Académie Wallonie-Europe
Université de Liège
Faculté des Sciences Appliquées
Mécanique Numérique Non Linéaire

On the development of an integrated bone remodeling law for orthodontic tooth movements models using the Finite Element Method.

Thèse présentée en vue de l'obtention du grade légal de
Docteur en Sciences de l'Ingénieur

Marlène MENGONI

Ingénieur civil physicien

Juin 2012

Académie Wallonie-Europe
Université de Liège
Faculté des Sciences Appliquées
Mécanique Numérique Non Linéaire

On the development of an integrated bone remodeling law for orthodontic tooth movements models using the Finite Element Method.

Thèse présentée en vue de l'obtention du grade légal de
Docteur en Sciences de l'Ingénieur

Marlène MENGONI

Ingénieur civil physicien

Juin 2012

Abstract

One of the guiding principles in orthodontics is to gradually impose progressive and irreversible bone deformations due to remodeling using specific force systems on the teeth. Bone remodeling leads the teeth into new positions with two tissues having a major influence: the periodontal ligament and the alveolar bone. Their mechanical and biological/physiological reactions to orthodontic forces are tightly linked. This mechanical biological coupling can be treated in biomechanical models, focusing on the mechanics and considering the phenomenological aspects of the biology/physiology. The development of such a model for bone tissue within a Finite Element framework is the core of this work.
We propose to reconcile two approaches of bone modeling (small strains linear elasticity for remodeling problems and complex constitutive models for other applications) by writing a constitutive model for trabecular bone at macroscopic level, built on morphological parameters to describe the anisotropy, and accounting for effects such as plasticity of the trabeculae. The continuum parameters such as the stiffness can evolve with morphology as remodeling occurs in the tissue. For this, we extend and enhance Doblaré and Garcia's remodeling phenomenological model. The remodeling process corresponds to an evolution of a damage tensor representing the bone morphology. To do so, we propose an integration method for an anisotropic Continuum Damage model coupled to plasticity. Adapting Doblaré and Garcia's remodeling law to our constitutive model, we extend it so that it can be used in the specific case of orthodontic tooth movement, still following Frost's mechanostat theory. We propose to include the hydrostatic pressure dependency of remodeling, due to the presence of the periodontal ligament, within the bone remodeling law. We finally present a validation method for the mechanical representation of the bone matrix through the knowledge of its morphology, both on engineered cellular solids with bone-like morphology (aluminum and polymeric foams) and on bone (Deer antler) samples.
Applying the model on the benchmark problem of the proximal femur remodeling, leads to results that are comparable to other models of the literature. We can therefore assume the way the remodeling model is built is valid. We finally apply the developed model to orthodontic tooth movement simulations. First we propose a model accounting for the non-linear mechanical response of the PDL through either bilateral contact conditions or spring models. We then present applications of orthodontic tooth movement, either displacement driven or force driven, both 2D and 3D. We thus show we can qualitatively represent the tooth movement, however outlining some of the drawbacks of the models (an unphysiological density distribution can arise due to the poor representation of the actual loads and a strong dependence on the boundary conditions is pointed out). However, we can represent the formation and resorption of hyaline areas, the non-linearity of the force/displacement relationship, and that applying a stepwise increasing force leads to higher displacements than a high initial force as there is no hyaline zone to resorb.

Avant-propos / Forewords

Un travail de thèse, bien qu'étant un projet seul, n'est pas un travail solitaire.
Avant d'entamer cette lecture, je vous propose de commencer par remercier les personnes qui, de près ou de loin, ont permis l'aboutissement de ce manuscrit...

Tout d'abord, Jean-Philippe, qui m'a toujours laissée libre de toute contrainte dans mes directions de recherche, m'encourageant à aller plus loin sur certains points et s'intéressant avec enthousiasme à un domaine qui ne lui est pas familier;
Monsieur Hogge, pour mon mandat et son soutien;
Monsieur Charlier, pour m'avoir initialement fait confiance sur le projet, même si je ne l'ai pas impliqué autant qu'il l'aurait sans doute désiré;
Lies, for her support and careful remarks about the "bio" in the biomechanics; Harry, for hosting me at ETH, a well as David for the foam meshes;
Professor Bourauel, for the time taken for the reading and for accepting to be a member of the jury; ainsi que Mme Mainjot, pour avoir accepté de faire partie du jury, lire et commenter une thèse dans un domaine qui lui est familier mais d'un point de vue qui l'est beaucoup moins;
Vinciane, pour tous les maillages et pour, elle aussi, s'être lancée quasi seule dans la biomécanique;
Le département A&M (malgré ma charge d'encadrement) qui s'implique de plus en plus dans le domaine biomécanique, mais aussi les collègues scientifiques pour tous ces moments de détente;
Séverine Levasseur, pour les cas-test sous Lagamine;
Les filles du décanat, pour la gestion pas forcément évidente de l'agenda du futur pro-doyen;
Luc, pour mes questions, et surtout ses réponses, après les heures; Christophe, d'avoir endossé seul les frustrations du doctora(n)t pour plusieurs générations; Philippe, pour son coup de main pour le remaillage; Romain, d'avoir bouclé sa thèse pour montrer la voie à suivre; Patricia, Axel, Sébastien, pour les temps de midi, parfois à rallonge, à réinventer le fonctionnement de l'unif;
Les étudiants, malgré le temps souvent perdu, permettant de me déconnecter de la recherche et de rire une bonne fois de temps à autre;
JPP encore, pour la maitrise forcée de LaTeX pour ses slides de cours et bien d'autres avant de commencer l'écriture de ce texte.

Je terminerai par remercier les personnes pas du tout impliquées dans ma vie professionnelle mais uniquement dans ma vie tout court, en commençant par ma famille, pour avoir fait semblant de s'intéresser, pas de soucis, cette fois, c'est (normalement) fait, je ne suis plus étudiante; les Therasse pour m'avoir considérée comme de la famille, en toute occasion; mes amis, y compris les collègues déjà cités qui le sont devenus, ainsi qu'en particulier Séverine H. et MC et Beto, pour le soutien de pairs non impliqués...

Table of Contents

Chapter 1
Introduction

One of the guiding principles in orthodontics is to gradually impose progressive and irreversible bone deformations using specific apparatus as force systems acting on the teeth. The bone deformation will lead the teeth into new locations. By optimizing load distribution, i.e. positions and intensities, orthodontic treatment could be reduced both in time and cost. However, nowadays, the nature and length of orthodontic treatments are mainly experience based, empirical, rather than simulation based. Therefore, even though some typical force conversion into movements is known, the physiological reaction is different for every patient, and the treatment needs to be adjusted regularly. A simulation based treatment using computer models would however allow to account for some patient-specific features, and therefore an orthodontic tooth movement software would be a valuable tool for the orthodontist.

Such a simulation tool needs to model not only the (patient- and treatment-specific) anatomy and system of forces through geometrical models of the tissues and the orthodontic appliances but also the biological and mechanical reactions of all tissues and materials involved.
The geometrical and mechanical description of the appliances is quite classical in mechanics, using for instance CAD models for the geometry and classical metallic alloys or polymer and rubber constitutive models.
Concerning the tissues however, tools are currently developed both to describe their geometry and their biological and mechanical effects. In patient-specific modeling, the state-of-the-art representation of the anatomy is to reconstruct its geometry from medical images, such as CT-scans or MRI's. However, these imaging technologies are not often used on a clinical basis. Therefore, tools to parametrize the geometry with classical imaging systems used in clinics such as X-rays classical radiography (or orthopantomogram a.k.a. dental panoramic radiography) need to be developed. This important geometrical issue will however not be dealt with in this work.
The biological and mechanical reactions of the tissues also need to be modeled. In orthodontic tooth movement, two tissues have a major influence: the periodontal ligament and the alveolar bone. Their mechanical and biological/physiological reactions to orthodon-

tic forces are tightly linked. This mechanical/biological coupling can be treated in biomechanical models, focusing on the mechanics and considering only the phenomenological aspects of the biology and physiology. In particular, such models should account for the coordinated bone resorption and formation (bone remodeling) in the alveolar bone that causes orthodontic tooth movement. The development of such a model for bone tissue is the core of this work, the goal of which is to provide a phenomenological constitutive model able to simulate those coupled phenomena.

As a tool to describe the mechanics of orthodontic tooth movement due to remodeling, we chose to work with the Finite Element Method (FEM). This FEM involves a series of computational procedures to calculate stresses and strains in each element, which produces a model solution for these fields. Such a structural analysis allows the determination of stresses and strains resulting from external force, displacement, and other factors. In particular, it can deliver not only the global mechanical behavior of the structures involved (in our case the teeth mobility), but also it gives access to local mechanical response of each tissue. Such a knowledge of the local behavior is essential to couple the mechanics and the biology. The FE method is extremely useful for indicating mechanical aspects of biomaterials and human tissues that can hardly be measured in vivo. It also allows the use of models on complex geometries and loading cases, accounting not only for structural and biological effects but also for contact and complex boundary conditions (BC's). To use a Finite Element model on a clinical basis, all aspects of the model (constitutive laws, contact problem, BC's representation, computational parameters, geometry representation, ...) need to be validated on a few representative cases. We will not address here all these aspects. We will focus our work on the development of specific biomechanical constitutive models for bone remodeling (therefore coupling the mechanical and biological behavior of bone tissue) and propose to validate the purely mechanical behavior of this model. We will also verify that simple cases of orthodontic tooth movements can be represented with our model when applied on geometries reconstructed from CT-scans images.

This work therefore constitutes a first essential step into the development of predictive tools in orthodontics. Such a tool should be completed with a systematic representation of BC's and geometry, as well as a simple procedure to adapt the constitutive parameters to a patient-specific physiology.

Outline of the thesis

Following this introductory chapter, we first present the general principles of orthodontics starting with an anatomical and physiological description of the tissues involved in orthodontic tooth movement. We will see in **chapter 2** that a physiological process named bone remodeling is at the origin of morphological changes in the bone surrounding the teeth and that these changes are responsible for tooth movement. On top of anatomical and physiological considerations and presentation of the principles of orthodontics, we also present the tools used to measure the morphology of bone based on image analysis.

After this presentation of basic principles in anatomy, physiology and orthodontics, we then present the basic tools used to mechanically describe the tooth movement. We therefore present in **chapter 3**, the general principles of Continuum Mechanics in finite strains and the discretization tool used in this work, the Finite Element Method. We close this chapter with a few insights on the different constitutive models, and their time integration, that will be used in this work.

As the basics of anatomy, physiology, orthodontics and computational mechanics have been described, we continue with a presentation of the state-of-the-art in modeling the biomechanics of bone remodeling in orthodontics tooth movement. In **chapter 4**, we focus our literature review on bone constitutive modeling and bone remodeling models.

We finally present the core of this work in **chapter 5**.
We first detail Doblaré and Garcia's [62, 83] remodeling phenomenological model we based our work on. This remodeling law is based on the Stanford model [16, 17, 30, 79], following Frost's mechanostat theory [74, 76]. Doblaré and Garcia's remodeling law is built on an anisotropic Continuum Damage framework in small strains, the remodeling corresponding to an evolution of the damage tensor representing the bone microstructure. Analyzing this model, we will see that it not only considers a simple linear elastic behavior of the bone matrix, but it also has a few disadvantages compared to the Stanford model it is built on, as well as a major inconsistency in its dimensional analysis.
We therefore propose to enhance Doblaré and Garcia's model not only to use our new model with an elastoplastic bone matrix expressed in a Finite Strain framework but also to solve the drawbacks and inconsistencies of Doblaré and Garcia's model. For this, we first present an integration method for an anisotropic Continuum Damage model coupled to plasticity (considering a von Mises plasticity of the bone matrix) in finite strains. We then show that if the damage tensor is constant, i.e. if there is no remodeling and the bone morphology is kept constant, our model is completely equivalent to an orthotropic elastoplastic model with a Hill-like plasticity criterion. We therefore verify our integration method with other integration methods dedicated to this type of models.
We close the presentation of our model by adapting Doblaré and Garcia's remodeling law to our constitutive framework. By using their concepts but starting over from the Stanford

model, we overcome their inconsistencies while keeping the full coupling between the constitutive law and the remodeling one. We also extend the remodeling law so that it can be used to the specific case of orthodontic tooth movement.
After presenting the sensitivity of our model to its main parameters (parameters describing the bone matrix behavior, its morphology, and remodeling parameters) on a simple geometric configuration, we eventually present a validation method for the mechanical representation of the bone matrix through the knowledge of its morphology. As our model is a phenomenological, continuum-based, constitutive law to be used in bone remodeling problems in a finite strain framework, it aims at describing the non-linear mechanical behavior of trabecular bone in the range of small to moderate strains. In this range, we will show that bone mechanically behaves as a cellular elastoplastic solid. We therefore validate our model both on engineered cellular solids with bone-like morphology (aluminum and polymeric foams) and on actual bone (Deer antler) samples.
We then present the benchmark case for remodeling algorithms that is the proximal femur remodeling, and compare our results to what can be found in the literature. This allows us to at least qualitatively and partly quantitatively verify the accuracy of our remodeling model.

As we presented a constitutive law accounting for bone remodeling, verified its integration, and validated its mechanical behavior and part of its remodeling one, we can finally in **chapter 6** use it in orthodontic tooth movement simulations. We therefore present first a specific representation of the periodontal ligament as it cannot geometrically be extracted from the CT images. Then we present several types of tooth movement simulations both for 2D and 3D geometries. For some simulations, the use of the ALE (Arbitrary Lagrangian-Eulerian) formulation and/or remeshing techniques is necessary for the finite element mesh to keep a good quality.

Original contributions of this work

As there is an increasing number of publications dealing with orthodontic tooth movement models, it is interesting to introduce here the novelties and original contributions of this thesis. These are of five different natures:

- development of a fully coupled non-linear model for bone remodeling;
- validation of the underlying mechanical behavior of the constitutive model;
- development of a numerical integration procedure for an elastoplastic anisotropic continuum damage model;
- presentation of a novel periodontal ligament mechanical and geometrical representation;
- use of the ALE formulation and remeshing techniques in orthodontic tooth movement problems.

Fully coupled non-linear model of bone remodeling

The goal of this work is to provide a constitutive model able to simulate the coupled biological and mechanical phenomenon within the bone in orthodontic tooth movement applications. Such models do already exist in the literature. However, they often do not account for a strong coupling between mechanics and biology, proposing to adjust the mechanical response of tissues with a remodeling phenomenological model in a lightly coupled manner. We here propose to fully include the remodeling behavior in the constitutive law. Also, we will see that remodeling models, even when strongly coupled to the mechanical behavior, are often associated to simplified constitutive behavior such as linear elasticity. As bone tissue is not a linear elastic material, we here associate remodeling to a non-linear model (plasticity-like model in finite strain). This is done by considering the trabecular bone is an anisotropic arrangement of elasto-plastic trabeculae. The anisotropy is measured by a fabric tensor. The remodeling phenomenon is considered as having effects both on the anisotropy and the density. The coupled biomechanical effect is therefore modeled as an anisotropic continuum damage model, coupled to elasto-plasticity.
The simplified isotropic version of this model gave rise to a published paper in the *Journal of Computational and Applied Mathematics* [172].

Validation of the underlying mechanical behavior of the constitutive model

Not only a model is developed accounting for the anisotropic morphology of trabecular bone and its non-linear response, but its purely mechanical component (not accounting for the remodeling) is validated against experimental data. For this, we use experimental data from

compression tests for bone and bone-like (morphologically speaking) material samples. We also propose a procedure to evaluate our model mechanical behavior for tension test by performing in-silico tension tests on these material samples.
The validation on experimental compression tests gave rise to a published paper in the *International Journal of Numerical Methods in Biomedical Engineering* [174].

Integration procedure for an elastoplastic anisotropic continuum damage model

As we develop an anisotropic continuum damage model coupled to elasto-plasticity, we also propose a numerical integration procedure for such a model in a finite strains context. We here propose a staggered scheme of integration instead of a fully coupled integration often found in the literature. This allows us to reduce drastically the computational cost of such an integration. Indeed we will show that using a staggered scheme, we switch from solving a fully coupled nonlinear system with 13 scalar unknowns (6 for the stress tensor, 1 for the plastic multiplier and 6 for the damage tensor) to two decoupled systems of 7 scalar unknowns (for the plasticity problem, nonlinear in only the plastic multiplier) and 6 scalar unknowns (the anisotropic linear damage problem). We also propose for this integration procedure the evaluation of an analytic consistent tangent operator that reduces again the computational cost.

Novel periodontal ligament mechanical and geometrical representation

We will see that the mechanical characterization of the periodontal ligament is essential in the predicted tooth movement. However, there is no clear agreement in the literature for the constitutive law that represents best the periodontal ligament mechanical behavior. Furthermore, we will see the ligament geometry cannot be obtained from the CT-scan images we build our geometry from. In most recent studies, the periodontal ligament is thus generated using scaling and/or Boolean operations on the teeth and bone interfaces in order to obtain a thin enclosure. This approximation is performed despite the fact that most authors agree on the importance of geometrical and material properties of the periodontal ligament in the achievement of orthodontic tooth movement. We therefore propose an alternative method to account for the mechanical role of the periodontal ligament without geometrically representing its thickness, using bilateral contact conditions.

Use of the ALE formulation and remeshing techniques

Finally, we will see that, due to remodeling and therefore softening of the bone tissue or when the periodontal ligament is geometrically represented, large deformations are encountered during the tooth movement. This leads to a finite element mesh deformation up to a point where the mesh quality can not be sufficient enough either to continue the computation

(if elements happen to get inverted) or simply to blindly trust the solution quality. To overcome this problem, we use both the Arbitrary Lagrangian-Eulerian (ALE) formulation and a remeshing method. The ALE formulation allows, at every time-step of the simulation, to represent the mesh movement independently from the material movement. The remeshing method allows, at given predefined time-step, to completely remesh the deformed geometry. To the best of our knowledge, this is the first time that both methods (separately or together) are used in orthodontic tooth movement problems. Indeed, a thorough search of the literature for the expressions "*orthodontic tooth movement*" and "*Arbitrary Lagrangian Eulerian*" leads to zero result on any search engine (PubMed, ScienceDirect, or Google Scholar) [1].
Relaxing the search to the words *tooth movements* and the expression "*Arbitrary Lagrangian Eulerian*" then gives two results (concerning biomechanical applications, there are dozens of results on gear teeth not at all related to the problem we are interested in), one on a temporomandibular joint model [189] and the other on bolus containment in the oral cavity [191]. Finally a search of the word *remesh* (as well as its derivatives *remeshing*, *remeshed*) and the words *tooth movements* leads to dozen of results in biomechanical related literature. However, analyzing these results shows that most of them refer to the REMESH module of MIMICS (a software from Materialise, Leuven, that allows you to create finite element meshes starting from medical images) which is used to refine a finite element mesh before conducting the simulation. The only two results [113, 114] (of the same author) found that actually use a remeshing technique during the simulation are studies about fracture models in biomaterials that use a remeshing algorithm around a crack propagation.

[1] Literature search performed on the 1st of April 2012.

Chapter 2
Anatomical Considerations and Principles of Orthodontics

The engineer's first problem in any design situation
is to discover what the problem really is.
- quote attributed to Sir Henry Royce

This chapter presents some generalities about the physiological phenomena present in orthodontic tooth movement. We therefore start by describing the anatomy of the facial skeleton and go down to the description of the tissues surrounding the teeth, including the different actors of the physiological equilibrium of the mouth. We then describe the mechanics of orthodontic tooth movement. This is in no way an exhaustive description of the physiological activity leading to either the physiological equilibrium or the orthodontic tooth movement. It is a basic description of these concepts aimed at introducing the topic to engineers, not to medical practitioners. We end this chapter by describing the morphological parameters (as well as the way to compute them) that will be needed to describe the anisotropy of the bone tissue.

Chapter Overview

2.1 Anatomical and Physiological Considerations

When dealing with anatomy description, it is necessary to mention the conventions concerning localization with respects to anatomical planes (Fig. 2.1).
Three anatomical planes (and axis) are mostly used:

- the *coronal* plane, corresponding in humans to a frontal view,
- the *sagittal* plane, corresponding in humans to a profile view,
- the *axial* or transverse plane, corresponding in humans to a bottom-up view.

Orientation is defined according to directions relative to the body axis:

- *antero-posterior*, in humans from front to back,
- *cranio-caudal*, in humans from head to toes,
- in the axial plane, *lateral* (either left or right) is towards the exterior of the body and *medial*, towards the center of the body,
- for the limbs, the *distal* end is at the tip of the limb, the *proximal* one is where it joins the body.

Finally, in facial anatomy a curved surface is defined along the jaw, the alveolar arch. Teeth may be aligned with their main axis identical to that of the jaw, but they can also be rotated. In such a case using terms like *anterior* or *lateral* can be confusing. Therefore, a special set of terms exists (see also Fig 2.6):

- *lingual*: facing the tongue,
- *labial*: facing the lips,
- *buccal*: facing the cheek,
- *apical*: toward the apex (extremity of the root) of a tooth,
- *coronal*: towards the crown of a tooth.

2.1.1 The Facial Skeleton

The facial skeleton (Fig. 2.2) is located anterior to the spinal column in an anterior and caudal location with respect to the skull [92]. It is composed of two main parts, the cranial immobile one, called the superior facial complex, and the caudal mobile one, called the mandible (sometimes also referred to as the lower maxilla).

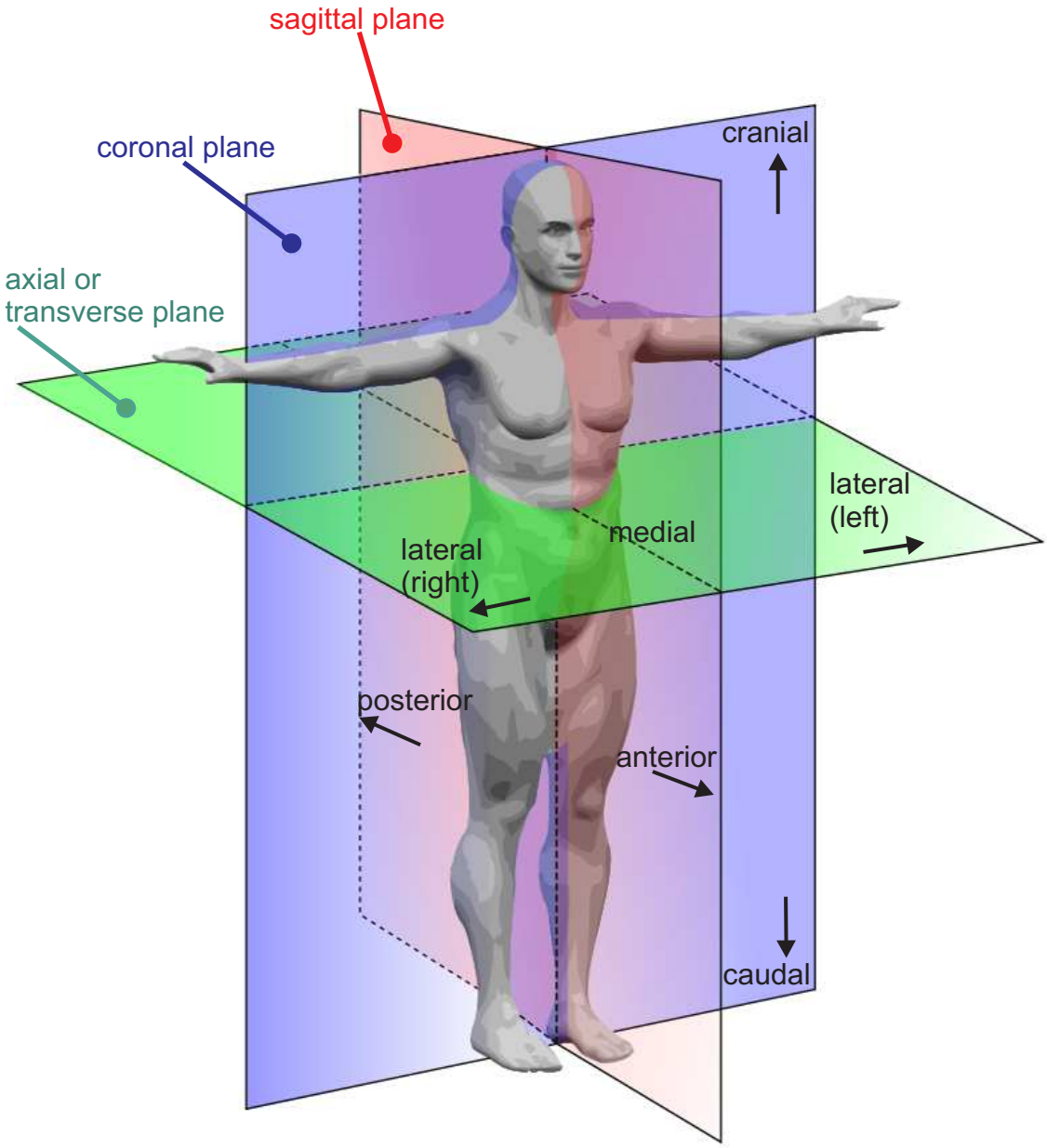

FIGURE 2.1: *Anatomical planes and orientations*

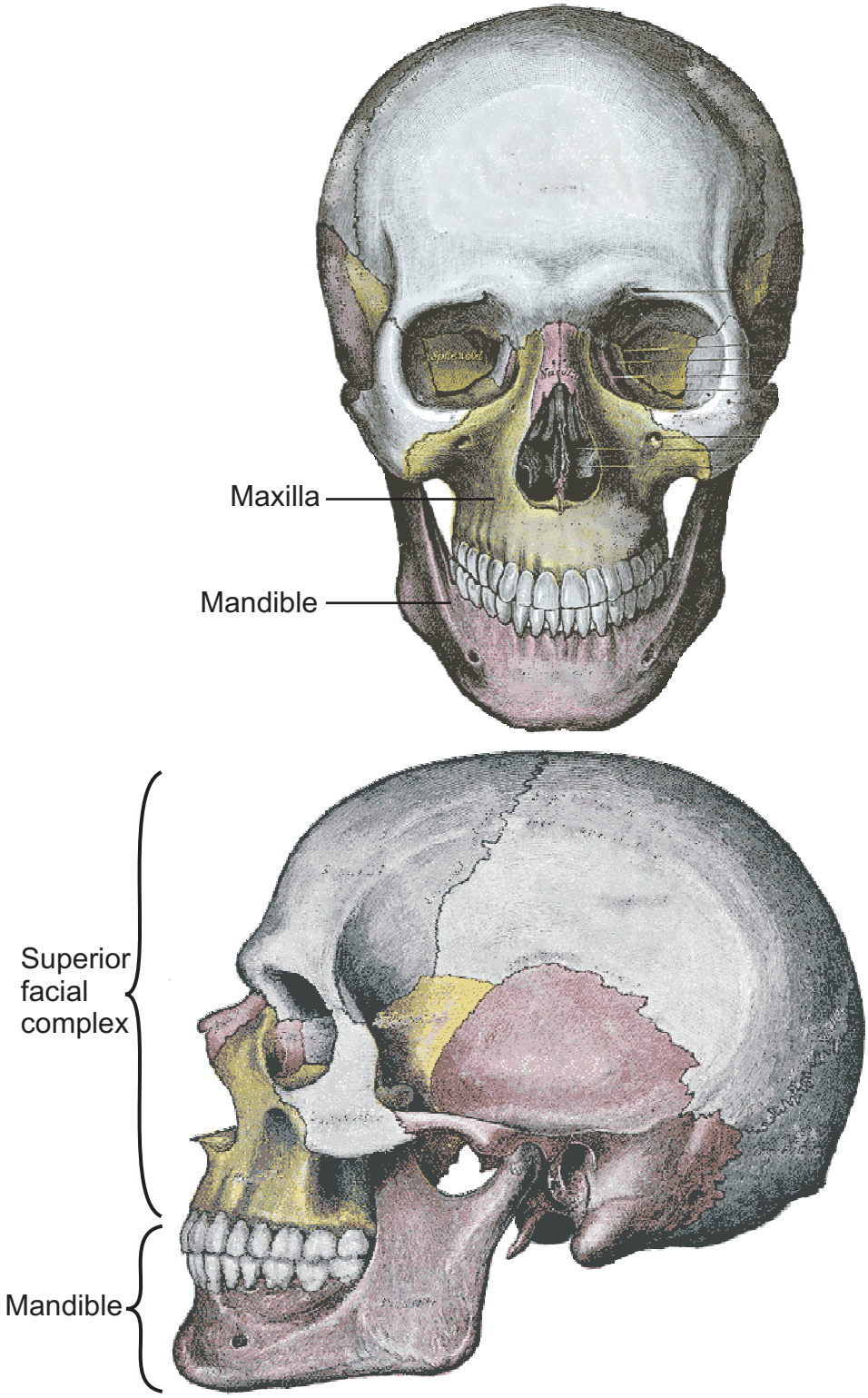

FIGURE 2.2: *Skull and face - anterior and lateral views, adapted from [92]*

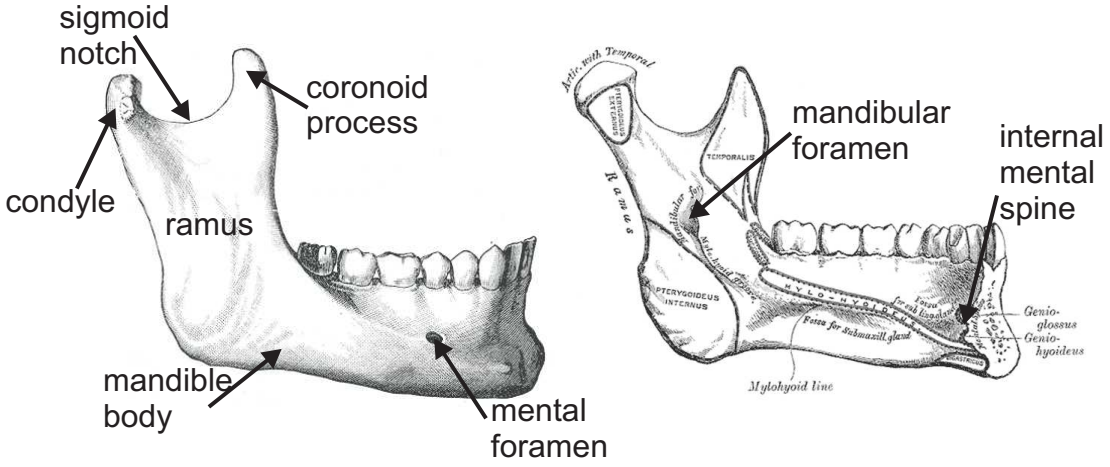

FIGURE 2.3: *mandible, adapted from [92]*

The superior facial complex

There are thirteen bones in the superior facial complex, anchored to the skull and fused together. The main one is the **maxilla** (actually composed of two symmetric parts linked by the palatal suture), or the superior jaw. It holds the superior alveolar arch. The function of the maxilla is to provide protection to the face, support of the orbits, hold the top half of the teeth in place, and form the floor of the nose.

The mandible

The mandible (lower jaw)'s main function is to support the lower part of the face and to hold the bottom half of the teeth in place (Fig. 2.3). The mandible is essential for movements of the mouth. It is the only mobile bone of the face. It is articulated on each side by the temporomandibular joints (TMJ), formed by the insertion of the mandibular condyles to the glenoïd cavity of the temporal bone.
The mandible *physiological rest position* is the position it occupies when all the elements of the stomatognathic system[1] are in equilibrium. Antagonist teeth are then separated by the occlusal space, lips are just in contact. At rest, a muscle can experience a residual tension, called the muscle tone, which is due to a continuous and passive partial contraction. The tone of the several muscles of the face is sufficient to compensate for the gravity effect on the mandible and to maintain it in the physiological rest position (Fig. 2.4).

Dentofacial equilibrium

In this physiological state, the teeth are in equilibrium in their sockets under the action of several types of forces, constant or intermittent, applied directly to the teeth or through the

[1]The stomatognathic system is composed by the mouth, the teeth, the pharynx, and related structures active in mastication, deglutition, and speech.

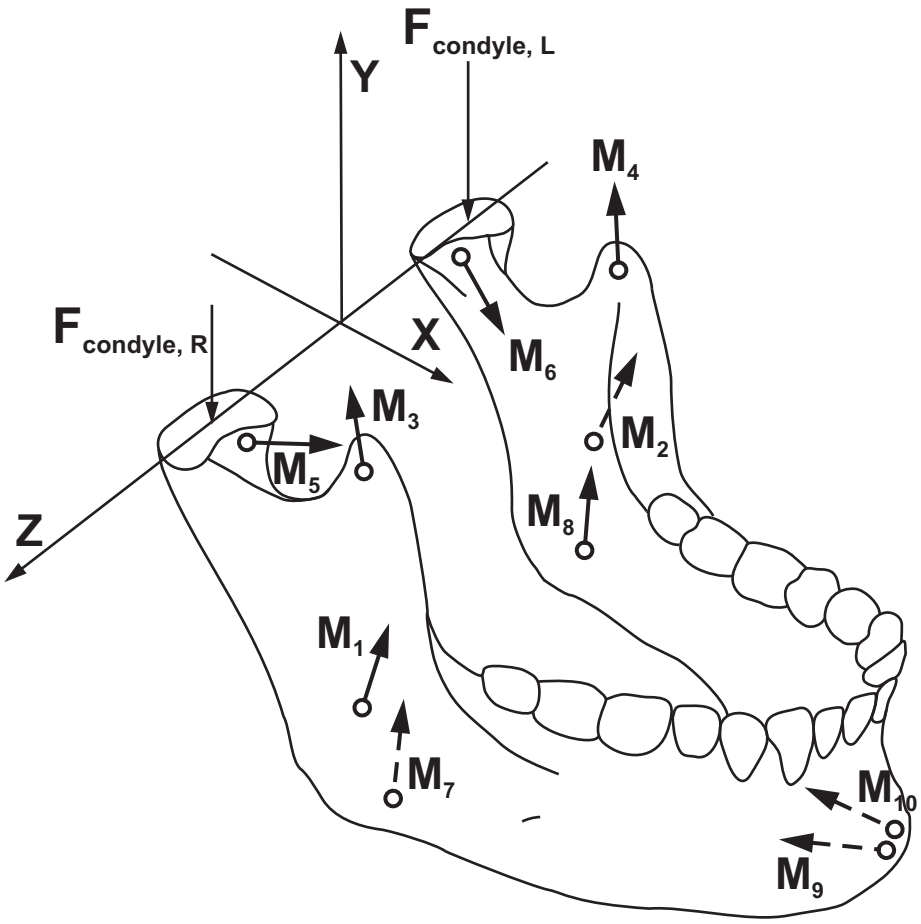

FIGURE 2.4: *Representation of muscular and anatomical forces on the mandible at physiological rest (adapted from [190]).*
Attachment sites on mandible for masseter (M_1, M_2), anterior temporalis (M_3, M_4), lateral pterygoid (M_5, M_6), medial pterygoid (M_7, M_8), and anterior digastric (M_9, M_{10}) muscles are shown. Arrows demonstrate approximate direction of muscle pull. Condylar forces point of application ($F_{condyle,R}$, $F_{condyle,L}$) and position of the mandibular teeth are also represented.

jaw. These forces generators are mainly the facial muscles, including the lips and tongue, either in a physiological rest position for which the muscles are active at muscle tone, or caused by any movement of the stomatognathic system.
The physiological teeth position depends on various factors apart from these forces, in particular:

- the tendency of the teeth to egress,
- the alveolar bone support,
- the elasticity of the periodontal ligament, a membrane of soft tissue seated between the tooth and its alveolar bone.

The combined action of these forces and factors are variable in time and operate on living tissues of high turn-over. The physiological equilibrium is therefore a fragile one.

2.1.2 The Teeth and their Environment

The teeth

Teeth are hard formations, implanted on the alveolar ends of both the maxilla and the mandible (Fig.2.5) [168, 194]. All teeth have the same structure (Fig. 2.6), with a **crown**, the visible part of the tooth, and one or several **roots**[1], embedded in the bone. The junction between root(s) and crown is called the **collar**. The crown is covered with **enamel**, which is the hardest, however very brittle, and most mineralized substance of the body.
The main mass of the tooth consists of **dentin**. It is softer than enamel but still the second hardest tissue of the body. In normal conditions, the dentin is fully covered either by enamel on the crown or by cementum on the root(s).
The inner part of the tooth consists of **dental pulp**, containing connective tissue, blood vessels and nerves. During development and tooth eruption, the dental pulp serves as a source of cells necessary for the formation of enamel and dentin.

The periodontium

The periodontium[2] is the term used to collectively describe the tissues involved in tooth support and attachment of the tooth [168]. It is composed of *gingiva*, *alveolar bone*, *periodontal ligament* (PDL) and *cementum*.

The gingiva (or gum) is formed by a free part surrounding the collar and a part attached to the external surface of the alveolar bone. It is part of the soft tissue lining the mouth. Compared with the soft tissue linings of the lips and cheeks, most of the gingiva is tightly bound

[1] The molars, and the premolars of the upper jaw, usually have two, three or four different roots and are called multi-rooted teeth.

[2] The word periodontium comes from the Greek terms “peri-”, meaning around and “-odons”, meaning tooth.

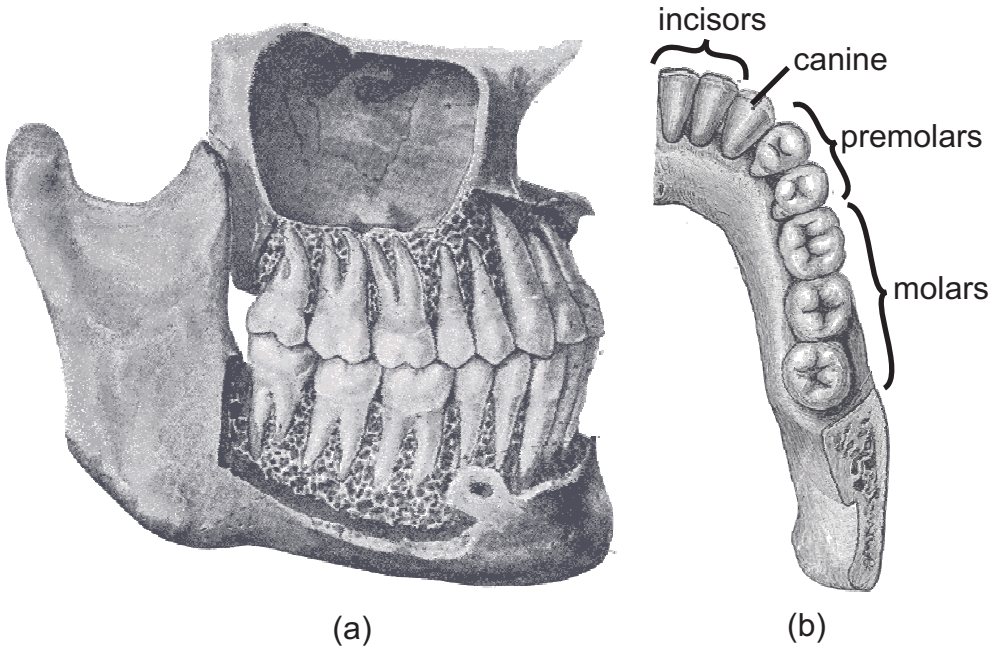

FIGURE 2.5: *(a) Dental insertions and (b) dental quadrant (adapted from [92])*

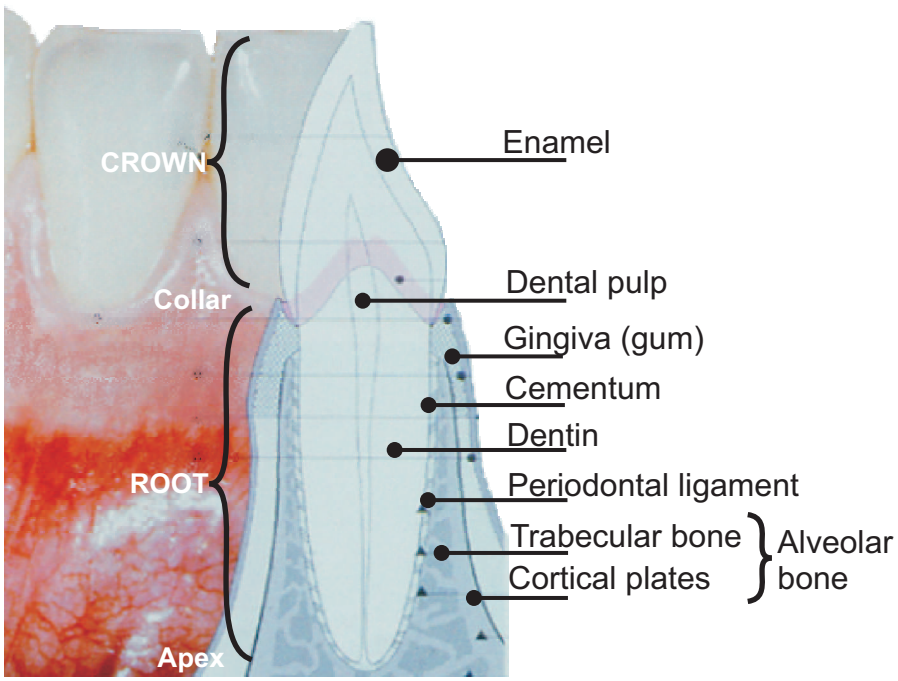

FIGURE 2.6: *Tooth and surrounding tissues - anatomy (adapted from [264])*

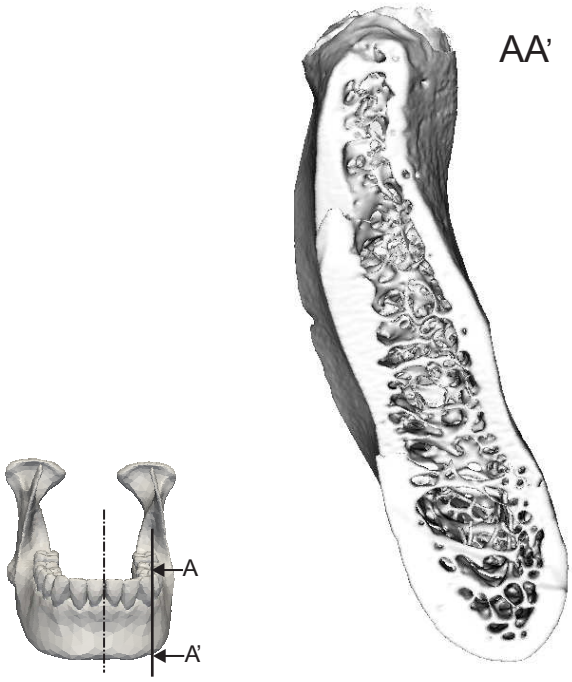

FIGURE 2.7: *Alveolar bone of a mandibular left canine (79-year-old male). Cancellous (or trabecular) internal structure and cortical shell.*
stl file available at `http://www.uni-ulm.de/uni/intgruppen/fem/` *[25]*

to the underlying bone which helps resist the friction of food passing over. It surrounds the teeth and provides a seal around them.

The alveolar bone is the main tissue linking the tooth to the mandible or maxilla [183]. The tooth bearing surfaces of the alveolar bone are made up of bundle bone, which is coarser and less mature than the lamellar bone of the cortical plates, while the inner part consists of trabecular bone and marrow (Fig. 2.7). This internal alveolar wall also shows many openings for blood vessels and marrow, and serves as an attachment for the Sharpey's fibers of the PDL. The main structure of the alveolar bone is similar to that of trabecular bone in other parts of the skeleton, but its turnover rate is much higher. The alveolar bone is dependent upon the presence of teeth for its preservation. When no teeth are present, alveolar bone does not form. Similarly, it tends to disappear slowly after the loss of teeth or when a tooth has no antagonist and is not loaded by occlusal contacts. The alveolar bone is covered with an outer cortex, thiner at the maxilla than at the mandible, continuing the basal bone without separation.

The periodontal ligament (PDL) is the encompassing structure of the tooth, attaching it to the alveolar bone [183, 262]. It consists mainly of collagen fibers stretching across the width of the ligament, which are embedded as Sharpey's fibers in the bone and the cementum. In humans, the PDL has an average thickness of 0.2mm.

The cementum is a calcified bone-like but avascular substance which is harder and more mineralized than bone. It serves as a protective layer (whose thickness varies typically from 20 to 1000μm from the cemento-enamel junction to the apex [158]) for the root, but the principal role for the cementum is to enable the attachment of the periodontal ligament fibers to the root.

2.1.3 Bone Tissue

Bones compose, together with cartilage, the skeletal tissues. They have three main functions:

- **a structural function**: bone tissue is one of the toughest tissues of the organism. It supplies a stiff structural support system for the other softer structures of the body, which cannot support themselves.

  Several bones have the additional role of protecting the soft tissues they surround from possibly damaging external loads and impacts.

- **a metabolic function**: bone tissue is a dynamic tissue that constantly remodels. This leads to the release or storage of mineral salts ensuring the phosphocalcic metabolism control.

- **an hematopoietic function**: bone tissue encloses the hematopoietic marrow (or red marrow), which produces blood cells.

Bone tissue composition

Bone tissue is made of water (about one quarter of the mass), organic components (about one third of the mass, most of it being collagen fibers) and non organic mineral salts (calcium, phosphate and magnesium mainly).
It furthermore contains a living component, the bone cells, which are surrounded by extracellular matrix.

The fundamental cellular component of mature adult bone is the **osteocyte**. The primary role of the osteocytes is to provide for the maintenance and continued vitality of the surrounding bone matrix.
The bone cell responsible for forming the bone is the **osteoblast**. Bone deposition is accomplished by the osteoblasts that form the various organic components of bone matrix and secrete them through the cell wall. Osteoblasts also play a role in the subsequent deposition of the crystalline inorganic constituents of bone, although the precise mechanisms of crystal formation is still the subject of investigation.

Bone removal or resorption is the job of the **osteoclast**. When large scale bone resorption is needed, osteoclasts can proliferate, become active, and degenerate in short order.

Bone structure and morphology

Bones are mainly made of bone tissue. They also contain marrow, adipose tissue (body fat), blood vessels, nerves, cartilaginous and conjunctive tissue.

There are four types of anatomical bones : long bones (e.g. the tibia or the femur), flat bones (e.g. the skull bones), irregular bones (e.g. the ones interesting us, the maxilla and the mandible) and finally sesamoid bones (embedded within a tendon such as the patella). Sesamoid bones are also referred to as short bones.

Bones are organized in structural patterns on several different length scales. On the highest level, human bone tissue comes in two basic varieties, cortical bone and cancellous bone [46]. Cortical (or compact) bone is distinguished from cancellous (or trabecular) bone by its low porosity (around five to ten percent).
Cancellous tissue is found mainly in short or flat bones as well as the epiphysis of long bones. The outer shell of most bones is compact bone, then one finds a deeper layer of cancellous bone which contains red bone marrow. However, for long bones, the interior part is the medullary cavity with the inner core of the bone cavity being composed (in adults) of yellow marrow. Except on the joints, bones are covered by layers of fibrous tissue called the periosteum. The medullary cavity of long bones is layered by the endosteum, a thin layer of fibrous tissue. Irregular bones consist of cancellous tissue enclosed within a thin layer of compact bone.

Cancellous bone (or trabecular bone) has an open-celled porous structure (Fig. 2.8). The empty spaces in cancellous bone are filled with red bone marrow. The porous nature of cancellous bone makes it well adapted to supporting the complex loading applied to the bone near the joints, without the extreme weight that a solid bone structure would entail. Furthermore, the structure of cancellous bone may be important in absorbing and distributing impact loads transmitted across the joints.

Cortical bone exhibits two forms of structure (Fig. 2.9):
Lamellar bone is found mostly in the outer and inner regions of the cortex. As the name suggests, it has a layered structure with individual lamella layered concentrically, centered on the intramedullary canal.
The lamellar structure is interrupted by *osteonal bone*. Each unit in this structure (osteons) runs roughly parallel to the long axis of the bone and is again made up of layers of alternating fiber orientations. Between these layers of bone, osteocytes are found in hollows called lacunae. The lacunae are interconnected by small tunnels known as canaliculi. At the center of each osteon is the Haversian canal, which contains a vascular bundle made up of blood vessels and nerves. Periodically, vascular tunnels, called Volkmann's canals, are found connecting the Haversian canals transversely.

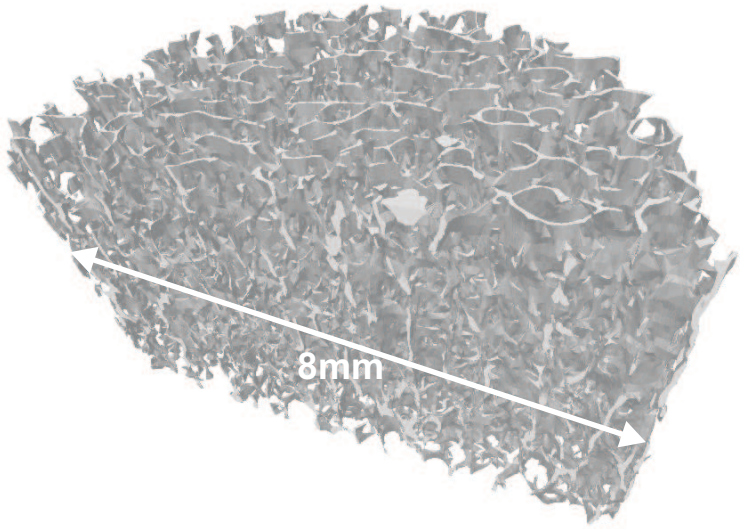

FIGURE 2.8: *Trabecular core of a deer antler (image obtained by volume reconstruction of µCT scan slices)*

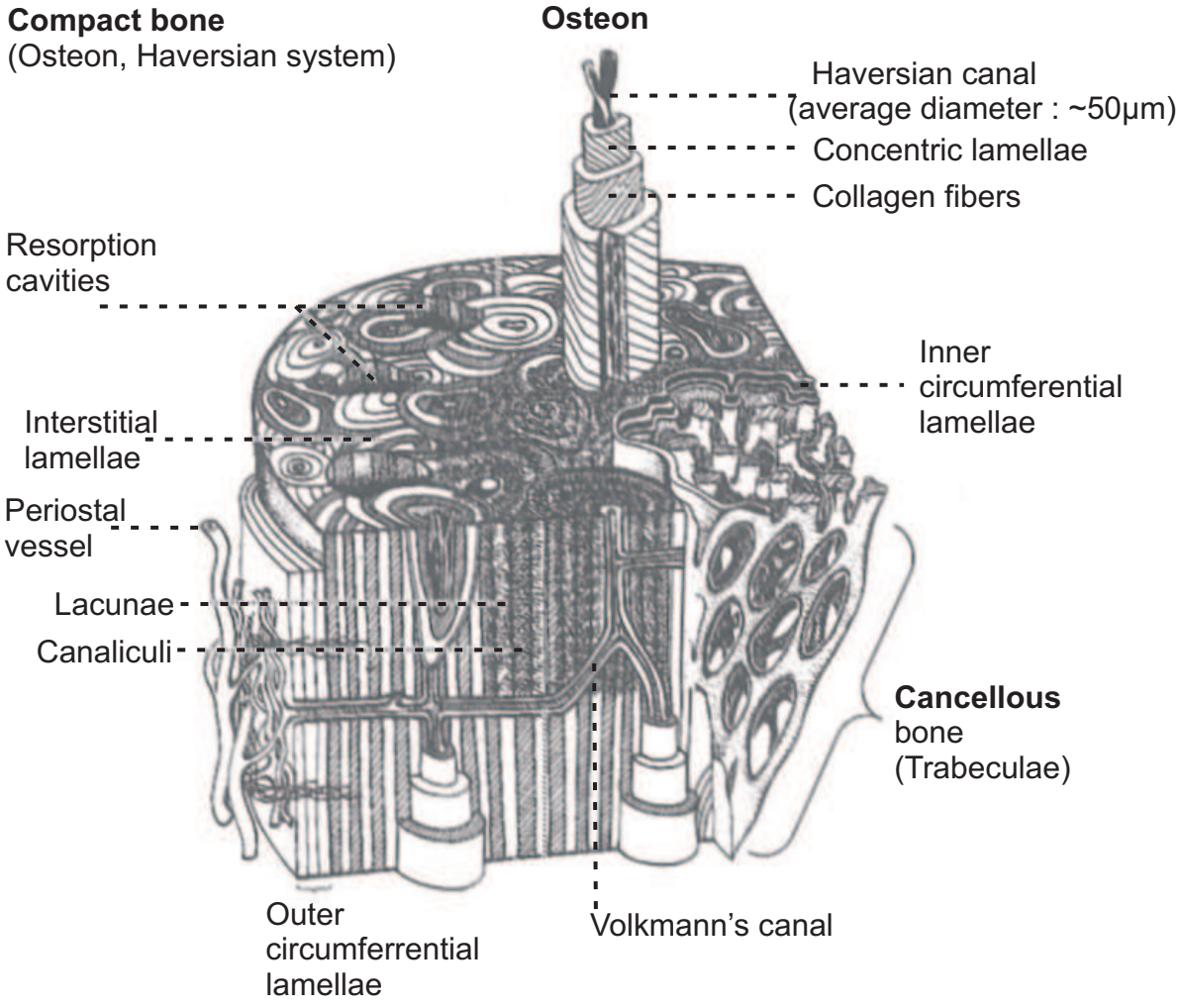

FIGURE 2.9: *Cortical bone tissue (reproduced from [46])*

Bone remodeling

Both cortical an cancellous bone, as adapted, adjustable, and optimized structures, are constantly renewed. This permanent remodeling is performed by functional units of remodeling (Basic Multicellular Units - BMU's) where osteoclasts and osteoblasts are closely associated (osteoclasts are in the front and osteoblasts follow). Bone contains of millions of BMU's, moving and progressing in bone. In a healthy adult, levels of resorption and formation remain identical, allowing the preservation of bone mass, but the process of remodeling is not uniform. Each year, an adult man renews about 25% of the trabecular bone and 4% of the cortical bone. In a child, to enable growth, apposition rate is higher than resorption rate. Finally, in the elderly (typically after menopause in women), there is a higher rate of resorption than apposition. This may result in phenomena such as osteoporosis[1].
Bone remodeling refers to two phenomena, as described by Frost [77, 78]:

- A physiological remodeling process, hormonally regulated, designed to maintain the concentration of calcium in the blood. This process is often referred to as internal remodeling (the word internal refers to the causes of remodeling, not the location). Its function is to maintain tissues in use, repairing micro-damage and ensuring a high turn-over.

- An adaptive process depending on the mechanical loading on the skeleton. It aims at preserving the mechanical properties of the bone and adapting its structure in response to the mechanical demands it experiences. This adaptive remodeling process is often referred to as modeling or external remodeling (the word external refers to the causes of remodeling, not the location) or even surface remodeling when it is a surface phenomenon.

  The physiological phenomenon of bone remodeling can be summarized in the following way [73]: osteoblasts appose bone in places calling for more reinforcements while the osteoclasts resorb it where the bone is no longer needed in its mechanical function. Osteoblastic formation and osteoclastic reduction are connected both in time and space as well as at the cellular scale.

Within the orthodontic literature however, the designation *remodeling* is used for both processes (see [171] for a discussion about the mis-understanding it can cause).
The word **(bone) remodeling** will be here used for the process due to external mechanical events. Internal remodeling is not accounted for in this work. We consider, as a simplifying assumption, that its function is to renew the tissue with no alteration of the overall bone mechanical properties. Therefore the internal remodeling is considered as being part only of the overall homeostatic equilibrium.

Remodeling processes take place in order to adjust the amount of tissue and its topology. There are also evidences of a link between fatigue damage in bone and the physiological

[1] More details on physiology of bone remodeling can be found in [43, 47, 118], among others.

processes of remodeling and adaptation [163, 249]. It is a biochemical process of skeletal adaptation to long term loading conditions, following what is called "Wolff's law"[1] of bone adaptation [47, 227, 228][2]. Bone resorption occurs when disuse is observed. This resorption tends to decrease the amount of bone where it is of no mechanical relevance. Bone apposition occurs in overloaded conditions, in order to reinforce bone where it is necessary. The bone therefore adapts its density in such a way as to achieve an homeostatic state of a given mechanical stimulus. Besides the density change, remodeling also occurs to modify the bone topology, mainly in trabecular tissue for which the trabeculae tend to align along the principal stress directions. Bone remodeling therefore depends not only on the load intensity but also on the load directions.
A well documented example can be observed on the human femur (Fig. 2.10): the trabecular architecture of its proximal end aligns with the principal stress trajectories (see a literature review in [238]). The human femur problem is so popular that it became the benchmark problem for most remodeling algorithms.

[1] **Wolff, J.** Das gesetz der transformation der knochen. A. Hirschwald, Berlin, 1892.
[2] A thorough historical review of this view of bone remodeling can be found in [117].

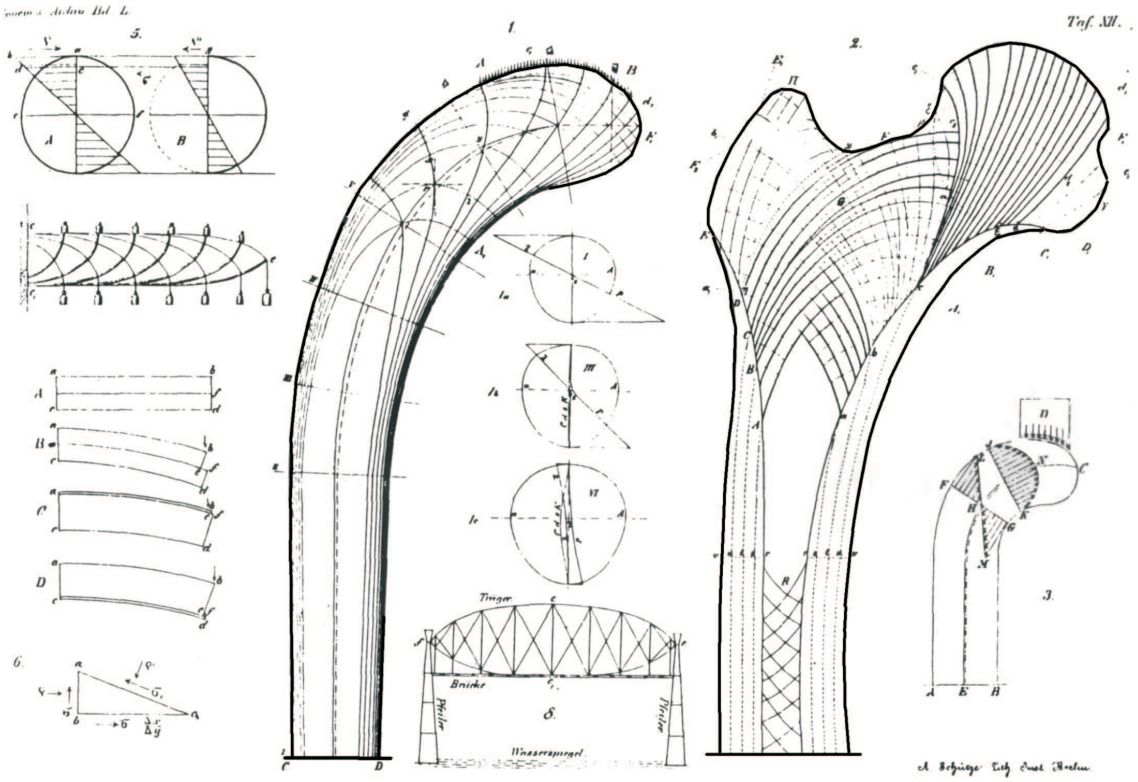

FIGURE 2.10: *On the left Culmann's graphical statics analysis of stress trajectories in a Fairbairn crane. On the right von Meyer's sketch of the trabecular architecture in a section through the proximal end of the human femur. This sketch (reproduced from [48]) is often cited as the first parallelism between biology and mechanics, leading to biomechanics, comparing the stress trajectories of a cantilever crane and the architecture of a femur proximal end.*

2.2 Principles of Orthodontics

Orthodontics is a specialty, using biomechanical principles of physiological mechanisms, that can correct dental malposition and malformations of the jaws to restore a functional and aesthetic dentition.
The primary goal of orthodontic treatment is often functional, obtaining an optimal occlusion, to improve chewing, respiration, or speech. A treatment can have several other goals such as a pathological correction (a bad tooth implantation can lead to caries or parodontal infections), aesthetics (of the dentition or the face), or prosthetic (orthodontic treatment preceding a prosthetic implantation).

Orthodontic treatments are limited to dental displacements, using either fixed or removable systems. Only the alveolar bone needs to be remodeled.

Dentofacial orthopedics treatments also include the control and modification of jaw positions and facial growth by controlling the growth sites in the maxilla and mandible.

Orthodontic treatment is possible at every age, but correction of jaw positions by control of facial growth is not possible in adults.

2.2.1 Orthodontic Tooth Movement

Both orthodontics and dentofacial orthopedics consist in the superposition of constant, intermittent or discontinuous loads through the use of external systems on one or more teeth leading to their movement and repositioning. Dental movement is achieved through the skeletal adaptation to external mechanical stimuli. Therapeutic forces, applied through orthodontic appliances, modify the physiological equilibrium (see Fig. 2.11). Loading of the skeletal system is therefore altered and bone cells are triggered to modify the bone shape and density in order to achieve a new equilibrium state and adjust the stress level. This state will be maintained until new mechanical external conditions trigger new remodeling events.

The optimal orthodontic force is considered as the force leading to maximal rate of movement without causing tissue damage or discomfort [141]. The application of forces of low magnitude (from 0.2 to 2.5N[1]) on the crown is traditionally recommended in orthodontics. Under forces of low magnitude, the vascularization of the ligament is partially occluded and cell activity within the ligament leads to bone remodeling. However, when the hydrostatic stress in the ligament is higher than the internal pressure of the blood capillaries (of about 2.5kPa [262]), there is a devascularization of the ligament and formation of hyaline zones[2]. These zones appear at the compression sites in the PDL and lead to a locally decreased cell

[1] Even tough a low force of 0.2N can produce tooth movement, lower values reported in the literature are usually around 0.5 or 0.7N [27, 227, 250, 276]

[2] A hyaline zone is composed solely of bundled collagen fibers, thus with a vitreous, hyaline, aspect.

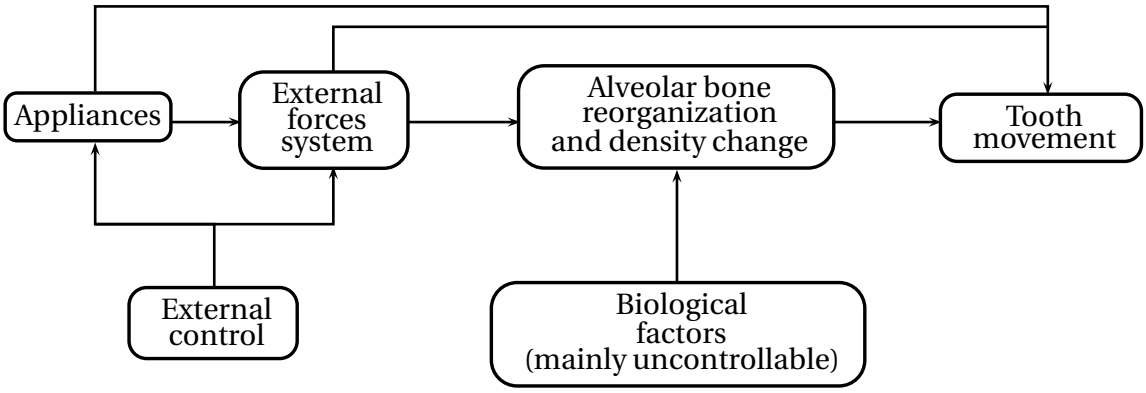

FIGURE 2.11: *Orthodontic Tooth Movement*

quantity and a loss of structure. Osteoblasts and osteoclasts cells can then no longer perform their work of bone remodeling. If the applied forces increase, there is then a pathological remodeling after resorption of the hyaline area by resorbing cells. Where low forces cause a physiological and stable movement, high forces induce abrupt starts and stops of synchronized migration with the collapse of necrotic bone and cementum. The stress state in the ligament is therefore the key factor on which depend the border between a favorable or unfavorable tooth movement [250].

Remodeling zones will depend on the type of movement induced by the appliances [107]:

- tipping movement (resulting from a pressure applied at the crown for instance) will increase the hydrostatic loads at the collar and therefore increase the remodeling around that area.
- bodily movement leaves the tooth axes parallel to its initial axes, the whole root height is therefore implicated in the remodeling process.
- intrusion movement leads to hyaline zone appearance followed by pathological remodeling at the apex.
- as roots are not symmetric around their main axes, rotation movement around this axes induces reciprocal compression and tension areas leading to remodeling.

Orthodontic tooth movement (OTM) occurs in three phases [141, 203] (see Fig 2.12 depicting experimental data of orthodontic tooth movement on Beagles):
The first phase is purely mechanical. Due to the force application the tissues surrounding the tooth, specially the PDL, (quasi-)elastically deform. The duration of this phase is very

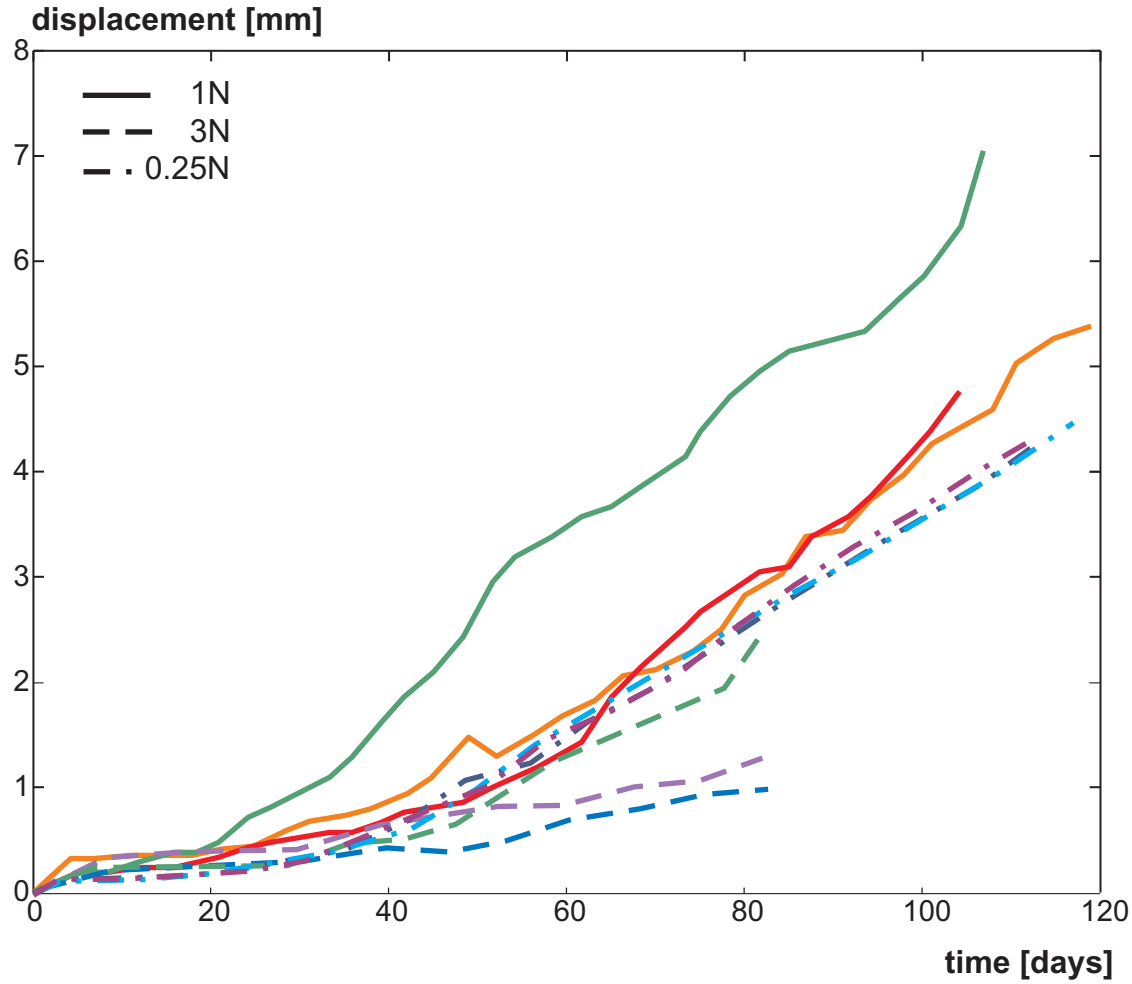

FIGURE 2.12: *Tooth displacement[mm] as a function of time [days] for constant translation forces applied on Beagles: data for a force of 0.25N extracted from [256] (dot-dash curves), of 1N extracted from [203] (plain curves), and of 3N extracted from [270] (dash curves). It is here clear that the highest forces do not lead to the highest displacements. However, it is also clear that there is a strong inter-subject variability.*

short as the characteristic time associated to deformation of both the periodontal ligament and the alveolar bone is very short (the displacement associated to this phase is never higher than the PDL width).
The second phase is the lag phase during which the movement is stopped. This phase is the result of hyaline zones appearing within the PDL. Its duration will depend on the time needed to resorb the hyaline zones and is highly variable (sometimes not existent, up to 30 days or more for moderate to high forces).
The third phase implies bone remodeling and is the actual, if possible permanent, tooth movement. Bone remodeling leads first to an accelerated then constant velocity movement of the tooth (up to $60\mu m$/day in the cases depicted in Fig. 2.12).

Contrary to the majority of bones, alveolar bone remodeling on a macroscopic scale seems to depend mainly on the hydrostatic pressure state [26, 27, 171]. Apposition occurs on the tension side of a tooth and resorption on the compression one (Fig. 2.13). However, the actual biomechanical processes causing such a difference between alveolar bone and other bones is not quite clear and uniformly accepted among biology and biochemistry literature (see e.g. discussions in [166, 228, 276]).
Without getting into details on mechanobiological processes, according to [276], the compression sites in the PDL result in an inflammatory event leading to focal necrosis. This creates chemo-attractant sites to resorb the hyaline zone and the underlying bone. On the tension sites however, there is no significant inflammatory component (even though tensile strains of low magnitude are anti-inflammatory and induce magnitude-dependent anabolic signals in osteoblast-like periodontal ligament cells) and these "overloaded" sites are osteogenic (the mechanism for osteogenesis at tension sites in tooth movement is not well-understood) and therefore lead to bone formation. The specific underlying role of the periodontal ligament in tooth movement is not well-understood, but its unique biomechanical, cellular, and molecular natures are undoubtedly important. Periodontal ligament cells respond to force by increases in cell proliferation and apoptosis. In particular, osteoprotegerin (OPG), a natural inhibitor of osteoclast differentiation and activation, is produced by fibroblasts[1] in the PDL (PDLFs), and RANKL, a receptor/activator ligand, is also expressed by the fibroblasts. The response of these PDLFs has been correlated to the stress in the PDL, especially the tensile and compressive stress [108, 142]. This tensile and compressive sensitivity at the cellular level corresponds to an hydrostatic pressure sensitivity at the macroscopic level.

2.2.2 Mechanics of Tooth Movement

Orthodontic appliances are nothing but devices able to generate forces acting on the teeth. It is therefore important to analyze these force systems to understand the effects they produce

[1] Fibroblasts are the most common cells in connective tissues. PDL fibroblasts (PDLFs) are known to be highly specialized fibroblasts.

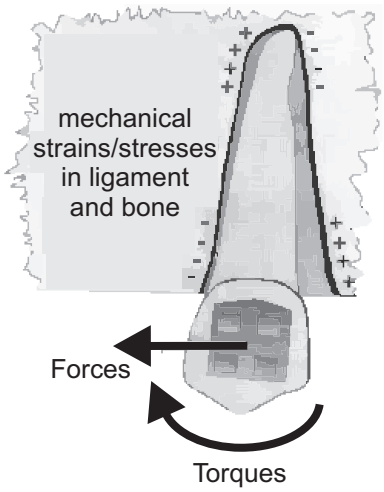

FIGURE 2.13: *OTM - Principles: tension sites, + and compression ones, - (reproduced from [107])*

on the teeth. Indeed, when a treatment plan is decided and the goals are set on the future dental implantation, the orthodontist should be able to choose the adequate force system to achieve this goal, i.e. to choose the necessary mechanisms and thus the type of appliances to use.

If the tooth movement were to be composed of rigid body movements only, it could be described by two characteristic points, the *center of resistance*, whose location depends solely on the geometry and tissue composition, and the *center of rotation*, whose location depends on the movement [154, 155].
Each tooth has its own **center of resistance** [1] whose location depends first on the characteristics of the tooth itself (shape, size, width, ...) and, secondly, on the physical characteristics of the alveolar bone surrounding the tooth. The location of this center of resistance is independent of the system of forces that can be applied to the tooth. On a young tooth whose apex is not yet formed, the center of resistance is located between the neck of the tooth and the growing root. On a tooth with a closed apex, it is approximately located at one third of the measured length between the alveolar crest and the apex of the root, from the apex. On an adult tooth, it is almost at the apex of the root.
When a force has its line of action passing exactly through the center of resistance, the tooth will present a pure translational movement. An identical force but not passing through the center of resistance will lead to a tooth movement involving two components: one identical to the previous translation and a rotation depending upon the force moment[2].
Rotation movement is around the **center of rotation** (Fig. 2.14) whose location depends di-

[1] The center of resistance can be considered as the center of mass of the tooth and its surrounding bone system.

[2] The moment of force is the product of the force by the length of its lever arm, or by the distance between the point of application of force and the center of resistance of the tooth.

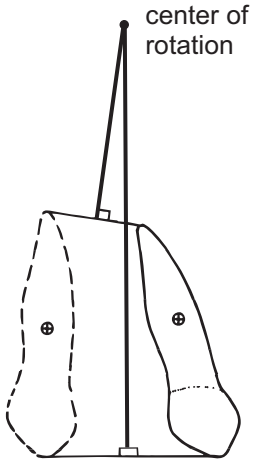

FIGURE 2.14: *Center of rotation for an arbitrary rigid movement (reproduced from [240]).*

rectly on the system of applied forces. The higher the moment, the more the center of rotation moves towards the center of resistance. Ultimately, when a pure moment is applied, the obtained movement is a pure rotation around the center of resistance. When the force passes through the center of resistance causing a translation, the center of rotation is then located at an infinite distance from the center of resistance. Therefore, the **moment-to-force ratio** is decisive for the type of movement produced.

2.2.3 Orthodontic Appliances

There are numerous dentofacial orthopedics and orthodontic appliances mainly because they are flexible and adaptable according to the needs and imagination of the practitioner. The first criterion that comes to mind to classify different types of devices is the distinction between removable appliances and fixed ones:

- **Removable appliances** (Fig. 2.15(a)) can be removed and put back at will by the patient (the time they are in use therefore depends on the willingness and motivation of the patient) and easily allow a proper dental hygiene.
- **Fixed appliances** (Fig. 2.15(b)) are sealed to the teeth for a variable period of time but, as they impede the practice of proper dental hygiene, an effort of attention and care is required to avoid the appearance of decalcification or caries.

One could also classify devices according to the nature of the forces that come into play:

- **Extrinsic forces**: all devices that deliver mechanical forces produced by expansion cylinders, springs of various configurations, rubber bands of various diameters, ligatures or steel arches of various forms. All these mechanical methods require frequent reactivation. The induced movements are artificial and/or coercive for the dentition, meaning the displacements are imposed directly by the device used, which often cannot guarantee to obtain a perfectly stable equilibrium.

- **Intrinsic forces**: they are appliances qualified as *functional* as they deliver no direct mechanical force but their presence in the mouth changes the tonic state and/or the dynamic musculature. They require not as frequent reactivations but need to be adapted to the progress made. These devices are the most physiological ones because in addition of inducing morphological correction, they integrate it into a new functional balance.

A third classification criterion emphasizes the difference between the effects of orthodontics and orthopedic appliances. However, it is not always possible to say that a given device has effects that are purely on the orthodontic or the orthopedic side.

(a) Removable type: Schwartz plates used to expand the palate `http://www.retainerlab.com/`

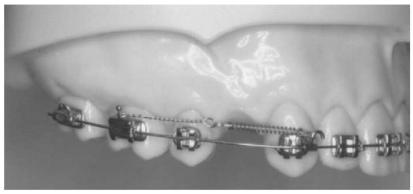

(b) Fixed type: brackets, springs, and wire used to induce a sliding movement [100]

FIGURE 2.15: *Two types of appliances*

2.3 Extraction of Morphological Parameters from CT-scans

As seen in the first section of this chapter (section 2.1), trabecular bone presents a complex microstructure. We are in this work interested in the macroscopic mechanical response of the trabecular bone to carry on models describing a full jaw without increasing beyond reason the number of unknowns. This macroscopic response is closely related to the underlying microstructure. As we do not want to describe in details the geometry and spatial arrangement of the trabeculae, we need tools to macroscopically describe the microstructure with only a few parameters. Although the volume fraction is the primary parameter in the geometric characterization of the microstructure of such cellular materials, it does not provide information about the arrangement and the orientation of the microstructure [195]. In Continuum Mechanics, the approach commonly used to model the material microstructure consists of introducing tensors of higher rank which characterize the microstructural architecture. In particular, in many applications, microstructural anisotropy seems to be sufficiently well described by a scalar and a symmetric second order tensor (the fabric tensor) which restricts the material symmetry to orthotropy. Fabric tensors may be defined in a wide number of ways but are required to be positive definite such as a quantitative stereological measure of the microstructural architecture. It is a tensor whose principal axis are coincident with the principal microstructural direction and whose eigenvalues are proportional to the distribution of the microstructure in the associated principal direction.
It is therefore necessary to introduce parameters able to describe such orientations. We therefore first need to acquire a 3D representation of the bone. This is done through the use of **tomography**. We then use a **morphological analysis** to describe the microstructure.

2.3.1 Computed Tomography

Tomography[1] refers to the cross-sectional imaging of an object from either transmission or reflection data collected by illuminating (by any kind of penetrating wave) the object from many different directions [125]. Fundamentally, tomographic imaging deals with the reconstruction of an image from its projections. The technique consists in irradiating a section of a sample from a number of positions angle and then measuring the intensity of the transmitted or reflected radiation. These projections can represent, for example, the attenuation of X-rays through an object as in conventional X-ray tomography, the decay of radioactive nucleoids in the body as in emission tomography, or the refractive index variations as in ultrasonic tomography. In X-ray tomography, such as used here, the projections consist of line integrals of the attenuation coefficient. This attenuation is due to photons either being absorbed by the atoms of the material, or being scattered away from their original directions of travel. Photoelectric absorption consists of an X-ray photon imparting all its energy to a tightly bound inner electron in an atom. The electron uses some of this acquired energy to

[1] The word tomography comes from the Greek terms “tome-”, meaning section and “-graphein”, meaning writing.

overcome the binding energy within its shell, therefore, the higher the atomic number of the material, the greater the absorption and the attenuation coefficient.
From the projections for each angular position, one can reconstruct an image and differentiate the constituting materials considering the variation of the attenuation coefficient and the initial energy of the rays. The images obtained are 2D maps of the distribution of the attenuation coefficient of X-rays. By stacking the obtained 2D images, one can reconstruct 3D images.
The attenuation coefficient is in the field of radiodensity measured in Hounsfield Units (HU). The HU scale is a linear transformation of the attenuation coefficient measurement into one in which the attenuation coefficient of distilled water at standard pressure and temperature (STP) is defined as zero HU, while the attenuation coefficient of air at STP is defined as -1000HU.

2.3.2 Morphological Analysis

Morphological analysis provides tools to extract characteristics or morphological parameters of an object. The actual values of the parameters extracted depend not only on the object but also on the quality of the object representation. In 3D images, it depends on the voxel size, in 2D, on the pixel size. The higher the resolution (the smaller the voxels/pixels), the higher the quality of the analysis.
Four parameters of the morphology are of particular interest for us[1]: TV, BV, Tb.Th, and MIL. The first three ones can be extracted from simple image analysis, the last one needs further stereological measurement of the microstructural arrangement. They are described in detail in the next paragraphs.

Tissue (or Total) Volume - TV

This parameter quantifies the total volume of the analyzed region (ROI - region of interest). Note that in the case of a bone, the word “tissue” includes the entire volume of pores and trabecular bone. It is computed by multiplying the total number of voxels contained in the region of interest (solid voxels and pores) by the volume of a voxel. This volume can also be measured from 2D images. In this case, the volume is calculated assuming that the thickness of a cut is equal to the length of the side of a pixel.

Bone Volume - BV

This parameter measures the total volume of 3D objects inside the region of interest. It is computed by multiplying the number of voxels of solid objects (i.e. excluding the pores) in

[1] We here use the bone nomenclature of morphology even though we will analyze the morphology on other type of materials such as engineered foams (see section 5.4 on our model validation.). Bone volume (BV) will therefore have to be understood as the solid phase volume and trabecular thickness (Tb.Th) as the thickness of the rods of the cellular solid.

the ROI by the volume of a voxel.

`BV/TV`

An important parameter is the ratio of the two previous parameters. Indeed, when dealing with density measures, we can define an apparent density (ρ) defined from the total mass (M) and `TV`, the bone density (ρ_0) defined from the total mass[1] and `BV`, and finally a reduced density ($\bar{\rho} \in [0,1]$), measuring the ratio of the apparent density to the bone density.
We therefore have:

$$\bar{\rho} = \frac{\rho}{\rho_0} = \frac{M/\mathtt{TV}}{M/\mathtt{BV}} = \frac{\mathtt{BV}}{\mathtt{TV}} \qquad \text{(Equ. 2.1)}$$

The reduced density is then the ratio `BV/TV` measured from the morphological analysis.
The porosity, denoted by f, is defined from the reduced density by :

$$f = \frac{\mathtt{TV} - \mathtt{BV}}{\mathtt{TV}} = 1 - \mathtt{BV/TV} = 1 - \bar{\rho} \qquad \text{(Equ. 2.2)}$$

Distribution of the thickness of trabeculae - `Tb.Th`

The local thickness at a location inside a solid is defined as the diameter of the largest sphere built so that it contains the point (but the point is not necessarily the center of the sphere) and is entirely contained within the surface of the solid.
Computing the trabecular thickness (`Tb.Th`) uses the concept of skeletonization of the object, identifying the center line (backbone) of all trabeculae. Then, for each trabecula, the thickness is measured as the radius of the largest fitting sphere for all voxels located along the backbone (`Tb.Th` measure defined in [106], see Fig. 2.16). For a given object, one can therefore compute the trabecular thickness distribution, extracting for instance the mean and standard deviation or the minimal and maximal values.

Mean Intercept Length - `MIL` **- and Degree of anisotropy -** `DA`

The Mean Intercept Length (`MIL`) [97] (and the degree of anisotropy - `DA`) is a measure of the symmetry of the three-dimensional solid object through the presence or absence of a preferential alignment on the component along an axis in a particular direction.
Consider a region or a volume containing two distinct phases (voids and solid), which are each characterized by a complex architecture, such as the one of the trabecular bone. This volume can be studied in order to determine its isotropy. If the volume is isotropic, then (statistically speaking) a straight line crossing the entire volume gives the same number of intersections of the solid phase in any 3D orientation. The basic principle of the `MIL` method is to count the number of intersections (I) between a linear grid (of a given spacing) and the solid/void interface as a function of the grid orientation (θ). The mean intercept length (an

[1] Assuming the pores are voids, and not marrow & (blood) vessels, gives a total mass equal to the bone mass.

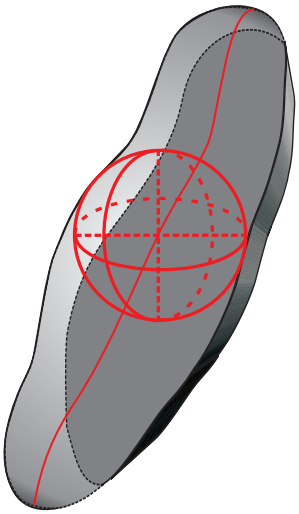

FIGURE 2.16: *Tb . Th measurement method: a sphere, whose center lies along the volume's center line, is fitted within the considered volume.*

intercept is the segment between two intersections) for this orientation is the total length L of the line grid divided by the number of intersections: $\texttt{MIL}(\theta) = L/I(\theta)$.
This calculation requires to define a spherical region within which the analysis of the MIL is performed. Indeed, in order to have an identical distribution of segment lengths, the bundles of lines of the grid all need to pass through the center of a sphere. Either one selects a spherical volume or the MIL can be computed for the sphere containing the entire ROI. The average length of the intersection (MIL) obtained using this method is therefore not measured directly but calculated based on the number of intersections in a given direction. Therefore, this method of calculating the MIL will give an accurate result when analyzing a volume containing a sufficiently large number of objects and it will not be appropriate for analyzing a volume containing a small number of objects.
Three dimensional MIL measurements may be fitted to an ellipsoid (or an ellipse for 2D measurements, see Fig. 2.17, 2.18) which can be expressed as the quadratic form of a second order tensor $\boldsymbol{M}$ in such a way that [97]:

$$\frac{1}{\texttt{MIL}^2(\theta)} = \mathbf{n}^T(\theta)\boldsymbol{M}\mathbf{n}(\theta) \qquad \text{(Equ. 2.3)}$$

where $\mathbf{n}(\theta)$ is the unit vector in the direction θ[1]. It is a symmetric tensor since by definition the ellipsoid axis are orthogonal to each other and the MIL values are positive ones (they denote a distance-like parameter). For an isotropic material, $\boldsymbol{M} = \boldsymbol{I}$.
Morphological analysis softwares can usually perform stereological measurements to extract the eigenvalues and eigenvectors of the MIL tensor $\boldsymbol{M}$.

[1]When fitting an ellipsoid onto a quadric form, the axis lengths are inversely proportional to the square of the eigenvalues of the tensor the ellipsoid is built from. Therefore, the ellipsoid fitted on $\boldsymbol{M}$ has its axis lengths proportional to the MIL measures

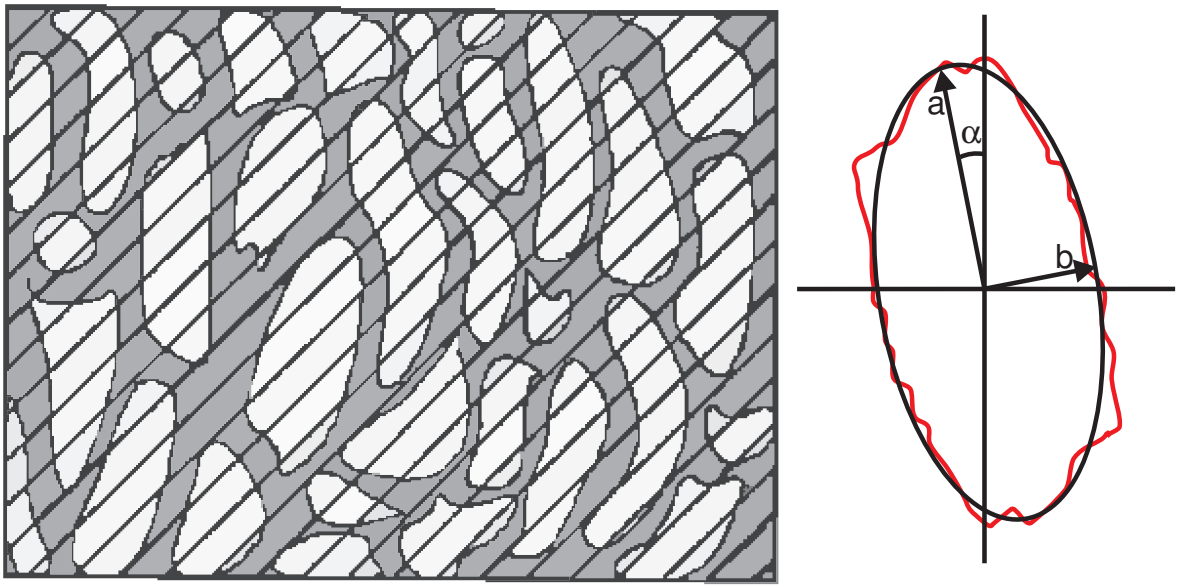

FIGURE 2.17: *An ellipse representation of the 2D anisotropic nature of trabecular bone architecture: a linear grid imposed over the image (left) and the measured* `MIL` *ellipse (right), adapted from [245]. At each grid direction correspond a* `MIL` *value (plotted in red on the polar diagram - right figure), an ellipse is then fitted on this data. The ellipse is defined through its axis half-lengths (a and b) and its main axis orientation,* α.

From these eigenvalues, it is possible to calculate a simplified parameter quantifying the anisotropy of the solid structure: the degree of anisotropy (`DA`) of the solid structure. This parameter is defined as the ratio between the highest eigenvalue and the lower eigenvalue:

$$\texttt{DA} = \frac{\max(\text{eigenvalues of } \boldsymbol{M})}{\min(\text{eigenvalues of } \boldsymbol{M})}$$

The degree of anisotropy values calculated by this method range from 1 (100% isotropic) to infinity (100% anisotropic).
Finally, the `MIL` tensor is used to build fabric tensors. Among other definitions, Cowin [51] defined a fabric tensor $\boldsymbol{T}$ as the inverse square root of $\boldsymbol{M}$:

$$\boldsymbol{T} = \boldsymbol{M}^{-1/2} \qquad \text{(Equ. 2.4)}$$

Such a tensor is well defined being the positive square root of the inverse of the positive definite symmetric tensor $\boldsymbol{M}$. For an isotropic material, $\boldsymbol{T} = \boldsymbol{I}$. The main advantage of this definition is that larger values of $\boldsymbol{T}$ will be associated with larger values of `MIL` and thus of the stiffness as it means that there is more solid phase present, the material is therefore stronger. An other advantage is that the eigenvalues of $\boldsymbol{T}$ are the MIL values in the eigen directions. This definition of the fabric tensor (Equ. 2.4) is the one used in this work.

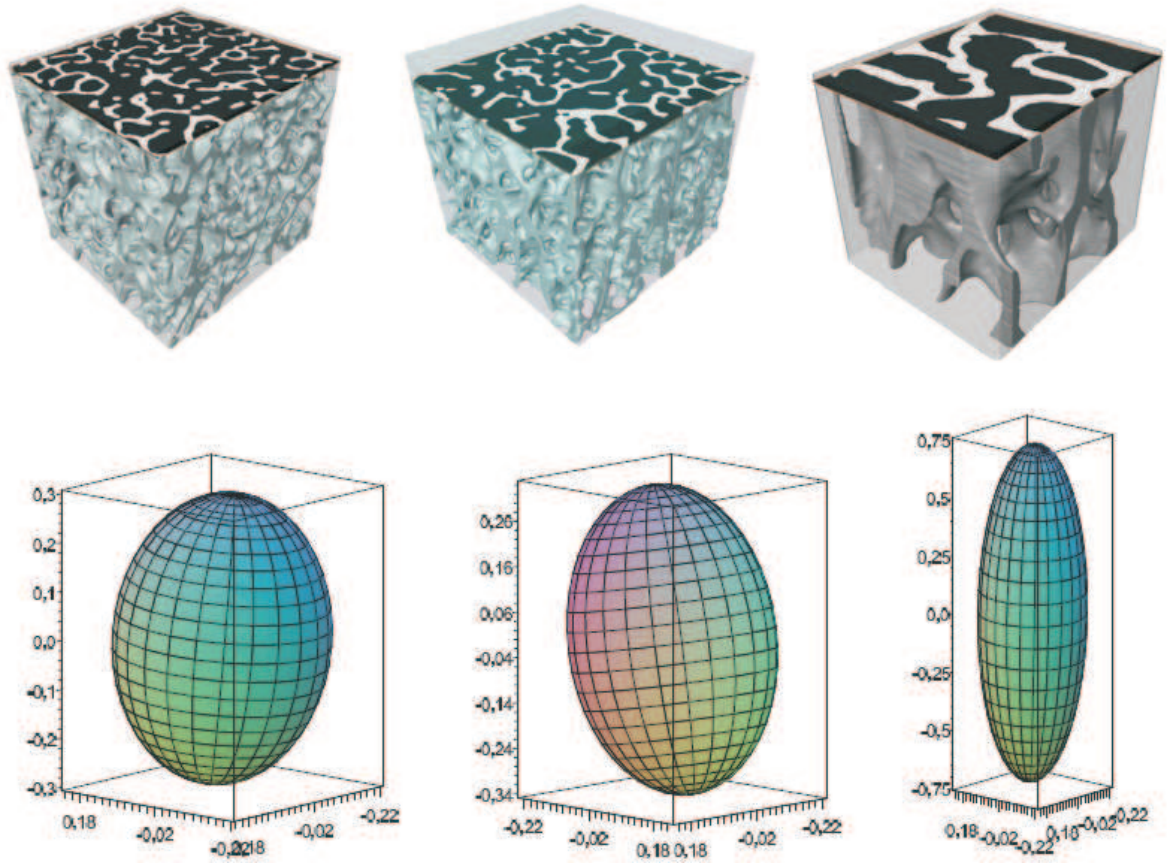

FIGURE 2.18: *An ellipsoid representation of the 3D anisotropic nature of trabecular bone architecture:* ***top row****-3D reconstruction from CT-scans, and* ***bottom row****-the associated measured* `MIL` *ellipsoids, adapted from [220].*

2.4 Conclusions

This chapter presented the basics of the anatomy and physiology involved in orthodontic tooth movement.

We saw bone is a living material whose main function is to form the skeleton and thus to allow, among other functions, mobility and protection of the body as well as to serve as a reservoir of calcium and phosphate to the body. It is subject to permanent and transients loads caused by everyday activities or special events such as accidents. Unlike inert materials, this tissue can respond adaptively to its environment. In addition to skeletal growth and resorption of fractures, which are of temporary nature, the structure of bone is continuously maintained and adapted internally and at its surface by a sustainable process, called remodeling (remodeling is used in the orthopedic literature to refer to the maintenance process; bone modeling is used for the adaptation and repair process; remodeling is however used in the orthodontic literature-as well as in this work-to refer to the adaptation process). The trabecular bone adaptation process leads to a morphology and density change of bone so that its main directions (measured for instance through the knowledge of a fabric tensor) are aligned with the privileged directions of stresses; while its density (measured through `BV/TV`) is higher where the mechanical stimulus is higher. The mechanical stimulus driving the bone remodeling process is believed to be either the strain energy-density, stress-related, strain-related or even related to the repair of micro-damage inside the bone.
Orthodontic tooth movement is possible due to combined resorption/apposition sites in the alveolar bone surrounding the tooth. The alveolar bone remodels along the orthodontic forces path and carries along the tooth, hence allowing the tooth movement. The bone remodeling process is closely related to the cellular activity in the periodontal ligament, especially to the activity of the fibroblasts. This cellular activity is known to be pressure sensitive. Orthodontic tooth movement therefore occurs in three phases: the first being the instantaneous deformation of the tissues (especially the periodontal ligament), followed by a lag phase sometimes present during the time needed to resorb possible hyaline zones in the PDL, and finally the movement strictly speaking, due to bone remodeling.

In order to model orthodontic tooth movement without considering detailed biology of both the periodontal ligament cell activity and the bone remodeling process, we will therefore present a model for bone remodeling accounting for the pressure dependency of the PDL by transferring this dependency into a pressure dependency in the bone remodeling law. The bone mechanical response will be modeled through the use of fabric tensor and `BV/TV` to account for morphology. The role of other tissues in orthodontic tooth movement will be neglected.

Chapter 3
On Non-Linear Computational Mechanics Principles

The motivation to perform research in biomechanics comes from the realization that mechanobiology cannot be understood without mechanics as much as an airplane cannot be understood without aerodynamics.
Biomechanics deals with movements and forces around and inside organisms. In the living world, atoms and molecules are organized in cells, tissues, organs and individual organisms. At the atomic or to some extend the cellular level, this has to be analyzed with the tools of quantum and statistical physics. At the tissue or organ level, i.e. at the scale of interest in this work, the tools provided by Continuum Mechanics will do the job.
This chapter therefore aims at presenting the theoretical and computational background of Continuum Mechanics required to understand the rest of the thesis. It is not an exhaustive review of the principles of Continuum Mechanics, only the useful tools in the present context are presented.

In this chapter, as everywhere else in this work, the notation used in mathematical expressions (except when index notation is used) is as follows: vector are in bold letters: e.g. $\mathbf{x}, \mathbf{a}$; second order tensors are in bold italic letters: e.g. $\boldsymbol{\sigma}$, $\boldsymbol{D}$ or $\boldsymbol{a}$; fourth order tensors in doubled line letters: e.g. $\mathbb{H}$ and $\mathbb{M}$, doubled line letters are also used for volumes: $\mathbb{V}$, and surfaces: $\mathbb{S}$.

Chapter Overview

3.1 Kinematics in Finite Strains

By assumption, we will work in a Continuum Mechanics framework.
The continuous medium is a representation of a quantity of matter that occupies a given space of volume $\mathbb{V}(t)$, with an outer surface $\mathbb{S}(t)$, at a given time t. By definition, a continuous medium is an environment in which physical properties vary spatially and temporally in a continuous way. The object of Continuum Mechanics is to predict the configurations of a body from a set of initial and boundary conditions. During deformation, in finite strains, the body shape evolves significantly. It is therefore not equivalent anymore to work either in the current or in the initial configurations (by opposition to the small displacement hypothesis widely used and for which no significant change of configuration exists). We therefore have to review some of the fundamentals of kinematics.

3.1.1 Lagrangian versus Eulerian Coordinate Systems

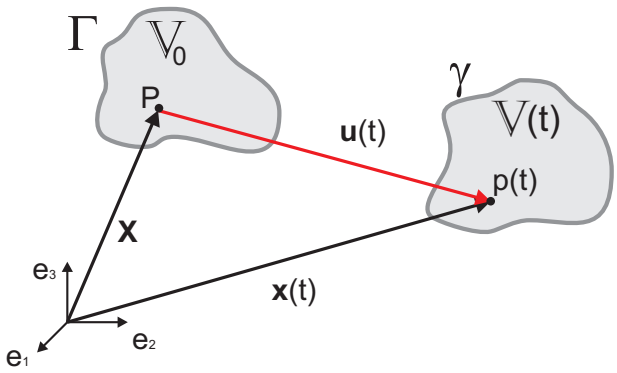

FIGURE 3.1: *A material point P associated to position $\mathbf{X}$ in the reference configuration becomes associated with position $\mathbf{x}(t)$ in the deformed configuration.*

Let $\mathbf{X}$ (**Lagrangian** coordinates) and $\mathbf{x}$ (**Eulerian** coordinates) be the position vector of a material point respectively in the reference configuration (Γ) of volume $\mathbb{V}_0$ and in the current configuration (γ) of volume $\mathbb{V}(t)$ as represented in Fig. 3.1.
It is generally assumed that the current position can be written in terms of the reference coordinates by the one-to-one relationship:

$$\mathbf{x} = \phi(\mathbf{X}, t) \qquad \text{(Equ. 3.1)}$$

Any property can thus be described as a function of either $\mathbf{x}$ (spatial representation) or $\mathbf{X}$ (material representation).

Lagrangian Formulation

In the Lagrangian, also called material, coordinate system, the initial position $\mathbf{X}$ must be known and is used as the independent variable. The displacement is:

$$\mathbf{u}(t) = \mathbf{x}(\mathbf{X}, t) - \mathbf{X} \tag{Equ. 3.2}$$

Thus, the Lagrangian formulation tracks material particles that are carried along with the deformation. In this case, the movement of the boundaries is easily followed and is computed automatically. Indeed, considering a spatial discretization method using a mesh, each mesh node is linked to the same material particle during the whole simulation. Therefore, the mesh boundaries define exactly (to the spatial discretization and integration errors) the material boundaries and the boundary displacement conditions can be immediately applied to the mesh nodes.
Another advantage of the Lagrangian mesh formalism is that history dependent materials, such as plastic materials treated here, are relatively easy to handle. Indeed, considering a spatial discretization method using a mesh, each integration point always represents the same material particle. Thus, this formalism is naturally chosen in nonlinear solid mechanics. However, in the case of large displacements and/or strains, such a Lagrangian mesh is generally distorted after some time. The mesh quality can then not be sufficient enough either to continue the computation (if elements happen to get inverted) or simply to blindly trust the solution quality (when elements are too much distorted).

Eulerian Formulation

The Eulerian, also called spatial, formulation describes the variations happening at a given spatial point. In the Eulerian coordinate system, the initial position $\mathbf{X}$ is treated as a dependent variable. In the case of computational fluid dynamics for which the Eulerian formulation is usually used, this initial position $\mathbf{X}$ is usually unknown. Thus, the velocity is estimated instead of the displacement:

$$\dot{\mathbf{u}} = \dot{\mathbf{x}} = \frac{d\mathbf{x}}{dt} \tag{Equ. 3.3}$$

Additional convective terms must then be taken into account in the conservation equations in order to represents the numerous different material particles seen by one point of the computational grid. Mathematically, these terms come from the fact that Eulerian coordinates are time dependent, so that, unlike Lagrangian coordinates, the time derivative of a physical quantity expressed in terms of such coordinates is different from the material time derivative. The evaluation of these convective terms, as well as their numerical computation, is complicated in the case of elaborated constitutive laws, like those representing the behavior of materials with memory (such as plasticity). Since the mesh is attached to spatial coordinates and thus fixed in space, the material flows through the mesh which remains perfectly undistorted. But a drawback of such a fixed mesh is that free boundaries are difficult to track.

ALE Formulation

In order to take advantages of both the Lagrangian and the Eulerian formulations, while avoiding their drawbacks, mixed Lagrangian-Eulerian approaches have been developed, like the ALE or Arbitrary Lagrangian-Eulerian formulation [22, 63, 209]. Other approaches, such as remeshing of the problem while the simulation is going on, can be carried out but are memory and CPU demanding, not to mention the difficulty to implement such a methodology, and can therefore only be used at critical times, not at all time steps.
For the ALE formulation, a new reference system is defined, the grid reference system. It can arbitrarily move independently from the material or spatial reference systems. It is associated with new coordinates, denoted $\boldsymbol{\chi}$, and the current positions can be expressed as an assumed one-to-one relationship of these coordinates as:

$$\mathbf{x} = \phi^{\star}(\boldsymbol{\chi}, t)$$

In the ALE method, the conservation equations are expressed on the grid reference system and additional convective terms also need to be considered to account for the difference between the material and grid velocity, $\mathbf{v}^{\star} = \left.\frac{\partial \mathbf{x}}{\partial t}\right|_{\boldsymbol{\chi}}$. This velocity field is a new unknown of the system that leads to twice as much kinematics unknowns with a strong coupling. However, the resolution of such a new system is eased by partitioning the Eulerian-Lagrangian operator and solve the equations sequentially. At each time step, the problem is therefore solved in two distinct stages:

1. In a first stage, a classical **Lagrangian step** is computed leading to an equilibrated configuration. The mesh follows the material particles and the conservation equations do not contain any convective terms. Issues like free boundaries and plasticity are easily handled.

2. In a second stage, called the **Eulerian step**, the equilibrated configuration is computed on a new mesh. This step consists into a node relocation sub-step (new nodal positions -the nodes are "simply" moved, there is no creation of new nodes and/or elements- and thus mesh velocities are computed under a compatibility constraint between the material and mesh boundaries) and a convective sub-step, for which the Lagrangian solution is projected onto the new mesh.

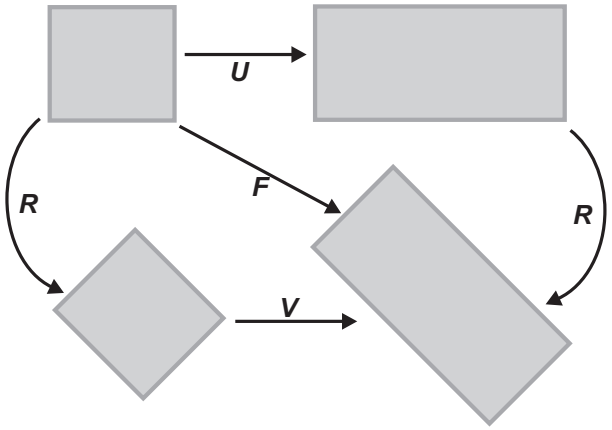

FIGURE 3.2: *Polar decomposition of the deformation gradient.*

3.1.2 Deformation Gradient and Strain Rate Tensors

The **deformation gradient**, which describes the motion from the reference configuration to the current one is the two-point tensor:

$$\boldsymbol{F} = \frac{\partial \mathbf{x}}{\partial \mathbf{X}} \text{ with } \det \boldsymbol{F} = J > 0 \qquad \text{(Equ. 3.4)}$$

This tensor can be decomposed in pure rotation and pure deformation tensors as:

$$\boldsymbol{F} = \boldsymbol{R}\,\boldsymbol{U} = \boldsymbol{V}\,\boldsymbol{R} \qquad \text{(Equ. 3.5)}$$

with $\boldsymbol{U} = \boldsymbol{U}^T$: (right) stretch tensor (Symmetric Positive Definite) ; $\boldsymbol{U} = \boldsymbol{R}^T\boldsymbol{V}\,\boldsymbol{R}$
$\boldsymbol{V} = \boldsymbol{V}^T$: (left) stretch tensor (Symmetric Positive Definite) ; $\boldsymbol{V} = \boldsymbol{R}\,\boldsymbol{U}\,\boldsymbol{R}^T$
$\boldsymbol{R}^T\boldsymbol{R} = \boldsymbol{I}$: rotation tensor (orthogonal)

Stretch ratios $(\lambda_1, \lambda_2, \lambda_2)$ are the eigenvalues of $\boldsymbol{U}$ (and $\boldsymbol{V}$). The principal directions of the deformation are their eigenvectors (the eigenvectors of $\boldsymbol{V}$ are those of $\boldsymbol{U}$ rotated in the final configuration with $\boldsymbol{R}$).

The **spatial gradient of velocity** is given by:

$$\boldsymbol{L} = \frac{\partial \dot{\mathbf{x}}}{\partial \mathbf{x}} = \dot{\boldsymbol{F}}\boldsymbol{F}^{-1} \qquad \text{(Equ. 3.6)}$$

That can be split into its symmetric and anti-symmetric parts, according to:

$$\boldsymbol{L} = \boldsymbol{D} + \boldsymbol{W} \qquad \text{(Equ. 3.7)}$$

with

$$\boldsymbol{D} = \frac{1}{2}(\boldsymbol{L} + \boldsymbol{L}^T) \qquad \textbf{strain rate} \text{ (symmetric)} \qquad \text{(Equ. 3.8)}$$

$$\boldsymbol{W} = \frac{1}{2}(\boldsymbol{L} - \boldsymbol{L}^T) \qquad \textbf{spin tensor} \text{ (anti-symmetric)} \qquad \text{(Equ. 3.9)}$$

By essence, the spin tensor is neglected under the small displacement hypothesis and is thus specific to large deformations.

3.1.3 Strain Tensors

Strain tensors can be defined using both the Lagrangian and the Eulerian formulations in such a way that they become zero for no deformation (including rigid body motions).

Lagrangian strain tensors:

$$\text{Generalized Lagrangian strain tensors: } \boldsymbol{E}^L = \begin{cases} \frac{1}{m}(\boldsymbol{U}^m - \boldsymbol{I}) & m \in \mathbb{R}_o \\ \ln \boldsymbol{U} & m = 0 \end{cases}$$

- $\boldsymbol{E}^N = \ln \boldsymbol{U}$ is also known as the **natural** strain tensor.
- Choosing $m = 1$ leads to $\boldsymbol{E}^B = \boldsymbol{U} - \boldsymbol{I}$ also known as the **Biot** strain tensor.

  In uniaxial problems, it is often referred to as the **engineering strain**.

  In such a case, it becomes $E^B = \dfrac{\ell - L}{L} = \dfrac{\Delta L}{L}$ where L is the reference length and ℓ is the deformed length.
- Choosing $m = 2$ gives the **Green-Lagrange** strain tensor: $\boldsymbol{E}^{GL} = \frac{1}{2}(\boldsymbol{F}^T\boldsymbol{F} - \boldsymbol{I})$.

  In uniaxial problem it becomes $E^{GL} = \dfrac{\ell^2 - L^2}{2L^2}$

Eulerian strain tensors:

$$\text{Generalized Eulerian strain tensors: } \boldsymbol{E}^E = \begin{cases} \frac{1}{m}(\boldsymbol{V}^m - \boldsymbol{I}) & m \in \mathbb{R}_o \\ \ln \boldsymbol{V} & m = 0 \end{cases}$$

- Choosing $(m = -2)$ gives the **Almansi** strain tensor: $\boldsymbol{E}^A = \frac{1}{2}(\boldsymbol{I} - \boldsymbol{F}^{-T}\boldsymbol{F}^{-1})$. In uniaxial problem it becomes $E^A = \dfrac{\ell^2 - L^2}{2\ell^2}$.

When used under a small strain hypothesis, all these strain tensors are identical to the first order (see zoom in Fig. 3.3), also given by the Cauchy strain tensor $\boldsymbol{\varepsilon} = \frac{1}{2}(\boldsymbol{F} + \boldsymbol{F}^T) - \boldsymbol{I}$ which makes only sense in a small displacement context and reads

$$\varepsilon_{ij} = \frac{1}{2}\left(\frac{\partial u_i}{\partial x_j} + \frac{\partial u_j}{\partial x_i}\right)$$

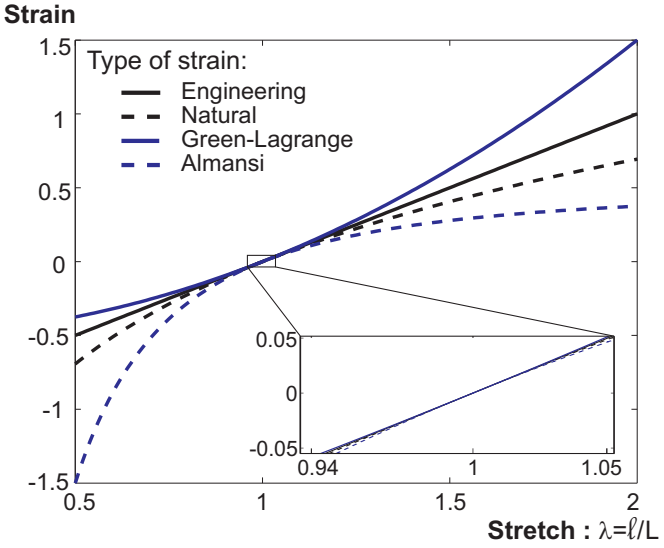

FIGURE 3.3: *Comparison of 1D strain measures as function of the stretch value,* $\lambda = \dfrac{\ell}{L}$

3.1.4 Stress Tensors

Stress tensors are physically defined as "a" force divided by "a" surface. Both the force and the surface the stress tensor refers to can be expressed in initial and deformed configuration.

- **Cauchy** stress tensor (deformed configuration) - $\boldsymbol{\sigma}$: loads are considered as the actual loads (**f**) and the surface is the deformed one ($\mathbb{S}$).

$$d\mathbf{f} = \boldsymbol{\sigma}\mathbf{n}d\mathbb{S} \tag{Equ. 3.10}$$

  with **n** the unit outward normal to the deformed surface.

- **Piola** stress tensor (initial configuration) - $\boldsymbol{P}$: loads are considered as the actual loads (**f**) and the surface is the initial one ($\mathbb{S}_0$). It is in uniaxial problems referred to as the **engineering stress** as it is the most obvious stress to compute (applied force and initial - generally known - surface).

$$d\mathbf{f} = \boldsymbol{P}\mathbf{N}d\mathbb{S}_0 \tag{Equ. 3.11}$$

  with **N** the unit outward normal to the reference surface.

- **Piola-Kirchhoff no. II** (PK2) stress tensor (initial configuration) - $\boldsymbol{S}$: loads are pushed back to the reference configuration ($\mathbf{F}_0$) and the surface is the initial one ($\mathbb{S}_0$).

$$d\mathbf{f}_0 = \boldsymbol{S}\mathbf{N}d\mathbb{S}_0 = \boldsymbol{F}^{-1}d\mathbf{f} \tag{Equ. 3.12}$$

3.2 Conservation Equations: Theory and Resolution Methods

The driving equations for mechanical problems are the conservation equations completed with the constitutive equations. Solving these non-linear equations is not generally conceivable in an analytical way, thus a numerical method has to be used. We choose to work with the Finite Element (FE) method (or FEM) for the spatial discretization. The FE method is one of the most used methods dealing with spatial discretization of partial differential equations. In the FE method, the state of the studied problem is described using variables defined in a limited number of discrete points representing the studied body: the nodes. To assess the state of the system at these points, the volume is subdivided into a finite number of subregions: the finite elements constituting the mesh. The equations are then solved on average over these elements.
As well as for the kinematics, the discretization can be expressed both in a Lagrangian or an Eulerian configuration. The choice made here is to express the discretization in the current configuration with a Lagrangian representation of the mesh. We therefore work with the Cauchy stress and the current positions as unknowns.
We will in this section present the conservation equations (strong form), their weak form and the general principles of the FE method for this configuration. The readers interested with detailed expressions of these equations and methods should read [18, 209] or [278] among many other detailed works on the subject. These references are those this section and the next one on constitutive theories in finite strains are inspired from.

3.2.1 Conservation Equations

The conservation equations express the conservation of some fundamental mechanical quantities, i.e. mass, momentum, angular momentum and energy. In the current configuration, they are simply expressed as:

- mass conservation: $\rho J = \rho_0$

  with ρ the current mass density (ρ_0 the initial mass density) and J the Jacobian of the transformation between the reference and current configurations ($J = \det \boldsymbol{F}$).

- momentum conservation: $\dfrac{\partial \sigma_{ij}}{\partial x_j} + \rho b_i = \rho a_i$

  with $\rho\mathbf{b}$ the body forces and $\mathbf{a}$ the acceleration field.

- angular momentum conservation: $\sigma_{ij} = \sigma_{ji}$

  This angular momentum conservation therefore simply states that the Cauchy stress tensor has to be symmetric.

- energy conservation (for athermal problems): $\rho \dot{u} = \sigma_{ij} D_{ij}$

  with u the specific internal energy.

3.2.2 Weak Form

As specified previously, in most cases, it is not possible to find an analytical solution for these equations (local-or strong-form of the solution) and thus one needs to recourse to an approximation method. To use the FE method as the discretization tool, these equations need to be rewritten in what is called a weak form, i.e. an integrated variational formulation. This weak form is here expressed thanks to the Principle of Virtual Works. This principle comes from expressing the conservation equations multiplied by a kinematically admissible virtual displacement ($\delta\mathbf{u}$, an arbitrary field of virtual displacements of $\mathcal{C}^0$ continuity-at least piecewise differentiable, respecting the continuity of the body, and the essential boundary conditions, presently imposed displacement) and integrated over an arbitrary volume. It reads:

$$\delta\mathcal{M} + \delta W_{\mathtt{int}} = \delta W_{\mathtt{ext}} \tag{Equ. 3.13}$$

stating that the sum of the virtual work of inertial forces ($\delta\mathcal{M}$) and internal forces ($\delta W_{\mathtt{int}}$) is equal to the virtual work of external force ($\delta W_{\mathtt{ext}}$).
In the current configuration, each of these terms reads[1,2]:

$$\delta\mathcal{M} = \int_{\mathbb{V}(t)} \rho \ddot{\mathbf{x}} . \delta\mathbf{u} \, d\mathbb{V} \tag{Equ. 3.14}$$

$$\delta W_{\mathtt{int}} = \int_{\mathbb{V}(t)} \boldsymbol{\sigma} : \frac{\partial \delta\mathbf{u}}{\partial \mathbf{x}} \, d\mathbb{V} \tag{Equ. 3.15}$$

$$\delta W_{\mathtt{ext}} = \int_{\mathbb{V}(t)} \rho\mathbf{b} . \delta\mathbf{u} \, d\mathbb{V} + \int_{\mathbb{S}(t)} (\boldsymbol{\sigma} . \mathbf{n}) . \delta\mathbf{u} \, d\mathbb{S} \tag{Equ. 3.16}$$

The principle of virtual work expresses the equilibrium of a body or any part of it, independently of the constitutive law and the formulation (even though we gave only the expressions of the virtual works integrated in the current configuration).
In particular, in this work, we express this equilibrium using an Updated Lagrangian Formulation, for which the reference configuration is the last known state of equilibrium.
The principle of virtual work also shows that the definition of a strain tensor is not required to express the equilibrium as only a virtual deformation ($\frac{\partial \delta\mathbf{u}}{\partial \mathbf{x}}$) is needed.
However, the energy conservation equation shows that to establish the constitutive equations, one cannot associate any strain tensor to any stress tensor. Indeed one can show that $\boldsymbol{\sigma}$ is energetically conjugated to $\boldsymbol{D}$, $\boldsymbol{P}$ to $\dot{\boldsymbol{F}}$ and $\boldsymbol{S}$ to $\dot{\boldsymbol{E}}^{GL}$.

[1] For two second order tensors $\boldsymbol{a}$ and $\boldsymbol{b}$, we use the notation ":" for the double contraction product: $\boldsymbol{A} : \boldsymbol{B} = A_{ij} B_{ij}$, summation over dummy indexes

[2] For two vectors $\mathbf{c}$ and $\mathbf{d}$, we use the notation "." for the vectorial product: $\mathbf{c}.\mathbf{d} = c_i d_i$, summation over dummy indexes

After space discretization, this weak form will result in the so-called semi-discretized equations (on space only). We will then use a classical finite difference method for the time discretization.

3.2.3 The Finite Element Method

The Finite Elements that are used in this work are basically kinematically admissible elements, i.e. the discretization concerns the displacement field only. The weak form of the equilibrium equations is written as a set of algebraic equations assuming a given shape of the displacement field through the use of shape functions ($\boldsymbol{N}$) and (unknown) nodal displacements ($\mathbf{q}$) so that:

$$\mathbf{u}(\mathbf{x}) = \boldsymbol{N}(\mathbf{x})\mathbf{q}$$

The nodal values $\mathbf{q}$ are determined by solving the weighted equilibrium equations (the previously introduced virtual work principle) over the elements using an incremental formulation (minimization formulations are usually not used in non-linear problems as their solutions are not uniquely defined). The semi-discretized virtual work principle is then written (after assembling all elementary contributions):

$$\delta\mathbf{q}\underbrace{\left[\boldsymbol{M}\,\ddot{\mathbf{q}} + \mathbf{F}_{\mathtt{int}} - \mathbf{F}_{\mathtt{ext}}\right]}_{\mathbf{F}^{oe}} = 0 \qquad \forall \delta\mathbf{q} \tag{Equ. 3.17}$$

with $\ddot{\mathbf{q}}$ the nodal accelerations, $\boldsymbol{M}$ the mass matrix and $\mathbf{F}_{\mathtt{int}}$ and $\mathbf{F}_{\mathtt{ext}}$ the (nodal consistent) internal and external forces.

$$\boldsymbol{M} = \int_{\mathbb{V}(t)} \rho \boldsymbol{N}^T \boldsymbol{N}\, d\mathbb{V} \tag{Equ. 3.18}$$

$$\mathbf{F}_{\mathtt{int}} = \int_{\mathbb{V}(t)} \boldsymbol{B}^T \sigma\, d\mathbb{V} \tag{Equ. 3.19}$$

$$\mathbf{F}_{\mathtt{ext}} = \int_{\mathbb{V}(t)} \rho \boldsymbol{N}^T \mathbf{b}\, d\mathbb{V} + \int_{\mathbb{S}(t)} \boldsymbol{N}^T \mathbf{t}\, d\mathbb{S} \tag{Equ. 3.20}$$

with $\boldsymbol{B} = \nabla \boldsymbol{N}^T$ (gradient relative to the current configuration, therefore evolving with time) and $\mathbf{t}$ the (known) applied surface tractions.
If the current configuration is not in an equilibrium state, since $\delta\mathbf{q}$ is arbitrary, the residue $\mathbf{F}^{oe}$ (Equ. 3.17) is not equal to zero for each and every component. It therefore represents the out-of-equilibrium, or residual, forces (hence the $\mathbf{F}^{oe}$ notation). In practice, this equilibrium cannot be exactly achieved and one will consider a configuration as equilibrated when

$$\frac{||\mathbf{F}^{oe}||}{||\mathbf{F}_{\mathtt{ext}}||} < \mathtt{prec} \tag{Equ. 3.21}$$

with `prec` a user defined precision.
The equilibrium equations Equ. 3.17 are iteratively solved using a Newton-Raphson method. Starting from a given trial nodal displacement $\mathbf{q}_0$ (several possibilities to evaluate such a trial

field exist but will not be treated in this work), the displacement field is iteratively updated in such a way that:

$$\begin{aligned} \Delta\mathbf{q} &= -\boldsymbol{K_T}^{-1}\mathbf{F}^{oe} \\ \mathbf{q}_{i+1} &= \mathbf{q}_i + \Delta\mathbf{q} \end{aligned} \qquad \text{(Equ. 3.22)}$$

with $\boldsymbol{K_T} = \dfrac{d\mathbf{F}^{oe}}{d\mathbf{q}}$ the tangent stiffness matrix.
These iterations are stopped when the previously defined equilibrium criterion (Equ. 3.21) is satisfied.
The tangent stiffness matrix, $\boldsymbol{K_T}$, can be decomposed into its geometrical and material parts. The geometrical part of the stiffness matrix depends only on the nature of the finite element and shape functions used.

As the main part of this work consists in proposing a constitutive model, only the material part of the stiffness matrix will be discussed here.
It is obtained by linearizing the Cauchy stress increment with respect to the strain increment. It can either be evaluated continuously or be discretized taking into consideration the integration scheme used to update the stress tensor. We here use a discretized material stiffness matrix, also called the material part of the **consistent tangent operator**, as it is evaluated consistently with the integration scheme. It is only a numerical operator (while the continuous one, when it exists, is a physical operator) as it depends on the stress update algorithm.

3.2.4 General Algorithm for a Finite Strain Problem

The resolution method for a finite strain problem can be expressed in several steps [as presented in 209, see Fig. 3.4]. We first need to define the data relative to the initial geometry, the mesh, the external loads and the material behavior. The integration algorithm then consists first in a loop over the load increments or time steps (which both number and size are a priori unknown). The configurations before and after this time loop are fully known and at equilibrium (provided the Newton-Raphson algorithm has converged to an equilibrated configuration). Within a time increment, one first has to define an approximation of the new geometry tentatively leading to a new equilibrium under the new load/time increment. The stresses are then evaluated in this new configuration, integrating the constitutive law relating (in the case of hypoelastic material models as treated here - see section 3.3) the stress evolution to the strain rate. The equilibrium is then checked in this configuration. If the equilibrium is not achieved, a new geometrical configuration has to be predicted using Newton-Raphson algorithm to correct the nodal positions.

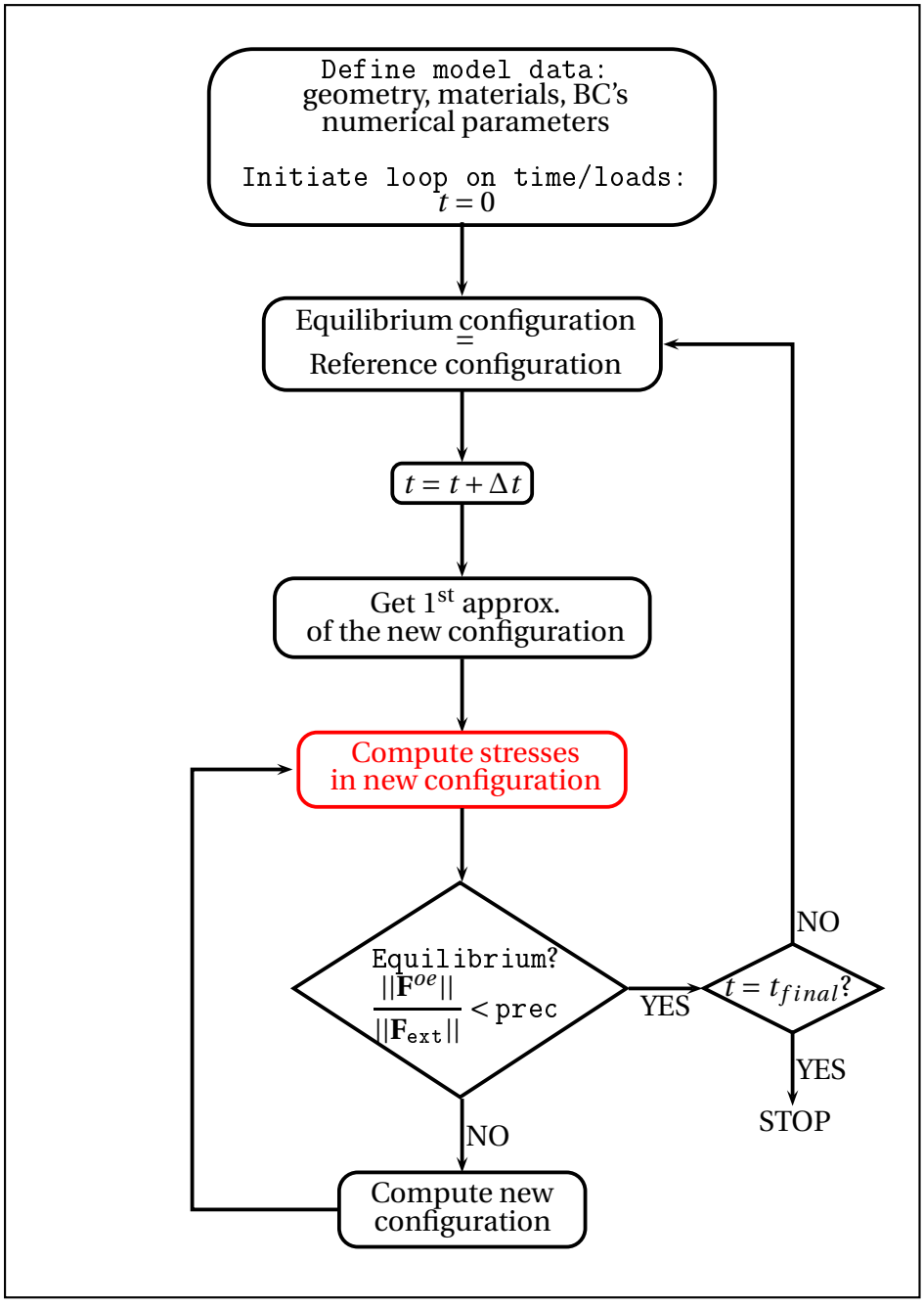

FIGURE 3.4: *Outline of the algorithm used in a non-linear FE analysis. The red box is the one that is of main interest to us in this work.*

We are here interested only in the integration of the constitutive law proposed for bone remodeling situations, the other steps of the general FE integration algorithm are not treated.

All numerical developments are implemented into Metafor [177], an in-house large strains finite element code. Its object-oriented architecture allows the developer not to master all the computational aspects of such a complex software. Indeed, this work focusing on the constitutive law, almost only the material integration procedure needs to be fully understood to work and develop in Metafor.

3.3 Constitutive Theory in Finite Deformations for Hypoelastic Solids

Hypoelastic materials are materials for which one can define a tensorial functional so that the Cauchy stress evolution can be written:

$$\dot{\boldsymbol{\sigma}} = \boldsymbol{f}(\boldsymbol{\sigma}, \boldsymbol{L}, \text{internal variables}) \qquad \text{(Equ. 3.23)}$$

3.3.1 Objective Derivative and Corotational Formulation

In finite strains, the current and initial configurations are generally significantly different. This implies that the expressions of variables, volume integrals, etc. depend on the configuration, which is not the case under the small strains hypothesis. So, the use of a specific formulation is required to deal with finite deformations. Especially, constitutive equations must be invariant under changes of frame of reference (i.e. a set of points moving in a rigid body motion - linked to an observer). The constitutive equations must be written in terms of objective quantities only (quantities that are frame independent, and thus transform according to the rules established for a change of frame).
However, the spin tensor $\boldsymbol{W}$, and thus the spatial gradient of velocity $\boldsymbol{L}$, is not objective. We can therefore, in Equ. 3.23, substitute $\boldsymbol{L}$ by its symmetric component (an objective quantity), the strain rate $\boldsymbol{D}$.
The time derivative of any Eulerian (second order) objective tensor is also not objective. Even though the Cauchy stress tensor $\boldsymbol{\sigma}$ is objective, it is easy to demonstrate that $\dot{\boldsymbol{\sigma}}$ is not. We therefore need to use an objective time derivative, such as the Jaumann derivative, which is written as:

$$\overset{\triangledown}{\boldsymbol{\sigma}}^{J} = \dot{\boldsymbol{\sigma}} - \boldsymbol{W}\boldsymbol{\sigma} + \boldsymbol{\sigma}\boldsymbol{W} \qquad \text{(Equ. 3.24)}$$

Therefore stresses are represented by an evolution law of the type :

$$\overset{\triangledown}{\boldsymbol{\sigma}} = \boldsymbol{f}(\boldsymbol{\sigma}, \boldsymbol{D}, \text{internal variables}) \qquad \text{(Equ. 3.25)}$$

where $\boldsymbol{\sigma}$ is the Cauchy stress tensor and $\overset{\triangledown}{\boldsymbol{\sigma}}$ is a generic objective time derivative of the Cauchy stress tensor (for instance the Jaumann derivative presented in Equ. 3.24). This somewhat

complicated expression can be transformed into a much simpler relation provided an appropriate change of frame, such as by introducing a corotational frame, is performed (see e.g. [210] for details). In this corotational frame, the Cauchy stress tensor $\boldsymbol{\sigma}^c$ (or any other tensor), as well as its time derivative $\overset{\bullet}{\boldsymbol{\sigma}}^c$, can be written respectively as:

$$\boldsymbol{\sigma}^c = \boldsymbol{\rho}^T \boldsymbol{\sigma} \boldsymbol{\rho} \tag{Equ. 3.26}$$

$$\overset{\bullet}{\boldsymbol{\sigma}}^c = \boldsymbol{\rho}^T (\overset{\bullet}{\boldsymbol{\sigma}} - \boldsymbol{\omega}\boldsymbol{\sigma} + \boldsymbol{\sigma}\boldsymbol{\omega})\boldsymbol{\rho} \;=\; \boldsymbol{\rho}^T \overset{\triangledown}{\boldsymbol{\sigma}} \boldsymbol{\rho} \tag{Equ. 3.27}$$

where $\boldsymbol{\omega}$ is any skew-symmetric tensor and $\boldsymbol{\rho}$ is a group of rotations generated thanks to this tensor. An objective derivative, when associated to a physical rotation tensor such as the Jaumann rate used here (choosing $\boldsymbol{\omega} = \boldsymbol{W}$ and therefore $\boldsymbol{\rho} = \boldsymbol{R}$), therefore transforms into a simple time derivative in the rotating frame.
For example, Equ. 3.25 can be rewritten :

$$\overset{\bullet}{\boldsymbol{\sigma}}^c = \overset{\bullet}{\boldsymbol{\sigma}}^c (\boldsymbol{\sigma}^c, \boldsymbol{D}^c, \text{internal variables}^c) \tag{Equ. 3.28}$$

In the next sections, when dealing with finite strains problems, since all quantities will be expressed in the corotational frame and for the sake of simplicity we will omit the exponent "^{c}". It should be clear that using a corotational frame is only a tool to help integrating in time the constitutive law (Equ. 3.28) and that once it has been integrated, the resulting stress tensor is brought back to the fixed Cartesian axis by using the inverse of Equ. 3.26. The interested reader should consult [210] for details on the corotational formulation.

3.3.2 Elasto-plasticity Integration

For an elasto-plastic material in an hypoelastic formulation, the basic assumption consists in an additive decomposition of the strain rate into two parts: an elastic and reversible part, $\boldsymbol{D}^e$, and an irreversible plastic part, $\boldsymbol{D}^p$:

$$\boldsymbol{D} = \boldsymbol{D}^e + \boldsymbol{D}^p \tag{Equ. 3.29}$$

Assuming that only the elastic part affects the stress rate, the constitutive law is therefore written as :

$$\overset{\bullet}{\boldsymbol{\sigma}} = \mathbb{C} : \boldsymbol{D}^e = \mathbb{C} : (\boldsymbol{D} - \boldsymbol{D}^p) \tag{Equ. 3.30}$$

where $\mathbb{C}$ is the stiffness tensor (4th order constant tensor, also referred to as the generalized Hooke's tensor).
In the case of an isotropic material, the stiffness tensor is known as Hooke's elasticity tensor, $\mathbb{H}$, function of only the two Lamé parameters, λ and μ:

$$\mathbb{H} = K\boldsymbol{I} \otimes \boldsymbol{I} + 2G\mathbb{1}$$

with $\mathbb{1}$ the fourth order symmetric unit deviatoric tensor[1]: $\mathbb{1} = \boldsymbol{I} \underline{\otimes} \boldsymbol{I} - \frac{1}{3}\boldsymbol{I} \otimes \boldsymbol{I}$, and

[1] For second order tensors $\boldsymbol{a}$ and $\boldsymbol{b}$, the product $A_{ijkl} = a_{ij} b_{kl}$ is noted $\mathbb{A} = \boldsymbol{a} \otimes \boldsymbol{b}$.

- $\mu = G = \frac{E}{2(1+\nu)}$, the shear modulus
- $K = \frac{E}{3(1-2\nu)} = \lambda + \frac{2}{3}G$, the bulk modulus
- E, Young's modulus
- ν, Poisson's ratio

The constitutive law Equ. 3.30 can thus be written in terms of the hydrostatic and deviatoric parts[1] of the strain rate tensor as:

$$\dot{\boldsymbol{\sigma}} = \underbrace{2G\hat{\boldsymbol{D}}^e}_{\dot{\boldsymbol{s}}} + \underbrace{K\,\mathtt{tr}\left(\boldsymbol{D}^e\right)\boldsymbol{I}}_{\dot{p}} \qquad \text{(Equ. 3.31)}$$

Elasto-plastic theories are based on the definition of three regions in the space of stresses (Fig. 3.5).
The first region is where the behavior is elastic. The second region is the border of the elastic region (plasticity criterion or yield function/surface). It is the region where the irreversible deformations appear. The third region is outside the surface of plasticity, its access is prohibited.

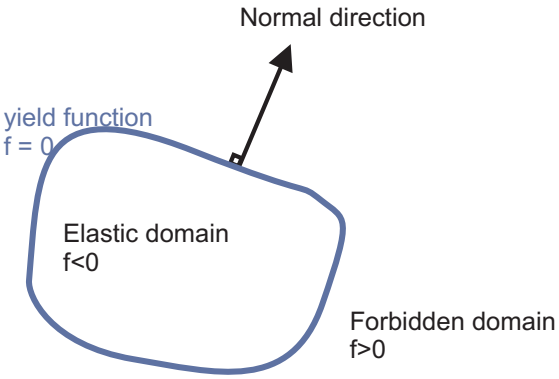

FIGURE 3.5: *The yield surface defines three regions in the space of stresses.*

The most convenient way to express a yield criterion, defined in the six-dimensional space of stresses, is to write it as

$$f(\boldsymbol{\sigma}, q) = 0 \qquad \text{(Equ. 3.32)}$$

In Equ. 3.32, q is the set of internal parameters (heredity parameters), which describe, at the macroscopic level, the microscopic state of the material and are an image of the past history of the deformation. Their value can evolve during plastic deformation only.

- The elastic region is characterized by: $f(\boldsymbol{\sigma}, q) < 0$
- The yield criterion is characterized by: $f(\boldsymbol{\sigma}, q) = 0$

[1] We use the notation $\hat{\boldsymbol{a}} = \mathtt{dev}(\boldsymbol{a})$ for the deviatoric part of a second order tensor $\boldsymbol{a}$: $\hat{\boldsymbol{a}} = \boldsymbol{a} - \frac{1}{3}\mathtt{tr}(\boldsymbol{a})\,\boldsymbol{I}$, and $\mathtt{tr}(\boldsymbol{a}) = a_{nn}$ for its trace.

- The "forbidden" region is characterized by: $f(\boldsymbol{\sigma}, q) > 0$

A restriction on the behavior evolution to admissible states should therefore be set up by $f(\boldsymbol{\sigma}, q) \leq 0$. This condition imposes that, during a plastic deformation, the yield function evolves and the undergone states must remain on the evolving function $f = 0$ or, in other words, that the stress state must remain on the subsequent yield surface. The mathematical expression for this condition, which is called the consistency condition, is:

$$\dot{f} = \frac{\partial f}{\partial \boldsymbol{\sigma}} : \dot{\boldsymbol{\sigma}} + \frac{\partial f}{\partial q}\dot{q} = 0 \tag{Equ. 3.33}$$

To be consistent with the Objectivity Principle, the yield surface has to be described in terms of objective quantities only. Therefore, it is usually described as a function of the invariants of the stress instead of the full stress tensor. A convenient way to do so is to express the yield function as the difference between a scalar representation of the stress (the equivalent stress, σ_{eq}) and a critical one (σ_{crit}):

$$f(\boldsymbol{\sigma}, q) = \sigma_{eq}(\text{invariants of } \boldsymbol{\sigma}) - \sigma_{crit}(q) \tag{Equ. 3.34}$$

There exist several expressions for the yield function depending on the definition of the equivalent stress σ_{eq} and on σ_{crit}. In the cases treated in this work, the von Mises criterion will be adopted, which means that the von Mises equivalent stress σ_{eq}^{vM} (which is an invariant of the stress tensor) and the yield stress σ_y will be used. The equation of this particular yield surface (when no kinematic hardening is considered) is written as:

$$\begin{cases} f(\boldsymbol{\sigma}, q) = \sigma_{eq}^{vM} - \sigma_y(q) \\ \sigma_{eq}^{vM} = \sqrt{\frac{3}{2}\boldsymbol{s} : \boldsymbol{s}} \end{cases} \tag{Equ. 3.35}$$

where $\boldsymbol{s}$ is the deviatoric part of the Cauchy stress tensor.
It is assumed (associative plasticity) that the evolution of the plastic part of the strain rate is collinear with the normal direction to the yield surface.

$$\boldsymbol{D}^p = \lambda \frac{\partial f}{\partial \boldsymbol{\sigma}} = \Lambda \frac{\boldsymbol{s}}{\sqrt{\boldsymbol{s} : \boldsymbol{s}}} = \Lambda \boldsymbol{N} \tag{Equ. 3.36}$$

where Λ is the consistency or flow parameter. It can be calculated using the consistency condition (Equ. 3.33). $\boldsymbol{N}$ is the outward unit normal to the yield surface.
The isotropic hardening law will complete the present constitutive formulation. It describes the evolution of the yield stress during a plastic deformation. For example, a linear isotropic hardening is written as:

$$\sigma_y(\bar{\varepsilon}^p) = \sigma_y^0 + h\bar{\varepsilon}^p \tag{Equ. 3.37}$$

where σ_y^0 is the initial yield stress, h is an hardening coefficient, and $\bar{\varepsilon}^p$ is an internal parameter, the equivalent plastic strain, defined through its rate by:

$$\dot{\bar{\varepsilon}}^p = \sqrt{\frac{2}{3}\boldsymbol{D}^p : \boldsymbol{D}^p} = \sqrt{\frac{2}{3}}\Lambda \tag{Equ. 3.38}$$

The von Mises criterion, which is written in terms of the deviatoric stress tensor, is independent of the hydrostatic pressure. The plastic strain rate (Equ. 3.36) is thus deviatoric and the trace of the elastic strain rate tensor is equal to the one of the total strain rate tensor. Considering Equ. 3.31, the pressure variation can be written as :

$$\dot{p} = K\mathtt{tr}\left(\boldsymbol{D}^e\right) = K\mathtt{tr}\left(\boldsymbol{D}\right) \tag{Equ. 3.39}$$

However, the deviatoric part of the elastic strain rate does depend on the plastic strain rate:

$$\hat{\boldsymbol{D}}^e = \hat{\boldsymbol{D}} - \hat{\boldsymbol{D}}^p = \hat{\boldsymbol{D}} - \boldsymbol{D}^p \tag{Equ. 3.40}$$

Considering Equ. 3.31 and Equ. 3.36, the deviatoric stress rate can be written as :

$$\overset{\bullet}{\boldsymbol{s}} = 2G(\hat{\boldsymbol{D}} - \Lambda \boldsymbol{N}) \tag{Equ. 3.41}$$

Finally, this set of equations (Equ. 3.33, Equ. 3.35, Equ. 3.37, Equ. 3.39 and Equ. 3.41) has to be integrated in time between time step n and time step $n+1$. It is a strain-driven problem. The strains at time $n+1$ are known[1], and a strain path has to be chosen to determine the strain rate $\boldsymbol{D}$. The increment of plastic strains has to be estimated so that Equ. 3.35 is satisfied.

We here choose to use an Updated Lagrangian Formulation, thus with a reference configuration which is the configuration at the beginning of the time step (last known equilibrated configuration), and kinematic quantities such as $\boldsymbol{F}, \boldsymbol{R}, \boldsymbol{U}$ are computed over the time step. We also use a corotational frame whose rotation is linked to $\boldsymbol{R}$ (see [209, 210] for details), thus with a corotational strain rate freed from rotation effects (using Equ. 3.5, Equ. 3.6, and Equ. 3.7 in a corotational frame):

$$\begin{aligned}
\boldsymbol{D} &= \rho^T \frac{1}{2}\left[\boldsymbol{L} + \boldsymbol{L}^T\right]\rho = \rho^T \frac{1}{2}\left[\overset{\bullet}{\boldsymbol{F}}\boldsymbol{F}^{-1} + \boldsymbol{F}^{-T}\overset{\bullet}{\boldsymbol{F}}^T\right]\rho \\
&\overset{(\boldsymbol{R}\boldsymbol{R}^T=\boldsymbol{I})}{=} \rho^T \boldsymbol{R}\frac{1}{2}\left[\overset{\bullet}{\boldsymbol{U}}\boldsymbol{U}^{-1} + \boldsymbol{U}^{-T}\overset{\bullet}{\boldsymbol{U}}^T\right]\boldsymbol{R}^T\rho \\
&\overset{(\rho^T\boldsymbol{R}=\boldsymbol{I})}{=} \frac{1}{2}\left[\overset{\bullet}{\boldsymbol{U}}\boldsymbol{U}^{-1} + \boldsymbol{U}^{-T}\overset{\bullet}{\boldsymbol{U}}^T\right]
\end{aligned}$$

Finally, we assume an exponential map of $\boldsymbol{U}$ over a time step:

$$\boldsymbol{U}(t) = e^{\boldsymbol{Cste}(t-t_n)/\Delta t}$$

with $\boldsymbol{Cste} = \boldsymbol{E}^N_{n+1}$ as $\boldsymbol{U}(t_{n+1}) = e^{\boldsymbol{Cste}}$.
Therefore, the corotational strain rate is written as:

$$\boldsymbol{D} = \frac{\boldsymbol{E}^N_{n+1}}{t_{n+1} - t_n} = \frac{\ln \boldsymbol{U}_{n+1}}{t_{n+1} - t_n} \tag{Equ. 3.42}$$

[1] Actually, they are iteratively evaluated inside the global Newton-Raphson loop of the finite element algorithm.

The time integration is done through an elastic predictor/plastic corrector (radial return) algorithm[1] in a time-step procedure where the stress tensor at time $n+1$ is computed from the stress tensor at time n in a iterative setup (Newton-Raphson algorithm) as:

$$\left\{ \begin{array}{rcl} \boldsymbol{s}_{n+1} & = & \boldsymbol{s}^e - 2G\Gamma \boldsymbol{N}_{n+1} \\ p_{n+1} & = & p^e = p_n + K\Delta \mathtt{tr}\left(\boldsymbol{E}^N_{n+1}\right) \end{array} \right. \tag{Equ. 3.43}$$

where $\Gamma = \int_{t_n}^{t_{n+1}} \Lambda \, dt$ and $\boldsymbol{s}^e$ is the elastic predictor of the deviatoric stress. It is computed as $\boldsymbol{s}^e = \boldsymbol{s}_n + 2G\hat{\boldsymbol{E}}^N_{n+1}$.
The unknown parameter Γ is computed through a Newton-Raphson algorithm so that:

$$\left\{ \begin{array}{rcl} \Gamma^{i+1} & = & \Gamma^i + \Delta\Gamma \\ r^i & = & \sigma^{vM}_{eq}(\Gamma^i) - \sigma_y(\Gamma^i) \\ \Delta\Gamma & = & -\dfrac{r^i}{\left.\dfrac{\partial \sigma^{vM}_{eq}}{\partial \Gamma}\right|_{\Gamma=\Gamma^i} - \left.\dfrac{\partial \sigma_y}{\partial \Gamma}\right|_{\Gamma=\Gamma^i}} \end{array} \right.$$

These iterations on the value of Γ end when the value of the residue r^{i+1} is below a given tolerance (a user defined precision): $\dfrac{r^{i+1}}{\sigma_y(\Gamma^{i+1})} < TOL_\Gamma$. The default value for this precision is typically chosen at 10^{-8}.
In the case of a linear isotropic hardening, the analytical solution reads (see [210] for details):

$$\Gamma = \frac{\sqrt{\boldsymbol{s} : \boldsymbol{s}} - \sqrt{\frac{2}{3}}\sigma_y^{(n)}}{2G + \frac{2}{3}h} \tag{Equ. 3.44}$$

where $\sigma_y^{(n)}$ is the yield limit at the beginning of the time step n.

Once these equations have been integrated in the corotational frame, all the (tensorial) quantities are rotated back in the fixed Cartesian frame by using the inverse of Equ. 3.26.

[1] During the elastic predictor step, it is assumed that $\boldsymbol{D} = \boldsymbol{D}^e$ and $\boldsymbol{D}^p = 0$ while for the plastic correction (if needed, i.e. if the elastic predictor does not satisfy the $f \leq 0$) $\boldsymbol{D} = 0$ and $\boldsymbol{D}^p = \Lambda \boldsymbol{N}$

3.4 Continuum Damage Mechanics

> *Drawing a parallel between bone remodeling and continuum damage mechanics may seem surprising. However, from the continuum constitutive modeling perspective, the two fields have a great deal in common. In both cases the material of interest is exposed to a large number of loading cycles over the period of interest. The material response within a given loading cycle can be accurately modeled as a linear elastic solid, and thus is not of great interest. Therefore, the problem becomes one of describing the time history or evolution of the elastic stiffness as it responds nonlinearly to the applied loading. In fact, the fundamental distinction is that a damaging material loses stiffness when it is overloaded and experiences no change when it is underloaded, bone is able to "heal" via remodeling and tends to gain stiffness when overloaded-up to a point-and lose stiffness when underloaded. It must be strongly emphasized that this analogy is only drawn in so far as the two processes can be modeled by similar mathematical formulations. In no way is this a proposal that the remodeling response is mediated by damage accumulation in the bone matrix and neither is it a proposal to the contrary.*
>
> *C.R. Jacobs,* Numerical simulation of bone adaptation to mechanical loading, *1994 [117]*

As well as remodeling models are either phenomenological or based on the knowledge of the microscopic behavior (mechanobiological approach to remodeling-see section 4.2), one can find two main approaches to damage mechanics. Either a phenomenological one, continuum damage mechanics, or a micromechanics based approach to damage such as the Gurson-Tvergaard-Needlemann (GTN, [96]) approach[1]. In this work, we will use the phenomenological approach of damage to represent remodeling. This section therefore present the principles of the Continuum Damage Mechanics theory.

3.4.1 Isotropic Damage

Continuum damage models based on the effective stress space were introduced by Kachanov (1958) and later by Rabotnov (1968) [as cited in 146, 271] who were the first to introduce, for the isotropic case, a one-dimensional damage variable which may be interpreted as the effective surface density of microdamage per unit volume. To illustrate their concept, consider a uniform bar subjected to a uniaxial tensile Cauchy stress, σ (see Fig 3.6). The cross-sectional area of the bar in the deformed damaged configuration is A. The uniaxial tensile force, f acting on the bar is easily expressed using the formula $f = \sigma A$. The principles of Continuum Damage Mechanics (CDM) introduce a fictitious undamaged configuration (called the effective configuration) of the bar. In this configuration the damage is removed from the

[1] GTN models define the damage variable as the void fraction, its evolution is due to the nucleation, growth and coalescence of these voids.

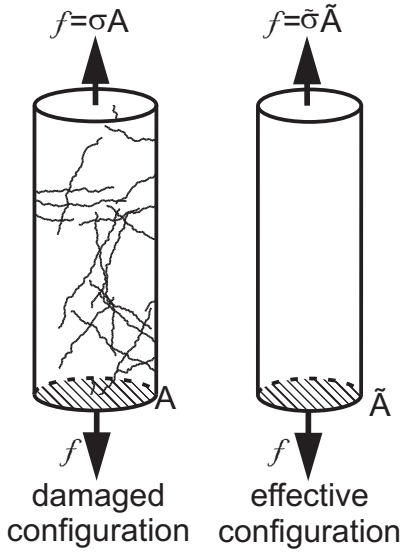

FIGURE 3.6: *Introduction of the effective state concept (adapted from [271])*

bar. The effective deformed cross-sectional area of the bar in this configuration is denoted by $\tilde{A}$ and the effective uniaxial stress is $\tilde{\sigma}$. The bars in both the damaged and the effective undamaged configurations are subjected to the same tensile force f. Therefore, considering the effective undamaged configuration, we obtain $f = \tilde{\sigma}\tilde{A}$. Equaling the two expressions of f obtained from both configurations, one obtains the following expression for the effective uniaxial stress $\tilde{\sigma}$:

$$\tilde{\sigma} = \sigma/(1-\phi) \text{ where } \phi = (A-\tilde{A})/A \qquad \text{(Equ. 3.45)}$$

Equ. 3.45 may be interpreted as the average stress acting on an effective area of the material [146]. In order to give it a general physical meaning, it is necessary to use the corresponding damage-free material (i.e. virgin material) to represent the "effective" concept of Equ. 3.45 for a damaged material, using a direction independent damage variable d, giving:

$$\tilde{\boldsymbol{\sigma}} = \frac{\boldsymbol{\sigma}}{1-d} \qquad \text{(Equ. 3.46)}$$

The damage variable d is then an internal variable related to the effective density of cracks or cavities at each point (for the isotropic case) or at each point and in each direction (anisotropic case), that is, to the microstructure. The CDM theory is thus a phenomenological description of damage. The damage variable is usually normalized, as in Equ. 3.46, in such a way that the value $d = 0$ corresponds to the undamaged material, while $d = 1$ represents the local rupture state or local failure of the mechanical component.

Strain energy equivalence

The strain energy equivalence approach of damage (subscript *see*) relates the stress level in the damaged material with the stress in the undamaged material that leads to the same strain energy density. Therefore the constitutive law in the effective configuration has to be

written in such a way that the strain energy density in this configuration is the same as the one in the actual configuration:

$$U = \frac{1}{2}\tilde{\boldsymbol{\sigma}} : \tilde{\boldsymbol{\varepsilon}}_{see} = \frac{1}{2}\boldsymbol{\sigma} : \boldsymbol{\varepsilon} \tag{Equ. 3.47}$$

One can therefore write, using Equ. 3.46

$$\tilde{\boldsymbol{\varepsilon}}_{see} = (1 - d_{see})\boldsymbol{\varepsilon}$$

And the constitutive law in the effective stress for small strain elasticity in the actual configuration is thus written:

$$\tilde{\boldsymbol{\sigma}} = \mathbb{H}^o : \tilde{\boldsymbol{\varepsilon}}_{see} \tag{Equ. 3.48}$$

where $\mathbb{H}^o$ is Hooke's fourth order elasticity tensor for the undamaged material (hence the exponent ^{o}):

$$\mathbb{H}^o = K\boldsymbol{I} \otimes \boldsymbol{I} + 2G\mathbb{1} \tag{Equ. 3.49}$$

This effective constitutive equation can also be written:

$$\boldsymbol{\sigma} = \mathbb{H}_{see} : \boldsymbol{\varepsilon} \tag{Equ. 3.50}$$

where $\mathbb{H}_{see} = (1 - d_{see})^2\mathbb{H}^o$ is Hooke's fourth order elasticity tensor for the damaged material. Therefore, the stiffness variation can be computed as

$$\dot{\mathbb{H}}_{see} = -2(1 - d_{see})\dot{d}_{see}\mathbb{H}^o \tag{Equ. 3.51}$$

Strain equivalence

The strain equivalence approach of damage (subscript *se*) relates the stress level in the damaged material with the stress in the undamaged material that leads to the same strain[1]. One can therefore write, in small strain elasticity:

$$\tilde{\boldsymbol{\sigma}} = \mathbb{H}^o : \boldsymbol{\varepsilon} \tag{Equ. 3.52}$$

This equation can also be written :

$$\boldsymbol{\sigma} = \mathbb{H}_{se} : \boldsymbol{\varepsilon} \tag{Equ. 3.53}$$

where $\mathbb{H}_{se} = (1 - d_{se})\mathbb{H}^o$ is Hooke's fourth order elasticity tensor for the damaged material. Therefore, the stiffness variation can be computed as

$$\dot{\mathbb{H}}_{se} = -\dot{d}_{se}\mathbb{H}^o \tag{Equ. 3.54}$$

The damage definition used in the strain equivalence approach yields to a different damage value than the previous one. In the strain equivalence approach, for an isotropic material and a 1D problem, damage can be related to Young's modulus as $d_{se} = 1 - \frac{E}{E_0}$ while for the strain energy equivalence approach, $d_{see} = 1 - \sqrt{E/E_0}$.

[1] This assumes the deformation behavior is affected by damage only through the effective stress.

Thermodynamics of damage in small strains

Taking (athermal) small strains in consideration, an assumption is made on the total strain in such a way that it is split into an elastic part and a plastic part :

$$\boldsymbol{\varepsilon} = \boldsymbol{\varepsilon}^e + \boldsymbol{\varepsilon}^p$$

The state variables are the strain field ($\boldsymbol{\varepsilon}$, an observable variable), the plastic deformation ($\boldsymbol{\varepsilon}^p$, an internal variable), the damage (d, an internal variable) and the variables associated with hardening (q, internal variables).
The state potential is considered by Lemaitre and Desmorat [146] as being the free energy: $\Psi(\boldsymbol{\varepsilon}, \boldsymbol{\varepsilon}^p, d, q)$. With an elastoplastic approach where the strain decomposition is assumed, the strain field and plastic strain dependence of the free energy is simply given by an elastic deformation dependence, hence $\Psi(\boldsymbol{\varepsilon}^e, d, q)$. Its variation can therefore be written:

$$\dot{\Psi} = \frac{\partial \Psi}{\partial \boldsymbol{\varepsilon}^e} : \dot{\boldsymbol{\varepsilon}}^e + \frac{\partial \Psi}{\partial d}\dot{d} + \frac{\partial \Psi}{\partial q}\dot{q}$$

The Clausius-Duhem inequality (second law of thermodynamics: $\boldsymbol{\sigma} : \dot{\boldsymbol{\varepsilon}} - \dot{\Psi} \geq 0$) therefore becomes:

$$\left(\boldsymbol{\sigma} - \frac{\partial \Psi}{\partial \boldsymbol{\varepsilon}^e}\right) : \dot{\boldsymbol{\varepsilon}}^e + \boldsymbol{\sigma} : \dot{\boldsymbol{\varepsilon}}^p - \frac{\partial \Psi}{\partial d}\dot{d} - \frac{\partial \Psi}{\partial q}\dot{q} \geq 0$$

In this formulation, the Cauchy stress is used and not the effective one as the effective stress is a stress on a virtual configuration that does not follow the laws of conservation defined in section 3.2. The Clausius-Duhem inequality has to be verified $\forall \dot{\boldsymbol{\varepsilon}}^e$, therefore, one can write:

$$\boldsymbol{\sigma} = \frac{\partial \Psi}{\partial \boldsymbol{\varepsilon}^e}$$

The Cauchy stress (and not the effective stress) tensor is therefore the variable which is the energy conjugate of the elastic strain field.
The other derivatives define the conjugated variables as follows:

$$Y = \frac{\partial \Psi}{\partial d}; \qquad Q = \frac{\partial \Psi}{\partial q}$$

Finally, the Clausius-Duhem inequality therefore shows the mechanical dissipation is positive:

$$\boldsymbol{\sigma} : \dot{\boldsymbol{\varepsilon}}^p - Y\dot{d} - Q\dot{q} \geq 0$$

Lemaitre and Desmorat [146] then assumes the existence of a dissipation potential, a convex scalar function of the conjugated variables $\varphi(\boldsymbol{\sigma}, Y, Q)$. The evolution laws are then written assuming the normality rule of generalized standard materials:

$$\dot{\boldsymbol{\varepsilon}}^p = \Lambda \frac{\partial \varphi}{\partial \boldsymbol{\sigma}}; \qquad \dot{d} = \Lambda \frac{\partial \varphi}{\partial Y}; \qquad \dot{q} = -\Lambda \frac{\partial \varphi}{\partial Q}$$

Practically, elastoplastic laws with damage use a dissipation potential φ which is a sum of the plastic dissipation potential (related to the yield criterion, f) and a damage dissipation potential, φ_d. The (associated) normality rule therefore yields (using one internal variable, the damaged equivalent plastic strain, $q = \bar{\varepsilon}^{p,d}$, associated to the yield limit of the material, $Q = \sigma_y$):

$$\dot{\boldsymbol{\varepsilon}}^p = \Lambda \frac{\partial f}{\partial \boldsymbol{\sigma}}; \qquad \dot{d} = \Lambda \frac{\partial \varphi_d}{\partial Y}; \qquad \dot{q} = -\Lambda \frac{\partial f}{\partial Q} = \Lambda$$

Damaged elastoplasticity

When coupling isotropic damage and plasticity, one needs to express the plastic criterion as well as the hardening laws in terms of damaged variables (details can be found in Desmorat and Otin [59], Lemaitre and Desmorat [146] for the small strains version or in Jeunechamps [122] for an extension to finite strains). For instance, using a von Mises criterion in a strain equivalence approach of damage leads to an equivalent stress defined as:

$$\tilde{\sigma}_{eq} = \sqrt{\frac{3}{2}\tilde{\boldsymbol{s}} : \tilde{\boldsymbol{s}}} = \frac{\sigma_{eq}}{1 - d_{se}} \qquad \text{(Equ. 3.55)}$$

Using an isotropic hardening for the yield limit gives:

$$\sigma_y = \sigma_y^0 + h\bar{\varepsilon}^{p,d} = \sigma_y^0 + h\frac{\bar{\varepsilon}^p}{1 - d_{se}} \qquad \text{(Equ. 3.56)}$$

with $\bar{\varepsilon}^{p,d}$ the damaged equivalent plastic strain.

3.4.2 Anisotropic Damage

To ensure a more general formulation of the principles of damage mechanics, the case of anisotropic damage can also be assumed. In this case different levels of damage are related to the principal directions of the physical space, and thus a simple scalar damage parameter is no longer sufficient to quantify damage in all directions. Instead, the anisotropic phenomenon of the damage distribution in the material is interpreted using a symmetric second-order damage tensor, $\boldsymbol{d}$. It has to be noticed however that assuming a linear relation between effective and Cauchy stress tensors should be described through the use of a fourth order tensor $\mathbb{D}$. Such a tensor is indeed the general representation of an operator that transforms the second order tensor $v_i n_j \delta S$ (defining the reference geometrical configuration with **n** the normal to the surface δS and v a reference vector) to a second order tensor defining the damaged configuration: $v_k \tilde{n}_l \delta \tilde{S}$ (see Fig. 3.7): $v_i n_j \delta S = \mathbb{D}_{ijkl} v_k \tilde{n}_l \delta \tilde{S}$
However, such a tensor is difficult to use and is not often necessary [146]. Defining an effective stress with a second order damage tensor is therefore an approximation of the exact effective stress.
The concept of effective stress in the case of anisotropic damage is more complex in order to ensure we keep the physical meaning of damage and stay compatible with the thermodynamics. The effective stress tensor is defined is such a way that it is a function of the second

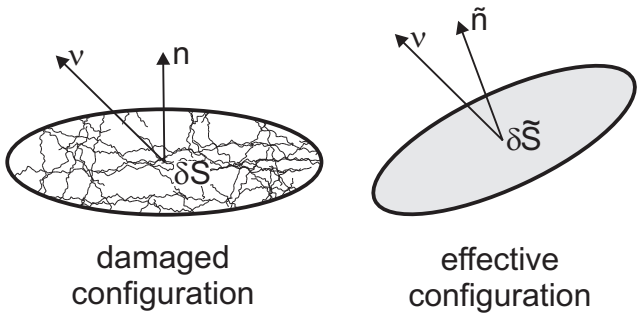

FIGURE 3.7: *Introduction of the effective state concept for anisotropic damage (adapted from [146])*

order damage variable and of the stress tensor. To keep a linear relationship between the effective and actual configurations, one often writes the effective stress so that

$$\tilde{\boldsymbol{\sigma}} = \mathbb{M}(\boldsymbol{d}) : \boldsymbol{\sigma}$$

Several definitions of $\mathbb{M}$ can be found in the literature [1, 146–148, 176, 271], we will here use the one proposed by Lemaitre *et al.* [147][1]:

$$\mathbb{M} = \boldsymbol{H}\underline{\otimes}\boldsymbol{H} - \frac{1}{3}\left(\boldsymbol{H}^2 \otimes \boldsymbol{I} + \boldsymbol{I} \otimes \boldsymbol{H}^2\right) + \frac{1}{9}\mathtt{tr}\left(\boldsymbol{H}^2\right)\ \boldsymbol{I} \otimes \boldsymbol{I} + \frac{1}{3}\frac{\boldsymbol{I} \otimes \boldsymbol{I}}{1 - \eta d^H} \qquad \text{(Equ. 3.57)}$$

where $\boldsymbol{H}$, the effective damage tensor, is defined in such a way that $\boldsymbol{d} = \boldsymbol{I} - \boldsymbol{H}^{-2}$, d^H is the hydrostatic damage ($d^H = \mathtt{tr}\,(\boldsymbol{d})\,/3$), and η is an hydrostatic sensitivity parameter[2]
It has the properties of

- being symmetric, therefore resulting in a symmetric effective stress (using a simple extension of the isotropic definition : $M_{ijkl} = \delta_{il}[\boldsymbol{I} - \boldsymbol{d}]^{-1}_{jk}$ does not lead to a symmetric result);
- not dependent of the Poisson's ratio value;
- compatible with the thermodynamics in a small strain approach: existence of a state potential and a principle of strain equivalence (the symmetrization $\mathbb{M} = \boldsymbol{I}\underline{\otimes}(\boldsymbol{I} - \boldsymbol{d})^{-1} + (\boldsymbol{I} - \boldsymbol{d})^{-1}\underline{\otimes}\boldsymbol{I}$ is not derived from a potential);

This list of requirements is also fulfilled by a fourth order damage tensor written as:

$$M_{ijkl} = (\boldsymbol{I} - \boldsymbol{d})^{-1/2}_{ik}(\boldsymbol{I} - \boldsymbol{d})^{-1/2}_{jl} \qquad \text{(Equ. 3.58)}$$

However, Lemaitre *et al.* [147] propose to also use a tensor (Equ. 3.57) able to represent different effects of damage on the hydrostatic and deviatoric stresses by means of an hydrostatic sensitivity parameter, η (this cannot be done using Equ. 3.58).

[1] For second order tensors $\boldsymbol{a}$ and $\boldsymbol{b}$, the product $A_{ijkl} = 1/2(a_{ik}b_{jl} + a_{il}b_{jk})$ is noted $\mathbb{A} = \boldsymbol{a}\underline{\otimes}\boldsymbol{b}$.

[2] $\eta \approx 3$ for metals [146] and taken to be equal to the degree of anisotropy (DA, defined in section 2.3) in the case of bone.

We can therefore write, using Equ. 3.57:

$$\tilde{\boldsymbol{\sigma}} = \mathtt{dev}\left(\boldsymbol{H}\boldsymbol{s}\boldsymbol{H}\right) + \frac{p}{1-\eta d^H}\boldsymbol{I} = \tilde{\boldsymbol{s}} + \tilde{p}\boldsymbol{I}$$

As for the isotropic case, both a strain energy equivalence approach or a strain equivalence one can be assumed for the constitutive law. In the first case, $\tilde{\boldsymbol{\varepsilon}}_{see}$ has to be chosen in such a way that $\boldsymbol{\sigma} : \boldsymbol{\varepsilon} = \tilde{\boldsymbol{\sigma}} : \tilde{\boldsymbol{\varepsilon}}_{see}$. Depending on the definition of the effective stress, computing the effective strain can therefore not be straightforward.

Exactly as it is done in the isotropic damage framework, one can show that, when defining $\boldsymbol{Y}$ as the energy conjugate of $\boldsymbol{H}$ ($\boldsymbol{Y} = \frac{\partial \Psi}{\partial \boldsymbol{H}}$), the Clausius-Duhem inequality is written

$$\boldsymbol{\sigma} : \dot{\boldsymbol{\varepsilon}}^p - \boldsymbol{Y} : \dot{\boldsymbol{H}} - Q\dot{q} \geq 0$$

The effective damage tensor evolution can thus be defined as:

$$\dot{\boldsymbol{H}} = \Lambda \frac{\partial \varphi_d}{\partial \boldsymbol{Y}} \qquad \text{(Equ. 3.59)}$$

with φ_d a damage dissipation potential.

Chapter 4
Biomechanics of Bone Remodeling in Orthodontics

Biomechanics is the study of the structure and function of biological systems by means of the methods of mechanics.

- Hatze, Herbert. (1974) The meaning of the term biomechanics.

This chapter presents the mechanical role of the main tissues involved in orthodontics tooth movement and the way this mechanical behavior is modeled in the literature, with an emphasis on bone remodeling theories as well as bone tissue constitutive modeling. This literature review is by no means exhaustive but presents the various modeling techniques used in orthodontics and dentofacial orthopedics, especially in the last two decades.

Chapter Overview

4.1 Models in Orthodontics

Within the dentistry related fields, mathematical models are increasingly used for research and treatment planning. We will here present the tendencies in mathematical models (either numerical FE models or analytical models) for tooth movement and in particular the constitutive models used for dental tissues. Numerous contributions also exist focusing on implant related problems, which are not considered here. We will also not treat the modeling of braces and force apparatuses used to obtain a given tooth movement but only detail the way the dental tissues are handled in initial or long term tooth movement models, considering only the forces applied to the teeth and not the means to apply these forces.

4.1.1 Dental Tissues and Periodontal Ligament Constitutive Modeling

The gingiva

The mechanism responsible for the asymmetrical behavior of the tooth when rotated around its main axis is sometimes assumed to be in the gingival tissue [54]: the complex fibrous structure of gingiva, that envelops the entire dental arch and provides an additional anchoring to the teeth, tends to contract. This creates a force acting on the different proximal teeth, producing an internal momentum and asymmetries.
Most studies about the gingiva are experimental, mostly on the response of the gum to certain types of toothbrushes or the materials used for dental impression. Almost no studies about the mechanical characterization of the gum can be found in the literature. However, as the gum is mainly composed of collagen fibers, it most probably has a viscous response [223]. In general, finite element studies on the movements of the dental arch do not account for the gum, thus assuming that its mechanical response is not predominant in the movement of the tooth.

The tooth materials

The enamel The enamel covering the crown is a highly mineralized tissue (about 99% of minerals against less than 1% organic matter). It is the hardest tissue in the body.
In general, the enamel is seen as a linear elastic material. Most studies about the mechanical response of enamel focus on its wear behavior [144, 151, 231, 283] as it is a material subject to several external constraints.

The cementum Few studies focus on characterizing the cementum, either mechanically or histologically. The group of Darendelier [36, 158, 159, 226] provides a comprehensive body of work on the physical characteristics of cementum.

The dentin Dentin tissue is reinforced by radial microscopic tubules. These tubules are filled with fluid and give the dentin a viscoelastic character. Since the mid-1970's [67], studies

have revealed the viscoelastic nature of the dentin. More recently, various studies [7, 120, 199], mainly experimental, proposed mechanical models of the dentin, considering it as a non-homogeneous and anisotropic material.

The dental pulp Studies of tooth movement in general do not account for the presence of dental pulp, or of the pulp chamber. No studies were actually found on the mechanical characterization of the dental pulp.

Even though the dental tissues are very different, as the tooth is composed mainly of two hard tissues (dentin and enamel), it is often modeled as consisting of one elastic material with a Young's modulus of about 19 GPa [121, 242, 250]. When the enamel and dentin are separated [such as in 27], Young's moduli are respectively 80 and 18 GPa . The Poisson's ratio is, regardless of the proposed study, taken at 0.3.

The periodontal ligament

The periodontal ligament connects the cementum to the alveolar bone. It is made of loose connective tissue, vascularized and innervated, traversed by numerous fibers. It allows for the maintenance of tooth/bone relationships, compensating dental abrasion of the enamel at the occlusal surfaces and contact points. It also stimulates the alveolar bone through its fibers. Finally, it regulates the movements of chewing through its sensory receptors.
The periodontal ligament plays an important role in the movement of the teeth. Indeed, its loose connective tissue serves as a buffer zone between the tooth and bone (two tissues much stiffer than the ligament). It is then responsible for the mobility of the tooth in its socket and transmits the force applied to the tooth to stresses applied to the bone. For these reasons, many studies have experimentally examined the mechanical behavior of this ligament. This characterization is adjusted by means of experimental tests on either human or animal (mainly bovine - considered equivalent to the human's [232]) periodontal ligament.
For instance, Rees and Jacobsen [224], Tanne *et al.* [247] showed that the mechanical response of the periodontal ligament was different for different dental forces. They showed an increase of the ligament stiffness with the tooth displacement, therefore proving the non-linearity of the periodontal ligament mechanical behavior. Following this, Ihlow *et al.* [115], Pini *et al.* [204, 205], Yoshida *et al.* [280] experimentally extracted stress/strain curves, confirming this non-linearity, which is furthermore different in tension and compression. Cronau *et al.* [54], Dorow *et al.* [64, 65] also showed that not only the PDL had to be considered as non-linear but also as time-dependent and demonstrating an hysteresis phenomenon in loading/unloading tests. Moreover, Komatsu *et al.* [134] and Pini *et al.* [205] showed the hysteresis in compression was much higher than in tension, suggesting that the dissipated energy was higher in compression than in tension.

Considering those experimental data, several constitutive models of the PDL can be found in the literature. These laws are generally bilinear elastic (and thus unable to represent any dissipation or time-dependence in the mechanical response) but there are also studies taking into account the fibrous tissue component (anisotropy) of the PDL or its non-linear (visco-)elastic behavior. The use of non-linear mechanical properties in PDL simulations provides more precision and reliability of the calculated stresses and strains for a wider range of tooth movements than in the case of linear material properties.

Elasticity Even though the non-linearity of the PDL is experimentally well established, several studies use an isotropic linear elastic model for the PDL, defined by two parameters, Young's modulus and Poisson's ratio. Most studies agree on the almost incompressible behavior of the PDL, using a Poisson's ratio $\nu \in [0.45, 0.49]$. However the value used for Young's modulus spreads over a wide range from 10^{-2} to 10^{2} MPa, i.e. over four orders of magnitude [5, 71, 112, 121, 197, 208, among others].
Such a wide range can be explained in two ways [230]. First a conversion error in a widely cited paper [274][1] that used a modulus in MPa while citing a numerical value in kN/m^2 (i.e. in kPa). Secondly, some authors used values determined to fit the results of a finite element analysis of tooth movement to experimental results [123, 224, 248]. As these studies were not performed on PDL analysis only, it might not only be the PDL parameters that needed to be identified with an inverse analysis but also all the other assumptions (either material modeling, or the geometry used or the imposed boundary conditions and even the finite element formulation - most often in small strains analysis while the PDL deforms beyond 50%). The validity of the results produced by these studies remains at least questionable in view of the fact that experimentally determined values exist and differ by order(s) of magnitude. Some authors also choose as Young's modulus a value representative of the average of the tangential modulus of the experimental data, therefore not representative anymore of the behavior at small strains as should be for a Young's modulus. A Young's modulus around 0.1 MPa is most likely to represent best the linear part of the PDL's mechanical behavior.
Bilinear elastic models are also found [24, 27, 65, 126, 211, 218, 225, 285]. They are defined with three values (or six when these values are different in tension or compression): Young's modulus (found between 0.05 and 0.15 MPa), a limit value of about 7% strains in tension tests (with the exception of [65] where a value of 62% is found) and a tangential modulus, 10 to 40 times larger than the Young's modulus (see Fig. 4.1).
Finally, Cattaneo *et al.* [34], Verna *et al.* [268] introduce a multi-linear model, different in tension and in compression.

Hyperelasticity Natali *et al.* [185, 186], Pietrzak *et al.* [202] consider the PDL as an hyperelastic material (Mooney-Rivlin material with, for Natali *et al.* [185, 186], reinforced fibers,

[1] The paper by Weinstein *et al.* is cited "only" 43 times (citations on the 20th of June 2012 by Google Scholar) but 17 of these citing papers are then cited over 30 times each (5 of which are cited over 200 times each).

expressed in an Ogden-type formulation). Natali *et al.* [185, 186] showed that the estimated strain corresponds well with the in vivo experimental data by Parfitt [198].

Viscoelasticity Aversa *et al.* [8], Menicucci *et al.* [175], Qian *et al.* [218], Slomka *et al.* [239], Toms *et al.* [251] all propose models accounting for a time dependency through the use of viscoelastic models using up to four time-constants. These models are either generalized Maxwell models [175, 218, 251] or a fitted Prony serie of the Bulk modulus [8].

Fibrous behavior Geramy [87] proposes a model considering a PDL composed solely of linear oriented fibers (modeled as spring elements which respond only in tension-compression and are never subject to torsion, shear or bending). Melsen [171], Provatidis [214], Qian *et al.* [217] propose a model considering a PDL solely composed of non-linear oriented fibers (also modeled as - non-linear - springs elements). Meyer *et al.* [178] propose a model considering the PDL composed of a linear elastic matrix reinforced by linear fibers.

Poroelasticity Finally, van Driel *et al.* [255] use a poroelastic model for the PDL, with a constant porosity. The poroelastic model allows to consider a time-dependent behavior through the fluid flow inside a porous matrix.

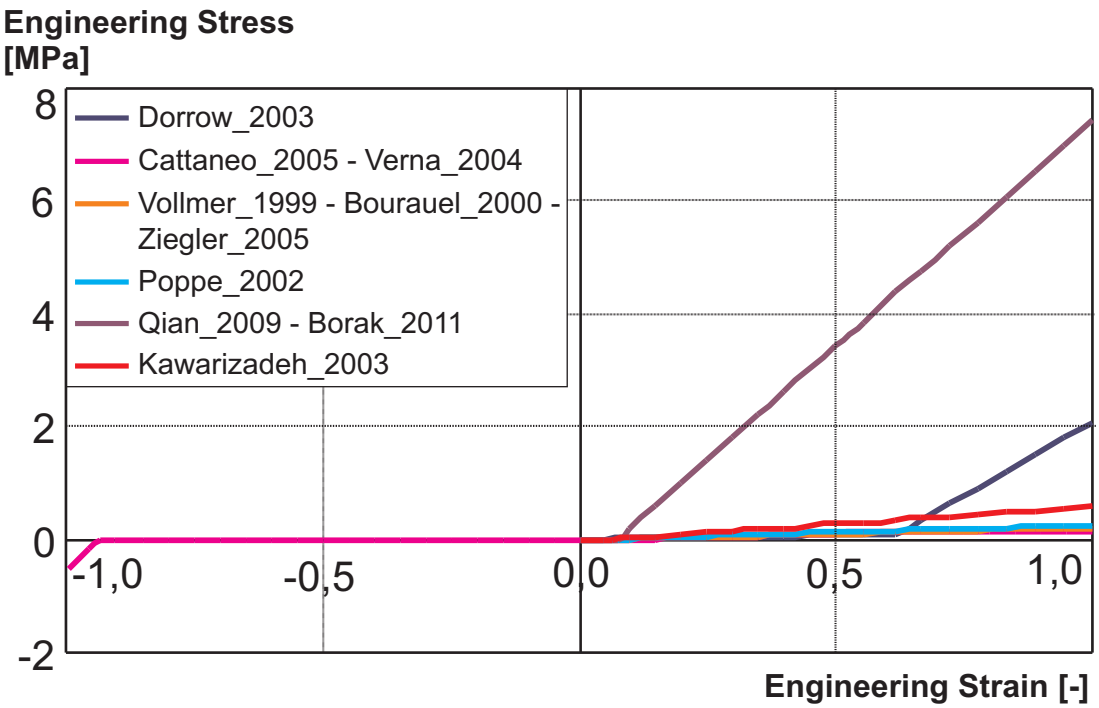

FIGURE 4.1: *Periodontal ligament: bi-(multi-)linear elastic models [24, 27, 34, 65, 127, 211, 218, 268, 285].*
In the literature, only the model proposed by Cattaneo et al. *[34], and Verna* et al. *[268] gives different behavior in tension and compression, it is therefore the only one for which stress values are given for negative strain values.*
The data is labeled after the name of the first author of the paper it comes from, followed by the year of publication.

4.1.2 Orthodontic Tooth Movement (OTM) Models

Initial tooth movement

Finite element models The finite element (FE) method is used in orthopedic biomechanics since the early 1970's [see 213, for a review of the early literature] to evaluate the stress levels in human bones. Since then, this method has been applied increasingly to the analysis of efforts in the bones, bone-prosthesis structures, fixations systems, and various other tissue types. The objectives of these early studies were to assess the relationships between function and morphology of the structures supporting the load, and optimize the design and techniques for fixing implants. The method is now well established as a basic tool for research and design in orthopedic biomechanics.
The FE method was introduced at the same time in the fields of dentistry, orthodontics and dentofacial orthopedics, to become an important tool for research in these areas. While the FE method is now widely used in dentistry and related fields, linear models are still the most common ones. Non-linearities in FE modeling can be one of the following three types:

- non-linear material behavior-more and more often used, especially for the PDL;
- geometrical non-linearities accounting for large displacements, strains and rotations-starting to be used as FE commercial packages nowadays handle finite deformations problems, but often not to the user's deliberate choice;
- and change of interrelations between objects such as contact or fracture-most often not present in dentistry related models [272] while contact phenomena are probably important at least in implant related problems.

The first FE models encountered in orthodontics were 2D or axisymmetric models and gradually moved to 3D models in the late 80's. Finite element studies in the literature are either predictive studies of tooth movement, the mechanical properties used in the constitutive models are then assumed to be correct, or use optimization procedures to identify the parameters of the assumed constitutive laws to experimental results (such as the amount of tooth movement). Most studies deal with tipping of the tooth or bodily movement (translation).

The geometry used for finite element analysis can be of three types (the last one emerging since the last ten years):

- idealized geometry, the root is often parabolic and the alveolar bone modeled as a surrounding box, the periodontal ligament has a constant thickness;
- parametrized geometry, based on standard anatomy;
- patient-specific geometry, reconstructed either from photographs (digital or digitized) of anatomical sections, or images from CT-scan (or μ CT).

Early models in the field of orthodontics were mainly directed to study the initial movement of the tooth in its socket (no bone remodeling included) following the implementation of a system of forces and moments by means of braces. Most current studies, although not mentioning it directly, still follow the same principle, using a geometry and a system of forces more and more complex.
Within the initial tooth movement models, mainly fully linear elastic homogeneous isotropic models are used [121, 132, 179, 207, 217, 248, among many others]. However, one can also find models with non homogeneous alveolar bone, where the Young's modulus is related to the bone density [35, 171]. Additionally, some studies assume an orthotropic behavior for alveolar bone [8, 23, 279]. Finally a number of models consider a non-linear material behavior for the periodontal ligament such as described in section 4.1.1.

Analytical models The studies involved in OTM usually are finite element based studies. However, from the concept of center of resistance and center of rotation [240], some authors characterize this movement through other modeling techniques.
Hayashi *et al.* [101] describe the tooth movement by a finite helical axis analysis. Provatidis [215] proposed an analytical model to describe the mechanical behavior of the periodontal ligament for a tooth of paraboloid shape, during translation. The PDL was assumed to be linear elastic, both the tooth and surrounding bone were rigid. van Schepdael [262] extended this model to mutli-rooted teeth and elliptic paraboloid shape of the roots as well as all types of tooth movement.

Long-term tooth movement

In order to model the tooth movement over time, it is necessary to account for bone remodeling that occurs in the alveolar bone.
Experience shows that the initial movement, mainly due to the elasticity of the periodontal ligament, is responsible for more than 80% of the movement of the tooth in the first week of treatment. Then, a stabilization of the tooth position is observed (for one to two weeks) to finally obtain a further movement due to bone resorption and bone apposition (respectively on the sites in compression and tension in the alveolar bone). Under the system of loads applied, the tooth will stabilize after a certain time in its new equilibrium position.
The laws of remodeling encountered in orthodontics FE modeling induce a change in the displacement of the tooth based on stress or strain in the bone or periodontal ligament. Kawarizadeh *et al.* [127] showed, by comparing the results of a finite element analysis with the distributions of osteoclast cells, that the strain in the periodontal ligament is related to bone remodeling.

Remodeling algorithms in orthodontics FE models usually involve an update of displacement (in addition to that due to external forces) or of forces based on an empirical bone remodeling law: The stimulus for remodeling is either the strain energy density [152], strain

dependent [26, 27, 85, 161, 219, 233], or stress dependent [130, 131, 133]. Remodeling algorithms usually run under an explicit time integration scheme: during a FE computation step, the displacement is computed to get an equilibrium as a function of the applied forces, the remodeling stimulus is then computed, and finally an update of the displacement is performed, without ensuring it results in a new mechanical equilibrium.
Provatidis [216] considers that the periodontal ligament, although elastic, has to maintain a constant thickness. He therefore corrects the tooth displacement obtained by an FE analysis by imposing a uniform thickness of the PDL. This method is consistent with the observation that no evidence of net changes in the thickness of the PDL is observed at the end of the treatment. Soncini and Pietrabissa [241], van Schepdael [262] proposed remodeling models considering a viscous behavior (viscoelastic Maxwell models) of the bone. Cronau *et al.* [54] proposed a remodeling algorithm considering a viscous behavior (viscoelastic Maxwell model) of the PDL. Finally, Field *et al.* [70], Lin *et al.* [153] proposed remodeling laws involving an explicit local change of the bone elastic properties based on the strain level.
These last two remodeling algorithms are the only ones found in the literature that are similar to the remodeling algorithms used within the biomechanics literature that is not dentistry related (see section 4.2 for more details on these models).

4.1.3 Dento-facial Orthopedics Modeling

Since the early 1980's, finite element models of maxillary and mandible are used. One can find [see 86, 139, 157, for a review of the literature] at that time, both 2D models and 3D ones. These models use elements whose size is comparable to the macroscopic dimensions of the bones. Generally, the authors seek either to define a map of stress due to the use of an orthopedics appliance, or to calibrate muscle activation patterns on the movements of the jaw. As for modeling the movement of the jaw, a great effort is made to characterize the temporomandibular joint (TMJ) [58, 99, 137, 190]. In most cases, the type of materials used for the bone is linear elasticity. Most authors distinguish cortical bone from trabecular bone. However, the presence/absence of teeth in the cranio-facial models is variable. As for the models of the TMJ, the cartilage and the disks are modeled either as linear elastic materials or as hyperelastic ones.
One also finds models including muscle activation of the jaw, either performing an inverse dynamic analysis to compute the activity of the large amount of muscles in the face, or modeling a given number of muscles, often by applying a spring model [80, 116, 135, 136, 201] to describe muscular forces.
Finally, one also finds models of the facial bones and skull analyzing the response to external orthopedic systems [21, 246].

4.2 Bone Remodeling Models

In addition to skeletal growth and resorption of fractures, which are of temporary nature, the structure of bone is, as discussed in section 2.1, continuously maintained and adapted internally and at its surface by a sustainable process, called remodeling.
The theoretical fundamentals of numerical models describing bone remodeling derive from the observations that the bone architecture is related to the mechanical loads encountered and controlled by a regulatory mechanism. This idea was proposed by Roux (1881), who stated that bone remodeling is a self-organizing process.
Martin *et al.* [165] give three main concepts in the representation of this observation: the optimization of the stiffness over loading, the alignment of trabeculae along the directions of principal stresses, and the self-regulatory nature of the response to a mechanical stimulus.
The first mathematical and mechanical formulations of bone remodeling date back from the 1960's, suggesting an optimal range of stress above and below which remodeling occurs. Frost [75, 76] captured these concepts in his mechanostat theory. It assumes that local strains regulate bone mass (without specifying the physiological background for this regulation). If strain levels exceed a reference state, new bone is formed. If strain levels are below this point, bone is removed. It is a qualitative theory, but it forms the theoretical basis for several mathematical and computational theories that were developed to study bone adaptation, including the one that is used here and will be fully described in section 5.1.
The first complete mathematical model of bone remodeling (theory of adaptive elasticity) appeared in the late 1970's by Cowin and Hegedus [49, 50, 103]. In this approach, bone is modeled as a poroelastic media with a solid phase surrounded and perfused by a fluid component. Bone remodeling is considered as a strain-controlled transfer of mass between the fluid phase and the solid phase.
Since then, models have encountered large evolutions and can be classified into two main approaches: phenomenological or mechanobiological models. The first approach includes models whose goal is to predict the global mechanical behavior (displacement, strains and stresses) of a tissue or an organ, taking into account the applied loads, the microstructure and the constraints imposed at the boundaries by the environment or the surrounding organs and tissues. Phenomenological models of bone remodeling therefore do not consider the detailed biological activity within the bone. Mechanobiological models are models used to predict the evolution of the microstructure and biological constitution of a tissue or an organ as a consequence of the mechanical environment.

4.2.1 Phenomenological Models

Most of phenomenological models [17, 47, 228] admit the existence of a mechanical stimulus (input) that produces bone apposition or resorption (output) in such a way that the stimulus tends to an homeostatic level in the long-term (homeostasis) most of them following the background advanced in Frost' mechanostat theory [75, 76]. These phenomenological mod-

els are mostly built on constitutive material laws (most often linear elasticity) linking global (or apparent) stresses to global (or apparent) strains with internal variables representative of the evolving local microstructure. For linear elasticity based models, the phenomenological models relate Young's modulus to the bone density. They then compute the change of bone apparent density (and therefore stiffness) as a function (the remodeling rate) of a given mechanical stimulus. Among these phenomenological models, the definition of a remodeling stimulus uses a wide range of mechanical quantities: stresses, strains, strain energy density, strain rate [188] or damage.

In the 1960's, Frost [74, 75] showed the natural presence of micro-fractures in the bones. Carter and his group [31, 32, 150, 200] then proposed a bone remodeling law as a function of damage due to fatigue. Damage based models were also proposed by Martin [163, 164] and Ramtani [221, 222].

In the eighties, two phenomenological models have been developed which have the advantage of involving much fewer parameters than the theory of adaptive elasticity, one at Stanford University (California) [16, 17, 30, 33, 79] and another at the University of Nijmegen (The Netherlands) [109, 110, 273]. The Dutch group chose the strain energy density (SED) per unit of bone volume for the remodeling stimulus while the US group proposed a daily tissue-level stress stimulus (referred to as the Stanford model). Both models originally considered an isotropic structural material, neglecting the role of the structural orientation in the remodeling process.

A second generation of models (based either on these two original ones or on the adaptive elasticity theory) couples material density with orientation or anisotropy [62, 68, 119, 195].

McNamara and Prendergast [169] proposed a model including both stress (or strain/SED) based remodeling laws and damage based laws, the coupling of which depends on the level of damage.

One can also find phenomenological bone remodeling laws considering only a viscoelastic response of the bone to loading [11, 284]. Bone adaptation has also been modeled considering its goal is a structural optimization process [9, 40, 117].

Finally, one can find phenomenological remodeling models based on a multi-scale representation of the bone. The anisotropic elastic parameters of the large scale model are adapted at each integration point based on the variation of a unit cell topology considered at the Gauss points [19, 72].

Some models are also based on a micro-finite element representation of the trabecular bone. Only a surface remodeling is therefore considered as there is no need to average the results over a continuum level. Tsubota *et al.* [252] proposed a model for which the surface displacement is function of the stress non-uniformity. Huiskes *et al.* [111], Ruimerman [229] proposed a surface model based on cell activities, this activity depending on the strain energy density. Recently, Müller's group at ETH Zurich [143, 234] correlated the formation and resorption areas in loaded mice tails to a computed strain-energy density using linear micro-finite elements models. They also showed a strain-energy density based growth algorithm

used on these models could reproduce the experimental remodeling pattern.

In orthodontics related problems however, as briefly described earlier, most remodeling models are not based on Frost's mechanostat theory. However some evidence proposed [171, 227] this theory should be applicable to OTM, showing the biological reaction was dependent on the force level and the stress/strain distribution. Using a finite element model of initial tooth movement due to translational forces with a highly non-linear model for the periodontal ligament (with a Young's modulus varying from 0.1 to 1000MPa in tension), Melsen [171] showed strains levels (without specifying the scalar measure of strain used) reached values that could be considered as below the reference state of the mechanostat theory in the compression side of the tooth, thus explaining direct resorption. He also showed strain levels reached values that would be above this reference state in the tension side of the tooth, thus explaining formation. Verna *et al.* [268], using lower stiffness level for the periodontal ligament, obtained strain values in the compression side that would lead, according to the mechanostat theory, to bone resorption. However, they also showed some microcracks could be observed in the compression sides, thus believing higher loads were sustained on that side than on the tension side (assuming the rupture level would be equal in tension and compression). Williams and Murphy [275] experimentally showed that, at light forces (below 3N), remodeling could be explained by the mechanostat theory. Milne *et al.* [181] also showed using FE models the mechanostat theory could explain the tooth displacement.
However, remodeling algorithms used in orthodontics are rarely based on the mechanostat theory (while they are in dental implants related models). Indeed, even though these remodeling algorithms are based on the measure of a deviation from a mechanical stimulus, they do not result in a change of bone mass but rather increase/decrease the overall tooth rate of movement in its alveolus [27, 85, 130, 161, 233].

4.2.2 Mechanobiological Models

Taking into account the detailed biological activity within the bone leads to more complex models, but allows a more realistic description of the processes involved. Such mechanobiological models have been developed for fracture healing in long bones and wound repair. McNamara and Prendergast [169], Prendergast *et al.* [213] proposed a mechano-regulatory model for which the differentiation of the stem cells into specific cell types is a function of shear, fluid flow and micro-damage. One also finds mechanobiological models dealing with the mechanisms of bone healing [10, 88, 89]. Some authors have proposed models of the interaction between osteoblasts and osteoclasts or osteocytes within the BMU's [3, 102, 105, 145].

4.3 Constitutive Laws for Trabecular Bone

Considering the complex microstructure of trabecular bone, two main approaches can be taken to model its mechanical response. The first one models precisely the microstructure morphology in all its geometric details (models referred to as μ-FE models), the other represents it in average over the entire volume or over defined volumes of interest (models referred to as continuum models).
The FE models for bone tissue are more and more often built on image datasets provided by CT. High resolution CT, with a resolution in the order of 10 to 100 μm (such as μ-CT or HR-pQCT), provides a precise description of the trabecular microstructure. Following segmentation, this trabecular geometry can then be converted into μ-FE models, describing the microstructure in all its geometrical details. Homogenizing the trabecular bone microstructure is usually done using the bone volume fraction or, recently, a fabric tensor [45, 167, 257, 288]. As in these continuum models the elements are larger than in μ-FE models, their volume includes several trabeculae, which are considered in the element properties by using density based or density and fabric-based stiffness tensors. Therefore, this homogenization eventually provides continuum FE models.
While bone geometry is provided by the CT images, performing finite element simulations requires also the knowledge of the relation between stresses and strains. Indeed, FE analysis require constitutive laws, describing the mechanical behavior of the modeled material. Several μ-FE studies use linear elastic laws [98, 196, 206] and only a few propose elastoplastic models [13, 193, 267]. In continuum FE models, to compensate for the lack of topological details, one needs however to use accurate non-linear material properties for the underlying constitutive law.
We present in this section the different trends of constitutive laws found in the literature, both for continuum FE models and for μ-FE models.

4.3.1 Homogenized Constitutive Laws (Continuum FE Models)

Trabecular bone is a complex material presenting at the continuum level large heterogeneities between anatomical sites, age and gender. This in turn affects its mechanical properties, resulting in strength and stiffness variations reaching one and three orders of magnitude respectively [128, 167]. Trabecular bone's mechanical behavior at large compressive strain resembles an elastoplastic cellular solid [90, 91]. The typical stress-strain curve from a compression experiment reaching high strain is depicted in Fig. 4.2.
Under compressive load, trabecular bone exhibits a behavior showing a decrease of the apparent tangent stiffness before reaching a maximal force. Beyond apparent strains at maximal force, smooth and gradual softening occurs until either a plateau is reached before hardening or the material hardens directly, thus creating a minimum point. After the plateau or the minimum point, the hardening consists in a quasi-linear increase of stress with strain. This corresponds to progressive pore closure at the microstructure level. It is followed, be-

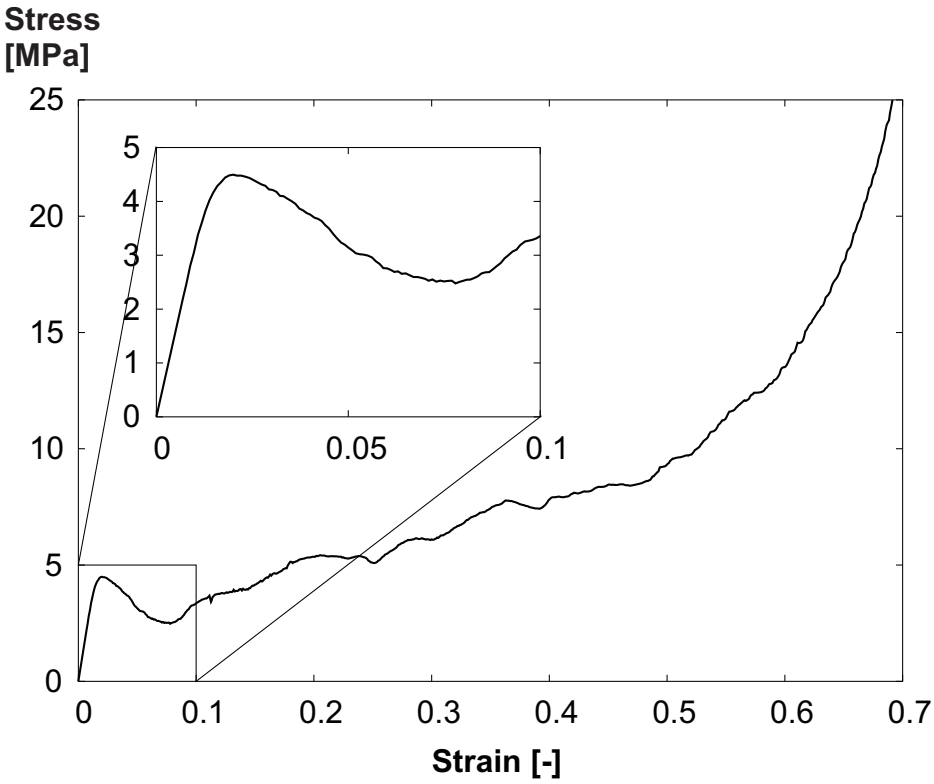

FIGURE 4.2: *Typical Cauchy stress/natural strain curves for trabecular bone in compression [37].*

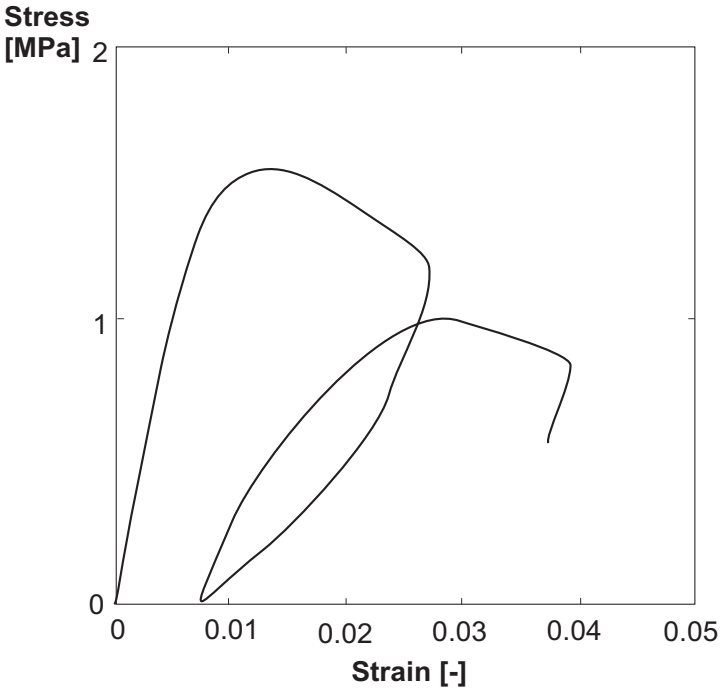

FIGURE 4.3: *Stress/strain cyclic behavior of human vertebral trabecular bone in compression [128], the type of stress and strain in the figure is not specified however at this strain level, all stress/strain measures are equivalent (see Fig. 3.3).*

fore the occurrence of failure, by a large increase of stress with strain due to the collapse of the cells. Using post-yield cyclic experiment [128, 167, see Fig. 4.3], it was shown that trabecular bone accumulates irreversible strains, presents a gradual decrease in stiffness, and that loading-unloading cycles create an hysteresis.

The reduction of apparent modulus and the appearance of irreversible strain, quantified upon unloading at null stress, are also featured by compact bone [81]. However, compact bone tissue is quasi-brittle, meaning that passed the ultimate point, a fracture directly occurs. Finally, the viscoelastic behavior was found to be negligible for strain rates associated to normal activities [259]. The elastic properties of trabecular bone depend largely on its morphology. For example in [167], using an analytical model based on volume fraction and fabric tensor, the correlation coefficient between experimental and predicted modulus was of 0.69, thus explaining large part of the modulus variations. Similar to the elastic modulus, the yield and ultimate stress can largely be explained by the structure morphology.

While these experimental data give evidence of the anisotropy and non-linearity of the mechanical behavior, a lot of models used at a continuum level assume an isotropic linear elastic model, most of them relating Young's modulus to the apparent bone density. When the continuum geometry is built from X-Ray images, this apparent density can be calculated using a correlation between Hounsfield Units and the density. Several correlations (depending on the tested site and the testing procedure) are then found between the apparent density and Young's modulus [see 104, for a review]. Finally, either the modulus is averaged over the entire volume of the modeled bone, or the modulus for each finite element is mapped against the volume it represents in the images. The bone is therefore considered as a non-homogeneous material.

Several morphology-elasticity relationships have been developed to account for the trabecular bone structure in the computation of the stiffness tensors [see 287, for a review]. Recently, yield criteria were developed specifically for trabecular bone [13, 38, 81, 95, 286]. Bayraktar and Keaveny [13] proposed as a yield surface a modified super-ellipsoid in strain space that was identified using micro-mechanical nonlinear FE models, Zysset and Rincón [286] proposed a fabric-based piecewise generalized Hill criterion in the stress-space with parameter identification made from multi-axial experiments. The use of such non-linear models based on morphological analysis has increased over the years [19, 41, 129].

However, some of these non-linear models are not suitable for using in a finite strains framework [38, 81, 95].

These models usually also do not consider the possibility for the internal variables to evolve with the morphology. They can therefore not easily be used in remodeling situations.

Other models describe the non-linear behavior of bone not as plasticity but as a bilinear elastic behavior, considering a reduction of the Young's modulus beyond a given strain level [14, 20, 193]. In particular, these bilinear elastic models do not allow for the existence, and thus accumulation, of irreversible strains.

Finally, one finds non-linear models for which the apparent parameters are extracted from

linear FE analysis on the micro-structure [14, 193].
In contrast with the above mentioned studies, as pointed out by Christen *et al.* [42], geometrically non-linear (finite strain) analysis should be used even when a micro-structure finite element approach to bone biomechanics is performed. Indeed, non-linear geometrical behavior due to large displacements and rotations such as buckling and bending of trabeculae has to be considered. However, mostly linear analyses were performed until recently in finite element analyses on the micro-structure, mainly because of the computational cost associated with such non-linear models.

4.3.2 Trabecular Level Constitutive Laws (μ-FE Models)

For μ-FE analyses, the constitutive law used is the stress/strain behavior for a single trabecula. The FEM analysis is then performed on a mesh representing the complex geometry of the trabecular morphology. There is no homogenization and therefore the elements are a direct representation of the real trabecular structure, the underlying constitutive law is then at trabecular level.
Historically, the first models at the trabecular level were idealized geometrical representations. These models used a network of beams and shells representing the trabeculae rods and plates [15, 94, 138]. This type of models easily allows a parametrization of the geometry. Therefore it can be used to produce random geometries with a controlled distribution so that generic trabecular architecture and variability can be produced. One can hence perform large parametric studies on the influence of the geometry on the apparent properties. However, these models do not include fidelity over the arrangement, size and shape of real trabeculae. This fidelity can be achieved by building these beams and shells models through image analysis. Using classification techniques on images, the real trabecular morphology can be decomposed into beam and shell structures with accurate thickness and shape data [156, 212, 243, 258, 263, Fig. 4.4].

With the advances in imaging techniques as well as computational power, finite element solid models representing "real"[1] trabecular structure emerged since the 1990's.
These μ-FE models are sensitive both to the method used to generate the mesh from the images and, obviously, to the constitutive law used to represent the bone behavior.

There are two main methods to create finite element meshes from images (Fig. 4.5). The first one, referred to as the voxel-based method, creates the elements by directly converting the images voxels into hexahedral elements [253, 260]. This method is straightforward, however it produces jagged surfaces and edges, and surface smoothing algorithms can be necessary. The second method requires a triangulation of the surface that first needs to be

[1] The trabecular structures that can be represented depend on the resolution of the images they are built from as well as the image analysis techniques, especially the thresholding technique, used to extract relevant data from images.

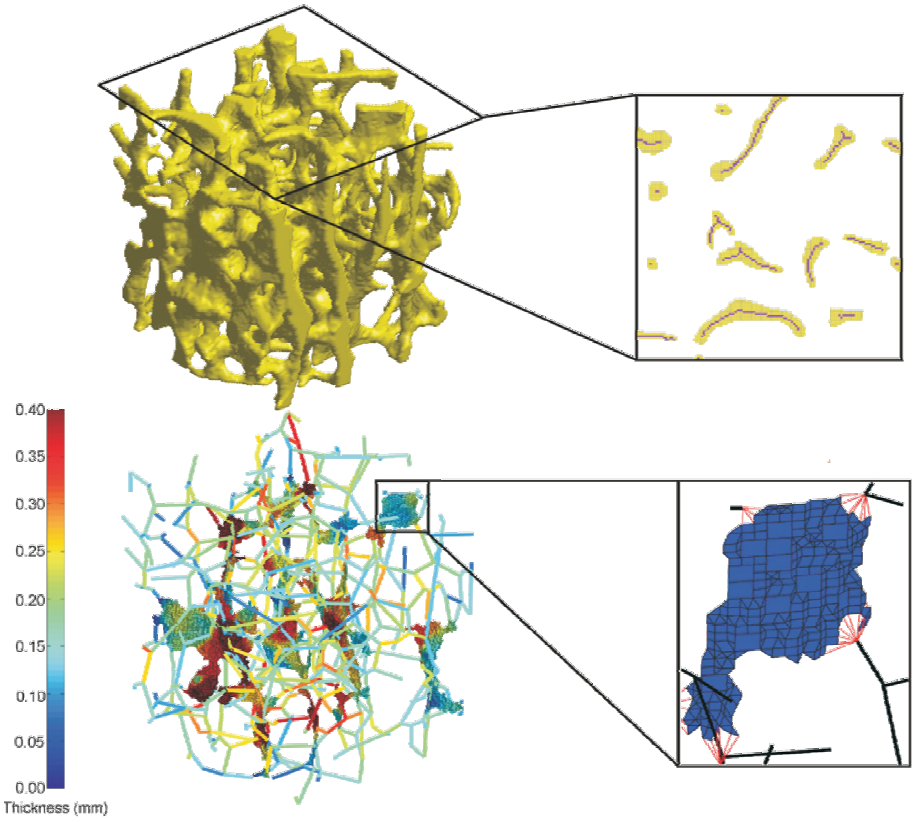

FIGURE 4.4: *Construction of beam-shell FE model from µ-CT scan: (top) 3D µ-CT scan reconstruction of lumbar spine sample, (bottom) skeleton-based mesh with beam and shell elements and color indicating local thickness (adapted from [263]).*

extracted from the images. The triangulated surface can then be filled with tetrahedral elements [66, 182]. These meshes are smoother and often more accurate than voxel-based meshes, however, tetrahedral elements do not perform as well as hexahedral elements from a computational point of view. When used in a small strain analysis with uniform elastic properties, the voxel-based meshes (using linear elements of classical formulation) are particularly efficient as all elements are the same (same fixed orientation and shape), allowing an elementary tangent operator to represent the entire linear system [261]. Convergence studies [192] have shown that the element size should be less than one fourth of the mean trabecular thickness as measured by the `Tb.Th` parameter described in section 2.3. However, for a given model accuracy, voxel-based models often require more elements than tetrahedral meshes.

Constitutive laws found in μ-FE models are mainly linear elastic laws [2, 28, 98, 196, 206]. Indeed, these models, when built with voxel-based meshes, perform very well in small strain analysis. Therefore, as in small strains the alveolar bone material behavior can be considered as elastic and linear, elasticity is sufficient. However, it is clear that this assumption is not valid anymore for a finite-strains problem, accounting for geometrical non-linearities. Even though these linear models do not give any insight into the local non-linear behavior, Pistoia *et al.* [206] correlated the linear prediction to an estimation of the failure load. They showed that failure occurred when, in the linear model, a given percentage of elements were strained beyond a critical limit.
Within the isotropic linear elastic models, a method can be used to bypass the difficult task of meshing the trabecular volume, which is often error prone. Indeed, the material parameters, i.e. only Young's modulus for isotropic linear elastic models as Poisson's ratio can be assumed constant, can be fitted directly from the μ-CT data using correlations between Hounsfiled Units and density as well as correlations between density and Young's modulus. The entire volume is then meshed and each element is mapped against its corresponding Hounsfield Unit in the voxel, giving a zero modulus to void elements. It is a similar procedure as for the non-homogeneous continuum FE models but with elements for which the size is smaller than the trabecular thickness.

Even though it is not widely used yet, the last decade showed the appearance of non-linear μ-FE models, either geometrically non-linear (finite strains models), materially non-linear, or both.
van Rietbergen *et al.* [260] first proposed an elastic-perfectly plastic model in small strains. Niebur *et al.* [193] then proposed a bilinear elastic model in small strains as well. Other more complex models appeared later using plastic like models accounting for hardening or softening [13, 244, 267] in a finite strains framework for compression tests. These studies lead to different conclusions about whether including geometrical non-linearities or softening in the material model is important or not. However, all these studies used samples of different mean `BV/TV` and at different compression level.

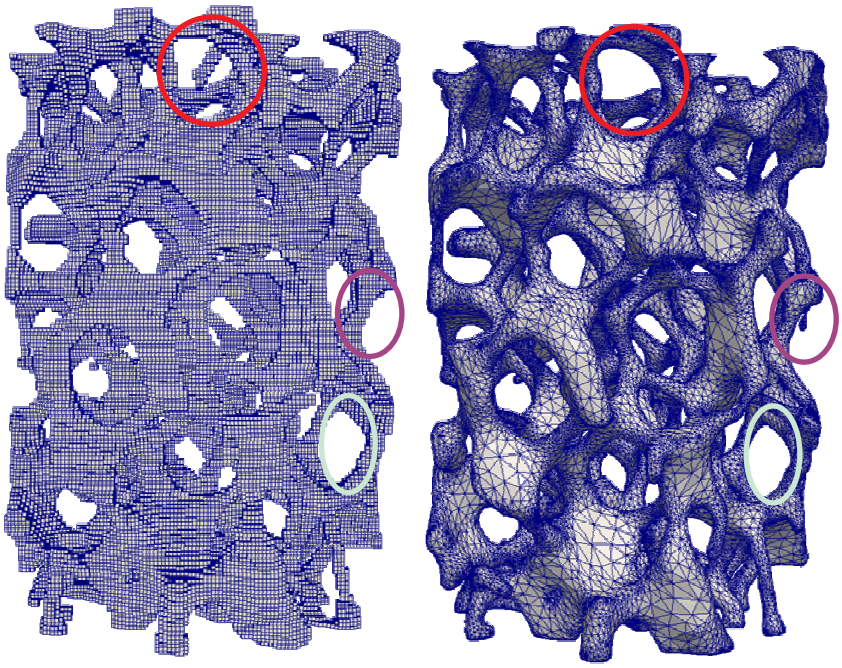

FIGURE 4.5: *Two general methods exist to create finite element meshes from images. The voxel-based method (on the left, producing "staircase" artifacts as enlightened in the green ellipse and the red circle) and the surface triangulation method (on the right, producing smooth surfaces with element sizes adapted to the local curvature). While meshing the same structure geometry and from the same CT images (hence with the same resolution), both techniques do not reproduce exactly the same volume: some elements can be eroded with both methods - enlightened in the red and purple ellipses (sample of Duocel aluminum foam, imaged at ETH Zürich [187] and meshes courtesy of D. Christen and V. d'Otreppe).*

It is our belief (see section 5.4 for a tentative explanation) that including geometrical nonlinearities is needed when reaching high compressive strains (for which there is a clear experimental evidence that buckling occurs in the trabeculae) and that softening effects might not be needed for low density samples (for which the apparent softening can be represented as a solely geometrical effect) but be necessary for higher density samples (as shown in [267] where the used samples had a mean reduced density of 30% and for which including softening effects was needed even using a finite strains framework).

4.4 Conclusions - Discussion on the modeling choices

From the presented literature review, we can see that the last decade showed a profusion of new models in orthodontic tooth movement (OTM). We therefore need to make a decision regarding the choices we have for different aspects of the models (geometry, constitutive laws for tissues, remodeling laws).

- We will use geometries obtained from clinical CT-scans. 2D models will be created by extracting the appropriate plane in the images, then meshed with quadrilateral elements. 3D models will be meshed with tetrahedral elements using a in-house software for the surface mesh construction from the images [66].

- Concerning the different tissues involved in OTM, we saw a lot of efforts have been made in the literature on the characterization of the periodontal ligament.

  It shows a mechanical behavior highly non-linear and plays an important role in orthodontic tooth movement. Its modeling therefore needs to be treated carefully. However, in order to focus our efforts on the bone behavior during remodeling, we will work with a simple elastic model for the periodontal ligament. We choose to work with a periodontal ligament mechanically described with a piecewise linear model for its tangent modulus (details are given later in section 6.1).

  Concerning the tooth materials, we saw even though some effort is produced in the literature to characterize its different composing tissues, it is often modeled as an isotropic homogeneous material. We choose to follow the same simplification and model the tooth as an elastic homogeneous material, not accounting for the pulp and the gingiva.

  Alveolar bone will be described as composed of an isotropic cortical outer layer and an inner anisotropic trabecular bone tissue.

- We saw that there is a profusion of models, either constitutive laws or remodeling laws, for trabecular bone at the macroscopic level. At this level, the constitutive laws for trabecular bone can account for morphological effects, including anisotropy through the use of fabric tensors, as well as non-linear materials effects, such as (anisotropic) plasticity or damage. However, these complex models usually consider a constant morphology. They are often not built to account for a change of morphological parameters due to remodeling.

  In OTM models and other orthopedic problems, the remodeling models usually assume small strain linear elasticity as a model for the bone matrix.

  We here propose to reconcile and unify both these approaches (small strains linear elasticity for remodeling problems and complex constitutive models for other applications) by proposing a constitutive model for trabecular bone at the macroscopic level,

built on morphological parameters such as the fabric tensor to describe the anisotropy, accounting for effects such as plasticity of the trabeculae, that can be used in a finite strains framework, and for which the continuum parameters such as the stiffness can evolve with morphology as remodeling occurs in the tissue.

We here remind the reader that the measure of the anisotropic morphology through the use of fabric tensor is a concept that can be applied mainly to the trabecular bone morphology. Thus, when dealing with cortical bone we will use an isotropic description of both the tissue and the remodeling.

- We saw even though experimental evidence concludes that the mechanostat theory for bone remodeling could explain the OTM, this theory is rarely used in long-term orthodontic tooth movement models. We will here use a remodeling law based on this theory. However, as in the non-linear FE code used, the strain is not stored (we showed in chapter 3 the strain tensor is not needed to express the equilibrium), we will not use the strain as the driving mechanical parameter for remodeling. A strain-energy density based model is chosen (stated by Doblaré and co-workers [62, 83], and fully described in the next chapter).

Chapter 5
Setting up a Bone Remodeling Model in a Finite Strains Framework

They did not know it was impossible, so they did it!

- Mark Twain

The original model which is proposed in this work is built on a damage/repair based model of remodeling. It is therefore a phenomenological model, stated first by Doblaré and co-workers [62, 83]. This model has been chosen as a framework because it is one of the few models whose stimulus variation is justified through thermodynamical concepts of Continuum Mechanics. It is also one of the few models for which the remodeling law is fully integrated into the constitutive model. In this work, it is extended and enhanced in order to be used for the alveolar bone and therefore it takes into consideration the hydrostatic stress state (compression or tension) of the tissue as one of the stimuli for bone remodeling. It is also coupled to an elasto-plastic material behavior in order to capture permanent strains of the tissue. The proposed model can therefore also be used to represent permanent irreversible tooth displacement and alveolar bone deformation due not only to remodeling but also to permanent deformation of the bone (plasticity-like deformation, although it is clear that the relevant inelastic process is different from that of the classical metal plasticity). It can also be used to describe a purely mechanical response of the bone, with no remodeling and therefore no variation of internal parameters. Finally, as it is built on the knowledge of micro-structural parameters, it can be used for other materials than bone that exhibit a similar microstructure.

In this chapter, we analyze in details the remodeling model proposed by Doblaré and co-workers.
We start in the first section by summarizing the required features of a remodeling model, explaining in details how the Stanford model is built and how Doblaré and co-workers used this model in a Continuum Damage formulation.
We then, in the second section, propose an extension to a non-linear model for the bone matrix as well as the use of a finite strain framework. To do so, we present an integration scheme for an anisotropic continuum damage model coupled to plasticity as well as the derivation of a consistent material tangent stiffness operator. The purely mechanical part of the model (with no remodeling) will be shown to be equivalent to an elastoplastic orthotropic material model with a Hill-like yield criterion. We therefore compare the results obtained for this

model with a constant damage tensor to an equivalent orthotropic model. This will allow us to verify the implementation of the integration method. The remodeling model of Doblaré and co-workers, based on the Stanford model, is finally modified to be used in such a framework.
We then (section three) perform a sensitivity analysis of both the purely mechanical part of the problem and the remodeling part on homogeneous cylindrical samples.
In section four, we propose a validation procedure for the mechanical part of the model. For this, we first simulate with our anisotropic model the compression of cylindrical samples of bone and bone-like structures. With this, we retrieve the general behavior of the experimental data obtained on the same samples. We then perform, on these samples, μ−FE simulations in tension to produce *in-silico* tension tests. We can then simulate the same tension tests with our anisotropic model. These compression and tension simulations partly validate the representation of the bone microstructure by an anisotropic behavior measured by the fabric tensor.
We close this chapter in section five, with a verification procedure for the remodeling part of our model. For this, We present what can be considered as "the" benchmark problem for remodeling algorithms: the trabecular adaptation of the femoral head to its physiological loading environment. We thus briefly present the problematics, reproduce as close as possible the description from the literature, and compare the behavior of our model with results available in the literature. This gives a verification but also underline some of the drawbacks of the model.

Chapter Overview

5.1 On the Genesis of Doblaré and Garcia's Model

Essentially, all models are wrong, But some are useful

- George E. P. Box

We first propose to introduce Doblaré and Garcia's model in its context and background (it is based on the Stanford model) in order to understand all its implications.

As described in the previous chapters, on a phenomenological point of view and as explained by the mechanostat theory, remodeling occurs in order to homogenize at the tissue level (noted with a subscript $_t$) a stimulus, ψ_t, in the neighborhood of an homeostatic tissue level value, $\psi_t^\star$. This stimulus is a scalar representation of the applied mechanical loads. Remodeling can be modeled relating, for isotropic remodeling models, the density rate, $\dot{\rho}$ to a remodeling rate, $\dot{r}$. This remodeling rate is a function of the difference between the current value of the chosen stimulus, ψ_t, and its homeostatic counterpart, $\psi_t^\star$. Most models also assume the existence of a "dead" or lazy zone (an interval, of half-width ω, around the homeostatic level for which no remodeling process takes place). The remodeling rate needs to be defined is such a way that remodeling takes place to resorb bone (decrease of density) where "underloaded" conditions are encountered, $\psi_t < \psi_t^\star - \omega$, and that formation of bone occurs (increase of density) where "overloaded" conditions are encountered, $\psi_t > \psi_t^\star + \omega$. These conditions for remodeling are usually called the remodeling criteria.
For isotropic remodeling models, it is then assumed that only the density is affected by remodeling. Mechanical parameters, such as Young's modulus, are affected only if they explicitly depend on the density. Anisotropic remodeling models also require to define the (anisotropic) stiffness variation as a function of the remodeling rate. This stiffness variation function needs to account for the tendency of bone to align its microstructure with the stress or strain principal directions. Therefore the stiffness tensor principal directions need to align themselves with these directions as well.

Phenomenological models therefore require to define three characteristics:

- first a function relating either the density rate (for isotropic models) or the density and the anisotropic stiffness rate (for anisotropic models) to the remodeling rate,
- then a function for the remodeling rate (function of the remodeling criteria),
- and finally a stimulus, motor of the remodeling phenomenon.

The Stanford model we first present was initially designed as an isotropic law for remodeling, later extended to an anisotropic one. The assumed stimulus responsible for remodeling is a stress-equivalent intensity at tissue level. The anisotropic extension of this model formulates the stiffness variation considering remodeling as an optimized process.
We then present Doblaré and Garcia's model of remodeling. Based on the Stanford model, it expresses the stiffness variation in a Continuum Damage Mechanics (CDM) framework,

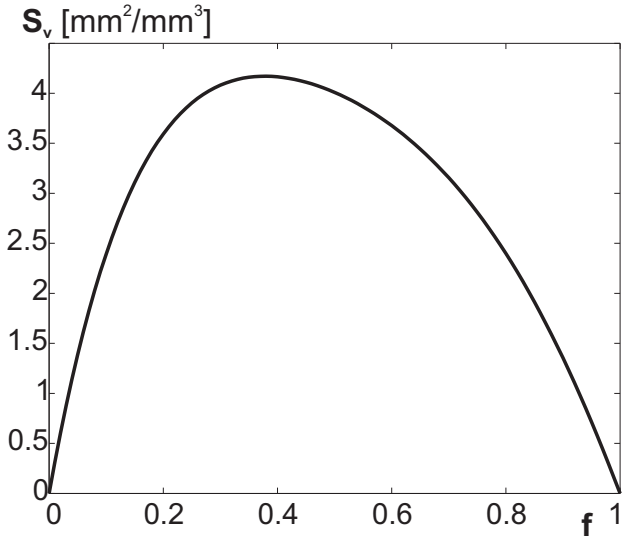

FIGURE 5.1: *Specific surface area, S_v, versus porosity $f = 1 - \rho/\rho_0$ as defined in [162].*

using an anisotropic damage-like tensor, $\boldsymbol{H}_{see}$. The stimulus responsible for this damage rate (and thus for remodeling) is, as usually assumed in CDM and presented in section 3.4, the energy conjugate of $\boldsymbol{H}_{see}$.

5.1.1 The Isotropic Stanford Model (Beaupré and Carter, 1986-1990)

Based on previous works, Beaupré, Carter and co-workers [16, 17, 30, 79] developed a model (called the isotropic Stanford model) proposing the three characteristics needed for a phenomenological model.

On a purely mechanical point of view, the isotropic Stanford model assumes the constitutive law for bone at continuum level is isotropic linear elasticity, therefore following Hooke's law, in small strains:

$$\boldsymbol{\sigma} = \mathbb{H} : \boldsymbol{\varepsilon}$$

The Stanford model assumes that all remodeled bone is fully mineralized (and thus has a density ρ_0), resulting in the following density rate:

$$\dot{\rho} = k S_v \rho_0 \, \dot{r} \qquad \text{(Equ. 5.1)}$$

The terms kS_v in Equ. 5.1 take into account the available ($k \in [0,1]$) bone specific surface area (S_v internal surface area per unit volume). They thus express the fact that a bone surface has to exist for bone cells to act and induce remodeling. The term k accounts for the fact that all this surface is not available for the cells to act. The specific surface area S_v can be related to the porosity $f = 1 - \frac{\rho}{\rho_0}$. Martin [162] showed from experimental data it can be accurately described by a fifth polynomial of the porosity. It is null for null porosity as well as for full porosity (see Fig. 5.1).

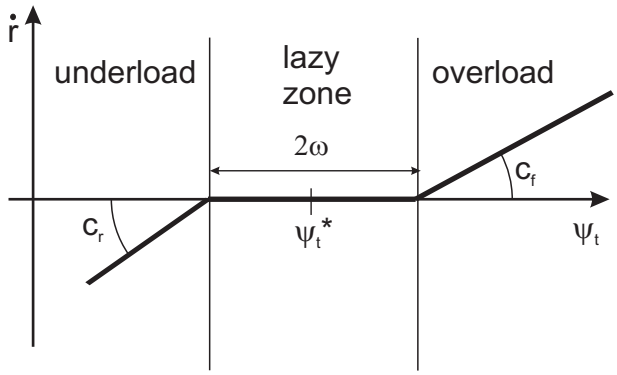

FIGURE 5.2: *Remodeling rate as a function of the tissue-level stimulus used in the Stanford model [16, 17]*

The Stanford remodeling rate considers as criteria for remodeling, $g_r^{\mathtt{St}\cdot}$ and $g_f^{\mathtt{St}\cdot}$, the out-of-equilibrium amplitudes of the stimulus ψ_t:

$$\begin{array}{lll} g_f^{\mathtt{St}\cdot} & = \psi_\mathrm{t} - (\psi_\mathrm{t}^\star + \omega) & \text{for formation conditions} \\ g_r^{\mathtt{St}\cdot} & = \psi_\mathrm{t} - (\psi_\mathrm{t}^\star - \omega) & \text{for resorption conditions} \end{array} \qquad \text{(Equ. 5.2)}$$

These criteria simply measure the (signed) distance between the current value of the stimulus (ψ_t) and the borders of the lazy-zone ($\psi_\mathrm{t}^\star \pm \omega$).
A simple piecewise linear relation between the remodeling rate, $\dot{r}$, and these criteria is then proposed, as depicted in Fig 5.2:

$$\dot{r}^{\mathtt{St}\cdot} = \begin{cases} c_f g_f^{\mathtt{St}\cdot} & \text{for } g_f^{\mathtt{St}\cdot} > 0, \\ 0 & \text{for } -\omega \le (\psi_\mathrm{t} - \psi_\mathrm{t}^\star) \le \omega, \\ c_r g_r^{\mathtt{St}\cdot} & \text{for } g_r^{\mathtt{St}\cdot} < 0 \end{cases} \qquad \text{(Equ. 5.3)}$$

where c_f and c_r are remodeling constants.
The density is therefore reduced (resorption, $\dot{\rho} < 0$) where underloaded conditions are encountered ($\psi_\mathrm{t} < \psi_\mathrm{t}^\star - \omega$, i.e. $g_r^{\mathtt{St}\cdot} < 0$). It is increased (formation, $\dot{\rho} > 0$) for overloaded conditions ($\psi_\mathrm{t} > \psi_\mathrm{t}^\star + \omega$, i.e. $g_f^{\mathtt{St}\cdot} > 0$).

Finally, the stimulus is chosen to be proportional to a stress-equivalent intensity at tissue level, $\bar{\sigma}_t$ (the proportionality coefficient accounts for a cyclic application -N cycles per unit time- of the loads leading to $\bar{\sigma}_t$):

$$\psi_\mathrm{t} = N^{1/m} \bar{\sigma}_t \qquad \text{(Equ. 5.4)}$$

In order to use this stimulus into a finite element code (or any other discretization tool used in computational mechanics at a continuum level), distinction between tissue level and apparent or continuum level[1] has to be made. To distinguish between values on tissue and

[1] The apparent level averages the tissue density and its topology in a continuum measure.

continuum level, the subscript t denotes tissue level. Obviously, stress averaged over a continuum cannot be the same as it really appears in the microstructure. Since marrow and blood vessels filling the pores are much softer than the calcified bone tissue, the (local) stress the tissue has to withstand will be actually larger than the (averaged) continuum stress. The relation between the tissue-level stress-equivalent intensity and the continuum-level one is given, from experimental considerations as

$$\bar{\sigma} = \left(\frac{\rho}{\rho_0}\right)^2 \bar{\sigma}_t \qquad \text{(Equ. 5.5)}$$

where ρ_0 is the density of the fully calcified bone and ρ is the apparent density.
In [16, 17], the continuum stress-equivalent intensity is computed from the strain energy density assuming small strains isotropic elasticity:

$$\bar{\sigma} = \sqrt{E\boldsymbol{\sigma} : \boldsymbol{\varepsilon}} \qquad \text{(Equ. 5.6)}$$

where $\boldsymbol{\varepsilon}$ is the Cauchy strain tensor, $\boldsymbol{\sigma}$ is the Cauchy stress tensor and E is the bone apparent Young's modulus which is dependent on the density. This stress-equivalent intensity is the stress one would obtain in a 1D averaged problem.
The stimulus (Equ. 5.4) can therefore be written in terms of continuum quantities as:

$$\psi_{\mathrm{t}} = N^{1/m}\left(\frac{\rho_0}{\rho}\right)^2 \sqrt{E\boldsymbol{\sigma} : \boldsymbol{\varepsilon}} \qquad \text{(Equ. 5.7)}$$

Using Equ. 5.1 (the density rate), together with Equ. 5.2 (the out-of-equilibrium amplitudes), Equ. 5.3 (the remodeling rate), and Equ. 5.7 (the stimulus definition) produce a remodeling model to update the density according to the stress intensity, defining the isotropic Stanford model. The mechanical parameters that are dependent on the density are also updated. A commonly accepted model for the bone elasticity parameters dependence on the density is:

$$\begin{aligned} E &= B(\rho)\rho^{\beta(\rho)} \\ \nu &= \nu(\rho) \end{aligned} \qquad \text{(Equ. 5.8)}$$

As a particular case of Equ. 5.8, Beaupré *et al.* [16] chose a constant Poisson's ratio and

$$E = \begin{cases} 2014\ \rho^{2.5}\ [MPa] & : \text{ if } \rho \leq 1.2\ g/cc \\ 1763\ \rho^{3.2}\ [MPa] & : \text{ if } \rho \geq 1.2\ g/cc \end{cases} \qquad \text{(Equ. 5.9)}$$

The stimulus can therefore be reformulated using Equ. 5.7 and Equ. 5.8 as

$$\psi_{\mathrm{t}} = \underbrace{N^{1/m}\rho_0^2\sqrt{B}}_{C}\frac{\sqrt{\boldsymbol{\sigma} : \boldsymbol{\varepsilon}}}{\rho^{2-\beta/2}} \qquad \text{(Equ. 5.10)}$$

The Stanford model is used in an explicit scheme: at the end of each time step of a finite element analysis, the density is updated according to its evolution rate and then the mechanical parameters are updated at each element for the next time step. However, this remodeling model could also be used more formally in an adaptive elasticity framework [49].

5.1.2 Anisotropic Extension (Jacobs, 1994)

In his PhD thesis, Jacobs [117] extended this isotropic Stanford model to an energy based anisotropic model for bone remodeling. His assumption is that bone remodeling is an optimal process in some energetic sense. The goal of bone adaptation is thus considered as obtaining a globally efficient mechanical structure. The efficiency is computed as the difference between the power associated with the external loads and the rate-of-change of the total internal energy (due to both the strains and the remodeling).

On a purely mechanical point of view, this extension of the Stanford model assumes the constitutive law for bone at continuum level is (anisotropic) linear elasticity, therefore depending on an anisotropic stiffness tensor $\mathbb{C}$:

$$\boldsymbol{\sigma} = \mathbb{C} : \boldsymbol{\varepsilon}$$

The stimulus used in this anisotropic extension is the same as the one used in the original isotropic Stanford model (Equ. 5.10). It cannot be interpreted as based on the stress-equivalent intensity (Equ. 5.6) as for an anisotropic stiffness Young's modulus is not uniquely defined. It is simply assumed that the stimulus is defined by Equ. 5.10.
Jacobs considers that the density and the stiffness tensor are independent variables. This can lead to general theoretical developments (see Appendix A) to write a stiffness variation law that fullfills an optimum energy principle. However, these two variables (the density and the stiffness tensor) are coupled when this general formulation is matched to the existing isotropic formulation in the case of an isotropic stress applied to an initially isotropic material.
Assuming that bone remodeling is an optimization process therefore leads to a constrained optimization problem (optimizing the efficiency under the remodeling criteria conditions) giving an (anisotropic) adaptation of stiffness as:

$$\dot{\mathbb{C}} = \frac{\beta \dot{\rho}}{\rho} \frac{\boldsymbol{\sigma} \otimes \boldsymbol{\sigma}}{\boldsymbol{\sigma} : \boldsymbol{\varepsilon}} \qquad \text{(Equ. 5.11)}$$

The stiffness tensor variation is thus proportional to the density variation and the stiffness principal directions align with the stress principal directions. Mechanically speaking, accounting for remodeling thus adds some viscosity to the bone stress/strain behavior.
The density rate can be computed from Equ. 5.1 ($\dot{\rho} = kS_v\rho_0\dot{r}$) where the remodeling rate is given by

$$\dot{r}^{\mathrm{An.}} = \begin{cases} c_f \dfrac{g_f^{\mathrm{An.}}}{\rho^{2-\beta/2}} & \text{for } g_f^{\mathrm{An.}} \geq 0 \\ 0 & \text{for } g_f^{\mathrm{An.}} < 0 \text{ and } g_r^{\mathrm{An.}} < 0 \\ -c_r \dfrac{g_r^{\mathrm{An.}}}{\rho^{2-\beta/2}} & \text{for } g_r^{\mathrm{An.}} \geq 0 \end{cases} \qquad \text{(Equ. 5.12)}$$

with the remodeling citeria:

$$\text{Formation: } g_f^{\mathtt{An}\cdot} = C\sqrt{\boldsymbol{\sigma}:\boldsymbol{\varepsilon}} - (\psi_t^\star + \omega)\rho^{2-\beta/2} \qquad \text{(Equ. 5.13)}$$

$$\text{Resorption: } g_r^{\mathtt{An}\cdot} = -C\sqrt{\boldsymbol{\sigma}:\boldsymbol{\varepsilon}} + (\psi_t^\star - \omega)\rho^{2-\beta/2} \qquad \text{(Equ. 5.14)}$$

An important concept of this model is that in the specific case of biological materials, the mechanical dissipation can be negative with no violation of thermodynamic laws because a certain magnitude of biological energy (which cannot be quantified) can be dissipated. The total dissipation is the sum of the mechanical dissipation and the biological one. Mechanical energy can therefore be gained while the total dissipation remains positive.

5.1.3 Continuum Damage Formulation (Doblaré and Garcia, 2001-2002)

As developed in the previous paragraph, Jacobs proposed two independent variables in his anisotropic extension of the Stanford model, the apparent density ρ and the stiffness tensor $\mathbb{C}$, whose evolution is the basis of his method. However, Jacobs'approach is closely related (and in fact inspired as mentioned in his thesis [117][1]) to the principles of Continuum Damage Mechanics (CDM).
As underlined by Doblaré, Garcia and co-workers [62, 83], the anisotropic Stanford's model presents several drawbacks when compared to the generalized CDM. First of all, the stimulus is defined as a global optimization function and not, as usual in the standard CDM theory, as a local variable. Also, the damage variable is not defined explicitly and the two internal variables ($\mathbb{C}$ and ρ) are not independent. They are dependent on each other as can be seen in Equ. 5.11, where it is shown that the evolution of the stiffness tensor depends on the density rate. The later really is an issue as Jacobs developed his optimization-based model assuming a stiffness tensor independent from the density but showed the variation of the first is computed from to the variation of the second. The independence assumption of the stiffness tensor on the density is therefore not valid anymore.
To solve these difficulties, Doblaré and Garcia proposed a remodeling model which, after identifying the internal variables associated to the bone microstructure, follows the extension of the CDM for the anisotropic case.

In the case of bone remodeling, "damage" has to be understood as a measure of the void volume fraction inside the bone tissue. The bone tissue at the continuum level is considered as an anisotropic "organization" of elastic trabeculae (local level). The continuum damage framework is used not to capture actual damage at the local level, i.e. micro-cracks of the trabeculae, but to represent the bone macroscopic porosity. Damage is therefore a measure of the volume fraction. In terms of morphological data provided by computed tomography (see definitions in section 2.3), damage is to be understood, as proposed in [62], as a measure of the reduced density of the tissue ($\bar{\rho}$ or the bone volume fraction, `BV/TV` i.e. the bone

[1] See citation on section 3.4, page 58

volume over the total specimen volume). Its anisotropy is quantified by the fabric tensor as introduced in the work of Cowin *et al.* [52] and in section 2.3 earlier in this work. The damage measure used is therefore virtual and actually reflects the bone density and orientation that can evolve in remodeling situations. There is no actual damage in the tissue. The undamaged material is the virtual situation of bone with zero porosity and perfect isotropy. It is the material considered at the trabecular tissue level, assumed to behave in an isotropic linear elastic way[1] in [62, 83]. The process of bone resorption corresponds to the classical damage evolution concept, since it increases the void fraction (porosity) and therefore damage (decreases the density). However, bone apposition can reduce damage and lead to bone repair, which has to be adequately considered in this extended damage theory. As stated earlier, mechanical energy can be gained and therefore damage repaired because the total energy dissipation includes biological dissipation due to metabolism on top of the mechanical dissipation (which is negative for damage repair).

Doblaré and co-workers in [62, 83] define a damage tensor, $\boldsymbol{d}_{see}$, used in a strain energy equivalence approach of CDM, by the expression

$$\boldsymbol{d}_{see} = \boldsymbol{I} - \bar{\rho}^{\beta/2}\sqrt{A}\boldsymbol{T} = \boldsymbol{I} - \boldsymbol{H}_{see}^2 \qquad \text{(Equ. 5.15)}$$

where $\bar{\rho}$ is the reduced density: $\bar{\rho} = \rho/\rho_0$, or the bone volume fraction, `BV/TV`, and A is a parameter obtained by particularizing the general anisotropic model to the isotropic case[2]:

$$A = \frac{B(\rho)}{B(\rho_0)}\rho_0^{\beta(\rho)-\beta(\rho_0)} \qquad \text{(Equ. 5.16)}$$

Using a Young's modulus function of density as defined in Equ. 5.9 simply leads to a value of $A = 1$ for $\rho > 1.2gr/cc$ and $A = 0.679$ when $\rho < 1.2gr/cc$.
This definition of damage fulfills the requirements of a damage variable, i.e. $\boldsymbol{d}_{see} = \boldsymbol{0}$ for $\rho = \rho_0$ and $\boldsymbol{T} = \boldsymbol{I}$, corresponding to the undamaged state; and $\boldsymbol{d}_{see} = \boldsymbol{I}$ for $\rho = 0$ and any value of $\boldsymbol{T}$, which means complete absence of bone mass. The damage values therefore increase with a decreasing density. The damage-like tensor $\boldsymbol{H}_{see}$ has its principal directions aligned with the fabric tensor $\boldsymbol{T}$ principal directions. We will call this damage-like tensor *Doblaré's remodeling tensor*. It includes not only the directionality of the bone microstructure through the fabric tensor, but also the porosity by means of the reduced density. We should here notice that this damage-like tensor $\boldsymbol{H}_{see}$ is not the effective damage tensor, $\boldsymbol{H}$, defined in section 3, page 64, and classically used in the anisotropic extension of Continuum Damage Mechanics. Indeed, we can see $\boldsymbol{d}_{see} = \boldsymbol{I} - \boldsymbol{H}_{see}^2$ while $\boldsymbol{d} = \boldsymbol{I} - \boldsymbol{H}^{-2}$.
Using a normalization condition for $\boldsymbol{T}$ (the fabric tensor $\boldsymbol{T}$ is here normalized in such a way that $\det \boldsymbol{T} = 1$) yields to the independence of the two internal variables $\boldsymbol{d}_{see}$ and ρ and therefore solves the issue of using coupled internal variables as in Jacob's model.

[1] Doblaré and co-workers consider only elastic trabeculae under a small strains hypothesis. We will extend this concept in the next section to an elasto-plastic trabecular model in a finite strains framework.

[2] For an isotropic tissue, $\boldsymbol{T} = \boldsymbol{I}$ and one can write $d_{see} = 1 - \sqrt{E/E_0}$

The expression of the effective stress tensor is chosen by Doblaré and co-workers as:

$$\tilde{\boldsymbol{\sigma}} = \boldsymbol{H}_{see}^{-1}\boldsymbol{\sigma}\,\boldsymbol{H}_{see}^{-1} \tag{Equ. 5.17}$$

which leads to an effective stress tensor, $\tilde{\boldsymbol{\sigma}}$, whose anisotropic directions coincide with those of the principal axes of Doblaré's remodeling tensor $\boldsymbol{H}_{see}$ and therefore of $\boldsymbol{d}_{see}$ and $\boldsymbol{T}$. This choice is equivalent to the fourth order damage tensor defined in Equ. 3.58.

With this continuum damage framework in mind, and as for any phenomenological bone remodeling model, the model is completed with the definition of the remodeling stimulus, the remodeling rate, and the density rate. As the remodeling model is anisotropic, a directional behavior needs to be taken into account. The stimulus therefore needs to be described, not by a scalar measure but by a tensorial one, built on the basis of the CDM framework in such a way that the Stanford remodeling model is retrieved when the directionality is not taken into account.
Doblaré and co-workers in [62, 83] chose a remodeling stimulus, $\boldsymbol{Y}$, as the variable thermodynamically conjugated with their remodeling tensor. In order to establish this stimulus, one has to define the mechanical variable (strain or stress) that externally "drives" the process. Doblaré and co-workers chose to use the strain as the "external driving force" (therefore as the independent field), although exactly the same results can be obtained if stress was considered. With this, the stimulus is defined as:

$$\boldsymbol{Y} = \left.\frac{\partial \Psi(\boldsymbol{\varepsilon}, \boldsymbol{H}_{see})}{\partial \boldsymbol{H}_{see}}\right|_{\boldsymbol{\varepsilon}=cst} \tag{Equ. 5.18}$$

with Ψ being the free energy:

$$\Psi = \frac{1}{2}\boldsymbol{\sigma} : \boldsymbol{\varepsilon} = \frac{1}{2}\tilde{\boldsymbol{\sigma}} : \tilde{\boldsymbol{\varepsilon}}_{see} \tag{Equ. 5.19}$$

The second equality of Equ. 5.19 holds since a strain energy equivalence approach of continuum damage is used.
$\boldsymbol{Y}$ is obtained in terms of the external independent variable (strain) and the internal variable (Doblaré's remodeling tensor), considering an elastic isotropic material behavior at tissue level ($\tilde{\boldsymbol{\sigma}} = \mathbb{H}^o : \tilde{\boldsymbol{\varepsilon}}_{see}$ with $\tilde{\boldsymbol{\varepsilon}}_{see} = \boldsymbol{H}_{see}\boldsymbol{\varepsilon}\boldsymbol{H}_{see}$), as[1]:

$$\boldsymbol{Y} = 2\left(2G\,\mathtt{sym}\left[(\boldsymbol{H}_{see}\boldsymbol{\varepsilon}\boldsymbol{H}_{see})(\boldsymbol{H}_{see}\boldsymbol{\varepsilon})\right] + \lambda\,\mathtt{tr}\left(\boldsymbol{H}_{see}^2\boldsymbol{\varepsilon}\right)\mathtt{sym}\left((\boldsymbol{H}_{see}\boldsymbol{\varepsilon})\right)\right) \tag{Equ. 5.20}$$

where the notation $\mathtt{sym}(\boldsymbol{a})$ for a second order tensor $\boldsymbol{a}$ means: $\mathtt{sym}(\boldsymbol{a}) = 1/2(\boldsymbol{a} + \boldsymbol{a}^T)$.
The damage function is the domain of the stimulus, $\boldsymbol{Y}$, for which damage is not modified (the lazy zone as used in the literature of bone remodeling). This function is therefore defined by the remodeling criteria. In [62, 83], Doblaré and co-workers propose two criteria, one for

[1] Expanding the expression of Ψ as a function of the independent variable and the internal variable only, we get: $\Psi = \frac{1}{2}(\boldsymbol{H}_{see}\boldsymbol{\varepsilon}\boldsymbol{H}_{see}) : \mathbb{H}^o : (\boldsymbol{H}_{see}\boldsymbol{\varepsilon}\boldsymbol{H}_{see})$

resorption conditions and one for formation conditions:

$$\text{Formation: } g_f^{\text{Dob.}} = C\rho_0^{-\beta/8}A^{1/8}\frac{3^{1/4}}{\sqrt{2(1-\mathrm{w})}}(\boldsymbol{J}:\boldsymbol{J})^{1/4} - (\psi_t^\star + \omega)\rho^{2-5\beta/8} \tag{Equ. 5.21}$$

$$\text{Resorption: } g_r^{\text{Dob.}} = \frac{\sqrt{2(1-\mathrm{w})}}{C\rho_0^{-\beta/8}A^{1/8}27^{1/4}}(\boldsymbol{J}^{-1}:\boldsymbol{J}^{-1})^{1/4} - \frac{1}{(\psi_t^\star - \omega)\rho^{2-5\beta/8}} \tag{Equ. 5.22}$$

where $\mathrm{w} \in [0,1[$ and $\boldsymbol{J}$ is a function of the stimulus, $\boldsymbol{Y}$, that quantifies, through the value of w, the relative influence of the hydrostatic ($\mathrm{w}=0$) and deviatoric ($\mathrm{w}=1$)[1] parts of the stimulus in the damage criterion:

$$\boldsymbol{J} = \frac{1}{3}(1-2\mathrm{w})\,\mathtt{tr}\,(\boldsymbol{Y})\,\boldsymbol{I} + \mathrm{w}\boldsymbol{Y} \tag{Equ. 5.23}$$

The damage flow rule is written, according to the thermodynamical approach of damage described in section 3.4 (therefore considering the remodeling criteria as being related to the damage dissipation potential),

$$\dot{\boldsymbol{H}}_{see} = \mu^r\frac{\partial g_r^{\text{Dob.}}}{\partial \boldsymbol{Y}} + \mu^f\frac{\partial g_f^{\text{Dob.}}}{\partial \boldsymbol{Y}} \tag{Equ. 5.24}$$

fulfilling the consistency condition:

$$\mu^r, \mu^f \geq 0;\ g_r^{\text{Dob.}}, g_f^{\text{Dob.}} \leq 0 \text{ and } \mu^r g_r^{\text{Dob.}} = \mu^f g_f^{\text{Dob.}} = 0 \tag{Equ. 5.25}$$

As the criteria definitions could lead to both of them being positive at the same time (unusual case but possible) an arbitrary decision has to be made in that case. [62, 83] consider that only formation occurs in that case.

Deriving the damage criteria (Equ. 5.21 and Equ. 5.22) and using Equ. 5.1 (so that the consistency parameters μ^r and μ^f would be function of the apparent density ρ), one finally gets an evolution law for Doblaré's remodeling tensor:

$$\text{Formation: } \dot{\boldsymbol{H}}_{see} = \frac{3\beta k S_v \dot{r}}{4\,\mathtt{tr}\left(\boldsymbol{H}_{see}^{-2}(\mathbb{W}:\boldsymbol{J})\boldsymbol{H}_{see}\right)}\frac{\rho_0}{\rho}\mathbb{W}:\boldsymbol{J} \tag{Equ. 5.26}$$

$$\text{Resorption: } \dot{\boldsymbol{H}}_{see} = \frac{3\beta k S_v \dot{r}}{4\,\mathtt{tr}\left(\boldsymbol{H}_{see}^{-2}(\mathbb{W}:\boldsymbol{J}^{-3})\boldsymbol{H}_{see}\right)}\frac{\rho_0}{\rho}\mathbb{W}:\boldsymbol{J}^{-3} \tag{Equ. 5.27}$$

where $\mathbb{W} = \frac{1}{3}(1-2\mathrm{w})\boldsymbol{I}\otimes\boldsymbol{I} + \mathrm{w}\mathbb{1}$ is a fourth order pseudo-unit tensor: for $\mathrm{w}=1$, it is a unit deviatoric tensor, for $\mathrm{w}=0$, it is a unit hydrostatic tensor.

The remodeling rate $\dot{r}$ is obtained from the remodeling criterion that is currently active

$$\dot{r}^{\text{Dob.}} = \begin{cases} c_f\dfrac{g_f^{\text{Dob.}}}{\rho^{2-\beta/2}} & \text{for } g_f^{\text{Dob.}} \geq 0 \\ 0 & \text{for } g_f^{\text{Dob.}} < 0 \text{ and } g_r^{\text{Dob.}} < 0 \\ -c_r\dfrac{g_r^{\text{Dob.}}}{\rho^{2-\beta/2}} & \text{for } g_r^{\text{Dob.}} \geq 0 \end{cases} \tag{Equ. 5.28}$$

[1] Let's note that for $\mathrm{w}=1$ however, Equ. 5.21 is not defined! Therefore $\mathrm{w} \in [0,1[$.

Finally, the density rate can be computed from Equ. 5.1.

5.1.4 Summary of the three presented models

As explained, phenomenological remodeling models are based on the definition of three characteristics: the **density rate function** ($\dot{\rho}$ function of $\dot{r}$), the **remodeling rate function** ($\dot{r}$ function of ψ_t and $\psi_t^\star$), and the **stimulus definition** (ψ_t and its homeostatic level $\psi_t^\star$). These models are coupled to a **constitutive law for the bone matrix**. Isotropic remodeling only couples the density to Young's modulus, while anisotropic models also align the stiffness principal directions to the loading path. Here are summarized the characteristics of the presented models (Stanford model, Jacob's anisotropic extension, and Doblaré and Garcia's formulation into a continuum damage framework).

Integration of the remodeling model into the constitutive law

All models assume an elastic material for the bone matrix.

Stanford: isotropic material (and remodeling) only;
described by Young's modulus: $E(\rho)$ and a constant Poisson's ratio;
Young's modulus is updated at each load/time step after a density update.

Jacobs: anisotropic material (and remodeling);
described by an anisotropic elastic stiffness matrix $\mathbb{C}$;
this stiffness matrix is updated according to $\dot{\mathbb{C}} = \frac{\beta\dot{\rho}}{\rho}\frac{\boldsymbol{\sigma}\otimes\boldsymbol{\sigma}}{\boldsymbol{\sigma}:\boldsymbol{\varepsilon}}$
at each load/time step after a density update.

Doblaré: anisotropic material (and remodeling);
described by means of an anisotropic damage tensor representative
of the morphology: $\boldsymbol{d}_{see} = \boldsymbol{I} - \bar{\rho}^{\beta/2}\sqrt{A}\boldsymbol{T} = \boldsymbol{I} - \boldsymbol{H}_{see}^2$ with $\boldsymbol{T}$ the fabric tensor.
The damage rate is due to remodeling:

$$\text{formation: } \dot{\boldsymbol{H}}_{see} = \frac{3\beta k S_v \dot{r}}{4\,\mathrm{tr}\left(\boldsymbol{H}_{see}^{-2}(\mathbb{W}:\boldsymbol{J})\boldsymbol{H}_{see}\right)}\frac{\rho_0}{\rho}\mathbb{W}:\boldsymbol{J}$$

$$\text{resorption: } \dot{\boldsymbol{H}}_{see} = \frac{3\beta k S_v \dot{r}}{4\,\mathrm{tr}\left(\boldsymbol{H}_{see}^{-2}(\mathbb{W}:\boldsymbol{J}^{-3})\boldsymbol{H}_{see}\right)}\frac{\rho_0}{\rho}\mathbb{W}:\boldsymbol{J}^{-3}$$

where $\boldsymbol{J}$ is linked to the variable thermodynamically conjugated to $\boldsymbol{H}_{see}$.

Jacobs' model degenerates completely into the Stanford model when hydrostatic stresses are applied to an initially isotropic stiffness.
Doblaré's model degenerates, when considering an isotropic damage only (thus considering an isotropic material as the damage tensor is the only source of anisotropy), into:
$\dot{d}_{see} = -\frac{1}{2}\beta k S_v \dot{r}\frac{\rho_0}{\rho}(1-d_{see})$

Stimulus definition

The stimulus, ψ_t defined by the Stanford model accounts for a cyclic application (N cycles per unit of time) of loads creating an equivalent stress at tissue level $\bar{\sigma}_t$: $\psi_t = N^{1/m}\bar{\sigma}_t$. This equivalent stress at tissue level is transformed into an apparent level measure based on the strain-energy density so that the stimulus reads:

$$\psi_{\mathrm{t}} = \underbrace{N^{1/m}\rho_0^2\sqrt{B}}_{C}\frac{\sqrt{\boldsymbol{\sigma}:\boldsymbol{\varepsilon}}}{\rho^{2-\beta/2}}$$

It is the stimulus used in the three models, even though it is expressed through the Continuum Damage framework in Doblaré and Garcia's model.

Remodeling rate function

All remodeling rate functions are built following the mechanostat theory, assuming a range of the stimulus value (of half-width ω) under which (underloaded conditions) bone resorption occurs and over which (overloaded conditions) bone formation occurs. All three models therefore propose remodeling criteria defining the borders between formation conditions, resorption conditions, and homeostatic conditions (no remodeling occurs).

- **formation criterion**:

Stanford:	$g_f^{\mathtt{St}\cdot} =$	ψ_{t}		$-(\psi_{\mathrm{t}}^{\star}+\omega)$
Jacobs:	$g_f^{\mathtt{An}\cdot} =$	$\psi_{\mathrm{t}}\rho^{2-\beta/2}$		$-(\psi_{\mathrm{t}}^{\star}+\omega)\rho^{2-\beta/2}$
Doblaré:	$g_f^{\mathtt{Dob}\cdot} =$	$\underbrace{C\frac{3^{1/4}}{\sqrt{2(1-\mathrm{w})}}(\boldsymbol{J}:\boldsymbol{J})^{1/4}}$	$\rho_0^{-\beta/8}A^{1/8}$	$-(\psi_{\mathrm{t}}^{\star}+\omega)\rho^{2-5\beta/8}$

equivalent to $\psi_{\mathrm{t}}\rho^{2-\beta/2}$ expressed with the continuum damage formulation

- **resorption criterion**:

Stanford:	$g_r^{\mathtt{St}\cdot} =$	ψ_{t}		$-(\psi_{\mathrm{t}}^{\star}-\omega)$
Jacobs:	$g_r^{\mathtt{An}\cdot} =$	$-\psi_{\mathrm{t}}\rho^{2-\beta/2}$		$+(\psi_{\mathrm{t}}^{\star}-\omega)\rho^{2-\beta/2}$
Doblaré:	$g_r^{\mathtt{Dob}\cdot} =$	$\underbrace{\frac{\sqrt{2(1-\mathrm{w})}}{C27^{1/4}}(\boldsymbol{J}^{-1}:\boldsymbol{J}^{-1})^{1/4}}$	$\rho_0^{\beta/8}A^{-1/8}$	$-\frac{1}{(\psi_{\mathrm{t}}^{\star}-\omega)\rho^{2-5\beta/8}}$

equivalent to $1/(\psi_{\mathrm{t}}\rho^{2-\beta/2})$ expressed with the continuum damage formulation

- **remodeling rate**

$$\text{Stanford: } \dot{r}^{\text{St.}} = \begin{cases} c_f g_f^{\text{St.}} & \text{for } g_f^{\text{St.}} > 0, \\ c_r g_r^{\text{St.}} & \text{for } g_r^{\text{St.}} < 0, \\ 0 & \text{otherwise.} \end{cases}$$

$$\text{Jacobs: } \dot{r}^{\text{An.}} = \begin{cases} c_f \dfrac{g_f^{\text{An.}}}{\rho^{2-\beta/2}} & \text{for } g_f^{\text{An.}} > 0, \\ -c_r \dfrac{g_r^{\text{An.}}}{\rho^{2-\beta/2}} & \text{for } g_r^{\text{An.}} > 0, \\ 0 & \text{otherwise.} \end{cases}$$

$$\text{Doblaré: } \dot{r}^{\text{Dob.}} = \begin{cases} c_f \dfrac{g_f^{\text{Dob.}}}{\rho^{2-\beta/2}} & \text{for } g_f^{\text{Dob.}} > 0, \\ -c_r \dfrac{g_r^{\text{Dob.}}}{\rho^{2-\beta/2}} & \text{for } g_r^{\text{Dob.}} > 0, \\ 0 & \text{otherwise.} \end{cases}$$

Density rate function

All models use the same function relating the density rate to the remodeling rate, considering the formed/resorbed bone is fully mineralized:

$$\dot{\rho} = kS_v \rho_0 \dot{r}$$

5.1.5 Discussion of Doblaré and Garcia's Model

Doblaré and co-workers propose an anisotropic CDM model for small strain elasticity characterized by its ability to reproduce the known experimental features of bone remodeling and using independent internal variables associated to the bone microstructure [62, 83]. Bone anisotropy is considered by means of the fabric tensor $\boldsymbol{T}$, which evolves in response to the stimulus tensor $\boldsymbol{Y}$. In a long-term analysis it aligns the fabric tensor principle directions with those of the applied stress state.

Behavior Analysis

In [62], the authors present five main properties of their model. These properties are here summarized and discussed. The reader interested with the proofs of some of the statements should read [62].

Property 1: The second term of the damage criteria (Equ. 5.21 and Equ. 5.22), depending only on the apparent density (called the damage hardening part of the criteria in [62]), is a function of the parameter β through $\rho^{2-5\beta/8}$ and tends toward a limit, constant value for $\beta = 3.2$. Indeed, the second term of each criteria does not depend on the reduced density anymore for this value of β. However, it is known from experimental data that β changes approximately between the bounds 2.5 and 3.2 (they are even the only used values for β in Equ. 5.9). Therefore, in this model the upper bound of β is interpreted as the limit value of a saturation process of the bone tissue with respect to the damage criterion. This value of 3.2 is thereby interpreted by Doblaré and García [62] as a direct consequence of the model and not as an external experimental value.
Discussion: The way to obtain this property is not quite clear. Indeed, the expressions of the damage criteria (Equ. 5.21 and Equ. 5.22) come from the expressions Equ. 5.13 and Equ. 5.14 of the anisotropic extension of the Stanford model proposed by Jacobs [117]. However, as outlined in the summary of the models on the previous section, both formulations are not identical. Indeed, Equ. 5.21 is respectively equal to Equ. 5.13 multiplied by $\rho^{-\beta/8}$ (thus the term $\rho_0^{-\beta/8} A^{1/8}$ in the first term of Equ. 5.21 and the exponent $(16-5\beta)/8$ in the second term). The remodeling rate proposed by Doblaré and co-workers therefore differs from the Stanford remodeling rate by this value for no apparent reasons. And only this difference is responsible of this claimed property.

Property 2: Doblaré and García [62] also claim that they retrieve the Stanford model when an initially isotropic bone loaded by a spherical stress state is considered.
Discussion: As said in the previous paragraph, their model differs from the Stanford model by a value $\rho^{-\beta/8}$ coming, to our understanding, out-of-nowhere. The remodeling criterion in resorption ($g_r^{\mathtt{Dob}\cdot}$) also differs significantly. This last difference is detailed at the end of this section when dealing with the disadvantages of the model.

Property 3: For an initially isotropic bone structure (with a fabric tensor $\boldsymbol{T} = \boldsymbol{I}$), Doblaré's remodeling tensor $\boldsymbol{H}_{see}$ starts its evolution, along each of the principal stress directions, proportionally in formation (or inversely proportionally in resorption) to the strain energy.
Discussion: This property is a direct consequence of the choice of the strain energy as a driving variable for bone remodeling, a choice made in the Stanford model. Indeed, for an initially isotropic bone structure, Doblaré's remodeling tensor becomes

$$\boldsymbol{H}_{see} = \bar{\rho}^{\beta/4} A^{1/4} \boldsymbol{I} = h_{see} \boldsymbol{I}$$

Therefore, its evolution, in formation conditions for instance (Equ. 5.26), becomes:

$$\dot{\boldsymbol{H}}_{see} = \frac{3}{4} \beta k S_v \dot{r} h_{see} \frac{\rho_0}{\rho} \frac{\mathbb{W} : \boldsymbol{J}}{\mathtt{tr}\,(\mathbb{W} : \boldsymbol{J})}$$

with $\dot{r} \propto (\boldsymbol{J} : \boldsymbol{J})^{1/4}$, i.e. to the strain energy density, and where $\mathbb{W} : \boldsymbol{J}$ is aligned with $\boldsymbol{Y}$ and thus $\boldsymbol{\varepsilon}$ as

$$\boldsymbol{Y} = 2h_{see}^3 \left[2G\boldsymbol{\varepsilon}^2 + \lambda \mathtt{tr}\,(\boldsymbol{\varepsilon})\, \boldsymbol{\varepsilon} \right]$$

Property 4: When Doblaré's remodeling tensor $\boldsymbol{H}_{see}$ is aligned with the Cauchy stress tensor (coincident eigenvectors), the rate of the fabric tensor eigenvectors vanishes. In this situation, the model is at an equilibrium state with respect to the principal directions of the reference system, with all the different tensors remaining aligned.
Proof: On one hand, since the remodeling tensor rate $\dot{\boldsymbol{H}}_{see}$ is proportional to the tensor $\boldsymbol{J}$ (Equ. 5.26) or $\boldsymbol{J}^{-3}$ (Equ. 5.27) and since $\boldsymbol{J}$ is defined in terms of the spherical and deviatoric components of the tensor $\boldsymbol{Y}$ (Equ. 5.23), it is clear that $\dot{\boldsymbol{H}}_{see}$ is aligned with $\boldsymbol{Y}$. On the other hand, if Doblaré's remodeling tensor $\boldsymbol{H}_{see}$ is aligned with the Cauchy stress tensor, so is the effective stress tensor. Therefore $\boldsymbol{Y}$ (Equ. 5.20) is also aligned with the Cauchy stress tensor as $\tilde{\boldsymbol{\varepsilon}}$ is aligned with $\tilde{\boldsymbol{\sigma}}$ through the isotropic constitutive law in the effective stress space, and since the product of two tensors that have the same eigenvectors results in another tensor with the same eigenvectors.
Therefore, if Doblaré's remodeling tensor $\boldsymbol{H}_{see}$ is aligned with the Cauchy stress tensor, the eigenvectors of $\dot{\boldsymbol{H}}_{see}$ are the same as those of $\boldsymbol{H}_{see}$. The rate of the eigenvectors of $\boldsymbol{H}_{see}$ thus vanishes. As the fabric tensor $\boldsymbol{T}$ is aligned by definition with Doblaré's remodeling tensor, the rate of the fabric tensor eigenvectors vanishes.
Discussion: This property therefore reflects the experimental features of bone remodeling described in Wolff's "law" of bone adaptation. Indeed, as described in section 2.1.3, it is experimentally shown that remodeling occurs to change the bone topology, mainly in trabecular tissue for which the trabeculae tend to align along the principal stress directions.

Property 5: Assuming that the remodeling criteria are convex, Doblaré and García [62] show a minimum mechanical dissipation (energy dissipation without taking into account the provided metabolic energy) principle is fulfilled. This is the opposite condition usually considered for non-living materials and normally used in Damage Mechanics which assumes the

fulfillment of the principle of maximum dissipation [236]. In the case of bone formation, the dissipation is negative and a certain amount of metabolic energy is necessary.
Discussion: This property is consistent with the theoretical work proposed by Jacobs in his PhD work [117]. This is an essential difference between the behavior of non-living (inert) and biologic (adaptive) materials. From a mechanical point of view, this different thermodynamical behavior comes from the different damage behavior in both cases: in non-living materials the energy dissipation is produced by the appearance of microcracks after reaching a certain stress level, while resorption in living materials appears in the region of low stress. In the case of bone formation, the dissipation is negative and a certain amount of metabolic energy is necessary.

Isotropic interpretation

This anisotropic model can easily be interpreted in its isotropic formulation (choosing an isotropic fabric tensor). As no more dependence on the orientation has to be represented, one can write $\boldsymbol{H}_{see} = h_{see}\boldsymbol{I}$ and w = 0 in Equ. 5.21 and Equ. 5.22.
We can show that $\boldsymbol{J} = \frac{2}{3}h_{see}^3\left[2G\mathtt{tr}\left(\boldsymbol{\varepsilon}^2\right) + \lambda(\mathtt{tr}\left(\boldsymbol{\varepsilon}\right))^2\right]\boldsymbol{I}$ and thus both criteria take a simple formulation given by:

$$\text{Formation: } g_f^{\mathtt{Dob.iso.}} = \overbrace{C\rho_0^{-\beta/8}A^{1/8}(1-d_{see})^{-1}\sqrt{u(\boldsymbol{\sigma})}}^{U(d_{see},\boldsymbol{\sigma})} - (1+\Omega)\overbrace{\psi_t^\star\rho^{2-5\beta/8}}^{U^\star} \quad \text{(Equ. 5.29)}$$

$$\text{Resorption: } g_r^{\mathtt{Dob.iso.}} = \frac{1}{U} - \frac{1}{(1-\Omega)U^\star} \quad \text{(Equ. 5.30)}$$

where $U^\star$ is a reference homeostatic value of U, a strain-energy density like function,
$\Omega\psi_t^\star = \omega$,
$d_{see} = 1 - h_{see}^2$, and
$u(\boldsymbol{\sigma})$ is the effective elastic energy density.

This effective elastic energy density u is as also defined in [146] for metallic materials modeled with CDM and accounting for the stress triaxiality[1]:

$$u(\boldsymbol{\sigma}) = \int \boldsymbol{\sigma} : d\boldsymbol{\varepsilon}_{see} = \frac{J_2^2}{E}\left[\frac{2}{3}(1+\nu) + 3(1-2\nu)\frac{p^2}{J_2^2}\right] = u(\tilde{\boldsymbol{\sigma}})(1-d_{see})^2 \quad \text{(Equ. 5.31)}$$

with $J_2 = \sqrt{\frac{3}{2}s_{ij}s_{ij}} = (1-d_{see})\sqrt{\frac{3}{2}\tilde{s}_{ij}\tilde{s}_{ij}} = (1-d_{see})\tilde{J}_2$.

The remodeling rate is thus a function of this strain-energy density like measure, U, as depicted in Fig 5.3.

[1]The stress triaxiality is defined by $\sigma^\star = \frac{p}{\sigma_{eq}} = \frac{p}{J_2}$ for a von Mises equivalent stress. In Equ. 5.31, the expression in square brackets is refered to as the "triaxiality function" in [146].

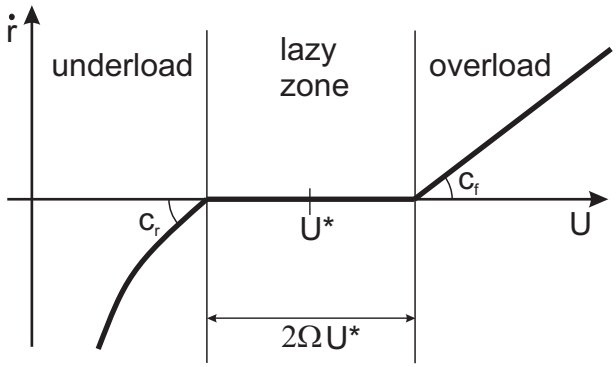

FIGURE 5.3: *Remodeling rate used in the isotropic version of Doblaré and co-workers's model [62]*

Finally, Equ. 5.26 and Equ. 5.27 both lead to the same damage rate:

$$\dot{d}_{see} = -\frac{1}{2}\beta k S_v(d_{see})\dot{r}(d_{see})\frac{\rho_0}{\rho(d_{see})}(1-d_{see}) \qquad \text{(Equ. 5.32)}$$

Fig. 5.4 shows a computation of the damage rate with the damage value, following Equ. 5.32. Results depend on the remodeling rate parameters (N, $\psi^\star$, actually only the ratio $\frac{\psi^\star}{N^{1/m}}$ has an influence on the rate, their values have just a stretching impact, c_f, c_r, and Ω) and the stress intensity through the values of p and J_2.
As the damage rate is positive for resorption and negative for formation, we can detect on Fig. 5.4 different remodeling zones as well as the lazy zone as a function of damage. As expected, the damage rate for values of damage close to 1.0 tend to (relatively) high (negative) values but is reduced to zero for full damage (not seen on the figure as, for a visibility purpose, damage rate below $-6\,10^{-4}[/s]$ is not depicted while for a damage value of 0.99, the damage rate is of $-0.0873[/s]$). In resorption, although the remodeling rate increases (in absolute value) for a damage decay, the damage rate does not reach high values due to the tendency of the specific surface area to decrease faster than the remodeling rate increases. The discontinuity of damage rate for a damage value of about 0.5 is due to the slight discontinuity introduced by Equ. 5.9 in the definition of bone Young's modulus (the damage value at which this discontinuity is observed is therefore function of the full density ρ_0).
As the resorption stimulus definition, Equ. 5.30, is non-linear with respect to the strain-energy density like measure, U, and as the homeostatic value, $U^\star$, is not constant but is a function of damage (except for high densities; when $\rho > 1.2g/cc$, $\beta = 3.2$ and $U^\star = \psi_t^\star$) the remodeling rate is not exactly as sketched in Fig. 5.3. It is (slightly) non-linear even when the formation criterion is positive. The actual remodeling rate as function of U is plotted in Fig. 5.5. As for the case of the damage rate, the computed remodeling rate depends on the remodeling rate parameters and the stress level.

As stated earlier, the damage evolution is proportional to the specific surface, S_v as defined in [162]. Its presence in the damage evolution law has a biological justification but also serves

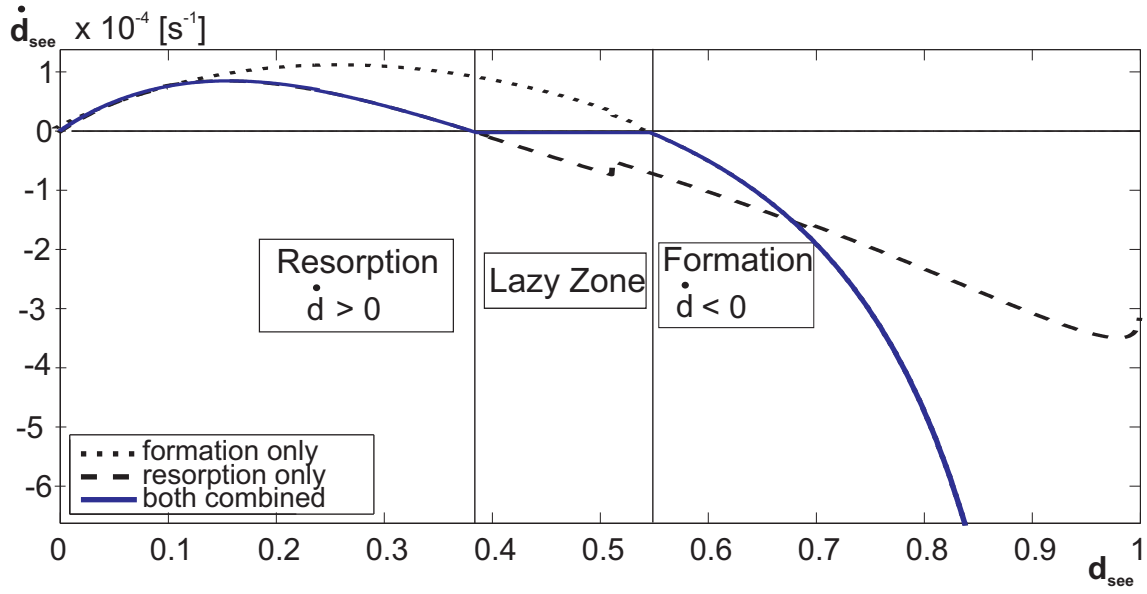

FIGURE 5.4: *Damage rate versus damage value (strain energy equivalence formulation) - parameters values:* $N = 1000$ *(nb of cycles per seconds),* $\psi_t^\star = 10[MPa]$ *(homeostatic stimulus value),* $k = 0.5$ *(percentage of available surface area),* $\Omega = 0.2$ *(half-width of the lazy-zone),* $p = J_2 = 0.5[MPa]$ *(assumed applied stress),* $c_f = 5\ 10^{-5}[mms^{-1}], c_r = 100c_f$ *(remodeling constants),* $\rho_0 = 1.9[g/cc]$*, the plain blue line is the actual damage rate computed.*

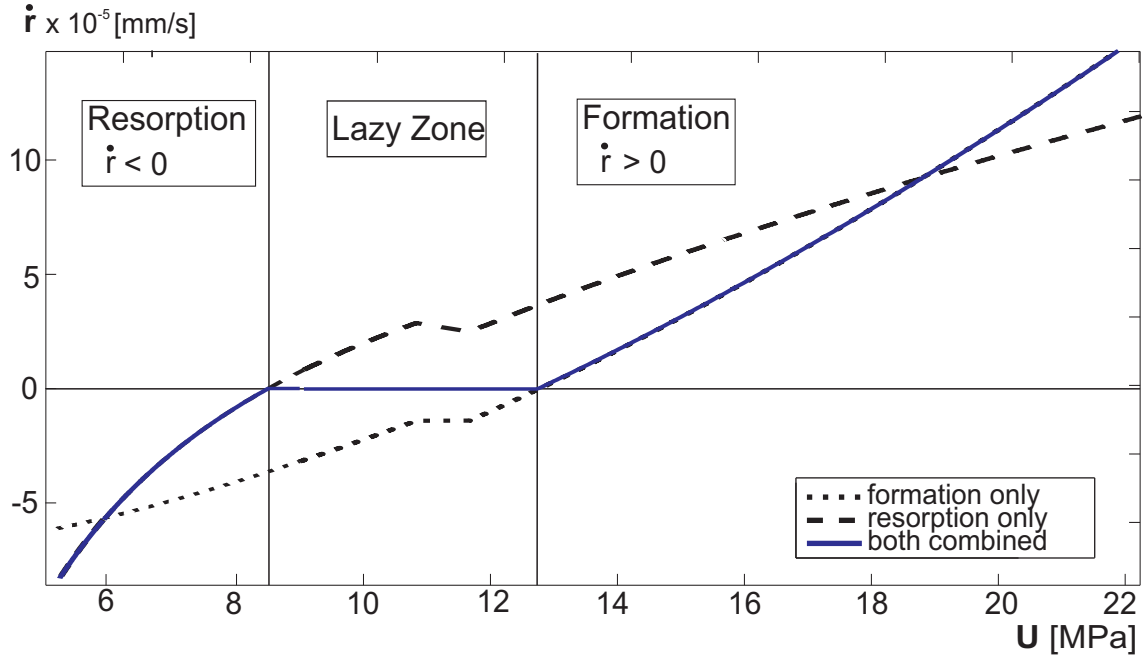

FIGURE 5.5: *Remodeling rate as a function of* U*:* $N = 1000$*,* $\psi_t^\star = 10[MPa]$*,* $k = 0.5$*,* $\Omega = 0.25$*,* $p = J_2 = 0.5[MPa]$*,* $c_f = 5\ 10^{-5}$ $c_r = 100c_f[mm/s]$*,* $\rho_0 = 1.9[g/cc]$*, the plain blue line is the actual remodeling rate computed*

a numerical purpose. Indeed, using this specific surface will decrease substantially the convergence problem that would arise when reaching high damage values: the effective stress definition of the continuum damage theory is written for an isotropic damage variable d_{see}, as Equ. 3.46. Therefore when obtaining a damage variable equal to 1.0 (full resorption of the bone), the model cannot be used anymore. Yet, this will tend not to happen in the model because when reaching the critical value, the damage rate decreases to zero thanks to the null value of the specific surface area.

Disadvantages of the model

As expressed earlier in this section, the first disadvantage of the model proposed in [62, 83] is that the Stanford model is not recovered in the case of an isotropic fabric tensor loaded by a purely hydrostatic stress. This difference is not only due to the parameter $\rho^{-\beta/8}$ appearing in Doblaré and Garcia's model, but also, as clearly seen in its isotropic formulation, to the definition of the resorption criterion Equ. 5.30 which, in a Stanford equivalent problem, would be written $-U+(1-\Omega)U^{\star}$ instead of $1/U-1/((1-\Omega)U^{\star})$.
It cannot be considered as a disadvantage if one does not want to recover the Stanford model but it becomes a disadvantage if one claims their model fully encompasses the Stanford model in the particular isotropic case.
Also, the Stanford model is a phenomenological model widely used, or on which most theories at a purely macroscopic scale (not involving fluid flow around cells or local trabecular change) are based, in the bone remodeling literature (the papers on which the Stanford theory is based [16, 30, 79] are cited respectively 321, 412 and 226 times[1]). Our goal in the development of a bone remodeling model is therefore at least being able to retrieve the behavior of the Stanford model.

It also has to be noticed that for an initial null bone porosity, there will be no damage creation, because of the null value of the specific surface at that point. This means that fully mineralized bone cannot be resorbed, it is a major drawback of the model. However, as we work with trabecular bone, we will not deal with bone of full porosity.

As emphasized in this chapter, one of the first assumption of the Stanford model (and therefore the anisotropic extension proposed by Jacobs and the re-formulation in a continuum damage framework by Doblaré and co-workers) is the linear elastic behavior of the bone matrix. This assumption of small strains, with a linear behavior of the bone trabeculae, might be valid for problems dealing only with bone remodeling. However, if one wants to use a bone remodeling algorithm in problems dealing with other behavior than bone remodeling, the bone matrix might need to be described with more sophisticated behavior than basic linear elasticity, such as elastoplasticity used in this work. Also, in situations such as remodeling produced by an orthodontic treatment, the goal of the procedure is to observe large displacements and/or rotations of the tooth in its socket. For such problems, a

[1] Citation on the 20th of June 2012, as given by Google Scholar.

finite strain framework is needed to properly (in a numerical way) account for these finite displacements/rotations.
However, to use Doblaré and Garcia's model [62, 83] with bone trabeculae described with a material model other than elasticity, the effective stress definition in the representation of damage has to be modified, as will be fully explained in the beginning of the next section.

Finally, a problem encountered in Doblaré and Garcia's model [62, 83] is an inconsistency in the dimensional analysis of the model.
As showed in Equ. 5.28, if c_r and c_f are both expressed as a velocity per unit stress ($\mu m/(\text{day}MPa)$ or $mm/(\text{day}MPa)$) as found in all their papers on the topic [61, 62, 82–84, among others], g_r and g_f both need to have the same units so that $\dot{r}$ is expressed in $1/\text{day}$ to be consistent with Equ. 5.1.
However, Equ. 5.21 and Equ. 5.22 defining $g_f^{\texttt{Dob}\cdot}$ and $g_r^{\texttt{Dob}\cdot}$ do not have the same dimensions. Indeed, it can be easily shown that both criteria have opposite dimensions as it clearly appears in their isotropic formulation (Equ. 5.29 and Equ. 5.30).
This is a major issue which fortunately can easily be treated in the isotropic formulation (the same is valid in the anisotropic formulation as well but will be treated in details in the next section) by choosing a new definition for the resorption criterion:

$$g_f^{\texttt{iso}\cdot} = U - (1+\Omega)U^\star < 0 \tag{Equ. 5.33}$$

$$g_r^{\texttt{iso}\cdot} = -U + (1-\Omega)U^\star < 0 \tag{Equ. 5.34}$$

instead of Equ. 5.29 and Equ. 5.30. This expression for g_r is negative when Equ. 5.30 is, as both U ans $U^\star$ are positive variables. Therefore, the resorption will be encountered for the same mechanical conditions for both formulations of the resorption criterion.
This expression, as stated earlier, also has the feature of being equivalent to the Stanford resorption criterion (apart from the $\rho^{-\beta/8}$ term discussed earlier).

These disadvantages need to be solved in the anisotropic bone remodeling model we propose in this work. Therefore, the mathematical framework proposed in Doblaré and Garcia's model will be used but the derivation of the remodeling tensor $\boldsymbol{H}$ will be built based on the results from Jacobs in his PhD thesis so that our model fully encompasses the Stanford model. Finally non-linearities of the bone matrix expressed as a plastic behavior and a finite strain framework will be considered.

5.2 Towards a Non-Linear Model in Large Strains

King of the lab!

- J.S.Hodgins IV, PhD

To use Doblaré and Garcia's model [62, 83] with bone trabeculae described with a material model other than linear elasticity, the effective stress definition in the representation of damage has to be chosen to enable a coupling between damage and material non-linearities such as plasticity. The main drawback of this model for coupling with plasticity is the use of a strain energy equivalence approach to represent the contribution of morphology. This continuum damage approach relates the stress level in the actual (damaged) material (Cauchy stress, $\boldsymbol{\sigma}$) with the stress in the undamaged material (effective stress, $\tilde{\boldsymbol{\sigma}}$) that leads to the same strain energy. Therefore, this damage approach looses the physical relation of damage to the surface density of defects, which is found in a strain equivalence approach of damage. Keeping this physical relation would however allow the coupling of damage to plasticity by expressing the yield criterion in terms of the effective stress tensor instead of the stress tensor. The yield criterion is then expressed for the undamaged material, here the trabecular material.

The first modification we therefore propose, compared to Doblaré and Garcia's model is to change the damage framework used and work in a strain equivalence approach of CDM[1].
We therefore define an anisotropic damage tensor that depends, as Doblaré's damage tensor did, on morphological parameters (`BV/TV`: $\bar{\rho}$ and fabric tensor: $\boldsymbol{T}$) by the expression:

$$\boldsymbol{d} = \boldsymbol{I} - \bar{\rho}^{\beta} A \boldsymbol{T} \qquad \text{(Equ. 5.35)}$$

where A is defined in Equ. 5.16.
This definition of damage[2] fulfills the requirements of a damage variable, i.e. $\boldsymbol{d} = \boldsymbol{0}$ for $\rho = \rho_0$ and $\boldsymbol{T} = \boldsymbol{I}$, corresponding to the undamaged state, and $\boldsymbol{d} = \boldsymbol{I}$ for $\rho = 0$ and any value of $\boldsymbol{T}$; which means complete absence of bone mass.
Using a normalization condition[3] for $\boldsymbol{T}$, such as $\mathtt{tr}(\boldsymbol{T}) = 3$, yields to the independence of the two internal variables, $\boldsymbol{d}$ and ρ, and therefore solves the issue of using coupled internal variables as in Jacob's model.

[1] The strain equivalence approach will be used from here. Subscript *se* introduced in chapter 3 will be omitted.

[2] For an isotropic tissue, $\boldsymbol{T} = \boldsymbol{I}$ and one can write for a strain equivalence approach of damage $d = 1 - E/E_0$. In the damage definition used by Doblaré and co-workers (Equ. 5.15), square roots appear as the strain energy equivalence approach is used and therefore the isotropic equivalent needs to retrieve $d_{see} = 1 - \sqrt{E/E_0}$

[3] Doblaré and co-workers showed the choice of normalization condition (either on the determinant or on the trace of the fabric tensor) did not influence much the theoretical results of the model. However, as computing a trace can be done with a better efficiency, numerically speaking, than a determinant, we choose to work with a normalization condition on the trace.

The second modification compared to Doblaré and Garcia's model is to assume a constitutive law for the undamaged material which is not restricted to basic small strain linear elasticity. We will work under a finite strains framework assuming an elastoplastic material with an hypoelastic decomposition of the strain rate:

$$\boldsymbol{D} = \boldsymbol{D}^e + \boldsymbol{D}^p$$

Working in a finite strains framework in a corotational formulation[1] gives an effective stress rate linked to the elastic part of the strain rate by the generalized Hooke's law:

$$\overset{\bullet}{\tilde{\boldsymbol{\sigma}}} = \mathbb{H}^o : \boldsymbol{D}^e \qquad \text{(Equ. 5.36)}$$

where $\mathbb{H}^o$ is the Hooke's tensor of elasticity, with parameters evaluated at the trabecular level (already introduced in Equ. 3.49):

$$\mathbb{H}^o = K\boldsymbol{I} \otimes \boldsymbol{I} + 2G\mathbb{1}$$

This general expression will be particularized for elasto-plastic materials in section 5.2.1. An integration scheme will be proposed as well as a consistent tangent operator.

As a third and final modification compared to Doblaré and Garcia's model, we also extend the Stanford model of bone remodeling to this generalized Continuum Damage Mechanics framework. With that, we will get in section 5.2.3 a model that overcomes Doblaré and Garcia's drawbacks underlined previously (i.e. we will completely retrieve the Stanford model and correct the dimensional inconsistency). In that section, we also propose some modifications compared to the Stanford model to account for the particularities of the alveolar bone (i.e. a model depending on the hydrostatic stress state - tension or compression - due to the activation of the periodontal ligament).

5.2.1 Anisotropic Continuum Damage Mechanics and Plasticity in Finite Strains

According to Lemaitre and Desmorat [59, 146, 147] as detailed in section 3.4, the only effective stress definition that fulfills the conditions of being symmetric, independent of Poisson's ratio, compatible with the thermodynamics (existence of a stress potential-when small strains are considered-, and a principle of strain equivalence[2]) and that can express different effect on the hydrostatic and deviatoric behavior, is represented by

$$\tilde{\boldsymbol{\sigma}} = \mathtt{dev}\left(\boldsymbol{H}\boldsymbol{s}\boldsymbol{H}\right) + \frac{p}{1-\eta d^H}\boldsymbol{I} = \tilde{\boldsymbol{s}} + \tilde{p}\boldsymbol{I} \qquad \text{(Equ. 5.37)}$$

[1] The exponent ^{c} of the corotational formulation is omitted. All the time derivatives noted $\bullet$ are to be understood as derivatives in the corotational frame.

[2] The energy equivalence approach in continuum damage mechanics does not relate the physical definition of damage to the surface density of defects, and its coupling to an elasto-plastic matrix is therefore less straightforward.

where $\boldsymbol{s}$ and p are respectively the stress deviator and the hydrostatic pressure (Cauchy stress $\boldsymbol{\sigma} = \boldsymbol{s} + p\boldsymbol{I}$), η is an hydrostatic sensitivity parameter[1], $d^H = \frac{1}{3}\mathtt{tr}(\boldsymbol{d})$, and where

$$\boldsymbol{d} = \boldsymbol{I} - \boldsymbol{H}^{-2} \tag{Equ. 5.38}$$

$\boldsymbol{H}$ is a second order symmetric tensor (we can here notice, compared to Doblaré's remodeling tensor, that $\boldsymbol{H}$ is the effective damage tensor defined in section 3.4). In the isotropic case, $\boldsymbol{d} = d\boldsymbol{I}$ thus $\boldsymbol{H} = (1-d)^{-1/2}\boldsymbol{I}$ and $\eta = 1$, and one retrieves $\tilde{\boldsymbol{\sigma}} = \frac{\boldsymbol{\sigma}}{1-d}$.
Considering Equ. 5.35 and Equ. 5.38, we see the effective damage tensor $\boldsymbol{H}$ has its principal directions aligned with the fabric tensor $\boldsymbol{T}$ principal directions:

$$\boldsymbol{H}^{-2} = \bar{\rho}^{\beta} A \boldsymbol{T}$$

This effective damage tensor includes not only the directionality of the bone microstructure through the fabric tensor, but also the porosity by means of the reduced density.

Plasticity in the effective stress space

We present here the driving equations of the plasticity problem when expressed in the effective stress space in order to couple plasticity and anisotropic damage. For this and since we will use, as detailed in the next paragraph, a staggered scheme for the integration of the coupled plastic-damage problem, we assume the damage tensor is constant. This assumption will allow us to derive the plastic flow rule independently from the the damage flow rule.

In order to keep a linear relation between effective and Cauchy stresses, one can write

$$\tilde{\boldsymbol{\sigma}} = \mathbb{M} : \boldsymbol{\sigma} \tag{Equ. 5.39}$$

where $\mathbb{M}$ is a fourth order tensor defined from $\boldsymbol{H}$ as[2] (reminder of Equ. 3.57):

$$\mathbb{M} = \boldsymbol{H}\underline{\otimes}\boldsymbol{H} - \frac{1}{3}\left(\boldsymbol{H}^2 \otimes \boldsymbol{I} + \boldsymbol{I} \otimes \boldsymbol{H}^2\right) + \frac{1}{9}\mathtt{tr}\left(\boldsymbol{H}^2\right)\ \boldsymbol{I} \otimes \boldsymbol{I} + \frac{1}{3}\frac{\boldsymbol{I} \otimes \boldsymbol{I}}{1-\eta d^H}$$

This relation can be inverted as:

$$\boldsymbol{\sigma} = \mathbb{M}^{-1} : \tilde{\boldsymbol{\sigma}} \tag{Equ. 5.40}$$

$$\text{with } \mathbb{M}^{-1} = \boldsymbol{H}^{-1}\underline{\otimes}\boldsymbol{H}^{-1} - \frac{\boldsymbol{H}^{-2} \otimes \boldsymbol{H}^{-2}}{\mathtt{tr}\left(\boldsymbol{H}^{-2}\right)} + \frac{1}{3}\left(1-\eta d^H\right)\boldsymbol{I} \otimes \boldsymbol{I}$$

Using Equ. 5.37, one can get for the effective pressure and stress deviator (see also Appendix B):

$$\left\{\begin{array}{rcccl} \tilde{p}\boldsymbol{I} & = & \dfrac{p}{1-\eta d^H}\boldsymbol{I} & = & p\,\mathbb{M} : \boldsymbol{I} \\ \tilde{\boldsymbol{s}} & = & \mathtt{dev}(\boldsymbol{H}\boldsymbol{s}\boldsymbol{H}) & = & \mathbb{M} : \boldsymbol{s} \end{array}\right. \tag{Equ. 5.41}$$

[1] $\eta \approx 3$ for metals [146] and taken to be equal to the degree of anisotropy (DA-as defined in section 2.3) in the case of bone.

[2] For second order tensors $\boldsymbol{a}$ and $\boldsymbol{b}$, the product $A_{ijkl} = a_{ij}b_{kl}$ is noted $\mathbb{A} = \boldsymbol{a} \otimes \boldsymbol{b}$.

Or conversely

$$\left\{\begin{array}{rcl} p\boldsymbol{I} &=& \left(1-\eta d^H\right)\tilde{p}\boldsymbol{I} \qquad = \quad \tilde{p}\,\mathbb{M}^{-1}:\boldsymbol{I} \\ \boldsymbol{s} &=& \boldsymbol{H}^{-1}\tilde{\boldsymbol{s}}\boldsymbol{H}^{-1}-\dfrac{\tilde{\boldsymbol{s}}:\boldsymbol{H}^{-2}}{\mathtt{tr}\left(\boldsymbol{H}^{-2}\right)}\boldsymbol{H}^{-2} \quad = \quad \mathbb{M}^{-1}:\tilde{\boldsymbol{s}} \end{array}\right. \tag{Equ. 5.42}$$

To couple damage and plasticity (considering a von Mises criterion for the undamaged material, i.e. the trabeculae in our case), an equivalent stress is defined in the effective stress configuration as:

$$\tilde{\sigma}_{eq}^{vM}=\sqrt{\frac{3}{2}\tilde{\boldsymbol{s}}:\tilde{\boldsymbol{s}}} \tag{Equ. 5.43}$$

The yield function then becomes:

$$f=\tilde{\sigma}_{eq}^{vM}-\sigma_y\leq 0 \tag{Equ. 5.44}$$

Assuming a constant damage tensor and a normality rule in the Cauchy stress space (as explained in section 3.4, it is the space where the conservation equations are fulfilled and the Clausius-Duhem inequality is respected) gives the flow rule (details of the derivation of this flow rule is found in Appendix B.1):

$$\boldsymbol{D}^p=\Lambda\boldsymbol{N} \tag{Equ. 5.45}$$

where Λ is the consistency or flow parameter and with the deviatoric unit normal defined[1] by:

$$\boldsymbol{N}=\frac{\dfrac{\partial f}{\partial\boldsymbol{\sigma}}}{||\partial f/\partial\boldsymbol{\sigma}||}=\frac{\boldsymbol{n}}{||\boldsymbol{n}||} \tag{Equ. 5.46}$$

with the notation

$$\boldsymbol{n}=\mathbb{M}:\tilde{\boldsymbol{s}}=\mathtt{dev}\left(\boldsymbol{H}\tilde{\boldsymbol{s}}\boldsymbol{H}\right) \tag{Equ. 5.47}$$

The equivalent plastic strain rate is given by:

$$\dot{\bar{\varepsilon}}^p=\sqrt{\frac{2}{3}\boldsymbol{D}^p:\boldsymbol{D}^p}=\sqrt{\frac{2}{3}}\Lambda \tag{Equ. 5.48}$$

However, it is the damaged equivalent plastic strain which is used as an internal parameter driving the plastic problem. It is defined through its rate, $\dot{\bar{\varepsilon}}^{p,d}$, in such a way that:

$$\boldsymbol{D}^p=\dot{\bar{\varepsilon}}^{p,d}\frac{\partial f}{\partial\boldsymbol{\sigma}} \quad\Rightarrow\quad \dot{\bar{\varepsilon}}^{p,d}=\frac{\Lambda}{||\partial f/\partial\boldsymbol{\sigma}||}=\sqrt{\frac{2}{3}}\Lambda\frac{||\tilde{\boldsymbol{s}}||}{||\boldsymbol{n}||}$$

The ratio of the equivalent plastic strain rate ($\dot{\bar{\varepsilon}}^p$) to the damaged equivalent plastic strain rate ($\dot{\bar{\varepsilon}}^{p,d}$) is given by $\dfrac{||\boldsymbol{n}||}{||\tilde{\boldsymbol{s}}||}$ and is simply $\dfrac{1}{1-d}$ if isotropic damage were considered.

[1] For a second order tensor $\boldsymbol{a}$, the norm used is defined as $||\boldsymbol{a}||=\sqrt{\boldsymbol{a}:\boldsymbol{a}}$

Finally, the last assumption for the plastic problem is to restrict the hardening law to be isotropic:

$$\sigma_y(\bar{\varepsilon}^{p,d}) = \sigma_y^0 + h\bar{\varepsilon}^{p,d}$$

with h an hardening parameter: $h = \dfrac{d\sigma_y}{d\bar{\varepsilon}^{p,d}}$.

This plastic problem is completed with the damage problem, defined through the damage evolution law. So far, we suppose the damage tensor rate can be described with any general damage model and we simply write: $\dot{\boldsymbol{H}} = \dot{\boldsymbol{H}}(\boldsymbol{H}, \boldsymbol{D}, \bar{\varepsilon}^{p,d}, \dot{\bar{\varepsilon}}^{p,d})$. It will be particularized to a remodeling problem at the end of this section.

Time integration algorithm for the constitutive model

The equations that are driving the coupled damage elastoplastic problem are therefore one scalar equation (definition of the yield criterion) and two tensorial ones (decomposition of the strain rate and the damage rate):

$$\begin{cases} \text{Strain rate decomposition :} & \boldsymbol{D} = \boldsymbol{D}^e + \boldsymbol{D}^p \\ \text{Yield function :} & f = \tilde{\sigma}_{eq}^{vM} - \sigma_y(\dot{\bar{\varepsilon}}^{p,d}, \bar{\varepsilon}^{p,d}) \leq 0 \\ \text{Damage evolution :} & \dot{\boldsymbol{d}} = \dot{\boldsymbol{d}}(\boldsymbol{d}, \boldsymbol{D}, \dot{\bar{\varepsilon}}^{p,d}, \bar{\varepsilon}^{p,d}) \\ \textbf{or } \text{Effective damage tensor evolution :} & \dot{\boldsymbol{H}} = \dot{\boldsymbol{H}}(\boldsymbol{H}, \boldsymbol{D}, \dot{\bar{\varepsilon}}^{p,d}, \bar{\varepsilon}^{p,d}) \end{cases} \quad \text{(Equ. 5.49)}$$

This system introduces one scalar and two tensorial unknowns, i.e. the damaged equivalent plastic strain rate $\dot{\bar{\varepsilon}}^{p,d}$, the elastic strain rate $\boldsymbol{D}^e$, and the damage evolution[1] $\dot{\boldsymbol{d}}$. Accounting for the symmetry of $\boldsymbol{D}^e$ and $\boldsymbol{d}$, we therefore have to solve a non-linear system of 13 scalar unknowns.

This principal system is completed with 3 tensorial equations (definition of the effective stress, the constitutive law, and the plastic flow rule) and a scalar one (defining the damaged equivalent plastic strain rate):

$$\begin{cases} \text{Definition of the effective stress :} & \tilde{\boldsymbol{\sigma}} = \mathbb{M} : \boldsymbol{\sigma} \\ \text{Constitutive law :} & \dot{\tilde{\boldsymbol{\sigma}}} = \mathbb{H}^o : \boldsymbol{D^e} \\ \text{Plastic flow rule :} & \boldsymbol{D}^p = \Lambda \dfrac{\mathtt{dev}\,(\boldsymbol{H}\tilde{\boldsymbol{s}}\boldsymbol{H})}{||\mathtt{dev}\,(\boldsymbol{H}\tilde{\boldsymbol{s}}\boldsymbol{H})\,||} \\ \text{Damaged equivalent plastic strain rate :} & \dot{\bar{\varepsilon}}^{p,d} = \sqrt{\dfrac{3}{2}}\Lambda \dfrac{||\tilde{\boldsymbol{s}}||}{||\boldsymbol{n}||} \end{cases} \quad \text{(Equ. 5.50)}$$

This introduces 19 new unknowns: the Cauchy stress tensor $\boldsymbol{\sigma}$ (6 unknowns), the effective stress tensor $\tilde{\boldsymbol{\sigma}}$ (6 unknowns), the plastic strain rate $\boldsymbol{D}^p$ (6 unknowns), and the consistency flow Λ (1 unknown).

[1] This damage rate will be computed through the knowledge of the effective damage tensor variation $\dot{\boldsymbol{H}}$

Solving this system (Equ. 5.49) with a fully coupled Newton-Raphson method would require to evaluate the derivatives for each of the 13 variables with respect to each other variables, i.e. 156 derivatives. The computation cost of such a method is therefore high and considered an issue to solve such a problem.

Thus, the principle of the integration scheme proposed for the present coupled problem (plasticity and anisotropic damage) is a staggered scheme. As mentioned in the previous paragraph, using such a scheme allowed us to derive the driving equations of the plastic problem independently from the damage flow rule. The full scheme of integration, inspired from Jeunechamps [122] who proposed in his PhD work an integration scheme for isotropic continuum damage coupled to von Mises plasticity, is represented in Fig. 5.6 and can be described as follows:

Starting from known values at time n ($\boldsymbol{\sigma}_n, \boldsymbol{d}_n, \bar{\varepsilon}_n^{p,d}$) the plastic problem is solved at constant damage in the effective stress space (the procedure to solve the plastic problem is detailed in the next paragraph). So we first determine the effective stress, $\tilde{\boldsymbol{\sigma}}_{n+1}$, and the damaged equivalent plastic strain rate, $\bar{\varepsilon}_{n+1}^{p,d}$.
From this result, the damage evolution (through the effective damage tensor variation) is computed at constant stress and plastic strain rate to obtain the final value[1] of the effective damage tensor $\boldsymbol{H}_{n+1}$.
The effective stress tensor and the equivalent plastic strain rate are then updated with this new effective damage tensor. The effective damage is then reevaluated.
This solving procedure is done iteratively, with iterations on the effective damage tensor ending when the difference between two consecutive tensors (measured by the norm $||\boldsymbol{H}_{n+1} - \boldsymbol{H}_n||$) is below a user precision (TOL_d). The default value for this precision has been chosen at 10^{-8}, i.e. the same value chosen in section 3 to evaluate the convergence of the plastic problem.

The stress integration and the plasticity are solved in the effective stress space. The Cauchy stress is obtained simply by applying the inverse of the anisotropic damage operator on the effective stress (Equ. 5.42).

We here remind the reader that the integration procedure of the constitutive law takes place in a corotational frame. To do so, before entering the integration algorithm, all tensorial quantities are rotated in the corotational frame using Equ. 3.26. Once the damage integration has converged, these quantities are rotated back in the fixed Cartesian frame by using the inverse of Equ. 3.26.

[1] The new value of the effective damage tensor is computed using an explicit scheme on the time derivative over the time-step: $\boldsymbol{H}_{n+1} = \boldsymbol{H}_n + \dot{\boldsymbol{H}}\Delta t$ with $\dot{\boldsymbol{H}}$ evaluated with the new effective stress and damaged equivalent plastic strain rate but with the effective damage tensor evaluated at the end of the previous time step: $\boldsymbol{H}_n$

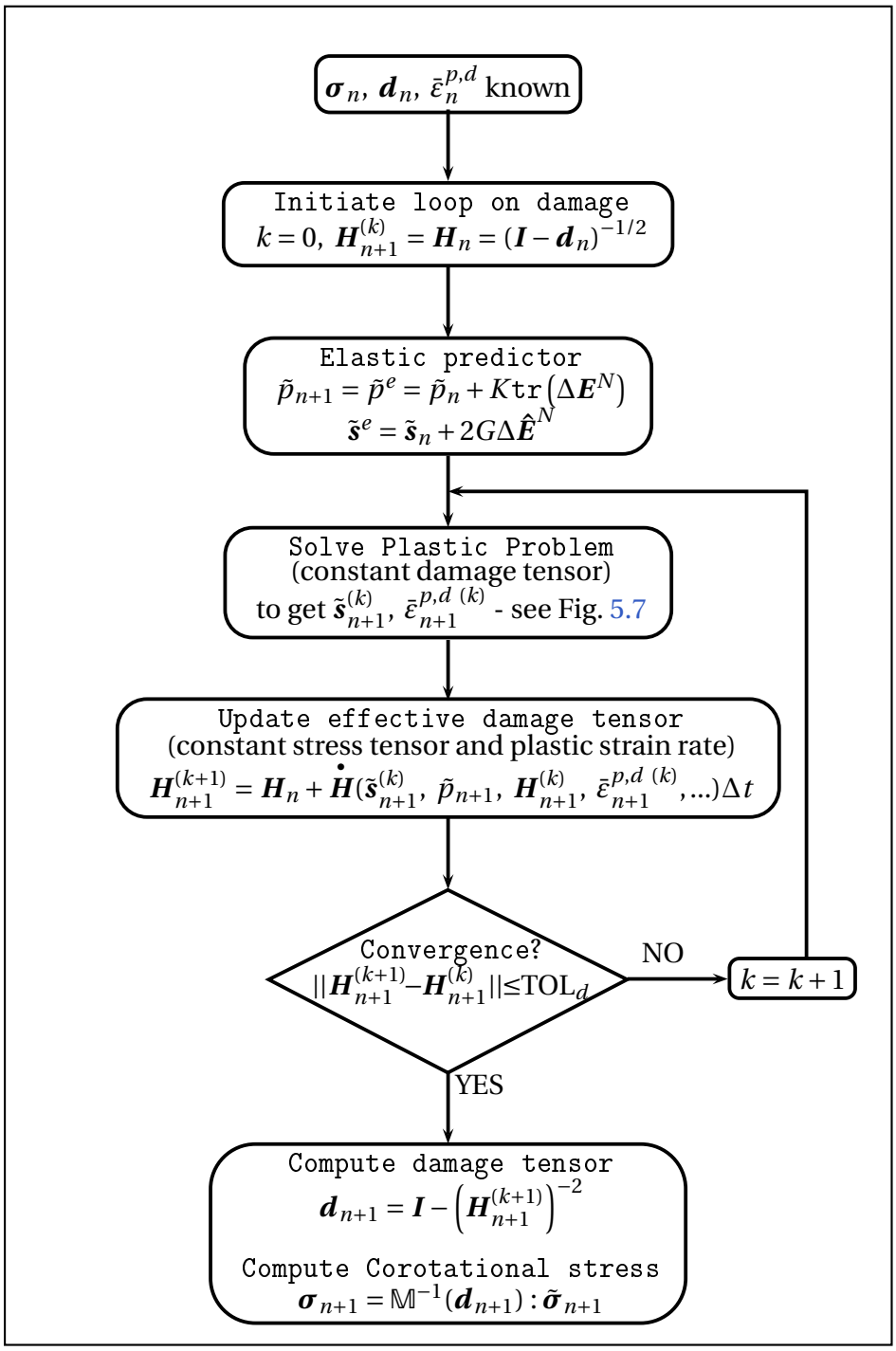

FIGURE 5.6: *Outline of the integration scheme for the coupled problem (elasto-plasticity and anisotropic damage) in the corotational frame, $\boldsymbol{\sigma}$, $\boldsymbol{d}$, $\bar{\varepsilon}^{p,d}$ are known at time step n and need to be computed for time step $n+1$.*

We now detail the algorithm used to solve the plastic problem (box `Solve Plasticity` in Fig. 5.6, extended in more details in Fig. 5.7).

Using the additive decomposition of the strain rate, the constitutive equation Equ. 5.36 becomes:

$$\overset{\bullet}{\tilde{\boldsymbol{\sigma}}} = \mathbb{H}^o : \boldsymbol{D} - \mathbb{H}^o : \boldsymbol{D}^p \tag{Equ. 5.51}$$

As seen in Equ. 5.45, Equ. 5.46 and Equ. 5.47, the plastic strain rate is purely deviatoric and the trace of the elastic strain rate tensor is equal to the one of the total strain rate tensor.
Considering an isotropic behavior for the undamaged material (i.e. at the trabecular level when speaking about bone), the hydrostatic and deviatoric parts of the effective stress rate therefore becomes:

$$\begin{cases} \overset{\bullet}{\tilde{p}} &= K\mathtt{tr}\left(\boldsymbol{D}\right) \\ \overset{\bullet}{\tilde{\boldsymbol{s}}} &= 2G\mathtt{dev}\left(\boldsymbol{D}\right) - 2G\Lambda\boldsymbol{N} \end{cases} \tag{Equ. 5.52}$$

with K the undamaged material bulk modulus and G its shear modulus.
The time integration is done thanks to an elastic predictor/plastic corrector algorithm (closest point algorithm)[1] in a time-step procedure where the stress tensor at time $n+1$ is computed from the stress tensor at time n in a iterative setup (Newton-Raphson algorithm).
The elastic predictor accounts only for the elastic strain rate and gives:

$$\begin{cases} \tilde{p}^e &= \tilde{p}_n + K\mathtt{tr}\left(\Delta\boldsymbol{E}^N\right) \\ \tilde{\boldsymbol{s}}^e &= \tilde{\boldsymbol{s}}_n + 2G\Delta\hat{\boldsymbol{E}}^N \end{cases} \tag{Equ. 5.53}$$

with $\Delta\hat{\boldsymbol{E}}^N = \mathtt{dev}\left(\ln\boldsymbol{U}\right)$ and $\mathtt{tr}\left(\Delta\boldsymbol{E}^N\right) = \mathtt{tr}\left(\ln\boldsymbol{U}\right)$ for $\boldsymbol{U}$ evaluated between the configurations at time n and time $n+1$ (incremental strain rate).
If needed (i.e. if $f = \tilde{\sigma}^{vM}_{eq} - \sigma_y > 0$), a plastic correction is performed for the deviatoric stress so that:

$$\begin{aligned} \tilde{\boldsymbol{s}}_{n+1} &= \tilde{\boldsymbol{s}}^e - 2G\Gamma\boldsymbol{N}_{n+1} \\ &= \tilde{\boldsymbol{s}}^e - 2G\Gamma\frac{\mathbb{M} : \tilde{\boldsymbol{s}}_{n+1}}{||\mathbb{M} : \tilde{\boldsymbol{s}}_{n+1}||} \end{aligned} \tag{Equ. 5.54}$$

with $\Gamma = \int_{t_n}^{t_{n+1}} \Lambda \, dt$ and with the normal to the yield surface $\boldsymbol{N}$ computed on $n+1$ as a closest point scheme is used.
The internal variable driving the plastic problem is updated by:

$$\bar{\varepsilon}^{p,d}_{n+1} = \bar{\varepsilon}^{p,d}_n + \sqrt{\frac{2}{3}}\Gamma\frac{||\tilde{\boldsymbol{s}}_{n+1}||}{||\mathbb{M} : \tilde{\boldsymbol{s}}_{n+1}||} \tag{Equ. 5.55}$$

where Γ is computed thanks to a Newton-Raphson scheme to fulfill the yield criterion.

[1] During the plastic predictor step, $\boldsymbol{D} = \boldsymbol{D}^e$ and $\boldsymbol{D}^p = 0$ while for the plastic correction (if needed, i.e. if the elastic predictor does not verify the yield criterion) $\boldsymbol{D} = 0$ and $\boldsymbol{D}^p = \Lambda\boldsymbol{N}$

This procedure (Equ. 5.54 and Equ. 5.55) for computing $\tilde{\boldsymbol{s}}_{n+1}$ and Γ however results in a fully coupled non-linear system. The resolution of this system through a Newton-Raphson method unfortunately results in strong convergence problems. However, we can modify this system so that we get a linear system for the deviatoric stress integration.

We can indeed choose to write the plastic strain rate in terms of a normal which is not a unit normal, such as $\boldsymbol{n}$ (Equ. 5.47):

$$\boldsymbol{D}^p = \lambda \boldsymbol{n} \tag{Equ. 5.56}$$

We then have

$$\lambda = \frac{\Lambda}{||\boldsymbol{n}||} = \frac{\Lambda}{||\mathbb{M} : \tilde{\boldsymbol{s}}||} \tag{Equ. 5.57}$$

Thus, the plastic correction (Equ. 5.54) becomes:

$$\tilde{\boldsymbol{s}}^{n+1} = \tilde{\boldsymbol{s}}^e - 2G\gamma\mathbb{M} : \tilde{\boldsymbol{s}}^{n+1} \tag{Equ. 5.58}$$

with $\gamma = \int_{t_n}^{t_{n+1}} \lambda \, dt$ the plastic increment.
The plastic correction can thus be written in the form of a linear system in $\tilde{\boldsymbol{s}}_{n+1}$:

$$\mathbb{P} : \tilde{\boldsymbol{s}}_{n+1} = \tilde{\boldsymbol{s}}^e \tag{Equ. 5.59}$$

where $\mathbb{P} = \boldsymbol{I} \underline{\otimes} \boldsymbol{I} + 2G\gamma\mathbb{M}$.
The internal variable driving the plastic problem is then computed as:

$$\bar{\varepsilon}^{p,d}_{n+1} = \bar{\varepsilon}^{p,d}_n + \sqrt{\frac{2}{3}}\gamma||\tilde{\boldsymbol{s}}_{n+1}|| \tag{Equ. 5.60}$$

To solve the plasticity, γ has to be computed so that $f = \tilde{\sigma}^{vM}_{eq}(\tilde{\boldsymbol{s}}) - \sigma_y(\bar{\varepsilon}^{p,d}) = 0$.
Starting with γ^0 as the value of the plastic multiplier at the beginning of the time-step, γ at the i^{th} iteration of the Newton-Raphson algorithm is given by:

$$\begin{cases} \gamma^{i+1} &= \gamma^i + \Delta\gamma \\ r^i &= \tilde{\sigma}^{vM}_{eq}(\gamma^i) - \sigma_y(\gamma^i) \\ \Delta\gamma &= -\dfrac{r^i}{\left.\dfrac{\partial \tilde{\sigma}^{vM}_{eq}}{\partial\gamma}\right|_{\gamma=\gamma^i} - \left.\dfrac{\partial\sigma_y}{\partial\gamma}\right|_{\gamma=\gamma^i}} \end{cases} \tag{Equ. 5.61}$$

The value of γ is iterated on until $\dfrac{r^{i+1}}{\sigma_y(\gamma^{i+1})} < TOL_\gamma$ with TOL_γ a fixed tolerance (as specified earlier, this tolerance is set by default to 10^{-8}).

Details on the way to solve the deviatoric stress (Equ. 5.59) and to compute the yield criterion derivative with respect to γ (Equ. 5.61) are given in Appendix B.2 and summarized in Fig. 5.7.

elastic predictor: compute $\tilde{p}^e$ and $\tilde{\boldsymbol{s}}^e$;

loop on damage - iterate on k

•**plastic correction** (`Solve Plasticity` box of Fig. 5.6)

initialization : $i=0$; $\gamma^{(i)}=\gamma_n$;

compute initial plastic criterion :

$$\tilde{\sigma}_{eq}^{vM(i)}=\sqrt{\frac{3}{2}\tilde{\boldsymbol{s}}^e:\tilde{\boldsymbol{s}}^e};$$

$$\sigma_y^{(i)}=\sigma_y^0+h\bar{\varepsilon}_n^{p,d} \quad \text{isotropic hardening only;}$$

$$f=\tilde{\sigma}_{eq}^{vM(i)}-\sigma_y^{(i)};$$

if $f>0$: **LOOP ON PLASTIC CORRECTION** - iterate on i

(termination criterion: $\frac{\text{residue}}{\sigma_y}<TOL_\gamma$)

$$\mathbb{P}^{(k,i)}=\underline{\boldsymbol{I}\otimes\boldsymbol{I}}+2G\gamma^{(i)}\mathbb{M}(\boldsymbol{H}^{(k)});$$

compute $\tilde{\boldsymbol{s}}^{(i)}$: solve $\mathbb{P}^{(k,i)}:\tilde{\boldsymbol{s}}^{(i)}=\tilde{\boldsymbol{s}}^e$; see appendix B.2

compute $\dfrac{\partial\tilde{\boldsymbol{s}}^{(i)}}{\partial\gamma^{(i)}}$: solve $\mathbb{P}^{(k,i)}:\dfrac{\partial\tilde{\boldsymbol{s}}^{(i)}}{\partial\gamma^{(i)}}=-2G\boldsymbol{n}$; see appendix B.2

$$\bar{\varepsilon}_{n+1}^{p,d(i)}=\bar{\varepsilon}_n^{p,d}+\sqrt{\frac{2}{3}}\gamma^{(i)}||\tilde{\boldsymbol{s}}^{(i)}||;$$

$$\tilde{\sigma}_{eq}^{vM(i)}=\sqrt{\frac{3}{2}\tilde{\boldsymbol{s}}^{(i)}:\tilde{\boldsymbol{s}}^{(i)}};$$

$$\sigma_y^{(i)}=\sigma_y^0+h\bar{\varepsilon}_{n+1}^{p,d(i)}; \quad \text{isotropic hardening only}$$

$$\text{residue}^{(i)}=\tilde{\sigma}_{eq}^{vM(i)}-\sigma_y^{(i)};$$

$$\Delta\text{residue}^{(i)}=\frac{\tilde{\boldsymbol{s}}^{(i)}}{||\tilde{\boldsymbol{s}}^{(i)}||}:\frac{\partial\tilde{\boldsymbol{s}}^{(i)}}{\partial\gamma^{(i)}}-\sqrt{\frac{2}{3}}h\left(||\tilde{\boldsymbol{s}}^{(i)}||+\frac{\gamma^{(i)}}{||\tilde{\boldsymbol{s}}^{(i)}||}\tilde{\boldsymbol{s}}^{(i)}:\frac{\partial\tilde{\boldsymbol{s}}^{(i)}}{\partial\gamma^{(i)}}\right);$$

$$\gamma^{(i+1)}=\gamma^{(i)}-\frac{\text{residue}^{(i)}}{\Delta\text{residue}^{(i)}};$$

when converged:

solve $\mathbb{P}^{(k,i+1)}:\tilde{\boldsymbol{s}}_{n+1}^{(k)}=\tilde{\boldsymbol{s}}^e$;

$$\bar{\varepsilon}_{n+1}^{p,d}=\bar{\varepsilon}_n^{p,d}+\sqrt{\frac{2}{3}}\gamma^{(i+1)}||\tilde{\boldsymbol{s}}_{n+1}^{(k)}||; \quad \gamma_{n+1}=\gamma^{(i+1)}$$

•**update effective damage tensor**

FIGURE 5.7: *Integration scheme: extension of the box* `Solve Plasticity` *of Fig. 5.6*

The coupled problem (plasticity/anisotropic damage) has to be completed by an evolution law for the damage tensor[1] (damage flow rule associated to a damage criterion or to a damage dissipation potential, Equ. 3.59). A priori, any thermodynamically consistent damage evolution could be used with this anisotropic damage elasto-plastic model.

As introduced in section 3.2, a tangent operator is needed to solve the force equilibrium of the finite element problem (Equ. 3.22). The consistent material part of the tangent operator can thus be derived for this integration procedure (the consistency of the tangent operator is verified by comparison of the convergence rate with an analytical operator and a numerical one). Details are given in Appendix C.

Summary of the Anisotropic CDM coupled to elastoplasticity

The equations that drive the coupled anisotropic damage/elastoplastic problem can be summarized as follows:

$$\left\{\begin{array}{rl}
\text{Definition of the effective stress :} & \tilde{\boldsymbol{\sigma}} = \mathbb{M} : \boldsymbol{\sigma} \\
\text{Strain rate decomposition :} & \boldsymbol{D} = \boldsymbol{D}^e + \boldsymbol{D}^p \\
\text{Constitutive law :} & \overset{\nabla}{\tilde{\boldsymbol{\sigma}}} = \mathbb{H}^o : \boldsymbol{D^e} \\
\text{Yield function :} & f = \tilde{\sigma}_{eq}^{vM} - \sigma_y(\dot{\bar{\varepsilon}}^{p,d}, \bar{\varepsilon}^{p,d}) \leq 0 \\
\text{Plastic flow rule :} & \boldsymbol{D}^p = \lambda \mathtt{dev}(\boldsymbol{H}\tilde{\boldsymbol{s}}\boldsymbol{H}) \\
\text{Damaged equivalent plastic strain rate :} & \dot{\bar{\varepsilon}}^{p,d} = \sqrt{\frac{3}{2}}\lambda||\tilde{\boldsymbol{s}}|| \\
\text{Damage evolution :} & \dot{\boldsymbol{d}} = \dot{\boldsymbol{d}}(\boldsymbol{d}, \boldsymbol{D}, \dot{\bar{\varepsilon}}^{p,d}, \bar{\varepsilon}^{p,d}) \\
\textbf{or } \text{Effective damage evolution :} & \dot{\boldsymbol{H}} = \dot{\boldsymbol{H}}(\boldsymbol{H}, \boldsymbol{D}, \dot{\bar{\varepsilon}}^{p,d}, \bar{\varepsilon}^{p,d})
\end{array}\right.$$

The integration of the effective hydrostatic and deviatoric stress over a time-step reads:

$$\begin{array}{rl}
\tilde{p}_{n+1} & = \tilde{p}^e = \tilde{p}_n + K\mathtt{tr}\left(\Delta \boldsymbol{E}^N\right) \\
\mathbb{P} : \tilde{\boldsymbol{s}}_{n+1} & = \tilde{\boldsymbol{s}}^e \\
\text{with} & \mathbb{P} = \boldsymbol{I}\underline{\otimes}\boldsymbol{I} + 2G\gamma\mathbb{M} \\
& \tilde{\boldsymbol{s}}^e = \tilde{\boldsymbol{s}}_n + 2G\Delta\hat{\boldsymbol{E}}^N \\
\bar{\varepsilon}_{n+1}^{p,d} & = \bar{\varepsilon}_n^{p,d} + \sqrt{\frac{2}{3}}\gamma||\tilde{\boldsymbol{s}}_{n+1}||
\end{array}$$

The update of the plastic multiplier γ over a time-step can be computed as

$$\Delta\gamma = \frac{\tilde{\sigma}_{eq}^{vM} - \sigma_y}{-\dfrac{\tilde{\boldsymbol{s}}}{||\tilde{\boldsymbol{s}}||} : \dfrac{\partial\tilde{\boldsymbol{s}}}{\partial\gamma} + \sqrt{\dfrac{2}{3}}h\left(||\tilde{\boldsymbol{s}}|| + \dfrac{\gamma}{||\tilde{\boldsymbol{s}}||}\tilde{\boldsymbol{s}} : \dfrac{\partial\tilde{\boldsymbol{s}}}{\partial\gamma}\right)}$$

The hardening rule is written: $\sigma_y = \sigma_y^0 + h\bar{\varepsilon}^{p,d}$

[1] Actually, an evolution law for $\boldsymbol{H}$ is needed.

5.2.2 Equivalence to an Orthotropic Material

When the damage tensor remains constant (i.e. if $\dot{\boldsymbol{H}} = \boldsymbol{0}$), this coupled anisotropic damage/elastoplasticity problem is completely equivalent to an elastoplastic orthotropic model. Indeed, for a constant damage tensor, the constitutive law (Equ. 5.36) can be used to derive a rate law for the Cauchy stress (applying Equ. 5.42):

$$\dot{\boldsymbol{\sigma}} = \frac{d}{dt}\left(\mathbb{M}^{-1} : \tilde{\boldsymbol{\sigma}}\right) = \mathbb{M}^{-1} : \dot{\tilde{\boldsymbol{\sigma}}} = \mathbb{M}^{-1} : \left(\mathbb{H}^o : \boldsymbol{D}^e\right) = \mathbb{C} : \boldsymbol{D}^e \tag{Equ. 5.62}$$

The orthotropic stiffness tensor is therefore given in terms of the fabric tensor $\boldsymbol{T}$ by:

$$\mathbb{C} = \mathbb{M}^{-1} : \mathbb{H}^o = \frac{1}{3}\tilde{K}\boldsymbol{I}\otimes\boldsymbol{I} + 2\tilde{G}\left(\boldsymbol{T}^{1/2}\underline{\otimes}\boldsymbol{T}^{1/2} - \frac{1}{3}\boldsymbol{T}\otimes\boldsymbol{T}\right) \tag{Equ. 5.63}$$

with $\tilde{K} = K \quad (1-\eta+\eta\bar{\rho}^{\beta}A)$
$\tilde{G} = G \quad \bar{\rho}^{\beta}A$

In the case of an isotropic damage tensor ($\boldsymbol{T} = \boldsymbol{I}$, $\eta = 1$ and $\bar{\rho}^{\beta}A = 1-d$), we can see that we retrieve the classical result for isotropic damage: $\mathbb{C}_{\text{iso}} = (1-d)\mathbb{H}^o$

We can express the stiffness tensor (Equ. 5.63) in the frame defined by the damage eigenvectors (i.e. the orthotropy axis). This can be done by a quadruple rotation of $\mathbb{C}$ using a rotation tensor ($\boldsymbol{Q}$) defined from the orthotropy axis (we use the notation * for quantities expressed in the orthotropy axis, thus Equ. 5.62 reads $\dot{\boldsymbol{\sigma}}^* = \mathbb{C}^* : \boldsymbol{D}^{e\,*}$):

$$\begin{aligned}
\mathbb{C}^* &= \boldsymbol{Q}^T\boldsymbol{Q}^T\mathbb{C}\boldsymbol{Q}\boldsymbol{Q} \\
&= \frac{1}{3}\tilde{K}\boldsymbol{I}\otimes\boldsymbol{I} + 2\tilde{G}\left(\boldsymbol{Q}^T\boldsymbol{Q}^T\left(\boldsymbol{T}^{1/2}\underline{\otimes}\boldsymbol{T}^{1/2}\right)\boldsymbol{Q}\boldsymbol{Q} - \frac{1}{3}\boldsymbol{Q}^T\boldsymbol{Q}^T\left(\boldsymbol{T}\otimes\boldsymbol{T}\right)\boldsymbol{Q}\boldsymbol{Q}\right) \\
&= \frac{1}{3}\tilde{K}\boldsymbol{I}\otimes\boldsymbol{I} + 2\tilde{G}\left(\left(\boldsymbol{Q}^T\boldsymbol{T}^{1/2}\boldsymbol{Q}\right)\underline{\otimes}\left(\boldsymbol{Q}^T\boldsymbol{T}^{1/2}\boldsymbol{Q}\right) - \frac{1}{3}\left(\boldsymbol{Q}^T\boldsymbol{T}\boldsymbol{Q}\right)\otimes\left(\boldsymbol{Q}^T\boldsymbol{T}\boldsymbol{Q}\right)\right) \\
&= \frac{1}{3}\tilde{K}\boldsymbol{I}\otimes\boldsymbol{I} + 2\tilde{G}\left(\boldsymbol{T}^{*\,1/2}\underline{\otimes}\boldsymbol{T}^{*\,1/2} - \frac{1}{3}\boldsymbol{T}^*\otimes\boldsymbol{T}^*\right)
\end{aligned} \tag{Equ. 5.64}$$

As the rotation tensor $\boldsymbol{Q}$ is defined from the orthotropy axis, i.e. the damage eigenvectors which are those of the fabric tensor $\boldsymbol{T}$, the tensor $\boldsymbol{T}^* = \boldsymbol{Q}^T\boldsymbol{T}\boldsymbol{Q}$ is by construction a diagonal tensor : $\boldsymbol{T}^* = \text{diag}(T_1, T_2, T_3)$ with T_1, T_2, T_3 the fabric tensor eigenvalues. This stiffness tensor expressed in the orthotropy axis therefore reads (using Voigt notation):

$$\mathbb{C}^* = \begin{pmatrix}
\frac{1}{3}\tilde{K}+2\tilde{G}\left(T_1-\frac{1}{3}T_1^2\right) & \frac{1}{3}\left(\tilde{K}-2\tilde{G}T_1T_2\right) & \frac{1}{3}\left(\tilde{K}-2\tilde{G}T_1T_3\right) & 0 & 0 & 0 \\
\frac{1}{3}\left(\tilde{K}-2\tilde{G}T_1T_2\right) & \frac{1}{3}\tilde{K}+2\tilde{G}\left(T_2-\frac{1}{3}T_2^2\right) & \frac{1}{3}\left(\tilde{K}-2\tilde{G}T_2T_3\right) & 0 & 0 & 0 \\
\frac{1}{3}\left(\tilde{K}-2\tilde{G}T_1T_3\right) & \frac{1}{3}\left(\tilde{K}-2\tilde{G}T_2T_3\right) & \frac{1}{3}\tilde{K}+2\tilde{G}\left(T_3-\frac{1}{3}T_3^2\right) & 0 & 0 & 0 \\
0 & 0 & 0 & 2\tilde{G}\sqrt{T_1T_2} & 0 & 0 \\
0 & 0 & 0 & 0 & 2\tilde{G}\sqrt{T_2T_3} & 0 \\
0 & 0 & 0 & 0 & 0 & 2\tilde{G}\sqrt{T_1T_3}
\end{pmatrix}$$

This expression is completely equivalent to the stiffness tensor used in orthotropic elasticity (generalized Hooke's law):

$$\mathbb{H}^*_{\text{ortho.}} = \begin{pmatrix} \frac{1-\nu_{23}\nu_{32}}{E_2E_3\mathtt{den}} & \frac{\nu_{21}+\nu_{31}\nu_{23}}{E_2E_3\mathtt{den}} & \frac{\nu_{31}+\nu_{21}\nu_{32}}{E_2E_3\mathtt{den}} & 0 & 0 & 0 \\ \frac{\nu_{12}+\nu_{13}\nu_{32}}{E_1E_3\mathtt{den}} & \frac{1-\nu_{13}\nu_{31}}{E_1E_3\mathtt{den}} & \frac{\nu_{32}+\nu_{31}\nu_{12}}{E_1E_3\mathtt{den}} & 0 & 0 & 0 \\ \frac{\nu_{13}+\nu_{23}\nu_{12}}{E_1E_2\mathtt{den}} & \frac{\nu_{23}+\nu_{21}\nu_{13}}{E_1E_2\mathtt{den}} & \frac{1-\nu_{21}\nu_{12}}{E_1E_2\mathtt{den}} & 0 & 0 & 0 \\ 0 & 0 & 0 & 2G_{12} & 0 & 0 \\ 0 & 0 & 0 & 0 & 2G_{23} & 0 \\ 0 & 0 & 0 & 0 & 0 & 2G_{13} \end{pmatrix}$$

with $\mathtt{den} = \dfrac{1-\nu_{13}\nu_{31}-\nu_{12}\nu_{21}-\nu_{23}\nu_{32}-2\nu_{31}\nu_{12}\nu_{23}}{E_1E_2E_3}$

and $\dfrac{\nu_{21}}{E_2} = \dfrac{\nu_{12}}{E_1}$; $\dfrac{\nu_{31}}{E_3} = \dfrac{\nu_{13}}{E_1}$; $\dfrac{\nu_{23}}{E_2} = \dfrac{\nu_{32}}{E_3}$ to ensure the symmetry of the tensor.

Identifying $\mathbb{C}^*$ with $\mathbb{H}^*_{\text{ortho.}}$ directly gives $G_{12} = \tilde{G}\sqrt{T_1T_2}$
$G_{23} = \tilde{G}\sqrt{T_2T_3}$
$G_{13} = \tilde{G}\sqrt{T_1T_3}$

The nine (six with the symmetry conditions) other unknowns (E_1, E_2, E_3, ν_{12}, ν_{21}, ν_{13}, ν_{31}, ν_{23}, ν_{32}) can be computed solving the nonlinear system given by the upper left quadrant of the tensors.

We can finally express the plastic criterion in the orthotropy axis in order to get the plastic flow rule.

$$\begin{aligned} \tilde{\sigma}_{eq} &= \sqrt{\frac{3}{2}\tilde{\boldsymbol{s}} : \tilde{\boldsymbol{s}}} \\ &= \sqrt{\frac{3}{2}\mathtt{dev}(\boldsymbol{HsH}) : \mathtt{dev}(\boldsymbol{HsH})} \\ &= \sqrt{\frac{3}{2}\left(\boldsymbol{Q}^T\mathtt{dev}(\boldsymbol{HsH})\,\boldsymbol{Q}\right) : \left(\boldsymbol{Q}^T\mathtt{dev}(\boldsymbol{HsH})\,\boldsymbol{Q}\right)} \\ &= \sqrt{\frac{3}{2}\mathtt{dev}(\boldsymbol{H}^*\boldsymbol{s}^*\boldsymbol{H}^*) : \mathtt{dev}(\boldsymbol{H}^*\boldsymbol{s}^*\boldsymbol{H}^*)} \\ &= \sqrt{\frac{3}{2}(\boldsymbol{H}^*\boldsymbol{s}^*\boldsymbol{H}^*) : (\boldsymbol{H}^*\boldsymbol{s}^*\boldsymbol{H}^*) - \frac{1}{2}(\mathtt{tr}(\boldsymbol{H}^*\boldsymbol{s}^*\boldsymbol{H}^*))^2} \end{aligned} \qquad \text{(Equ. 5.65)}$$

where $\boldsymbol{H}^*$ is a diagonal tensor since $\boldsymbol{H}$ is aligned with the damage tensor:

$$\boldsymbol{H}^* = \mathrm{diag}(h_1, h_2, h_3)$$

The tensor $\boldsymbol{H}^*\boldsymbol{s}^*\boldsymbol{H}^*$ is therefore very simple to compute and gives:

$$\boldsymbol{H}^*\boldsymbol{s}^*\boldsymbol{H}^* = \begin{pmatrix} h_1^2 s^*_{11} & h_1h_2 s^*_{12} & h_1h_3 s^*_{13} \\ h_1h_2 s^*_{12} & h_2^2 s^*_{22} & h_2h_3 s^*_{23} \\ h_1h_3 s^*_{13} & h_2h_3 s^*_{23} & h_3^2 s^*_{33} \end{pmatrix}$$

We should here underline that the yield criterion, while written as a von Mises criterion for the effective stress tensor, cannot be written in terms of classical yield criterion for the Cauchy stress, even when expressed in the orthotropy axis. However, it is similar to Hill 48 plastic criterion, indeed $\boldsymbol{H}^*$ being diagonal, we get:

$$\tilde{\sigma}_{eq} = \sqrt{\boldsymbol{s}^* : \mathbb{A}^* : \boldsymbol{s}^*}$$

with

$$\mathbb{A}^* = \begin{pmatrix} h_1^4 & -\frac{1}{2}h_1^2h_2^2 & -\frac{1}{2}h_1^2h_3^2 & 0 & 0 & 0 \\ -\frac{1}{2}h_1^2h_2^2 & h_2^4 & -\frac{1}{2}h_2^2h_3^2 & 0 & 0 & 0 \\ -\frac{1}{2}h_1^2h_3^2 & -\frac{1}{2}h_2^2h_3^2 & h_3^4 & 0 & 0 & 0 \\ 0 & 0 & 0 & 3h_1^2h_2^2 & 0 & 0 \\ 0 & 0 & 0 & 0 & 3h_2^2h_3^2 & 0 \\ 0 & 0 & 0 & 0 & 0 & 3h_1^2h_3^2 \end{pmatrix}$$

The flow rule is therefore, considering associated plasticity:

$$\boldsymbol{D}^{p\,*} = \Lambda \frac{\partial \tilde{\sigma}_{eq}}{\partial \boldsymbol{\sigma}^*}$$

The derivative $\dfrac{\partial \tilde{\sigma}_{eq}}{\partial \boldsymbol{\sigma}^*}$ is given by:

$$\frac{\partial \tilde{\sigma}_{eq}}{\partial \boldsymbol{\sigma}^*} = \frac{1}{\tilde{\sigma}_{eq}} \underbrace{\left[\mathbb{A}^* : \boldsymbol{s}^* - \frac{1}{3}\left(A^*_{kkmn} s^*_{mn}\right) \boldsymbol{I} \right]}_{\boldsymbol{N}\boldsymbol{N}} \qquad \text{(Equ. 5.66)}$$

where $\boldsymbol{N}\boldsymbol{N}$ is the outward normal to the yield surface in the orthotropy axis.
The equivalent plastic strain rate is thus given by, $\boldsymbol{N}\boldsymbol{N}$ being deviatoric:

$$\dot{\bar{\varepsilon}}^p = \sqrt{\frac{2}{3}\boldsymbol{D}^{p\,*} : \boldsymbol{D}^{p\,*}} = \Lambda \sqrt{\frac{2}{3}\frac{\partial \tilde{\sigma}_{eq}}{\partial \boldsymbol{\sigma}^*} : \frac{\partial \tilde{\sigma}_{eq}}{\partial \boldsymbol{\sigma}^*}} = \frac{\Lambda}{\tilde{\sigma}_{eq}} \sqrt{\frac{2}{3}\boldsymbol{N}\boldsymbol{N} : \boldsymbol{N}\boldsymbol{N}} \qquad \text{(Equ. 5.67)}$$

Considering as previously an integration scheme with an elastic predictor and a plastic corrector gives:

$$\begin{aligned} \boldsymbol{\sigma}^e &= \boldsymbol{\sigma}^*_n + \mathbb{C}^* : \boldsymbol{E}^{N\,*}_{n+1} \\ \boldsymbol{\sigma}^*_{n+1} &= \boldsymbol{\sigma}^e - \mathbb{C}^* : \left(\Gamma \left. \frac{\partial \tilde{\sigma}_{eq}}{\partial \boldsymbol{\sigma}^*} \right|_{n+1} \right) \\ &= \boldsymbol{\sigma}^e - \Gamma \left(\mathbb{C}^* : \left. \frac{\partial \tilde{\sigma}_{eq}}{\partial \boldsymbol{\sigma}^*} \right|_{n+1} \right) \\ &= \boldsymbol{\sigma}^e - \Gamma \boldsymbol{N}^*_{n+1} \end{aligned} \qquad \text{(Equ. 5.68)}$$

The plastic problem therefore consists into finding Γ, using a Newton-Raphson algorithm, in such a way that $f = \tilde{\sigma}_{eq} - \sigma_y(\bar{\varepsilon}^p) = 0$.

Such an orthotropic material stress integration is implemented into Metafor [177] using a generic yield criterion. In order to use it with a yield criterion defined by Equ. 5.65, we only have to implement four functions, defining $\tilde{\sigma}_{eq}$ (Equ. 5.65), $\frac{\partial \tilde{\sigma}_{eq}}{\partial \boldsymbol{\sigma}^*}$ (Equ. 5.66), $\dot{\bar{\varepsilon}}^p$ (Equ. 5.67) and $\boldsymbol{N}^*$ (Equ. 5.68).

Verification method for the integration scheme at constant damage

For the purpose of verifying the integration scheme developed (anisotropic damage and elastoplasticity, with a constant damage tensor only), we will define simple test cases for which the results and the computational costs will be compared between the two approaches (orthotropic elastoplasticity and anisotropic damage with elastoplasticity at constant damage). We will also compare the same test cases with results obtained for an orthotropic material implemented in *Lagamine* [39, 60]. *Lagamine* is an implicit nonlinear FE code with an updated Lagrangian formulation developed in the ArGEnCo department at the University of Liège since 1984. It has a large element library as well as numerous constitutive laws. However, only an elastic orthotropic material will be considered for this comparison. Indeed, as expressed earlier, the yield criterion used here cannot be written in terms of classical criteria in the Cauchy stress space, therefore it cannot easily be related to classical plastic criteria used for orthotropic materials available in *Lagamine*.

The test cases presented are constituted of the following features (see Fig. 5.8):

- **geometry**: cube with a side width of $L = 10$ cm meshed with hexahedra of 2cm width (i.e. 125 elements).
- **boundary conditions for elastic tests**: one side (the side situated in the $z = 0$ plane) has all its nodes fixed in all directions, the opposite one (the side situated in the $z = L$ plane) has all its nodes moved to create 4 test cases: tension (20% stretch in the Z-direction), compression (-20% stretch in the Z-direction), 20% shear in the X-direction (referred to as the 'positive shear test') and finally -20% shear in the X-direction (referred to as the 'negative shear test').
- **boundary conditions for elastoplastic tests**: one side (the side situated in the $z = 0$ plane) has all its nodes fixed in all directions, the opposite one (the side situated in the $z = L$ plane) has all its nodes moved to create 2 loading-unloading-reloading test cases: tension/compression (loading to 20% stretch in the Z-direction, unloading to 0% stretch, reloading to -20% stretch and final unloading to 0% stretch) and shear in the X-direction (loading to 20% shear in the X-direction, unloading to 0% shear, reloading to -20% shear and final unloading to 0% shear).
- **material properties**: we consider the cube to be made of trabecular bone (Young's modulus computed from Equ. 5.9 and Poisson's ratio $\nu = 0.33$, with a specific mass of $1.9 g/cc$) whose fabric tensor eigenvectors are $(1,1,1)$ and $(0,-1,1)$ and fabric tensor

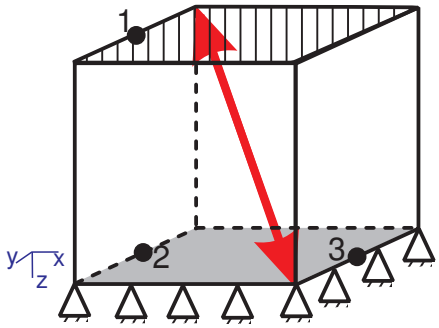

FIGURE 5.8: *Test cases used for the verification method: the side in gray is fixed, the hatched one is moved to create either a compression test, a tension test or shear tests. The red arrow shows the direction for which the cube is considered twice as dense as in the other directions. The black dots are the three points from which the data are extracted.*

eigenvalues are respectively 1.5 and 0.75[1] (i.e. a bone twice as dense in the $(1,1,1)$ direction than in the perpendicular directions). The reduced density is chosen as a mean density for trabecular bone, i.e. $\bar{\rho} = 20\%$.[2] For elastoplastic tests, the yield limit is chosen at $\sigma_y = 200MPa$ (median value of the one calculated with an reverse engineering approach on linear finite element models in [193, 244, 266]) with an isotropic hardening of $h = 725MPa$ (corresponding to a tangential modulus 5% the value of Young's modulus as in the same studies).

We compare for the elastic cases (i.e. orthotropic model in Metafor, damage-based model in Metafor as developed in this work, and orthotropic model in Lagamine) simple mechanical features such as the hydrostatic stress and the von Mises equivalent stress. These values are extracted at three characteristic points of the volume represented in Fig. 5.8 (the data are extracted from the closest Gauss points, which actually represent the same particle in all cases).

We can see in Fig. 5.9 and 5.10 that the overall mechanical behavior for all four tests is similar for the three constitutive models. A closer look tells us there is no difference (to the numerical precision of the integration) between both methods implemented in Metafor. However, the difference is larger between these two cases and the Lagamine integration, especially for the compression and tension tests. Indeed, the Lagamine results show a difference up to 8% relatively to the Metafor results for the compression and tension tests.
This difference is most probably due to the numerical strategy concerning the way the finite element computation is performed (evaluation of equilibrium, non-linear numerical

[1] The third fabric eigenvector is perpendicular to the first two. The third eigenvalue is computed in such a way that the sum of the three eigenvalues is 3 (normalization condition of the fabric tensor).

[2] Such a choice of parameters gives for the classical orthotropic parameters: $E_1 = 223.4MPa$, $E_2 = 163.26MPa$, $E_3 = 163.26MPa$, $\nu_{12} = 0.473$, $\nu_{13} = 0.615$, $\nu_{23} = 0.473$, $G_{12} = 71.48MPa$, $G_{23} = 50.58MPa$, and $G_{13} = 71.48MPa$

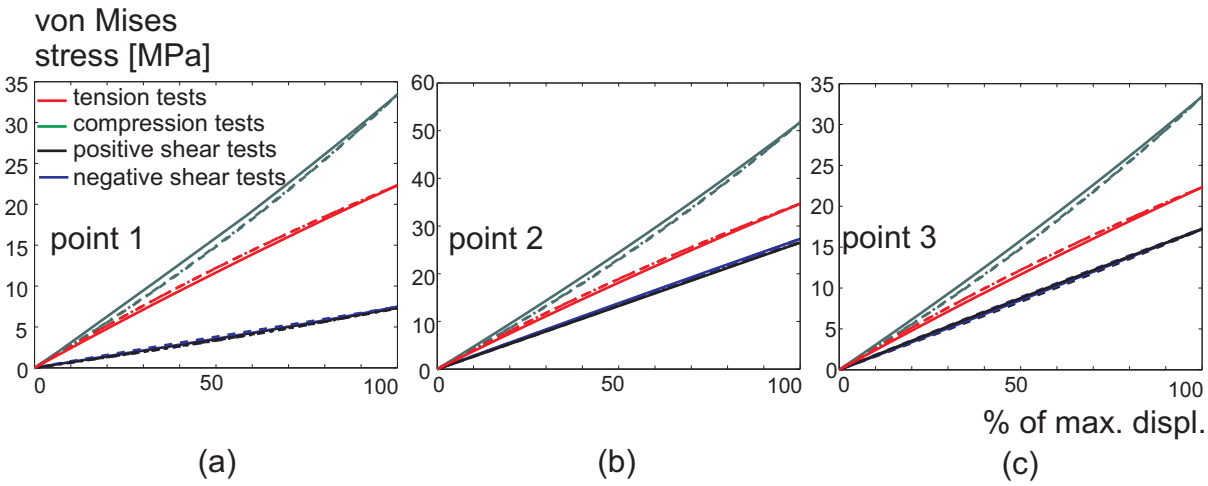

FIGURE 5.9: *von Mises stress for the four test cases (tension: red, compression: green, positive shear test: black, negative shear test: blue) and the three different integration methods (orthotropic Lagamine: plain curves, anisotropic damage-i.e. this work: dashed curves, orthotropic Metafor: dotted curves) - elastic models.*

scheme, time integration, ...). All these parameters are strictly the same for both methods using Metafor while there are most probably differences between Metafor and Lagamine. However, we are confident to conclude that, on the elastic case, our constitutive law integration scheme can be considered as verified.
We can also briefly analyze the implications of the orthotropy in the deformation of the samples (Fig 5.11). We can see that the von Mises equivalent stress for tension (Fig 5.11(a)) and compression (Fig 5.11(b)) tests is higher in the direction of the larger stiffness (more than five times higher) than in the other directions. For the shear tests, while an isotropic behavior would produce exactly the same distribution of stress on both shear tests, we observe not only that the stress intensities are slightly different (higher stress when the main orthotropic direction is submitted to negative hydrostatic stress, i.e. for negative shearing) but also that the deformation is slightly different. Indeed, the positive shearing (Fig 5.11(c)) forces the faces situated in the Oyz plane (vertical and perpendicular to the paper/screen) to curve outwards, while the negative shearing (Fig 5.11(d)) forces the same faces to curve inwards.

For the elastoplastic cases (comparison between orthotropic models in Metafor and damage-based model in Metafor as developed in this work), we compare the same mechanical features as for the elastic case on the same material points as well as the equivalent plastic strain, and, for the whole volume, the force intensity needed for the cube to be deformed.

We can see in Fig. 5.12 that no differences (to the precision of the integration) can be observed on both the hydrostatic stress and the von Mises equivalent stress values computed either with the elastoplastic orthotropic model or with the elastoplastic anisotropic damage one. The same holds true both for the equivalent plastic strain values (Fig. 5.13) and for the

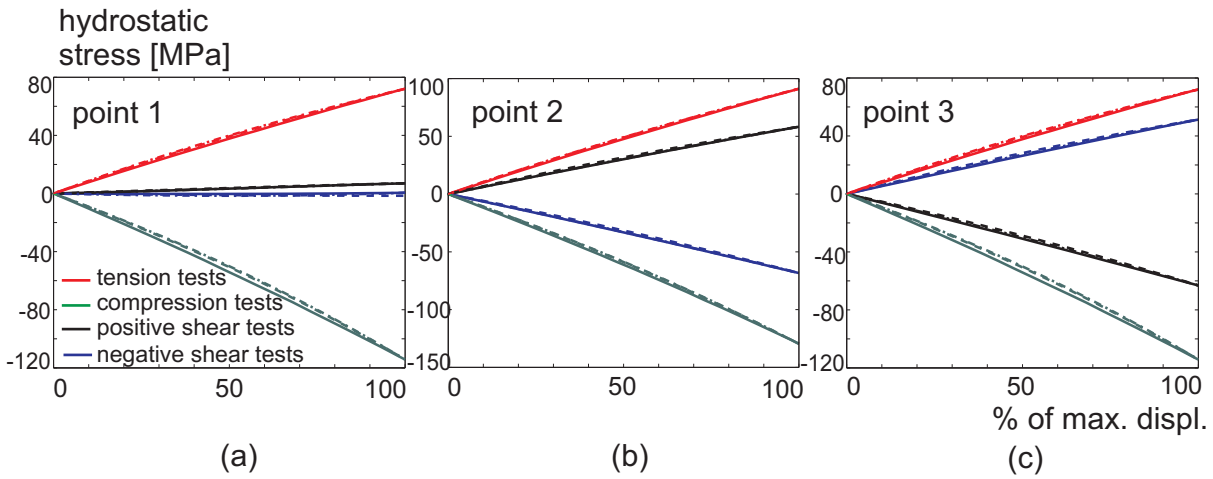

FIGURE 5.10: *hydrostatic stress for the four test cases (tension: red, compression: green, positive shear test: black, negative shear test: blue) and the three different integration methods (orthotropic Lagamine: plain curves, anisotropic damage-i.e. this work: dashed curves, orthotropic Metafor: dotted curves) - elastic models.*

force needed to deform the samples (Fig. 5.14, the shear force is initially negative because the first imposed displacement is along $-\mathbf{e}_x$ while the component of the force along $\mathbf{e}_x$ is depicted). The overall deformation pattern is slightly different from the elastic cases (Fig. 5.15) as the strain is higher due to plasticity.

We should notice here that not only do both models give the same mechanical results but also they converge at the same rate. Indeed, for the computation of the two test cases for elastoplastic material models, we imposed a maximal authorized loading step a hundredth of the maximal displacement (thus minimum 400 steps per test case). Both models needed 406 mechanical iterations to get a solution, i.e. 1 iteration per loading step except when the imposed displacement changed direction (after the maximal displacement and after the minimal displacement were reached) for which 3 mechanical iterations were needed. However, the time needed for each mechanical iteration (i.e. the time needed for the constitutive law to converge) was different. The anisotropic damage model is almost ten times slower than the orthotropic model. This is due mainly to the presence of two systems to solve (computing $\tilde{\boldsymbol{s}}_{n+1}$ following Equ. 5.59 and its derivative with respect to γ) within the Newton-Raphson iterations of the plastic correction. These systems do not exist in the orthotropic model, which is thus faster. The presence of these systems in the anisotropic model is due to the coupling between stresses and damage.

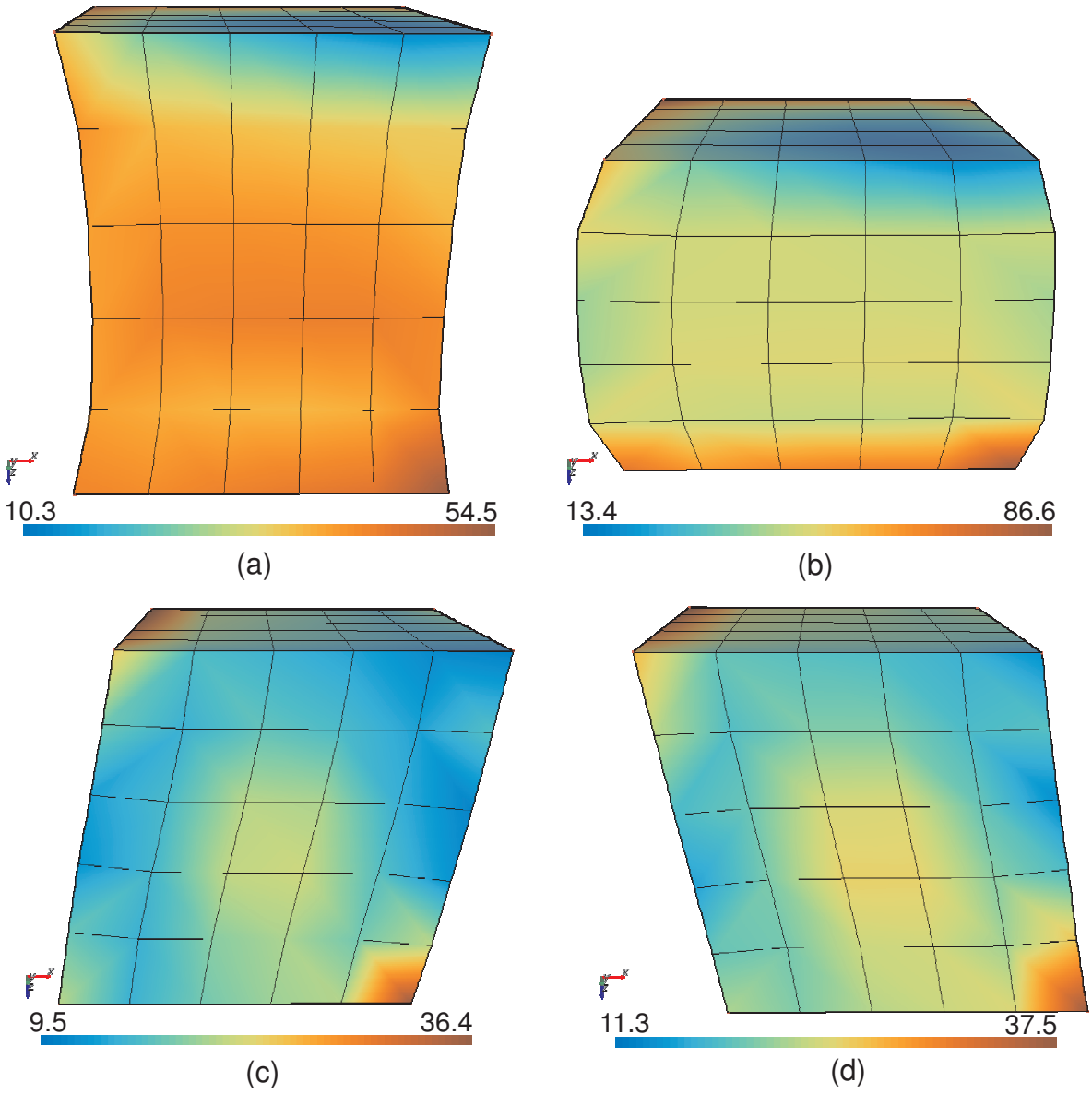

FIGURE 5.11: *von Mises equivalent stress map [MPa] for the four test cases: (a) tension, (b) compression, (c) positive shear, and (d) negative shear - elastic models. The presented stress maps are those of the orthotropic elastic model implemented in Metafor.*

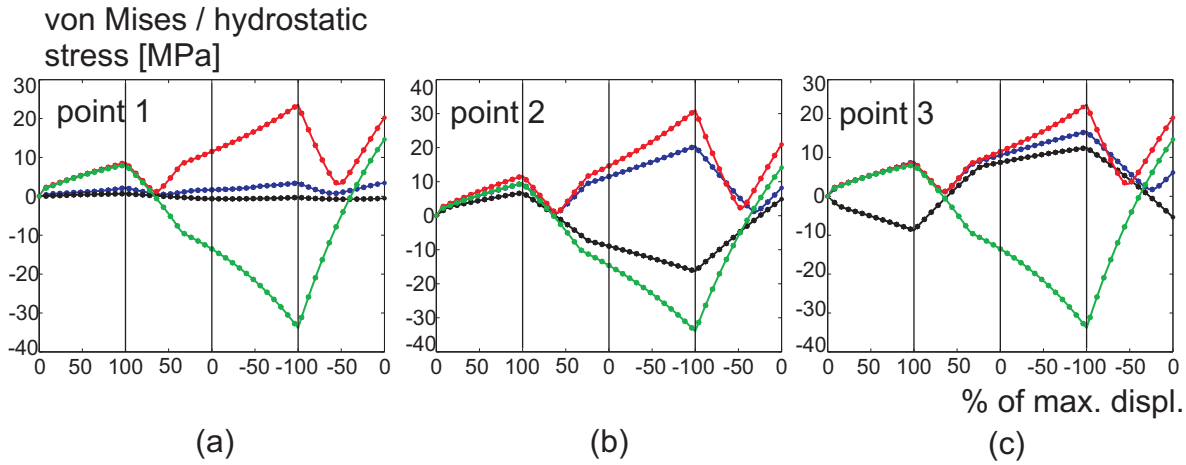

FIGURE 5.12: *stresses for the two test cases (von Mises stress for tension tests: red, von Mises stress for shear tests: blue, hydrostatic stress for tension tests: green, hydrostatic stress for shear tests: black) and the two different integration methods (anisotropic damage-i.e. this work: plain curves, orthotropic Metafor: dots) - elastoplastic models.*

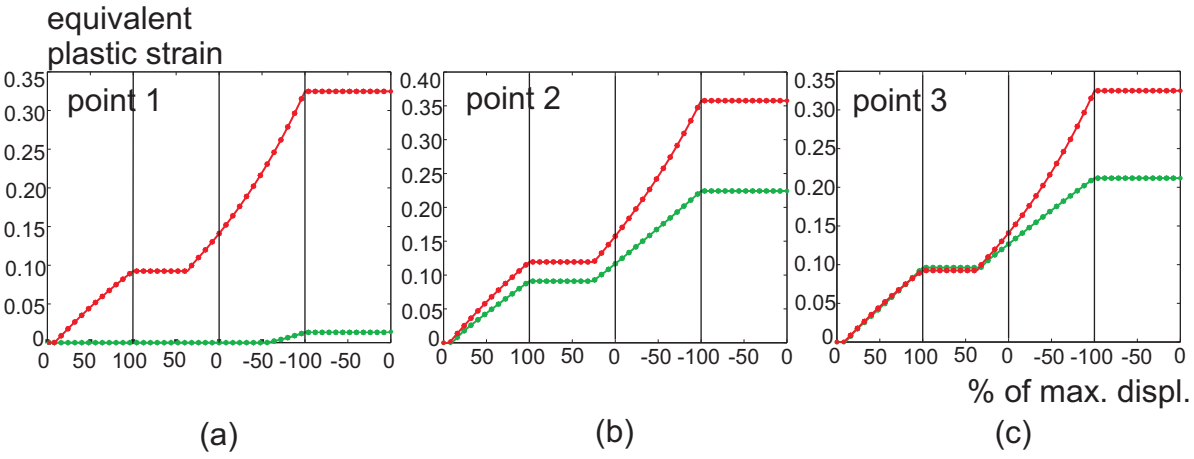

FIGURE 5.13: *equivalent plastic strains for the two test cases (tension: red, shear: green) and the two different integration methods (anisotropic damage-i.e. this work: plain curves, orthotropic Metafor: dots) - elastoplastic models.*

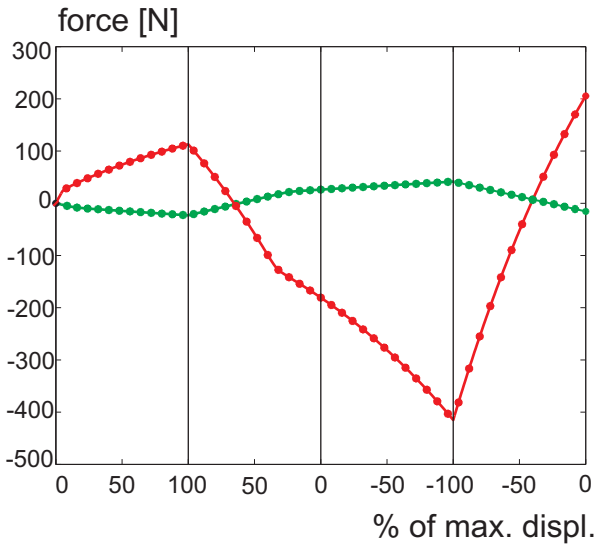

FIGURE 5.14: *force intensity for the two test cases (tension: vertical force, red; shear: horizontal force, green) and the two different integration methods (anisotropic damage-i.e. this work: plain curves, orthotropic Metafor: dots) - elastoplastic models.*

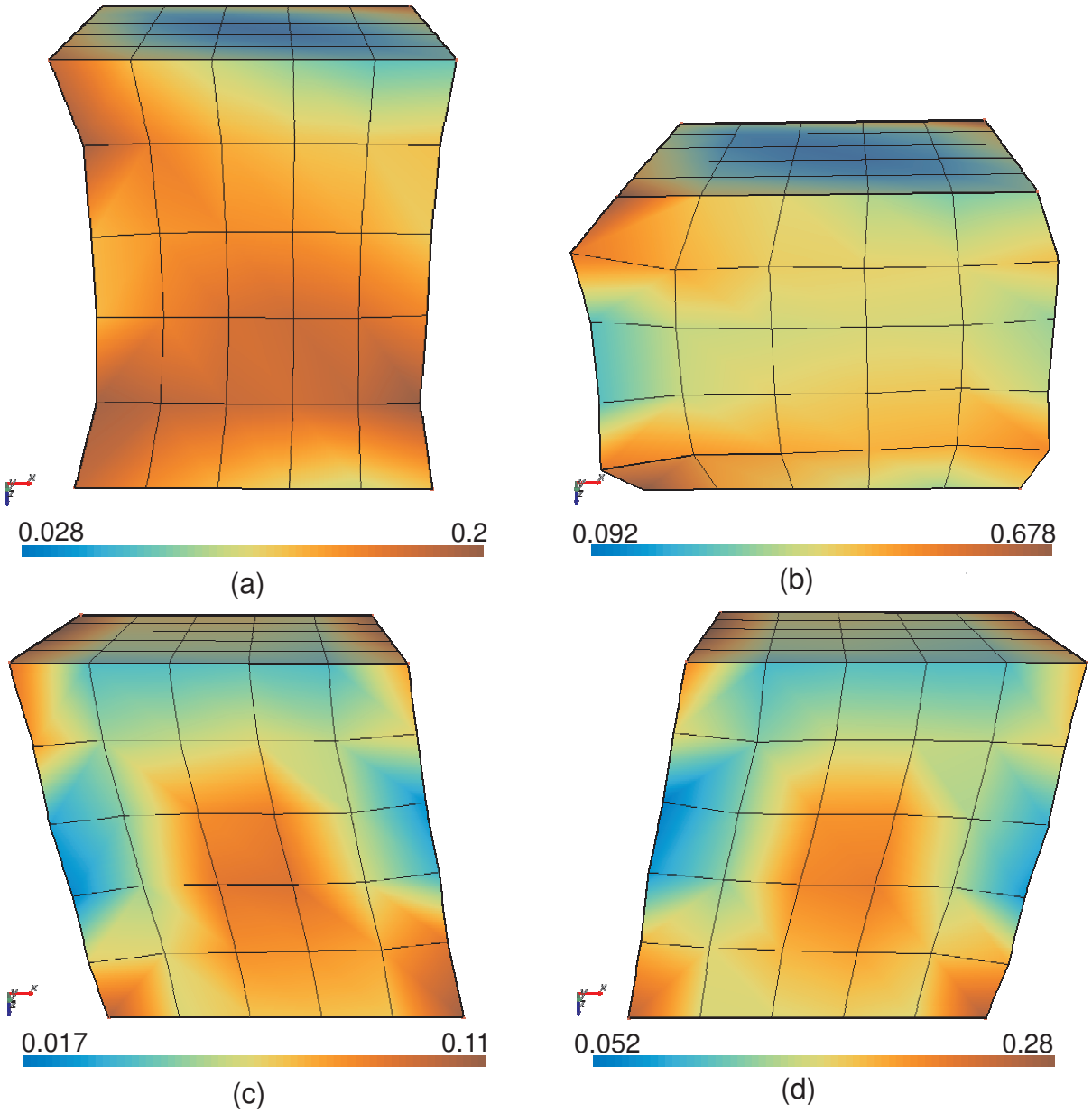

FIGURE 5.15: *equivalent plastic strain map for the two test cases: (a) tension at maximal loading, (b) tension at minimal loading, (c) shear at maximal loading, and (d) shear at minimal loading - elastoplastic models. The presented strain maps are those of the orthotropic elastoplastic model implemented in Metafor.*

5.2.3 Remodeling Law in the Non-Linear Constitutive Framework

As said earlier, the constitutive model needs to be completed with a damage rate model representative of remodeling. We thus close this section by extending the Stanford model (described in section 5.1.1) to a generalized anisotropic theory by means of the principles of continuum damage mechanics, using the ideas suggested by Doblaré and Garcia [62, 83] but overcoming the disadvantages discussed in section 5.1.5.
As discussed, the remodeling law is written in terms of an evolution law for the effective damage tensor: $\dot{\boldsymbol{H}}$.
As for any phenomenological remodeling models considering Frost's mechanostat theory, we need to define a stimulus, a remodeling rate, and a density rate model.

Anisotropic formulation

In order to derive an evolution law for the effective damage tensor $\boldsymbol{H}$, or equivalently for the fabric tensor $\boldsymbol{T}$, we define (as in section 3.4) an external mechanical stimulus, $\boldsymbol{Y}$, identified with the variable thermodynamically associated with the effective damage tensor in terms of the free energy density function (Ψ), choosing to use the stress as the "external driving force".

$$\boldsymbol{Y} = -\left.\frac{\partial \Psi(\boldsymbol{\sigma}, \boldsymbol{H})}{\partial \boldsymbol{H}}\right|_{\boldsymbol{\sigma} \text{ constant}} \tag{Equ. 5.69}$$

This free energy density is calculated considering an isotropic material behavior at trabecular level (and assuming we can extend the expression of the free energy density in small strains to a finite strain problem) and expressing it in terms of either effective or Cauchy stress as:

$$\Psi = \frac{1}{2}\left(\frac{\tilde{p}^2(1-\eta d^H)}{K} + \frac{1}{2G}\left(\mathtt{tr}\left(\boldsymbol{H}^{-1}\tilde{\boldsymbol{s}}\boldsymbol{H}^{-1}\tilde{\boldsymbol{s}}\right) - \frac{(\boldsymbol{H}^{-2}:\tilde{\boldsymbol{s}})^2}{\mathtt{tr}\left(\boldsymbol{H}^{-2}\right)}\right)\right) \tag{Equ. 5.70}$$

$$= \frac{1}{2}\left(\frac{p^2}{K(1-\eta d^H)} + \frac{1}{2G}\mathtt{tr}\left(\boldsymbol{H}\boldsymbol{s}\boldsymbol{H}\boldsymbol{s}\right)\right) \tag{Equ. 5.71}$$

$\boldsymbol{Y}$ is then obtained in terms of the external independent variable (effective stress, $\tilde{p}$, $\tilde{\boldsymbol{s}}$) and the internal variable (effective damage tensor, $\boldsymbol{H}$) as (deriving Equ. 5.70 with respect to $\boldsymbol{H}$):

$$\boldsymbol{Y} = \frac{1}{3K}\eta\tilde{p}^2\boldsymbol{H}^{-3} + \frac{1}{2G}\left[\boldsymbol{H}^{-1}\tilde{\boldsymbol{s}}\boldsymbol{H}^{-1}\tilde{\boldsymbol{s}}\boldsymbol{H}^{-1} - \frac{\boldsymbol{H}^{-2}:\tilde{\boldsymbol{s}}}{\mathtt{tr}\left(\boldsymbol{H}^{-2}\right)}\left(\boldsymbol{H}^{-2}\tilde{\boldsymbol{s}}\boldsymbol{H}^{-1} + \boldsymbol{H}^{-1}\tilde{\boldsymbol{s}}\boldsymbol{H}^{-2} - \frac{\boldsymbol{H}^{-2}:\tilde{\boldsymbol{s}}}{\mathtt{tr}\left(\boldsymbol{H}^{-2}\right)}\boldsymbol{H}^{-3}\right)\right] \tag{Equ. 5.72}$$

It can be written as well in terms of Cauchy stress as

$$\boldsymbol{Y} = \frac{1}{3K}\frac{\eta p^2}{(1-\eta d^H)^2}\boldsymbol{H}^{-3} + \frac{1}{2G}\boldsymbol{s}\boldsymbol{H}\boldsymbol{s} \tag{Equ. 5.73}$$

The damage criterion is the domain of the external mechanical stimulus, $\boldsymbol{Y}$, for which damage is not modified (the lazy zone as used in the literature of bone remodeling) both in over-

load and underload conditions. Following Doblaré and Garcia's approach with Jacob's definitions, we propose two damage criteria, one for formation and one for resorption:

$$\text{Formation}: g_f = C\frac{3^{1/4}}{\sqrt{1-\mathrm{w}}}(\boldsymbol{J}:\boldsymbol{J})^{1/4} - (\psi_t^\star + \omega)\rho^{2-\beta/2} \qquad \text{(Equ. 5.74)}$$

$$\text{Resorption}: g_r = -C\frac{3^{1/4}}{\sqrt{1-\mathrm{w}}}(\boldsymbol{J}:\boldsymbol{J})^{1/4} + (\psi_t^\star - \omega)\rho^{2-\beta/2} \qquad \text{(Equ. 5.75)}$$

with $\boldsymbol{J} = \mathbb{W}:\boldsymbol{Y} = \frac{1}{3}(1-2\mathrm{w})\mathtt{tr}(\boldsymbol{Y})\,\boldsymbol{I} + \mathrm{w}\boldsymbol{Y}$ and C defined in Equ. 5.10.
As two parameters, w in the definition of $\boldsymbol{J}$, and η in the definition of $\tilde{\boldsymbol{\sigma}}$, are defined to weigh the deviatoric and hydrostatic parts of tensors, and as they are defined on two distinct intervals ($\mathrm{w} \in [0,1[$ and $\eta \in [1,+\infty[$), we actually use $\mathrm{w} = 1 - e^{-(\eta-1)}$ to reduce the number of parameters to one (this (w,η) mapping is a continuous mapping between a parameter, η, defined in an infinite interval and one, w, defined in a finite interval). As η is usually bound (about 3 for metals [146] and taken to be equal to the degree of anisotropy (DA) in the case of bone), there is no numerical difficulties using this function (while it would tend to 1 for large values of η and the division by $(1-\mathrm{w})$ in Equ. 5.74, Equ. 5.75 would not be possible otherwise).
Considering an associated evolution law for the effective damage tensor[1], we can write:

$$\dot{\boldsymbol{H}} = \mu^f \frac{\partial g_f}{\partial \boldsymbol{Y}} + \mu^r \frac{\partial g_r}{\partial \boldsymbol{Y}} \qquad \text{(Equ. 5.76)}$$

with the consistency conditions $\mu^f, \mu^r \geq 0; \quad g_f, g_r \leq 0; \quad \mu^f g_f = \mu^r g_r = 0$.
Deriving the remodeling criteria (Equ. 5.74 and Equ. 5.75), combining with the effective damage tensor definition (Equ. 5.38) and the density variation of the Stanford model (Equ. 5.1), the evolution law of the effective damage tensor is written for both formation and resorption conditions as (details available in Appendix D):

$$\dot{\boldsymbol{H}} = -\frac{\beta k S_v \dot{r}}{2}\frac{\mathtt{tr}\left(\boldsymbol{H}^{-2}\right)}{\mathtt{tr}\left(\boldsymbol{H}^{-3}(\mathbb{W}:\boldsymbol{J})\right)}\frac{\rho_0}{\rho}\mathbb{W}:\boldsymbol{J} \qquad \text{(Equ. 5.77)}$$

with $\mathbb{W} = \frac{1}{3}(1-2\mathrm{w})\boldsymbol{I}\otimes\boldsymbol{I} + \mathrm{w}\mathbb{1}$ as defined earlier.
The remodeling rate $\dot{r}$ is obtained from the remodeling criterion that is currently active:

$$\dot{r} = \begin{cases} -c_r \dfrac{g_r}{\rho^{2-\beta/2}} & \text{for } g_r \geq 0, g_f < 0, \\ 0 & \text{for } g_r < 0, g_f < 0, \\ c_f \dfrac{g_f}{\rho^{2-\beta/2}} & \text{for } g_f \geq 0, g_r < 0, \end{cases} \qquad \text{(Equ. 5.78)}$$

Finally, the density variation can be computed from Equ. 5.1 defined in the Stanford model. It has to be emphasized however that this density change is not actually used to compute

[1] This is the equivalent to the effective damage tensor evolution defined from the damage dissipation potential in Equ. 3.59.

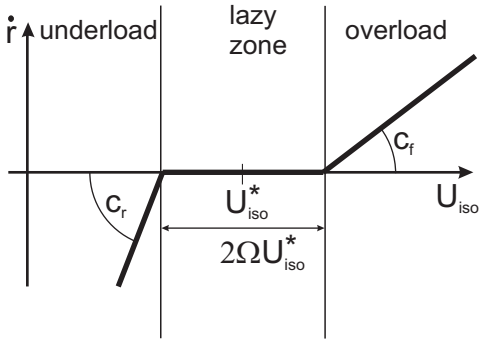

FIGURE 5.16: *Remodeling rate used in the isotropic version of our model*

a change of mass. Only the stiffness variation due the density rate is used as the density is considered having an influence on stiffness only. Therefore, there is no actual change of mass considered in the bone.

This remodeling law is used with the generic anisotropic damage model presented in section 5.2.1. To use it with the consistent tangent operator, the derivatives of $\dot{\boldsymbol{H}}$ with respect to p, $\boldsymbol{s}$ and $\boldsymbol{H}$ have to be computed[1].

Isotropic formulation [172]

This anisotropic model can easily be reduced to an isotropic formulation. The damage variable is then : $\boldsymbol{d} = d\boldsymbol{I}$ and therefore $\boldsymbol{H} = h\boldsymbol{I} = (1-d)^{-1/2}\boldsymbol{I}$ (choosing $\eta = 1$).
We can show that in this case both remodeling criteria (Equ. 5.74 and Equ. 5.75) take the simpler form:

$$\text{formation} : g_f = \underbrace{C(1-d)^{-1/4}\sqrt{\frac{1}{2G}\boldsymbol{s}:\boldsymbol{s}+\frac{1}{K}p^2}}_{U_{\text{iso}}} - (1+\Omega)\psi_t^{\star}\rho^{2-\beta/2} < 0 \qquad \text{(Equ. 5.79)}$$

$$\text{resorption} : g_r = -U_{\text{iso}} + (1-\Omega)\psi_t^{\star}\rho^{2-\beta/2} < 0 \qquad \text{(Equ. 5.80)}$$

Equ. 5.77 leads to the siotropic damage rate:

$$\dot{d} = -\beta k S_v \dot{r}\frac{\rho_0}{\rho}(1-d) \qquad \text{(Equ. 5.81)}$$

with $\dot{r}$ defined by Equ. 5.78.
The remodeling rate is thus a function of this strain-energy density like measure, U_{iso}, as depicted in Fig 5.16.

[1] For any damage evolution law, the derivatives of $\dot{\boldsymbol{H}}$ with respect to p, $\boldsymbol{s}$, $\boldsymbol{E}^N$, γ and $\boldsymbol{H}$ are needed to compute the tangent operator. In the case of damage representing the microstructure, and its evolution a bone remodeling law, the derivatives with respect to $\boldsymbol{E}^N$ and γ are equal to zero.

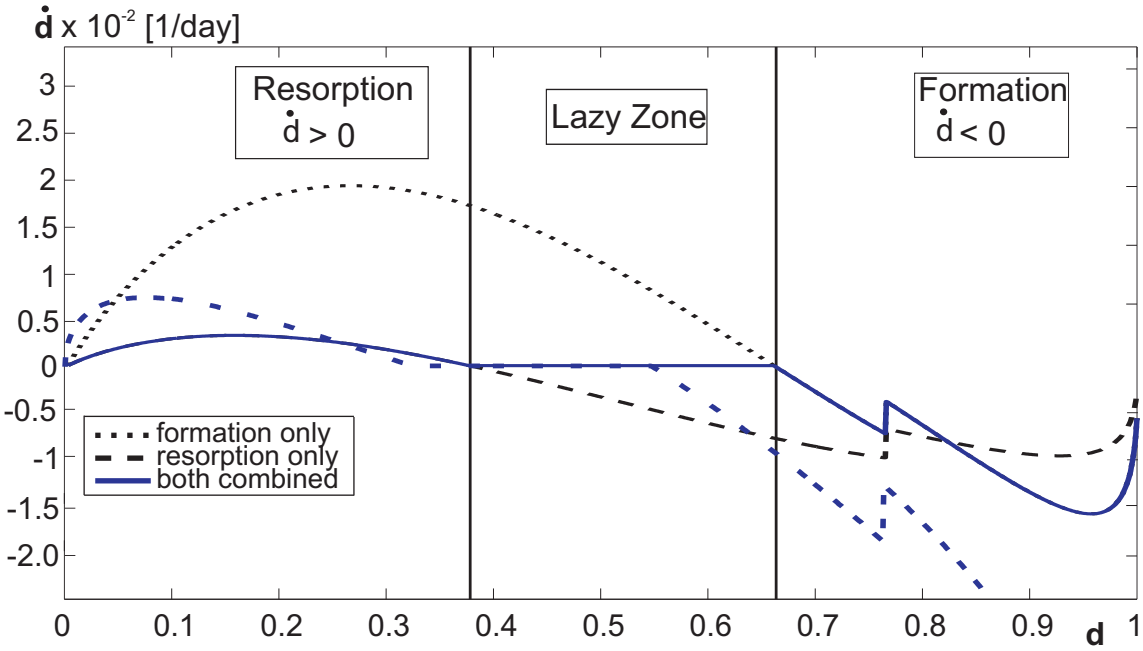

FIGURE 5.17: *Damage rate versus damage value (strain energy equivalence formulation) - parameters values:* $N = 1000$ *(nb of cycles per day),* $\psi_t^\star = 1[MPa]$ *(homeostatic stimulus value),* $k = 0.5$ *(percentage of available surface area),* $\Omega = 0.25$ *(half-width of the lazy-zone),* $p = J_2 = 5.0[MPa]$ *(assumed applied stress),* $c_f = 0.01[mm/day], c_r = c_f/2.$ *(remodeling constants),* $\rho_0 = 1.9[g/cc]$*, the plain blue line is the actual computed damage rate, the dashed blue line represents the damage rate as if computed with Doblaré's model (transformed into a strain equivalence damage for comparison purposes). The jump around* $d = 0.78$ *corresponds to the jump in the Young's modulus computation as a function of the apparent density*

While Doblaré and Garcia's model was not, this isotropic formulation is completely equivalent to the Stanford theory (described in details in section 5.1.1), when a small strain elastic problem is considered.

Fig. 5.17 shows a computation of the damage rate with the damage value, according to Equ. 5.81.
As with Doblaré's model, the three remodeling zones (formation, resorption, and lazy zone) are easily distinguished. For direct comparison purposes, the damage rate obtained with Doblaré and Garcia's model but shifted to a strain equivalent representation of damage (simply using $1-d = (1-d_{see})^2$ in the damage rate formulation) is also depicted. We can see that for high values of damage, therefore in formation conditions, the damage rate obtained with a model fully equivalent to the Stanford model (such as the one presented here) is much reduced compared to Doblaré and Garcia's model. This difference at high damage values comes mainly from the $\rho^{-\beta/8}$ discussed earlier with other drawbacks of Dobablaré and Garcia's model. However, it should be noticed that the definition of the a "strain-energy density

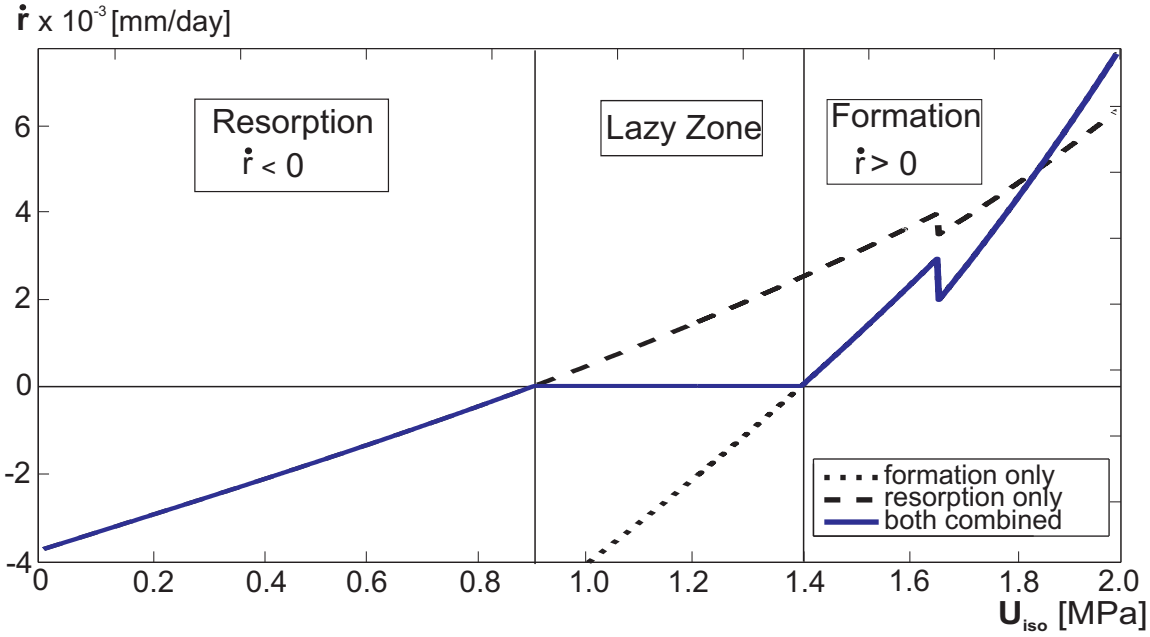

FIGURE 5.18: *Remodeling rate as a function of U:* $N = 1000$, $\psi^\star = 1[MPa]$, $k = 0.5$, $\Omega = 0.25$, $p = J_2 = 5.0[MPa]$, $c_f = 0.01[mm/day]$, $c_r = c_f/2.$, $\rho_0 = 1.9[g/cc]$, *the plain blue line is the actual computed remodeling rate.*

like function", U in Doblaré and Garcia's model, and U_{iso} in our model, differ between both models not only by this enigmatic factor found in Doblaré and Garcia's model but also by a $(1-d)^{-0.25}$ factor due to the different representation of the free energy between both approaches of damage and not accounted for in this comparison. It is also the combination of both of the above reasons that can explain the difference in the width and position of the lazy zone. Finally, the differences in resorption (low damage values) are explained also by the difference in the definition of the remodeling criteria in resorption. We here remind the reader that Doblaré and Garcia used the relation $g_r^{\texttt{Dob.iso.}} = \dfrac{1}{U} - \dfrac{1}{(1-\Omega)U^\star}$ and therefore introduced not only an inconsistency in the dimensional analysis of their model but also a difference in the value of this criterion compared to our model (difference of a factor $(1-\Omega)UU^\star$).

As for Doblaré and Garcia's model, the homeostatic value, $(\psi_t^\star \pm \omega)\rho^{2-\beta/2}$, is not constant but is a function of damage (through the value of ρ). Thus, the remodeling rate variation is not exactly as sketched in Fig. 5.16 and shows a slight non-linearity. The actual remodeling rate of the present model as function of U_{iso} is plotted in Fig. 5.18. It does not show a downward concavity in resorption as it was the case for Doblaré and Garcia's model as the remodeling stimulus is linear in U_{iso} (while Doblaré and Garcia's is not linear in U).

Summary of the characteristics and differences between the presented remodeling model and Doblaré and Garcia's

We here summarize the main characteristics (an their differences) of the developed and presented model and the one it is based on, Doblaré and Garcia's model.
As explained, phenomenological remodeling models are based on the definition of three characteristics: the **density rate function** ($\dot{\rho}$ function of $\dot{r}$), the **remodeling rate function** ($\dot{r}$ function of $\psi_t, \psi_t^\star$), and the **stimulus definition** (ψ_t and its homeostatic level $\psi_t^\star$). These models are coupled to a **constitutive law for the bone matrix**.
These four characteristics are therefore the one we summarize here.

• Integration of the remodeling model into the constitutive law

Doblaré's model assumes an elastic material for the bone matrix, we assume an elastoplastic material, with von Mises yield criterion.

Doblaré: anisotropic material (and remodeling);
described by means of an anisotropic damage tensor
(strain energy equivalence)
representative of the morphology:
$\boldsymbol{d}_{see} = \boldsymbol{I} - \bar{\rho}^{\beta/2}\sqrt{A}\boldsymbol{T} = \boldsymbol{I} - \boldsymbol{H}_{see}^2$ with $\boldsymbol{T}$ the fabric tensor.
The damage rate is due to remodeling:

$$\text{formation: } \dot{\boldsymbol{H}}_{see} = \frac{3\beta k S_v \dot{r}}{4} \frac{1}{\mathtt{tr}\left(\boldsymbol{H}_{see}^{-2}(\mathbb{W}:\boldsymbol{J})\boldsymbol{H}_{see}\right)} \frac{\rho_0}{\rho}\mathbb{W}:\boldsymbol{J}$$

$$\text{resorption: } \dot{\boldsymbol{H}}_{see} = \frac{3\beta k S_v \dot{r}}{4} \frac{1}{\mathtt{tr}\left(\boldsymbol{H}_{see}^{-2}(\mathbb{W}:\boldsymbol{J}^{-3})\boldsymbol{H}_{see}\right)} \frac{\rho_0}{\rho}\mathbb{W}:\boldsymbol{J}^{-3}$$

where $\boldsymbol{J}$ is linked to the variable thermodynamically conjugated to $\boldsymbol{H}_{see}$.

Developed: anisotropic material (and remodeling);
described by means of an anisotropic damage tensor
(strain equivalence)
representative of the morphology:
$\boldsymbol{d} = \boldsymbol{I} - \bar{\rho}^{\beta} A\boldsymbol{T} = \boldsymbol{I} - \boldsymbol{H}^{-2}$ with $\boldsymbol{T}$ the fabric tensor.
The damage rate is due to remodeling:

$$\dot{\boldsymbol{H}} = -\frac{\beta k S_v \dot{r}}{2} \frac{\mathtt{tr}\left(\boldsymbol{H}^{-2}\right)}{\mathtt{tr}\left(\boldsymbol{H}^{-3}(\mathbb{W}:\boldsymbol{J})\right)} \frac{\rho_0}{\rho}\mathbb{W}:\boldsymbol{J}$$

where $\boldsymbol{J}$ is linked to the variable thermodynamically conjugated to $\boldsymbol{H}$.

• Stimulus definition

Both models derive a stimulus from the variable energetically associated to either Doblaré's remodeling tensor (for Doblaré and Garcia's model) or from the effective damage tensor in the case of the model presented here.

• Remodeling rate function

Both remodeling rate function are built following the mechanostat theory, assuming a range of the stimulus value (of half-width ω) under which (underloaded conditions) bone resorption occurs and over which (overloaded conditions) bone formation occurs. Both models therefore propose remodeling criteria defining the borders between formation conditions, resorption conditions, and homeostatic conditions (no remodeling occurs).

- **formation criterion**:

Doblaré: $$g_f^{\mathtt{Dob.}} = \underbrace{C\frac{3^{1/4}}{\sqrt{2(1-\mathrm{w})}}(\boldsymbol{J}:\boldsymbol{J})^{1/4}}_{\substack{\text{equivalent to } \psi_{\mathrm{t}}\rho^{2-\beta/2} \text{ expressed} \\ \text{with the continuum damage formulation}}} \rho_0^{-\beta/8} A^{1/8} \quad -(\psi_{\mathrm{t}}^{\star}+\omega)\rho^{2-5\beta/8}$$

Developed: $$g_f = \underbrace{C\frac{3^{1/4}}{\sqrt{1-\mathrm{w}}}(\boldsymbol{J}:\boldsymbol{J})^{1/4}}_{\substack{\text{equivalent to } \psi_{\mathrm{t}}\rho^{2-\beta/2} \text{ expressed} \\ \text{with the continuum damage formulation}}} - (\psi_t^{\star}+\omega)\rho^{2-\beta/2}$$

- **resorption criterion**:

Doblaré: $$g_r^{\mathtt{Dob.}} = \underbrace{\frac{\sqrt{2(1-\mathrm{w})}}{C27^{1/4}}(\boldsymbol{J}^{-1}:\boldsymbol{J}^{-1})^{1/4}}_{\substack{\text{equivalent to } 1/(\psi_{\mathrm{t}}\rho^{2-\beta/2}) \text{ expressed} \\ \text{with the continuum damage formulation}}} \rho_0^{\beta/8} A^{-1/8} \quad -\frac{1}{(\psi_{\mathrm{t}}^{\star}-\omega)\rho^{2-5\beta/8}}$$

Developed: $$g_r = - \underbrace{C\frac{3^{1/4}}{\sqrt{1-\mathrm{w}}}(\boldsymbol{J}:\boldsymbol{J})^{1/4}}_{\substack{\text{equivalent to } \psi_{\mathrm{t}}\rho^{2-\beta/2} \text{ expressed} \\ \text{with the continuum damage formulation}}} + (\psi_t^{\star}-\omega)\rho^{2-\beta/2}$$

- **remodeling rate** Both remodeling rate are defined from the criterion currently active:

$$\text{Doblaré: } \dot{r}^{\mathtt{Dob.}} = \begin{cases} c_f \dfrac{g_f^{\mathtt{Dob.}}}{\rho^{2-\beta/2}} & \text{for } g_f^{\mathtt{Dob.}} > 0, \\ -c_r \dfrac{g_r^{\mathtt{Dob.}}}{\rho^{2-\beta/2}} & \text{for } g_r^{\mathtt{Dob.}} > 0, \\ 0 & \text{otherwise.} \end{cases}$$

$$\text{Developed: } \dot{r} = \begin{cases} c_f \dfrac{g_f}{\rho^{2-\beta/2}} & \text{for } g_f > 0, \\ -c_r \dfrac{g_r}{\rho^{2-\beta/2}} & \text{for } g_r > 0, \\ 0 & \text{otherwise.} \end{cases}$$

• Density rate function

Both models use the same function relating the density rate to the remodeling rate, considering the formed/resorbed bone is fully mineralized:

$$\dot{\rho} = kS_v\rho_0\dot{r}$$

Properties of the model

As the tools used are equivalent to the one proposed in Doblaré and Garcia's model [62, 83], the properties 3 to 5 of their model discussed in section 5.1.5 are fulfilled in the present model as well:

- for an initially isotropic bone structure, the effective damage tensor $\boldsymbol{H}$ starts its evolution along each of the principal stress directions, proportionally to the stress triaxiality.
- when the effective damage tensor $\boldsymbol{H}$ is aligned with the Cauchy stress tensor (coincident eigenvectors), the rate of the fabric tensor eigenvectors vanishes. In this situation, the model is at an equilibrium state with respect to the principal directions of the reference system, with all the different tensors remaining aligned.
- assuming that the remodeling criteria is convex, a minimum mechanical dissipation (energy dissipation without taking into account the provided metabolic energy) principle is fulfilled.

Properties 1 and 2, which have been analyzed as limitations of Doblaré and Garcia's model since the Stanford model could not be retrieved, do not apply to the model proposed in this work. This implies that the upper bound of β cannot be interpreted as the limit value of a saturation process of the bone tissue with respect to the remodeling criterion. The upper bound of β ($\beta = 3.2$) is thus considered as an external experimental parameter.
An extensive parameters analysis of the model is given in section 5.3.

As specified earlier, the density change due to remodeling is not actually computed, only its effect on the stiffness through the fabric tensor is. In particular, there is no actual change of mass considered in the bone. Therefore the model cannot be used in problems for which mass is critical.
For instance, it cannot be used in dynamical analysis (the mass matrix, Equ. 3.18, is not properly updated) or in applications sustaining body forces such as gravity (the volume integral of the external forces vector, Equ. 3.20, is not properly updated). This is therefore one of the main drawbacks of the model (or rather of its implementation[1]). However, in the applications considered in this work, not only will we work in quasi-static analysis (not accounting for the inertia effects affected by the mass matrix) and neglecting gravity effects, but also both the variation of mass and the velocity field will be small, therefore working at constant mass is not far from reality.

One of the other drawbacks of the model comes from the nonlinear relationship between the apparent density $\bar{\rho}$ and the associated stiffness (Equ. 5.9). This relationship leads to a

[1] Taking into account a mass variation would rigorously change the mass balance equation and therefore the momentum balance equation. A term accounting for the source of mass, here the biological remodeling, and its advection would be added in each of these equations.

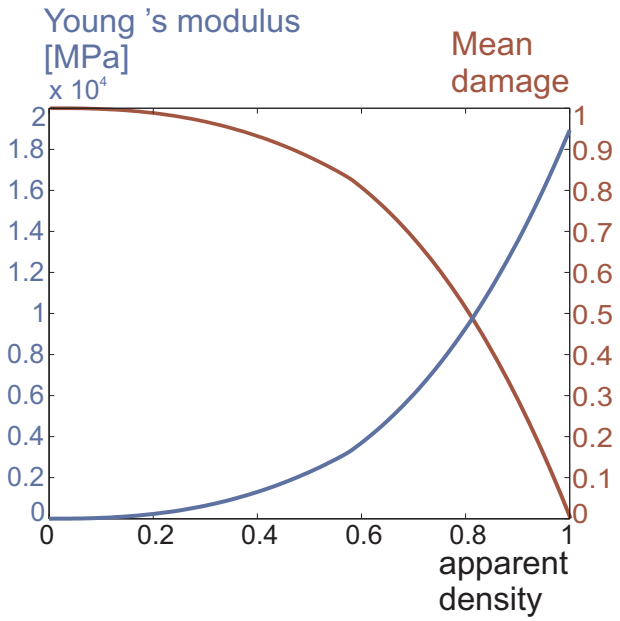

FIGURE 5.19: *Young's modulus and mean damage as a function of the apparent density using Equ. 5.9 and a strain equivalence representation of damage*

mean damage whose value is almost constant and above 0.99 for apparent densities below 0.18 (see Fig. 5.19). Even though, as already specified, the damage value does not reach 1.0 thanks to the decaying specific surface area, a value above 0.97/0.98 correspond to a plausible (yet low) apparent density but to a very low Young's modulus. This therefore means that for values of the apparent density below about 0.2, the bone is considered as very compliant and traditional Lagrangian techniques do not allow to follow the material deformation with the initial mesh. However, this major drawback will here be most of the time overcome using mesh management techniques such as the ALE method and/or remeshing.

Modifications for the Alveolar Bone [172]

As stated earlier, alveolar bone remodeling seems on a macroscopic scale to depend mainly on the hydrostatic pressure state [26, 27, 171]. Apposition occurs on the tension sites of a tooth and resorption on the compression ones. To model these processes, several authors do not consider a pressure dependency of the bone remodeling process but focus only on the periodontal ligament's non-linear response [183, 185, 214, 250, 268]. Its non-linearity and opposite behavior in tension and compression leads to opposite loading conditions (considering the remodeling problem) of the bone on each side of the tooth.
However, the present work concentrates on the bone behavior during remodeling. We assume, as explained in section 2.2, the hydrostatic pressure state (positive or negative) in the bone matrix as the key stimulus to differentiate between apposition and resorption in overloaded conditions. Indeed, as specified, the bone remodeling process in orthodontics tooth movement is closely related to the cellular activity in the periodontal ligament, especially to the activity of the fibroblasts. This cellular activity is believed to be pressure sensitive. Moreover, the cell supply needed for bone remodeling is delivered by the blood vessels. However, the alveolar bone's main blood and cell supply is delivered through the periodontal ligament. As this membrane's stiffness is much less than the surrounding tissues, the strain levels are higher. It is therefore often postulated [141, 262] that a disruption in the blood supply within the periodontal ligament stops the nutrients supply and therefore impedes remodeling. The remodeling process is therefore triggered by the hydrostatic pressure state in the PDL and stopped when these stresses are too high. Moreover, during their experimental work, Yousefian *et al.* [281] correlated the response of cells active in the remodeling process to the hydrostatic pressure within the ligament. We therefore assume that it is the same stimulus which is responsible for the differentiation between apposition and resorption and for the triggering of the phenomenon.
Thus, a bone remodeling rate $\dot{r}$ of the type Equ. 5.78 cannot be directly applied to the alveolar bone. It would indeed not differentiate formation and resorption sites of the bone regardless of the tension or compression state. Indeed the external mechanical stimulus on which $\dot{r}$ depends does not involve the sign of the pressure but only on its intensity ($\boldsymbol{Y} \propto p^2$ Equ. 5.73). We thus propose a model that uses an approach similar to the one exposed, for both the damage definition and variation as well as for the damage criteria. However, in accordance to the observation of a pressure dependent phenomenon, the remodeling rate definition is modified (Fig. 5.20, Equ. 5.82) taking into account the pressure state. We here therefore consider an overload criterion g_o that can be expressed as the previous formation criterion (Equ. 5.74) and an underload criterion g_u, expressed as the previous resorption criterion (Equ. 5.75). In underloaded conditions ($g_u \geq 0$), we consider resorption is always observed. In overloaded conditions ($g_o \geq 0$), we consider formation for positive hydrostatic pressure conditions and resorption for negative ones.
Finally, in compression, remodeling is limited by the capillary blood pressure. Therefore, in compression, when the pressure is higher than a critical pressure, p_{crit}, no remodeling at

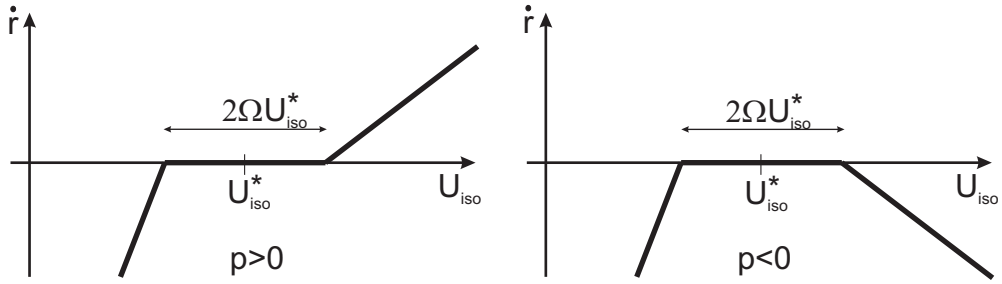

FIGURE 5.20: *Pressure dependent remodeling rate, pressure p being positive in tension.*

all is observed due to the lack of access to remodeling cells. The remodeling rate is therefore equal to zero below this hydrostatic stress value in overloaded conditions. This critical value of the hydrostatic pressure within the periodontal ligament is converted into a critical value for the hydrostatic pressure within the alveolar bone using as a scaling factor the bulk modulus ratio of the two tissues.
This new remodeling rate is thus given by :

$$\dot{r}_p = \begin{cases} c_f \dfrac{g_o}{\rho^{2-\beta/2}} & \text{if } g_o \geq 0,\ g_u < 0 \quad \text{and} \quad p > 0 \\ -c_r \dfrac{g_o}{\rho^{2-\beta/2}} & \text{if } g_o \geq 0,\ g_u < 0 \quad \text{and} \quad p < 0 \text{ and } |p| < p_{crit} \\ -c_r \dfrac{g_u}{\rho^{2-\beta/2}} & \text{if } g_u \geq 0,\ g_o < 0 \\ 0 & \text{if otherwise} \end{cases} \qquad \text{(Equ. 5.82)}$$

where c_r and c_f are two remodeling constants, β is the density related parameter introduced in Equ. 5.8 and p, the pressure is positive in tension. For numerical purposes, the differentiation between formation and resorption when $g_o \geq 0$ is not exactly at $p = 0$ but at $p = \pm\delta p \ll 1$. A linear interpolation for the coefficient between $p = -\delta p$ ($c = -c_r$) and $p = \delta p$ ($c = c_f$) is used. The remodeling coefficient function of the hydrostatic pressure is depicted in Fig. 5.21.

The damage evolution is proportional to the defined remodeling rate so that repair will occur in the case of tissue formation, for overloaded tension conditions. Damage will increase in the case of tissue resorption, both in the case of overloaded compression conditions and underloaded conditions. Therefore, when underloaded, the alveolar bone would resorb, as it is observed following the loss of a tooth. However, when overloaded, such as when following orthodontic treatment, the bone will resorb where it is compressed and will be formed where it is in tension so that the tooth will move in its socket along the direction of the applied force.

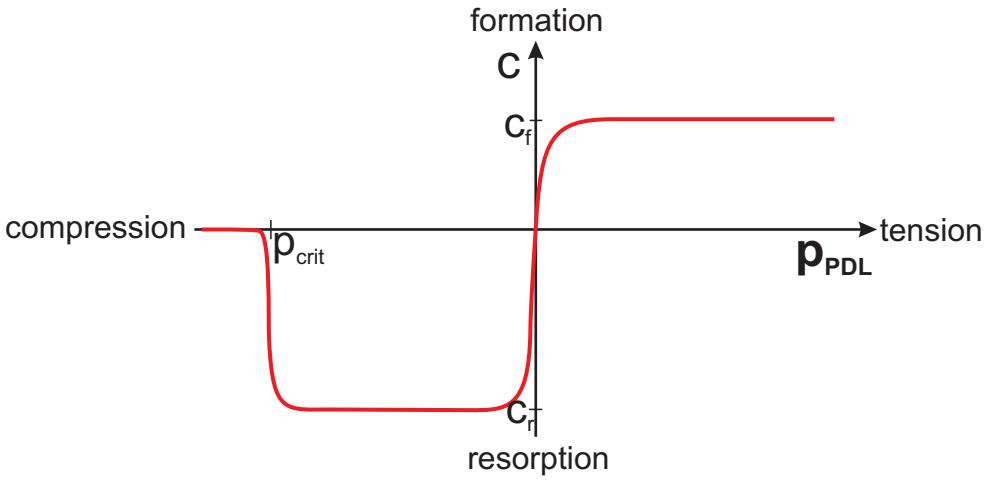

FIGURE 5.21: *Value of the remodeling coefficient c as a function of the hydrostatic pressure for the remodeling law adapted to the specific case of alveolar bone in overloaded conditions.*

5.3 Sensitivity Analysis on Homogeneous Cylinders

Le début d'la fin s'enchaîne avec la fin du début
lorsque le milieu n'est pas ben long. *- P. Geluck*

In this section we systematically present an analysis on the different parameters of the model. This analysis is performed on homogeneous anisotropic cylindrical samples submitted either to compression, tension or shear conditions. We will first present the purely mechanical response and especially the influence of the anisotropy of the morphology. No remodeling is therefore considered. The model is thus the constitutive law one can use for an elastoplastic cellular solid. To do so, the damage rate of the model is simply set to zero. We then present the remodeling behavior, considering all the remodeling parameters on an adaptable elastic material such as trabecular bone.

5.3.1 Anisotropy parameters analysis

The main morphological parameters (orthotropic directions and porosity) are analyzed on simple compression and shear test cases. For this, we produced cylindrical models of bone samples (2cm of height, 1cm of diameter, see Fig. 5.22(a))). For the compression tests, one circular side is considered in frictionless contact conditions with a rigid fixed plane ; while the other side is submitted to a vertical displacement of one fifth of the initial height and free in the horizontal plane to produce compression tests (see Fig. 5.22(b)). For the shear tests, one circular side is completely constrained (the nodes are fixed in space) while the other side is submitted to a horizontal displacement of one fifth of the diameter (see Fig. 5.22(c)). The initial set of parameters considers an isotropic bone sample of 40% apparent density (leading to an apparent Young's modulus of $1014MPa$, while the Young's modulus of the trabeculae is considered to be $13748MPa$ - bone full density of $1.9gr/cc$), a yield limit at tissue level of $500MPa$ with a hardening parameter of 1.0, i.e. almost perfectly plastic at tissue level.
The morphology parameters are examined using the anisotropic remodeling model developed in this work. We compare four different morphologies on the cylindrical samples. The first one is isotropic, the second is mainly aligned with the cylinder axis (vertical), the third is mainly perpendicular to the cylinder axis (horizontal) and the last one is aligned with an oblique direction with respect to the cylinder's axis. The purely mechanical response (no damage rate due to remodeling) of the model is then analyzed in displacement driven problems. As no remodeling is accounted for, there is no change of either density or orientation with time. We analyze here the force intensity versus displacement. We will also look at maps of the von Mises equivalent stress for the maximal imposed displacement. The deviatoric stress is assumed to be more affected by the anisotropy than the hydrostatic one (affected only through the η parameter, here varying from 1.0 for an isotropic test to $\sqrt{2}$ for the three other morphologies). The von Mises equivalent stress is therefore the only variable we will discuss for the shear tests. As the compression tests are less constrained (through the con-

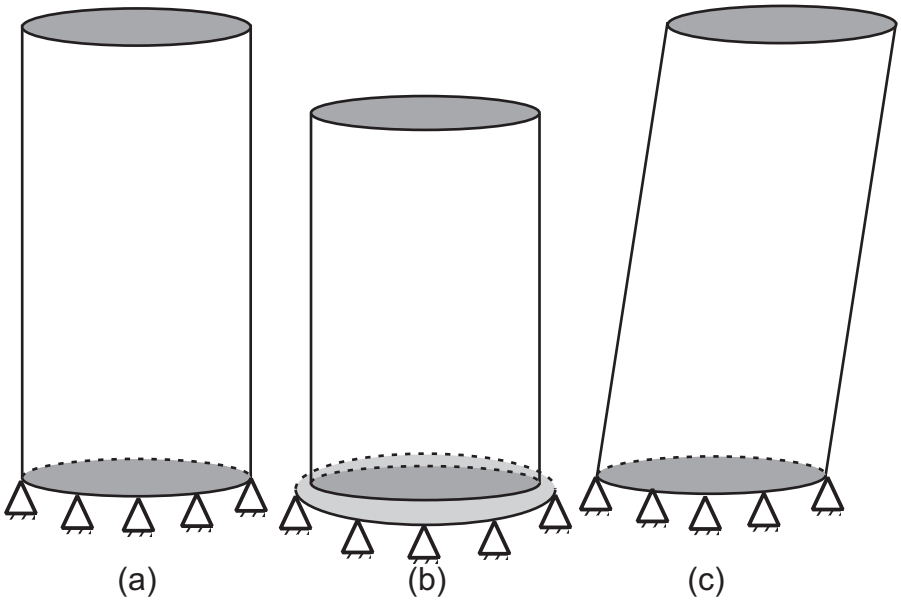

FIGURE 5.22: *Test cases defined for the analysis of the purely mechanical response of the developed constitutive model. (a) initial configuration, (b) compression tests with contact, and (c) simple shear tests.*

tact conditions) than the shear tests, we will as well have a look for these tests at the shape the cylinders take after deformation.

- **Isotropic morphology**: this corresponds to the reference case for the three next cases. The morphology is defined only by the apparent density. We will therefore analyze the influence of this parameter on the mechanical response. For this, we vary the apparent density from 0.2 (low density trabecular bone) to 1.0 (fully mineralized bone).

  As we have a simple isotropic behavior, the only useful characteristic to analyze is the force needed for the displacement (see Fig 5.23). As expected the force level is increasing with the density, not linearly as the density/stiffness relationship is not linear. We can also see that the force level at which yielding occurs depends on the density as well. However, the displacement at which this occurs (about 19% of the max displacement for compression tests) is independent of the density. Distribution of von Mises equivalent stress is pretty much classical (see Fig 5.24(a)) and not worth much discussion.

- **Morphology vertical**: this corresponds to a bone sample four times denser vertically than horizontally (for the same apparent density of 40%). As, for the same density, the stiffness is higher vertically than for the equivalent isotropic case, the force needed for the same vertical displacement (Fig. 5.25, red curves) is higher than the previous one (Fig. 5.25, green curves). The effect is however less important for shear tests.

  We can also see, as expected, that yielding starts for the compression test at the same level of displacement, but for a lower force than for the equivalent isotropic case.

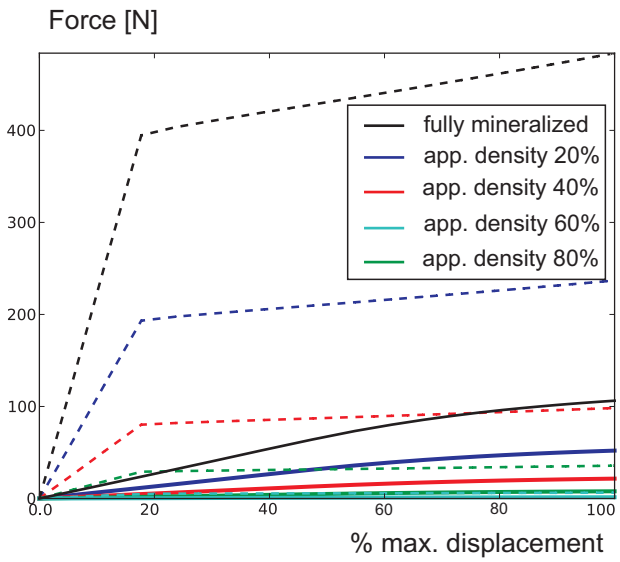

FIGURE 5.23: *Force [N] as a function the percentage of maximal displacement for a compression test (dashed curves) and a shear test (plain curves) for an isotropic morphology for four different values of the apparent density.*

For a vertical morphology and shear test, the von Mises equivalent stress (Fig 5.24(b)) shows pretty much the same distribution but larger values (about 15% higher) than the equivalent isotropic case.

As for the compression test, the outline of the deformed cylinder on the contact plane has a larger diameter than the equivalent isotropic morphology as the sample is weaker radially than vertically (Fig. 5.26).

- **Morphology horizontal**: this corresponds to a bone sample four times denser horizontally than vertically (for the same apparent density of 40%). Decreasing the vertical stiffness leads to the necessity to apply a lower force (not four times lower as the relationship between density and stiffness is not linear) to achieve the same displacement (Fig. 5.25, dark blue curves).

  Once more, yielding happens for the compression test at the same level of displacement, for a lower force than for the isotropic case as the sample is vertically weaker than the isotropic sample.

  Concerning the von Mises equivalent stress (Fig. 5.24(c)), an horizontal morphology shows the opposite effect as for the vertical morphology, i.e. a lowering of the stress intensity. It also shows a stress distribution somehow more homogeneous than for the two previous cases. Indeed as the cylinder is vertically softer, there is less stress concentration at the most strained elements.

  The outline of the deformed cylinder on the contact plane has a smaller diameter than the equivalent isotropic morphology as the sample is stiffer radially than vertically

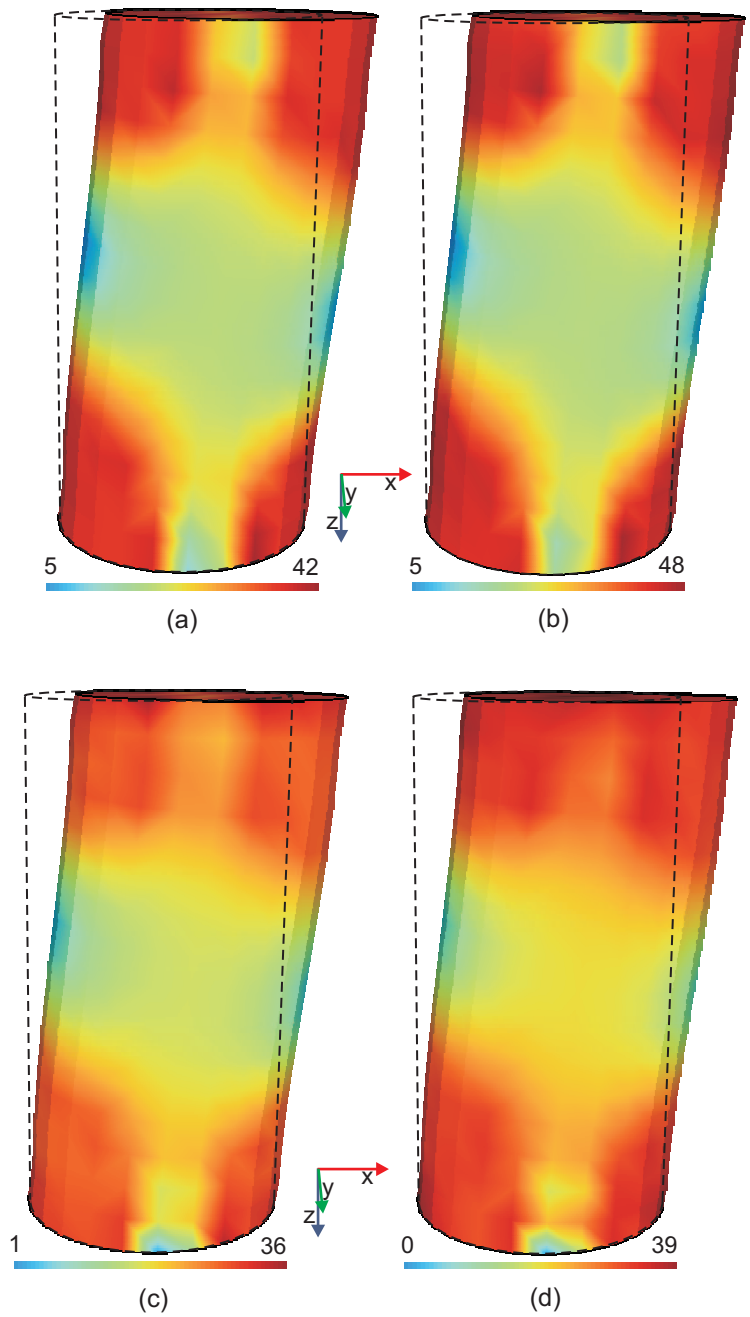

FIGURE 5.24: *Maps of von Mises equivalent stress [MPa] for the initial set of material parameters on (a) an **isotropic** morphology, (b) a **vertical** morphology , (c) an **horizontal** morphology, and (d) an **oblique** morphology for the shear tests. In dashed lines the initial configuration.*

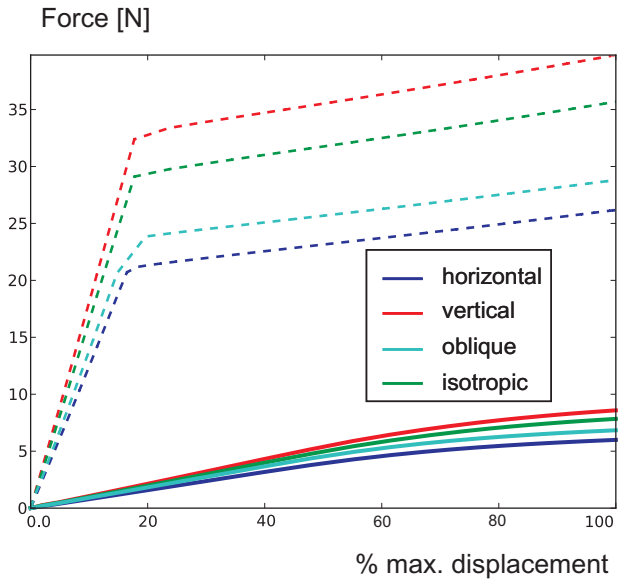

FIGURE 5.25: *Force [N] as a function the percentage of maximal displacement for a compression test (dashed curves) and a shear test (plain curves) for four different morphologies.*

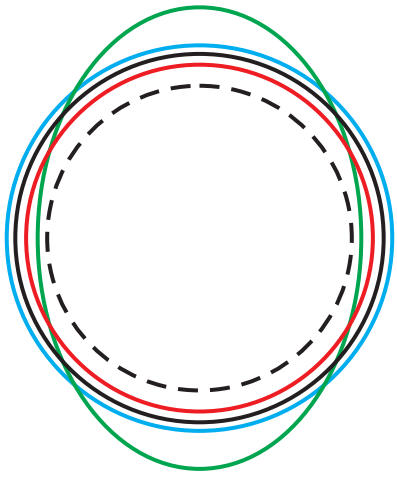

FIGURE 5.26: *Outline of the deformed cylinder on the contact plane in compression contact conditions. Dashed black circle: initial outline; plain black circle: isotropic morphology; red circle: horizontal morphology; blue circle: vertical morphology; green ellipse: oblique morphology*

(Fig. 5.26).

- **Oblique Morphology**: this corresponds to a bone sample four times denser at 45^o to the vertical than in the perpendicular directions (for the same apparent density of 40%). The oblique case falls, concerning the vertical stiffness, in between the vertical and the horizontal cases. Therefore the force intensity is as well in between the two previous intensities (Fig. 5.25, light blue curves).

  The von Mises stress map (Fig. 5.24 (d)) includes features of the horizontal morphology map (more homogeneous distribution) but showing higher intensities as the cylinder is vertically stronger than on the previous case.

  As the stiffness is different in both directions of the horizontal plane for the compression test, the outline of the deformed cylinder on the contact plane is an ellipse instead of a cylinder (Fig. 5.26).

We saw that while the apparent deformed outline of the cylindrical samples is similar for all morphologies in shear tests (as we produced constrained displacement driven tests), the apparent behavior (measured by the force intensity) is different from one morphology to the other. However, the least constrained compression tests show large differences not only on the measure of the force intensity needed for the applied displacement but also, and mainly, on the shape the cylinder takes under compression (the circular cylinder becomes elliptic when the morphology principle axis are not aligned with the force direction).
In this section, we glanced through the differences between each type of morphologies for simple tests so that the slight differences in the mechanical behavior have been outlined.

5.3.2 Remodeling Behavior

Remodeling parameters analysis

Each of the remodeling parameters are here varied within physical and physiological intervals. The response of the model is then analyzed for tension and compression conditions. For this, as previously, we produced cylindrical models of bone samples (2cm of height, 1cm of diameter, and a bone apparent density of 40%). One circular side is completely constrained (the nodes are fixed in space) while the other side is submitted to a constant vertical force of 5N through the application of rigid contact conditions (the force is applied linearly from 0N to 5N in a tenth of a day and then kept constant for a year, i.e. 365 days; the contact is considered frictionless). While the previous section considered displacement driven problems, we here consider force driven problems.
We first present an analysis considering an isotropic material as well as isotropic remodeling (we here present the remodeling model without its extension to account for the pressure dependent model proposed for the alveolar bone). The mechanical response that is analyzed is therefore the displacement of the contact plane versus time as well as the bone density evolution.
We will then present the same analysis of an initially isotropic bone but anisotropic remodeling. We will therefore mainly analyze the orientation evolution with time.

Isotropic remodeling The initial set of parameters is as follows: homeostatic tissue level value of the stimulus, $\psi_{\mathrm{t}}^{\star} = 10MPa$, remodeling constant $c = 0.02\mu m/(\mathrm{day}MPa)$, available surface area $k = 0.6$, lazy zone half-width $\Omega = 0\%$ (in percentage of the homeostatic tissue level value), i.e. no lazy zone.
The loading and material parameters lead to a value of the stimulus ($U_{\mathrm{iso}}/\rho^{2-\beta/2}$, which is the value compared to the homeostatic tissue level value to assess the overload/underload status) varying from $18MPa$ to $25MPa$. The whole cylindrical sample of bone is therefore for the initial set of remodeling parameters in overload conditions. The tendency of the remodeling is therefore to increase the bone density. This increase in density will act as a toughening of the material. There is therefore a tendency to reverse the movement imposed by the applied force.

- Influence of the homeostatic tissue level value of the stimulus, $\psi_{\mathrm{t}}^{\star}$.

  The first value of $10MPa$ (full overload conditions) is increased to $20MPa$ (mixed overload and underload conditions), $50MPa$ (full underload conditions), and $100MPa$ (full high underload conditions).

  Fig. 5.27(a) shows that the case for which the whole volume is initially in overload conditions (red curves, for which $\psi_t^{\star} = 10MPa$), the tendency of remodeling is to reverse the imposed movement. Therefore, the (absolute) value of the contact plane displacement decreases with time. For mixed (elements either in overloaded conditions or

in underloaded depending of their position in the cylinder) initial conditions (green curves, $\psi_t^\star = 20MPa$), since the majority of the elements are in overloaded conditions, the tendency is also to decrease the displacement. However, this decrease is twice as slow as for the previous value. Increasing even more the value of the homeostatic stimulus (light blue curves, $\psi_t^\star = 50MPa$) allows for the whole volume to be initially in underloaded conditions and therefore gives a tendency to increase the imposed movement. However, as the bone remodels, the speed at which the surface moves decreases. Finally, for high underload conditions over the whole volume (dark blue curves, $\psi_t^\star = 100MPa$), a high (but decreasing) rate of displacement is observed for a period of 250 days. The stimulus increases, as pictured in Fig. 5.27(c), up to the homeostatic stimulus. However, as no lazy zone is present, the speed would reach zero and lead to an equilibrium only if the stimulus reaches exactly the homeostatic stimulus, which is, at least from a numerical point-of-view, not feasible. Therefore, the stimulus 'over-shots' the homeostatic values and the bone sample is in overload conditions, with a tendency therefore to reduce the displacement. We can also notice that there is no difference on the stimulus values (Fig. 5.27(c)) between the compression or tension tests. We can finally see that, for overloaded conditions, the density (Fig. 5.27(b), here the mean density over the sample) increases, while underloaded conditions lead to a decrease of the density, whatever the hydrostatic stress state.

- Influence of the remodeling constant, $c_f = c_r$.

  The first value of $0.02\mu m/(\text{day}MPa)$ is decreased to $0.01\mu m/(\text{day}MPa)$ and then increased to $0.05\mu m/(\text{day}MPa)$ and $0.1\mu m/(\text{day}MPa)$.

  Fig. 5.27(d) shows, as expected, that increasing the value of the remodeling constant simply acts on the rate of displacement. Indeed, the variation of the remodeling constant leads simply to different slope of the remodeling rate $\dot{r}$.

- Influence of the available surface area, k.

  The first value of 60% is modulated to 40%, 80%, and 100%, representing a low surface activity in the bone, an average one, and finally a maximal one (theoretical value only, not physiological).

  Fig. 5.28(a) shows, that increasing the value of the available surface area simply acts on the rate of displacement. Indeed, the variation of the available surface area leads simply to different slope of the density variation $\dot{\rho}$.

- Influence of the lazy zone half-width, Ω.

  To observe the effect of this parameter, we chose to use a value of the homeostatic tissue level stimulus set to $100MPa$. Indeed, we showed on Fig. 5.27(c) that only for this value the stimulus reaches the homeostatic value. Varying the lazy-zone half width with the other values of the homeostatic level would only slightly reduce the speed of

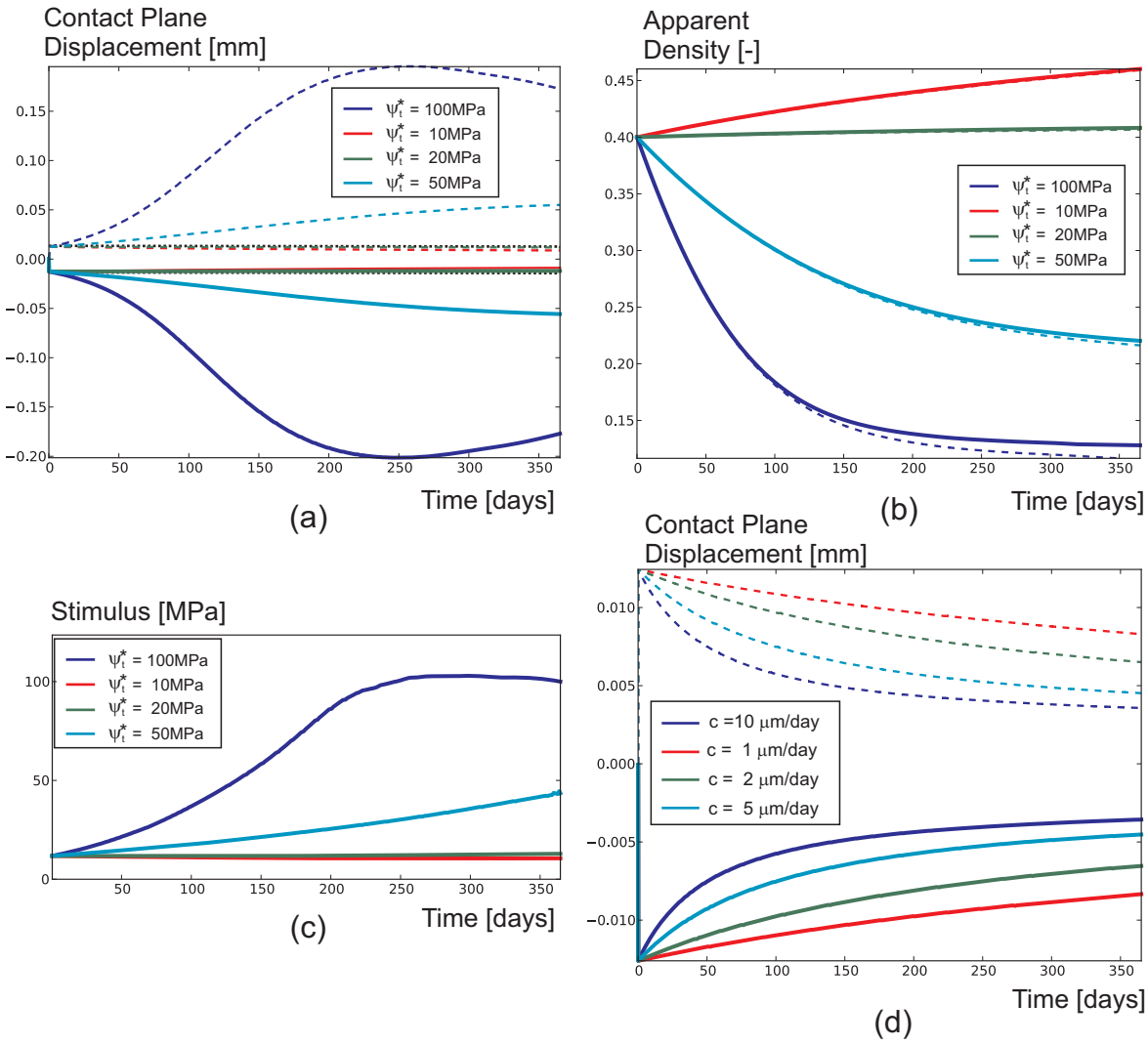

FIGURE 5.27: *Displacement of the contact plane [mm] versus time [days] for different values of (a) the homeostatic stimulus value ($\psi_t^\star$, the dotted black lines correspond to the value of the initial displacement) and (d) the remodeling constant ($c_f = c_r = c$). For the variation of the homeostatic stimulus, the evolution of the mean density (b) and the maximal stimulus (c) are also depicted. Plain curves are for tension tests while dashed curves are for compression tests. Note that by convention the displacement is negative when the cylinder is in tension.*

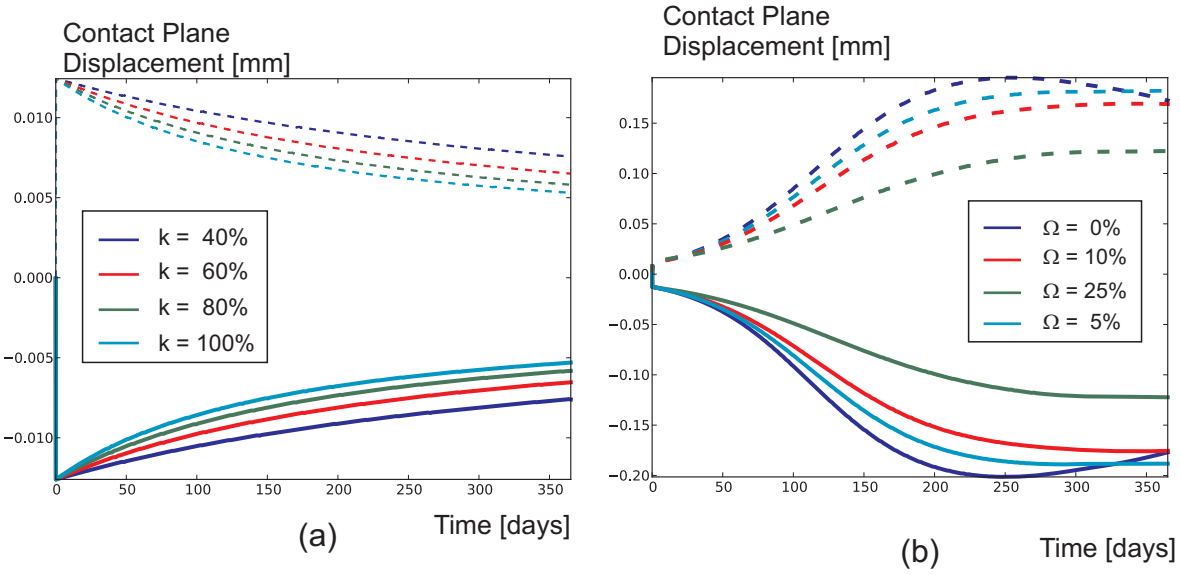

FIGURE 5.28: *Displacement of the contact plane [mm] versus time [days] for different values of (a) the available surface area (k) and (b) the lazy zone half-width (ω). Plain curves are for tension tests while dashed curves are for compression tests. Note that by convention the displacement is negative when the cylinder is in tension.*

displacement as the difference between the stimulus and its homeostatic value, corrected by the lazy zone, decreases. The first value of Ω (0%) is increased, for high underload conditions, to 5%, 10%, and 25%.

We can first observe (Fig. 5.28(b)) that while the lazy-zone width increases, the displacement speed is reduced as explained previously. Accounting for a small lazy zone of 5% half-width allows for the stimulus to reach the lazy zone and thus to stop its evolution (light blue curve). This happens for a smaller displacement (of 2mm) but a larger time (about 3 weeks later) than for the case with no lazy zone. The displacement then does not evolve anymore with time as the equilibrium is reached. Larger values of the lazy zone half-width do not allow the stimulus to reach the lazy zone as its evolution is slower than with a smaller lazy zone width.

We saw in this section that among the parameters on which the remodeling law depends, some have a very straightforward, linear, influence on the overall behavior of the model (the available surface area and the remodeling constant). However, other have a more complex influence on the behavior (the value of the homeostatic tissue-level stimulus and the width of the lazy zone). The calibration of these last parameters should therefore be performed with caution. Especially, the presence of the lazy zone and its width have to be analyzed in details from a physiological point-of-view.

Anisotropic remodeling The set of parameters is as the previous initial one. We will not here analyze the remodeling parameters influence but only the influence of the anisotropy on the remodeling. For this, we compare the displacement and the density evolution versus time for four different initial structures (Fig. 5.29).

- **Morphology initially isotropic**: this corresponds initially to the same test as in the previous section. However, the remodeling is anisotropic and thus tends to align the morphology with the applied loads.
- **Morphology initially vertical**: this corresponds to a bone sample twice denser vertically than horizontally (for the same overall density). The sample is therefore stiffer (not twice as stiff, the relationship between stiffness and density is non-linear) in the direction of the applied loads. The displacement as well as the density evolution are therefore smaller than in the isotropic case (Fig. 5.29). The remodeling leads to a decrease of displacement which is slightly smaller as well. Indeed, the tendency of remodeling is to increase the stiffness in the direction of the applied loads. As the sample is already stiffer vertically, the remodeling action is smaller than for the initially isotropic case.
- **Morphology initially horizontal**: this corresponds to a bone sample twice denser horizontally than vertically (for the same overall density). This sample is the weakest in the vertical direction. The displacement is therefore the largest and so is the decrease in displacement due to remodeling (Fig. 5.29).
- **Morphology initially oblique**: this corresponds to a bone sample twice denser at 45^o to the vertical than in the perpendicular directions (for the same overall density). This sample therefore shows a stiffness in the vertical direction with a value between the one of the horizontal morphology case and the vertical morphology case. Therefore, the initial displacement lies between the two corresponding initial displacements, so does the displacement decrease due to remodeling (Fig. 5.29).

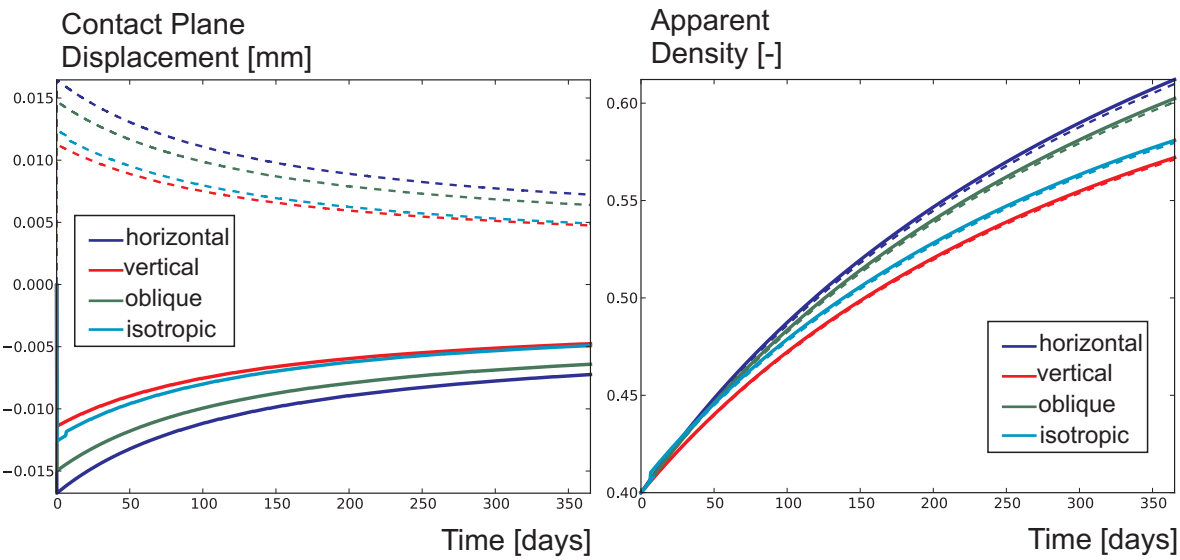

FIGURE 5.29: *Displacement of the contact plane [mm] and mean apparent density [-] versus time [days] for different orientations of the morphology. Plain curves are for tension tests while dashed curves are for compression tests. Note that by convention the displacement is negative when the cylinder is in tension.*

Differences due to the modifications for the alveolar bone

Finally, we show here the difference in the model response used with a generic bone remodeling model (as used up to here) or with the modifications proposed for the alveolar bone (pressure dependent model). We here also study the influence of the use of different remodeling constants in formation or resorption.
The response of the model is analyzed for shear conditions and a horizontal morphology (twice as dense horizontally than vertically). These shear conditions give, on the same sample, some elements with a positive hydrostatic stress and some with a negative one, therefore allowing to better highlight the influence of a pressure-dependent model.
The first remark to outline before starting this comparison of remodeling laws is the presence of a possible hyaline zone in the pressure dependent model. Indeed, this model is built to account for the lack of bone cell migration due to the interruption of the blood flow within the periodontal ligament. This happens at a low pressure of about $-2.5kPa$ in the ligament. To adapt this value to an hydrostatic threshold within the bone, we consider as a scaling factor the ratio of both material bulk's modulus, i.e. $\frac{K_{\text{bone}}}{K_{PDL}} = 745$ (considering the mechanical parameters for the bone as used in this section and a periodontal ligament with a Young's modulus of $68kPa$ and a Poisson's ratio of 0.45). Therefore, the critical pressure under which the hyaline zone forms is initially set at $-1.8MPa$ (this value depends on the apparent density value, as does the bone bulk's modulus).
The initial extend of the hyaline zone for different values of shear (1, 5, and 10% of the diameter) is depicted in Fig 5.30.

In order to compare the influence of the pressure dependent remodeling law only, without the influence of this hyaline zone, we will therefore apply a low shear displacement, insuring the hydrostatic stress stays above this critical value. For this, shear conditions are obtained with an imposed horizontal displacement of one side of 0.5% the cylinder diameter, kept constant for a full year (as previously the full displacement is imposed in a tenth of a day), the opposite side is fully constrained. As we have a displacement driven problem, instead of analyzing the rate of displacement as a sign of remodeling, we will therefore analyze the change of applied force.
The initial set of parameters is as follows: homeostatic tissue level value of the stimulus, $\psi_{\text{t}}^{\star} = 10MPa$, remodeling constant $c_f = c_r = 0.02\mu m/(\text{day}MPa)$, available surface area $k = 0.6$, lazy zone half-width $\Omega = 20\%$ (in percentage of the homeostatic tissue level value), and proportionality coeficient between the stimulus and the stress-equivalent intensity at tissue level $N^{1/m} = 5$ while it was chosen at 1 so far. This change of proportionality coefficient (accounting for a cyclic application of the loads, with an equivalent number of cycle of 5^4 as m is chosen at 4) allows to use the same homeostatic values than previously even though the stress intensities are reduced due to the low shearing. This will allow us to obtain either underloaded conditions or overloaded conditions using physiological levels of the homeostatic

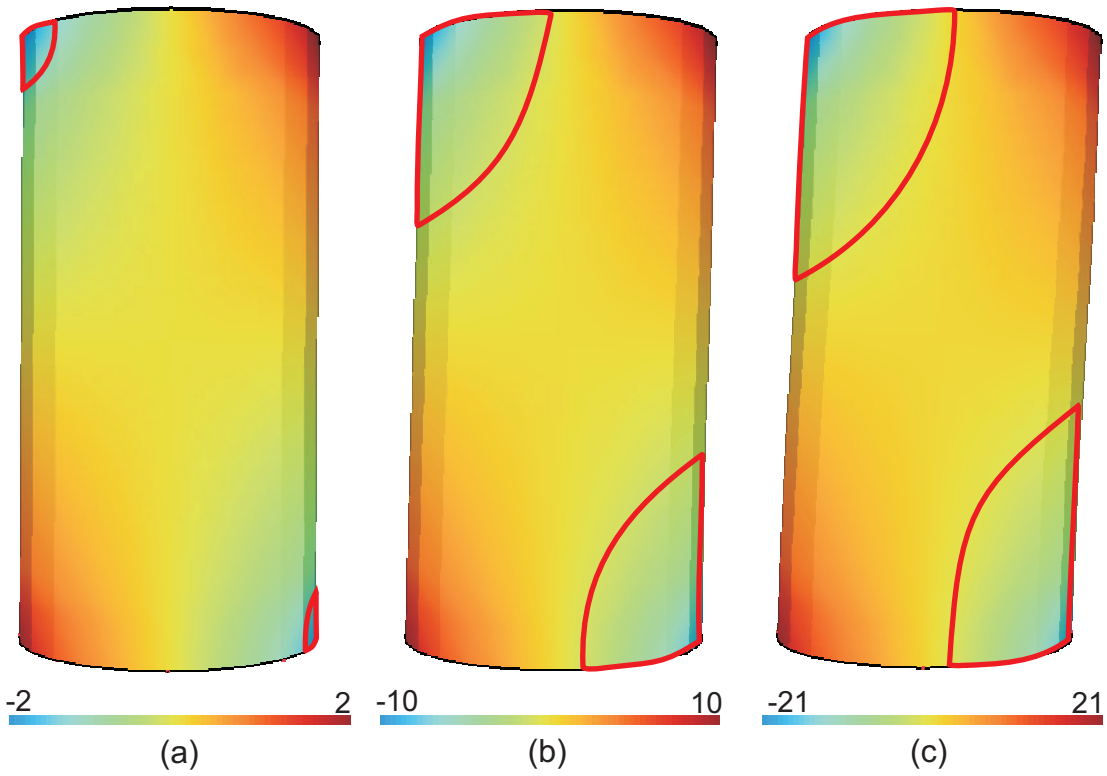

FIGURE 5.30: *Hydrostatic pressure maps [MPa] for an initial shear of (a) 1% of the diameter, (b) 5% of the diameter, and (c) 10% of the diameter. The highlighted red zones show the surfacic extend of the hyaline zone.*

stimulus[1].

As expected as there is no difference between the classical model and the pressure dependent one in underloaded conditions, no difference can be seen between both models behavior in these conditions (Fig. 5.31, plain curves). As these conditions lead to resorption for which the remodeling constant is not changed between a single value or two different values for resorption and formation, there is also no visible difference between these type of tests. In overload conditions however (Fig. 5.31, dashed curves), a classical remodeling model will always produce formation conditions while the presented pressure dependent model presents either formation or resorption depending on the hydrostatic state. Both models tend to increase the maximal stimulus value (Fig. 5.31(a), dashed curves), at two different rates depending whether one ($c_f = c_r$) or two ($c_f \neq c_r$) values are used as remodeling constants. The change of stimulus is not exactly the same in both models as the maximal stimulus is affected by the whole sample and not only the local behavior. However, the difference can be marked analyzing the mean density variation (Fig. 5.31(b), dashed curves). Indeed, the classical remodeling model tends in overload conditions to increase the density (at a rate dependent on the remodeling constant in formation) while the pressure dependent model will either increase or decrease the density depending on the hydrostatic stress. This difference has a clear impact on the mean density over the sample which always increases with a classical remodeling law. However, it will remain almost constant for a pressure dependent model for which $c_f = c_r$ as the volume for which the density decreases is the same as the one for which it increases and the rate at which this variation occurs is the same for formation and resorption, thus leading to a constant mean value. When resorption is considered a faster phenomenon than formation ($c_r > c_f$), there is a decrease of the mean density in time.

[1]The previous value of $N = 1$ is not exactly physiological, but allowed to apply higher loads and to get a better visualization of what is happening due to remodeling

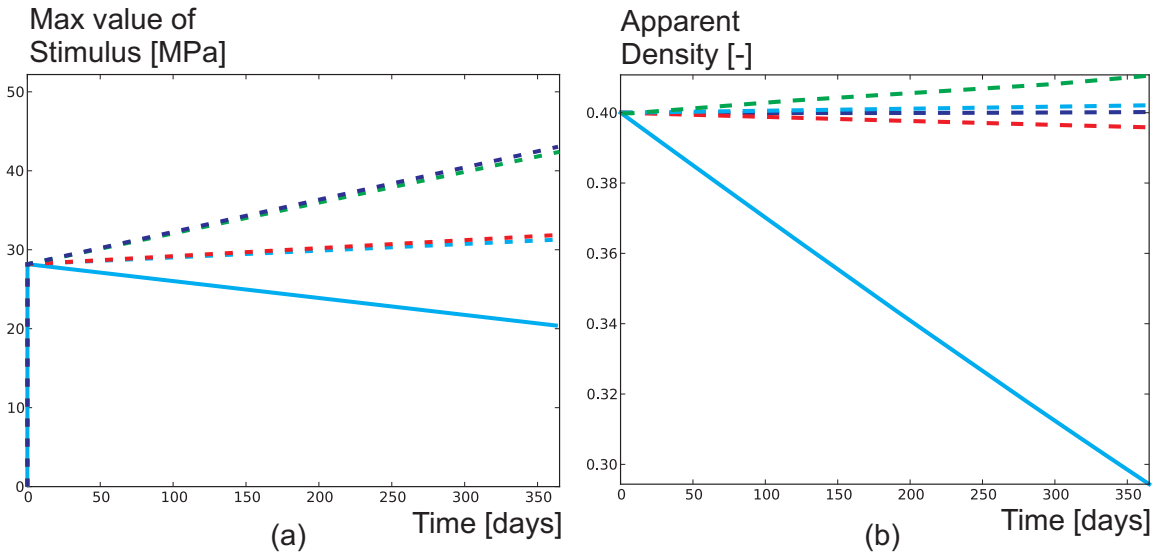

FIGURE 5.31: *(a) Maximal stimulus [MPa] and (b) mean density, versus time [days] for different remodeling laws (classical remodeling, in green - classical remodeling with $c_f = c_r/4$, in light blue - pressure dependent remodeling, in dark blue, and pressure dependent remodeling with $c_f = c_r/4$, in red). Dashed curves are for initial overload conditions ($\psi_t^\star = 10.$) while plain curves are for initial underload conditions ($\psi_t^\star = 60.$).*

5.4 Validation of the Mechanical Representation of Trabecular Bone

640K ought to be enough for anybody.

- quote mis-attributed to Bill Gates (1981)

This chapter presented a phenomenological, continuum-based, constitutive law that can be used in bone remodeling simulations in a finite strain framework. The constitutive law therefore aims at describing the non-linear mechanical behavior of trabecular bone in the range of small to moderate compressive strains. It considers an accumulation of plastic deformation and possible low softening due to early buckling of the microstructure. As on the local level the remodeling leads to a variation of the morphology, the phenomenological constitutive law is based on internal variables representative of this morphology. These internal variables are included in the model in such a way that they can evolve according to a remodeling law. Considering validation, this model therefore needs not only to be validated against remodeling data but the global constitutive law itself needs to be validated as well.
In this work, we will not try however to validate the model against remodeling data during orthodontic tooth movement. Indeed, a full validation procedure of remodeling would require to work with patients. It would require to acquire the actual geometrical and morphological data of the bone and considered tooth for the selected patient. The knowledge of all boundary conditions should also be taken into account (i.e. not only the appliances interaction but also the muscle and other soft tissues activity). The progress of treatment should also be measured by acquiring the changes in bone morphology (therefore having regular images), the tooth movement (either by the images acquisition or by measuring the displacement in-situ) and by measuring the different applied forces. This would require quite invasive techniques and does not enter in the frame of this work.
We will therefore only try to validate the purely mechanical representation of the bone morphology (and not its change due to remodeling), i.e. not considering its active part. As only the passive mechanical behavior of bone is therefore considered, it can be done on extracted bone samples, tested ex-vivo. We will actually not validate our model on human bone but we will use bone-like engineered material as well as deer antlers, which are actually made of bone.

The next section about validation of the model for compression experiments has been published in-extenso in the *International Journal for Numerical Methods in Biomedical Engineering* [174].
As experimental tension tests were not available to us, we then present a methodology to validate the model for this type of tests using only the knowledge on compression tests. To do so, we numerically produced tension tests:

- We first propose to model the compression tests using μ-Finite Element models (and

therefore using a constitutive law relative to the trabeculae, not to the apparent tissue level).

- As these μ-Finite Element models in compression can be considered valid, we then assume they are also valid for tension tests and therefore perform numerical tension tests using the same models. Doing so, we can obtain force/displacement curves in tension used to validate our model for tension tests.

5.4.1 Validation on Experimental Compression Tests [173, 174]

Under compressive load, the mechanical behavior of trabecular bone exhibits a behavior showing a decrease of the apparent tangent stiffness before reaching a maximal force (see Fig. 4.2 page 78). Beyond apparent engineering strains at maximal force, smooth and gradual softening occurs until a plateau is reached. It is followed, before the occurrence of failure, by a final apparent hardening due to collapse of the cells. The proposed continuum based mechanical behavior should therefore be validated against experimental data obtained for mechanical tests of trabecular bone as well as materials with bone-like microstructure undergoing small to moderate strains. As the constitutive law is to be used eventually in remodeling problems for which apparent strains are limited, the proposed law has to be validated up to the reaching of the plateau.

Methods

The presented continuum-based formulation was applied to three different materials: two engineered cellular solid materials showing bone-like microstructure, aluminum and Polylactic acid (PLA) foams (Fig. 5.32 shows 3D visualization of one of the tested aluminum foam samples), and cancellous bone tissue of a deer antler (Fig. 2.8, page 20).
For each type of material, cylindrical specimens were used. Images of the microstructure were acquired using a X-Ray micro-tomography imaging system (μCT). For each specimen, the following structural parameters were determined from the μCT data (software CT-Analyser, Skyscan, Belgium): bone volume fraction (`BV/TV`), the eigenvalues ($E1$, $E2$, $E3$) and eigenvectors (E-vectors 1 to 3) of the Mean Intercept Length (MIL) tensor, and the degree of anisotropy (`DA`), which is the ratio of the max eigenvalue to the min one (see complete data collection in Appendix E). The samples were then compressed along their main axis in a mechanical testing device and load-displacement data were acquired. The experimental setups were performed either at the Department of Applied Chemistry, Laboratory of Chemical Engineering [56] or at ETH-Zurich, Institute for Biomechanics [187].
The first material that has been tested is fabricated from highly porous aluminum alloys. The Duocel aluminum foam (ERG, Oakland, CA) from which the samples were extracted is composed of 6101 T6 aluminum alloy. Fifteen specimens were used (diameters and heights of respectively about 8 and 16 mm), five of which will be referred as “dense” (mean bone volume fraction over the five samples $\bar{\rho}$ = 12.8%), five have a “middle” density ($\bar{\rho}$ = 7.3%), and

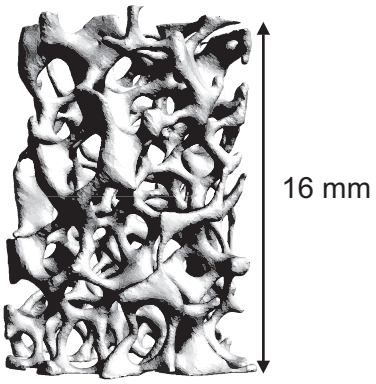

FIGURE 5.32: *3D visualization of a specimen of aluminum foam obtained from μCT images.*

TABLE 5.1: *Material parameters at the local level*

Material	Young's modulus $[GPa]$	Poisson's ratio $[-]$	Yield stress $[MPa]$	Hardening parameter $[MPa]$
Duocel Foam	69.0	.33	200.0	200.0
PLA	3.2	.33	75.0	0
Deer antler	8.1	.33	95.0	820.0

the last five have a "low" density ($\bar{\rho} = 4.4\%$). Images were generated using a X-Ray microtomography imaging system (μCT 20, Scanco Medical, Switzerland), a compact fan-beam type tomograph [187], also referred to as a desktop μCT, at a $34 \times 34 \times 34\ \mu m^3$ resolution. The samples were compressed in a stepwise fashion from 0% to 16% apparent engineering strain (mechanical testing and μCT acquisition are detailed by Nazarian and Müller in [187]). The material parameters used to describe the local level (the "trabecular" mechanical behavior) were chosen from the literature on this specific alloy [6, 12, 44, 57] and are reported in table 5.1. We assumed a low linear isotropic hardening ($h = 200\ MPa$, leading to a tangent modulus of $E_t = 200.5\ MPa$).

The second material is a foam composed of Polylactic acid (PLA) and an amphiphilic block copolymer of lactide and ethylene oxide (PEO), prepared by the CERM, University of Liège [160]. PLA is a biocompatible, biodegradable, and easy processable polymer and has therefore received considerable attention for the manufacturing of three-dimensional polymer scaffolds. Their properties can be easily tuned, for example the wettability can be increased by adding a hydrophilic copolymer. The freeze-drying technique allows the preparation of PLA foam with highly organized longitudinal and random pores. Mixtures of PDLLA (Purac, $Mn = 136000\ g/mol$) and PEO-b-PDLLA [$Mn(PEO) = 5000\ g/mol$; $Mn(PDLLA) = 17700\ g/mol$] were prepared as follows: the (co)polymers were dissolved in dimethylcarbonate at a concentration of 3 $wt : vol\%$ with a proportion of 5 $wt\%$ of PEO in respect to

the whole polymer mass. The solution was frozen for one night at $-70\,^oC$, dried by vacuum sublimation for 48 h at $-10\,^oC$, followed by a 48 h period at $0\,^oC$, and finally at room temperature until it reached a constant weight. A single specimen was used (8.2 mm in diameter and 12.5 mm in height, with an apparent volume density of 15%). Tomographic images of the sample were generated using a μCT imaging system (Skyscan 1172, Skyscan, Belgium), a compact closed cone-beam type desktop tomograph, at a $8.64 \times 8.64 \times 86.4\ \mu m^3$ resolution. It was compressed from 0% to 42% apparent engineering strain. Only a few studies have investigated the mechanical behavior of PLA as in most applications PLA is reinforced by fibers [124, 170, 180]. However, the elastic behavior of the PLA is usually assumed linear. The plasticity is here assumed to be a von Mises perfectly plastic behavior. The yield stress has been chosen to fit the experimental results. The set of material parameters used to describe the local level is reported in table 5.1.

The last material presented is cancellous tissue of a deer (*Cervus Elaphus*) antler, prepared at the Department of Clinical Sciences, Faculty of Veterinary Medicine, University of Liège [53, 149]. The antlers of cervids are constituted of bone tissue covered with velvet in the early stage of growth. This bone tissue is composed of a central core of cancellous bone surrounded by a thick outer layer of compact bone (Figure 5.33). The core cancellous bone presents a cellular structure. It is the part used here. A single deer antler specimen was used in this work (7.8 mm in diameter and 11.96 mm in height, with an apparent volume density of 18.7%). It was collected before antler casting, during the active growth phase when the antler is still covered by velvet. The sample, made of primary bone tissue, was machined from the core of the antler main beam [149]. Tomographic images were taken using the same tomograph used for the previous material. It was compressed from 0% to only 4.1% apparent engineering strain. As for the the PLA, only few studies have investigated the mechanical properties of the cancellous part of deer antler [4] while the cortical part has been widely investigated ([41, 55, 140] among many more). One of the reasons to this difference is the difficulty of isolating the cancellous core of the antler as it is very brittle. The yield properties of the trabeculae are here assumed to be equivalent to the one calculated in [41] for cortical bone as the Young's modulus in [41] is similar to the Young's modulus reported in [4] for cancellous bone. The set of material parameters used to describe the local level is reported in table 5.1.

All the specimens described were modeled as cylinders of appropriate dimensions. They were meshed with 3136 elements (hexahedral 8-nodes elements with selective reduced integration) i.e. 16 layers of 196 elements (Fig. 5.34). The morphology of each specimen was described through the use of the damage tensor. This tensor was computed (Equ. 5.35) using morphology data (`BV/TV`, fabric tensor) extracted from the structural analysis on the μCT images of the corresponding tested specimen. For each specimen, this damage tensor and the other material parameters (table 5.1) were assigned to each element of the FE mesh. To represent the experimental boundary conditions, a displacement was applied on one side of the cylinder (vertical displacement with free in plane movement) while the other side of

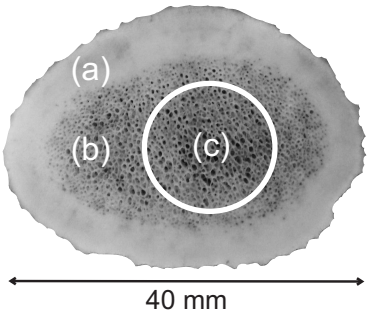

FIGURE 5.33: *Transverse view of a deer antler: (a) compact bone - (b) cancellous bone - (c) extraction site.*

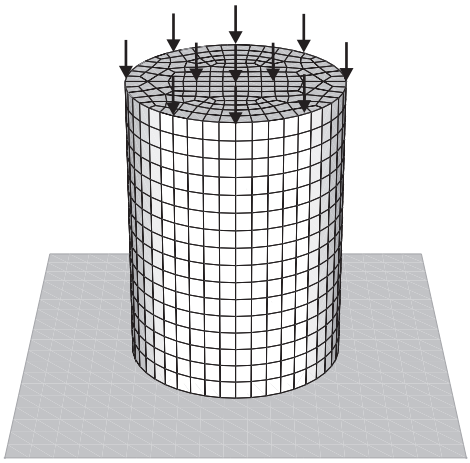

FIGURE 5.34: *Hexahedral mesh of the homogeneous cylinder model of a specimen with its boundary conditions.*

the cylinder was modeled to be in contact (frictionless conditions) with a rigid plane. On the contact plane, one central node of the cylinder was constrained in the horizontal plane to prevent rigid body modes. The displacement was applied so that it leaded to a 10% (Duocel foam), 20% (PLA foam) or 4% (deer antler) apparent compressive engineering strain. The apparent strain levels achieved justify the use of a finite strains formalism for the finite element computation. FE analyses were performed with Metafor [177] to compute the external force needed to apply the displacement for each sample. It was then compared to the experimental one. We finally also compared the results obtained with the presented anisotropic elastoplastic model to materials models accounting only for anisotropic elasticity or only for elastoplasticity. The anisotropic elasticity model was achieved by setting to zero Equ. 5.45. The isotropic elastoplastic model needed an isotropic damage variable accounting only for `BV/TV`. This was achieved by setting the fabric tensor to the unit tensor instead using of a structural fabric to compute the damage tensor.
The morphological analysis software CT-Analyser allows for a definition of a region of interested (ROI) to extract the morphological data. Initially, the morphological data were extracted over the whole volume of the specimens (Table 5.2). The ROI was therefore set for

TABLE 5.2: *Morphological parameters extracted from the CT images analysis (mean (± std) for the Duocel foam samples)*

Material	BV/TV [%]	DA [−]
Duocel Foam (high density)	12.800 (1.007)	1.059 (0.009)
Duocel Foam (middle density)	7.262 (0.502)	1.084 (0.013)
Duocel Foam (low density)	4.431 (0.276)	1.137 (0.033)
PLA	14.5	4.596
Deer antler	8.53	2.588

each specimen as one cylinder over the whole volume. Later, the impact of the volume on which the morphological data were extracted was analyzed. Each cylinder was virtually divided into 4 or 8 cylinders, each of one quarter or one eighth of the full height. The morphological data were then extracted on each of these ROIs. Instead of one damage tensor for the whole specimen, the FE model therefore presents 4 or 8 damage tensors, each assigned to the corresponding finite elements in the discretization.

Results

Although the samples used are all cellular materials, they present, within their testing range, different types of behaviors in compression (Fig. 5.35): Duocel foams (Fig. 5.35(a)) exhibit a mechanical behavior typical of cellular solids as described earlier. Specially, the experimental force presents a characteristic plateau for the lower and middle density samples. Fig. 5.35(a) also demonstrates the dependence of the mechanical apparent behavior on the reduced density. Lower density samples exhibit lower apparent stiffness in the linear part of the force-displacement curves and their maximal forces are lower than for higher densities samples. However, within the testing range, none of the low density and middle density samples seems to present final hardening. The PLA sample (Fig. 5.35(b)) is tested only up to the appearance of softening after reaching the maximal force, the force plateau is not present in the experimental data. Both the Duocel foam and PLA foam material exhibit within their testing range an apparent yielding behavior. Regarding the deer antler cancellous tissue specimen (Fig. 5.35(c)), only the initial increase of tangent stiffness is present as the sample is tested only to a low strains level. The maximal displacement tested seems to be lower than the one needed to reach the maximal force.
Fig. 5.36 to 5.40 present the results of the FE analyses in term of a comparison between the computed force and the experimental one for the corresponding sample. For the Duocel foam samples, the results for each set of density level are presented as a mean (and standard deviation) over the set for the relative difference between the computed force and the experimental one (Fig. 5.36(a) to 5.38(a)). Detailed results for an arbitrary sample are also presented (Fig. 5.36(b) to 5.38(b)).

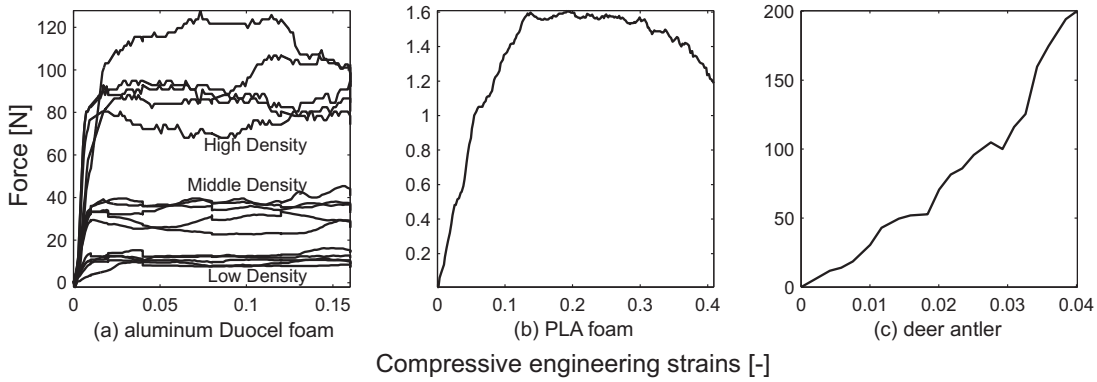

FIGURE 5.35: *Experimental forces vs. compressive engineering strains for the three types of material presented.*

The results are first analyzed for morphological data extracted over the whole volume of the specimens. This case is referred to as "1 ROI" in the corresponding figures.
The predicted force-engineering strain behavior for both the Duocel samples (Fig. 5.36 to 5.38) and the PLA foam sample (Fig. 5.39) present the same overall behavior as the experimental one in the range of strains considered here. We can retrieve the apparent linear behavior as well as the maximal force. This maximal force is represented with an error of less than 10% for the high density Duocel samples (Fig. 5.36(a)) and of about 11% for the middle density ones (Fig. 5.37(a)). Moreover, the low density Duocel samples show an error on the maximal force (achieved for all samples at about 3% of compression - Fig. 5.35(a)) of only 2.5%. Finally, this maximal force is computed with an error of less than 0.5% for the PLA foam (Fig. 5.39). However, one has to keep in mind that the yield limit for this sample was chosen to fit the experimental results, having such a small error was thus expected. The transition between the linear part of the curves and the reach of maximal force is however ill represented. Indeed, the appearance of yield shows a difference up to more than 1% of engineering strain for the high density Duocel samples (Fig. 5.36) or the PLA foam (Fig. 5.39). For the Duocel samples (Fig. 5.36 to 5.38), the only material reaching the plateau in the experimental data, the softening occurring before reaching the plateau cannot be represented with this morphological data. Indeed, the computed force tends to increase almost linearly after reaching the maximal force. Therefore, the error on this force increases as well. Specially, the abrupt decrease of the experimental force such as present in the low density Duocel samples at about 4% of engineering strains (Fig. 5.35(a)) cannot be represented by the model. The error on the computed force increases in these conditions from 2.5% to 15% (Fig. 5.38). Concerning the deer antler sample (Fig. 5.40), only the mean stiffness over the computed strain range can be represented. The use of structural parameters averaged over the entire volume seems therefore not appropriate to represent the non-linear behavior of the force for all materials. It should be noticed however that for the PLA foam and deer antler, as only one specimen was used, the presented results (both experimental and computational) may not

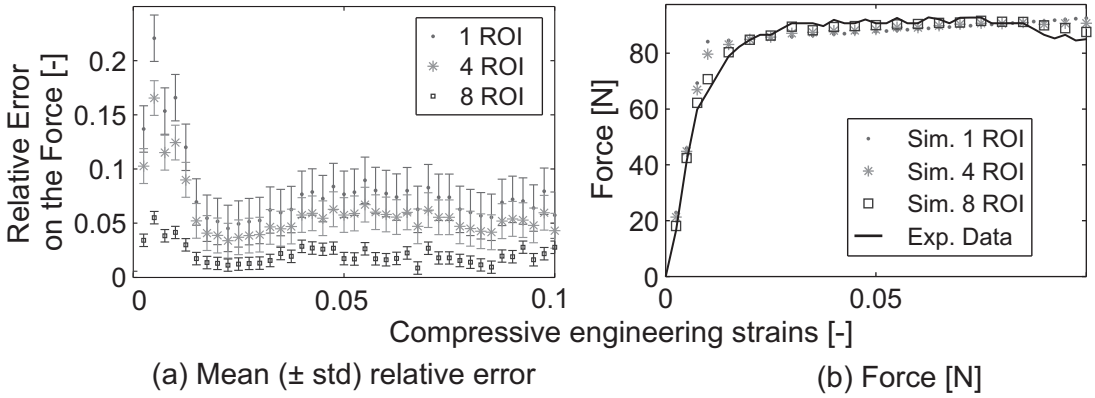

FIGURE 5.36: *Dense Duocel Foam Samples: computed (Sim.) and experimental forces [N] vs. compressive engineering strains [-]. (a) relative error on the force - mean and std., (b) force for an arbitrary sample*

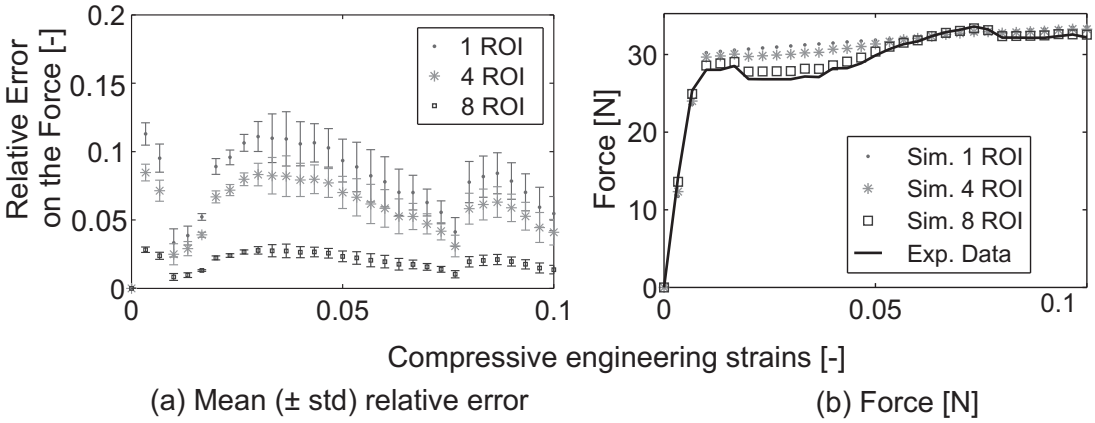

FIGURE 5.37: *Middle Density Duocel Foam Samples: computed (Sim.) and experimental forces vs. compressive engineering strains (a) relative error on the force - mean and std., (b) force for an arbitrary sample.*

be representative.

A closer analysis of the μCT images (such as the 3D visualization on Fig. 5.32) shows that the repartition of the density and its orientation is not homogeneous on the specimens. Therefore, the choice to compute one set of morphological parameters to represent the whole specimen is not representative of the actual specimen structure. The same morphological parameters were then extracted for each cylinder on smaller regions of interest. This therefore allows for the representation of force variations due to more local behavior. Extracting the material parameters over 4 ROIs (referred to as "4 ROI" in Fig. 5.36 to 5.40) already reduces the error observed on the linear part of the force by about 20%. It also allows a better computation of early softening for which the error is reduced by about 4% (Fig. 5.38(b)). When computing the force with material parameters extracted over 8 ROIs (referred to as "8 ROI" in Fig. 5.36 to 5.40), the predicted force can fit details of the experimental force vari-

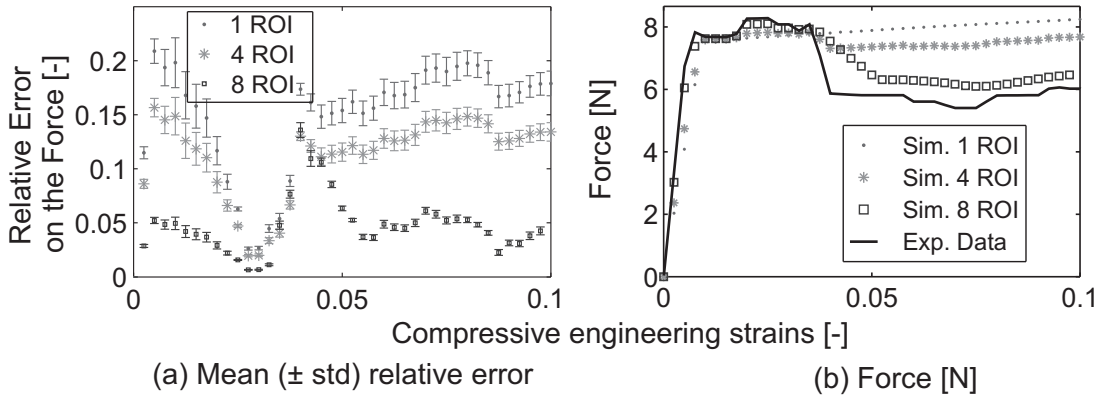

FIGURE 5.38: *Low Density Duocel Foam Samples: computed (Sim.) and experimental forces vs. compressive engineering strains (a) relative error on the force - mean and std., (b) force for an arbitrary sample.*

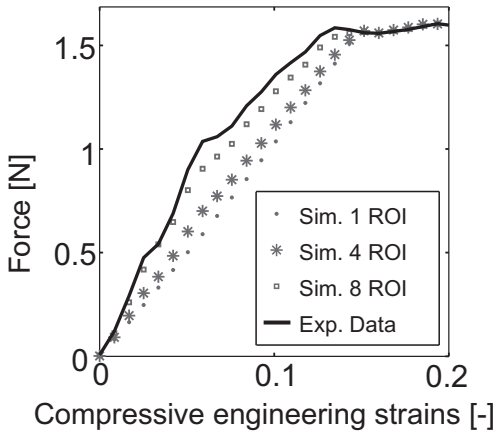

FIGURE 5.39: *PLA Sample: computed (Sim.) and experimental forces vs. compressive engineering strains.*

ations on the non-linear part of the curve. The relative error on the force is reduced for all samples below 5% over the computed strain range except when the experimental force shows abrupt variations such as the abrupt reduction of force before reaching the plateau (Fig. 5.38(a) and (b)). For both the PLA foam and the deer antler sample, reducing the size of the ROI allows to better fit the curvature of the almost linear part of the force (Fig. 5.39 and 5.40), reducing the maximal error from 40% to less than 10% for the PLA foam and from 100% to 15% for the deer antler. We therefore seem to get a convergence of the computed force to the experimental one using small ROIs. However, this convergence is achieved at the expense of the computational cost.

Discussion

Even though the Duocel foam samples all have a low degree of anisotropy (Table 5.2), the use of an anisotropic material accounting for the fabric directions, instead of an isotropic one

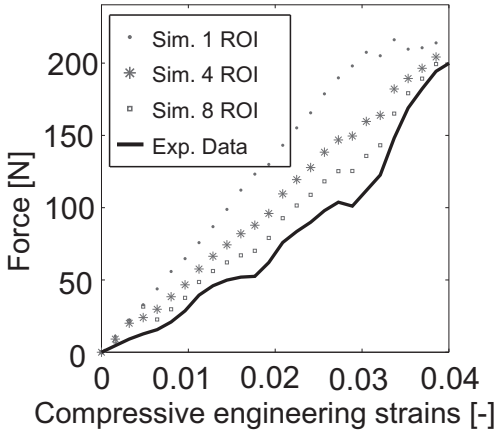

FIGURE 5.40: *Deer antler Sample: computed (Sim.) and experimental forces vs. compressive engineering strains.*

accounting only for `BV/TV` (Fig. 5.41), allows to better capture not only the apparent stiffness of the sample but also the apparent yield stress and the engineering strain at which apparent yield is achieved. The use of an isotropic model for the Duocel foams in applications where the maximal force is of importance would conclude to an overestimation of about 11% on the force for both the high density and the middle density samples (Fig. 5.41(a) and (b)). For the low density samples, the use of an isotropic model would lead to an accurate estimation of the maximal force at the correct strain level but the post-yield behavior is ill-represented, leading to errors up to 30% (Fig. 5.41(c)).

The importance of using an elastoplastic model for the Duocel samples is also outlined in Fig. 5.41(a) to (d). It can be seen that an elastic material can account only, as can be expected of such a linear behavior, for the initial stiffness of the samples. The use of an elastic anisotropic material would here lead to assume a slight increase of the tangent stiffness instead of a decrease before yield. This leads, for the maximal simulated strain, to an error on the force of more than 1000% for some samples. The introduction of elastoplasticity for this material is therefore even more essential than the use of an anisotropic material.

Concerning the PLA foam sample, Fig. 5.42(a) shows the importance of using a non-linear material model. Indeed, the force computed with an elastic material model continues to increase monotonously after reaching the experimental yield limit. This leads, for the maximal simulated strain, to an error on the force of about 300%. In this case, the use of an anisotropic model, while the degree of anisotropy is higher than for the Duocel foams (Table 5.2), is less determinant than the use of a non-linear one. The error on the computed force at the end of loading is indeed of only 6% with an isotropic elastoplastic model. This would allow to conclude, on this particular sample for the given test conditions, that the non-linearity of the material has more impact on its response to load than its anisotropic structure.

The deer antler sample however shows almost no difference on the force computed with an elastic or an elastoplastic material model when the anisotropy is considered (Fig. 5.42(b)). This can be explained as the maximal strain achieved in this compression test is small (only

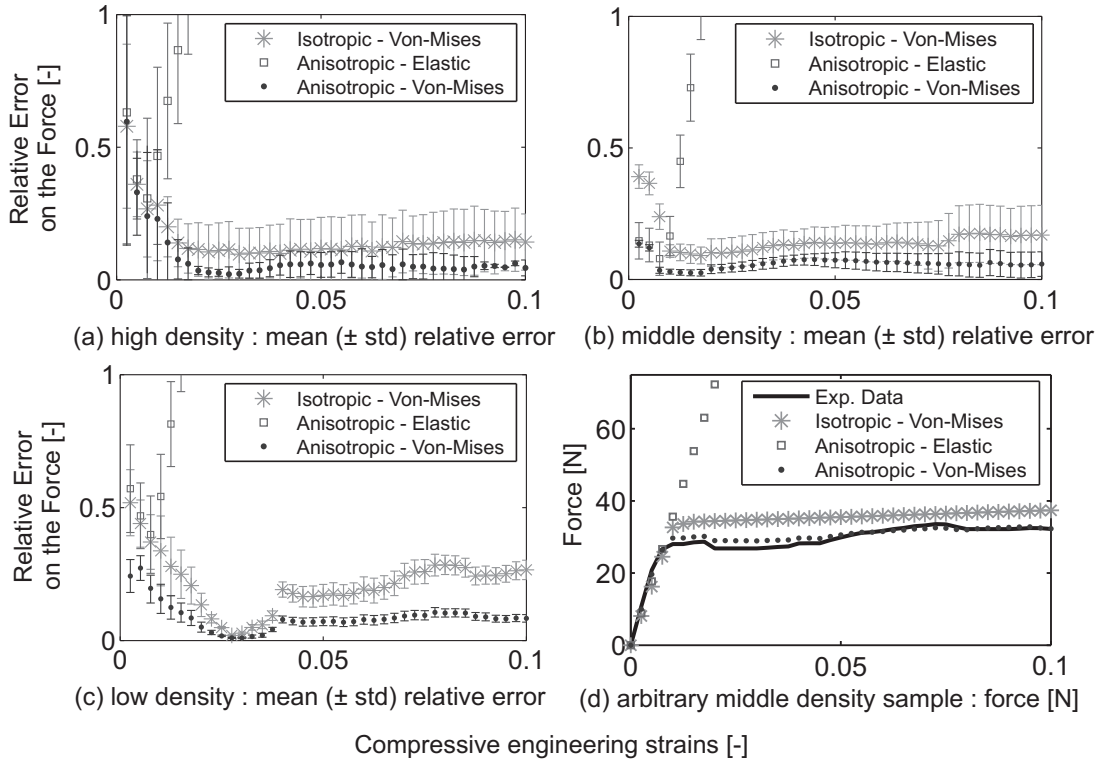

FIGURE 5.41: *Comparison of the force vs. compressive engineering strains for three different material models (Duocel foam samples, 8 ROI): anisotropic elastoplastic (von Mises) material - material model presented in this study ; isotropic elastoplastic (von Mises) material ; anisotropic elastic material*

4% of engineering strain), the elastic model therefore seems to be sufficient to describe the antler mechanical behavior. However, the use of an isotropic model for the deer antler leads to errors on the computed force of about 30% throughout most of the strain range. This would therefore allow to conclude, on this particular sample for the given test conditions, that the anisotropic structure of the material has more impact on its response to load than its non-linearity.

Conclusions

We showed that, for the presented materials and test conditions, the representation of the morphology through `BV/TV` and the fabric tensor is required to capture the apparent yield stress and strains even for low degrees of anisotropy. The introduction of a non-linearity such as elastoplasticity is essential to the understanding of the mechanical behavior in compression for strains beyond the yield limit. However, for applications where the strains are limited, the use of an elastic anisotropic model is sufficient to represent the force accurately. Using this model for morphological data extracted for regions of interests (ROI) small enough, we showed that one can retrieve not only the linear behavior of the structure but also the non-linear behavior such as the apparent yield stress and strain and early post yield

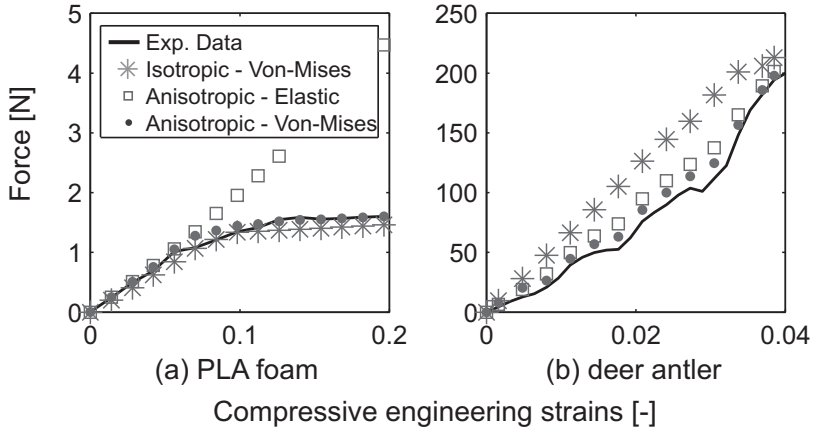

FIGURE 5.42: *Comparison of the force vs. compressive engineering strains for three different material models (PLA foam and deer antler, 8 ROI): anisotropic elastoplastic (von Mises) material - material model presented in this study ; isotropic elastoplastic (von Mises) material ; anisotropic elastic material*

softening. Using ROIs one eighth of the total volume of the specimens, we reduced the relative error on the force below 5% over the computed strain range except when abrupt variations of the force are observed. While the state-of-the-art in the use of material parameters extracted from the morphology is to assign different material parameters to each finite element [20, 95, 129, 265], the presented results show that the computation of the maximal force as well as some non-linear measures (yield stress and strain for instance) can be achieved without the need to consider very small ROIs. The determination of the optimal size of these ROIs should consider several parameters such as the degree of local behavior needed in the macroscopic model but also the discretization (and therefore computational) cost. This type of global mechanical models is indeed presented as a possible solution for computationally costly models such as micro finite elements. The integration of more local behavior should therefore not lead to an excessive increase of the computation cost.

While the application of this material model seems to be valid for the presented materials in compression, it still has to proof itself on other materials, specially using more samples of bone and not mainly bone-like materials. Furthermore, for material for which the local non-linear behavior is not well established (here the PLA foam and the deer antler), loading/unloading tests should be carried out to ensure the non-linear behavior is indeed an irreversible (plastic-like) behavior and not another type of non-linearity (non-linear elasticity, micro-cracks leading to damage, ...). Finally, the model should also be tested on other mechanical tests such as tension, bending or torsion.

5.4.2 Validation on Computational Tension Tests

As said in the previous paragraph, we should also test our model with respect to other mechanical tests than compression. However, only experimental compression tests are available to us. We will therefore create computational tension tests on the microstructure and then use the numerical force/displacement curves obtained with these simulations to test our material model. For this, we will simulate tension tests with μ-Finite Element models. However, we need first to validate such μ-Finite Element models, using the compression data as on the previous section. We therefore first propose to model the compression tests using μ-Finite Element models (and therefore using a constitutive law relative to the trabeculae, not to the apparent tissue level).
In order to validate these models, we compare the main characteristics of the engineering stress/engineering strain curves obtained at the apparent level (i.e. apparent Young's modulus, apparent yield stress and strain, and ultimate stress) as well as the root mean square error on the force over the displacement range. The validation concerns not only the constitutive law (well known for the Duocel aluminum foam samples that will therefore be the only one used here) but also the mesh, the element integration scheme and the representation of the boundary conditions.
If we can consider the μ-FE models of compression tests as valid, we will assume this remains true for tension tests. This assumption comes from the observation that the μ-FE simulations of compression tests involve not only compression of elements but also shear and tension. All types of loading are represented in the compression tests as they would be for tension tests. With this hypothesis, we therefore perform numerical tension tests using the same models. Doing so, we can obtain force/displacement curves in tension and use them to validate our model for tension tests as done in the previous section for compression tests.

The first step to perform μ-FE analysis on the samples used in the previous section is to build finite element meshes from the μ-CT images. These meshes were produced at ETH after thresholding of the images (only μ-FE analysis on the Duocel foams are considered as the constitutive law at the trabecular -or rather strut- level is better known than for the two other materials). Hexahedral meshes were then built using a voxel-based approach. Convergence studies [192] have shown that the element size should be less than one fourth of the mean strut thickness as measured by the `Tb.Th` parameter described in section 2.3. As presented in Table E.1, the mean strut thickness for the tested Duocel foam samples are of $0.360, 0.261$ and $0.167mm$ for respectively the dense, middle density and low density samples. As the resolution of the images (and therefore the minimum element size for voxel-based meshes) is $30\mu m$, all the samples could be used for simulation with a mesh considered as a converged mesh (i.e. fine enough). However, using the smallest linear hexahedral elements possible leads to meshes (for the middle density samples) with more than 4.5 millions degrees-of-freedom (this number is higher for dense samples and lower for low density ones). This leads

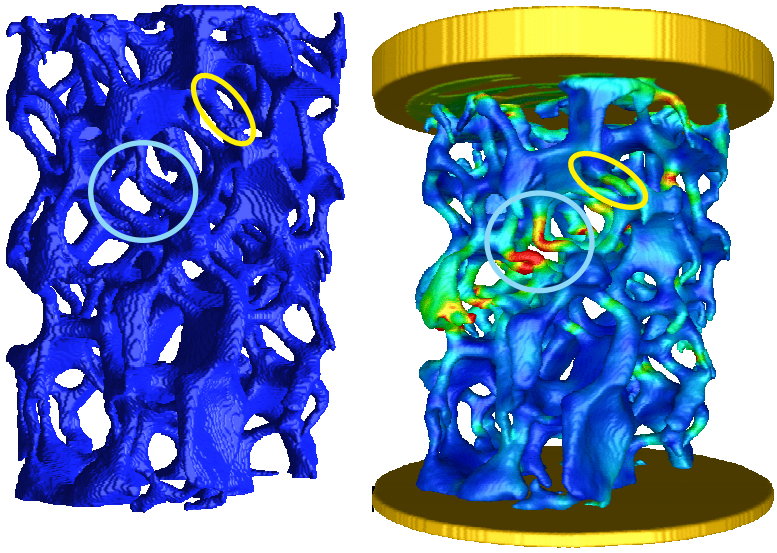

FIGURE 5.43: *3D reconstruction of one dense Duocel foam. On the left, initial configuration; on the right, configuration at 4% compression (color shows experimental strains map - scalar measure of the Green-Lagrange strain tensor (second invariant of the deviatoric part of the Green-Lagrange strain tensor); courtesy of D. Christen, ETH). Evidence of finite deformations are enlightened in the blue circle (buckling of the aluminum struts) and of large rotations in the yellow ellipse.*

to a huge cost in computational memory that cannot be handled with our current computing capabilities. Therefore, we decided to use $60\mu m$ resolution models, i.e. each hexahedral element represent 8 voxels. However, the meshes obtained with this resolution for the low density samples cannot be considered as satisfactory (less than 3 elements over the strut thickness). This might also be true for the middle density samples (just about 4 elements over the strut thickness). Therefore, this validation procedure will be performed only to the densest samples we have (for which there is a mean of 6 elements over the strut thickness).

Nonlinear micro finite element modeling of aluminum foam in compression

The meshes were then imported into Metafor [177], and converted into eight nodes hexahedral elements at $60\mu m$ per side, leading to a mean of almost 500000 nodes per sample.The use of a finite deformations code (geometrically and materially non-linear) is essential because the compressed samples showed evidence of localized large deformations and large rotations (see Fig. 5.43).
Finite deformations simulations were also required to show the softening effect was a structural softening, i.e. due to local buckling of the aluminum struts, and not a material softening. Such a structural effect cannot indeed be produced with a geometrically linear analysis. The material parameters used in the μ-FE models for each sample are reported in table 5.1, they are the same as the one used in the validation of the continuum law in compression tests.

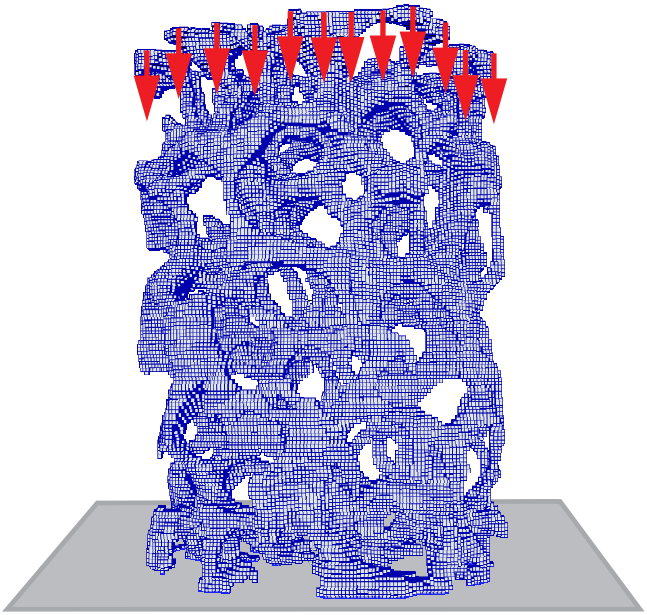

FIGURE 5.44: *Mesh and boundary conditions for an arbitrary sample: the red arrows show the imposed displacement, the gray surface is the contact plane.*

The experimental setup boundary conditions (two contact plates, one fixed, on top of which the sample lays, and one moving down, crushing the sample along the vertical direction) were numerically reproduced as close as possible. However the use of two rigid plates with frictional or sticking contact conditions led to a simulation setup that was not stiff enough compared to the experimental setup and could not lead to an equilibrium convergence. Therefore a choice was made to use a rigid plate with frictionless contact conditions at the bottom of the setup and impose vertical displacement of the top nodes (allowing a free horizontal movement). One node at the bottom center of the sample was also constrained in the horizontal plane to prevent rigid body modes (see Fig. 5.44).
All samples are submitted to an imposed displacement of the top surface corresponding to 16% of the initial height (maximal displacement obtained during the experiments). However, as no self-contact is accounted for in the simulation (contact between the struts due to compression of the sample), some simulations had to be stopped earlier (as soon as $\approx$ 12% of height reduction - see Table 5.3). A visual check has been performed at the end of the allowed height reduction for all samples, each showing self-contact should be accounted for at that level of displacement (no quantitative check can be performed without taking into account the self-contact, which cannot be performed due to the high computing memory requested by the self-contact algorithm).

It should first be noticed that the experimental data show different type of behavior according to the sample. As can be seen in Fig. 5.45 and described in Table 5.4, two of the samples (sample $D1$ and $D5$) exhibit an apparent stiffness (proportional to the slope of the linear part of the force/displacement curve) which is significantly lower than the three others. The

TABLE 5.3: *Total displacement achieved for each sample*

sample	$D1$	$D2$	$D3$	$D4$	$D5$
Height variation [%]	16	11.82	16	12.27	12.83

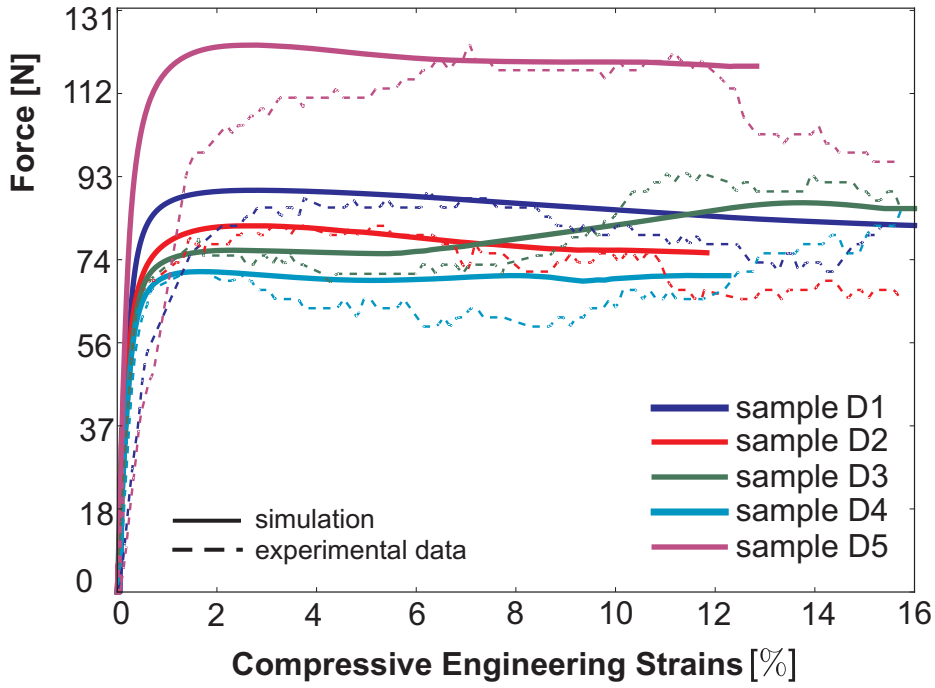

FIGURE 5.45: *Duocel Foam Dense Samples: computed (plain line) and experimental (dashed line) forces vs. sample displacement.*

differences in the reduced densities (assuming apparent quantities are proportional to the reduced density - $\bar{\rho}$) cannot explain this differences on the stiffness. Indeed, while the reduced density of sample $D1$ is slightly lower than the mean reduced density, $\bar{\rho}$ for sample $D5$ is significantly higher and should therefore lead to a higher apparent stiffness. The differences in apparent stiffnesses could therefore be explained by either a slight difference in the testing conditions (alignment of the sample, contact conditions, ...) or by a difference in the alloy itself. As both these types of differences are not accounted for in the model, no significant difference on the simulated apparent stiffness should be found.
One can also notice a difference in the experimental data of apparent ultimate stress (the term stress refers to the engineering stress, computed from the applied force and the initial cross-section area, if this area were to be plain), $\sigma_{\mathrm{u}}^{\mathrm{app}}$, which is significantly higher for sample $D5$ than for the other four samples. However, as sample $D5$ has a reduced density significantly higher than the other samples, the difference may be explained solely by the density. If this is the case, the simulated ultimate stress should also be higher for this sample.
Finally, the post-yield behavior (behavior for displacements higher than the displacement corresponding to the apparent ultimate stress) of all samples first exhibits a softening of the force, followed for some samples (samples $D3$ and $D4$ mainly) by a hardening. This secondary hardening could be explained either by the densification regime or by an increase in the contact area as some struts initially not in contact with the plates could come into contact due to high deformations and rotations. While the densification regime is not accounted for, the contact area increase is taken into account by the model.

From these observations, we can define the apparent variables needed to describe the force displacement relation (Fig. 5.46). The apparent linear part depends on the apparent Young's modulus, $\mathrm{E}^{\mathrm{app}}$, the end of the linear part is the apparent yield stress, $\sigma_{\mathrm{y}}^{\mathrm{app}}$. It is followed by an apparent hardening up to the ultimate stress, $\sigma_{\mathrm{u}}^{\mathrm{app}}$. These are the three quantities we can compare between the experimental data and the simulated ones. After the ultimate stress, follows a softening that we suppose to be only due to a structural effect (no softening is present in the constitutive law) and finally, in some samples, a secondary hardening due to an increase in the contact area and self-contact of the struts. The accuracy of the post-yield behavior can be quantified by the difference in force for a given displacement between the measured and the simulated force.
The simulated apparent Young's modulus is measured using a linear regression of the engineering stress/engineering strain computed data up to an apparent strain level (apparent yield strain, $\varepsilon_{\mathrm{y}}^{\mathrm{app}}$) defined as follows: it is the apparent strain for which the tangent modulus ($\frac{\partial \sigma}{\partial \varepsilon}$, theoretically constant and equal to Young's modulus for the linear part) falls below a threshold value (here taken at 15% of the mean experimental apparent Young's modulus, i.e. $37MPa$). This threshold value as been chosen arbitrarily and visually verified a posteriori (visual verification that with the chosen threshold, the apparent yield strain represents approximatively the apparent strain at the end of the linear part, leading to a mean apparent

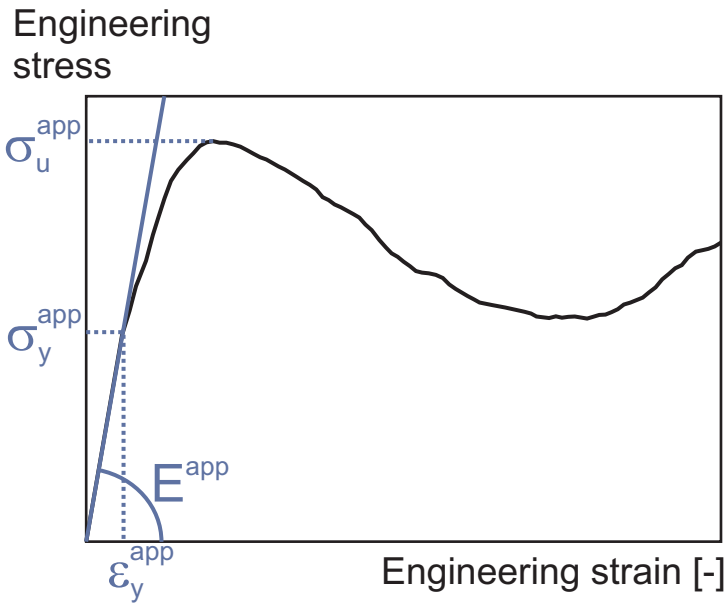

FIGURE 5.46: *Definitions used to describe the characteristic points of the non-linear stress/strain curve (beware of the unusual notation, σ, ε, for the non-linear stress and strain measure, used to simplify the reading).*

TABLE 5.4: *Apparent mechanical values : Young's modulus ($\mathrm{E}^{\mathrm{app}}$), yield limit ($\sigma_{\mathrm{y}}^{\mathrm{app}}$), ultimate stress ($\sigma_{\mathrm{u}}^{\mathrm{app}}$) ; for experimental data ($_{exp}$) and simulations ($_{sim}$) for each sample (plus mean, and standard deviation - std).*

sample	$D1$	$D2$	$D3$	$D4$	$D5$	Mean	Std
$\bar{\rho}$ [%]	11.86	13.46	11.89	12.60	14.17	12.8	1.0
$\mathrm{E}^{\mathrm{app}}{}_{exp}$ $[MPa]$	193.46	304.29	304.26	265.48	179.21	249.34	53.55
$\mathrm{E}^{\mathrm{app}}{}_{sim}$ $[MPa]$	296.58	278.77	246.03	285.64	309.39	283.28	21.32
$\sigma_{\mathrm{y}}^{\mathrm{app}}{}_{exp}$ $[MPa]$	1.248	1.6	1.6	1.573	1.04	1.41	0.23
$\sigma_{\mathrm{y}}^{\mathrm{app}}{}_{sim}$ $[MPa]$	1.584	1.623	1.437	1.554	2.386	1.72	0.34
$\sigma_{\mathrm{u}}^{\mathrm{app}}{}_{exp}$ $[MPa]$	1.987	1.887	2.123	2.024	2.639	2.13	0.26
$\sigma_{\mathrm{u}}^{\mathrm{app}}{}_{sim}$ $[MPa]$	1.752	1.829	1.817	1.68	2.616	1.94	0.34

yield strain of $\varepsilon_{\mathrm{y}}^{\mathrm{app}}{}_{sim} \approx 0.64\%$ [1] while it is $\varepsilon_{\mathrm{y}}^{\mathrm{app}}{}_{exp} \approx 0.73\%$ in the experimental data[2] , i.e. not a very good representation but an approximative one).

This definition leads to a mean apparent Young's modulus, $\mathrm{E}^{\mathrm{app}}$, of $283.28MPa$ while it is of $249.34MPa$ in the experimental data (Table 5.4). Performing an unpaired t-test assuming unequal variances (assessed with an f-test) and normality distribution (assessed with Kolmogorov-Smirnov test) on these values shows that the simulated apparent Young's modulus shows no significant difference with the experimental one. As expected, no difference can be seen in the computed apparent stiffness between all the samples. The difference that is seen on the experimental data is therefore not due to a reduced density effect. The same statistical conclusion (assuming an equality of variances) can be made for the apparent yield stress and apparent ultimate stress but with a lower correlation for the last one (for this quantity, the normality assumption cannot be considered as valid, a Mann-Whitney test is therefore performed). However, computing an apparent strength from the apparent yield strain and the apparent Young's modulus ($\sigma^{\mathrm{app}} = \mathrm{E}^{\mathrm{app}}\,\varepsilon_{\mathrm{y}}^{\mathrm{app}}$) gives significantly different results than the equivalent quantity for the experimental data ($p < 0.05$). This last result is mainly due to the deficient representation of the apparent yield strain discussed previously.

Finally, we can compute the Root-Mean-Square error on the force representation (see Table 5.5). As could have been expected, the RMS error for both samples displaying an apparent stiffness significantly lower than the three others (sample $D1$ and $D5$) is high compared to the three other samples (from three to nine times higher). This is explained mainly by the improper computation of the apparent stiffness. Indeed, when computing the RMS error on the linear part of the data, we can see that the error values are high (over 100% error for sample $D5$). However, computing the same error on the nonlinear part of the data (and shifting the simulated behavior as if the apparent stiffness had been well represented), we can see all error values drop to get to a mean error of about 10%. For the three other samples, we have an RMS error below 13% on the whole computed strain range with higher values (up to three times higher) for the linear part than for the nonlinear one.

For apparent strains higher than the one achieved at the ultimate stress level, one can see that all simulations show a decrease of the stress and thus a softening behavior. As the material behavior always exhibits hardening, this softening is only a structural effect. It can therefore be represented only in a non-linear analysis considering finite deformations and large rotations. Sample $D3$ specially allows a pretty good representation of the first softening and the following hardening (RMS relative error on the computed range $\approx 6\%$).

We therefore showed, as intended in this section, that both the apparent yield and ultimate stress can be reproduced with an elastoplastic material model (von Mises yield surface) and that the post-yield softening is solely due to a structural effect.

[1] Values of .62%, .60%, .62%, .59%, .78% for sample $D1$, $D2$, $D3$, $D4$, $D5$ respectively
[2] Values of .75%, .72%, .72%, .75%, .73% for sample $D1$, $D2$, $D3$, $D4$, $D5$ respectively

TABLE 5.5: *Apparent root-mean-square error on the force computation, in % of the experimenta force, over the whole strain range (RMS error), over the linear part of the apparent behavior (RMS error, linear), and over the nonlinear part of this behavior (RMS error, nonlinear).*

sample	$D1$	$D2$	$D3$	$D4$	$D5$	Mean	Std
RMS error	34.51	6.25	6.23	12.99	92.43	31.28	35.89
RMS error, linear	77.42	10.67	8.45	31.69	134.25	52.49	53.44
RMS error, nonlinear	10.53	5.16	4.93	10.46	15.16	10.25	3.55

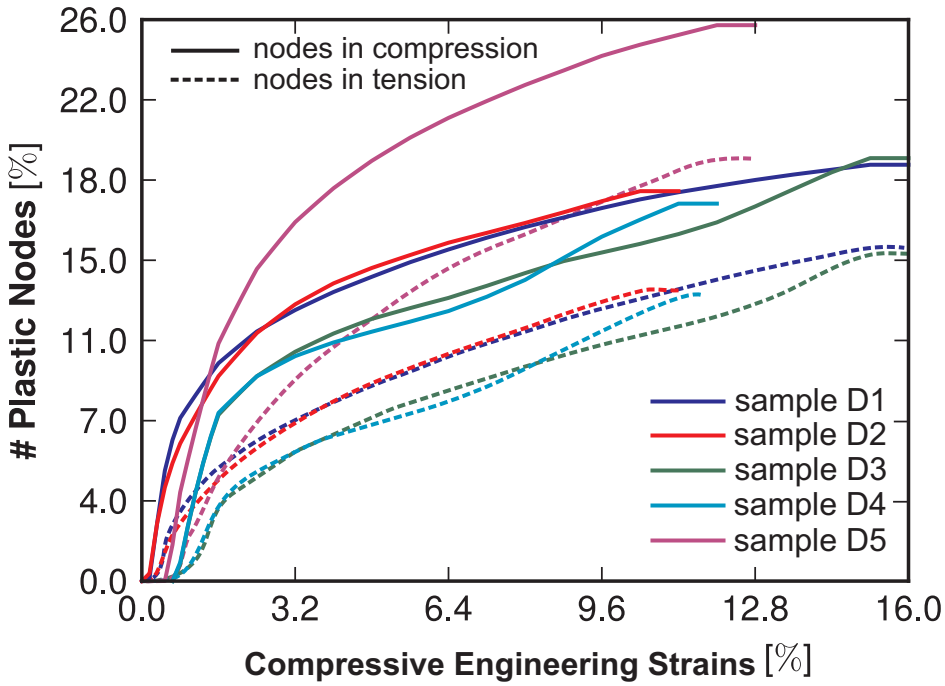

FIGURE 5.47: *Percentage of nodes in plasticity as a function of sample displacement (plain lines: nodes in compression, dashed lines: nodes in tension).*

On the apparent linear behavior at the beginning of the loading (up to the apparent yield strain, ≈ 0.64%), it should be noticed that the linearity is only apparent. Indeed, if one computes the number of nodes in plasticity[1] (i.e. with a non zero equivalent plastic strain), we can see the importance of the non-linear behavior of the material in the deformation process. Fig. 5.47 shows that elements start to sustain plastic deformations as soon as the apparent strain reaches a mean value of 0.22%. The first yielding elements are elements sustaining negative hydrostatic pressure (compression). Indeed, as the samples are compressed, the elements showing the highest equivalent stress early in the process are elements in compression. However, as soon as some elements show yielding in compression, local deformations become larger due to plastic flow and some yielding elements sustain positive hydrostatic pressure (tension). Elements sustaining a positive hydrostatic pressure start to show a yielding behavior at an apparent strain about 20% higher than elements in compression. Among the elements in plasticity, it is shown that about 40% (throughout the displacement level) are elements submitted to a positive hydrostatic stress while the sample is submitted to compression. At an apparent strain of 0.6% (i.e. below the apparent yield strain), already 3 to 5% of the elements are in plasticity. When an apparent strain of 1% is achieved, the number of element in plasticity becomes significant (≈ 8% of elements). These results show once more that a non-linear material behavior is needed even at low compression levels. As can be seen in Fig. 5.47, most samples show approximately the same post-yield behavior with about the same percentage of nodes in plasticity. However, the number of elements in plasticity of sample $D5$ is about 40% higher than in the other four samples. This is most probably one of the explanations to the force reached for this sample in compression being significantly higher than for the others.
From these observations (accurate representation of the apparent mechanical values: E^{app}, σ_y^{app}, σ_u^{app} and low RMS error on the nonlinear part of the force), we can conclude without taking too much risk that the μ-FE models used for these simulations can be considered as valid.
As introduced previously, we will consider on the next section they are also valid for tension tests. We will for this keep the mesh, the constitutive law, the contact condition at the bottom plate but the top nodes will be moved away from the contact plate to create tension-tests.

Nonlinear finite element modeling of aluminum foam in tension

As proposed in the previous section, we provide here *in-silico* tension tests on the microstructure of our dense Duocel foam samples. The samples are considered rigidly fixed on the bottom plate and the upper nodes are moved away from this plate with a displacement equivalent to 6% of their initial height. This value of displacement is smaller than in the *in-silico* compression tests as some elements on the thinner struts are substantially stretched

[1]The scalar value measuring the equivalent plastic strain is obtained by integrating $\dot{\bar{\varepsilon}}^p$ (Equ. 3.38). This value is computed at the integration points (Gauss points) and extrapolated over the mesh to get a nodal value.

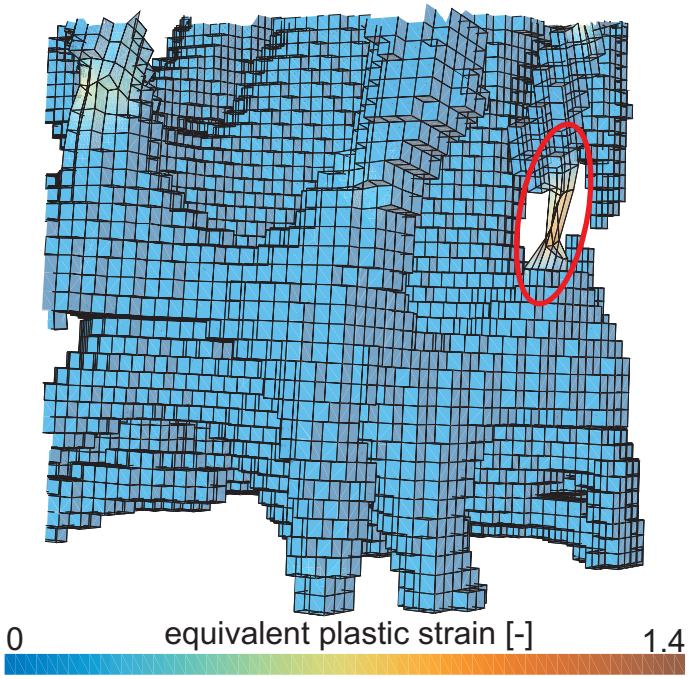

FIGURE 5.48: *Mesh distortion on tension tests at high plastic strain in the μ-FE model at* 7% *apparent engineering strains.*

beyond a point where the mesh is so distorted that the solution cannot be trusted anymore (see Fig. 5.48). Mesh management solutions such the Arbitrary Lagrangian-Eulerian formulation are not used in this problem as the number of nodes is high (about half a million) and the additional computational cost to use such a formulation would be too high for its potential benefits.

We can first of all notice (Fig. 5.49) that, as for compression tests, sample $D5$ reaches higher forces than the other samples for the same displacement level. We can also notice that, for a given absolute value of engineering strains, the force needed in tension is about 66% higher than the force needed to compress the sample.

For the comparison between *in-silico* tension curves (referred to as the *in-silico* results) and results obtained for the same problem with our model, the methods employed to obtain and present the results are completely equivalent to the ones presented in section 5.4.1 and will not be reminded here. All morphological and material parameters are kept constant with respect to the ones used in that section.
The results are first analyzed for morphological data extracted over the whole volume of the specimens. This case is referred to as "1 ROI" in the corresponding figures.
The predicted force-engineering strain behavior with our model does not present at all the same overall behavior as the *in-silico* one in the range of strains considered here (Fig. 5.50). We can retrieve some of the apparent linear behavior and the maximal force but not at all the strain at which it is achieved (represented with an error of more than 100%). The transition

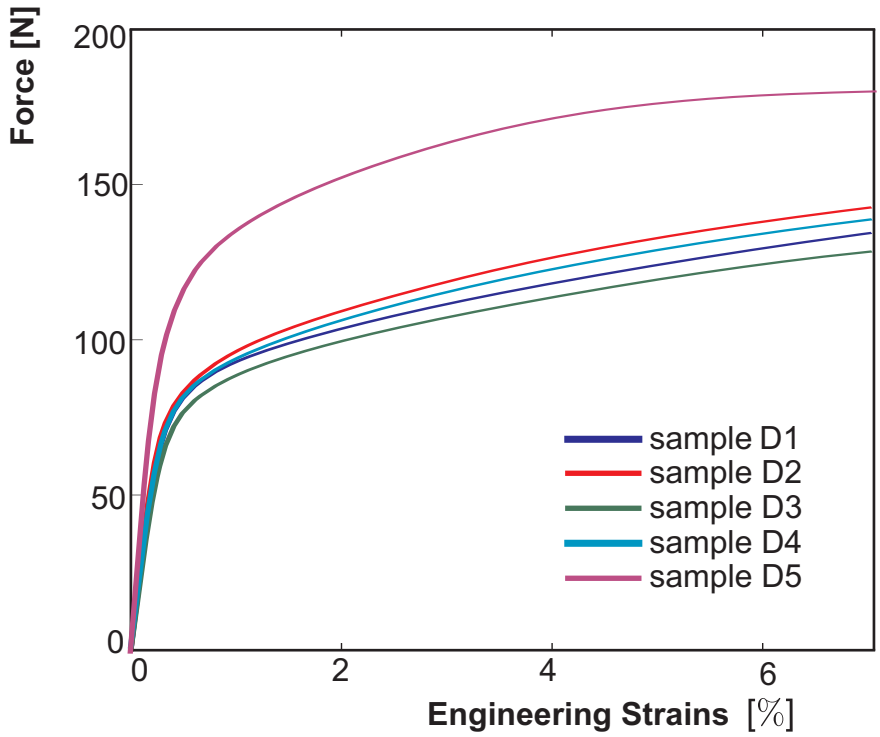

FIGURE 5.49: *Tension curves obtained with the µ-FE simulations (referred to as* in-silico *results)*

between the linear part of the curves and the reach of maximal force are as well badly represented. Indeed, yielding appears at an engineering strain level about 1% higher than it does in the *in-silico* curves. The computed force tends to decrease almost linearly after reaching the maximal force while it increases for the *in-silico* results. The use of structural parameters averaged over the entire volume seems therefore not appropriate to represent the non-linear behavior of the force for all samples.

Extracting the material parameters over 4 ROIs (referred to as "4 ROI" in Fig. 5.50) already reduces the error observed on the linear part of the force by about 20%. When computing the force with material parameters extracted over 8 ROIs (referred to as "8 ROI" in Fig. 5.50), the predicted force can fit details of the experimental force variations on the non-linear part of the curve. We therefore seem to get a convergence of the computed force to the experimental one using small ROIs. Not only the linear part of the force is better represented but also the appearance of yield and the post-yield behavior are represented with an error below 10%.

Even though the Duocel dense foam samples all have a low degree of anisotropy (Table 5.2), the use of an anisotropic material accounting for the fabric directions, instead of an isotropic one accounting only for `BV/TV` (Fig. 5.51), allows to better capture not only the apparent stiffness of the sample but also the apparent softening at low strains. The use of an isotropic model for the Duocel foams in applications where the maximal force is of importance would conclude to an overestimation on the force in this case.

The importance of using an elastoplastic model for the Duocel samples is also outlined in

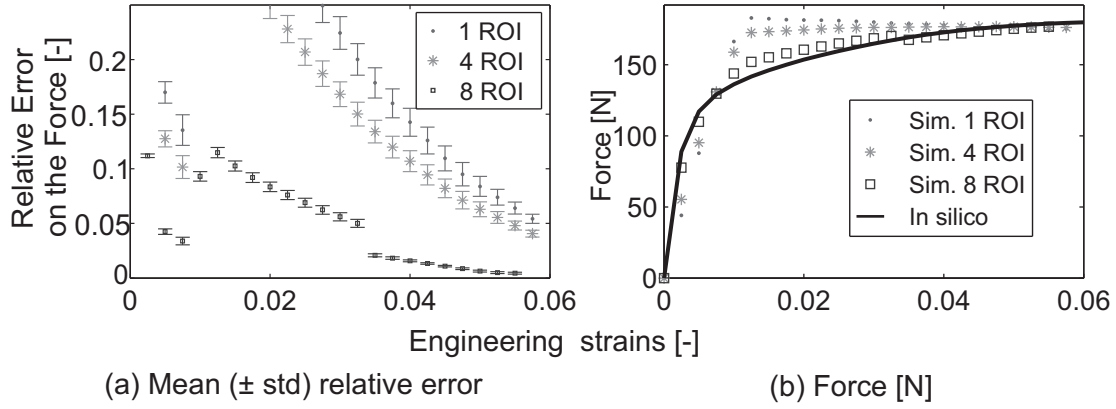

FIGURE 5.50: *Dense Duocel Foam Samples: computed (Sim.) and* in-silico *forces [N] vs. compressive engineering strains [-]. (a) relative error on the force - mean and std., (b) force for an arbitrary sample*

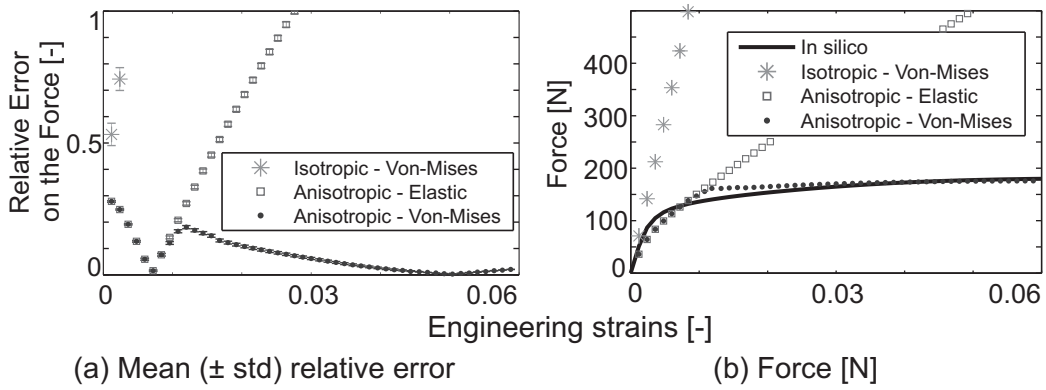

FIGURE 5.51: *Comparison of the force vs. compressive engineering strains for three different material models (Duocel foam samples, 4 ROI): anisotropic elastoplastic (von Mises) material - material model presented in this study ; isotropic elastoplastic (von Mises) material ; anisotropic elastic material*

Fig. 5.51. It can be seen that an elastic anisotropic material can account only for the force up to 1% of apparent engineering strains. The introduction of elastoplasticity for this material is essential for larger strain levels.

We should outline the fact that for these results in tension, the consideration of anisotropy seems as important as the consideration of non-elasticity while for the compression tests on the same samples, the anisotropy did not seem to play such an important role in the overall behavior of the samples.
As for the compression tests, for applications where the strains are limited, the use of an elastic anisotropic model is sufficient to accurately represent the force. Using our model for morphological data extracted for regions of interests (ROI) small enough, we showed that one can reproduce not only the linear behavior of the structure but also the non-linear behavior such as the apparent yield stress and strain and the early post-yield behavior. Using

ROIs one eighth of the total volume of the specimens, we reduced the relative error on the force below 10% over the computed strain range except when abrupt variations of the force are experimentaly observed.

With these observations it seems fair to conclude the use of our model on tension tests can be considered as valid (considering the material and testing conditions) using small enough ROI's. As stated earlier, it still has to proof itself on other materials, specially using more samples of bone and not mainly bone-like materials as well as a larger panel of densities.

We showed in this section that accounting either for nonlinearities (through a von Mises plastic criterion) or for the anisotropy (or both) is important for all the simulations we performed on our test samples.
Indeed for the Duocel foam samples, accounting for the nonlinearities of the material was needed for 3%, 1%, and 0.5% of compressive engineering strains for respectively the low density, middle density and dense samples. In tension tests, both the anisotropy and the nonlinearity was to be accounted for from 1% of engineering strains for the dense samples. For the two other materials in compression tests, the nonlinearity of the material was to be accounted for starting at 8% compressive engineering strains for the PLA foam, while accouting for the anisotropy was of importance for the deer antler as soon as 0.3% compressive engineering strains were reached.

5.5 Remodeling of the Proximal Femur

The developed bone remodeling model is here used and verified, without its pressure dependent extension specific to the alveolar bone, to analyze the bone structure and density evolution on models of the proximal extremity of a femur submitted to loads representative of a daily normal activity. The idea is to assess (at least qualitatively) the capacity of the remodeling algorithm to represent normal density and morphology of the proximal femur submitted to physiological loads, starting from a virtual situation of homogeneous isotropic bone.

5.5.1 2D model and verification

As a simplification and to compare our results with standard results from the literature, a two-dimensional model is used for an in-plane analysis (plane strain analysis). The model used here is reproduced from [17]. It has also been used in [62, 69, 117]. The geometry is depicted in Fig. 5.52 where, in order to describe the bone dimensions, some points are plotted. The distance between points A and B (the diameter of the diaphysis) is 30 mm and the distance between point C and D is 57.76 mm.
The applied loading [17] represents an approximation of the mean daily loads due to normal gait (the most frequent and a reasonable load application to the femur). In this sense, the gait cycle is discretized into three loadings representative of the single leg stance (the joint reaction force, JRF) and the extremes of abduction and of adduction. The magnitudes, orientations and applied daily cycles of each load are given in Table 5.6 and Fig. 5.53. In order to take into account a variety of activities, like standing, stair-climbing, etc., the first load case (single leg stance) was assigned 6000 daily cycles while the two others are assigned 2000 cycles. Each load case consists in a force acting on the femoral head at the articulation (representative of the joint reaction to the leg stance) plus a reaction force induced in the abductor muscle.
Due to an analysis of Jacobs [117], the order in which these loads are applied has no significant impact on the numerical results. Thus, they can be grouped together. Instead of a uniform mixture of all three cyclic loading cases, they are reordered such that, each day, during three fifth of the time the first loading case is applied while during the fourth and fifth parts of the day load cases 2 and 3 are applied, respectively (Fig. 5.54). With a constant cycle number of 10 000, this sums up to the same distribution as in Table 5.6. We remind here that the number of cycles is accounted for in the remodeling model (see definition of the stimulus Equ. 5.4). The loads are not applied in a cyclic manner but uniformly, with an intensity representative of a single cycle.
A limitation of this 2D model was pointed out [117] as the lack of connection between the two cortical layers (lateral and medial parts of the cortex) of the diaphysis, while it appears in reality due to the cylindrical structure of the cortex. Here, we follow the (artifact) solution used by several authors [62, 69, 117]. This artifact consists into including an additional “side

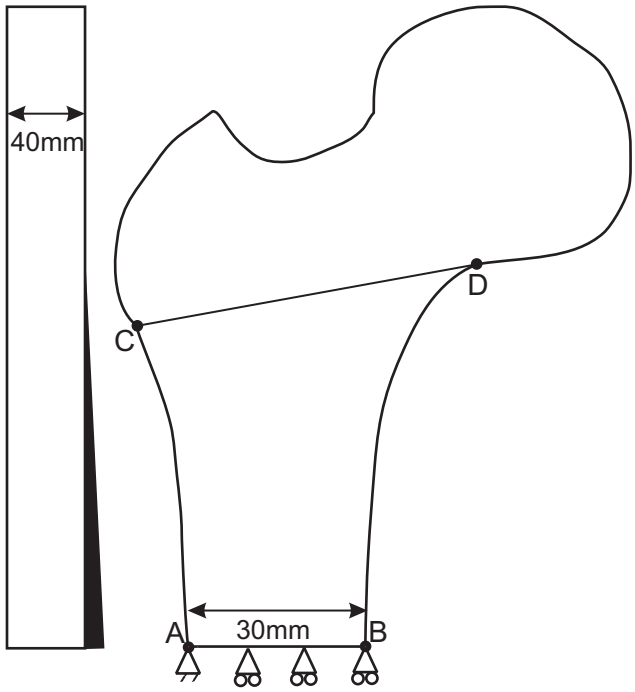

FIGURE 5.52: *Geometry and boundary conditions used in the 2D model of the proximal femur. On the left, lateral view of the model's thickness with in black the additional (artificial) thickness due to the side plate (not to scale with the main model).*

Load	Cycles	Joint reaction (F)		Abductor reaction (R)	
case	per day	Magnitude (N)	Orientation (^{o})	Magnitude (N)	Orientation (^{o})
1	6000	2317	24	703	28
2	2000	1158	-15	351	-8
3	2000	1548	56	468	35

TABLE 5.6: *Magnitude and orientation of the applied forces for each load case. Case 1 is a single leg stance, case 2 and 3 represent the extremes of abduction and adduction, respectively. The angle are given with respect to the vertical axis, positive in a clockwise direction [17].*

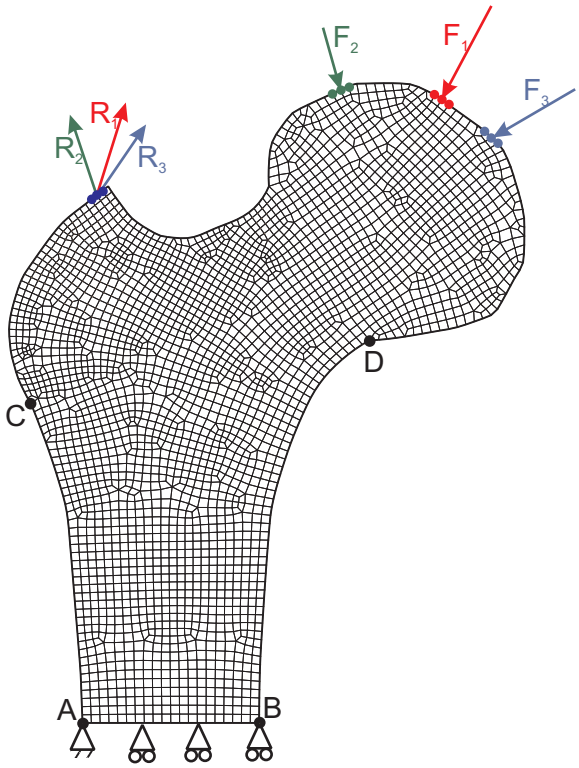

FIGURE 5.53: *Mesh and boundary conditions used in the 2D model of the proximal femur (red: joint reaction and muscle reaction-case 1, green: joint reaction and muscle reaction-case 2, and blue: joint reaction and muscle reaction-case 3).*

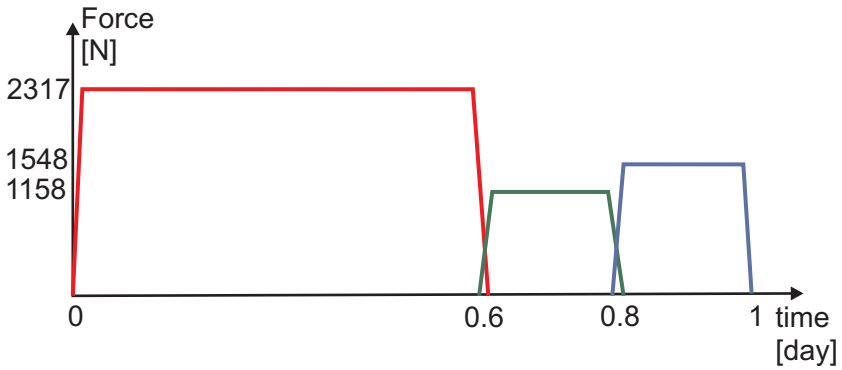

FIGURE 5.54: *Daily cycle of the forces as applied (red: force at the joint-case 1, green: force at the joint-case 2, and blue: force at the joint-case 3).*

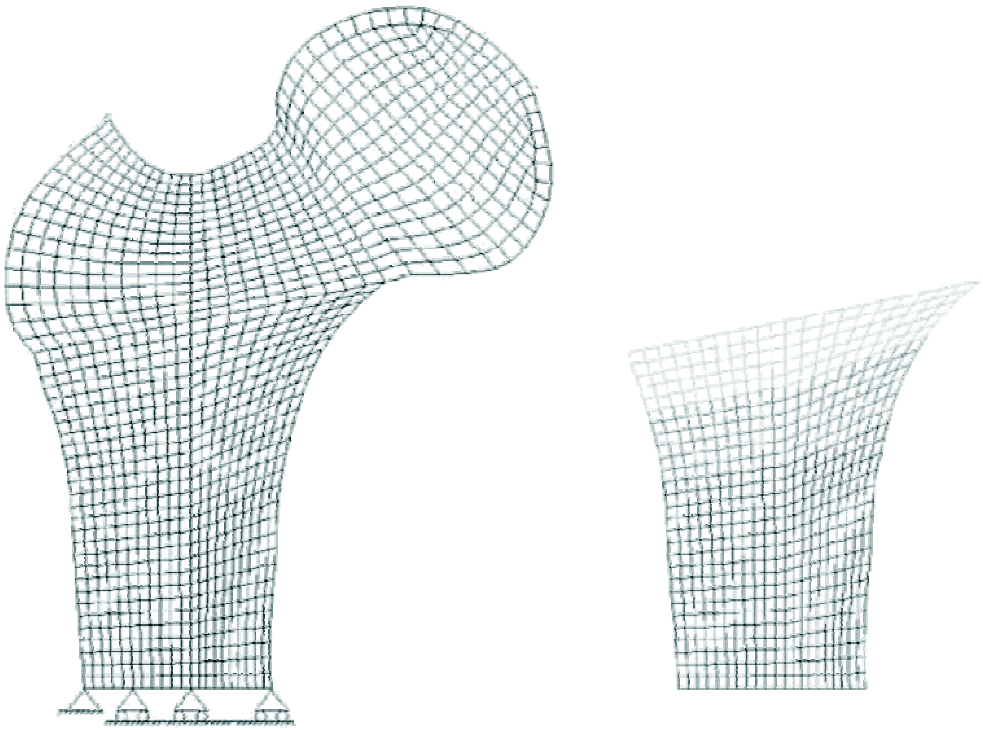

FIGURE 5.55: *Mesh of the 2D model of the proximal femur used by Doblaré and García [62]. On the left, mesh of the main model, on the right of the side plate.*

plate" (between the four points $ABCD$) of bone tissue, joining both cortical layers and not allowed to remodel. This so called side plate (even though it is more "in front" of the main model than side to it), when discretized, has its left nodes directly bound to the left nodes of the main model (i.e. the curve AC belongs to both the main model and the side plate) and analogously the right nodes to the right side (i.e. the curve BD belongs to both models). To take into account that the cortical cylinder smoothly merges into the trabecular structure of the metaphysis, the cited authors use a plate with varying thickness, from 1mm at the epiphysis to 5mm at the diaphysis, while the main model's thickness is 40mm (see geometry in Fig. 5.52 and mesh in Fig. 5.55). This side plate therefore artificially adds stiffness to the model.

As, in Metafor, we use 2D plane strain analysis elements with 1mm thickness, this thickness difference in 2D elements is adjusted by means of the applied loads (reduced by a factor of 40 to account for the main model thickness), and the stiffness of the side plate (increased by 3.5 compared to the equivalent trabecular bone stiffness to account for the side plate mean thickness). The mesh (Fig. 5.53) consists of 2742 linear quadrilaterals elements for the main model and 931 for the side plate, the left lower point (A) is fixed and the rest of the lower horizontal line (AB) is fixed along the vertical direction.

The initial situation corresponds to an isotropic homogeneous state with initial density $\rho = 0.63 g/cc$ (corresponding to a porosity of 0.70 and a mean damage value of $d_h = 0.97$). This

initial situation corresponds also to the material of the side plate. Each force is distributed on three adjacent mesh nodes as depicted in Fig. 5.53 in order to decrease loads concentration effects. The time-step of the simulation is controlled and set to a maximum of a tenth of a day to ensure that each loading case is applied during at least two consecutive time-steps. Since the three models we compare our results with use a simple elastic material to describe the bone matrix and as the purpose of this section is to verify the remodeling algorithm, we here use also a simple elastic material at the trabecular level. The following set of remodeling parameters is used (corresponding to the set of parameters used in [62]):

number of daily load cycles	: $N = 10000$
homeostatic value of the stimulus	: $\psi^\star = 50\ MPa$
exponent of the stress stimulus	: $m = 4$
remodeling velocity for resorption and formation	: $c_r = c_f = 0.02\mu m/(\text{day}MPa)$
half-width of the lazy zone	: $\omega = 25\%\psi^\star$
parameter weighing the hydrostatic and deviatoric parts of the effective stress definition	: $\eta = 1.2$

We first compare our results with the density maps of the literature for the same problem, solved considering an anisotropic remodeling law. For this, we compare the bone density after 100 days of application of the loading cycles with results in Doblaré and García [62] and Fernandez *et al.* [69], and after 300 days of loading cycles with results in Doblaré and García [62] and Jacobs [117]. We should first of all outline the fact that the results of these three models, even though they show similar patterns in the bone density map do not exactly produce the same spatial distribution.

All models show (Fig. 5.56) cortical formation in the medial and lateral part of the diaphysis (thicker at the medial part), decrease of the density in the intramedullary canal, a region of higher density in the proximal part of the femoral neck, and a head bounded by two low density regions. In addition, Doblaré's model (Fig. 5.56(a,c)) shows reduced density in the area referred to as Ward's triangle (while it is only slightly present in Jacob's model, Fig. 5.56(d)). These are the main features, similar to reality in morphological terms (see most of them on the X-Ray of a proximal femur Fig. 5.56(e)), we want our model to be able to reproduce, within the same range of density values.
First of all, we can observe in the results from our model (Fig. 5.57) that, even though we distributed the loads on three nodes, we cannot avoid concentration effects at the points of applications, thus explaining the over formation around these points. This over increase of the density is particularly present after a simulation of 300 days and diffuse all the way to point D.

The initial geometric model by Beaupré *et al.* [17] (used with an anisotropic remodeling model in [62, 69, 117]) contained a layer of cartilage at the epiphysis. This layer was not used in the three models we compare our results with (Jacobs announces some load distribution

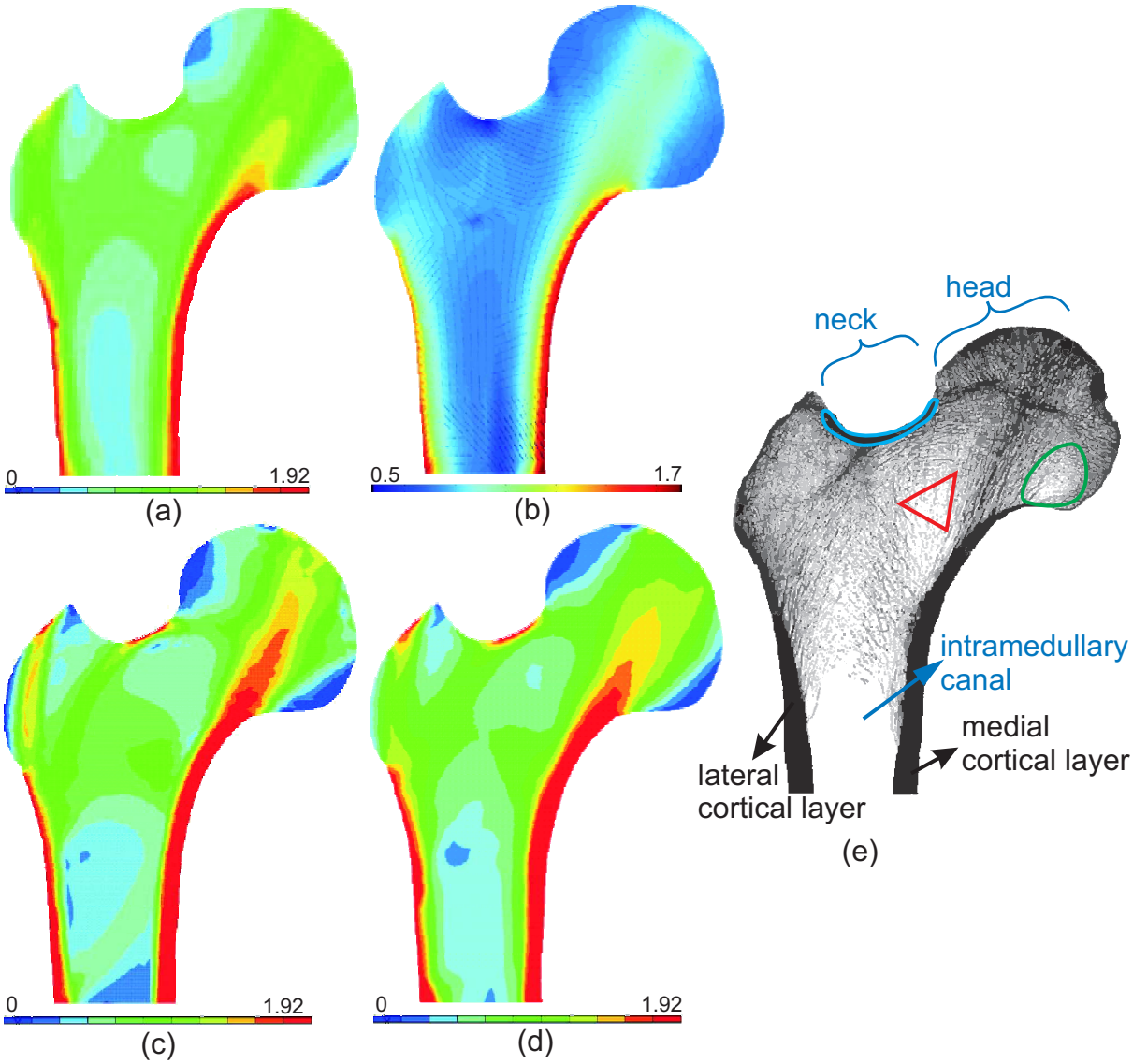

FIGURE 5.56: *Bone density [gr/cc] due to remodeling - **top row**: after 100 days of load cycles (a) results by Doblaré and García [62], (b) results by Fernandez* et al. *[69] -notice the different min/max values reported on the color map; **bottom row**: after 300 days of load cycles (c) results by Doblaré and García [62], (d) results by Jacobs [117] (as reported in [62]). (e) Femur X-Ray: clear cortical formation in the inner and outer part of the diaphysis and decrease of the density (to zero) at the intramedullary canal, a region of higher density in the proximal part of the femoral neck (in blue), Ward's triangle (in red), and a low density region on the distal part of the head (in green).*

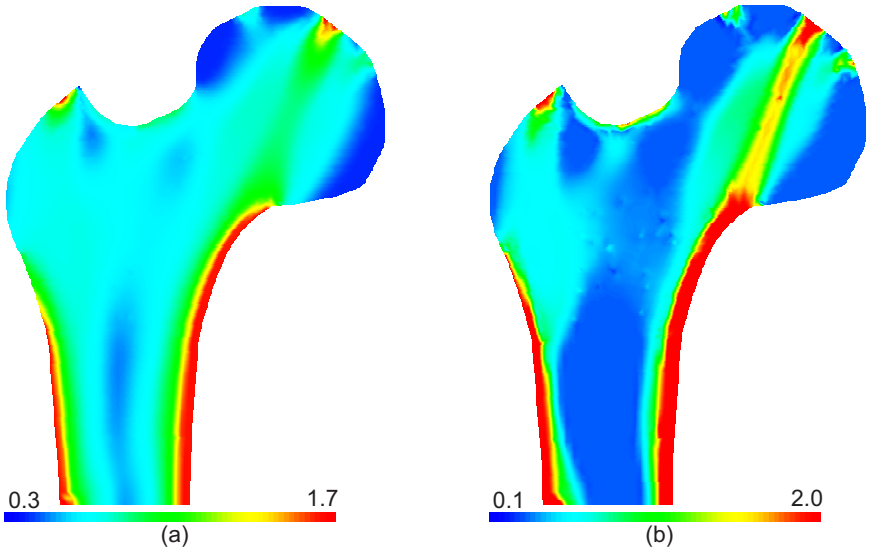

FIGURE 5.57: *Bone density [gr/cc] due to remodeling - (a) after 100 days of load cycles; (b) after 300 days of load cycles*

is used in his model but not the way it is accounted for), however, it would improve drastically the concentration effect as the cartilage (even if modeled as a simple elastic material) has a diffusion effect. Adding such a cartilage layer to the model will be analyzed later.

However, we can see that our model can reproduce the main features of the proximal femur morphology as expressed by the other remodeling models. In particular, Ward's triangle is clearly present, even after a simulation corresponding to only 100 days of remodeling. The cortical layer at the diaphysis is well represented. The other described features are also present, but not quantitatively accurate. This difference is mainly due to the concentration effect discussed previously. As the area of high bone formation is larger between the neck and the proximal part of the head, the stress intensities on the whole neck have a different distribution as the more solicited part gets stiffer and carries thus more loads (remote density changes influence local stimulus magnitude). Therefore, the density decreasing areas have a stimulus further away to the homeostatic level than it would have without this stress concentration. In these regions, the remodeling rate is thus higher.

As said earlier, we can decrease this concentration effect by considering the cartilage layer on the femoral head, at the articulation. For this, we add a 2mm layer of cartilage (meshed with 140 linear quadrilaterals, Fig. 5.58), considered as a simple elastic material, with a Young's modulus of 5.9GPa and a Poisson's ratio of 0.47 (these values are identical to the ones initially proposed by the model of Beaupré *et al.* [17]).
This leads to a density distribution (Fig. 5.59) where the formation sites are less concentrated than compared to the previous model. Therefore the resorption sites are well defined and we can observe already after a simulation of 100 days most features the model is supposed to represent, except for the lateral cortical layer at the diaphysis. In particular, the

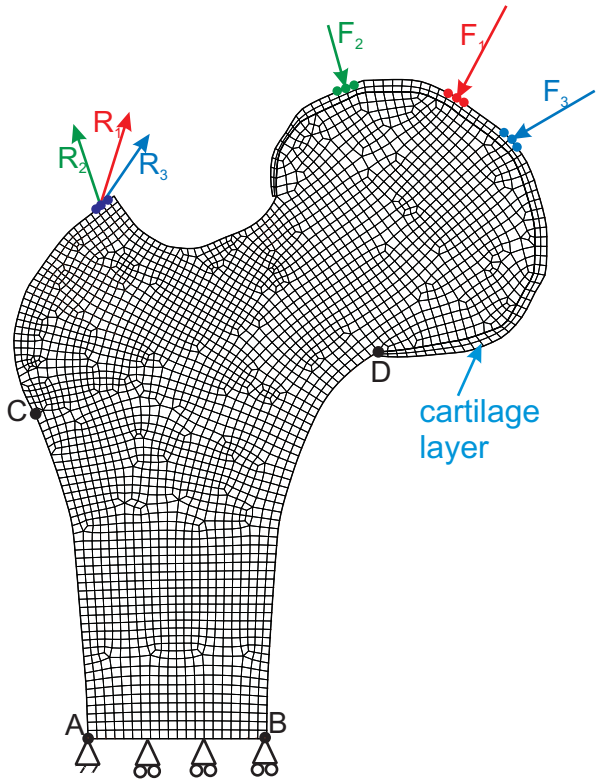

FIGURE 5.58: *Mesh, geometry, and boundary conditions used in the 2D model of the proximal femur with a cartilage layer (red: load and reaction case 1, green: load and reaction case 2, and blue: load and reaction case 3).*

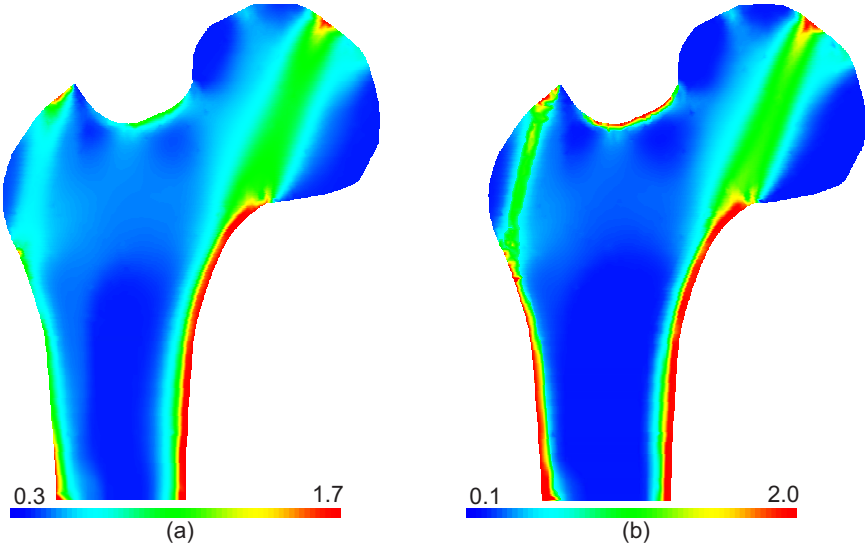

FIGURE 5.59: *Bone density [gr/cc] due to remodeling, model with a cartilage layer - (a) 100 days of load cycles; (b) 300 days of load cycles*

intramedullary canal is well defined, as is the region of higher density at the proximal neck. After a simulation of 300 days, the lateral cortical layer at the diaphysis is also present. The reduction of density goes down to 0.1gr/cc (at the intramedullary canal, the region of Ward's triangle, and the regions of the head). In the three other models we compare our results to, a minimal value of 0gr/cc is presented (the density maps presented show density values down to 0gr/cc) while in all three cases, the range of acceptable density values was decalred to be set from 5% to 95% of the fully mineralized bone, i.e. from 0.105gr/cc to 1.995 gr/cc. Our minimal density value of 0.1gr/cc is due to the fact that a maximal value authorized of mean damage is set at 0.998, mainly for convergence purposes. Indeed, as outlined previously, this leads to a stiffness which is 500 times smaller than the maximal stiffness, thus inducing a large stiffness variation over the model. Setting a maximal value of mean damage higher leads to two numerical issues, first an even larger stiffness gradient, reducing the numerical convergence, second a stiffness so low that the strain could become too large to be handled without using specific mesh management techniques. The fact that a lower density value (i.e. lower than 0.1gr/cc) cannot be easily reached can be considered as a drawback of the remodeling model. However, in the present case, it is not different from what is seen in the literature when a maximal and a minimal values are imposed for the density.

We also compare for this case the variation of the orientation of the trabecular bone. Once more, comparing the results by Jacobs and Doblaré and García shows differences, that can be considered as major differences (Fig. 5.60(a,b)). A first remark should be highlighted before discussing our results. We showed the bone density values were the same between these two models and presented the same features, even though the distribution is not exactly identical. Therefore, the mean stiffness (that can be measured by the average value of the stiffness in the principal axis) at each point should be the same. However Fig. 5.60(a) and (b)

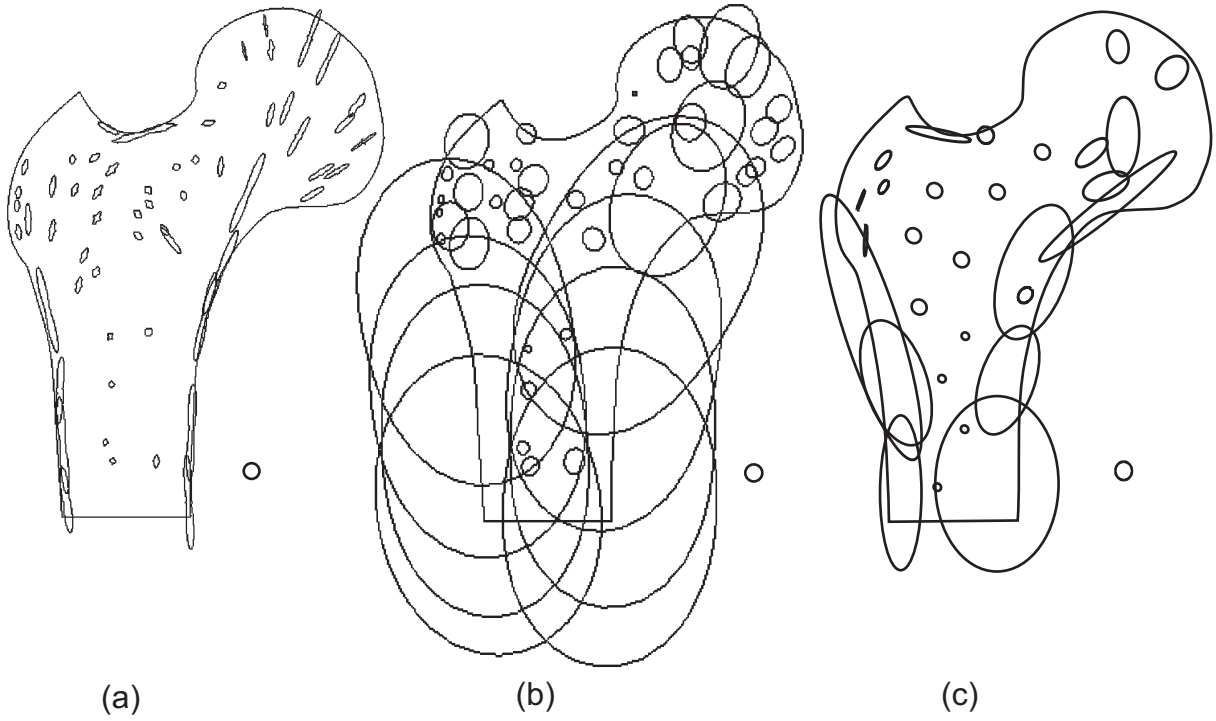

FIGURE 5.60: *Trabecular bone orientation after a simulation of 300 days. The ellipses represent the stiffness value, a 1GPa isotropic stiffness circle indicator is also depicted. (a) results by Jacobs, (b) results by Doblaré and García, and (c) results by the present model.*

clearly do not present the same mean stiffness, while the orientation is pretty much identical. The anisotropy (measured by the degree of anisotropy, visually by the ratio of the long axis to the small axis of the ellipses) is also significantly different, of about eight for Jacobs's model and about two for Doblaré and García's, along the diaphysis.
The difference in the plotted mean stiffness can be explained as follows. Using a plane strain analysis gives a 3D stress and therefore the stiffness matrix is also 3D (and the damage tensor as well for damage based model). However, the plot proposed by Jacobs does not account for this third dimension to compute the plotted stiffness. What is depicted in Fig. 5.60(a) is not exactly the stiffness but the ratio of a uniaxial applied stress to the resulting normal strain in the direction of stress application as a function of direction.
Despite the difference in the anisotropy, both authors claim their model represent properly measured values in the head and neck regions. However, the model by Jacobs gives, as the author recognises, a degree of anisotropy in the diaphysis too high for too low values of the longitudinal stiffness.
As there is no clear evidence of what the anisotropy is in the head and neck regions, we will therefore mainly extract the anisotropy at the cortical parts of the diaphysis. We will however check the trabecular bone orientation at the head and neck is acceptable.
The obtained results (Fig. 5.60(c)) show the same orientations than the two other models do over the whole proximal femur. Particularly, the bone tissue is oriented along the diaphysis

on its cortical sides, towards the proximal head in the stronger part of the head and is pretty much isotropic in the mediaphysis and the intramedullary canal. In the diaphysis, we observe a mean stiffness situated in between the two other two models mean stiffness values. The degree of anisotropy is closer to the results by Doblaré than those by Jacobs.

From these results, we can conclude that our model is verified considering its remodeling behavior. We were able to represent the remodeling of the proximal femur submitted to physiological loading. However, we also saw the remodeling behavior is very sensitive to boundary conditions, specially to concentration effects due to the way these boundary conditions are applied. This is one of the limitations of our model (the firsts have been discussed in section 5.2.3).

5.5.2 3D model

We here analyze the bone structural evolution of a 3D model of the proximal femur.
The 3D mesh is obtained from a discretized surface data available from the VAKHUM [254] dataset (consisting for the whole femur of 4232 triangular cells). The proximal end of the femur is extracted from this surface and a volume mesh is generated by the use of Tetgen [235]. The proximal 3D mesh consisting of 22669 linear tetrahedron and 4661 nodes is shown on Fig. 5.61.

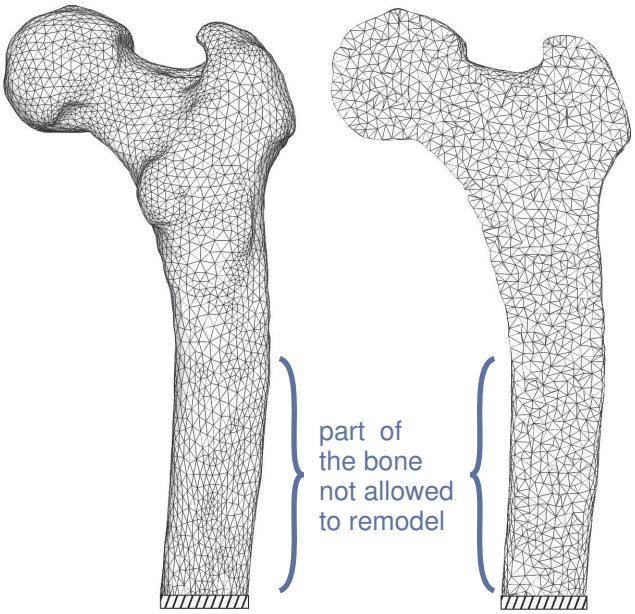

FIGURE 5.61: *Left - 3D mesh of the proximal femur. Right - frontal cut through the mesh.*

We here compare the density maps obtained accounting either for the same loading cases as the previous 2D model (joint reaction forces + abductor forces), or for the same forces but taking into account their 3D orientation, or as a third case adding the forces of Iliopsoas and Vastus lateralis muscles (see Fig.5.62).
Only half the length of the diaphysis and the proximal end are modeled. The distal part is considered fully clamped. The diaphysis is considered as composed of cortical bone of porosity 0.30 (thus Young's modulus of 6GPa), not allowed to remodel. If we do not consider this cortical bone part and since stress concentrations are observed at the clamped base, we would get unphysiological remodeling at the model base due to this concentration. For the proximal part, the initial situation and the set of remodeling parameters are the same as in the 2D case presented previously. The loads however are applied simultaneously instead of one after each other as in Fig 5.54 (only one application site is considered for the joint reaction forces), their intensities are weighted by their duration of application in the 2D case (these modified conditions in 2D deilver results close to the previous application of loads, however reducing the dense region of the head). The loads orientation are as proposed in [237] in an experimental setup. The load intensities are adjusted so that the JRF

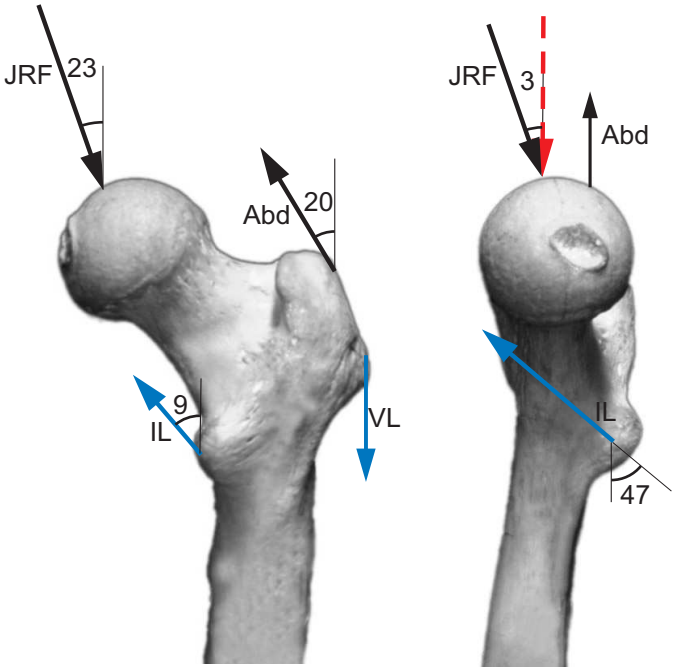

FIGURE 5.62: *Load case as presented in [237]. Joint reaction forces (JRF-in red, the equivalent 2D loads; in black, their 3D orientation), Abductors (Abd); and in blue the added muscles: Iliopsoas (IL) and Vastus lateralis (VL).*

and abductor resultants are similar to those of the 2D case. Thus, the resultant of the joint reactions forces is considered to be 1832 N, the abductor forces 590 N, the iliopsoas's 914 N, and the vastus lateralis's 1419 N.

First of all, looking at the deformed proximal femur (see Fig. 5.63(b)), we can see that accounting for the three-dimensionality of the joint reaction forces and the abductors without taking into account other muscles such as the iliopsoas and the vastus lateralis gives a solution that cannot be considered as physiological. This is mainly due to the added frontal component of the JRF, which is compensated by that of the iliopsoas but not by the abductor. We will therefore compare the results only between the 2D loading case (not accounting for the frontal component of the JRF, see Fig. 5.63(a)) and the 3D case with three muscles (abductor, iliopsoas, and vastus lateralis, see Fig. 5.63(c)).

Analyzing the density distribution after a simulation of 100 remodeling days (see Fig. 5.64) shows that the cortical formation at the diaphysis is not distributed axisymmetrically for the 2D loading case (Fig. 5.64(a) and (c)), therefore concentrating the bone formation on the lateral and medial sides of the diaphysis. Applying 3D muscles (Fig. 5.64(b) and (d)) leads to a overall lower bone formation but with some formation in the neck region while there is almost no formation in that region for the 2D loading case. The cortical layer in the diaphysis has density values lower in the 3 muscles, 3D, case than in the 2 muscles, 2D, one, with the higher values more posterior in the 3D case. There is also more resorption in the 3D case than in the 2D one, with a larger volume reaching the minimal density.

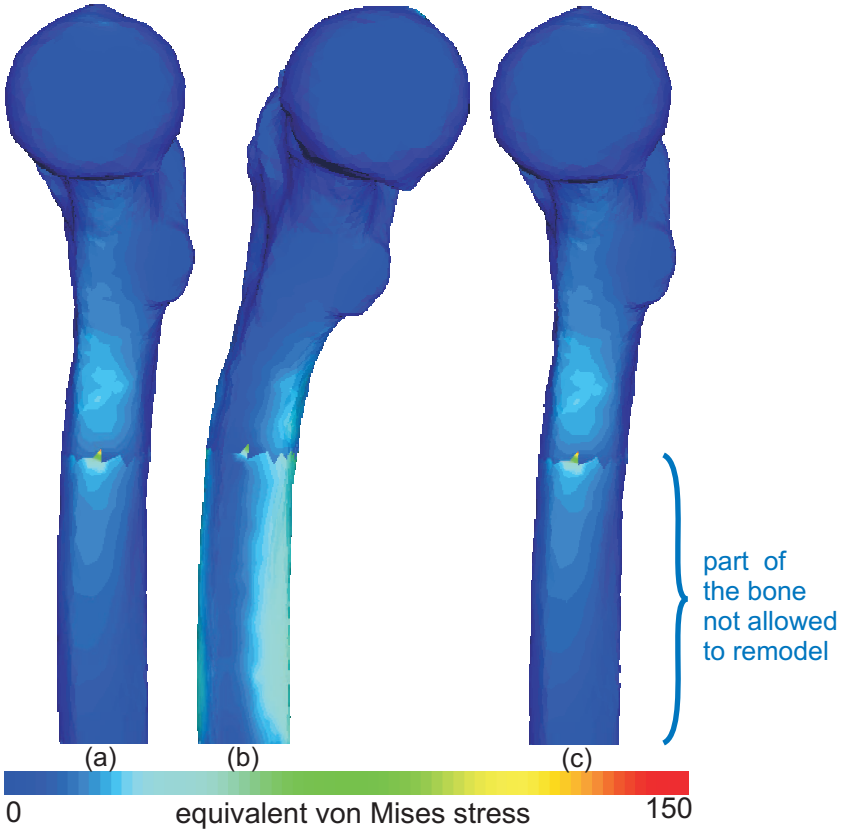

FIGURE 5.63: *Proximal Femur Deformation (equivalent von Mises stress [MPa]): (a) 2D case loading, (b) 3D loading, JRF and abductor only, and (c) adding the illiopsoas and vastus lateralis. The same sagittal view is depicted for the three load cases.*

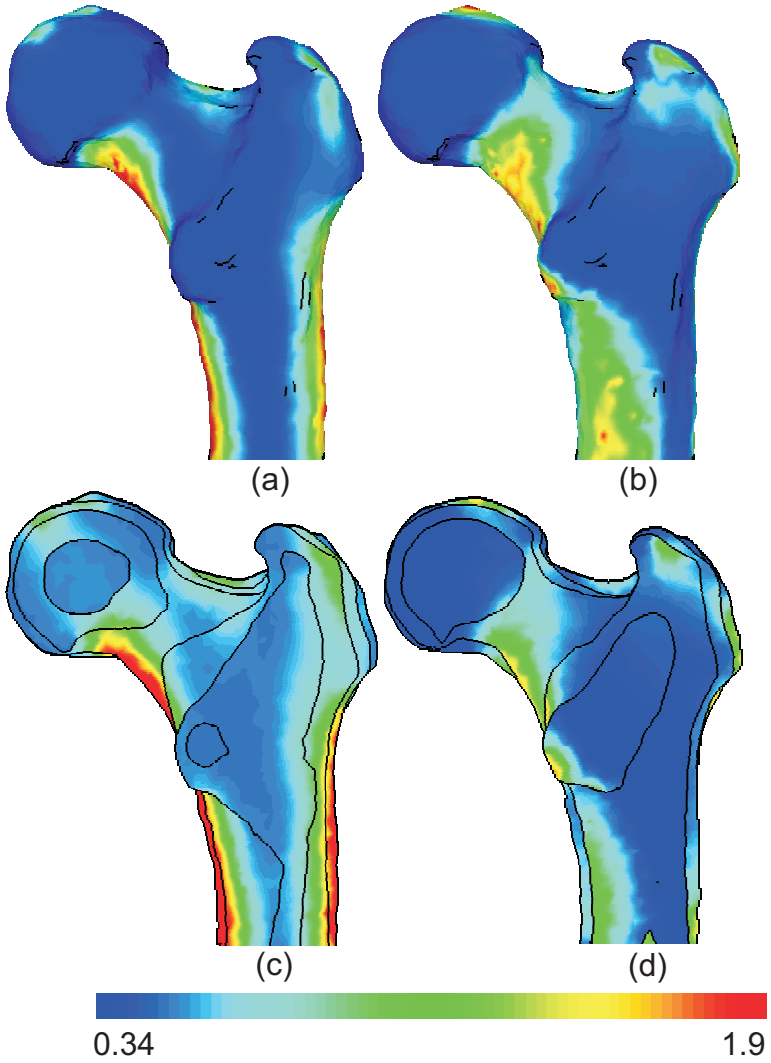

FIGURE 5.64: *Proximal Femur, Bone Remodeling - distribution of the density [gr/cc]: (a) outline for the 2D loading case, (b) outline for the 3D loading case-3 muscles, (c) frontal slices through the volume for the 2D loading case, and (d) frontal slices through the volume for the 3D loading case-3 muscles.*

Even tough we cannot formally verify our model on 3D simulations of the proximal femur because the 3D remodeling cases found in the literature are not as detailed as the previous 2D cases concerning the geometry and applied boundary conditions, we can still conclude our model is able to represent in a physiological way 3D cases. Here we showed once more that the application of the remodeling model is very sensitive to the applied boundary conditions. Especially, the pattern of remodeling is here completely different whether 2D our 3D loading cases are considered.

5.6 Conclusions

This chapter is really the core of this work.

We started by detailing Doblaré and Garcia's remodeling phenomenological model we based our work on. This remodeling law was chosen as the base of our model as it elegantly proposes a framework to combine the anisotropy of the bone morphology through macroscopic measures such as the fabric tensor and the apparent density while allowing an adaptation of both these morphological measures. However, we showed it presented some weaknesses, as not only it considers a simple linear elastic behavior of the bone matrix, but it also has a few disadvantages compared to the Stanford model it is built from. It also present a major inconsistency in its dimensional analysis.
We then proposed to enhance this model not only to use our new model with an elastoplastic bone matrix but also to lift the drawbacks and inconsistencies of Doblaré and Garcia's model. As Doblaré and Garcia's model is built on a Continuum Damage framework, we developed a numerical integration method for an anisotropic Continuum Damage model coupled to plasticity (considering a von Mises plasticity for the bone matrix) in finite strains. This integration method has been verified first considering a constant damage tensor, i.e. if there is no remodeling and the bone morphology is thus kept constant. Our model and its integration scheme is in this case completely equivalent to an orthotropic elastoplastic model with a Hill-type plasticity.
Finally, an adaptation of the remodeling law was proposed to consider the specific case of the alveolar bone for which the periodontal ligament is believed to play a major role, which exhibits a pressure-dependent behavior.
We then performed an analysis on the sensitivity of our model with respect to its numerous parameters (parameters describing the bone matrix behavior through the apparent density value, its morphology, and remodeling parameters) on a simple cylindrical configuration and simple mechanical tests. It showed the remodeling model is mainly influenced by the value taken for the homeostatic measure of the remodeling stimulus as well as the width of the lazy-zone. In the eventuality of a future calibration study, these two parameters have to be treated with caution. On a purely mechanical point-of-view, we showed the appreciation of the proper apparent density is of major importance. So are the orthotropy axis orientations.
This chapter was finally closed proposing a validation methodology for the mechanical representation of the bone matrix through the knowledge of its morphology and a verification procedure for the biological representation of the remodeling phenomenon. We validated our model both on engineered cellular solids with bone-like morphology (aluminum and polymeric foams) and on bone (Deer antler) samples. This validation was performed on experimental compression tests and we produced *in-silico* tension tests to carry on further validation. These *in-silico* tension tests were produced considering validated μ-FE models on the same samples used in the experimental compressive tests. We verified the remodel-

ing model comparing the results we have for the benchmark case for remodeling algorithms that is the proximal femur remodeling with results in the literature for the same problem. We showed our model can represent normal density and morphology of the proximal femur submitted to physiological loads, starting from a virtual situation of homogeneous isotropic bone.

Chapter 6
Simulation of Orthodontic Tooth Movement

We here present the application of the remodeling model developed in the previous chapter on orthodontic tooth movement (OTM) problems. For this, we first have to choose a mechanical representation for the periodontal ligament. The first section of this chapter is therefore dedicated to the presentation of a contact model for the PDL representation. For 2D models, we will examine the improvements mesh management methods, such as ALE and/or remeshing techniques, can bring to the model. We then present in the second section of this chapter different simulations of OTM, both in 2D (tipping and bodily tooth movement) and in 3D (rotation and intrusion) models.
In this chapter, all finite element simulations are performed using Metafor [177]. A quasi-static analysis is carried on for all cases. 2D models are plane strain models.

Chapter Overview

6.1 Problematic Representation of the Periodontal Ligament

As presented in chapter 4, the periodontal ligament plays an important role in the mechanics of tooth movement. However, a broad choice of mechanical models are found in the literature. Therefore, a decision has to be made with respect to its modeling. In order to focus on the non-linear description of the bone and not of the ligament, we assume an elastic behavior for the PDL. However, we decided to use a multi-linear model as we will see the periodontal ligament is subjected to large deformations and therefore describing the highly non-linear behavior with a simple two parameters (Young's modulus and Poisson's ratio) elastic model seems to be a strong assumption we can easily by-pass.

6.1.1 A Piecewise Linear Model for the Periodontal Ligament

As the bi-(multi-)linear models found in the literature [24, 27, 34, 65, 127, 211, 218, 268, 285], while giving appropriate results in tooth movement modeling, do not fit well with experimental mechanical tests performed on the PDL (see Fig. 6.1), we decided to propose another model, consistent with the experimental data available [8, 65, 134, 184, 185, 204, 205, 250]. We therefore first carried out a review of the experimental data found in the literature. We extracted from this data either the given stress/strain curves, when the measure of stress and the measure of strain used were known[1], or the load/displacement curves when all geometrical data was available to transform it into stress/strain data[2] (Table 6.1). We then transformed[3] the usable data into Piola stress/Biot strain curves (or, as the experimental data are all uniaxial tests, engineering stress/engineering strain curves) and fitted a piecewise-linear curve on the average (see results in Fig. 6.1 and Appendix F).
Doing so, we obtain a piecewise linear model of the periodontal ligament behavior in uni-

TABLE 6.1: *Periodontal Ligament - available experimental data used to derive the PDL stress/strain relationship [in alphabetical order].*

Data	Stress	Strain
Aversa *et al.* [8]	Piola	Biot
Dorow *et al.* [65]	Piola	Biot
Komatsu *et al.* [134]	Load	Displacement
Natali *et al.* [184, 185]	Piola	Stretch
Pini *et al.* [204, 205]	Piola-Kirchhoff II	Green-Lagrange
Toms and Eberhardt [250]	Piola	Biot

[1] Indeed, the experimental testing of the PDL leads to large strains, one therefore needs to explicit the measure of strain and stress used (see the definitions of these measures in chapter 3).

[2] From the 27 initial studies from which experimental data was available, only 8 correspond to one of these conditions.

[3] The transformation used assumes uniaxial tests and an incompressible behavior.

axial tests. Assuming a nearly incompressible material and that the $3D$ mechanical behavior of this fibrous tissue can be represented with a simple two parameters (variable tangent modulus and constant Poisson's ratio) therefore gives a model for the periodontal ligament, following Hooke's law with a variable stiffness tensor. Even though this representation is not straightforward to implement in a large strain environment (transforming $1D$ engineering stress/engineering strain curves into a $3D$ behavior using an hypoelastic formulation), we will see in the next section that the knowledge of the $1D$ behavior is sufficient to build the models we propose for the representation of the periodontal ligament.
We therefore obtained a non-linear representation of the mechanical behavior of the periodontal ligament. This mechanical behavior will be used in a contact representation of the periodontal ligament as detailed in the next section. Doing so, we only represent the buffer role of the PDL, we do not have access to the actual stress distribution within the PDL. Hence, in the remodeling law for the alveolar bone in which the fibroblast pressure sensitivity is accounted for (see section 5.2.3), the critical values of the hydrostatic pressure within the periodontal ligament are converted to critical values for the hydrostatic pressure within the alveolar bone using as a scaling factor the bulk modulus ratio of the two tissues.

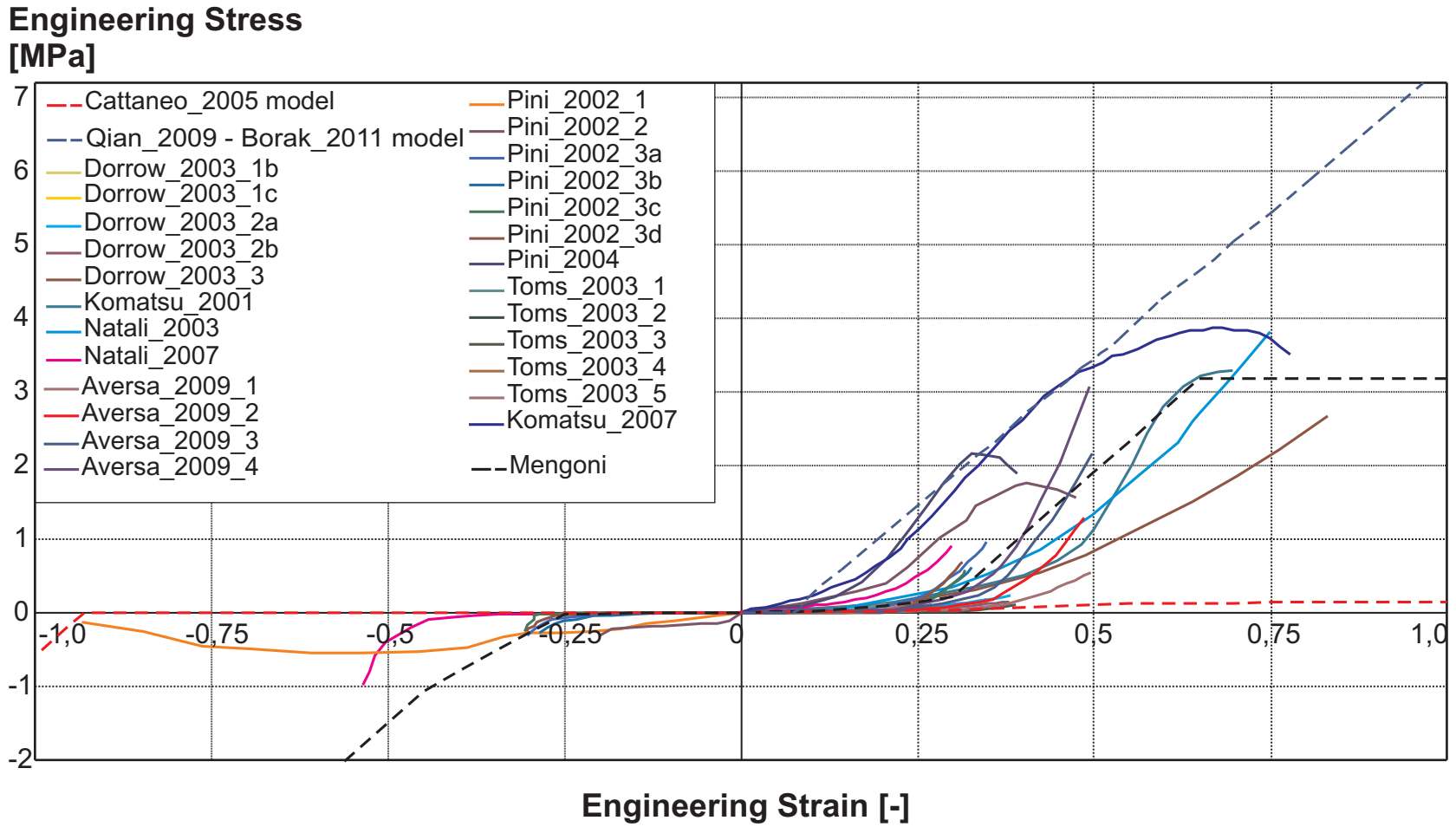

FIGURE 6.1: *Periodontal Ligament - experimental data [8, 65, 134, 184, 185, 204, 205, 250] : Engineering Strain vs. Engineering Stress for uniaxial tests. The data is labeled after the name of first author of the paper it comes from, followed by the year of publication and the number of the figure in the paper (a letter is added if several curves appear on the same figure). As a comparison, in blue and red dashed line, two multi-linear models [24, 34, 218] that surround this experimental data. In black dashed line, the model used in this work.*

6.1.2 Contact Representation of the Periodontal Ligament

As discussed in chapter 4, for the past few years, 3D finite element models based on CT scans are increasingly used in the field of orthodontics [71, 207, 282, among many others]. This shows great improvement from the previous decades where most models were derived from 2D then 3D standard geometries. The production of FE meshes from CT data for orthodontic tooth movement modeling requires a description of several important tissues to be segmented. From this segmentation, a surface reconstruction and triangulation followed by a volumetric meshing technique produce the required FE model. However, clinical CT resolution allows only for differentiation of bone (both cortical and alveolar) and teeth (distinction of dentin and enamel). Specially, the surface geometry of the periodontal ligament cannot be directly derived from CT images. One of the solutions is to derive a model from $\mu-$CT data. However, $\mu-$CT technology is not available on a clinical basis, a clinical tool therefore has to be developed. In most recent studies [93, 208, 282], the PDL is generated using scaling and/or Boolean operations on the teeth and bone interface in order to obtain a thin enclosure. This approximation is performed despite the fact that most authors agree on the importance of geometrical and material properties of the PDL in the achievement of orthodontic tooth movement. The aim of this section is therefore to propose alternative methods to account for the mechanical role of the PDL without geometrically representing its thickness. Particularly, we will focus on two mechanical representation of the periodontal ligament, either a (non-)linear spring model or a (non-)linear contact model.

Springs are $1D$ elements linking two nodes by a stiffness. The force exerted by a spring is related to the spring elongation, $\Delta\ell$, through a stiffness parameter, k, following Hooke's law: $F_{\text{spring}} = -k\Delta\ell$. Considering a small strain approach, the stiffness parameter can be related to Young's modulus of a material as $k = EA/L$ where A is the cross-section area of the spring and L is the spring natural length.
Considering the PDL is mainly resisting in compression or tension perpendicularly to its interfaces with the tooth and bone (a plausible assumption as the PDL is composed of fibers oriented mainly it this direction), therefore allows to model the PDL mechanical behavior as spring elements. A linear PDL model assumes a constant stiffness k, while a non-linear model, such as proposed in the previous section, assumes a stiffness varying with the elongation. These spring elements need to be added in the model at the bone/tooth interface.

In the finite element method, contact problems can be modeled with several approaches (a very brief introduction to the treatment of contact problems in Finite Elements is proposed in Appendix G). In particular, the penalty method allows for two bodies to penetrate each other provided that a force, proportional to the gap between the bodies (the proportionality coefficient is called the penalty), is applied on the surfaces.
The PDL can therefore also be modeled as a contact interface between the tooth and the bone. For this, we consider a penalty coefficient proportional to the tangent modulus. A

linear PDL model assumes a constant penalty (thus proportional to Young's modulus), while a non-linear model, such as proposed in the previous section, assumes a penalty varying with the gap.
In a $1D$ problem, this contact approach is completely equivalent to a spring element.

It should be noticed that representing the PDL with the simple models proposed here does not give any insight on the stress distribution within the PDL. It can therefore not be used with a remodeling law based on values of the stress in this structure. More over, the fluid flow within the PDL is believed to play an important role in the remodeling of the surrounding bone, it is here only accounted for in an hydrostatic pressure dependent model. Especially, a mechanobiological approach of bone remodeling could not be used with such simple models for the PDL as there is no way the biological activity and its coupling with the mechanical environment could be accounted for in a contact or spring model as they represent only the phenomenological mechanics. However, it should be possible to develop more complex interface models of the PDL that could be used in such cases.

The use of either a spring model or a contact one to represent the PDL mechanical behavior assumes that this mechanical behavior is a simple one. We will therefore assess the validity of these representations comparing the results with an other simple mechanical assumption for the PDL, i.e. an elastic behavior represented by a single Young's modulus and considering a quasi-incompressible material. As this PDL representation has to be used with the phenomenological remodeling model proposed in this work, we will compare for the different representation of the PDL the relevant mechanical features used in this model, i.e. von Mises equivalent stress, hydrostatic stress, and the strain-energy density like parameter used in the remodeling law: $U_{\text{iso}} \propto \frac{1}{2G}\boldsymbol{s}:\boldsymbol{s}+\frac{1}{K}p^2$.

Methods for a $2D$ analysis

A mandible geometry was obtained from the INRIA/GAMMA repository[1], consisting of a surface reconstruction of the mandibular bone (no differentiation between cortical and trabecular bone is available) and its 14 teeth (crown and root). These surfaces are typically the output of a CT data segmentation and triangulation. The 2D outline in the mesiodistal plane of the left central incisor was extracted (Figure 6.2).
However, the PDL is not present in the geometry. Indeed, it cannot be extracted from CT data. From this geometry, four FE models were thus created:

1. A first model for an actual PDL generation (referred to as the linear reference model).

   This required to duplicate the geometrical points at the interface and move them normally to the surface to create an enclosure of $0.2mm$ thickness for the PDL. The three

[1] INRIA/GAMMA repository http://www-roc.inria.fr/gamma/gamma.php

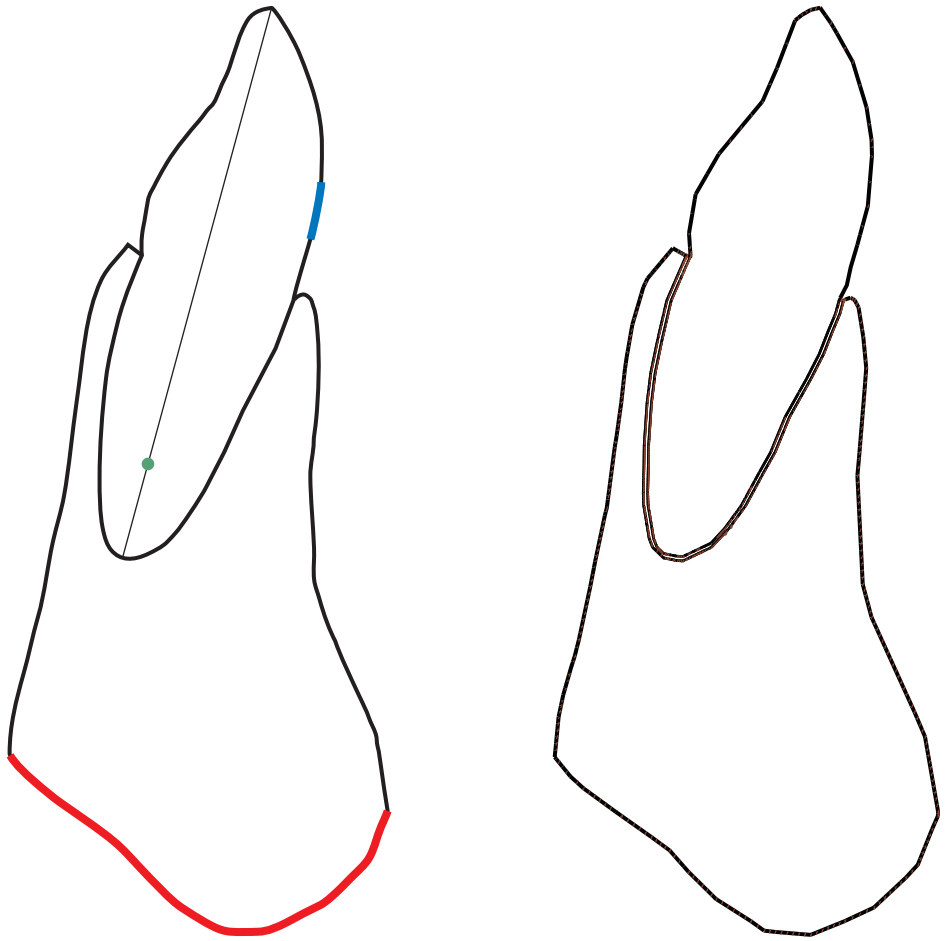

(a) Geometry with no periodontal ligament

(b) Geometry for the inclusion of a $0.2mm$ periodontal ligament

FIGURE 6.2: *2D geometries in the mesiodistal plane of the left central incisor extracted from the INRIA/GAMMA 3D model. When we refer to the basal bone which is considered fixed, we refer to the red curve; the blue curve is the position of the applied pressure (for problem with applied pressure); the green dot is the position around which the tooth is rotated (for controlled rotation problems); the main axis of the tooth is also represented (axis perpendicularly to which the tooth is translated for translation controlled problems)*

surfaces (PDL, tooth, and alveolar bone) were then meshed with linear quadrilateral elements. The resulting unstructured mesh (see Fig. 6.3) is composed of 1000 elements for the PDL, 1820 for the alveolar bone, and 2294 for the tooth (the number of elements representing the tooth is mainly controlled by the number of elements in the PDL).

2. A second model for a spring representation of the PDL.

   This required to first discretize the interface line, then duplicate the nodes and meshed lines and create spring elements between the nodes at the same position. The two other surfaces (tooth and alveolar bone) where then meshed with linear quadrilateral elements. The mesh is thus composed of 200 spring elements, 1820 quadrilateral elements for the alveolar bone, and 2294 for the tooth (the mesh of the tooth and alveolar bone are identical to the previous case so that the comparison of the models is not a comparison of the meshes.)

3. A third model for a contact representation.

   This required only to duplicate the geometric points at the interface and mesh with linear quadrilateral elements the two surfaces (identical mesh than previously).

4. A fourth and final model with no PDL.

   This did not require any pre-processing operations as the tooth and bone were supposed to be bound. The two surfaces were also meshed with linear quadrilateral elements (identical mesh than the previous ones).

Material behavior of the PDL was assumed first to be linear (see Table 6.2, the value for the periodontal ligament is the value of Young's modulus obtained in the previous section on the non-linear mechanical behavior of the PDL), bone Young's modulus depending on the bone apparent density. For the spring model, the spring stiffness takes into account the PDL Young's modulus and the distance between consecutive springs (cross section area of each spring). Some non-linearity was to be accounted for as the springs'initial length is zero while the PDL thickness is $0.2mm$. For the contact model, bilateral contact conditions were used. The normal penalty accounts for the PDL Young's modulus, the tangential penalty is adjusted, proportionally to the normal penalty, using a proportionality coefficient (representative of the friction) of 0.6. This coefficient has been adjusted so that the displacement of the tip of the tooth for the tipping problem is equivalent using the contact model and the solid periodontal ligament model.
We also compare material models between the nonlinear spring representation and the nonlinear contact representation of the PDL, accounting for its stiffness dependence on the strain as presented at the beginning of the section (material parameters used for the tooth and the alveolar bone are as in the linear analysis, see Table 6.2).

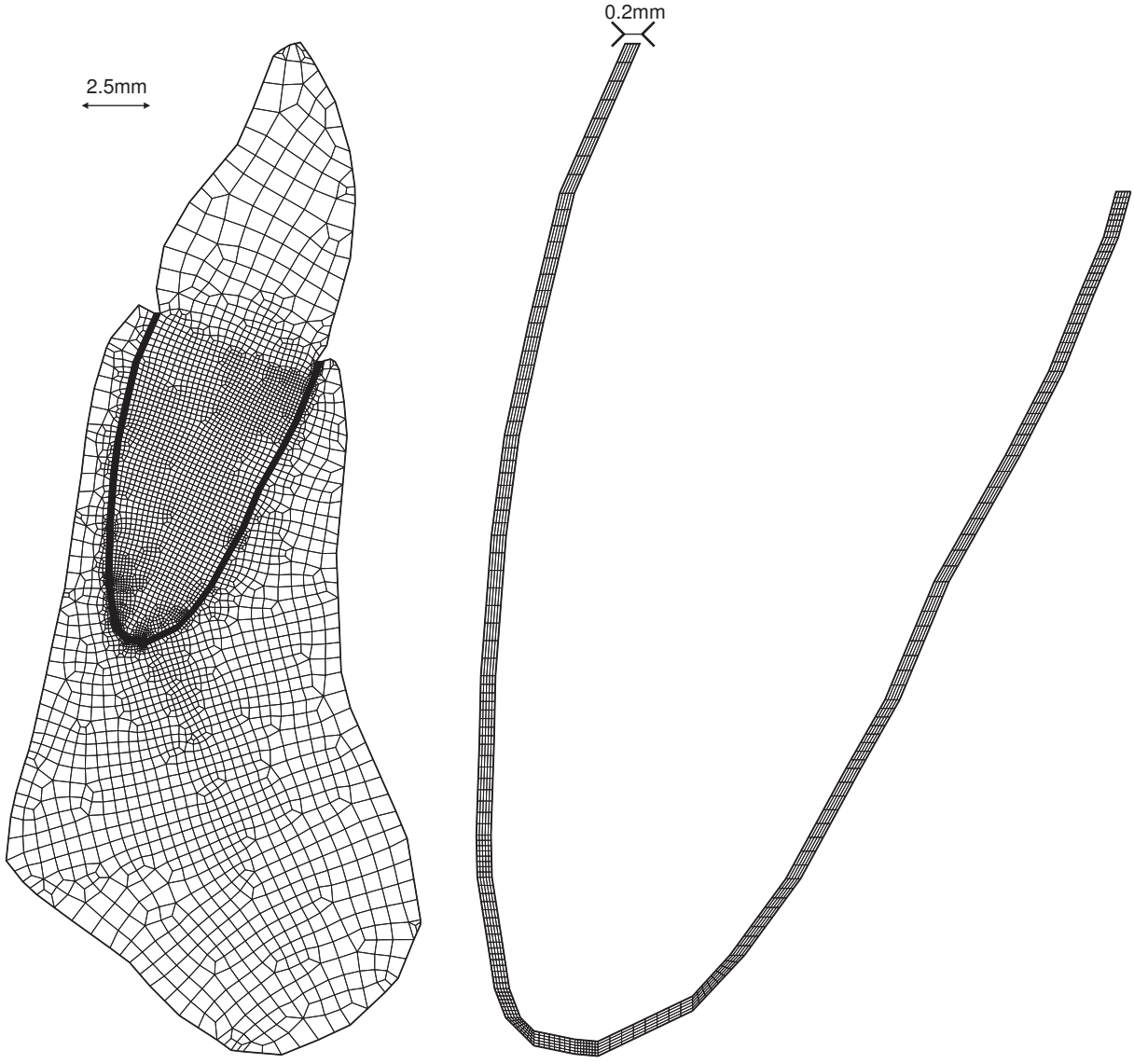

FIGURE 6.3: *left: 2D mesh of the tooth, surrounding alveolar bone with the inclusion of a periodontal ligament; right: zoom on the periodontal ligament mesh.*

TABLE 6.2: *Material parameters for the evaluation of the periodontal ligament mechanical representation, linear analysis*

	Young's Modulus [MPa]	Poisson's ratio [-]
Alveolar Bone	1770.0[a]	0.3
Tooth	20230.0	0.3
PDL	0.068	0.49

[a] i.e. a bone reduced density of 50%

Three types of boundary conditions are considered. First a pressure driven problem, then a rotation driven problem and, finally a translational one, all with a basal line of the bone considered totally fixed. The pressure driven problem consists in applying a pressure representative of a total $0.3N$ force on the labial side of the tooth crown (see Fig. 6.2, blue curve). The rotation consists in rotating the tooth of a 2^o angle around a point situated at one third of the tooth root height (see Fig. 6.2, green dot). The translation consists in translating the tooth perpendicularly to its main axis (see Fig. 6.2) on a distance of one quarter the periodontal ligament width ($0.05mm$).
One simulation of a rotation driven problem is also presented on a multi rooted tooth. For this we extracted the outline of the first left molar along the alveolar arch and produced 4 meshes as previously for the incisor. A rotation of a 2^o angle around a point situated above the joining of the roots is considered.
As this study is a comparative study for the PDL mechanical behavior models, only the tooth initial movement is accounted for, no remodeling algorithm is present.

Methods for a $3D$ analysis

Using the same geometrical data as for the 2D analysis, a multiple-material surface mesh of the left central incisor (tooth and surrounding bone, no PDL is available in the geometrical data) was constructed in a two steps procedure [66]: first a surface reconstruction method is used to extract a smooth representation of the boundaries from the discrete data (and avoid tedious smoothing of the mesh in post-processing steps) ; then, the mesh is produced using an enhanced Marching Tetrahedra procedure. This surface meshing algorithm generated two conform discrete surfaces at the bone/teeth interface. From these surface meshes, four FE models were derived to represent the PDL, as previously done for the $2D$ case.

1. The first one (reference model) includes an enclosure (whose width is 0.2mm) between the teeth and bone interface (moving the two surfaces away from each other), allowing the inclusion of prismatic elements for a linear elastic PDL of user-controlled width (here, we use two elements on the PDL width, see Fig 6.4, i.e. a total of 4204 elements).

2. A second one includes linear springs between corresponding nodes of the interface (i.e. 1076 spring elements).

3. A third one represents the PDL mechanical behavior by bilateral contact conditions between the two surface meshes. For this model, the use of conform discrete surface meshes for the teeth and bone is not required.

4. A fourth and final model with no representation of the PDL at all, thus considering the nodes of the two discrete surfaces of the bone/tooth interface as being connected.

From the obtained multiple-material surface mesh, composed of a set of closed triangulations, a linear 4-node tetrahedral volume mesh was easily obtained using TetGen [235] (Fig. 6.5). This tetrahedral mesh is composed of 11624 elements for the tooth and 52075 for the alveolar bone.
As boundary conditions for the FE analysis, a rigid translation ($0.05mm$) of the tooth was applied perpendicularly to its main axis in a labio-lingual direction and the basal line of the mandibular bone was considered fixed.
Once again, as this study is a comparative study for the PDL mechanical behavior, only the tooth initial movement is accounted for, no remodeling algorithm is present.

Results and discussion for a $2D$ analysis

The results for the $2D$ tipping movement simulations (pressure driven problem) of the tooth initial mobility produced by the $0.3N$ force are presented in Figures 6.6 and 6.7. The stress distribution in the bone along the root for all linear models shows (Figure 6.6(a) - plain line is the reference model) that the mechanical role of the PDL is of major importance as in the fourth model (no PDL - dotted line) both the stress intensity (hydrostatic and von Mises stress) and its distribution are poorly represented. Models with linear springs or bilateral linear contact can both fit the hydrostatic stress distribution. Both these models ensure the transfer of the pressure through the ligament with the same intensity as for the reference model. However, the spring model (dash-dotted line) shows shear intensity half the reference one on the labial side. On the lingual side, the shear intensity of the spring model is up to 19% higher than the reference one and its maximum position is 50% less apical than the reference maximal position. The contact model (dashed line) shows a shear intensity 17% lower in compression and 16% higher in tension with the same position for the maximal value of shear.
For the two non-linear simulations (i.e. the non-linear spring model and the non-linear contact model), one can see (Figure 6.6(b)) the shear intensity as well as the hydrostatic pressure are lower (in absolute values for the pressure) for the non-linear contact model than for the non-linear spring model. The non-linear contact model also shows hydrostatic pressure and shear intensities twice lower than the linear model produces. Note also that the change in the pressure state (from tension to compression) on the lingual side is exactly at the same

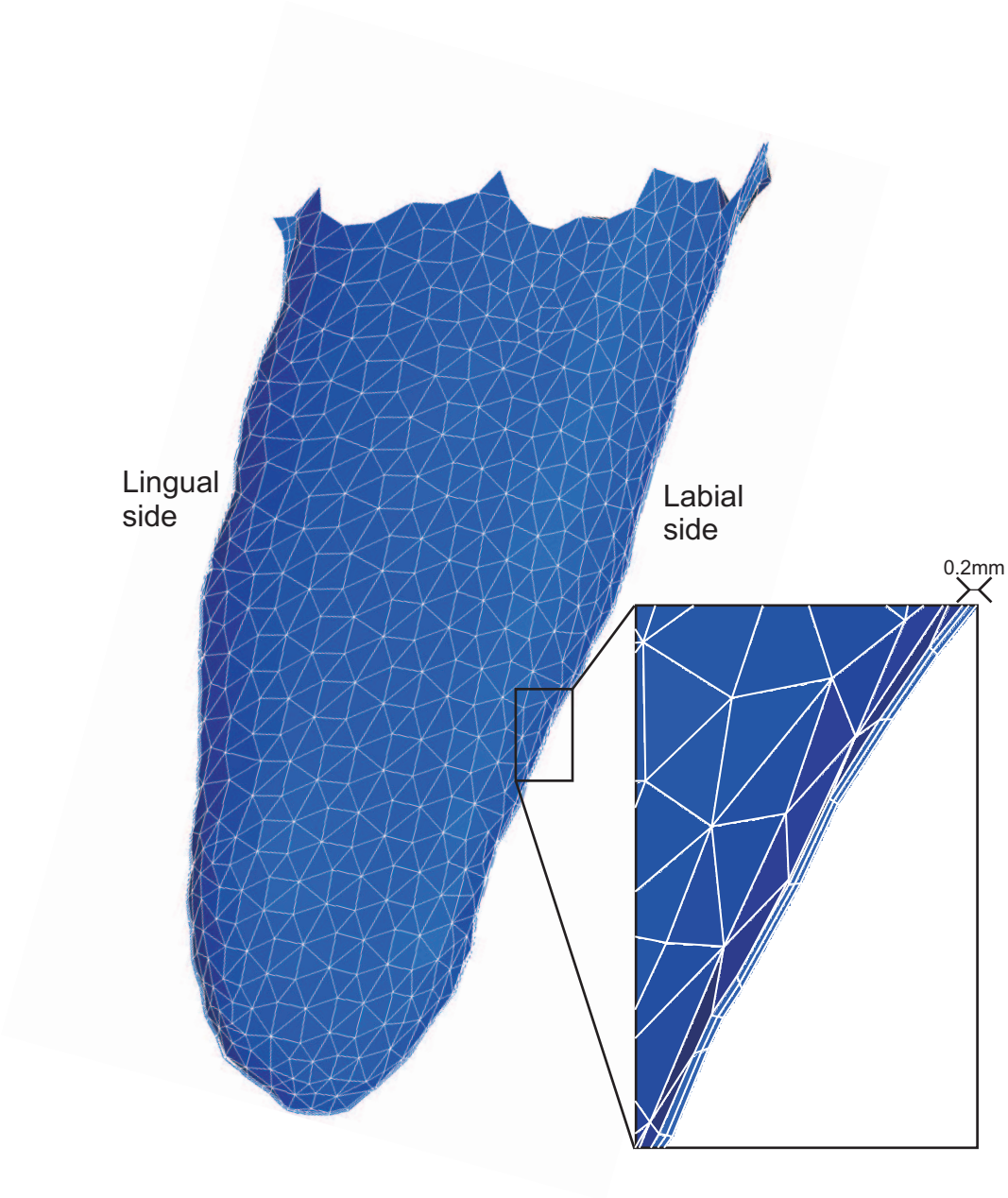

FIGURE 6.4: *Periodontal ligament mesh (mesiodistal view): prismatic elements are built between the tooth external surface and the bone internal one.*

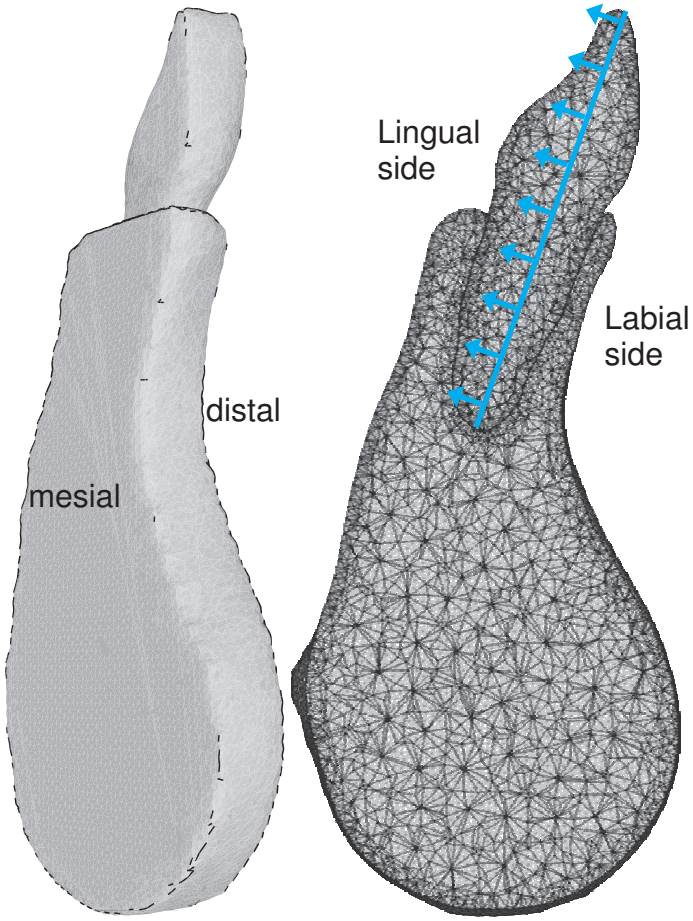

FIGURE 6.5: *Geometry and mesh of the tooth and its surrounding alveolar bone. The blue arrows represent the direction of the applied translation movement.*

position for both linear and non-linear models. On the labial side however, using a non-linear model moves this point of pressure change more coronally. The non-linearity of the PDL material therefore has a significant impact on the results, even for the application of a low pressure level at the crown.
The obtained displacement can be observed in Figure 6.7 (linguo-labial displacement) for the bilateral linear contact model. It shows a maximal displacement of the root in the labial side of 36 μm at the apex. This displacement is due only to the PDL compression. The close up at the apex shows a penetration of the tooth surface into the bone representative of the PDL deformation in compression. At the collar, the tooth unties from the bone while the PDL is widening.
The same discussion can be made for the rotation and translation driven problems (Fig. 6.8) as well as for the mutli-rooted tooth (Fig. 6.9 and 6.10). We present the results considering only a linear behavior of the PDL.

We see that the accuracy of the representation of the periodontal ligament by bilateral contact conditions remains valid for all considered types of movement for the incisor. For both the rotation (Fig. 6.8a) and the translation (Fig. 6.8b) problems, the results obtained with contact conditions are closer to the use a geometrical representation of the PDL on the lingual side than on the labial one with comparison to the spring representation of the PDL.
For the model of the rotation of the molar, there is no obvious evidence (Fig. 6.9) on whether the contact or the spring representation of the periodontal ligament better reflects the results obtained with an actual geometrical representation. The sagittal displacement is depicted in Fig. 6.10 and shows displacement up to 0.13mm at the apexes, i.e. 65% of the periodontal ligament width.

Results and discussion for a $3D$ analysis

We here present maps of both the equivalent von Mises stress and the hydrostatic pressure on a slice cut in the mesiodistal plane of the incisor (Figs. 6.11 to 6.14).
The first look at the von Mises equivalent stress maps shows no obvious differences between the contact and spring models (Fig. 6.11). The stress distribution is exactly the same between both models with a difference in the stress intensity up to only 1%. The same assessment can be made comparing these two models with the results obtained including a solid periodontal ligament (Fig. 6.12(a)), however, both the von Mises stress distribution and its intensity are different if we do not use any representation of the periodontal ligament (Fig. 6.12(b)). In particular, stress concentrations are observed on the lingual side of the tooth apex and of the external surface of the alveolar bone. The von Mises stress intensity is twice as low as for the three previous cases. The same discussion can be made for the hydrostatic stress, except that the intensity for the “no ligament” model is almost five times higher than for the three other models.

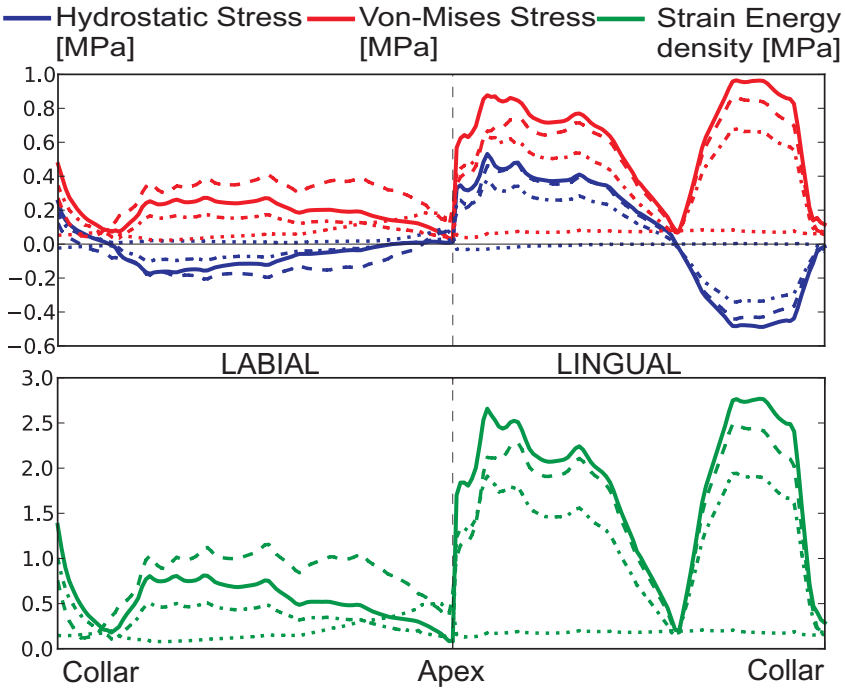

(a) Linear mechanical behavior

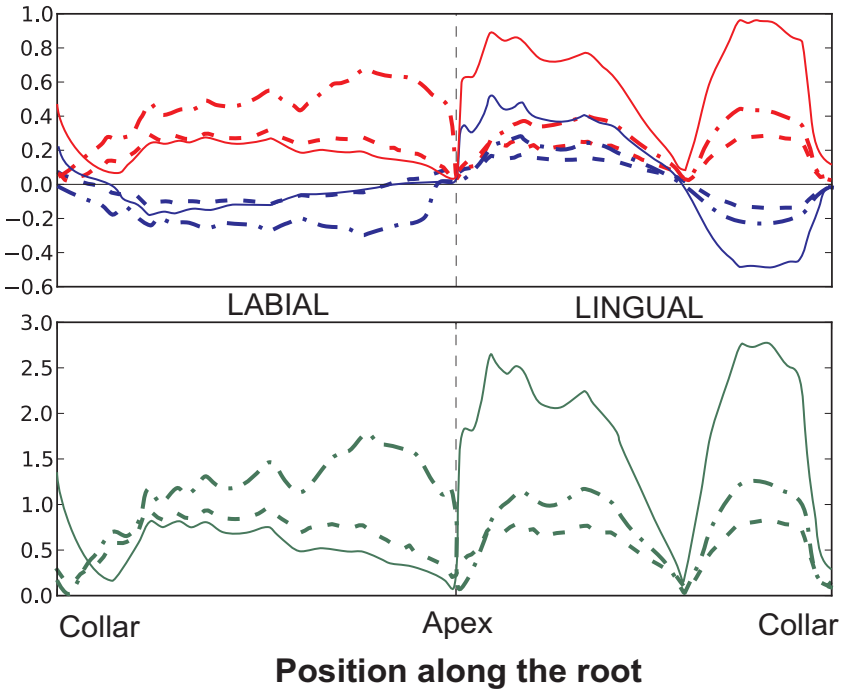

(b) Non-Linear mechanical behavior

FIGURE 6.6: *Pressure driven problem in the incisor: stresses and strain energy (computed as needed in the strain-energy density like parameter U_{iso}, i.e. $\frac{1}{2G}\boldsymbol{s}:\boldsymbol{s}+\frac{1}{K}p^2$) in the bone along the root. Plain lines are obtained for the linear reference model (in both figures), dashed-dotted lines for springs, dashed lines for a bilateral contact condition, and dotted lines for no PDL representation.*

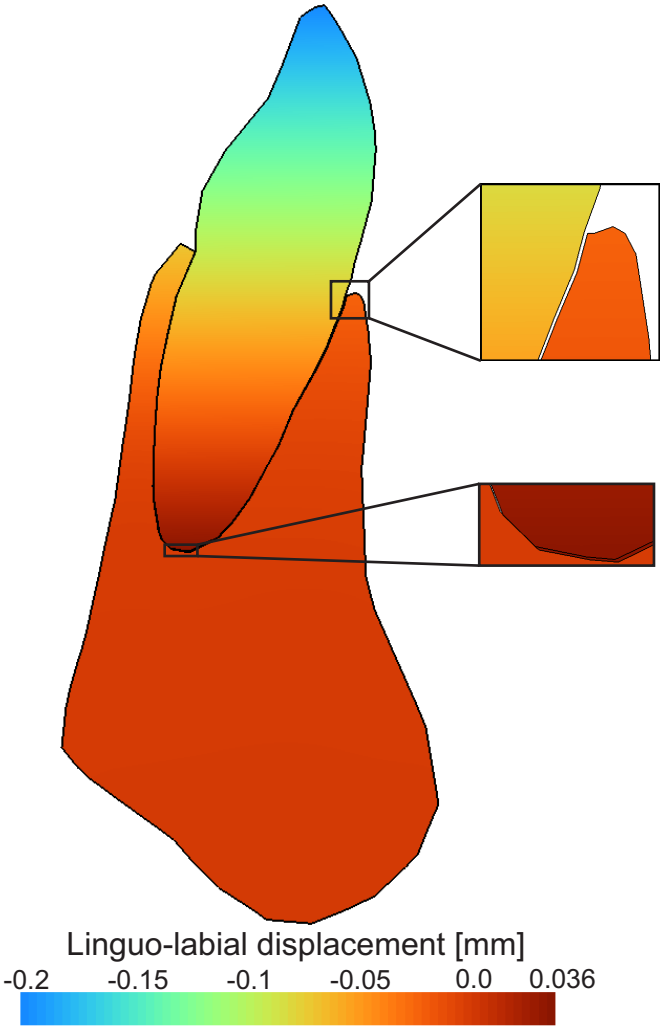

FIGURE 6.7: *Pressure driven problem in the incisor: displacement in the linguo-labial direction for a bilateral linear contact condition representative of the PDL. Close-ups on the tooth/bone contact at the labial collar and the apex.*

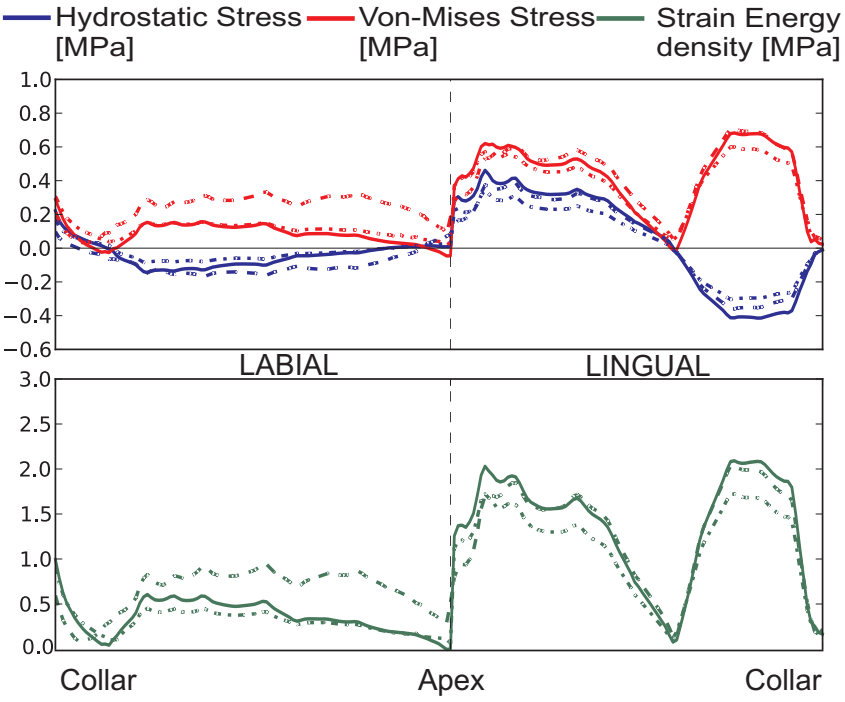

(a) Rotation

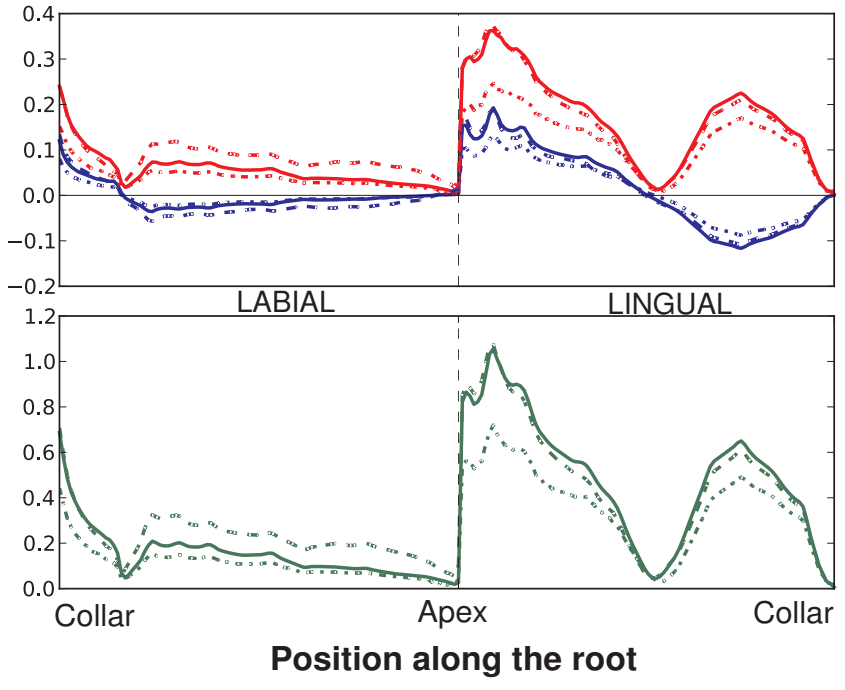

(b) Translation

FIGURE 6.8: *Displacement driven problems in the incisor: stresses and strain energy (computed as needed in the strain-energy density like parameter U_{iso}, i.e. $\frac{1}{2G}\boldsymbol{s}:\boldsymbol{s}+\frac{1}{K}p^2$) in the bone along the root. Plain lines are obtained for the linear reference model, dashed-dotted lines for springs, and dashed lines for a bilateral contact condition.*

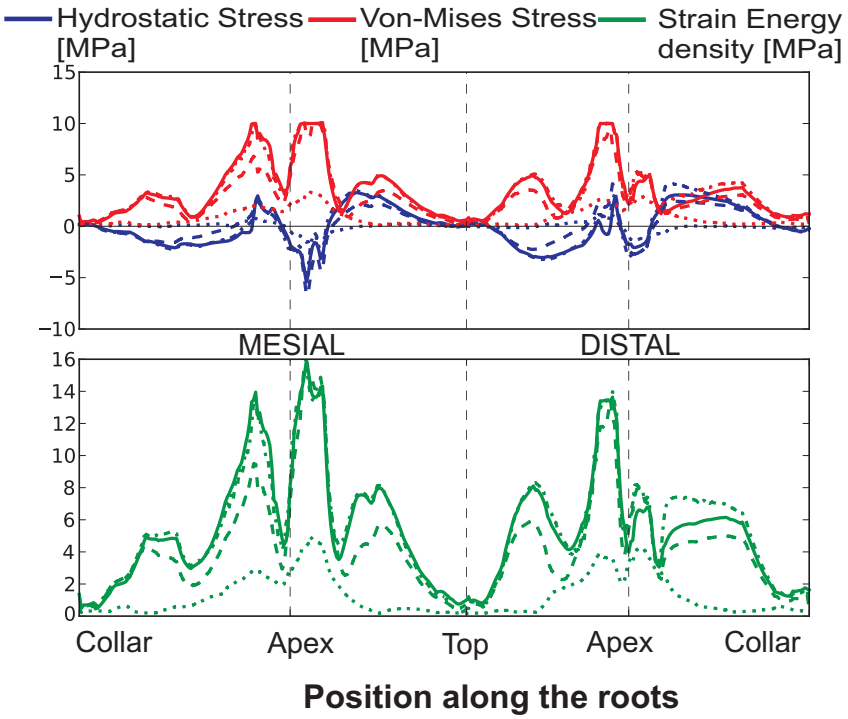

FIGURE 6.9: *Rotation driven problem in the molar: stresses and strain energy (computed as needed in the strain-energy density like parameter U_{iso}, i.e. $\frac{1}{2G}\boldsymbol{s}:\boldsymbol{s}+\frac{1}{K}p^2$) in the bone along the roots. Plain lines are obtained for the linear reference model (in both figures), dashed-dotted lines for springs, dashed lines for a bilateral contact condition and dotted lines for no PDL representation.*

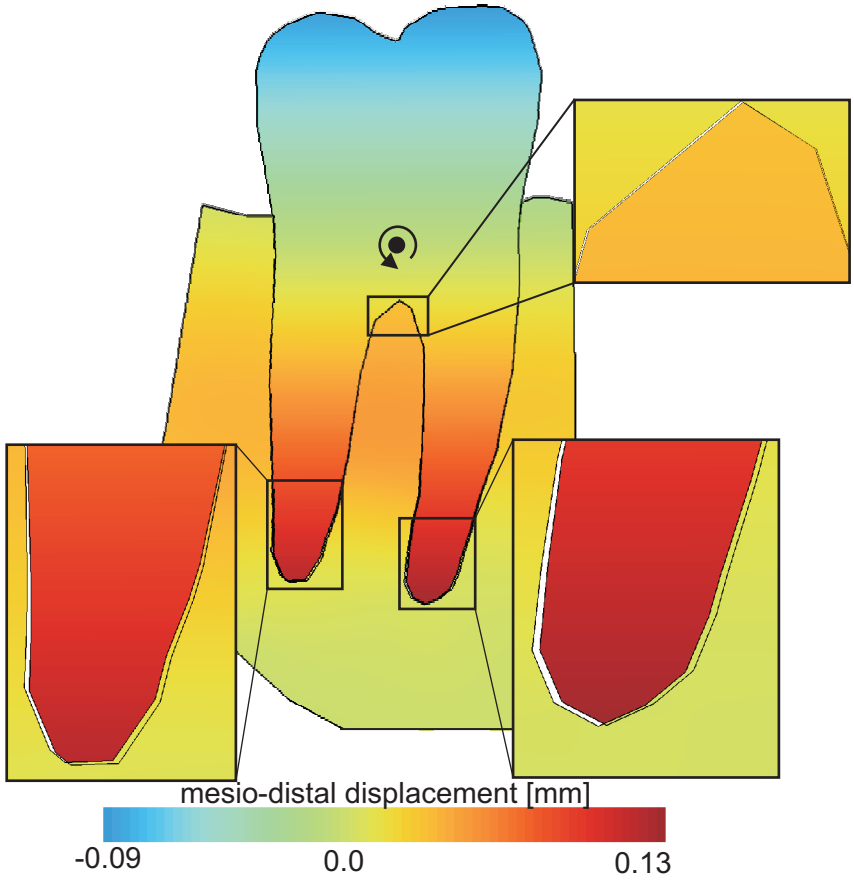

FIGURE 6.10: *Rotation driven problem in the molar: sagittal displacement in the alveolar arch (curved) plane for a bilateral linear contact condition representative of the PDL. Close-ups on the tooth/bone contact at the central collar and the apexes.*

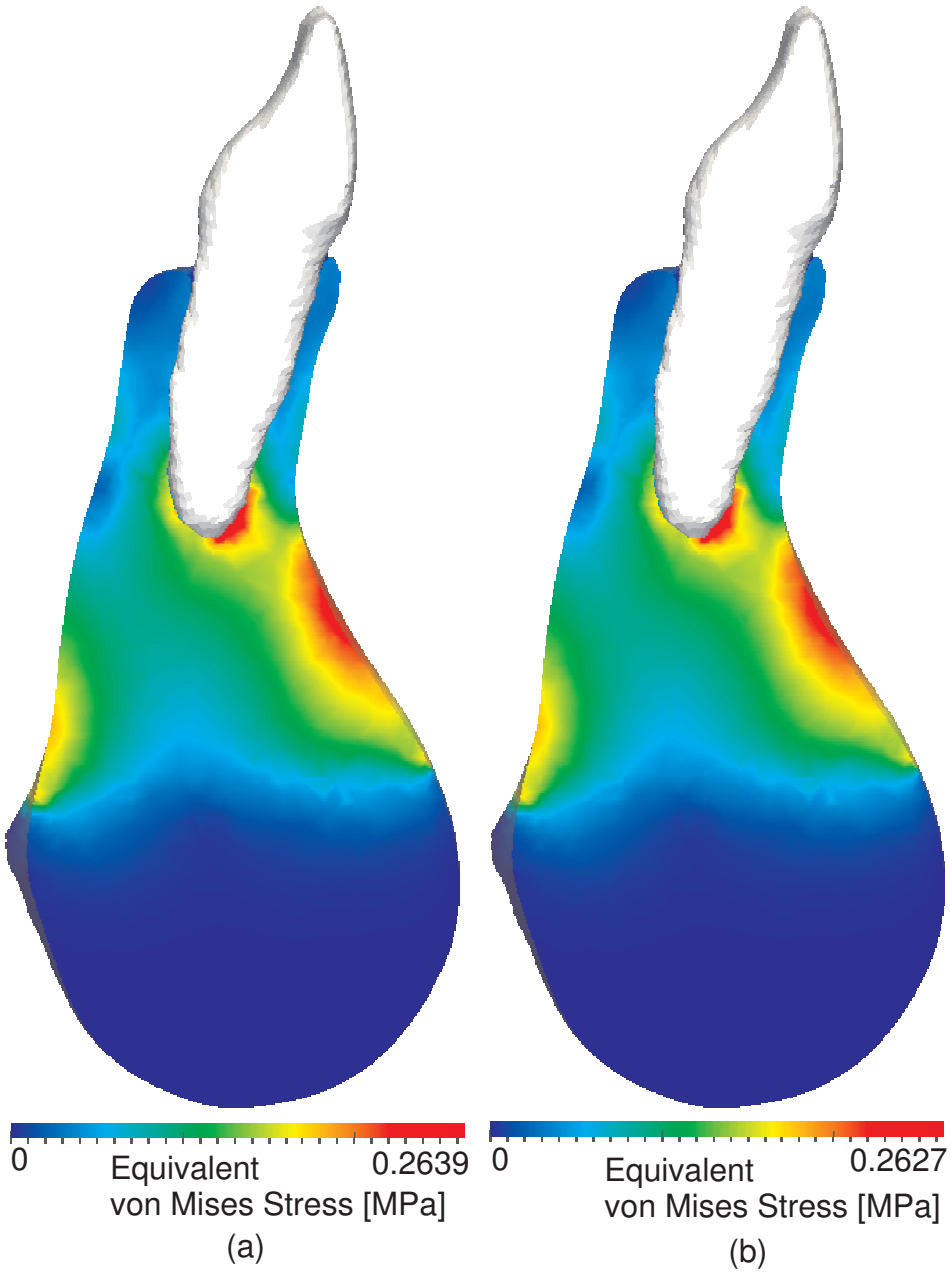

FIGURE 6.11: *3D translation driven problem in the incisor: equivalent von Mises stress [MPa] (a) spring model, (b) contact model*

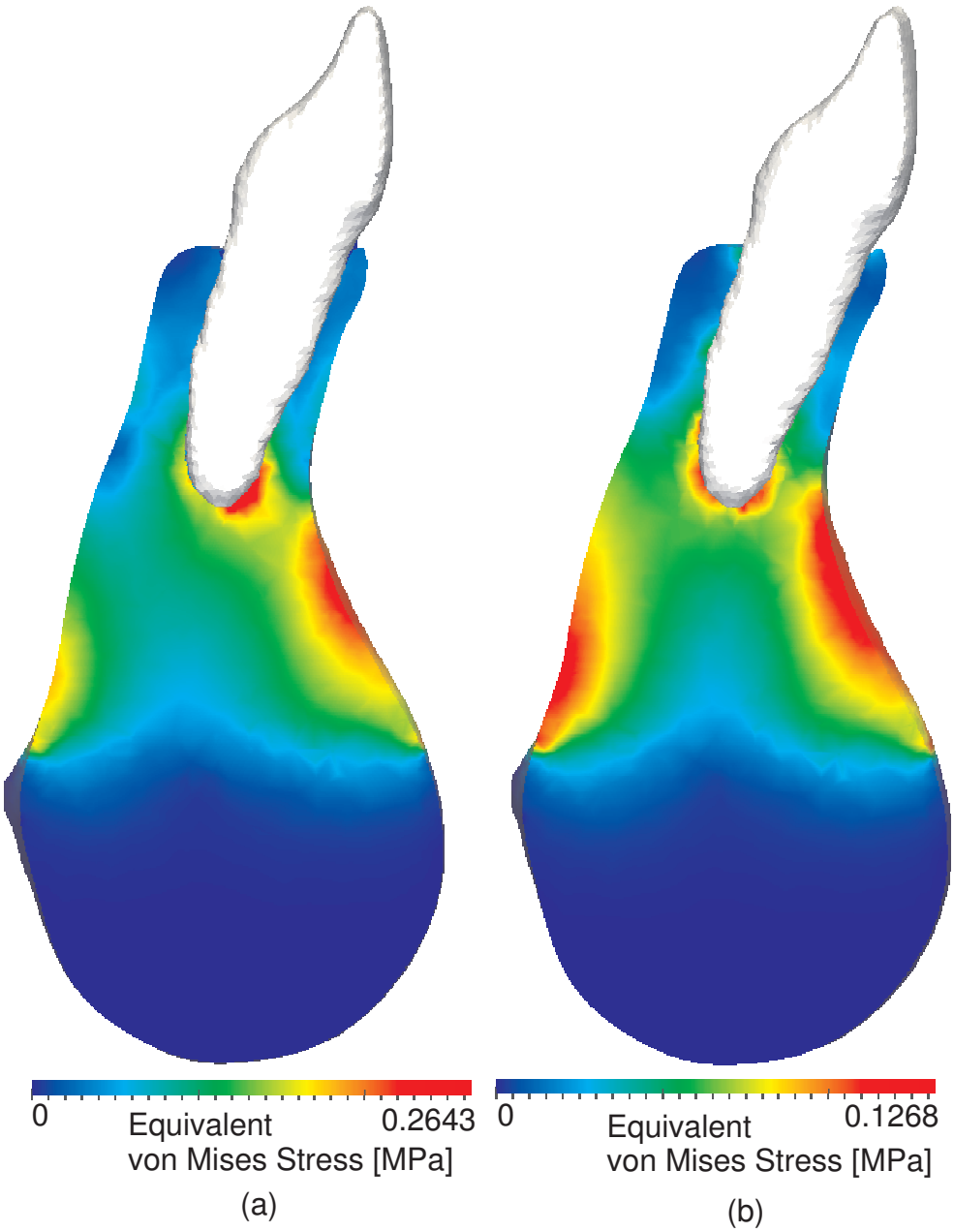

FIGURE 6.12: *3D translation driven problem in the incisor: equivalent von Mises stress [MPa] (a) solid PDL model, (b) no PDL model*

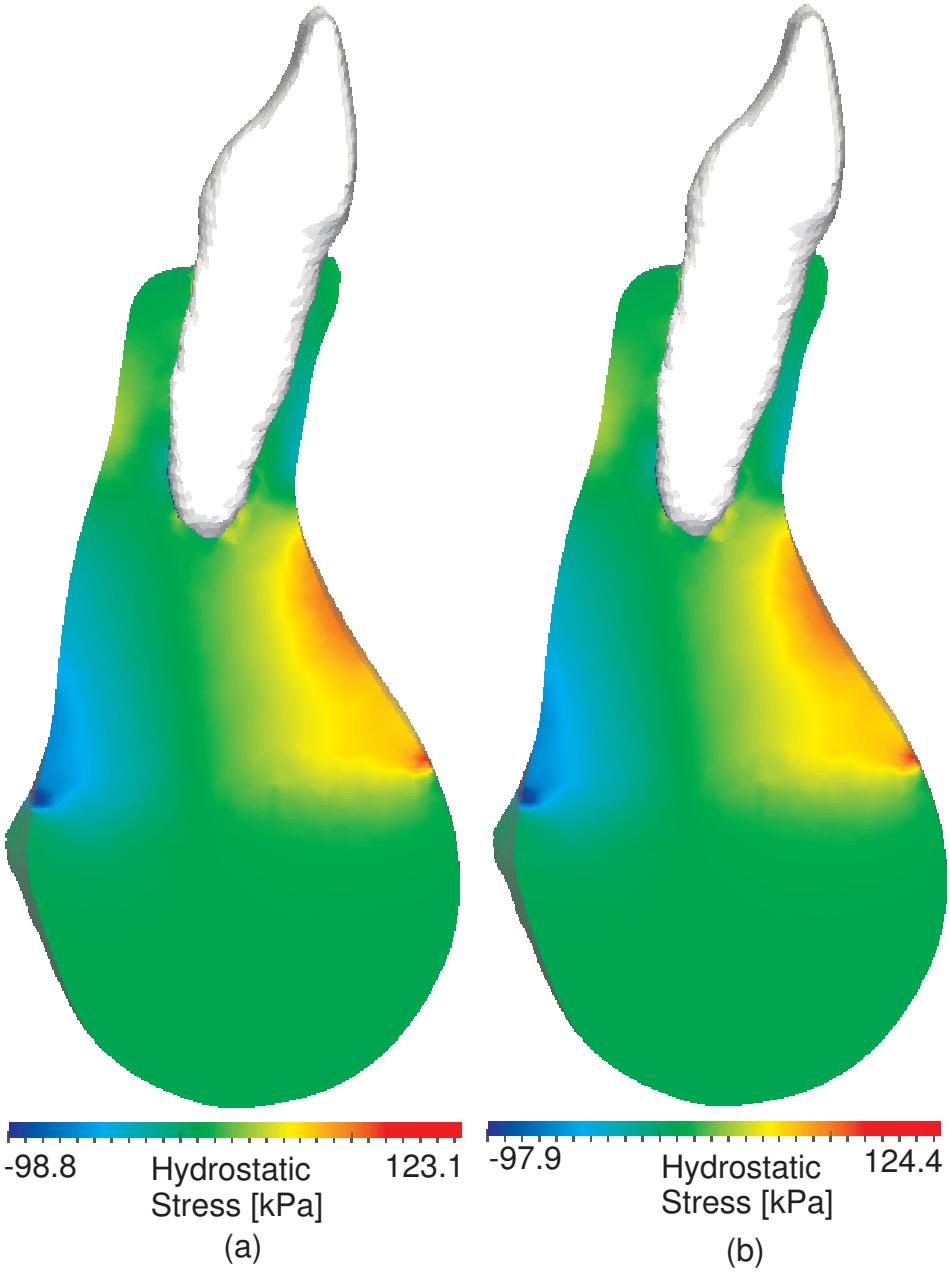

FIGURE 6.13: *3D translation driven problem in the incisor: hydrostatic stress [MPa] (a) spring model, (b) contact model*

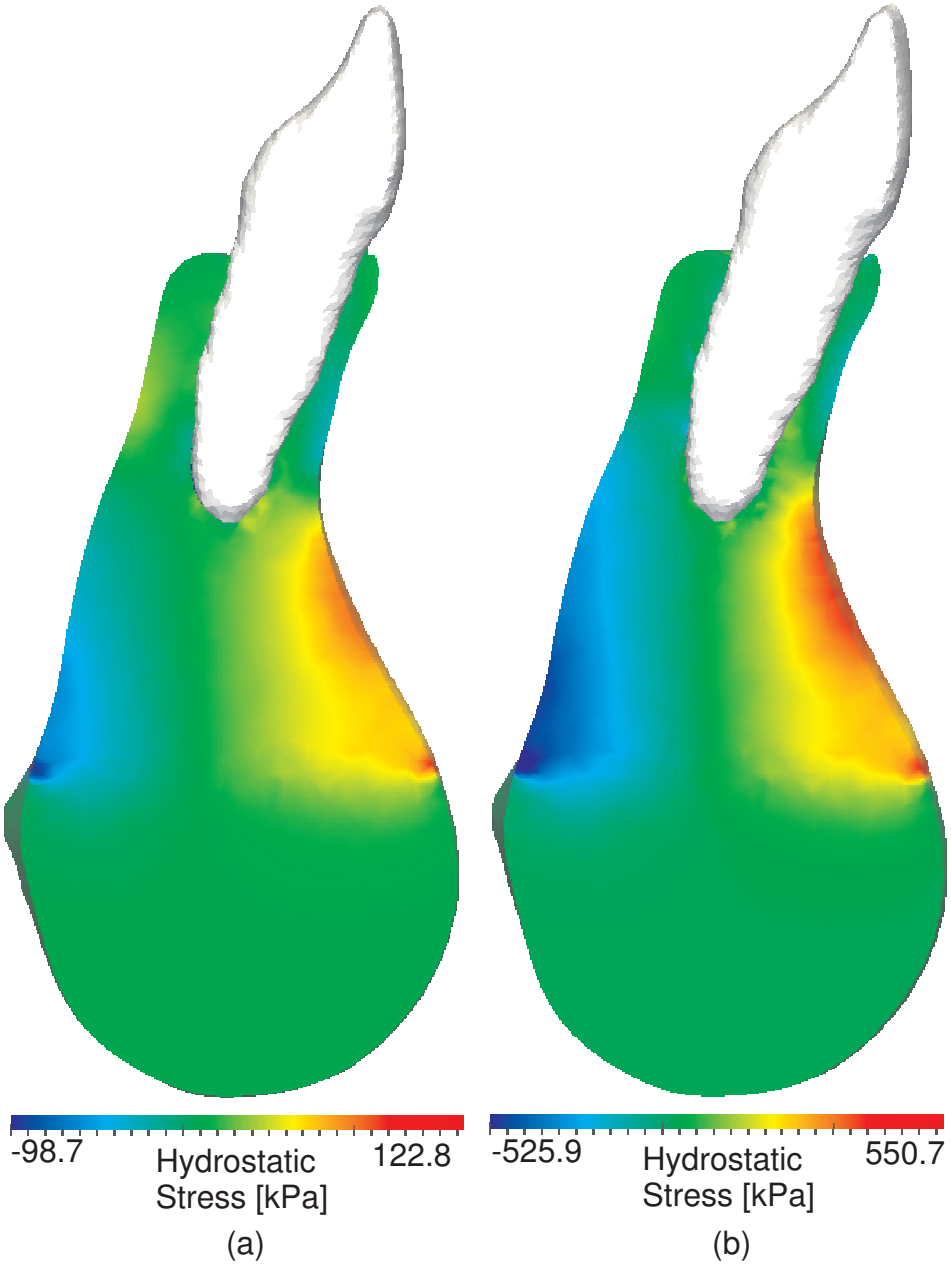

FIGURE 6.14: *3D translation driven problem in the incisor: hydrostatic stress [MPa] (a) solid PDL model, (b) no PDL model*

Conclusions

Clinical CT data precision does not allow for the PDL surface reconstruction. Extensive pre-processing is often used to create a PDL. This study demonstrated the potential of using customized contact conditions on the bone/tooth interface, as both the hydrostatic and shear stress in the bone could be represented while reducing the preprocessing of the model. In the pre-processing steps, it should also be noticed that the duplication of the mesh nodes (and not only of the geometry) is not required for the contact model as compatible meshes of the contour/surfaces are not needed (while they are for the spring model). This therefore allows for a lower number of duplicated geometrical data. The contact model can thus also be used if the bone and teeth have been triangulated separately, creating non-conforming interface meshes. From these different observations, we can conclude that using a non-linear contact method to represent the periodontal ligament mechanical response gives results on the stress and strain intensity in the bone that are similar to a non-linear spring model. Both the spring and the contact models also give similar results in the linear case as the use of a solid elastic PDL (inclusion of elastic PDL elements between the tooth and the bone). However, we should notice that using a contact method can be considered only if the interface is smooth enough, otherwise tuning the contact parameters to have a good enough convergence, and more over avoid artificial stress concentration, can be tricky.

As a result, the contact model will be used from now on for geometries where the PDL geometry cannot be extracted. The advantages of this choice are that the bone/tooth geometrical interface does not need to be moved to include the PDL and it also does not require conforming meshes. As specified earlier, this contact representation of the PDL is a good alternative to an elastic material behavior, it does not however account for complex behavior such as viscosity or fluid flow within the PDL.

6.1.3 Remarks about the Mesh Distortion in the Periodontal Ligament

In this section, the applied loads or displacements were low with comparison to actual treatment loading or displacements. For instance, the tipping movement was obtained applying a force of $0.3N$. However, this level of force is quite low for orthodontic forces, more often reported around 0.5 to $1.5N$. As said earlier (see chapter 4), the periodontal ligament is also often represented with a up to ten times stiffer material than the one we used.
Using a periodontal ligament with a low Young's modulus however leads to mesh distortions within the ligament, if a high force level is applied, as the material exhibit a low stiffness. Such large strains cannot be computed with a Lagrangian approach of the mesh displacement (the mesh follows the material displacement), or at least the elements of the mesh become so distorted that the solution cannot be trusted anymore.
Therefore, mesh management techniques should be used for any problem involving high forces and low stiffness periodontal ligament, when the ligament is geometrically represented. In the case of a contact representation of the ligament, this problem does not arise anymore.
We here present two solutions used either apart or simultaneously: the Arbitrary Lagrangian-Eulerian (ALE) method (as presented in section 3) and a remeshing technique.
In the ALE method, the mesh is managed separately from the material displacement, using a priori defined rezoners (described in details in [22]). In the case of the periodontal ligament, we use a spline rezoner for the two free boundaries delimiting the surface of the PDL (purple lines in Fig. 6.15). It allows to relocate the nodes of the PDL boundary assuming it is represented by a cubic spline. We then use a rezoner on the inner nodes of the mesh using an iterative smoothing method. This method tends to homogenize the area of the elements. After rezoning of the nodes, the different internal fields are transfered onto the new mesh with a first order Godunov scheme [22].

This ALE method allows to better represent the large strains at the collar (see initial and deformed meshes, with and without ALE in Fig. 6.16(a-d)). A tipping force up to $0.65N$ can therefore be applied while keeping a good mesh quality but a higher force cannot be used. Indeed in the cervical area, the free boundaries of the ligament deform so much (mainly because of the almost incompressible behavior of the ligament, creating a convex and a concave menisci[1]) that the elements tend to get inverted, whatever the ALE rezoning algorithm used (Fig. 6.16(e), red element).
Therefore, full remeshing of the deformed geometry has to be considered. For this, we need to extract the deformed geometry on which a new mesh will be built. This task is not too difficult in the 2D case for which cubic splines can be built on the outline of the deformed geometry. However it is more complex in 3D and therefore will not be treated in this work.

[1] We should note that we here use a linear model for the periodontal ligament. Using a non-linear model would increase the stiffness as the lengthening and narrowing of the ligament goes on, and therefore decrease the deformation.

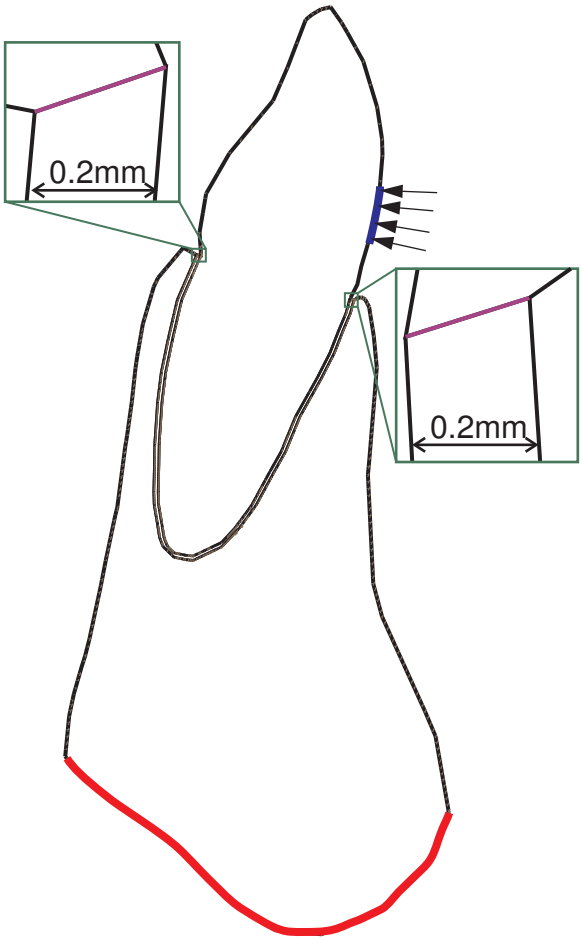

FIGURE 6.15: *Geometry and BC's of the tipping problem used with ALE and/or remeshing techniques. The nodes on the red curve are clamped, the force is applied on the blue curve. Purple lines are the one for which an ALE rezoning algorithm is used, the two zooms are the area presented in Fig. 6.16.*

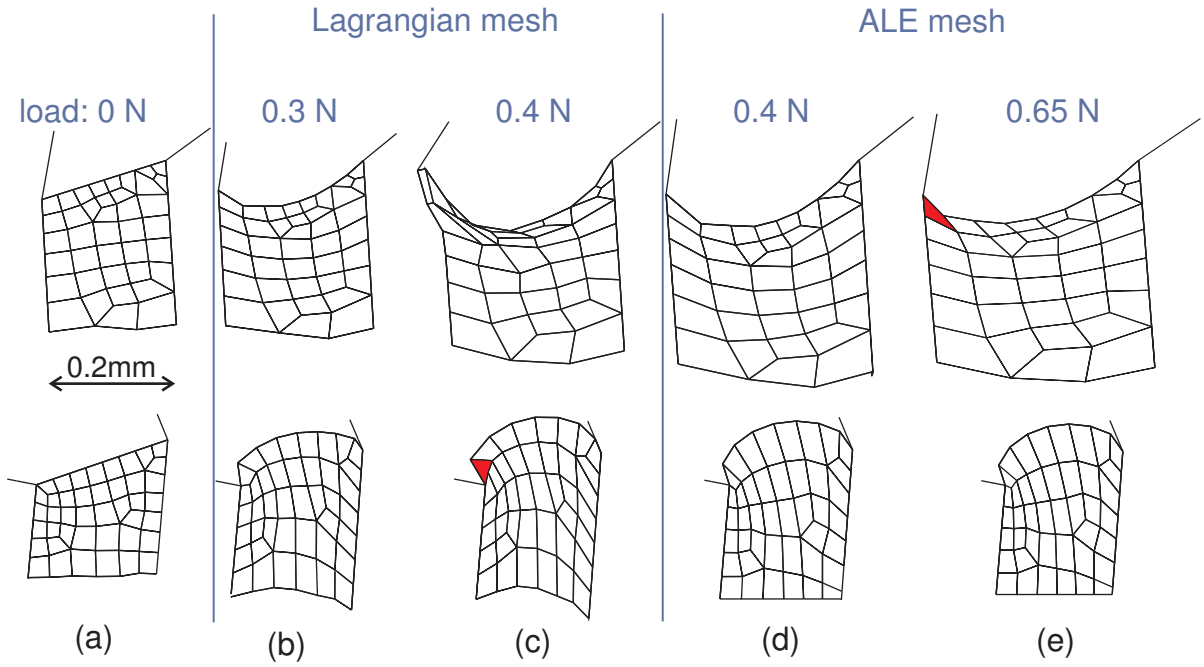

FIGURE 6.16: *Mesh evolution of the periodontal ligament at the collar.* ***Top row****: labial (right) side in tension;* ***bottom row****: lingual (left) side in compression. (a) initial mesh, (b) deformed mesh for a force of 0.3N, (c) deformed mesh for a force of 0.4N, (d) deformed mesh for a force of 0.4N with ALE, and (e) deformed mesh for a force of 0.65N with ALE. In red, two of the problematic elements (not counting most of the top elements in top row (c).)*

After having extracted the deformed geometry, it can be remeshed and then data between the two meshes are transfered. For this, we have to define steps at which the remeshing has to take place. As the ALE method gives results accurate enough up to at least the application of $0.65N$ but that elements get too much distorted for a higher force, the first load step defined for remeshing is after an application of $0.65N$. This new mesh (Fig. 6.17(b)) allows to continue loading (still applying the ALE method at each time-step) up to a $0.83N$ force. At a higher force level however the mesh gets once more too distorted on the tension side (Fig. 6.17(c)). Therefore, a new remeshing point is defined at $0.83N$, allowing to carry on the computation up to a force level of $0.95N$, for which a new remeshing point is defined. In the same way, a final remeshing point is defined at a forec of $1.01N$. This fourth and final mesh can be used for forces up to $1.2N$. This remeshing technique could be used further, every time defining new time steps at which remeshing takes place. However, at each remeshing step, data needs to be transfered between the two meshes. This operation is not only CPU demanding, but also it involves a loss of accuracy as some numerical diffusion is inevitable, specially at the boundaries between materials.

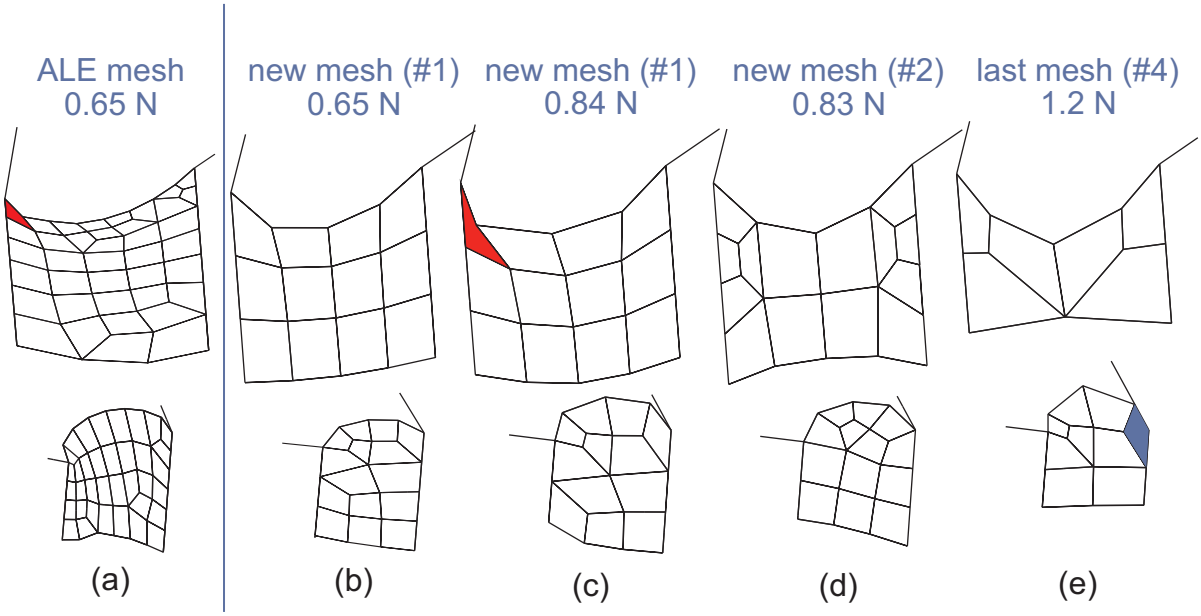

FIGURE 6.17: *Mesh of the periodontal ligament at the collar.* ***Top row****: labial (right) side in tension;* ***bottom row****: lingual (left) side in compression. (a) ALE mesh at 0.65N (identical to 6.16(e)), (b) first new mesh for a force of 0.65N, (c) first new mesh for a force of 0.84N (in red, the problematic element), (d) second new mesh for a force of 0.83N, and (e) last new mesh (the fourth one) for a force of 1.2N. For this last mesh, the blue element is in contact with the base of the crown.*

Analyzing the evolution of the mesh, we can see that there are less and less elements describing the free boundaries. Indeed, initially to catch the creation of the menisci due to the deformation, a fine mesh needs to be used. However, once the menisci are formed, building

a fine mesh is not possible without creating badly shaped elements at the corners that cannot deform properly. Indeed, at the tension side, the contact angles of the concave meniscus decrease as the force increases, with a tendency to deform the quadrangles into triangles. At the compression side however, the contact angle between the convex meniscus and the bone boundary tends to increase and become obtuse. Therefore, the description of the geometry of the free boundary (mainly its curvature) is less and less accurate in order to be able to mesh it properly.
We can also finally see that, from a force equal to 1N, the periodontal ligament comes into contact with the tooth crown on the compression side. This implies that the use of a finite element code that can deal with contact problems is mandatory if one wants to represent forces at therapeutic level.

6.2 Remodeling in Orthodontic Tooth Movement (OTM)

In this section, we finally consider the potential of the pressure dependent model to predict the density evolution of alveolar bone tissue, allowing for a tooth displacement due to orthodontic boundary conditions.
First of all, we have to remind that the remodeling model tends to homogenize a stimulus towards an homeostatic value representative of the equilibrium solution. In all the models we present in this section, only orthodontic loads are applied. We do not consider any physiological loading due to muscle tone, or other movements of the stomatognatic system. Therefore, the initial conditions for all models (null stress and strain) are considered as an equilibrium state. Thus the equilibrium stimulus is assumed to be zero and any application of external load will lead to an overload of the tooth/alveolar complex systems.

The first problem we will consider is a purely academic case, testing the capabilities of the remodeling model for tooth movement applications. For this problem, we do not consider a real geometry of the tooth and surrounding tissues. Indeed, we saw in section 5.5 that the remodeling behavior is very sensitive to the boundary conditions and in particular to stress concentrations due to the BC's application. Thus, we free ourself from these BC's effects by considering a 2D root shape geometry moving into an alveolus of unrealistic thickness. For this problem, we will see how the ALE method can be used to model large displacements of the tooth within the bone while remodeling is going on. We will consider the contribution of the plasticity of the trabecular bone and of the anisotropic remodeling to the model. Finally, we will also analyze the sensitivity of the model to the two parameters that have been described as sensitive in section 5.3.

We then will consider two types of OTM problems with patient-specific geometries. First of all academic cases for which the force variation due to remodeling is observed for constant displacement problems (i.e. displacement driven tooth movement). Then more realistic cases for which a displacement is observed under the application of a constant force (i.e. force driven tooth movement). It should be clear however that real orthodontic appliances lead neither to displacement driven problems nor to force driven ones but rather to a mixed situation for which there is an initial imposed force level that decreases as the displacement due to remodeling is going on.

6.2.1 Large displacement numerical tooth movement

The first problem we consider is a purely academic case. For this problem, we do not consider real geometries of the tooth and surrounding tissues as presented in the previous section. We free ourself from boundary conditions effects by increasing the thickness of the bone. We thus model a 2D single-rooted tooth whose root thickness is 7mm at the collar and root height is 16mm, surrounded by alveolar bone (composed solely of trabecular tissue) whose thickness is 49 mm on each side of the tooth, and height (more realistic value) is 40 mm (see Fig. 6.18). The tooth is considered as being a rigid tissue (and is therefore not represented in Fig. 6.18, only the root is). The periodontal ligament is modeled through bilateral contact conditions as presented in the previous section. The alveolar bone is assumed to follow a remodeling constitutive model as presented in this work (material and remodeling parameters are given in table 6.3). At the tissue level, the yield limit is chosen at $\sigma_y = 200MPa$ (median value of the one calculated with an reverse engineering approach on linear finite element models in [193, 244, 266]). The isotropic hardening depends on the bone apparent density (so that it corresponds to a tangential modulus equal to 5% of the value of the Young's modulus -density dependent- as in the previously cited studies). The tooth root is horizontally translated at a constant speed so that travels a distance 1.5 times its width in a year (i.e. 10.5 mm/365 days). The bone is considered clamped on its basal line while it is restrained vertically on its top line and horizontally on its vertical extremities (see Fig. 6.18). This model could correspond to a simulation of a tooth moving along the alveolar arch, with no other teeth present. In this section, we will analyze the force variation versus time for this tooth displacement, as well as the obtained density field.

As the imposed tooth displacement is large compared to the tooth characteristic length, a mesh management technique such as the ALE method is required. Indeed, the large deformation cannot be handled with a Lagrangian formulation as it will eventually lead to completely distorted elements. Initially, the quadrangular mesh is built so that fine elements lie around the tooth (see Fig. 6.18). For that, an unstructured mesh (composed of 566 quadrangular elements) is built in the section delimited by the central $BEKH$ rectangle, including the tooth outline (whose geometry is built on a spline). Structured quadrangular meshes are built in the sections delimited by the lateral $ABHG$ and $EFLK$ rectangles (each composed of 224 quadrangular elements).

As the loading is an imposed displacement (at constant velocity), the kinematics of the mesh is a priori known and the ALE mesh management can be specific to this kinematics. The ALE method is used to keep a good mesh quality all along the displacement. The easiest way to do that is to translate the finer central section mesh with the tooth. This translation is obtained as follows: we impose that the displacement of the (bone) nodes B, H, and I (blue points in Fig. 6.18) is identical to that of the (bone) node C (in contact with the tooth root). In the same way, the displacement of the nodes E, J, and K is identical to that of the node D. We here remind the reader that the ALE method allows for the mesh to move independently from the material, so all these nodes are not associated to the same material particle along the

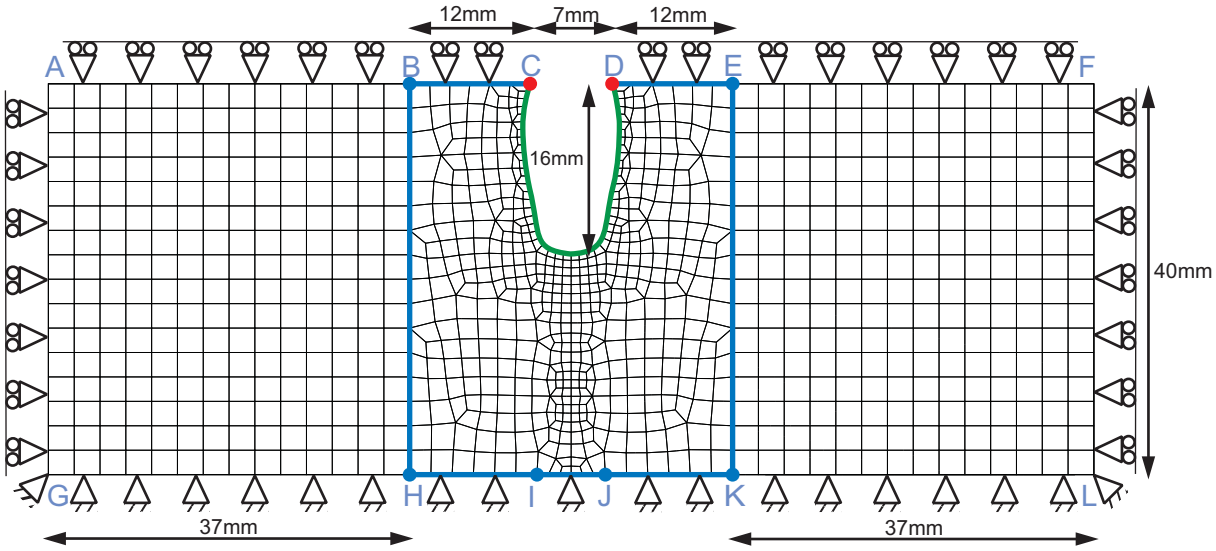

FIGURE 6.18: *purely academic case: geometry, mesh, and ALE mesh management: the nodes on the green curve are relocated using spline curves, the blue points have an horizontal displacement which is the same as the red points, the blue lines are remeshed (with a constant number of elements) as if they remained straight between their extremities.*

TABLE 6.3: *Material parameters*

Material	Young's modulus $[GPa]$	Poisson's ratio $[-]$	Yield stress $[MPa]$	Hardening parameter $[MPa]$
Tooth	rigid	-	-	-
Bone at tissue level	13.75[a]	0.3	200.0	723.7

Remodeling model	
initial apparent density	: $\rho = 1.33 gr/cc$
equivalent Young's modulus[a]	: $E = 4.39 GPa$
number of daily load cycle	: $N = 1$
homeostatic value of the stimulus	: $\psi^\star = 0\ MPa$
exponent of the stress stimulus	: $m = 4$
remodeling velocity for resorption	: $c_r = 0.02 \mu m/(\text{day} MPa)$
remodeling velocity for formation	: $c_r = 0.01 \mu m/(\text{day} MPa)$
half-width of the lazy zone	: $\omega = 0.1\ MPa$
parameter weighing the hydrostatic and deviatoric parts of the effective stress definition[b]	: $\eta = 1.$

[a] Values obtained using Equ. 5.9 and considering a tissue density ρ_0 of 1.9gr/cc

[b] Chosen as the initial degree of anisotropy, i.e. 1.0 as the tissue is considered as being initially isotropic.

movement. The mesh nodes along the root surface (green curve in Fig. 6.18) are relocated using spline curves. Finally, the lines BC, DE, EK, KJ, JI, IH, and HB are remeshed (with a constant number of elements as the ALE method does not modify the topology of the initial mesh) so that they remain straight during the material displacement. All the other (inner) nodes of the central section are repositioned using an iterative smoothing method (Giuliani's method [22]). The same method is used to reposition the inner nodes of the two lateral sections (sections $ABHG$ and $EFLK$).
After repositioning the nodes, the different internal fields are transfered onto the new mesh using a first order Godunov scheme [22].

First of all, we will look at the contribution the Arbitrary Lagrangian-Eulerian brings to the model. For this, we simply analyze the equivalent plastic strain field at 35% of the maximal displacement, i.e. 3.7 mm (see Fig. 6.19). We can see that, when using the classical Lagrangian method, not only the mesh is distorted around the tooth apex, but also the equivalent plastic strain field reaches higher values (0.98 without the ALE method, 0.71 with) around the tooth apex. The tooth can be displaced using the Lagrangian mesh only up to a distance of 3.9 mm. Higher displacement cannot be computed as the elements get too distorted, up to the inversion of elements.

We can then analyze the results of the model, i.e. the force variation with displacement. The first analysis that can be done is to compare the force intensity required for the imposed displacement as a function of the material law and morphology used. The initial bone model considers it is initially isotropic, described with an elastoplastic material at tissue level, and is submitted to an anisotropic remodeling. We here compare the required force intensity modifying these three characteristics (see Fig. 6.20 - initial model, dark blue curve).
First, considering initial morphologies that are not isotropic but either twice stiffer horizontally than vertically (red curve in Fig. 6.20) and vice-versa (purple curve in Fig. 6.20). Since the movement is horizontal and thus that the remodeling acts so that the morphology becomes horizontal, the morphology which is stiffer horizontally requires a larger force to initiate the displacement. However, the rate at which the force increases is lower than for an initially isotropic model. The observation is the exact opposite for a morphology initially stiffer vertically. This model requires a lower force initially (as the bone is less stiff in the movement direction) but the rate at which the force increases is higher as the morphology becomes horizontal due to remodeling.
Secondly, the use of an elastoplastic material at tissue level gives results completely different than if the material was considered elastic at tissue level. We can indeed see (light blue curve in Fig. 6.20) that the force level is twice higher when the material is elastic as the plastic flow has for effect to reduce the force for a given displacement.
Finally, using an anisotropic remodeling has for effect to align the morphology with the imposed direction of displacement, thus requiring a higher force than if the bone was submitted to an isotropic remodeling (green curve in Fig. 6.20).

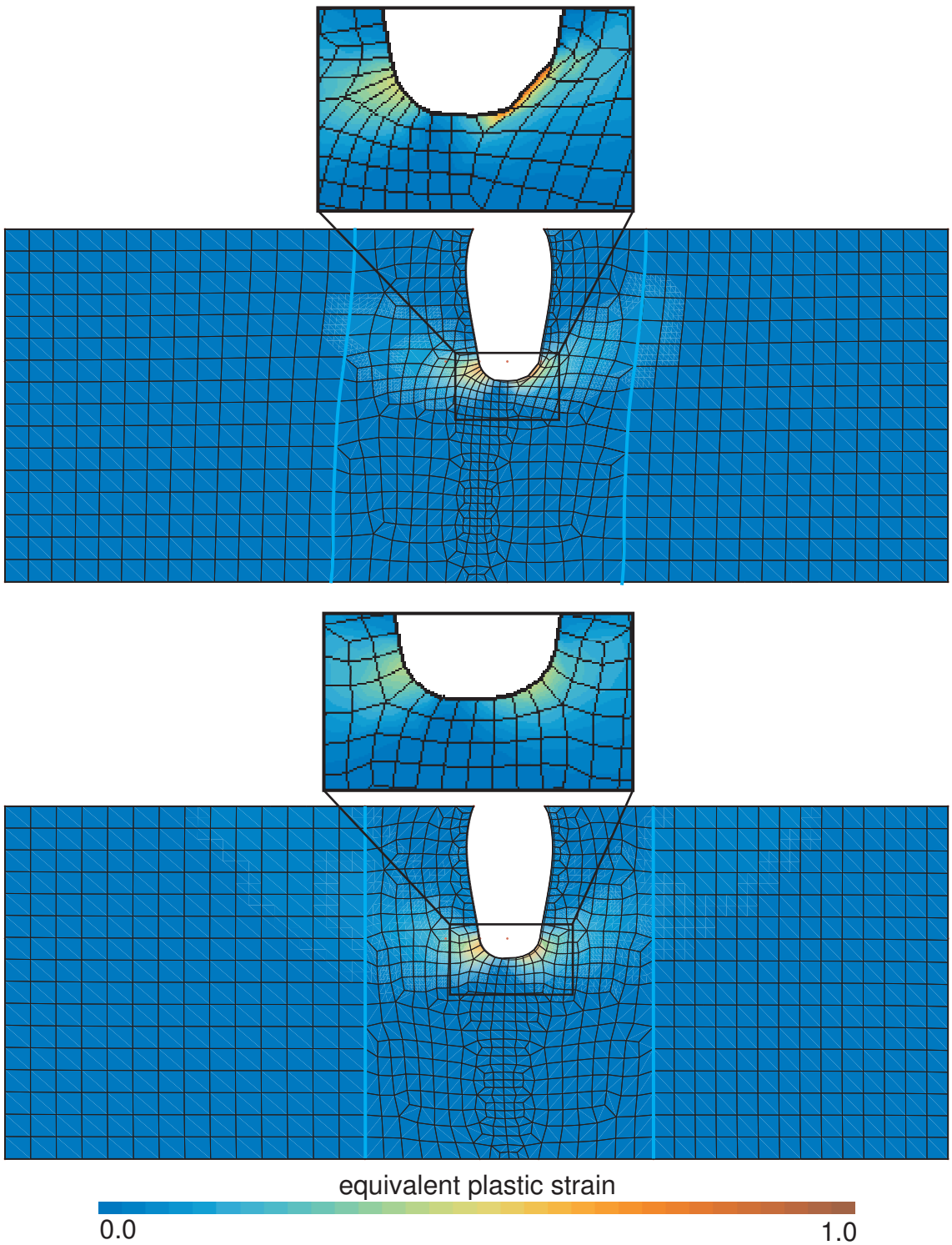

FIGURE 6.19: *Use of the ALE mesh management method in the model. Top panel: Lagrangian mesh, bottom panel: ALE mesh. The equivalent plastic strain in the bone around the tooth apex reaches vales of 0.98 in the (distorted) Lagrangian mesh while a value of 0.71 only is reached when using the ALE method.*

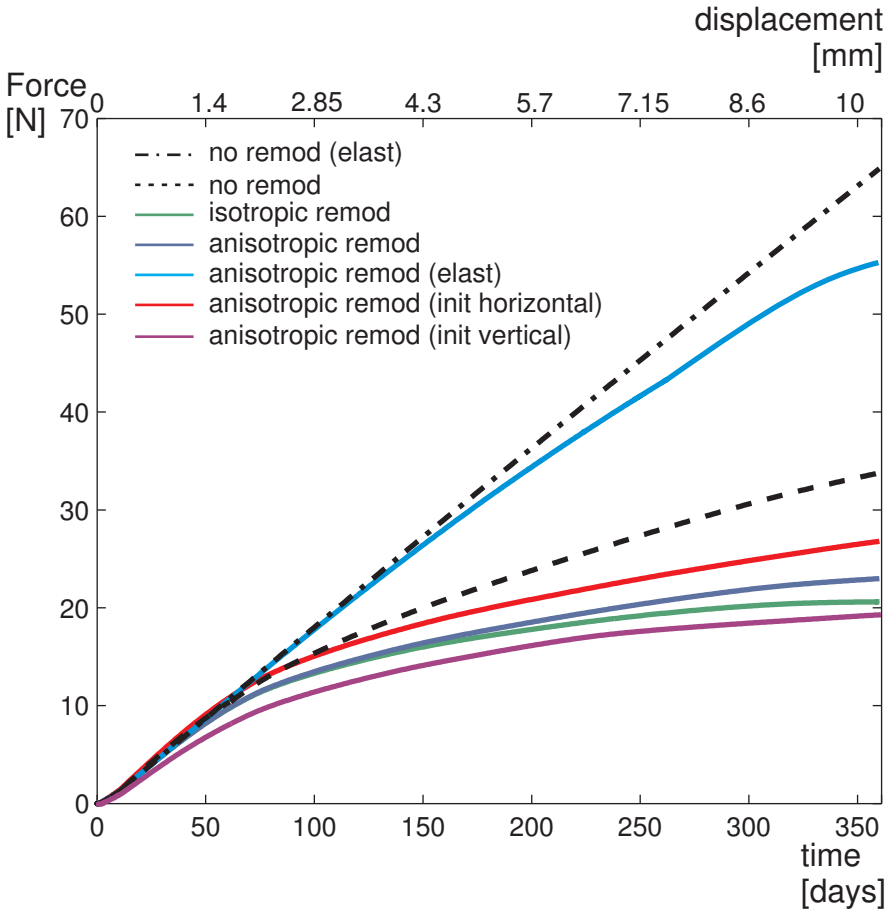

FIGURE 6.20: *Force [N] vs. time [days] and displacement [mm] for the imposed velocity and different bone material models.*

For comparison purpose, we also depicted the required force obtained if the bone was considered a passive material, i.e. if no remodeling was accounted for, both for an elastoplastic model (dashed curves in Fig. 6.20) and an elastic model (dashed-dotted curves in Fig. 6.20). We can see that, as expected, the remodeling has for effect to facilitate the tooth movement, thus involving a lower force (about 10N lower, i.e. 50% of the required force) than for a passive material.

We should notice that this model is not representative of an actual tooth movement in the force levels it involves. Indeed, we see that, for an anisotropic remodeling and considering an elastoplatic material at tissue level, the required force reaches values from 20 to 27N depending on the initial morphology considered, i.e. at least ten if not twenty times higher than the forces used in orthodontic treatments. This difference is due to the not physiological model considered. Indeed, we consider a 2D model of a tooth whose geometry does not at all accurately represents the reality but, also, without any physiological forces but the orthodontic one. The constant velocity is probably not physiological either, especially over such a distance and/or duration.

For the initial model (bone with an initially isotropic morphology, submitted to an anisotropic remodeling and with an elastoplastic material at tissue level) we can then examine the density (Fig. 6.21), stimulus (Fig. 6.22), and equivalent plastic strain fields (Fig. 6.23) at the end of the simulation.
We can see that as expected, the bone density decreased downstream (where the bone is in compression) while it only very slightly increased upstream (where the bone is in tension). However, analyzing the stimulus level on each side of the tooth does not show a significant difference. Therefore, using a remodeling model that would not be based on the pressure sign as developed in this work would lead either to resorption or to formation on both sides of the tooth.
Finally, the use of a model accounting for plasticity at tissue level leads to plastic strains that are not negligible around the tooth apex. They also lead to a force level required for the movement which is significatively different from the one required with an elastic model.

We showed in section 5.3 that the remodeling model was quite sensitive to the values used for the homeostatic stimulus and for the half-width of the lazy-zone. We here present the sensitivity of the required force intensity on these two parameters. We use three other values than the initial one for the homeostatic level of the stimulus (initially chosen at zero), i.e. $\Psi_t^\star$ =0.1 MPa, 5 MPa, and 10 MPa. We also use three other values than the initial one for the half-width of the lazy zone (initially chosen at 0.1 MPa), i.e. ω =0.001 MPa, 0.01 MPa, and 1 MPa.
We can see (Fig. 6.24) that a small increase in the homeostatic value of the stimulus decreases the force. An increase to $\Psi_t^\star = 0.1MPa$ (i.e. not producing underloaded areas since $\omega = 0.1MPa$) reduces the force required for the displacement.

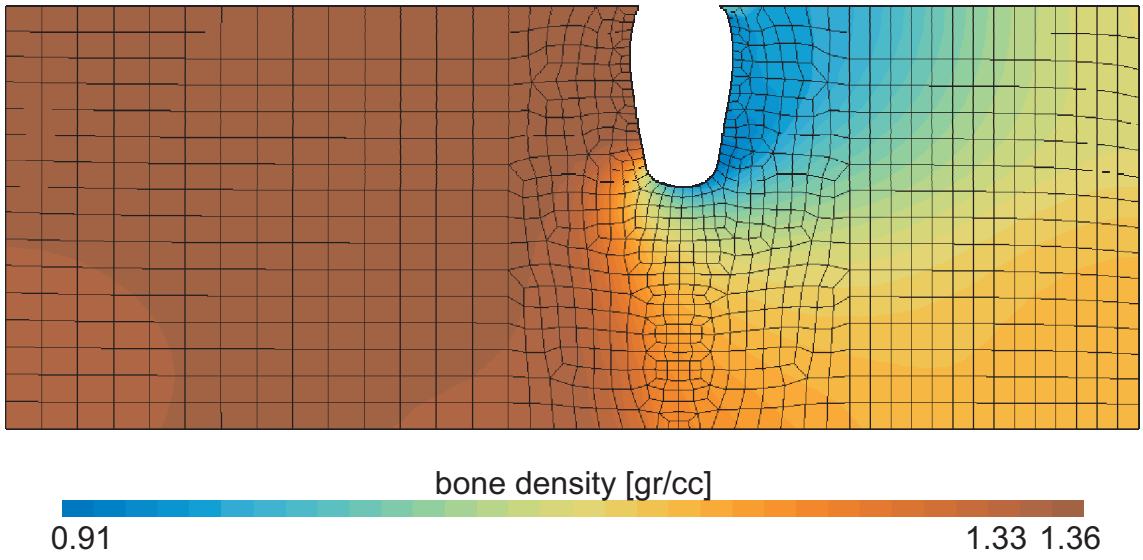

FIGURE 6.21: *Bone density field [gr/cc] at the end of the tooth displacement.*

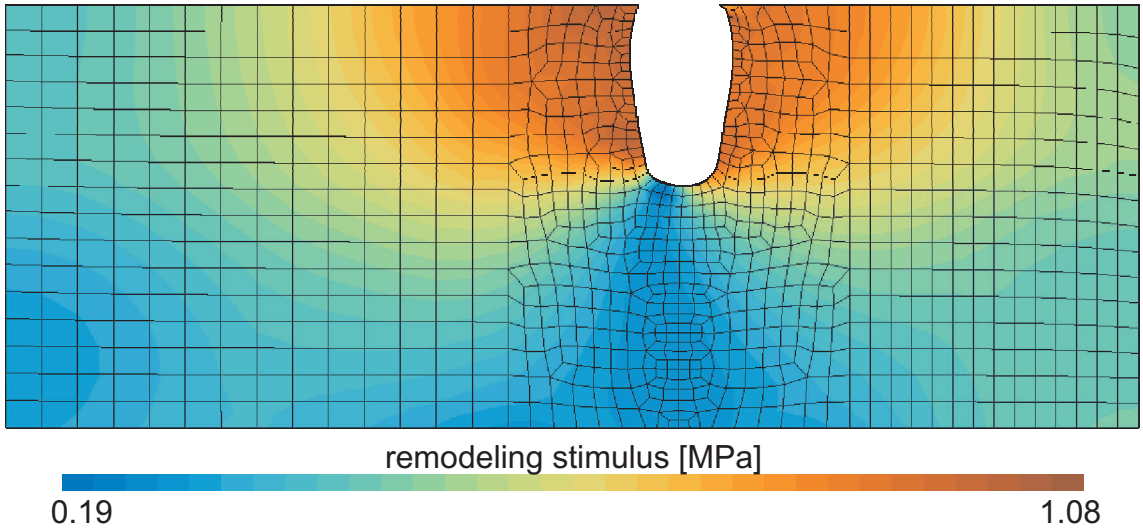

FIGURE 6.22: *Bone stimulus [MPa] at the end of the tooth displacement.*

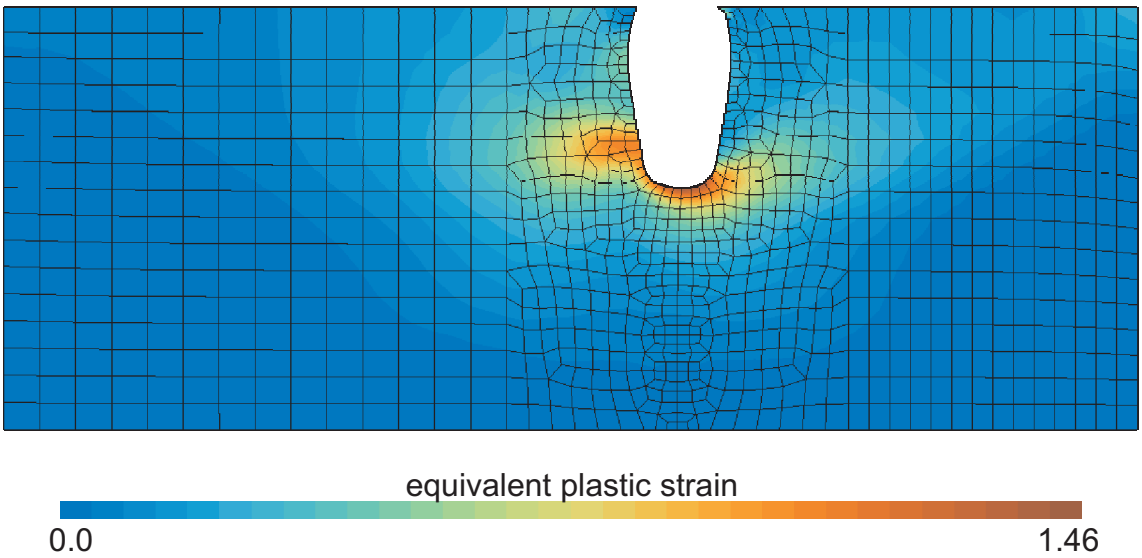

FIGURE 6.23: *Equivalent plastic strain at the end of the tooth displacement.*

Increasing further the homeostatic value of the stimulus does not have much impact on the force intensity. Indeed, increasing the homeostatic stimulus leads for the whole bone volume to be in underloaded conditions (while initially there are only overloaded areas). These areas will undergo resorption only. As the initial model is submitted mainly to resorption (we saw in Fig. 6.21 that the bone formation is almost not present), the global impact of this increase in the homeostatic level is pretty small.
The same discussion is valid for the half-width of the lazy-zone. A decrease of the half-width reduces the force while an increase up to the point where the whole volume is in underloaded conditions does not have much effect on the required force intensity.

On a purely computational point of view, the use of an anisotropic remodeling model increases the costs compared to an isotropic one. Comparing the CPU costs (time needed for the computation) between the initial model and the isotropic remodeling equivalent one, shows the anisotropic model is 3 times longer than the isotropic one (see table 6.4). It should be noticed that using the ALE method in this model does not increase much the CPU cost as less than 3% of the time is spent for the ALE rezoning and transfer. The CPU cost increase for the anisotropic case is due to two issues: first the need to use smaller time steps for the remodeling model to converge (so that 810 iterations are needed for an anisotropic remodeling model instead of 530 for an isotropic remodeling model), and, second, each iteration is longer since when computing the plastic correction we showed (see appendix B) that two linear systems have to be solved (while the isotropic model has an analytical solution for the update of the plastic multiplier, see [122]). This need to solve two more systems increases a bit the required memory to compute the solution (from 103.5Mb for the isotropic model to 104.9Mb). Therefore, there is a cost to use the anisotropic model but for a solution which is significantly different. This additional cost is thus worth it.

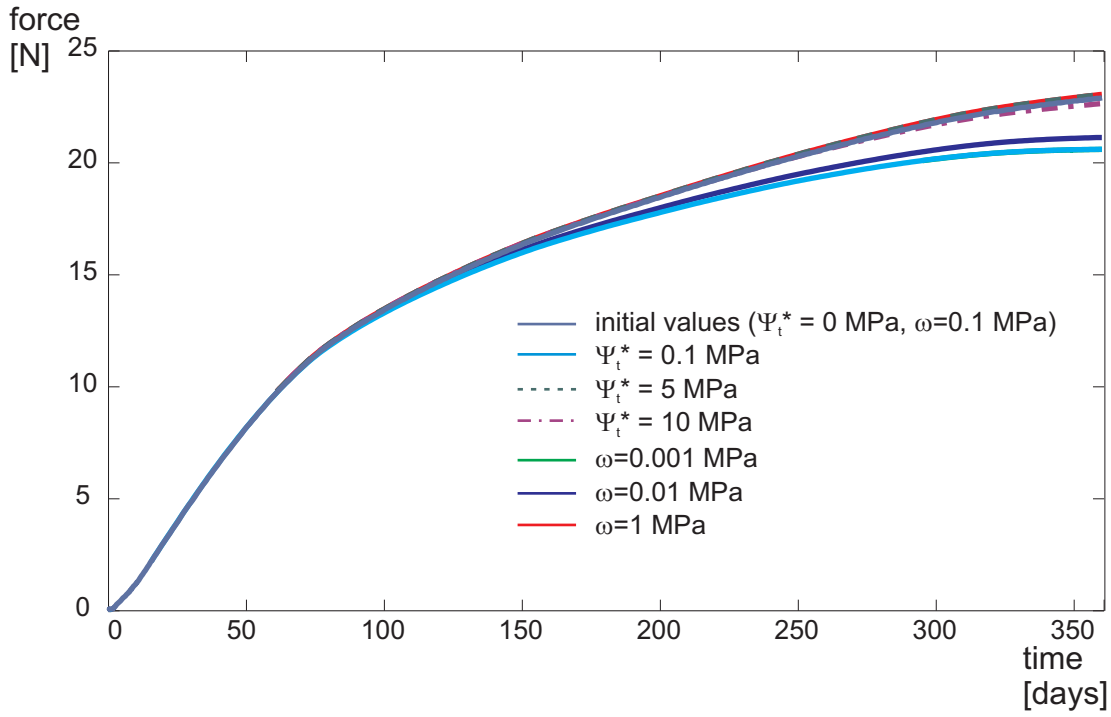

FIGURE 6.24: *Force [N] vs. time [days] and displacement [mm] for the imposed velocity and different values of the two main parameters. The green curves is, at that scale, merged to the light blue one.*

TABLE 6.4: *Comparison of the computational costs between an anisotropic remodeling model and an isotropic one.*

Remodeling Model	CPU Time[a]	Number of mechanical iterations	Memory
	[s]	[-]	[Mb]
anisotropic	2467.23	810	104.9
isotropic	824.06	530	103.
% difference $\left(100\frac{\text{value anisotropic-value isotropic}}{\text{value isotropic}}\right)$	199.4	52.83	1.8

[a] CPU times for the computation on an Intel Core i7-950, 3.07GHz with 8Gb memory and a Win7 64bits OS.

We thus showed in this section that our model can be used to simulate large displacements of the tooth within the bone. This can be achieved using mesh management methods, such as the Arbitrary Lagrangian-Eulerian method used in this case.
We showed the use of an anisotropic remodeling accounting for the elastoplasticity of the material brings significant differences, in terms at least of the required force, compared to either an isotropic remodeling or an elastic material at tissue level.
Within the anisotropic remodeling model, we also showed the characterization of the initial orientation of the morphology (considered here either isotropic, or vertical, or horizontal) is important to evaluate the force, with a difference up to 25% of the required force intensity.
Finally, we showed the remodeling stimulus reaches about the same value in the side of the bone in compression and in the side in tension, even when using a non-linear model for the periodontal ligament (here modeled as bilateral sticking contact conditions). Therefore, the use of remodeling rate definition adapted for the alveolar bone and accounting for the compression or tension state is important to be able to simulate the tooth displacement.
To the best of our knowledge, there is no OTM model in the literature considering a morphological change of the bone that represent tooth translations over such a distance.

6.2.2 Models settings for orthodontic tooth movement applications

For remodeling applications with patient-specific geometry, the geometry used in section 6.1 cannot be used anymore. Indeed, it does not distinguish between trabecular and cortical bone within the alveolus. However, the cortical layer is of high importance as it provides a relatively rigid support to the alveolar complex.
We thus extracted a geometry from CT-scans images (coming from the OSIRIX samples image dataset[1], see Fig. 6.25). These CT images of a mandible were segmented (courtesy of V. d'Otreppe), differentiating cortical bone, trabecular bone, and teeth.

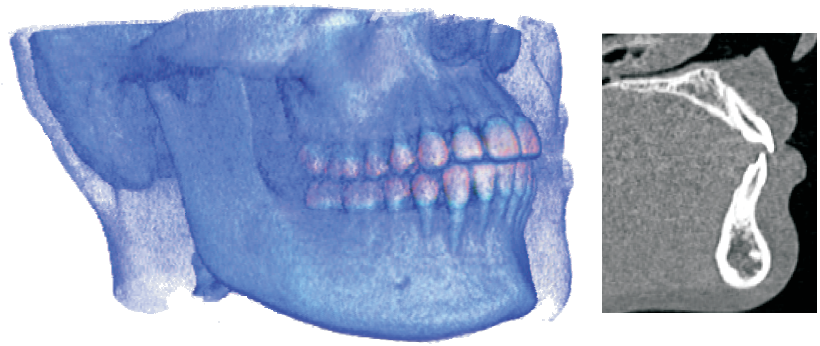

FIGURE 6.25: *OSIRIX/INCISIX dataset - 3D reconstruction of the CT scan images and sagittal slice from which the 2D tooth is reconstructed.*

For the 2D analysis (plane strain), we extracted a slice of the left central incisor in the mesio-distal plane (see Fig. 6.26). We then built the 2D geometry with cubic splines for the tooth, trabecular bone, and cortical bone, with distinct splines at the tooth/bone interfaces (to allow a contact representation of the periodontal ligament) but with only one spline representing the (trabecular) bone/ (cortical) bone interface (which are therefore fully bound to each other). The three built surfaces (cortical bone, trabecular bone, and tooth) were then meshed as previously with quadrilateral elements (with respectively 1161, 2566, and 1022 elements, see Fig. 6.26).
For the 3D analysis, a multiple material surface mesh was constructed [66] from this segmentation, with a duplication of the surface nodes at the tooth/bone interface (Fig. 6.27). A tetrahedron volumic mesh was obtained for each volume using Tetgen [235]. The mesh is thus composed of 57878 tetrahedron elements representing the tooth, 188845 elements for the cortical bone, and 213882 elements for the trabecular bone (Fig. 6.28). However, the surface at the bone/tooth interface is not smooth enough to apply contact conditions representative of the periodontal ligament. In order to still use a non-linear representation of the mechanical behavior of the PDL, we will here use non-linear spring elements between the tooth root and the bone surfaces (as described in section 6.1).
For all the following analysis, the tooth is assumed either to behave as an elastic material (Young's modulus of 19GPa and Poisson's ratio of 0.3) or to be a rigid body. Bone tissue is

[1] OSIRIX/INCISIX dataset http://www.osirix-viewer.com/datasets/

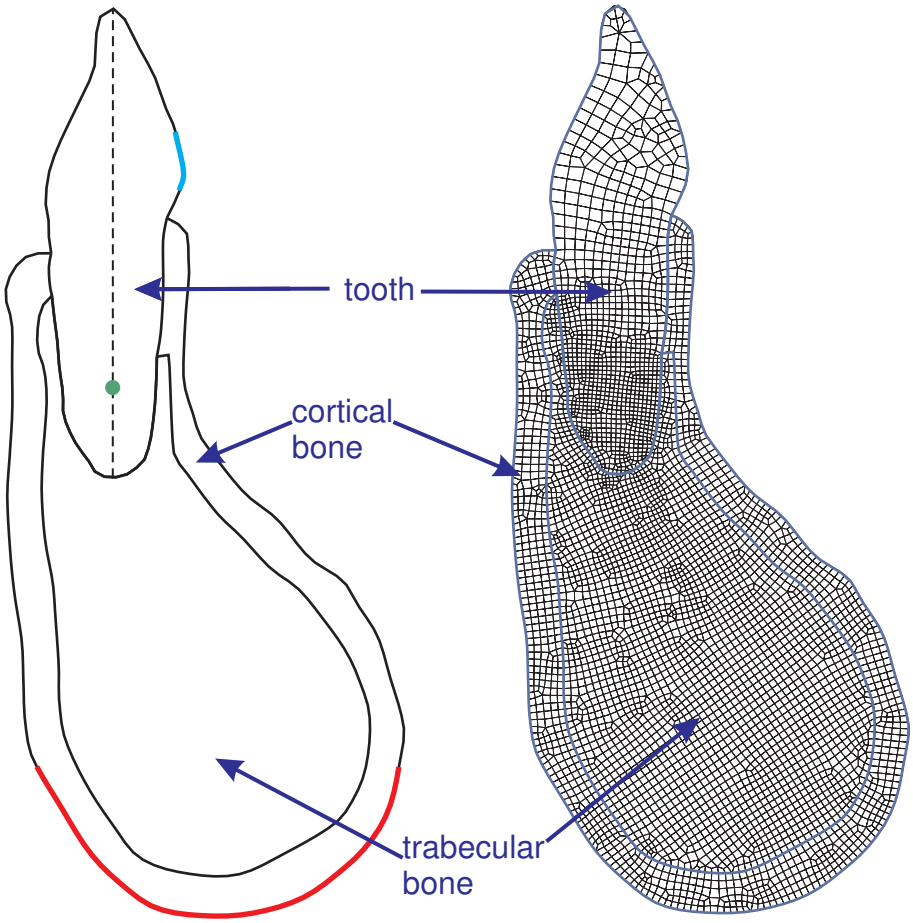

FIGURE 6.26: *2D geometry and associated mesh in the mesiodistal plane of the left central incisor extracted from the OSIRIX/INCISIX image dataset. When we refer to the basal bone which is considered fixed, we refer to the red curve; the light blue curve is the position of the applied pressure (for problems with applied pressure); the green dot is the position around which the tooth is rotated (for controlled rotation problems); the main axis of the tooth is also represented (axis perpendicularly to which the tooth is translated for translation controlled problems or a force is applied on the bone for bodily tooth movements).*

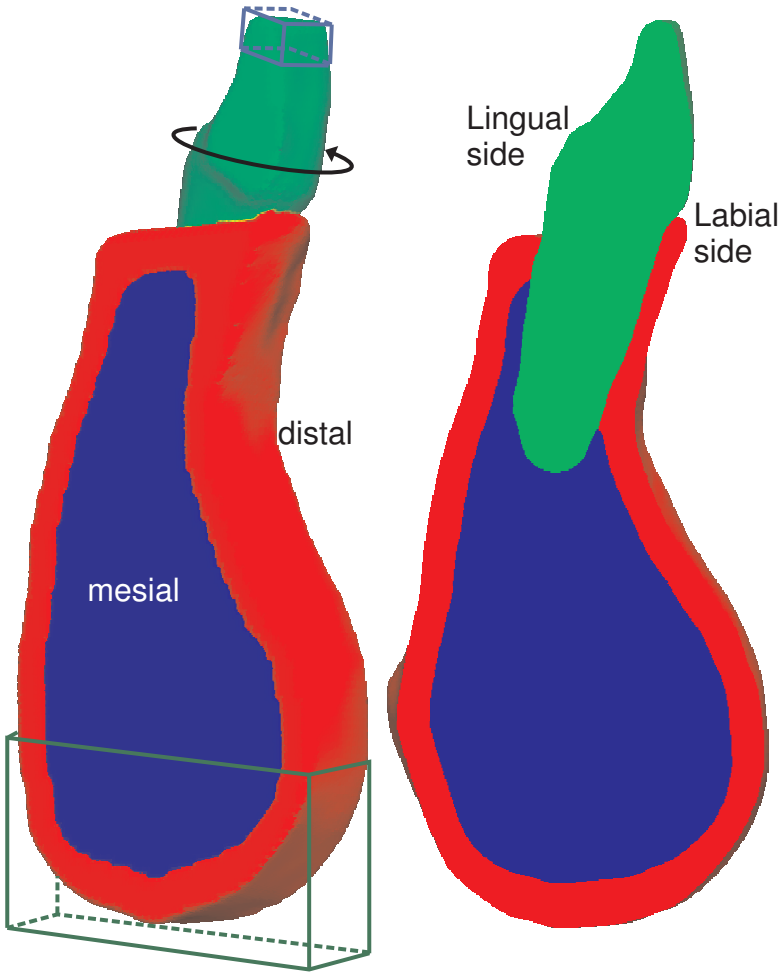

FIGURE 6.27: *3D geometry and cut in the mesiodistal plane of the left central incisor extracted from the OSIRIX/INCISIX image dataset. In green, the tooth, in red cortical bone, and blue trabecular bone. The applied boundary conditions are either imposed rigid rotation of the tooth around its main axis (black circular arrow) or the application of an intrusion force on the surface nodes situated in the blue box. The surface nodes situated in the green box are clamped.*

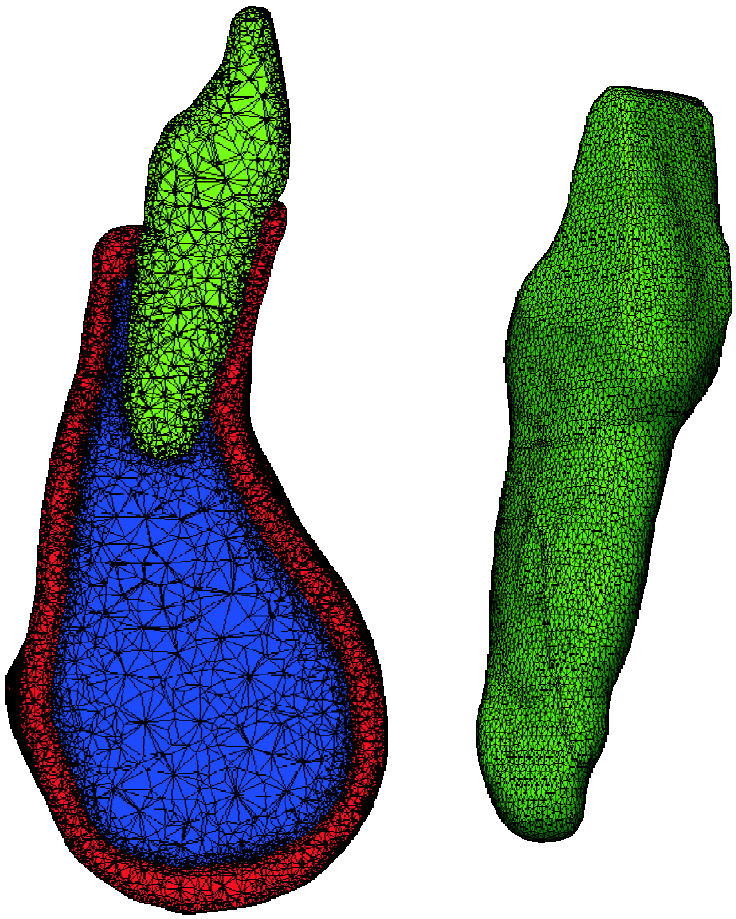

FIGURE 6.28: *3D mesh and cut in the mesiodistal plane of the left central incisor extracted from the OSIRIX/INCISIX image dataset. In green, the tooth (whose surface mesh is highlighted on the right), in red cortical bone, and blue trabecular bone. The mesh is fine at the surface and interfaces but coarser in volume.*

TABLE 6.5: *Summary of the material parameters*

Material	Young's modulus $[GPa]$	Poisson's ratio $[-]$	Yield stress $[MPa]$	Hardening parameter $[MPa]$
Tooth	19.0	0.3	-	-
Bone at tissue level	13.75[a]	0.3	200.0	723.7

Type of bone tissue	Initial apparent density $[gr/cc]$	Equivalent Young's modulus[a] $[GPa]$
Trabecular	0.95	1.77
Cortical	1.805	11.67

[a]Values obtained using Equ. 5.9 and considering a tissue density of 1.9gr/cc

assumed to behave as a material following the developed remodeling constitutive model, for both types of bones (with a fully mineralized density of 1.9gr/cc, cortical initial porosity of 0.05, trabecular initial porosity of 0.5 - see table 6.5). We consider a trabecular bone initially isotropic but subject to anisotropic remodeling. The cortical bone is however, as discussed in section 4.4, subject to isotropic remodeling only, it therefore maintains its initial isotropy. In the 2D analysis, the periodontal ligament mechanical behavior is described by contact conditions as detailed in the previous section. In the 3D analysis, it is described with equivalent spring elements.

The boundary conditions differ for each analysis but for all of them, the basal bone is considered as fully clamped in all directions. As mentioned earlier, the initial conditions and the loading conditions do not accurately represent actual orhtodontic problems but are rather academic cases. In particular, the time span of the problems is determined only by the remodeling constants c_r and c_f. We express these constants in $\mu m/(\text{day}MPa)$, the time needed for the application of the applied loading (imposed displacement or force) is, if not specified otherwise, a tenth of a day and we observe the force or displacement variation over a period of six months. In resorption conditions, if not specified otherwise, we use a remodeling constant c_r of $10\mu m/(\text{day}MPa)$. In formation conditions, the remodeling constant is twice lower [71, 262]. The other remodeling parameters are given in table 6.6.

TABLE 6.6: *Remodeling parameters*

number of daily load cycle	: $N = 1$
homeostatic value of the stimulus	: $\psi^\star = 0\ MPa$
exponent of the stress stimulus	: $m = 4$
remodeling velocity for resorption	: $c_r = 0.01 mm/(\text{day} MPa)$
remodeling velocity for formation	: $c_r = 0.005 mm/(\text{day} MPa)$
half-width of the lazy zone	: $\omega = 0.1\ MPa$
parameter weighing the hydrostatic and deviatoric parts of the effective stress definition[a]	: $\eta = 1.$

[a] Chosen as the initial degree of anisotropy, i.e. 1.0 as the tissue is considered as being initially isotropic.

6.2.3 Displacement driven tooth movement

The first applications on realistic geometries are displacement driven, i.e. either tooth rotations or tooth translations. We will present here both 2D and 3D models, considering rigid displacements of the tooth. The effect of remodeling is a variation of the force needed to maintain a given displacement. We will also analyze the effects of the remodeling anisotropy.

Tooth rotation

A rotation movement is applied to the tooth root with a center of rotation situated at $3mm$ from the root apex (Fig. 6.26), i.e. below one third of the root length (which is of $10.2mm$) as proposed in [269] among others. Tipping is kept to obtain an angle of three degrees with respect to the tooth axis, in the lingual direction. Getting from an angle of zero to the final angle is done is a tenth of a day and this angle is maintained constant during 180 days. Bone density variation is observed during this constant displacement period, leading to a reduction of the force required to maintain the movement.

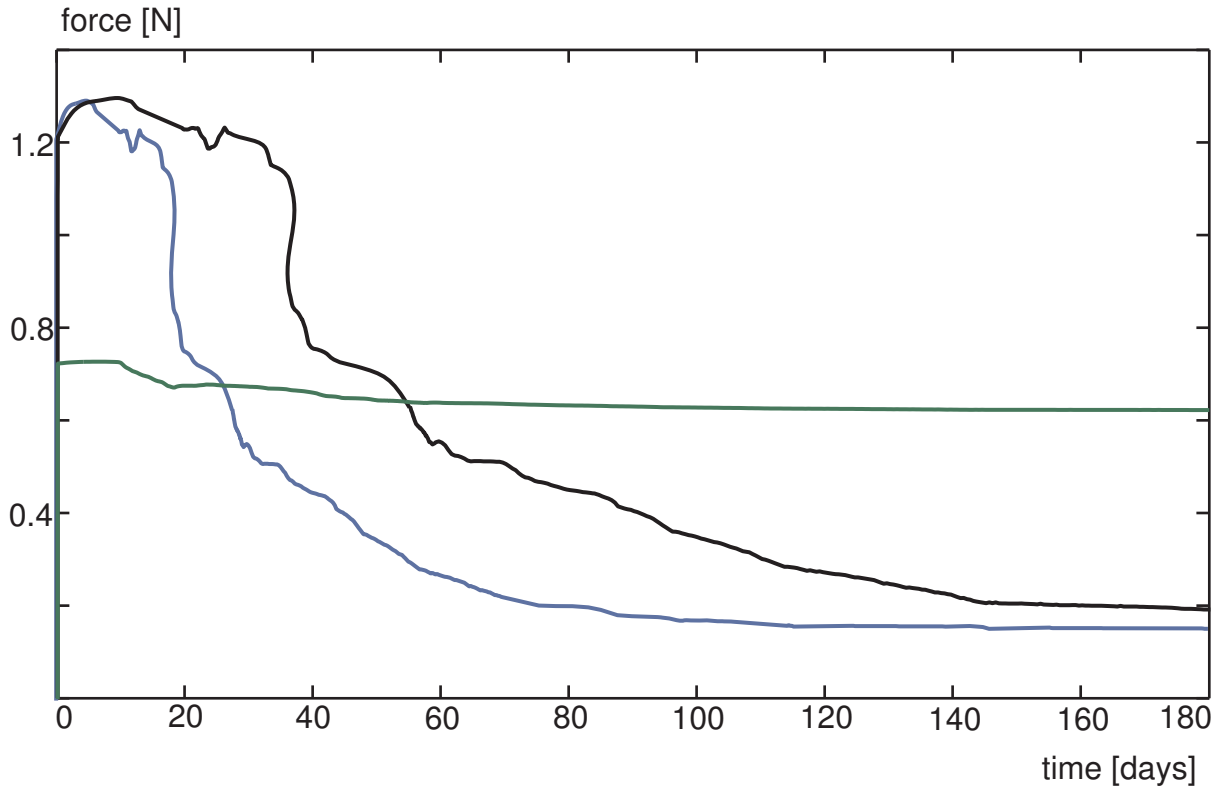

FIGURE 6.29: *Displacement driven tooth movements - intensity of the force [N] needed to maintain a displacement over time [days]. In green: rotation movement, in black: translation movement, and in blue: translation with a remodeling constant twice as low as the previous one.*

The tooth movement is rigid around the center of rotation, therefore, the displacement (see

Fig. 6.30, left), due to the imposed rotation, is at the top of the tooth of $843\mu m$ towards the lingual side and at the apex of $154\mu m$ towards the labial side. The force needed to get such a rigid rotation is about $0.72N$ (see Fig. 6.29, green curve). This force level is consistent with orthodontic forces reported in the literature [27, 227, 250, 276] This force remains constant for the two first weeks as a small hyaline zone formed at the apex and impedes a direct remodeling leading to a reduction of the total force. Remodeling is going on around this zone in such a way that the hydrostatic pressure decreases (in absolute value). This decrease in pressure is equivalent to a removal of the hyaline zone. Once the pressure is low enough (below the critical level defined by the vascular pressure), the remodeling goes on in this zone and the total force needed to maintain the rotation starts decreasing. The force decreases for about five more weeks down to $0.64N$ and then remains constant over time. The bone density varies rapidly on the lingual side to reach its maximal value at some places after 50 days (Fig. 6.31, left). The stimulus has not reached its equilibrium at that time (Fig. 6.31, right) but as the bone density cannot change anymore, the remodeling stimulus does not change either. The trabecular bone, while initially with an isotropic morphology, orients itself so that it is aligned with the principal stress directions which themselves are oriented along the rotation lines (see Fig. 6.32(a)).

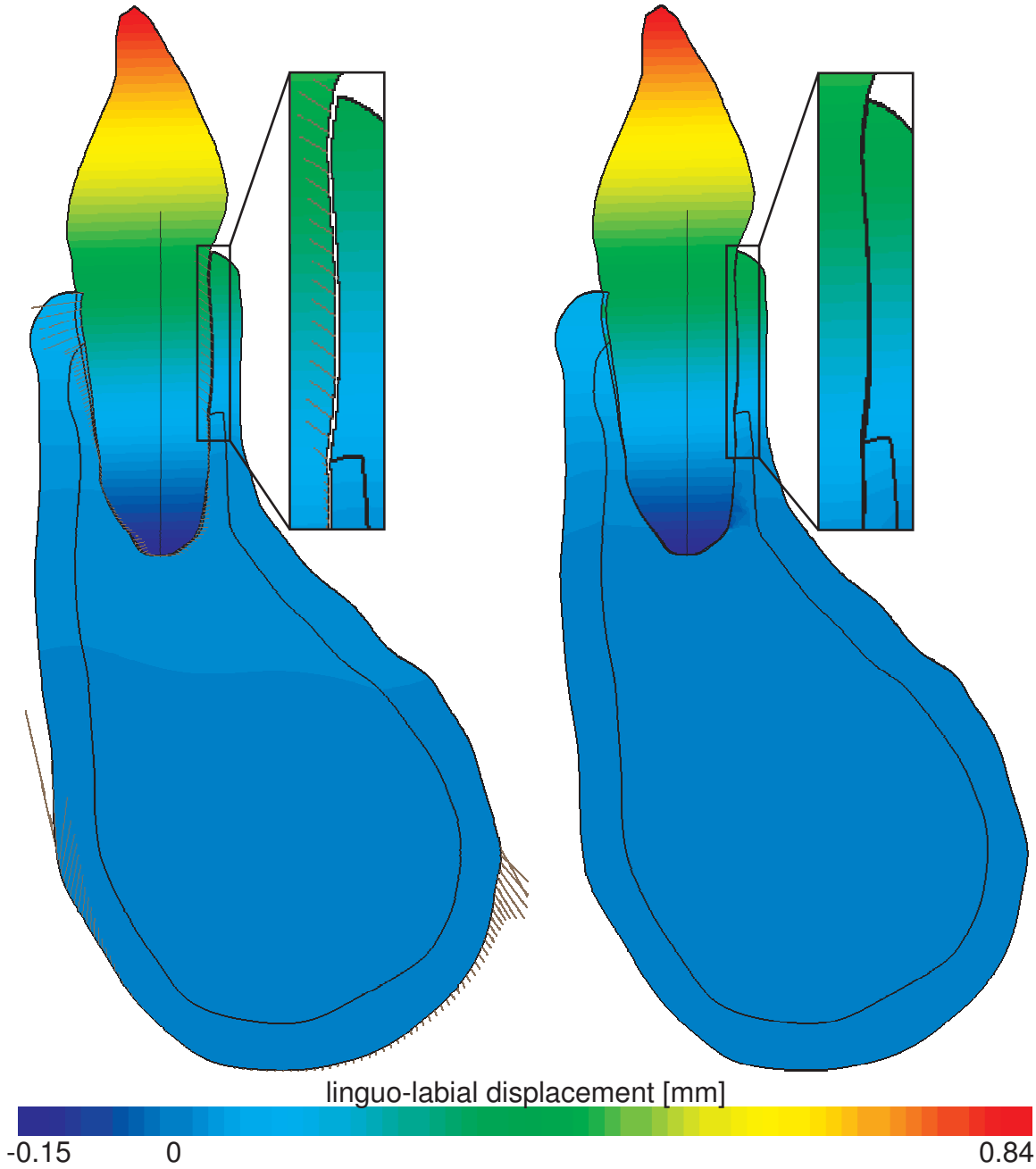

FIGURE 6.30: *Movement of rotation - linguo-labial displacement [mm]. On the left: at the end of the loading phase (the lines show the force direction and intensity needed to maintain the rotation); on the right after 3 weeks of remodeling. Notice the gap closing on the labial side.*

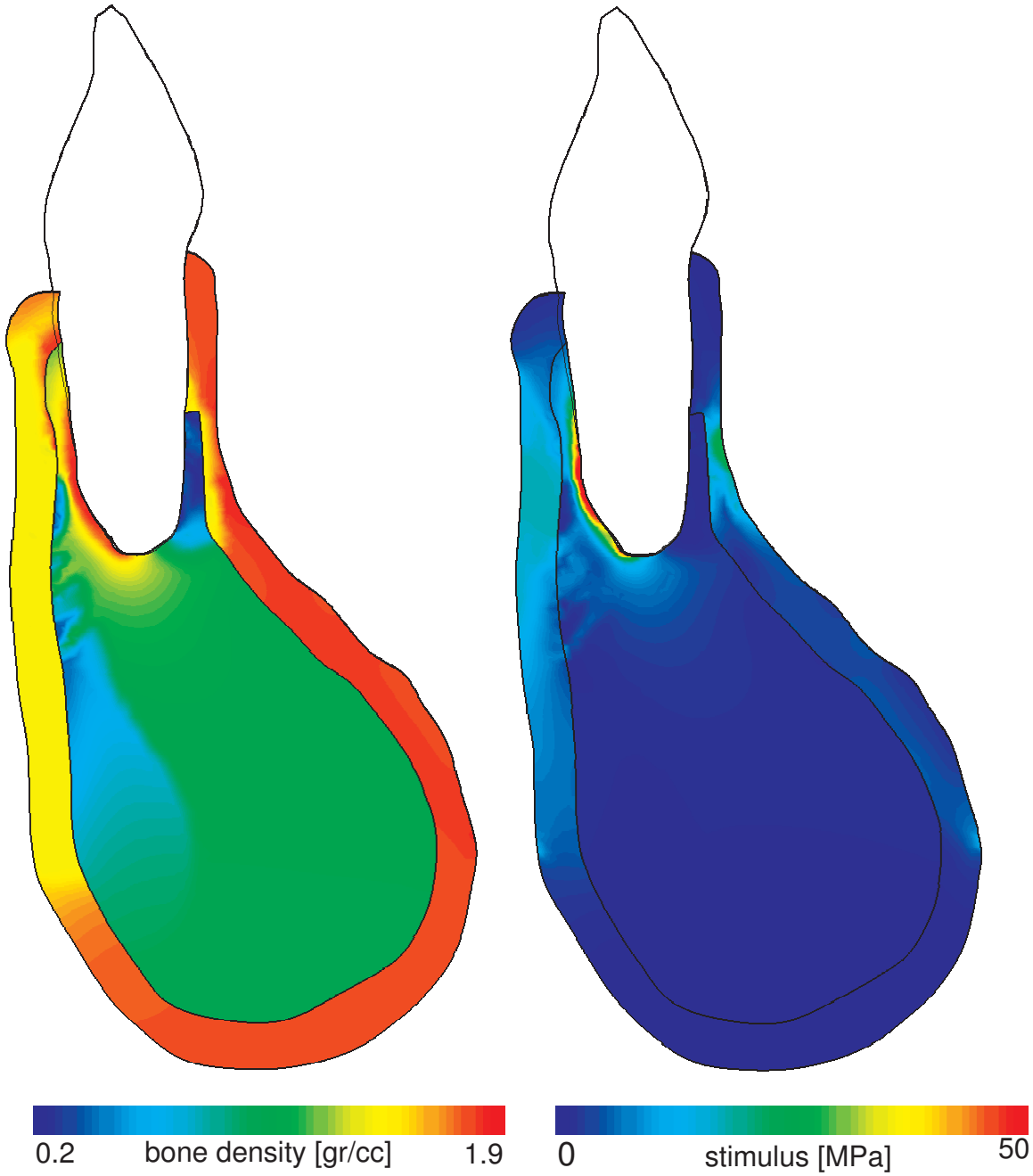

FIGURE 6.31: *Movement of rotation after 50 days - on the left: bone density [gr/cc]; on the right: bone remodeling stimulus [MPa].*

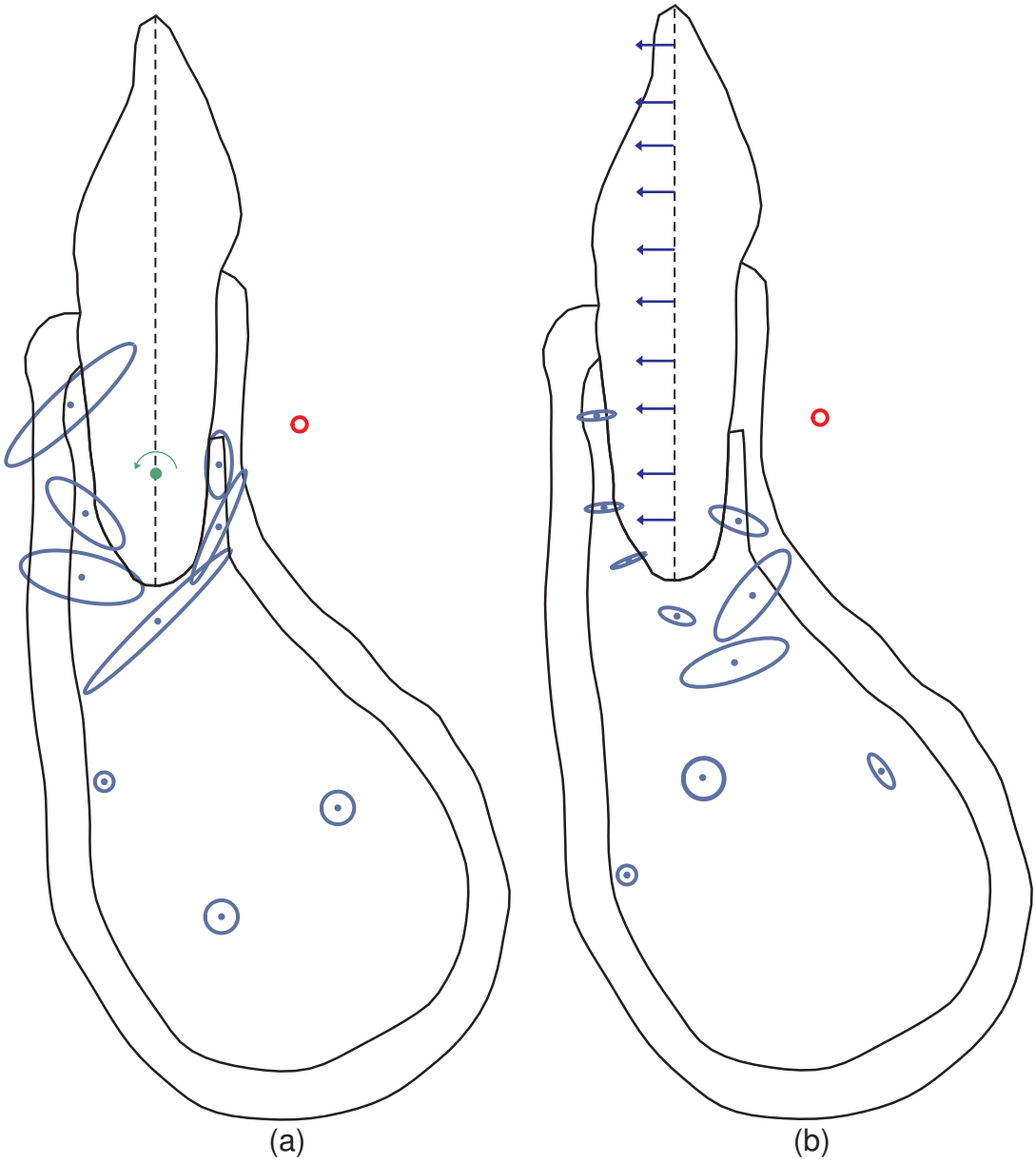

FIGURE 6.32: *Trabecular bone orientation - (a) Movement of rotation after 50 days, (b) Movement of translation after 180 days. The ellipses represent the stiffness value (the axis orientations are those of the fabric tensor eigenvectors and their lengths are proportional to the fabric tensor eigenvalues), a 1GPa isotropic indicator is also depicted in red.*

Tooth translation

A translation movement whose amplitude is identical to the periodontal ligament width (i.e. a movement of 0.2mm) is applied to the tooth root perpendicularly to its main axis, towards the lingual side of the tooth (Fig. 6.26). The movement is applied is a tenth of a day and this displacement is kept constant during 180 days. Bone density variation is observed during this constant displacement period, leading to a reduction of the needed force.
The force needed to obtain such a translation movement is higher than for the rotation, about $1.2N$ (see Fig. 6.29, black curve). The formation of hyaline zones appear only on one side of the tooth (Fig. 6.33), allowing however for formation to occur on the tension side. Therefore, the initial trend of remodeling is to increase the force needed to keep the displacement constant. During the time hyaline zones are present, remodeling occurs mainly around these zones, resorbing them (see Fig. 6.34, left). Once the hyaline zones are resorbed due to peripheral remodeling (after about forty days, see Fig. 6.34, right), the force decreases fast as the bone density can decrease lingually (the compression side of the tooth). A force reduction by a factor of two is observed in only 20 days. The force then continues to slowly decrease down to about $0.2N$ after 150 days, time after which not much variation can be observed. We can also notice that after 70 days (Fig. 6.34, zoomed areas), the contours of the bone at the bone/tooth interface matches those of the tooth, as remodeling tends for the bone to 'follow' the tooth.

Applying exactly the same boundary and loading conditions but considering a remodeling constant twice higher (both for the formation and resorption constants), leads, as expected since the remodeling constants are the only drivers of the time dependence of the problem, to the same results but twice as fast. Therefore, the level of $0.2N$ is reached in about 75 days (see Fig. 6.29, blue curve). After this period, the force level continues to decrease but very slowly, reaching only $0.16N$ after the 180 days of observation. This leads to believe the equilibrium is obtained after this time.

We should notice that because of the boundary conditions at the basal bone, some computational hyaline zone form around the end of the bone anchorage in compression (see Fig. 6.33, right, dark blue zone). This zone is qualified as a computational hyaline zone because it would not be present physically. Thee area-of-influence of these boundary conditions however does not extend all the way to the tooth on the compression side.
On the tension side however, the anchorage end point seems on the long term to extend its influence all the way to the tooth (see Fig. 6.33, right, yellow zone). This can be a major issue if the effect of remodeling (i.e. the force variation) is mainly influenced by the application of boundary conditions. Changing the boundary conditions by fixing a boundary twice smaller, leads to an initial force required to apply the translation higher than previously (Fig. 6.35) as more volume of bone is displaced by the movement (less bone is fixed). The stress is lower around the tooth, therefore the extend of the hyaline zone around the tooth is smaller, almost non existent. There is thus no hyaline zone to resorb before remodeling can occur and

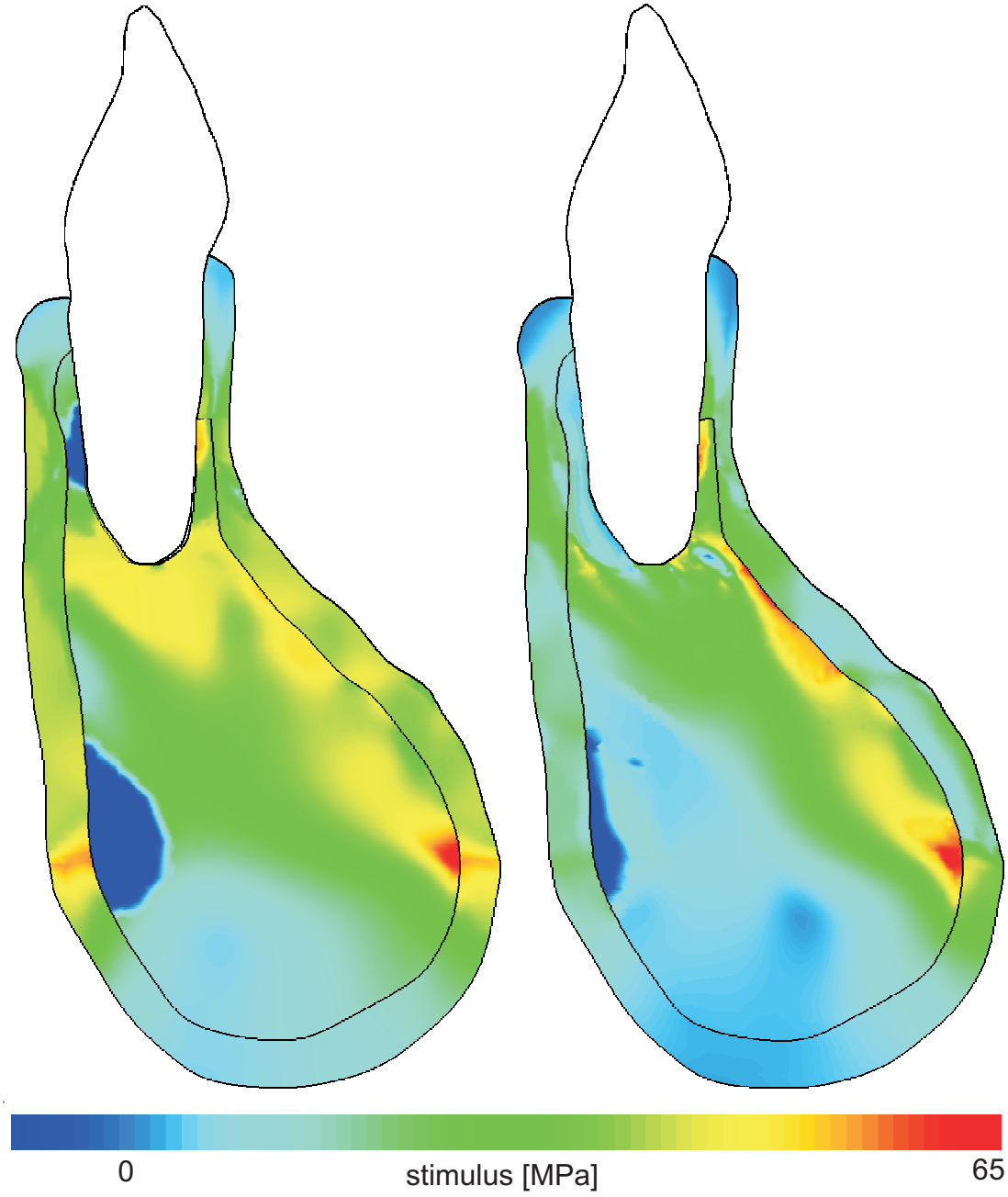

FIGURE 6.33: *Tooth translation: bone remodeling stimulus [MPa] at the end of the loading phase (left) and after 40 days (right). Values below zero are representative of the hyaline zones.*

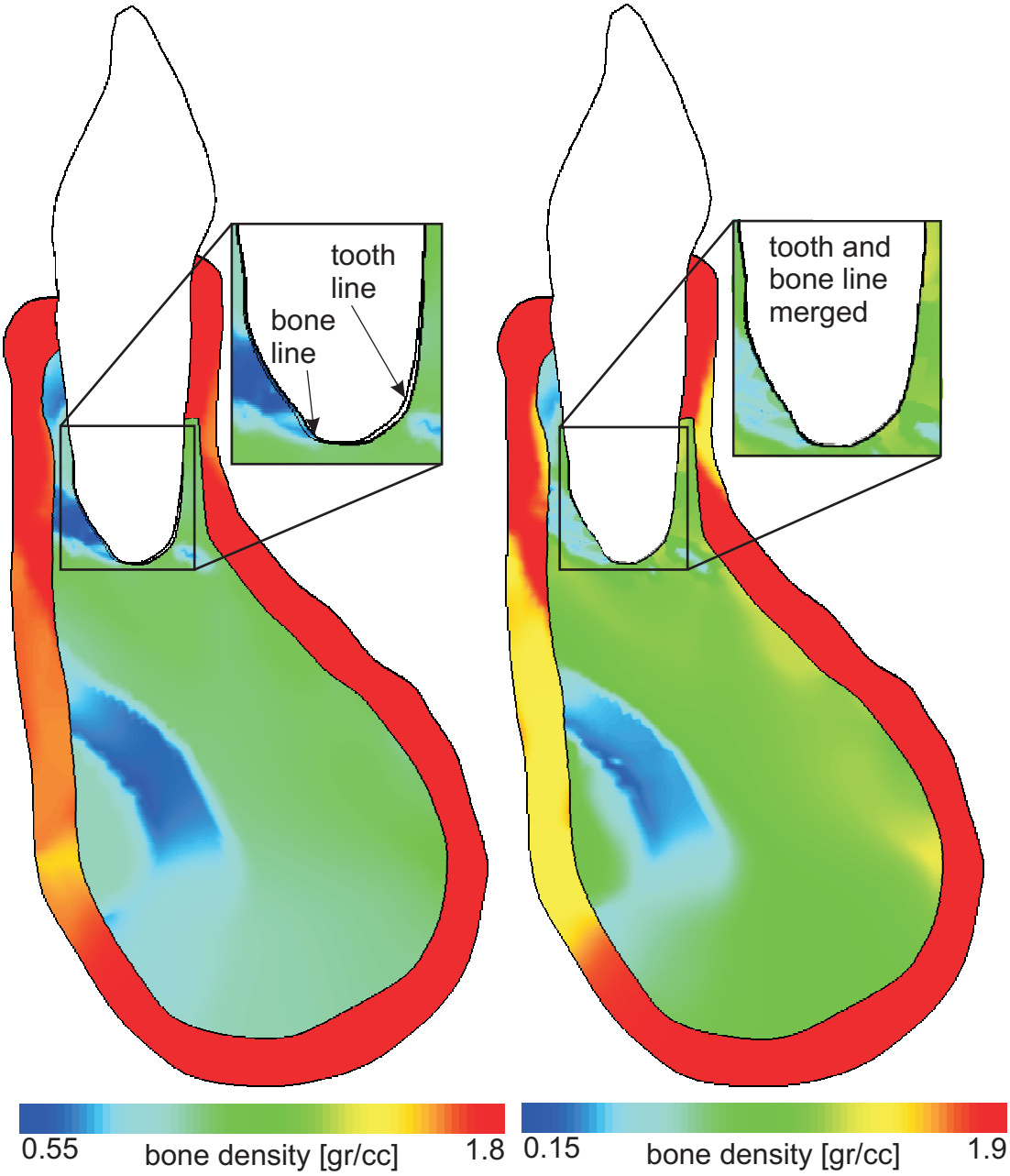

FIGURE 6.34: *Tooth translation: bone density [MPa] after 35 days (left) and after 70 days (right).*

the force variation starts immediately. However, the force level eventually reaches about the previous one but staying a bit higher (about $0.05N$ higher as from the 35th day of remodeling). Therefore, we can consider that on the long term, the boundary conditions do not have much of an effect but the initial remodeling is however strongly affected by the boundary conditions.

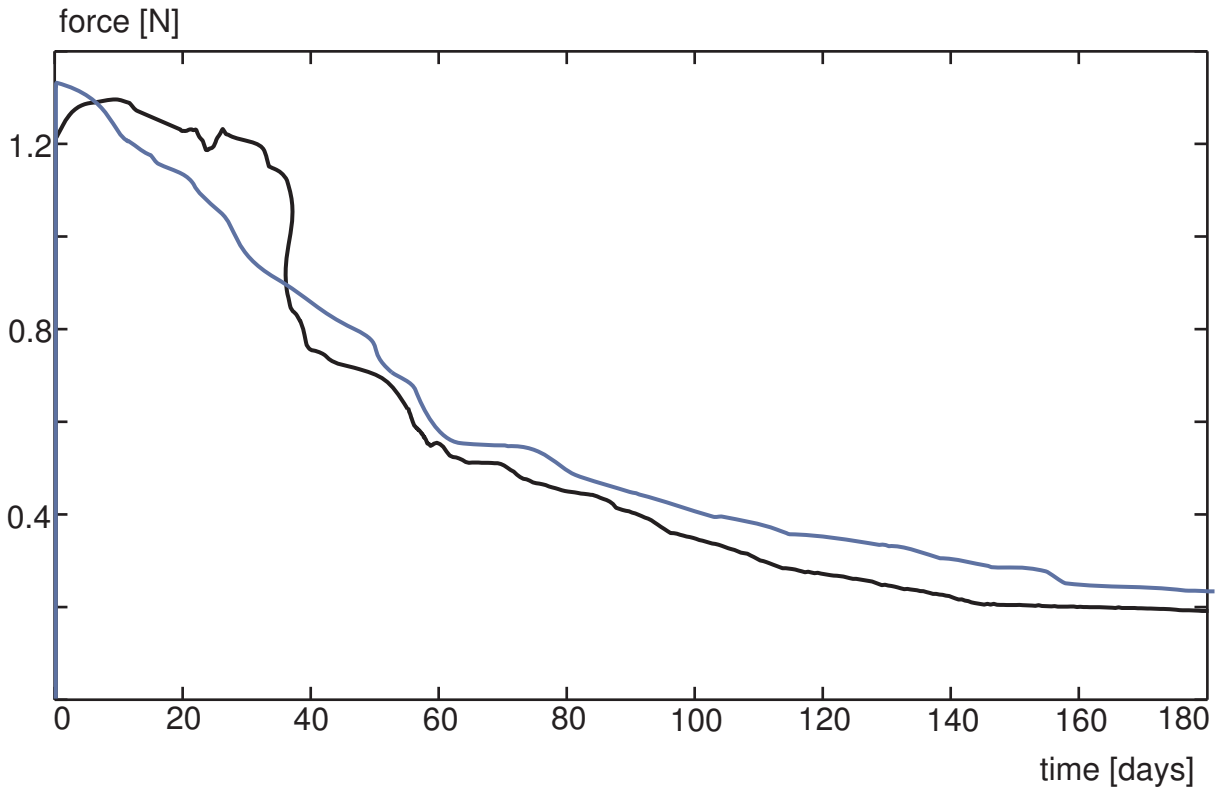

FIGURE 6.35: *Intensity of the force [N] needed to maintain a translation over time [days]. In black: initial boundary conditions, and in blue: clamping boundary conditions applied on a reduced zone.*

Rotation of the tooth around its axis

In a 3D model, a third type of displacement can be applied, a rotation of the tooth around its main axis. We here consider a 2^o rotation of the tooth (see Fig. 6.27) around its main axis. The movement is applied in a tenth of a day and this rotation is kept constant during a month (31 days). Bone density variation is observed during this constant rotation period, leading to a reduction of the needed force.
The required force intensity to obtain such a movement is consistent with typical force levels used in orthodontic treatments, i.e. 1.15N (Fig. 6.36).

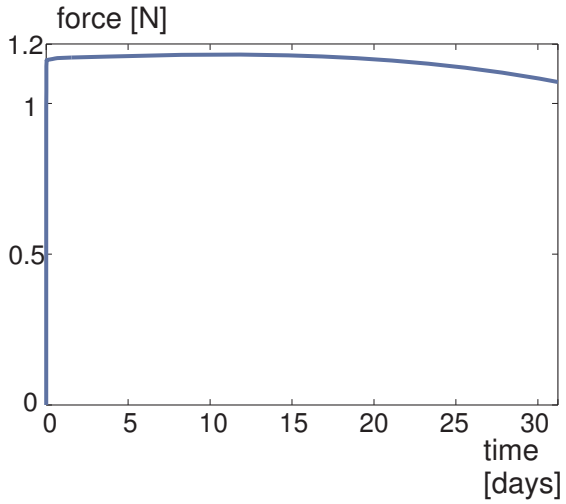

FIGURE 6.36: *Intensity of the force [N] needed to maintain a rotation of the tooth around its axis over time [days].*

Because of the rotation movement and since the root is not symmetric around its main axis, the bone surrounding the tooth is alternatively in tension and in compression, leading to the creation (Fig. 6.37) of either formation zones or hyaline zones (since the compression is high). The beginning of remodeling in resorption does therefore not appear at the bone/tooth interface but further away, resorbing the hyaline areas. The remodeling occurs in such a way that the rotation movement is facilitated (Fig. 6.38), decreasing the density where the bone is compressed due to the rotation, and increasing the density where it is in tension. The amount of resorption after 15 days of remodeling is however less than the amount of formation as the remodeling in the compression areas first occurs to remove the hyaline zones and not to resorb bone. These area are still present after the 31 days of observation, slowly moved away. The bone density after 31 days therefore shows the same pattern as after 15 days, with less resorption than formation (Fig. 6.39). Thus, the force to maintain the rotation, while slightly increasing at an early stage, stays almost constant for about two weeks, then decreases when most of the hyaline areas are removed (Fig. 6.36). After 31 days of remodeling, there are however still hyaline areas present at some places, thus areas where the bone density does not change.

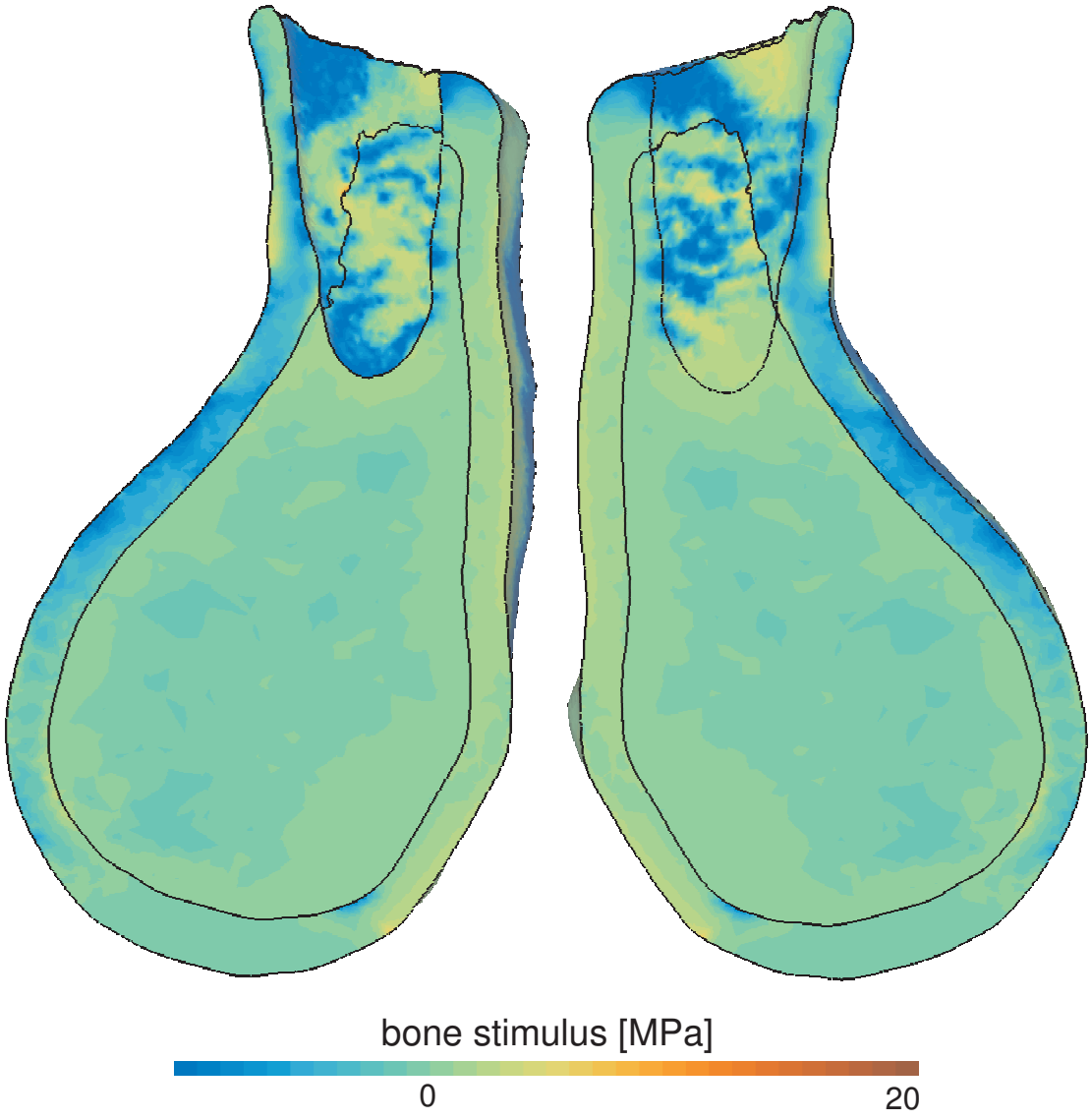

FIGURE 6.37: *Rotation: bone remodeling stimulus [MPa] at the end of the loading phase. Sagittal cuts - left: lateral view, right: medial view. Values below zero are indicative of the presence of a hyaline zone.*

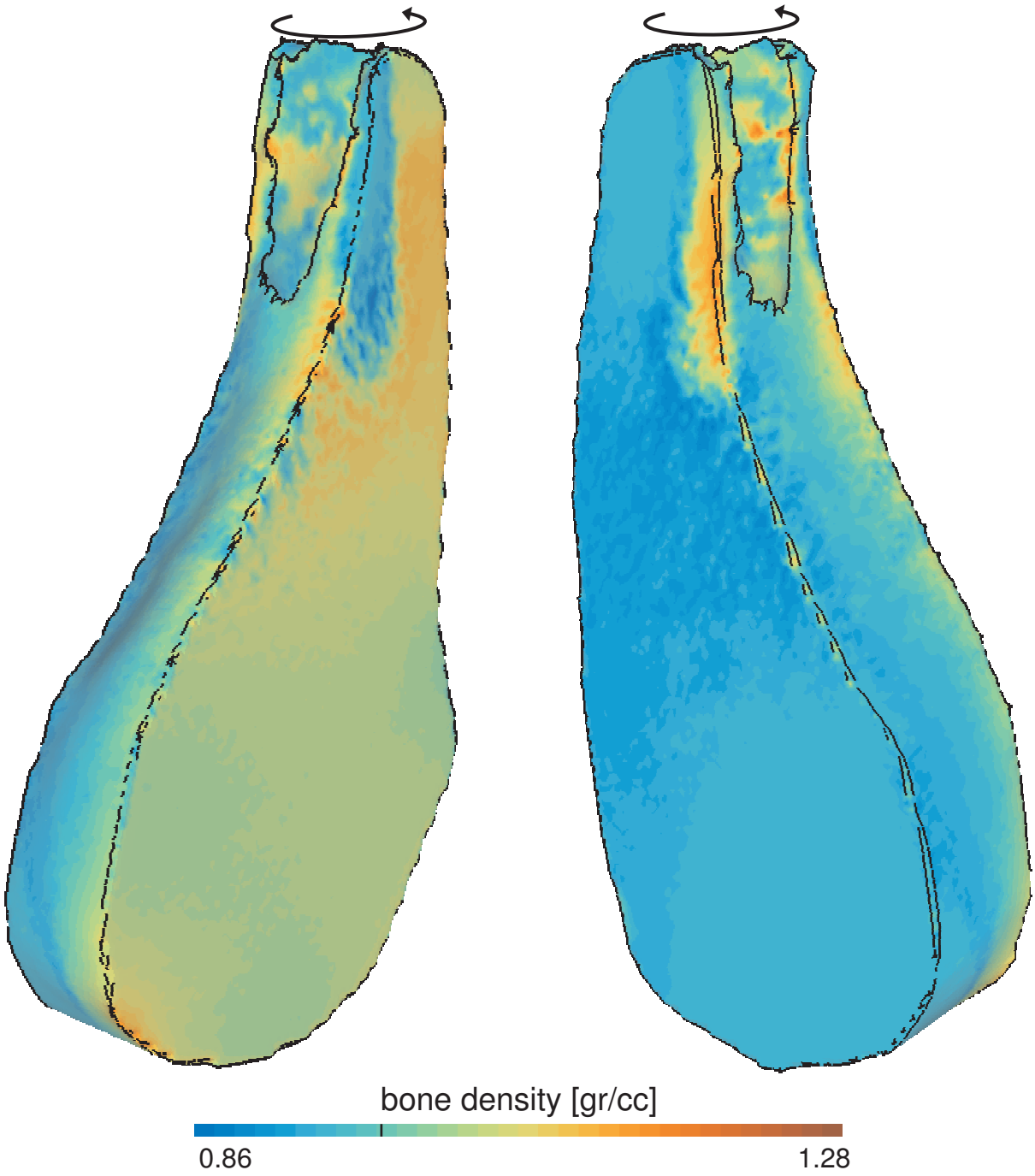

FIGURE 6.38: *Rotation: bone density [gr/cc] after 15 days of remodeling. Trabecular bone only, left: lateral view, right: medial view. The curves arrows remind the imposed tooth movement. The black line in the colorbar is the initial density, i.e. 0.95gr/cc.*

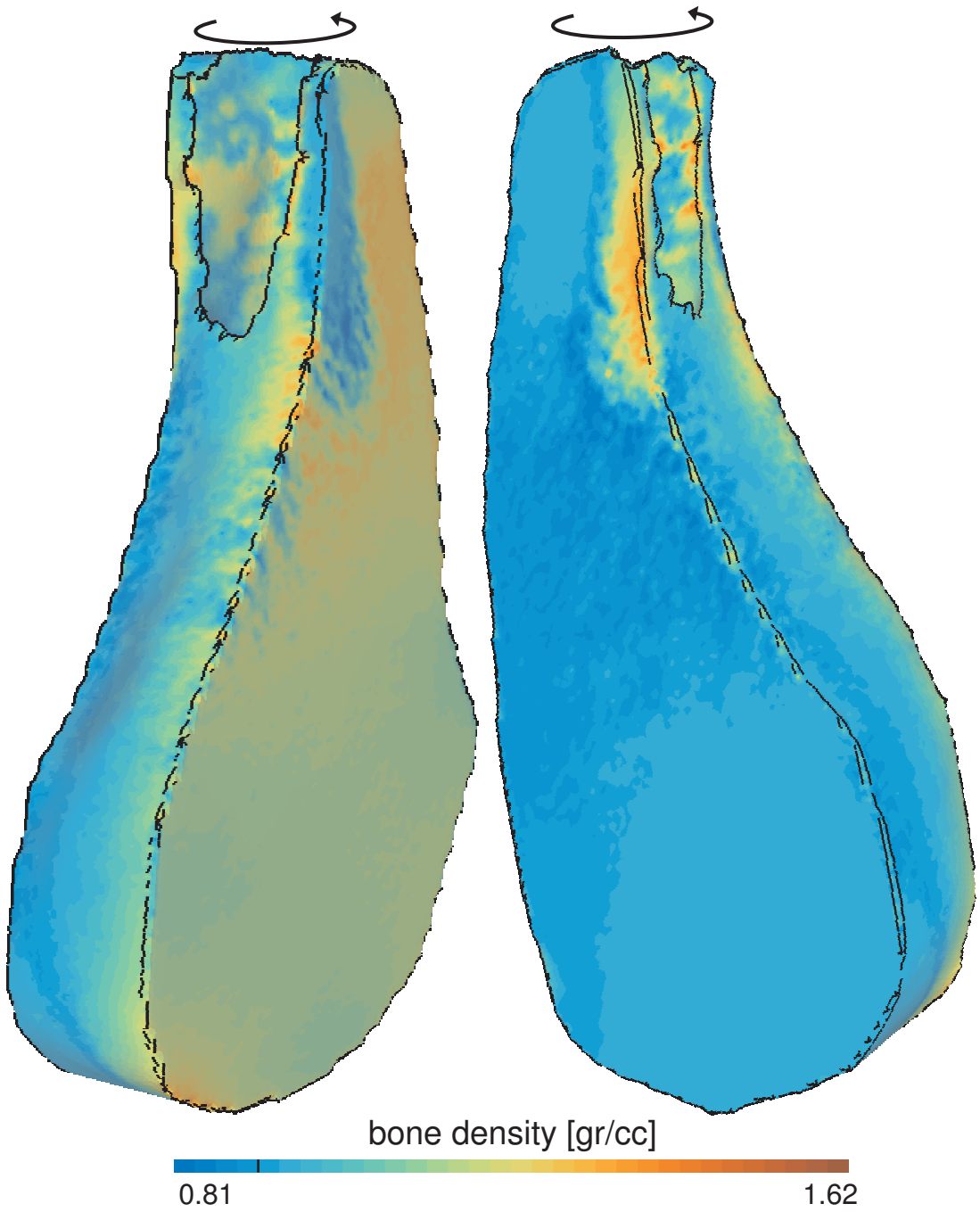

FIGURE 6.39: *Rotation: bone density [gr/cc] after 31 days of remodeling. Trabecular bone only, left: lateral view, right: medial view. The curves arrows remind the imposed tooth movement. The black line in the colorbar is the initial density, i.e. 0.95gr/cc.*

6.2.4 Force driven tooth movement

The second type of applications are force driven, i.e. either tipping, en-masse tooth movement, or intrusion movements. We will present here both 2D and 3D models, considering either rigid displacements of the tooth (the force being then directly applied to the bone, through the contact interface of the PDL) or a deformable tooth (the force being then applied to the tooth). The effect of remodeling is a variation of the displacement required to maintain a given force intensity and direction.

Tipping of the tooth

A tipping movement is obtained by applying a pressure force on the crown (Fig. 6.26). Starting from a 0N force, a 0.7N force is reached by applying a continuous variation of the load during a tenth of a day. This force intensity is kept constant during 180 days. Bone density variation is observed during this constant force period, leading to an increase of displacements.
As expected the movement induced by the pressure on the crown is a tipping movement, i.e. a rotation of the tooth around a point situated at about one third of the root height (see Fig. 6.40). As the applied force can be characterized as low (as long as orthodontic forces are considered), no hyaline area is formed on the compression sites of the tooth (lingual apex and labial collar). The density variation due to remodeling can therefore start directly. After 20 days, the resorption at the labial apex is already high with a density down to 0.25gr/cc (see Fig. 6.41). After 40 days, the bone has reached at some places its minimal density at the labial apex while a cortical-like (density-speaking, not morphologically) layer appears at the lingual apex. Remodeling at the collar (composed of cortical bone) is however slower, therefore the tooth movement is impeded.
There is not much further remodeling going on around the apex. After 100 days, we can see the predicted bone density begins to exhibit a probably unphysiologic appearance. This takes the form of a progressive replacement of regions of continuous apparent density with strut-like structures (see Fig. 6.41, right - resorption on the lingual side of the trabecular bone). This phenomenon as already been reported in [117] where strut-like structures were observed in the remodeling of the proximal femur. The explanation proposed then is that such structures are more metabolically efficient to maintain since they involve less total bone mass and are thus preferred to a more continuous morphology. They are represented by the remodeling model as its principle is to optimize a mechanical stimulus involving bone density with respect to the strain energy density. These structures are a numerical phenomenon and will not appear in real situations for two main reasons: First, the simplification of the complex physiological and therapeutic loadings (and their histories) to a simple pressure load allows for numerical predictions of strut structures that are precisely oriented to support the numerically applied loads. These structures would experience high bending when exposed to other load cases, and would thus be inhibited. Second, it is well accepted that

within a zone near remodeling equilibrium, other non-adaptive aspects of bone physiology dominate the remodeling response, and are not represented in the numerical model. Concerning the obtained displacements, even tough it is limited, we can see that initially the bone at the apex tends to move lingually and progressively as remodeling is going on, the bone adapts itself around the apex to move labially (see Fig. 6.42).

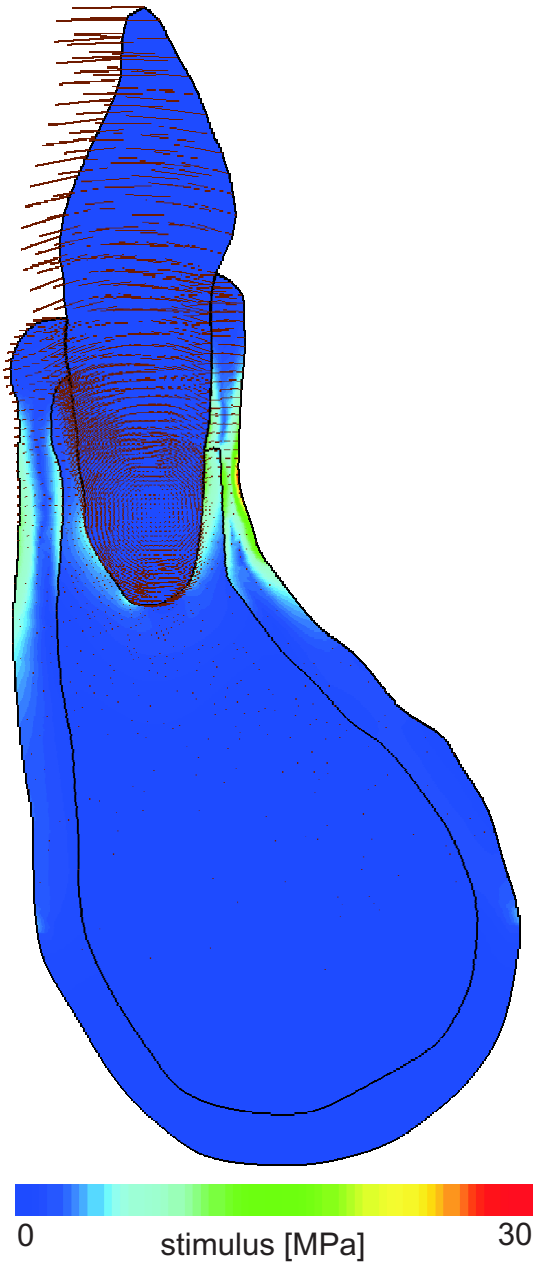

FIGURE 6.40: *Tipping: bone remodeling stimulus [MPa] at the end of the loading phase. The lines correspond to the displacement field and emphasize the rotation movement.*

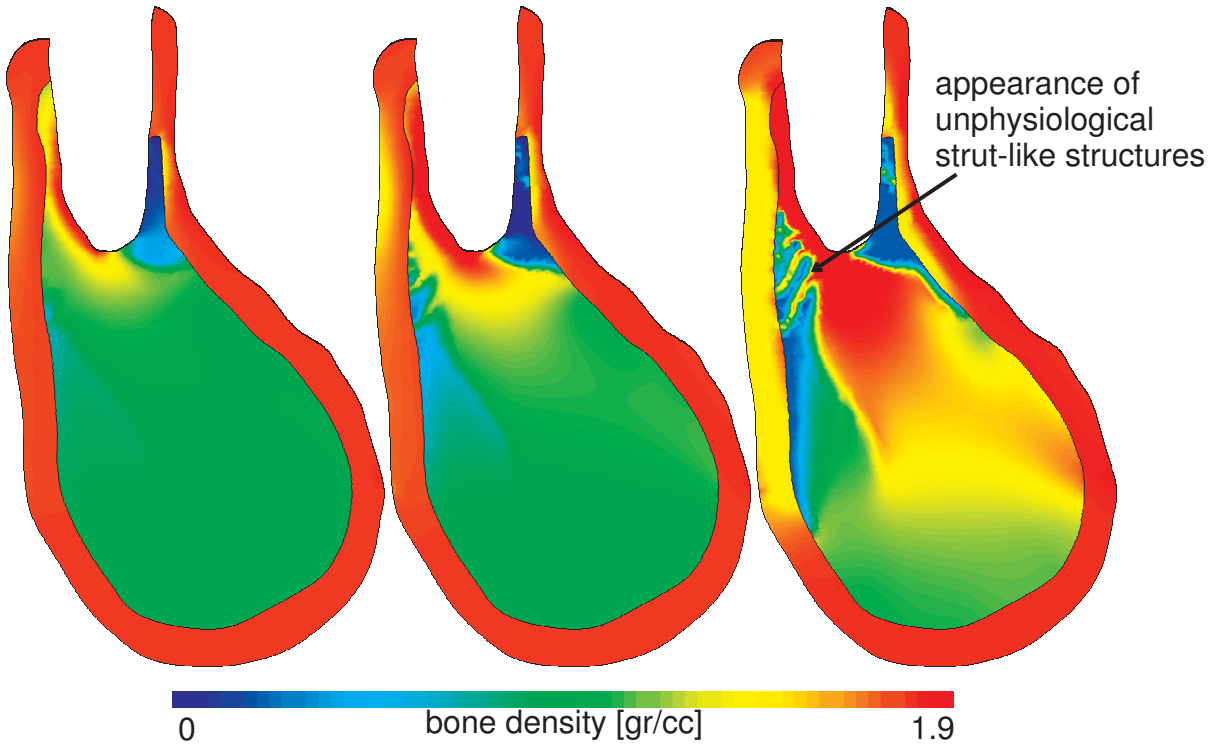

FIGURE 6.41: *Tipping: bone density [gr/cc] during the remodeling period. Left: after 20 days, center: after 40 days, right: after 100 days.*

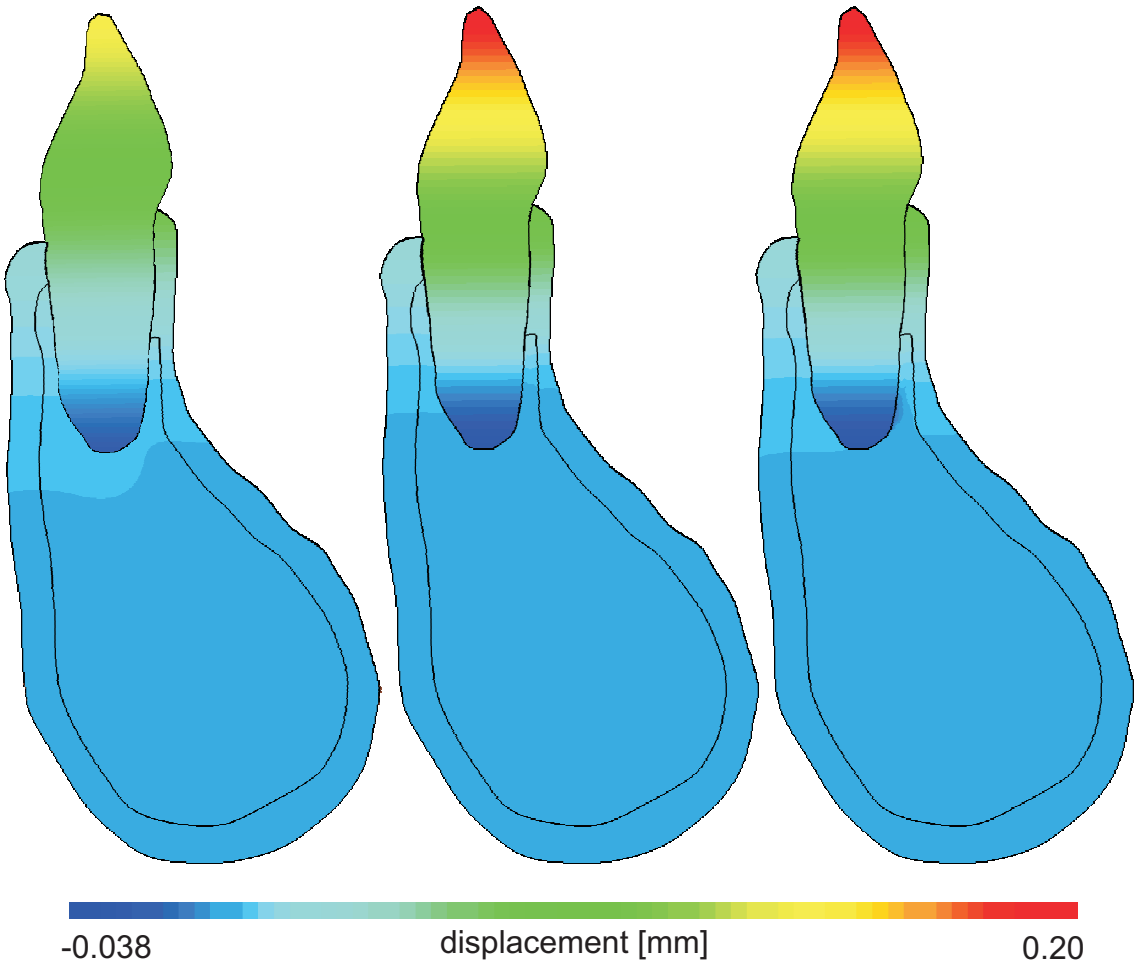

FIGURE 6.42: *Tipping: displacement [mm] in the labio-lingual direction (i.e. positive to the left) during the remodeling period. Left: initial displacement, center: after 20 days, right: after 60 days.*

Bodily tooth movement

A bodily tooth movement is obtained when the tooth moves en-masse in one direction, thanks to the application of a force passing through its center of rotation, therefore leading to a pure translation. In order to obtain such a movement, clinically, a combination of forces and moments are applied on the crown. Numerically however, we will consider the result of the application of a force to the tooth (Fig. 6.26). This force is obtained thanks to a force-driven rigid contact between tooth and bone (the contact law representing the periodontal ligament). The contact is applied in such a way that the contact force reaches in a tenth of a day an intensity of $0.7N$ in a direction perpendicular to the tooth main axis. With this problem, we will also analyze the effect of applying a higher force level, twice as high as the previous one (i.e. 1.4N). Finally, we will check the implication of a treatment-like application of forces, i.e. starting from a low force level of 0.7N, increasing this force by 50% after three weeks of treatment (up to 1.05N), and finally increasing the force by the same amount (i.e. up to 1.4N) four weeks later, keeping it constant for seven more weeks (up to 98 days). The final force applied with this treatment-like problem is therefore the same as the previous one.The displacements of three lingual points (whose positions are depicted in Fig. 6.43) are depicted in Fig. 6.44 (beware of the different displacement scales for each point).

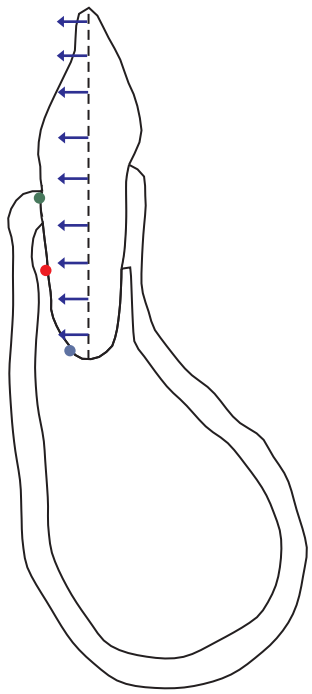

FIGURE 6.43: *Bodily tooth movement: applied load and positions of the three points for which the labio-lingual displacement is extracted in Fig. 6.44.*

Even tough the tooth displacement due to the force is rigid, the bone displacement however is not. The displacement at the collar (green curves in Fig. 6.44) is for the three load cases higher (at least twice as important) than for the two other points. The displacement at the

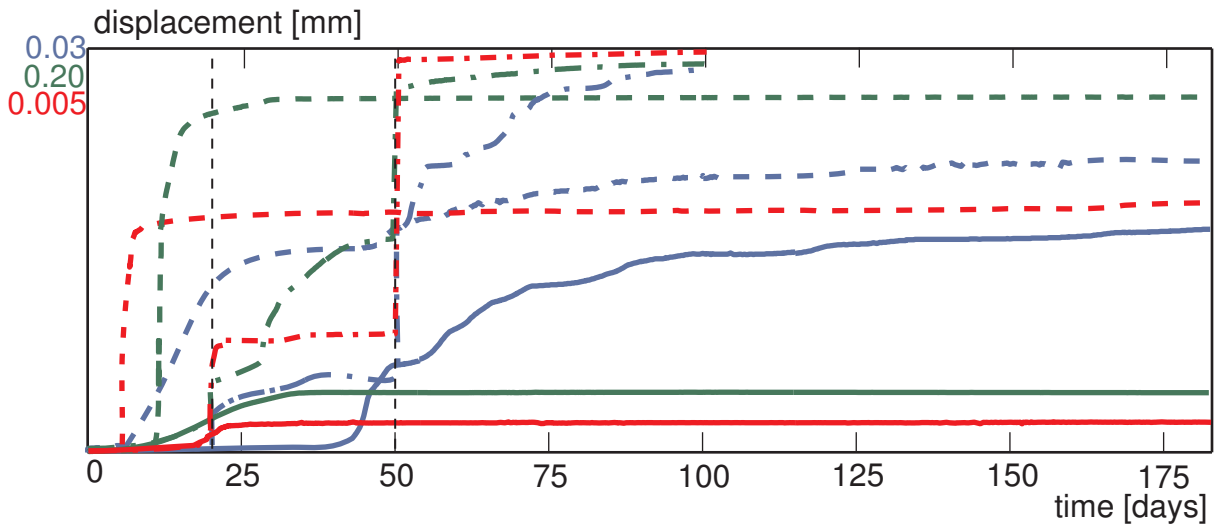

FIGURE 6.44: *Bodily tooth movement: displacement of the bone/tooth interface for three points on the lingual side. In blue, 1mm from the apex; in green, at the collar; in red, mid-height of the root. Plain lines are for the 0.7N force; dashed lines are for the 1.4N force, and dash-dotted lines are for the treatment like force.*

mid-height (red curves in Fig. 6.44) is at least ten times smaller than at the apex (blue curves in Fig. 6.44). The rate of displacement is different for all three points and all three load cases (except for the treatment-like model which shows exactly the same results as the low force model before the first force increment as these two models are identical up to then). The time after which the displacement seems to have reached a stationary value is also different for each point and each load case.

The displacement is not proportional to the applied force. Indeed, for a low force, it is not twice lower than the one for a twice larger force. It is six times lower at the collar and mid-height, but only 80% of the higher displacement at the apex. Therefore, the strain field induced by the force is totally different for each load case.

For the application of the higher force, even tough there are some areas of hyaline zone formation (see Fig. 6.45), these areas are not continuous and therefore do not completely impede the displacement initially. Applying the higher force steps by step as in a treatment-like application always leads to higher displacement than applying the higher force at once. Indeed, there is no hyaline zone to resorb at all and therefore the density variation contributes totally to the displacement.

The application of the 1.4N force produces remodeling stimulus values up to ten times higher than a low force does (Fig. 6.45). This leads, where possible, to a faster remodeling at the beginning of the loading, causing after 20 days a displacement over one hundred times higher (Fig 6.46). This fast remodeling however does not last on the long term as large areas reach the maximal and minimal values of density (Fig 6.47). Thus, after only 14 weeks, the treatment-like application of high forces reaches a higher displacement than the high force does after 26 weeks (Fig 6.48).

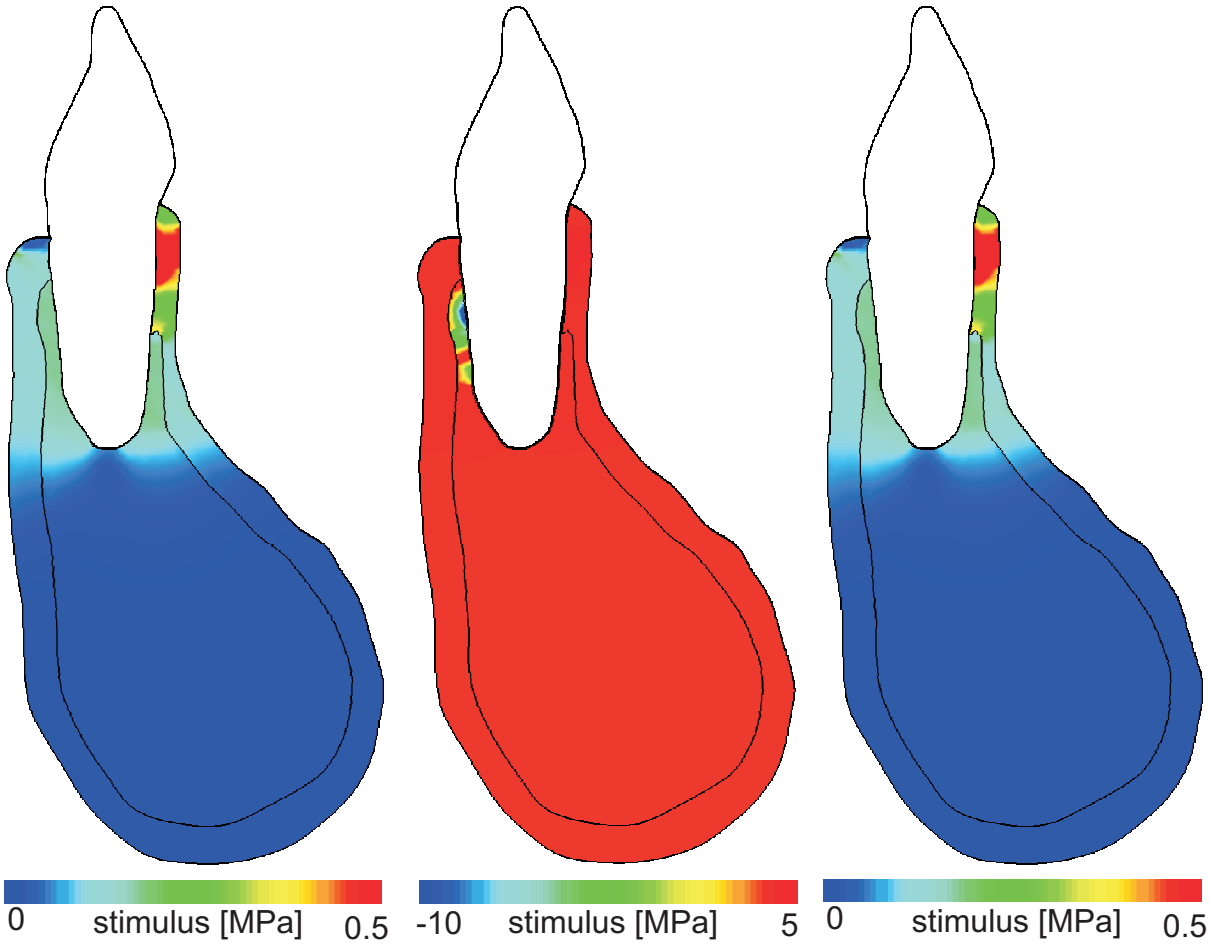

FIGURE 6.45: *Bodily tooth movement: bone remodeling stimulus [MPa] at the end of the loading phase. Left: low force, center: high force, right: treatment-like model. Values below zero are indicative of the presence of a hyaline zone.*

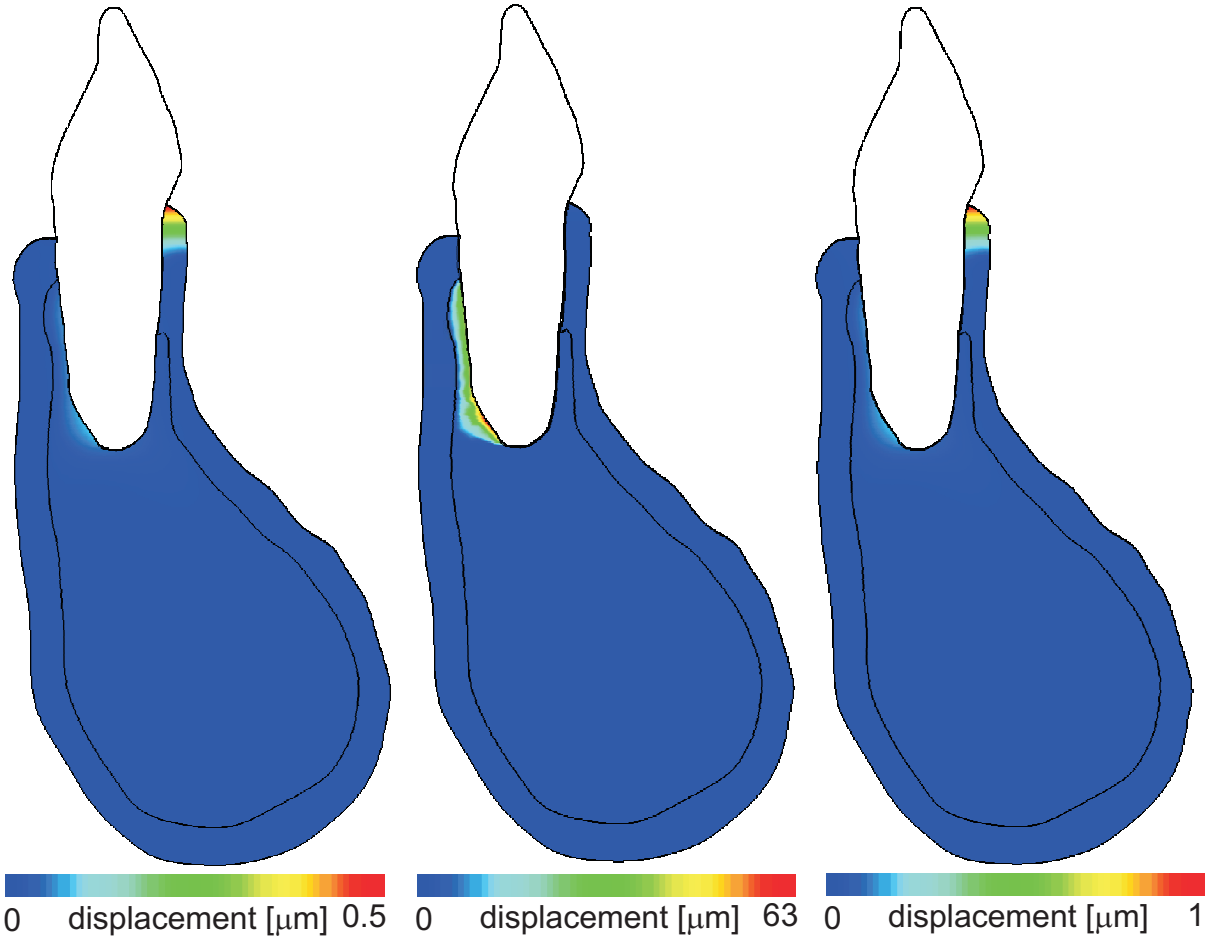

FIGURE 6.46: *Bodily tooth movement: displacement [μm] in the labio-lingual direction (i.e. positive to the left) after 20 days. Left: low force, center: high force, right: treatment-like model (after the first force increment).*

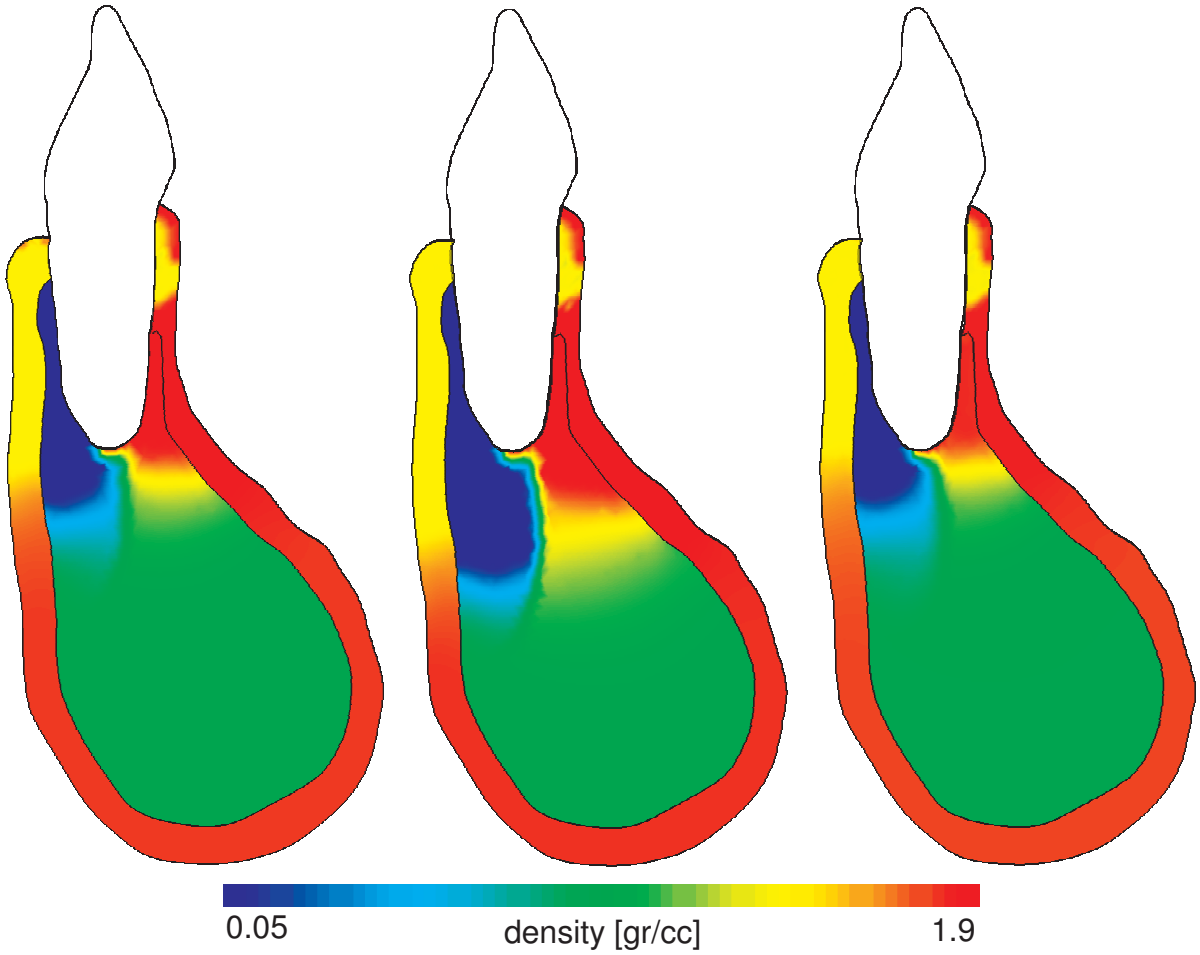

FIGURE 6.47: *Bodily tooth movement: bone density [gr/cc] at the end the remodeling period. Left: low force (180 days), center: high force (180 days), right: treatment-like model (98 days).*

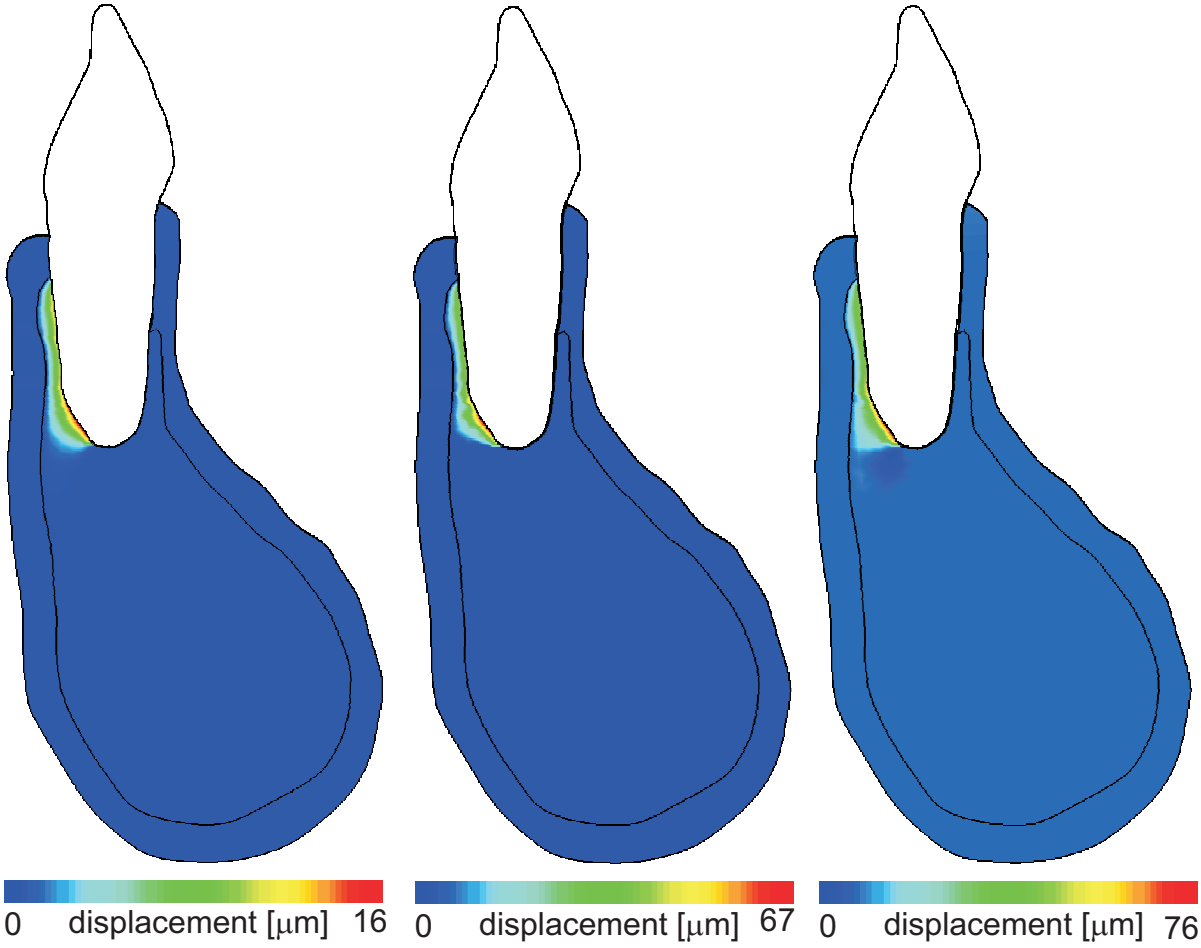

FIGURE 6.48: *Bodily tooth movement: displacement [µm] in the labio-lingual direction (i.e. positive to the left) at the end the remodeling period. Left: low force (180 days), center: high force (180 days), right: treatment-like model (98 days).*

Intrusion movement in 3D

We finally consider the results of an intrusion movement. This movement is obtained applying a $0.7N$ force on the tip of the crown (see Fig. 6.27), towards the apex of the tooth (the force is applied with a constant direction, whatever the tooth movement). The force is applied from 0N to its maximal value in a tenth of a day and is kept constant during a month (31 days). Bone density variation is observed during this constant force period, leading to an increase of the tooth displacement. The tooth displacement is almost rigid and thus only the displacement of an arbitrary point is analyzed.
As expected, the obtained displacement is directed towards the tooth apex. However, the non-linearity of the PDL mechanical behavior (we remind the reader the PDL is here modeled with non-linear spring elements) leads to a tooth movement which is not purely apical but has a component in the labial direction for the crown and a lingual component for the root, thus giving a rotation movement to the tooth (see Fig. 6.49).

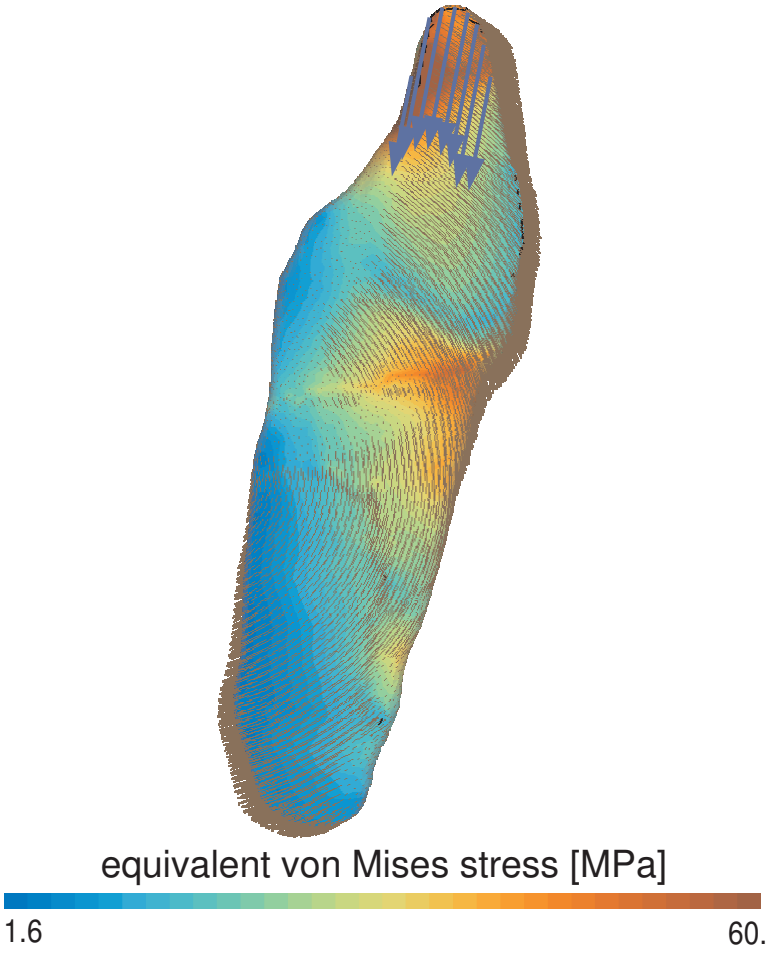

FIGURE 6.49: *Intrusion: von Mises equivalent stress [MPa] at the end of the loading phase. The blue arrows represent the application of the intrusion ofrce. The brown lines represent the displacment field.*

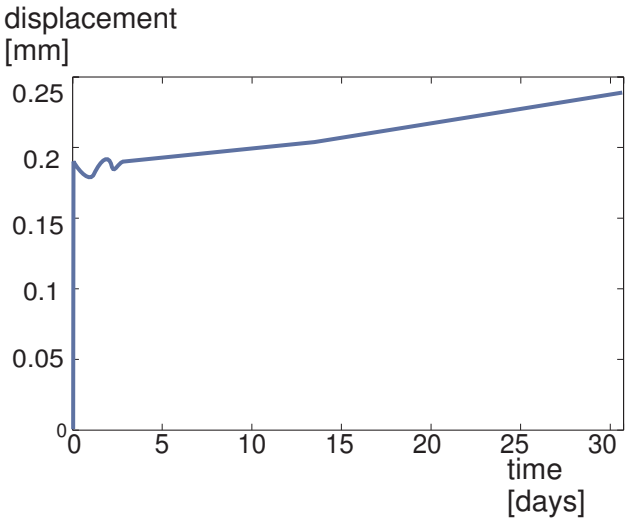

FIGURE 6.50: *Intrusion: displacement of the tooth [mm] vs. time [days]. The tooth displacement is almost rigid, only the displacement intensity of an arbitrary surface node is depicted. The direction of the displacement however is not constant in space as seen in Fig. 6.54.*

The initial displacement (see Fig. 6.50), due to the periodontal ligament deformation mainly, is 0.18mm, i.e. 90% of the PDL width .
It creates high compression of the bone along most of the tooth/bone interface, thus creating hyaline areas (see Fig. 6.51). Moreover, all areas at the bone/tooth interface that are not hyaline are in tension because of the rotation movement. The remodeling thus takes initially place either away from the surface, removing these hyaline areas, or to form new bone. Over the 31 days of observation, the hyaline zone are only partially removed, with most of the bone at its surface still not able to remodel (see Fig. 6.52). Therefore, only bone formation occurred during this observation period (see Fig. 6.53).
The tooth displacement (Fig. 6.50), while initially decreasing because of the bone formation apically, slowly increases to reach 0.24 mm in a month, i.e. an increase of 27% of the initial (instantaneous) displacement. This increase in displacement is mainly due to the formation of bone along the root, increasing the rotation movement.

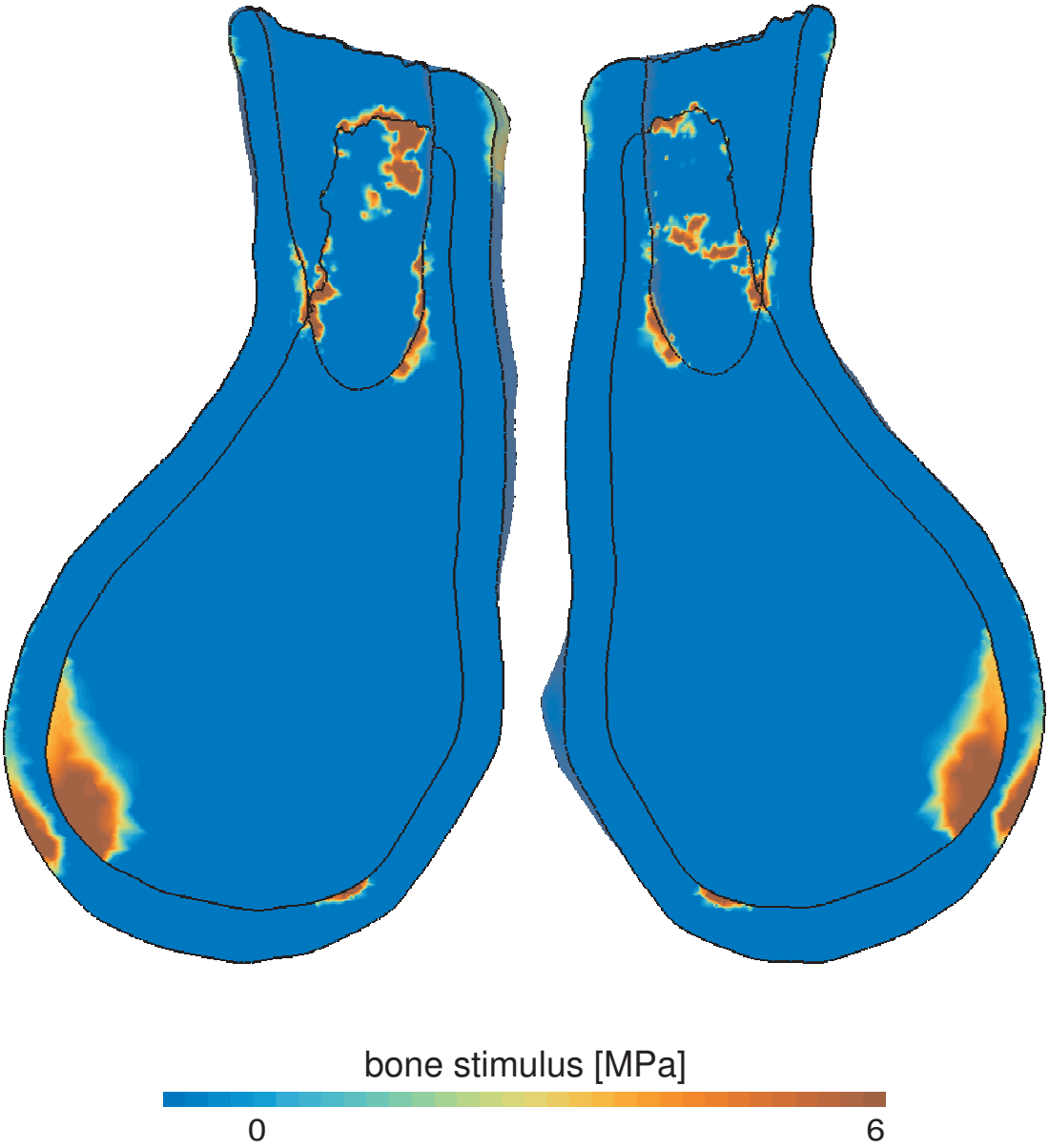

FIGURE 6.51: *Intrusion: bone remodeling stimulus [MPa] at the end of the loading phase. Sagittal cuts - left: lateral view, right: medial view. Values below zero are indicative of the presence of a hyaline zone.*

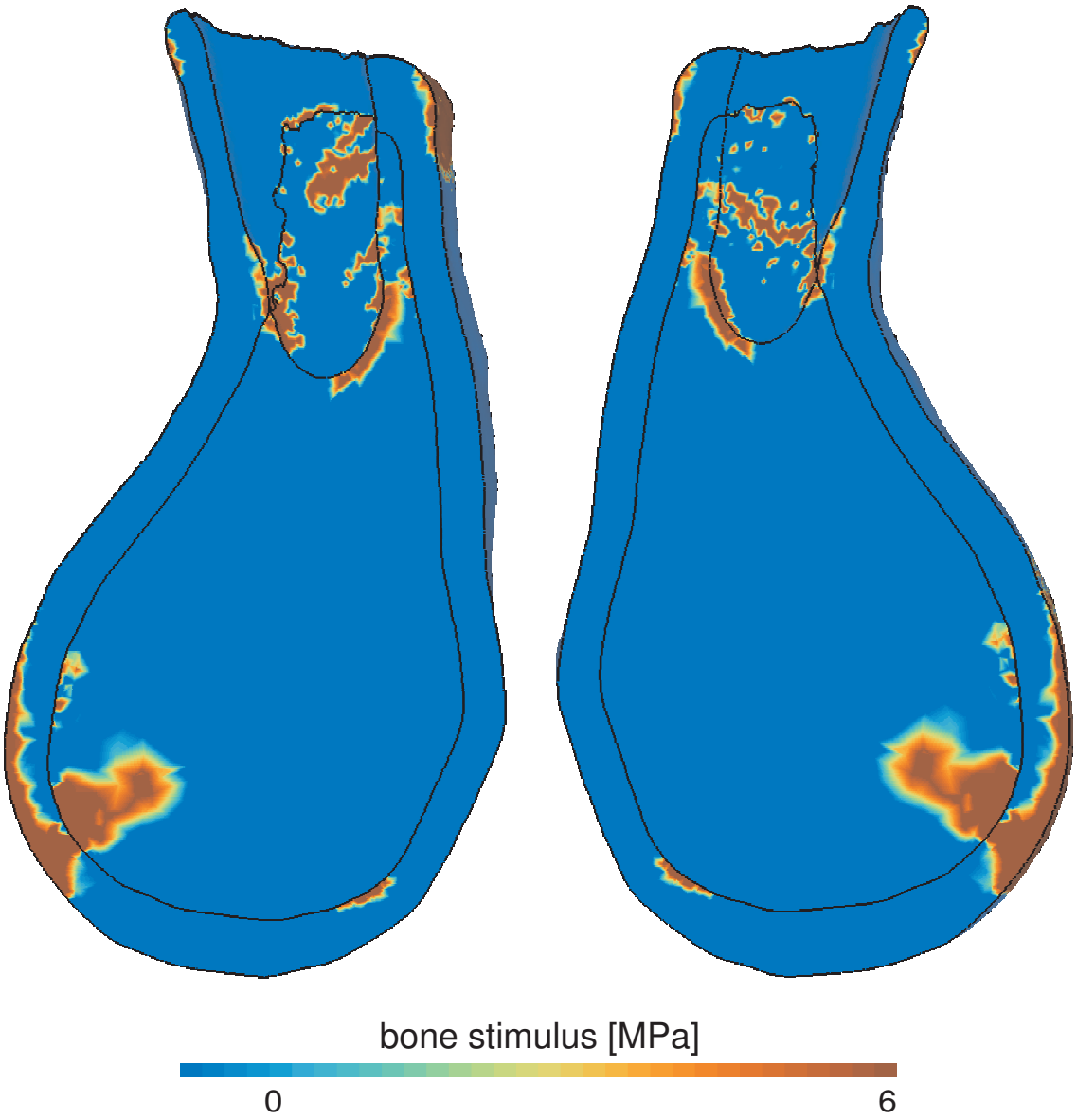

FIGURE 6.52: *Intrusion: bone remodeling stimulus [MPa] after a month of remodeling. Sagittal cuts - left: lateral view, right: medial view. Values below zero are indicative of the presence of a hyaline zone.*

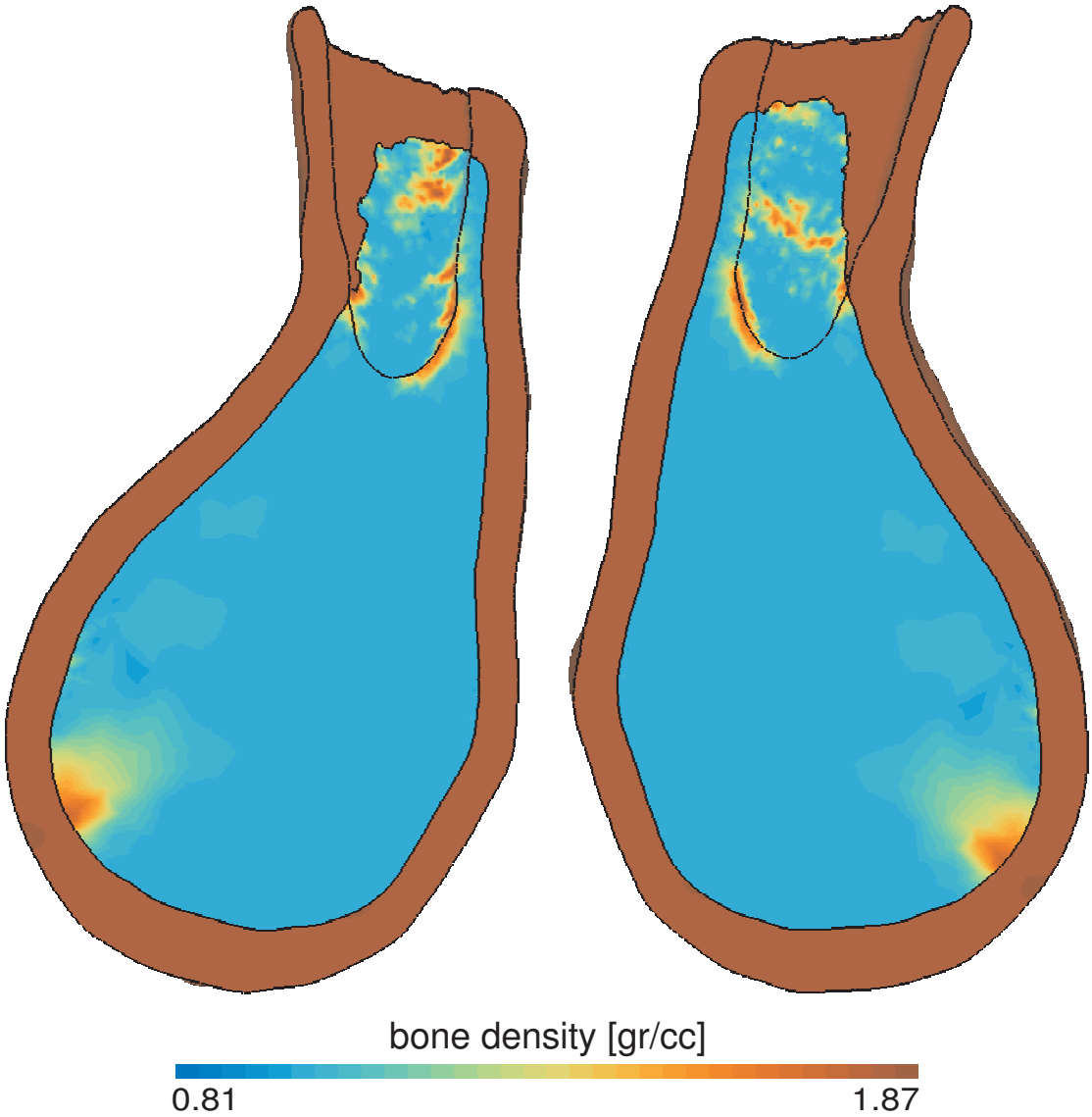

FIGURE 6.53: *Intrusion: bone density [gr/cc] after a month of remodeling. Sagittal cuts - left: lateral view, right: medial view.*

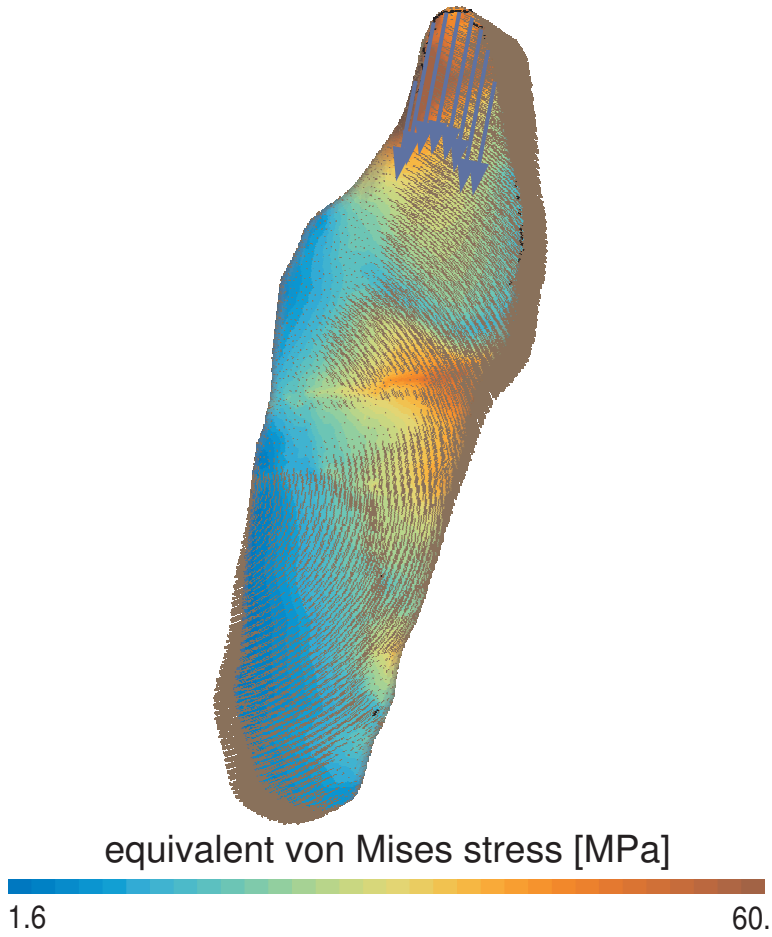

FIGURE 6.54: *Intrusion: von Mises equivalent stress [MPa] after a month of remodeling. The blue arrows represent the application of the intrusion ofrce. The brown lines represent the displacment field.*

6.2.5 Conclusions

The presented applications introduced numerical models for the simulation of orthodontic tooth movement based on the assumption that bone remodeling processes during tooth movement are controlled by the elastic energy density as well as pressure state of the alveolar bone. In spite of the necessary idealizations, the proposed phenomenological description of bone remodeling specified for alveolar bone allows to qualitatively represent density variation of the bone surrounding a tooth when submitted to loadings representative of orthodontic appliances. The need to use a pressure dependent remodeling rate is shown to be useful to represent tooth movement. These hypothesis may be too restrictive but have yet to be shown not valid as the use of an appliance would most of the time increase the strain energy on all sides of the tooth root, a non pressure dependent model of remodeling would therefore either lead to resorption or formation on all sides of a tooth.
The different applications modeled all present qualitative results that are satisfactory. Displacement driven simulations also present quantitative results on the force reduction due to remodeling that seems plausible. However, force driven simulations mainly outline the drawbacks of the model. The obtained displacements are too small compared to clinical tooth displacements while the bone density reduction is often too high. This is due to several aspects of the models as described in this section. First, an unphysiological density distribution can arise due to the poor representation of the physiological and therapeutic loads. Second, a strong dependence on the boundary conditions has been shown to affect at least the early stages of remodeling. Third, the force driven models are not exactly representative of a treatment as during treatment both the force and displacement would vary over time. Finally, the bone formation/resorption does not have a direct effect on the amount of bone (as the change of mass is not computed) but rather on its stiffness. A stiffer bone appears in formation sites, it therefore lowers the deformation capability of the tissue. In translation movement for instance, the bone softens downstream, willing to increase the movement, but at the same time it toughens upstream, impeding this movement, while the clinical observation is that the bone volume increases downstream.
However, we showed that we can represent the formation and resorption of hyaline areas, the non proportionality between applied forces and the obtained displacement, and that applying a stepwise increasing force leads to higher displacements than a high initial force as there is no hyaline zone to resorb. Specifically, when freeing ourself from boundary conditions effects, we showed we can produce large displacements of the tooth within the bone.

Chapter 7
Conclusions

The main principle in orthodontics is to gradually impose progressive and irreversible bone deformations due to remodeling using specific force systems on the teeth. The bone remodeling will lead the teeth into new positions.
The hypothesis of this work is that a simulation-based treatment using computer models could allow to account for some patient-specific features, and therefore an orthodontic tooth movement software would be a valuable tool for the orthodontists. Such a simulation tool needs to model the biological and mechanical reactions of all tissues and materials involved. In orthodontic tooth movement, two tissues have a major influence: the periodontal ligament and the alveolar bone. Their mechanical and biological/physiological reactions to orthodontic forces are tightly linked. This coupling can be treated in biomechanical models, focusing on the mechanics and considering the phenomenological aspects of the biology/physiology[1]. The development of such a model for bone tissue is the core of this work.
As a tool to describe the mechanics of orthodontic tooth movement due to remodeling, we chose to work with the Finite Element Method (FEM). This FEM involves a series of computational procedures to calculate the stress and strain in each element, which produces a model solution. In particular, it gives access to local mechanical response of each tissue, essential to couple the mechanics and the biology.

In **chapter 2**, we first presented the general principles of orthodontics starting with a brief description of the anatomy and physiology of the tissues involved in orthodontic tooth movement. Bone remodeling is at the origin of morphological changes in the bone surrounding the teeth that are responsible for tooth movement. Bone remodeling occurs in order to homogenize the mechanical response of the bone morphology, increasing the bone density where the bone is highly loaded and decreasing it where its presence is not (mechanically) necessary. Also, the remodeling occurs in such a way that the bone trabecular morphology aligns with the external force orientation. By comparison to remodeling in other bones than the alveolar bone, the surrounding tissues play a major influence on the remodeling behav-

[1] It should be noticed that mechanobiological models could also be used. These models focus on the biological reaction, accounting for the mechanical environment. However, they are often more complex and computationally demanding than biomechanical models, therefore probably less efficient than the latter.

ior. Here, the periodontal ligament pressure state seems to be the key factor to differentiate formation and resorption conditions.

In **chapter 3**, we reviewed the general principles of Continuum Mechanics and the Finite Element Method. As we use damage-based models we presented the basic concepts of both isotropic and anisotropic continuum damage models.

In **chapter 4**, we focused on a literature review on bone constitutive modeling and bone remodeling models. At the macroscopic level, the constitutive laws for trabecular bone account for morphological effects, including anisotropy, as well as non-linear materials effects, such as (anisotropic) plasticity or damage. However, these complex models usually consider a constant morphology, and therefore cannot be used in remodeling situations. Besides, remodeling laws usually assume small strain linear elasticity as a model for the bone tissue. Moreover, while observations lead to conclude Frost's mechanostat theory of bone remodeling could explain orthodontic tooth movement, it is rarely used in orthodontics related literature.

With these observations, we finally present the heart of this work in **chapter 5**. We proposed to reconcile both approaches of bone modeling (small strains linear elasticity for remodeling problems and complex constitutive models for other applications) by writing a constitutive model for trabecular bone at macroscopic level, built on morphological parameters to describe the anisotropy, accounting for effects such as plasticity of the trabeculae, and for which the continuum parameters such as the stiffness can evolve with morphology as remodeling occurs in the tissue. For this, we extended and enhanced Doblaré and Garcia's [62, 83] remodeling phenomenological model based on Frost's mechanostat theory. This remodeling law is built on an anisotropic Continuum Damage framework in which the remodeling corresponds to an evolution of the damage tensor representing the bone morphology. We enhanced their approach to use their model with an elastoplastic model for the bone trabeculae, as well as to retrieve the Stanford model it is built from, and to correct a major dimensional inconsistency, keeping however the strong coupling between the constitutive law and the remodeling one.
To build this new model, we first presented an integration method for an anisotropic Continuum Damage model coupled to plasticity (considering a von Mises plasticity of the bone matrix) in a finite strains formulation. We verified this integration method considering a constant damage tensor by comparing results on simple cases with other equivalent models. Adapting Doblaré and Garcia's remodeling law to our constitutive framework, we extended it so that it can be used to the specific case of orthodontic tooth movement. We therefore proposed to insert the hydrostatic pressure dependency of remodeling, due to the presence of the periodontal ligament, within the bone remodeling law.
We then analyzed the sensitivity of our model to its numerous parameters (parameters describing the bone matrix behavior, its morphology, and remodeling parameters) on a simple

geometric configuration and simple mechanical tests. This study showed that the remodeling model is mainly influenced by the values used for the homeostatic measure used as a stimulus for remodeling as well as the lazy-zone width. On a purely mechanical point-of-view, we showed the evaluation of the proper apparent density is of major importance, so are the orthotropy axis.
We then proposed a validation method for the mechanical representation of the bone matrix through the knowledge of its morphology. As our model is developed to be used in bone remodeling problems in a finite strain framework, it aims at describing the non-linear mechanical behavior of trabecular bone in the range of small to moderate strains. In this range, we have seen that bone mechanically behaves as a cellular elastoplastic solid. We therefore validated our model both on engineered cellular solids with bone-like morphology (aluminum and polymeric foams) and on bone (Deer antler) samples. This validation was performed on experimental compression tests and we produced *in-silico* tension tests to carry on further validation. These *in-silico* tension tests were produced considering validated μ-FE models on the samples used in the experimental compressive tests. We showed that accounting either for material nonlinearities (through a von Mises plastic criterion) or for the anisotropy (or both) is important for all the simulations we performed on our test samples. Indeed for the aluminum foam samples, accounting for the nonlinearities of the material was needed for 3%, 1%, and 0.5% of compressive engineering strains (i.e. at strains levels that are often considered as small enough to consider the problem as linear) for respectively the low density (mean apparent density of 4.43%), middle density (mean apparent density of 7.26%) and dense samples (mean apparent density of 12.8%). In tension tests, both the anisotropy and the nonlinearity was to be accounted for from 1% of engineering strains for the dense samples. For the two other materials in compression tests, the nonlinearity of the material was to be accounted for from 8% compressive engineering strains for the PLA foam while accouting for the anisotropy was of importance for the deer antler as soon as 0.3% compressive engineering strains.
We finally showed our remodeling model can reproduce results from the literature when used on the benchmark problem of the proximal femur remodeling. Indeed, we obtained results on the density distribution and on the morphological orientation that are comparable both qualitatively and quantitatively for this 2D problem. However, we also showed the remodeling behavior is very sensitive to the boundary conditions application.

In **chapter 6** we finally applied the developed model to orthodontic tooth movement (OTM) problems.
First we presented a specific mechanical representation of the periodontal ligament as it cannot be extracted from CT-scans images and its geometry is therefore unknown. We developed a model accounting for the non-linear mechanical response of the PDL through either bilateral contact conditions or spring elements.
We then presented applications of the numerical model for the simulation of orthodontic tooth movement based on the assumption that bone remodeling processes during tooth

movement are controlled by the energy density as well as the pressure state of the alveolar bone. In spite of the necessary idealizations, the proposed phenomenological description of bone remodeling specified for alveolar bone allows to qualitatively represent density variation of the bone surrounding a tooth when submitted to loading representative of orthodontic appliances.
As we showed on the femur benchmark case that the model is very sensitive to boundary conditions, we produced a first model whose geometry is not representative of the reality but allows us to free ourselves from BC's effects. With this purely academic test case, we showed that our model can be used to simulate large displacements of the tooth within the bone. This can be achieved using mesh management methods, such as the Arbitrary Lagrangian-Eulerian method used in this case. We showed the use of an anisotropic remodeling accounting for the elastoplasticity of the material brings significative differences, in terms at least of the required force, compared to either an isotropic remodeling or an elastic material at tissue level. Within the anisotropic remodeling model, we also showed the characterization of the initial orientation of the morphology (considered here either isotropic, or vertical, or horizontal) is important to evaluate the force, with a difference up to 25% of the required force intensity. Finally, we showed the remodeling stimulus reaches about the same value in the side of the bone in compression and in the side in tension, even when using a non-linear model for the periodontal ligament (here modeled as bilateral contact conditions). Therefore, the use of remodeling rate model adapted for the alveolar bone and accounting for the compression or tension state is important to be able to simulate the tooth displacement.
Then we built geometrically realistic models of a tooth and surrounding tissues. These models consider either displacement driven problems or force driven problems, both 2D and 3D, and all qualitatively represent the observed phenomenon of OTM. We also outlined some of the drawbacks of the models. First, an unphysiological density distribution can arise due to the poor representation of the application of the physiological and therapeutic loads. Second, a strong dependence on the boundary conditions has been shown to affect at least the early stages of remodeling. Finally, the bone formation does not have a direct effect on the amount of bone but rather on its stiffness. A stiffer bone appears in formation sites, it therefore lowers the deformation capability of the tissue.
However, we showed that we can represent the formation and resorption of hyaline areas, the non-linearity of the force/displacement relationship, and that applying a stepwise increasing force leads to higher displacements than a high initial force as there is no hyaline zone to resorb.

With this work, we therefore explored the possibility to build an integrated remodeling law into a non-linear constitutive model of trabecular bone accounting for morphological effects measured through CT-scan stereological analysis. Simple cases of orthodontic tooth movements can be represented with our model when applied to geometries reconstructed from CT-scans images. However further work should focus on a more realistic representa-

tion of boundary and initial conditions. Indeed, we assumed that the only forces present during OTM where the orthodontic forces, neglecting all physiological forces (muscle tone, chewing forces and other mouth activities, as well as gravitational forces). We thus used a value of the remodeling stimulus that is not physiological. We also showed that the fixation conditions we used can be of major influence in the short-term response of the model. Finally, the loading cases considered are not exactly representative of the application of orthodontic apparatus. Further work could focus not only on a more systematic extraction of the anatomy from CT-images (or better classical panoramic radiographies used daily in the dental clinics), as well as a systematic meshing procedure, but also on the representation of both the geometry and mechanics of the orthodontic apparatus. We indeed showed that an accurate representation of the force system is of major importance to the model response. Finally, we used material and biological parameters extracted from literature data. However most of the parameters we used are empirical. A better and more systematic work should be carried out to evaluate these parameter values. For the material parameters and the non-linearities of the trabecular bone for instance, several ongoing studies seem to lead not to a von Mises criterion for the trabeculae but a pressure dependent one (such as degenerated -with only two parameters for the description of the yield surface- Hill 48 models). For the remodeling parameters, most of them are both patient-specific and site specific. A multi-scale model accounting for the cellular activity could be used to get more accurate values of these parameters. As mentioned earlier, the determination of the homeostatic stimulus and the width of the lazy-zone should be evaluated with caution. Finally, in the developed model the resorption and formation of bone has an effect only on mechanical parameters such as the stiffness. There is no actual creation or disappearance of mass/volume within the bone. Criteria such as developed in fracture models could be used to deal with the loss of elements when the bone is completely resorbed. Methods to add bone elements at the surface or within the volume should be examined in the case of bone formation.

Appendix A
Anisotropic Extension of the Stanford Model

This appendix relates the details of the optimization approach of anisotropic remodeling as proposed by Jacobs [117]. We first remind the reader with standard results in Continuum Mechanics when dealing with energy conservation. We then present the theoretical developments proposed by Jacobs to account for remodeling.

A.1 Energy Conservation in Continuum Mechanics

When dealing with inert isothermal materials, the time derivative of the total energy (internal energy and kinetic energy) is equal to the power developed by the applied forces, $\mathcal{P}_{\texttt{ext}}$:

$$\frac{d}{dt}\int_{\mathbb{V}(t)} (\rho u + \frac{1}{2}\rho \mathbf{v}.\mathbf{v})\, d\mathbb{V} = \mathcal{P}_{\texttt{ext}} \tag{Equ. A.1}$$

with u the internal energy density due only to the strain field (by opposition to an internal energy density accounting also for remodeling, χ) and $\mathbf{v}$ the velocity field.
Applying the standard techniques of Continuum Mechanics, the external mechanical power can be expressed as

$$\mathcal{P}_{\texttt{ext}} = \underbrace{\int_{\mathbb{S}(t)} (\boldsymbol{\sigma}.\mathbf{n}).\mathbf{v}\, d\mathbb{S}}_{\text{power from surface traction forces}} + \underbrace{\int_{\mathbb{V}(t)} \rho \mathbf{b}.\mathbf{v}\, d\mathbb{V}}_{\text{power from body forces}} \tag{Equ. A.2}$$

Applying Gauss's theorem and accounting for the momentum conservation equation (defined in section 3.2), the first term of Equ. A.2 can be written:

$$\int_{\mathbb{S}(t)} \sigma_{ij} n_j v_i\, d\mathbb{S} = \int_{\mathbb{V}(t)} \frac{\partial}{\partial x_j}(\sigma_{ij} v_i)\, d\mathbb{V} \tag{Equ. A.3}$$

$$= \int_{\mathbb{V}(t)} \frac{\partial \sigma_{ij}}{\partial x_j} v_i + \sigma_{ij}\frac{\partial v_i}{\partial x_j}\, d\mathbb{V} \tag{Equ. A.4}$$

$$= \int_{\mathbb{V}(t)} (\rho \dot{v}_i - \rho b_i) v_i + \sigma_{ij} D_{ij}\, d\mathbb{V} \tag{Equ. A.5}$$

or

$$\int_{\mathbb{S}(t)} (\boldsymbol{\sigma}.\mathbf{n}).\mathbf{v}\, d\mathbb{S} = \int_{\mathbb{V}(t)} (\rho\dot{\mathbf{v}} - \rho\mathbf{b}).\mathbf{v} + \boldsymbol{\sigma} : \boldsymbol{D}\, d\mathbb{V}$$

Therefore, the external mechanical power simplifies as:

$$\mathcal{P}_{\mathtt{ext}} = \int_{\mathbb{V}(t)} \rho\dot{\mathbf{v}}.\mathbf{v} + \boldsymbol{\sigma} : \boldsymbol{D}\, d\mathbb{V} \qquad \text{(Equ. A.6)}$$

The LHS of Equ. A.1 can be transformed, using Reynold's theorem, as:

$$\frac{d}{dt}\int_{\mathbb{V}(t)} (\rho u + \frac{1}{2}\rho\mathbf{v}.\mathbf{v})\, d\mathbb{V} = \int_{\mathbb{V}(t)} \rho\dot{u} + \rho\mathbf{v}.\dot{\mathbf{v}}\, d\mathbb{V}$$

Finally, Equ. A.1 reads:

$$\int_{\mathbb{V}(t)} \rho\dot{\mathbf{v}}.\mathbf{v} + \boldsymbol{\sigma} : \boldsymbol{D}\, d\mathbb{V} = \int_{\mathbb{V}(t)} \rho\dot{u} + \rho\mathbf{v}.\dot{\mathbf{v}}\, d\mathbb{V}$$

And one can see that the variation of the internal energy density is, for an isothermal process:

$$\rho\dot{u} = \boldsymbol{\sigma} : \boldsymbol{D}$$

In a small strain theory such as used in Jacobs's work, $\boldsymbol{D} = \dot{\boldsymbol{\varepsilon}}$ and therefore $\rho\dot{u} = \boldsymbol{\sigma} : \dot{\boldsymbol{\varepsilon}}$.

A.2 Anisotropic Remodeling Considered as an Optimization Process

Concerning the remodeling model proposed by Jacobs, the first assumption is that the stress-strain relationship in small strain elasticity, i.e.

$$\boldsymbol{\sigma} = \mathbb{C} : \boldsymbol{\varepsilon} \qquad \text{(Equ. A.7)}$$

is no longer necessarily isotropic (in the isotropic case, $\mathbb{C} = \mathbb{H}$) and cannot be represented by the two parameters E and ν only. The idea of Jacobs is to find an evolution law for the stiffness tensor $\mathbb{C}$, i.e., a rule for its variation, $\dot{\mathbb{C}}$. His assumption is that bone remodeling is an optimal process in some energetic sense.
The efficiency of the adaptive process, $\mathcal{E}$, is measured as the mechanical dissipation. It is computed as the difference between the power associated with the external loads and the rate-of-change of the total energy in which the internal energy, χ, is due both to the strains and to the remodeling.

$$\mathcal{E} = \mathcal{P}_{\mathtt{ext}} - \int_{\mathbb{V}_0} \dot{\chi} + \rho\mathbf{v}.\dot{\mathbf{v}}\, d\mathbb{V}_0 \qquad \text{(Equ. A.8)}$$

The total energy dissipation is the sum of the mechanical and the biological dissipation. In inert materials, the latter does not exist and, therefore the mechanical dissipation $\mathcal{E}$ has to be non-negative (and for isothermal elastic problems, $\dot{\chi} = \rho\dot{u}$ and $\mathcal{E}$ is zero as seen in the first

part of this appendix.). In the specific case of biological materials, this mechanical dissipation can be negative with no violation of thermodynamic laws because a certain magnitude of biological energy (which cannot be quantified) can be dissipated. Mechanical energy can therefore be gained.
The internal energy variation is not due only to the strain variation as for inert materials but also to the stiffness variation and the density variation. Assuming χ can be decomposed into an internal energy associated with the strain rate and the stiffness rate and an internal energy associated with the density rate ($\Theta(\rho)$), Jacobs gets:

$$\chi = \frac{1}{2}\boldsymbol{\varepsilon} : \mathbb{C} : \boldsymbol{\varepsilon} + \Theta(\rho)$$

and

$$\dot{\chi} = \boldsymbol{\sigma} : \dot{\boldsymbol{\varepsilon}} + \frac{1}{2}\boldsymbol{\varepsilon} : \dot{\mathbb{C}} : \boldsymbol{\varepsilon} + \Theta'\dot{\rho}$$

As a result, the efficiency, $\mathcal{E}$, is finally quantified as:

$$\mathcal{E} = -\int_{\mathbb{V}_0} \left[\frac{1}{2}\boldsymbol{\varepsilon} : \dot{\mathbb{C}} : \boldsymbol{\varepsilon} + \Theta'\dot{\rho}\right] d\mathbb{V}_0 \qquad \text{(Equ. A.9)}$$

Note that in the case of atrophy $\boldsymbol{\varepsilon} : \dot{\mathbb{C}} : \boldsymbol{\varepsilon}$ is negative (for which we will see that all terms of $\dot{\mathbb{C}} \leq 0$) and in the case of hypertrophy it is positive. In the case of isothermal elasticity, Equ. A.9 is identically null, it is restricted to a positive value for inert materials but can be negative in the case of living tissues.
Jacobs then assumes that bone remodeling is an optimal process in some energetic sense. It therefore means the efficiency has to be optimized, under the conditions for which bone remodeling is activated. These conditions are derived from Equ. 5.2 of the isotropic Standford model and can be formulated using Equ. 5.10 as[1]

$$g_f^{\mathtt{An}\cdot} = C\sqrt{\boldsymbol{\sigma} : \boldsymbol{\varepsilon}} - (\psi_t^\star + \omega)\rho^{2-\beta/2} \geq 0 \qquad \text{(Equ. A.10)}$$

$$g_r^{\mathtt{An}\cdot} = -C\sqrt{\boldsymbol{\sigma} : \boldsymbol{\varepsilon}} + (\psi_t^\star - \omega)\rho^{2-\beta/2} \geq 0 \qquad \text{(Equ. A.11)}$$

Forming the Lagrangian of the constraint optimization problem yields (with the Lagrange multipliers μ_i):

$$\mathcal{L} = \mathcal{E} + \int_{\mathbb{V}_0} \mu_i g_i^{\mathtt{An}\cdot}\, d\mathbb{V}_0$$

The stationary condition requires that the first variations with respect to the variables ($\boldsymbol{\varepsilon}$ and ρ) vanish, giving (Jacobs considers that the density and the stiffness tensor are independent variables):

$$\int_{\mathbb{V}_0} \left[\mu_i \frac{\partial g_i^{\mathtt{An}\cdot}}{\partial \boldsymbol{\varepsilon}} - \dot{\mathbb{C}} : \boldsymbol{\varepsilon}\right] \delta\boldsymbol{\varepsilon} + \left[\mu_i \frac{\partial g_i^{\mathtt{An}\cdot}}{\partial \rho} - \Theta''\dot{\rho}\right] \delta\rho \; d\mathbb{V}_0 = 0 \qquad \forall \delta\boldsymbol{\varepsilon} \text{ and } \delta\rho$$

[1] $g_r^{\mathtt{An}\cdot} \propto -g_r^{\mathtt{St}\cdot}$ so that both conditions for formation and resorption can be written as conditions for which remodeling occurs when their value are positive. They can therefore be treated in the same way in the optimization procedure.

This finally leads to the optimality conditions:

$$\dot{\mathbb{C}} : \boldsymbol{\varepsilon} = \mu_i \frac{\partial g_i^{\mathtt{An.}}}{\partial \boldsymbol{\varepsilon}} \quad \text{and} \quad \Theta'' \dot{\rho} = \mu_i \frac{\partial g_i^{\mathtt{An.}}}{\partial \rho}$$

with the Kuhn-Tucker conditions: $\mu_i \leq 0, \quad g_i^{\mathtt{An.}} \geq 0 \quad \text{and} \quad \mu_i g_i^{\mathtt{An.}} = 0.$

Particularizing this result to Equ. A.10 and Equ. A.11 and requiring that the anisotropic behavior gives the same results as the isotropic one when hydrostatic stress are applied to an initially isotropic stiffness, Jacobs finally shows that one gets:

$$\dot{\mathbb{C}} = \frac{\beta \dot{\rho}}{\rho} \frac{\boldsymbol{\sigma} \otimes \boldsymbol{\sigma}}{\boldsymbol{\sigma} : \boldsymbol{\varepsilon}}$$

The remodeling model is completed with a density update identical to the one used in the isotropic Stanford model and with the definition of a remodeling rate:

$$\dot{r}^{\mathtt{An.}} = \begin{cases} c_f \dfrac{g_f^{\mathtt{An.}}}{\rho^{2-\beta/2}} & \text{for } g_f^{\mathtt{An.}} \geq 0 \\ 0 & \text{for } g_f^{\mathtt{An.}} < 0 \text{ and } g_r^{\mathtt{An.}} < 0 \\ -c_r \dfrac{g_r^{\mathtt{An.}}}{\rho^{2-\beta/2}} & \text{for } g_r^{\mathtt{An.}} \geq 0 \end{cases}$$

Appendix B
Deriving and Solving the Plastic Flow Rule

This appendix relates the details of the equations needed to derive and solve the plastic flow rule in the anisotropic damage model coupled to plasticity as introduced in section 5.2.1.
In order to understand all the notation, let's first consider how a diagonal tensor and a deviatoric tensor transform when they are submitted to the corotational stress/effective stress mapping, i.e. let's compute $\mathbb{M} : \boldsymbol{I}$ and $\mathbb{M} : \hat{\boldsymbol{a}}$ with

$$\mathbb{M} = \boldsymbol{H} \underline{\otimes} \boldsymbol{H} - \frac{1}{3}\left(\boldsymbol{H}^2 \otimes \boldsymbol{I} + \boldsymbol{I} \otimes \boldsymbol{H}^2\right) + \frac{1}{9}\mathtt{tr}\left(\boldsymbol{H}^2\right)\ \boldsymbol{I} \otimes \boldsymbol{I} + \frac{1}{3}\frac{\boldsymbol{I} \otimes \boldsymbol{I}}{1-\eta d^H}$$

or, using an index notation:

$$\begin{aligned}\mathbb{M}_{ijkl} &= H_{ik}H_{jl} - \frac{1}{3}(H_{in}H_{nj}\delta_{kl} + H_{kn}H_{nl}\delta_{ij}) + \frac{1}{9}\mathtt{tr}\left(\boldsymbol{H}^2\right)\delta_{ij}\delta_{kl} + \frac{1}{3}\frac{1}{1-\eta d^H}\delta_{ij}\delta_{kl} \\ &= \mathbb{M}_{klij}\end{aligned} \tag{Equ. B.1}$$

We get

$$\begin{aligned}\{\mathbb{M} : \boldsymbol{I}\}_{ij} &= \mathbb{M}_{ijkl}\delta_{kl} \\ &\overset{\delta_{kl}\delta_{kl}=3}{=} H_{ik}H_{jk} - \frac{1}{3}(3H_{in}H_{nj} + H_{kn}H_{nk}\delta_{ij}) + \frac{1}{3}\mathtt{tr}\left(\boldsymbol{H}^2\right)\delta_{ij} + \frac{1}{1-\eta d^H}\delta_{ij} \\ &\overset{\boldsymbol{H}\text{ symmetric}}{=} H_{ij}^2 - (H_{ij}^2 + \frac{1}{3}\mathtt{tr}\left(\boldsymbol{H}^2\right)\delta_{ij}) + \frac{1}{3}\mathtt{tr}\left(\boldsymbol{H}^2\right)\delta_{ij} + \frac{1}{1-\eta d^H}\delta_{ij} \\ &= \frac{1}{1-\eta d^H}\delta_{ij}\end{aligned}$$

Thus,

$$\mathbb{M} : \boldsymbol{I} = \frac{1}{1-\eta d^H}\boldsymbol{I} \tag{Equ. B.2}$$

We also have

$$
\begin{aligned}
\{\mathbb{M}:\hat{\boldsymbol{a}}\}_{ij} &= \mathbb{M}_{ijkl}\left(a_{kl}-\frac{1}{3}\mathtt{tr}\left(\boldsymbol{a}\right)\delta_{kl}\right)\\
&\overset{\text{using Equ. B.2}}{=} \mathbb{M}_{ijkl}a_{kl}-\frac{1}{3}\mathtt{tr}\left(\boldsymbol{a}\right)\left(\frac{1}{1-\eta d^H}\delta_{ij}\right)\delta_{kl}\\
&= H_{ik}a_{kl}H_{jl}-\frac{1}{3}(H_{in}H_{nj}a_{kl}\delta_{kl}+H_{kn}a_{kl}H_{nl}\delta_{ij})+\frac{1}{9}\mathtt{tr}\left(\boldsymbol{H}^2\right)\delta_{ij}a_{kl}\delta_{kl}\\
&\quad +\frac{1}{3}\frac{1}{1-\eta d^H}\delta_{ij}a_{kl}\delta_{kl}-\frac{1}{3}\frac{\mathtt{tr}\left(\boldsymbol{a}\right)}{1-\eta d^H}\delta_{ij}\delta_{kl}\\
&\overset{\boldsymbol{H}\text{ symmetric}}{=} \{\boldsymbol{HaH}\}_{ij}-\frac{1}{3}\mathtt{tr}\left(\boldsymbol{a}\right)H^2_{ij}-\frac{1}{3}\left[\mathtt{tr}\left(\boldsymbol{HaH}\right)-\frac{1}{3}\mathtt{tr}\left(\boldsymbol{a}\right)\mathtt{tr}\left(\boldsymbol{H}^2\right)\right]\delta_{ij}\\
&= \{\boldsymbol{H\hat{a}H}\}_{ij}-\frac{1}{3}\mathtt{tr}\left(\boldsymbol{H\hat{a}H}\right)\delta_{ij}\\
&= \{\mathtt{dev}\left(\boldsymbol{H\hat{a}H}\right)\}_{ij}
\end{aligned}
$$

Thus,

$$\mathbb{M}:\hat{\boldsymbol{a}}=\mathtt{dev}\left(\boldsymbol{H\hat{a}H}\right) \qquad \text{(Equ. B.3)}$$

B.1 Deriving the Plastic Flow Rule for the Anisotropic Damage Model

The plastic strain rate is assumed to follow the normality rule (associated plasticity) in the Cauchy stress space. For a von Mises yield function, it gives:

$$\boldsymbol{D}^p = \Lambda \boldsymbol{N} = \Lambda \frac{\dfrac{\partial f(\tilde{\boldsymbol{s}})}{\partial \boldsymbol{\sigma}}}{||\partial f / \partial \boldsymbol{\sigma}||}$$

with $f = \tilde{\sigma}_{eq}^{vM} - \sigma_y$ and $\dfrac{\partial f(\tilde{\boldsymbol{s}})}{\partial \boldsymbol{\sigma}} = \dfrac{\partial f(\tilde{\boldsymbol{s}})}{\partial \tilde{\boldsymbol{s}}} \dfrac{\partial \tilde{\boldsymbol{s}}}{\partial \boldsymbol{\sigma}}$

$$\begin{aligned}
\boldsymbol{D}^p &= \Lambda \frac{\dfrac{\partial f(\tilde{\boldsymbol{s}})}{\partial \boldsymbol{\sigma}}}{||\partial f / \partial \boldsymbol{\sigma}||} \\
&= \Lambda \frac{3}{2} \frac{1}{\tilde{\sigma}_{eq}^{vM} \, ||\partial f / \partial \boldsymbol{\sigma}||} \tilde{\boldsymbol{s}} : \frac{\partial \tilde{\boldsymbol{s}}}{\partial \boldsymbol{\sigma}} \\
&= \Lambda \frac{3}{2} \frac{1}{\tilde{\sigma}_{eq}^{vM} \, ||\partial f / \partial \boldsymbol{\sigma}||} \tilde{\boldsymbol{s}} : \frac{\partial \tilde{\boldsymbol{s}}}{\partial \boldsymbol{\sigma}} \\
&= \Lambda \frac{\tilde{\boldsymbol{s}} : \dfrac{\partial \tilde{\boldsymbol{s}}}{\partial \boldsymbol{\sigma}}}{||\tilde{\boldsymbol{s}} : \dfrac{\partial \tilde{\boldsymbol{s}}}{\partial \boldsymbol{\sigma}}||}
\end{aligned} \tag{Equ. B.4}$$

or, using an index notation:

$$D_{kl}^p = \Lambda \frac{\tilde{s}_{ij} \dfrac{\partial \tilde{s}_{ij}}{\partial \sigma_{kl}}}{\sqrt{\tilde{s}_{mn} \dfrac{\partial \tilde{s}_{mn}}{\partial \sigma_{op}} \tilde{s}_{qr} \dfrac{\partial \tilde{s}_{qr}}{\partial \sigma_{op}}}} \tag{Equ. B.5}$$

Upon writing

$$\tilde{\boldsymbol{s}} = \mathtt{dev}(\boldsymbol{HsH}) = \boldsymbol{HsH} - \frac{1}{3}\mathtt{tr}(\boldsymbol{HsH})\,\boldsymbol{I} \tag{Equ. B.6}$$

or

$$\tilde{s}_{ij} = H_{im} s_{mn} H_{nj} - \frac{1}{3} H_{qr} s_{rs} H_{sq} \delta_{ij} \tag{Equ. B.7}$$

one gets (assuming $\boldsymbol{H}$ constant[1])

$$\begin{aligned}
\frac{\partial \tilde{s}_{ij}}{\partial \sigma_{kl}} &= \frac{\partial H_{im} s_{mn} H_{nj}}{\partial \sigma_{kl}} - \frac{1}{3} \frac{\partial H_{qr} s_{rs} H_{sq}}{\partial \sigma_{kl}} \delta_{ij} \\
&= \left[H_{im} \delta_{mk} \delta_{nl} H_{nj} - \frac{1}{3} H_{im} \delta_{kl} \delta_{mn} H_{nj} \right] - \frac{1}{3} \left[H_{qr} \delta_{rk} \delta_{sl} H_{sq} - \frac{1}{3} H_{qr} \delta_{kl} \delta_{rs} H_{sq} \right] \delta_{ij} \\
&= \left[H_{ik} H_{lj} - \frac{1}{3} H_{im} H_{mj} \delta_{kl} \right] - \frac{1}{3} \left[H_{qk} H_{lq} - \frac{1}{3} H_{qr} H_{rq} \delta_{kl} \right] \delta_{ij}
\end{aligned} \tag{Equ. B.8}$$

[1] This assumption is valid considering a staggered scheme of integration for the coupled plastic/damage problem.

One can therefore write ($\tilde{\boldsymbol{s}}$ being deviatoric et $\boldsymbol{H}$ symmetric[1])

$$\tilde{s}_{ij}\frac{\partial \tilde{s}_{ij}}{\partial \sigma_{kl}} = \tilde{s}_{ij}\left[H_{ik}H_{lj} - \frac{1}{3}H_{im}H_{mj}\delta_{kl}\right] = H_{ki}\tilde{s}_{ij}H_{jl} - \frac{1}{3}H_{mi}\tilde{s}_{ij}H_{jm}\delta_{kl} \tag{Equ. B.9}$$

or equivalently

$$\tilde{\boldsymbol{s}} : \frac{\partial \tilde{\boldsymbol{s}}}{\partial \boldsymbol{\sigma}} = \mathtt{dev}\left(\boldsymbol{H}\tilde{\boldsymbol{s}}\boldsymbol{H}\right) \tag{Equ. B.10}$$

and eventually

$$\boldsymbol{D}^p = \Lambda \boldsymbol{N} = \Lambda \frac{\mathtt{dev}\left(\boldsymbol{H}\tilde{\boldsymbol{s}}\boldsymbol{H}\right)}{||\mathtt{dev}\left(\boldsymbol{H}\tilde{\boldsymbol{s}}\boldsymbol{H}\right)||} \tag{Equ. B.11}$$

The flow direction (unit normal to the yield function) is given by

$$\boldsymbol{N} = \frac{\dfrac{\partial f}{\partial \boldsymbol{\sigma}}}{||\partial f / \partial \boldsymbol{\sigma}||} = \frac{\mathtt{dev}\left(\boldsymbol{H}\tilde{\boldsymbol{s}}\boldsymbol{H}\right)}{||\mathtt{dev}\left(\boldsymbol{H}\tilde{\boldsymbol{s}}\boldsymbol{H}\right)||} \tag{Equ. B.12}$$

This normal fulfills the following properties:

$$\boldsymbol{N} : \boldsymbol{N} = 1 \qquad \boldsymbol{N} : d\boldsymbol{N} = 0 \tag{Equ. B.13}$$

The equivalent plastic strain rate is therefore given by:

$$\dot{\bar{\varepsilon}}^p = \sqrt{\frac{2}{3}\boldsymbol{D}^p : \boldsymbol{D}^p} = \Lambda\sqrt{\frac{2}{3}\boldsymbol{N} : \boldsymbol{N}} = \sqrt{\frac{2}{3}}\Lambda \tag{Equ. B.14}$$

We also define $\boldsymbol{n}$ as (using Equ. B.3):

$$\boldsymbol{n} = \mathtt{dev}\left(\boldsymbol{H}\tilde{\boldsymbol{s}}\boldsymbol{H}\right) = \mathbb{M} : \tilde{\boldsymbol{s}} \tag{Equ. B.15}$$

It gives:

$$\boldsymbol{N} = \frac{\mathbb{M} : \tilde{\boldsymbol{s}}}{||\mathbb{M} : \tilde{\boldsymbol{s}}||} = \frac{\boldsymbol{n}}{||\boldsymbol{n}||} \tag{Equ. B.16}$$

[1] The symmetry of $\boldsymbol{H}$ has to be ensured by its initial symmetry and a symmetric evolution function.

B.2 Solving the Plastic Problem

The equations that drive the plastic update are as follows (Equ. 5.58 and Equ. 5.60)

$$\tilde{\boldsymbol{s}}^{n+1} = \tilde{\boldsymbol{s}}^{e} - 2G\gamma\mathbb{M} : \tilde{\boldsymbol{s}}^{n+1} \tag{Equ. B.17}$$

$$\bar{\varepsilon}^{p,d}_{n+1} = \bar{\varepsilon}^{p,d}_{n} + \sqrt{\frac{2}{3}}\gamma||\tilde{\boldsymbol{s}}^{n+1}|| \tag{Equ. B.18}$$

and the update of the plastic multiplier in the Newton-Raphson process can be written:

$$\Delta\gamma = -\frac{r_i}{\left.\dfrac{\partial\tilde{\sigma}^{vM}_{eq}}{\partial\gamma}\right|_{\gamma=\gamma_i} - \left.\dfrac{\partial\sigma_y}{\partial\gamma}\right|_{\gamma=\gamma_i}} \tag{Equ. B.19}$$

The first equation (Equ. B.17) is a linear system in $\tilde{\boldsymbol{s}}$. It can be written in the form:

$$\mathbb{P} : \tilde{\boldsymbol{s}}^{n+1} = \tilde{\boldsymbol{s}}^{e} \tag{Equ. B.20}$$

where

$$\begin{aligned}\mathbb{P}_{ijkl} &= \frac{1}{2}(\delta_{ik}\delta_{jl} + \delta_{il}\delta_{jk}) + 2G\gamma\mathbb{M}_{ijkl}\\ \mathbb{P} &= \boldsymbol{I}\underline{\otimes}\boldsymbol{I} + 2G\gamma\mathbb{M} = \mathbb{P}(\gamma, \boldsymbol{H})\end{aligned}$$

The solution to this system is:

$$\tilde{\boldsymbol{s}}^{n+1} = \mathbb{S} : \tilde{\boldsymbol{s}}^{e} \tag{Equ. B.21}$$

where $\mathbb{S}$ is the inverse of $\mathbb{P}$. It has to be noticed however that $\mathbb{P}$ is not actually inverted. $\mathbb{S}$ is used as a notation, a linear system has to be solved to compute $\tilde{\boldsymbol{s}}^{n+1}$.

The update of the plastic multiplier (Equ. B.19) requires to compute $\left.\dfrac{\partial\tilde{\sigma}^{vM\ n+1}_{eq}}{\partial\gamma}\right|_{\gamma=\gamma_i}$ and $\left.\dfrac{\partial\sigma^{n+1}_{y}}{\partial\gamma}\right|_{\gamma=\gamma_i}$.

- $$\begin{aligned}\frac{\partial\tilde{\sigma}^{vM\ n+1}_{eq}}{\partial\gamma} &= \sqrt{\frac{3}{2}}\frac{1}{\tilde{\sigma}^{vM\ n+1}_{eq}}\tilde{\boldsymbol{s}}^{n+1} : \frac{\partial\tilde{\boldsymbol{s}}^{n+1}}{\partial\gamma}\\ &= -\sqrt{\frac{3}{2}}\frac{2G}{\tilde{\sigma}^{vM\ n+1}_{eq}}\tilde{\boldsymbol{s}}^{n+1} : \left(\mathbb{S} : \boldsymbol{n}^{n+1}\right)\end{aligned} \tag{Equ. B.22}$$

The latest equality is valid since (derivation of Equ. B.20 with respect to γ):

$$\begin{aligned}\frac{\partial\mathbb{P} : \tilde{\boldsymbol{s}}^{n+1}}{\partial\gamma} &= 0\\ &= \frac{\partial\mathbb{P}}{\partial\gamma} : \tilde{\boldsymbol{s}}^{n+1} + \mathbb{P} : \frac{\partial\tilde{\boldsymbol{s}}^{n+1}}{\partial\gamma}\\ &= 2G\mathbb{M} : \tilde{\boldsymbol{s}}^{n+1} + \mathbb{P} : \frac{\partial\tilde{\boldsymbol{s}}^{n+1}}{\partial\gamma}\\ &= 2G\boldsymbol{n} + \mathbb{P} : \frac{\partial\tilde{\boldsymbol{s}}^{n+1}}{\partial\gamma}\end{aligned}$$

Thus

$$\mathbb{P} : \frac{\partial \tilde{\boldsymbol{s}}^{n+1}}{\partial \gamma} = -2G\boldsymbol{n} \tag{Equ. B.23}$$

or,

$$\frac{\partial \tilde{\boldsymbol{s}}^{n+1}}{\partial \gamma} = -2G\mathbb{S} : \boldsymbol{n} \tag{Equ. B.24}$$

for which, once more, the latest equality is only a notation, a linear system has to be solved to compute $\frac{\partial \tilde{\boldsymbol{s}}^{n+1}}{\partial \gamma}$.

The last assumption to solve the plastic problem is to use only an isotropic hardening law for the yield limit:

$$\sigma_y(\bar{\varepsilon}^{p,d}) = \sigma_y^0 + h\bar{\varepsilon}^{p,d} \quad \text{thus} \quad \sigma_y^{n+1} = \sigma_y^n + h(\bar{\varepsilon}_{n+1}^{p,d} - \bar{\varepsilon}_n^{p,d})$$

with h the hardening parameters: $h = \frac{d\sigma_y}{d\bar{\varepsilon}^{p,d}}$.
We thus have

$$\begin{aligned}
\bullet \quad \frac{\partial \sigma_y^{n+1}}{\partial \gamma} &= h\frac{\partial(\bar{\varepsilon}_{n+1}^{p,d} - \bar{\varepsilon}_n^{p,d})}{\partial \gamma} \\
&\overset{\text{using Equ. 5.60}}{=} \sqrt{\frac{2}{3}}h\left(||\tilde{\boldsymbol{s}}^{n+1}|| + \gamma\frac{\partial||\tilde{\boldsymbol{s}}^{n+1}||}{\partial\gamma}\right) \\
&= \sqrt{\frac{2}{3}}h\left(||\tilde{\boldsymbol{s}}^{n+1}|| + \frac{\gamma}{||\tilde{\boldsymbol{s}}^{n+1}||}\tilde{\boldsymbol{s}}^{n+1} : \frac{\partial \tilde{\boldsymbol{s}}}{\partial\gamma}\right) \\
&\overset{\text{using Equ. B.24}}{=} \sqrt{\frac{2}{3}}h\left(||\tilde{\boldsymbol{s}}^{n+1}|| - \frac{2G\gamma}{||\tilde{\boldsymbol{s}}^{n+1}||}\tilde{\boldsymbol{s}}^{n+1} : \left[\mathbb{S} : \boldsymbol{n}^{n+1}\right]\right)
\end{aligned} \tag{Equ. B.25}$$

Finally, the update of the plastic multiplier is given by combining Equ. B.19, Equ. B.22, and Equ. B.25:

$$\Delta\gamma = \frac{||\tilde{\boldsymbol{s}}^{n+1}|| - \sqrt{\frac{2}{3}}\sigma_y(\gamma_i, \tilde{\boldsymbol{s}}^{n+1})}{\frac{2G}{\tilde{\sigma}_{eq}^{n+1}}\tilde{\boldsymbol{s}}^{n+1} : \left[\mathbb{S}(\gamma_i) : \boldsymbol{n}^{n+1}\right] + \frac{2}{3}h\left(||\tilde{\boldsymbol{s}}^{n+1}|| - \frac{2G\gamma_i}{||\tilde{\boldsymbol{s}}^{n+1}||}\tilde{\boldsymbol{s}}^{n+1} : \left[\mathbb{S}(\gamma_i) : \boldsymbol{n}^{n+1}\right]\right)}$$

Once more, we should insist on the point that $\mathbb{S}$ is used only as a notation. At each iteration of the Newton-Raphson procedure used to compute the plastic multiplier, two linear systems have to be solved to get $\tilde{\boldsymbol{s}}^{n+1}$ (Equ. B.20) and $\frac{\partial \tilde{\boldsymbol{s}}^{n+1}}{\partial \gamma}$ (Equ. B.23).

Appendix C
Computation of a Consistent Material Tangent Stiffness Operator

This appendix relates the details of the equations needed to derive the consistent tangent operator (as defined in section 3.2) for the proposed integration procedure.
The material tangent stiffness operator can be written :

$$\mathbb{H} = \frac{d\boldsymbol{\sigma}}{d\boldsymbol{E}^N} = \mathbb{H}^{vol.} + \mathbb{H}^{dev.} = \boldsymbol{I} \otimes \frac{dp}{d\boldsymbol{E}^N} + \frac{d\boldsymbol{s}}{d\boldsymbol{E}^N} \tag{Equ. C.1}$$

with $\mathbb{H}^{vol.}$ and $\mathbb{H}^{dev.}$ the volumic and deviatoric parts of the tangent stiffness operator and $\boldsymbol{\sigma} = \mathbb{M}^{-1} : \tilde{\boldsymbol{\sigma}}$ and $\tilde{\boldsymbol{\sigma}} = \tilde{\boldsymbol{\sigma}}(\boldsymbol{E}^N, \boldsymbol{H}, \gamma)$:

$$\begin{cases} \mathbb{H}^{vol.} &= \boldsymbol{I} \otimes \left(\tilde{p} \dfrac{\partial (1 - \eta d^H)}{\partial \boldsymbol{H}} : \dfrac{d\boldsymbol{H}}{d\boldsymbol{E}^N} + (1 - \eta d^H) \dfrac{\partial \tilde{p}}{\partial \boldsymbol{E}^N} \right) \\ \mathbb{H}^{dev.} &= \dfrac{\partial \boldsymbol{s}}{\partial \boldsymbol{E}^N} + \dfrac{\partial \boldsymbol{s}}{\partial \boldsymbol{H}} : \dfrac{d\boldsymbol{H}}{d\boldsymbol{E}^N} + \dfrac{\partial \boldsymbol{s}}{\partial \gamma} \otimes \dfrac{d\gamma}{d\boldsymbol{H}} \end{cases} \tag{Equ. C.2}$$

with $\boldsymbol{H} = \boldsymbol{H}_0 + \boldsymbol{g}$, $\tilde{p} = \tilde{p}(J)$ with $J = \mathtt{tr}\left(\boldsymbol{E}^N\right)$ and $\boldsymbol{s} = \boldsymbol{s}(\hat{\boldsymbol{E}}^N, \gamma, \boldsymbol{H})$

$$\begin{cases} \mathbb{H}^{vol.} &= \boldsymbol{I} \otimes \left(-\dfrac{\eta}{3} \tilde{p} \dfrac{\partial \mathtt{tr}(\boldsymbol{d})}{\partial \boldsymbol{H}} : \dfrac{d\boldsymbol{H}}{d\boldsymbol{E}^N} + (1 - \eta d^H) \dfrac{\partial \tilde{p}}{\partial \boldsymbol{E}^N} \right) \\ \mathbb{H}^{dev.} &= \mathbb{M}^{-1} : \dfrac{\partial \tilde{\boldsymbol{s}}}{\partial \boldsymbol{E}^N} + \left(\dfrac{\partial \mathbb{M}^{-1}}{\partial \boldsymbol{H}} : \tilde{\boldsymbol{s}} + \mathbb{M}^{-1} : \dfrac{\partial \tilde{\boldsymbol{s}}}{\partial \boldsymbol{H}} \right) : \dfrac{d\boldsymbol{H}}{d\boldsymbol{E}^N} + \mathbb{M}^{-1} : \dfrac{\partial \tilde{\boldsymbol{s}}}{\partial \gamma} \otimes \dfrac{d\gamma}{d\boldsymbol{E}^N} \end{cases} \tag{Equ. C.3}$$

Stress tensor partial derivative

One gets, almost trivially for the partial derivatives with respect to $\boldsymbol{E}^N$ (see appendix B.2 for the details on the derivative with respect to γ - the derivative with respect to $\boldsymbol{H}$ is computed in the same way.):

$$\frac{\partial \tilde{p}}{\partial \boldsymbol{E}^N} = \frac{\partial \tilde{p}}{\partial J} \frac{\partial J}{\partial \boldsymbol{E}^N} = K \frac{\partial J}{\partial \boldsymbol{E}^N} \tag{Equ. C.4}$$

$$\frac{\partial \tilde{\boldsymbol{s}}}{\partial \boldsymbol{E}^N} = \frac{\partial \tilde{\boldsymbol{s}}}{\partial \hat{\boldsymbol{E}}^N} : \frac{\partial \hat{\boldsymbol{E}}^N}{\partial \boldsymbol{E}^N} \tag{Equ. C.5}$$

$$= 2G\mathbb{S} : \frac{\partial \hat{\boldsymbol{E}}^N}{\partial \boldsymbol{E}^N} \tag{Equ. C.6}$$

with

$$\left\{ \begin{array}{rcl} \dfrac{\partial J}{\partial \boldsymbol{E}^N} & = & \boldsymbol{I} \\ \dfrac{\partial \hat{\boldsymbol{E}}^N}{\partial \boldsymbol{E}^N} & = & \mathbb{1} \end{array} \right. \tag{Equ. C.7}$$

Computation of $\dfrac{d\gamma}{d\boldsymbol{E}^N}$ (isotropic hardening only)

The derivation of $\dfrac{d\gamma}{d\boldsymbol{E}^N}$ uses the stationarity property of the yield function: $\dfrac{df}{d\boldsymbol{E}^N} = 0$.

$$\frac{df}{d\boldsymbol{E}^N} = 0 \tag{Equ. C.8}$$

$$= \frac{d\tilde{\sigma}_{eq}(\tilde{\boldsymbol{s}})}{d\boldsymbol{E}^N} - \frac{d\sigma_y(\tilde{\boldsymbol{s}},\gamma)}{d\boldsymbol{E}^N} \tag{Equ. C.9}$$

$$= \left(\frac{\partial \tilde{\sigma}_{eq}}{\partial \tilde{\boldsymbol{s}}} - \frac{\partial \sigma_y}{\partial \tilde{\boldsymbol{s}}}\right) : \frac{d\tilde{\boldsymbol{s}}}{d\boldsymbol{E}^N} - \frac{\partial \sigma_y}{\partial \gamma}\frac{d\gamma}{d\boldsymbol{E}^N} \tag{Equ. C.10}$$

with :

$$\frac{\partial \tilde{\sigma}_{eq}}{\partial \tilde{\boldsymbol{s}}} = \sqrt{\frac{3}{2}}\frac{\tilde{\boldsymbol{s}}}{||\tilde{\boldsymbol{s}}||} \tag{Equ. C.11}$$

$$\frac{\partial \sigma_y}{\partial \tilde{\boldsymbol{s}}} = \sqrt{\frac{2}{3}}h\gamma\frac{\tilde{\boldsymbol{s}}}{||\tilde{\boldsymbol{s}}||} \tag{Equ. C.12}$$

$$\frac{\partial \sigma_y}{\partial \gamma} = \sqrt{\frac{2}{3}}h||\tilde{\boldsymbol{s}}|| \tag{Equ. C.13}$$

$$\frac{d\tilde{\boldsymbol{s}}}{d\boldsymbol{E}^N} = \frac{\partial \tilde{\boldsymbol{s}}}{\partial \boldsymbol{E}^N} + \frac{\partial \tilde{\boldsymbol{s}}}{\partial \boldsymbol{H}} : \frac{d\boldsymbol{H}}{d\boldsymbol{E}^N} + \frac{\partial \tilde{\boldsymbol{s}}}{\partial \gamma} \otimes \frac{d\gamma}{d\boldsymbol{E}^N} \tag{Equ. C.14}$$

One therefore gets:

$$\left(\sqrt{\frac{3}{2}} - \sqrt{\frac{2}{3}}h\gamma\right)\frac{\tilde{\boldsymbol{s}}}{||\tilde{\boldsymbol{s}}||} : \frac{d\tilde{\boldsymbol{s}}}{d\boldsymbol{E}^N} - \sqrt{\frac{2}{3}}h||\tilde{\boldsymbol{s}}||\frac{d\gamma}{d\boldsymbol{E}^N} = 0$$

We therefore get:

$$\sqrt{\frac{3}{2}}\frac{\tilde{\boldsymbol{s}}}{||\tilde{\boldsymbol{s}}||} : \left(\frac{\partial \tilde{\boldsymbol{s}}}{\partial \boldsymbol{E}^N} + \frac{\partial \tilde{\boldsymbol{s}}}{\partial \gamma} \otimes \frac{d\gamma}{d\boldsymbol{E}^N} + \frac{\partial \tilde{\boldsymbol{s}}}{\partial \boldsymbol{H}} : \frac{d\boldsymbol{H}}{d\boldsymbol{E}^N}\right) - h\sqrt{\frac{2}{3}}\left(||\tilde{\boldsymbol{s}}||\frac{d\gamma}{d\boldsymbol{E}^N} + \gamma\frac{\tilde{\boldsymbol{s}}}{||\tilde{\boldsymbol{s}}||} : \left(\frac{\partial \tilde{\boldsymbol{s}}}{\partial \boldsymbol{E}^N} + \frac{\partial \tilde{\boldsymbol{s}}}{\partial \gamma} \otimes \frac{d\gamma}{d\boldsymbol{E}^N} + \frac{\partial \tilde{\boldsymbol{s}}}{\partial \boldsymbol{H}} : \frac{d\boldsymbol{H}}{d\boldsymbol{E}^N}\right)\right) = 0 \tag{Equ. C.15}$$

We can re-arrange the terms of this equation to obtain an equation for $\dfrac{d\gamma}{d\boldsymbol{E}^N}$:

$$\left[\left(\sqrt{\frac{3}{2}} - h\sqrt{\frac{2}{3}}\gamma\right)\frac{\tilde{\boldsymbol{s}}}{||\tilde{\boldsymbol{s}}||} : \frac{\partial \tilde{\boldsymbol{s}}}{\partial \gamma} - h\sqrt{\frac{2}{3}}||\tilde{\boldsymbol{s}}||\right]\frac{d\gamma}{d\boldsymbol{E}^N} = h\sqrt{\frac{2}{3}}\gamma\frac{\tilde{\boldsymbol{s}}}{||\tilde{\boldsymbol{s}}||} : \left(\frac{\partial \tilde{\boldsymbol{s}}}{\partial \boldsymbol{E}^N} + \frac{\partial \tilde{\boldsymbol{s}}}{\partial \boldsymbol{H}} : \frac{d\boldsymbol{H}}{d\boldsymbol{E}^N}\right) - \sqrt{\frac{3}{2}}\frac{\tilde{\boldsymbol{s}}}{||\tilde{\boldsymbol{s}}||} : \left(\frac{\partial \tilde{\boldsymbol{s}}}{\partial \boldsymbol{E}^N} + \frac{\partial \tilde{\boldsymbol{s}}}{\partial \boldsymbol{H}} : \frac{d\boldsymbol{H}}{d\boldsymbol{E}^N}\right) \tag{Equ. C.16}$$

This gives

$$\frac{d\gamma}{d\boldsymbol{E}^N} = \boldsymbol{\alpha} + \boldsymbol{\zeta} : \frac{d\boldsymbol{H}}{d\boldsymbol{E}^N} \tag{Equ. C.17}$$

with

$$\boldsymbol{\alpha} = \frac{1}{\text{den}} \left(\boldsymbol{A}_1 : \frac{\partial \tilde{\boldsymbol{s}}}{\partial \boldsymbol{E}^N} \right) \tag{Equ. C.18}$$

$$\boldsymbol{\zeta} = \frac{1}{\text{den}} \left(\boldsymbol{A}_1 : \frac{\partial \tilde{\boldsymbol{s}}}{\partial \boldsymbol{H}} \right) \tag{Equ. C.19}$$

and

$$\boldsymbol{A}_1 = \left(h\sqrt{\frac{2}{3}}\gamma - \sqrt{\frac{3}{2}} \right) \frac{\tilde{\boldsymbol{s}}}{||\tilde{\boldsymbol{s}}||} \tag{Equ. C.20}$$

$$\text{den} = -\boldsymbol{A}_1 : \frac{\partial \tilde{\boldsymbol{s}}}{\partial \gamma} - h\sqrt{\frac{2}{3}}||\tilde{\boldsymbol{s}}|| \tag{Equ. C.21}$$

Computation of $\frac{d\boldsymbol{H}}{d\boldsymbol{E}^N}$

The derivative of $\boldsymbol{H}$ with respect to the natural strain ($\boldsymbol{E}^N$) depends explicitly on the damage evolution law (terms written as $\frac{\partial \boldsymbol{g}}{\partial \boldsymbol{.}}$):

$$\frac{d\boldsymbol{H}}{d\boldsymbol{E}^N} = \frac{d\boldsymbol{g}}{d\boldsymbol{E}^N} = \frac{\partial \boldsymbol{g}}{\partial \boldsymbol{E}^N} + \frac{\partial \boldsymbol{g}}{\partial \boldsymbol{s}} : \frac{d\boldsymbol{s}}{d\boldsymbol{E}^N} + \frac{\partial \boldsymbol{g}}{\partial p} \otimes \frac{dp}{d\boldsymbol{E}^N} + \frac{\partial \boldsymbol{g}}{\partial \boldsymbol{H}} : \frac{d\boldsymbol{H}}{d\boldsymbol{E}^N} + \frac{\partial \boldsymbol{g}}{\partial \gamma} \otimes \frac{d\gamma}{d\boldsymbol{E}^N} \tag{Equ. C.22}$$

Using Equ. C.2 and Equ. C.17 allows one to write Equ. C.22 as:

$$\left[\boldsymbol{I} \underline{\otimes} \boldsymbol{I} - \frac{\partial \boldsymbol{g}}{\partial \boldsymbol{s}} : \left(\frac{\partial \boldsymbol{s}}{\partial \gamma} \otimes \boldsymbol{\zeta} + \frac{\partial \boldsymbol{s}}{\partial \boldsymbol{H}} \right) - \frac{\partial \boldsymbol{g}}{\partial p} \otimes \frac{\partial p}{\partial \boldsymbol{H}} - \frac{\partial \boldsymbol{g}}{\partial \boldsymbol{H}} - \frac{\partial \boldsymbol{g}}{\partial \gamma} \otimes \boldsymbol{\zeta} \right] : \frac{d\boldsymbol{H}}{d\boldsymbol{E}^N} = \frac{\partial \boldsymbol{g}}{\partial \boldsymbol{E}^N} + \frac{\partial \boldsymbol{g}}{\partial \boldsymbol{s}} : \left(\frac{\partial \boldsymbol{s}}{\partial \boldsymbol{E}^N} + \frac{\partial \tilde{\boldsymbol{s}}}{\partial \gamma} \otimes \boldsymbol{\alpha} \right) + \frac{\partial \boldsymbol{g}}{\partial p} \otimes \frac{dp}{d\boldsymbol{E}^N} + \frac{\partial \boldsymbol{g}}{\partial \gamma} \otimes \boldsymbol{\alpha} \tag{Equ. C.23}$$

where all the derivatives both on the left and right hand side of the equation are known. This equation is generically written $A_{ijkl} X_{klmn} = B_{ijmn}$ with A and B known and can be solved by solving 9 equations of the type $A_{ijkl} x_{kl} = b_{ij}$ which are systems of 9 linear equations in x_{kl}.

Derivatives of $\mathbb{M}$ and $\mathbb{M}^{-1}$

Derivatives of $\mathbb{M}$ and $\mathbb{M}^{-1}$ with respect to damage remain to be computed. These are in general sixth order tensors. However, in the computation of the stiffness operator, the general sixth order tensors are therefore not needed. Only the fourth order tensors $\frac{\partial \mathbb{M}}{\partial \boldsymbol{H}} : \tilde{\boldsymbol{s}}$, $\frac{\partial \mathbb{M}^{-1}}{\partial \boldsymbol{H}} : \tilde{\boldsymbol{s}}$ as well as $\frac{\partial \mathtt{tr}(\boldsymbol{d})}{\partial \boldsymbol{H}}$ are to be computed.

Computation of $\dfrac{\partial \mathbb{M}}{\partial \boldsymbol{H}} : \tilde{\boldsymbol{s}}$

$$[\mathbb{M} : \tilde{\boldsymbol{s}}]_{ij} = [\mathtt{dev}(\boldsymbol{H}\tilde{\boldsymbol{s}}\boldsymbol{H})]_{ij} = [\boldsymbol{H}\tilde{\boldsymbol{s}}\boldsymbol{H}]_{ij} - \frac{1}{3}[\boldsymbol{H}\tilde{\boldsymbol{s}}\boldsymbol{H}]_{nn}\delta_{ij}$$

Therefore

$$\left.\frac{\partial [\mathbb{M} : \tilde{\boldsymbol{s}}]_{ij}}{\partial H_{kl}}\right|_{\tilde{\boldsymbol{s}}\ \mathrm{cst}} = \delta_{ik}[\boldsymbol{H}\tilde{\boldsymbol{s}}]_{jl} + \delta_{jl}[\boldsymbol{H}\tilde{\boldsymbol{s}}]_{ik} - \frac{1}{3}([\boldsymbol{H}\tilde{\boldsymbol{s}}]_{kl} + [\boldsymbol{H}\tilde{\boldsymbol{s}}]_{lk})\delta_{ij} \qquad \text{(Equ. C.24)}$$

$$\frac{\partial \mathbb{M}}{\partial \boldsymbol{H}} : \tilde{\boldsymbol{s}} = \boldsymbol{I}\underline{\otimes}(\boldsymbol{H}\tilde{\boldsymbol{s}}) + (\boldsymbol{H}\tilde{\boldsymbol{s}})\underline{\otimes}\boldsymbol{I} - \frac{1}{3}\boldsymbol{I}\otimes\left[(\boldsymbol{H}\tilde{\boldsymbol{s}}) + (\boldsymbol{H}\tilde{\boldsymbol{s}})^T\right] \qquad \text{(Equ. C.25)}$$

Computation of $\dfrac{\partial \mathbb{M}^{-1}}{\partial \boldsymbol{H}} : \tilde{\boldsymbol{s}}$

$$\left[\mathbb{M}^{-1} : \tilde{\boldsymbol{s}}\right]_{ij} = \underbrace{(H^{-1})_{io}\tilde{s}_{op}(H^{-1})_{pj}}_{\star_{ij}} - \underbrace{\frac{H^{-2}_{ij}(\tilde{s}_{mn}H^{-2}_{mn})}{\mathtt{tr}\left(\boldsymbol{H}^{-2}\right)}}_{\star\star_{ij}} \qquad \text{(Equ. C.26)}$$

With

$$\begin{aligned}\left.\frac{\partial \star_{ij}}{\partial H_{kl}}\right|_{\tilde{\boldsymbol{s}}\ \mathrm{cst}} &= \frac{\partial H^{-1}_{io}}{\partial H_{kl}}\tilde{s}_{op}H^{-1}_{pj} + H^{-1}_{io}\tilde{s}_{op}\frac{\partial H^{-1}_{pj}}{\partial H_{kl}} \\ &= -H^{-1}_{ik}\left(H^{-1}\tilde{s}H^{-1}\right)_{jl} - \left(H^{-1}\tilde{s}H^{-1}\right)_{ik}H^{-1}_{jl}\end{aligned}$$

and

$$\left.\frac{\partial \star\star_{ij}}{\partial H_{kl}}\right|_{\tilde{\boldsymbol{s}}\ \mathrm{cst}} = \frac{\partial H^{-2}_{ij}}{\partial H_{kl}}\frac{\tilde{s}_{mn}H^{-2}_{mn}}{\mathtt{tr}\left(\boldsymbol{H}^{-2}\right)} + H^{-2}_{ij}\frac{\tilde{s}_{mn}}{\mathtt{tr}\left(\boldsymbol{H}^{-2}\right)}\frac{\partial H^{-2}_{mn}}{\partial H_{kl}} - \frac{H^{-2}_{ij}\tilde{s}_{mn}H^{-2}_{mn}}{(\mathtt{tr}\left(\boldsymbol{H}^{-2}\right))^2}\frac{\partial \mathtt{tr}\left(\boldsymbol{H}^{-2}\right)}{\partial H_{kl}}$$

with

$$\frac{\partial H^{-2}_{ij}}{\partial H_{kl}} = \frac{\partial H^{-1}_{io}}{\partial H_{kl}}H^{-1}_{oj} + H^{-1}_{io}\frac{\partial H^{-1}_{oj}}{\partial H_{kl}} = -(H^{-1}_{ik}H^{-2}_{jl} + H^{-2}_{ik}H^{-1}_{jl})$$

$$\frac{\partial \boldsymbol{H}^{-2}}{\partial \boldsymbol{H}} = -(\boldsymbol{H}^{-2}\underline{\otimes}\boldsymbol{H}^{-1} + \boldsymbol{H}^{-1}\underline{\otimes}\boldsymbol{H}^{-2})$$

and

$$\frac{\partial \mathtt{tr}\left(\boldsymbol{H}^{-2}\right)}{\partial \boldsymbol{H}} = \frac{\partial \boldsymbol{H}^{-2} : \boldsymbol{I}}{\partial \boldsymbol{H}} = -2\boldsymbol{H}^{-3}$$

One can therefore write

$$\begin{aligned}\left.\frac{\partial \star\star_{ij}}{\partial H_{kl}}\right|_{\tilde{\boldsymbol{s}}\ \mathrm{cst}} = -\Bigg[&\left(H^{-1}_{ik}H^{-2}_{jl} + H^{-2}_{ik}H^{-1}_{jl}\right)\frac{\tilde{s}_{mn}H^{-2}_{mn}}{\mathtt{tr}\left(\boldsymbol{H}^{-2}\right)} + \frac{H^{-2}_{ij}}{\mathtt{tr}\left(\boldsymbol{H}^{-2}\right)}\left([\boldsymbol{H}^{-1}\tilde{\boldsymbol{s}}\boldsymbol{H}^{-2}]_{kl} + [\boldsymbol{H}^{-2}\tilde{\boldsymbol{s}}\boldsymbol{H}^{-1}]_{kl}\right) \\ &- H^{-2}_{ij}\frac{2\tilde{s}_{mn}H^{-2}_{mn}}{(\mathtt{tr}\left(\boldsymbol{H}^{-2}\right))^2}H^{-3}_{kl}\Bigg]\end{aligned}$$

Finally the fourth order tensor $\dfrac{\partial \mathbb{M}^{-1} : \tilde{\boldsymbol{s}}}{\partial \boldsymbol{H}}$ can be written :

$$\begin{aligned}\frac{\partial M^{-1}_{ijop}}{\partial H_{kl}}\tilde{s}_{op} = &-H^{-1}_{ik}\left(H^{-1}\tilde{s}H^{-1}\right)_{jl} - \left(H^{-1}\tilde{s}H^{-1}\right)_{ik}H^{-1}_{jl} \\ &+ \frac{\tilde{s}_{mn}H^{-2}_{mn}}{\mathtt{tr}\left(\boldsymbol{H}^{-2}\right)}\left[H^{-1}_{ik}H^{-2}_{jl} + H^{-2}_{ik}H^{-1}_{jl} - \frac{2}{\mathtt{tr}\left(\boldsymbol{H}^{-2}\right)}H^{-2}_{ij}H^{-3}_{kl}\right] \\ &+ \frac{H^{-2}_{ij}}{\mathtt{tr}\left(\boldsymbol{H}^{-2}\right)}\left([\boldsymbol{H}^{-1}\tilde{\boldsymbol{s}}\boldsymbol{H}^{-2}]_{kl} + [\boldsymbol{H}^{-2}\tilde{\boldsymbol{s}}\boldsymbol{H}^{-1}]_{kl}\right)\end{aligned} \tag{Equ. C.27}$$

or else

$$\begin{aligned}\frac{\partial \mathbb{M}^{-1}}{\partial \boldsymbol{H}} : \tilde{\boldsymbol{s}} = &-\boldsymbol{H}^{-1}\underline{\otimes}\left(\boldsymbol{H}^{-1}\tilde{\boldsymbol{s}}\boldsymbol{H}^{-1}\right) - \left(\boldsymbol{H}^{-1}\tilde{\boldsymbol{s}}\boldsymbol{H}^{-1}\right)\underline{\otimes}\boldsymbol{H}^{-1} \\ &+ \frac{\tilde{\boldsymbol{s}} : \boldsymbol{H}^{-2}}{\mathtt{tr}\left(\boldsymbol{H}^{-2}\right)}\left[\boldsymbol{H}^{-1}\underline{\otimes}\boldsymbol{H}^{-2} + \boldsymbol{H}^{-2}\underline{\otimes}\boldsymbol{H}^{-1} - \frac{2}{\mathtt{tr}\left(\boldsymbol{H}^{-2}\right)}\boldsymbol{H}^{-2}\otimes\boldsymbol{H}^{-3}\right] \\ &+ \frac{\boldsymbol{H}^{-2}}{\mathtt{tr}\left(\boldsymbol{H}^{-2}\right)}\otimes\left[\boldsymbol{H}^{-1}\tilde{\boldsymbol{s}}\boldsymbol{H}^{-2} + \boldsymbol{H}^{-2}\tilde{\boldsymbol{s}}\boldsymbol{H}^{-1}\right]\end{aligned} \tag{Equ. C.28}$$

Computation of $\dfrac{\partial \mathtt{tr}\,(\boldsymbol{d})}{\partial \boldsymbol{H}}$

As $\boldsymbol{d} = \boldsymbol{I} - \boldsymbol{H}^{-2}$ and as, for any invertible symmetric tensor such as $\boldsymbol{H}$, one has: $\dfrac{\partial \boldsymbol{H}^{-1}}{\partial \boldsymbol{H}} = -\boldsymbol{H}^{-1}\underline{\otimes}\boldsymbol{H}^{-1}$, one can write:

$$\frac{\partial \boldsymbol{d}}{\partial \boldsymbol{H}} = \boldsymbol{H}^{-2}\underline{\otimes}\boldsymbol{H}^{-1} + \boldsymbol{H}^{-1}\underline{\otimes}\boldsymbol{H}^{-2} \tag{Equ. C.29}$$

The computation of $\dfrac{\partial \mathtt{tr}\,(\boldsymbol{d})}{\partial \boldsymbol{H}}$ is therefore directly given by:

$$\frac{\partial \mathtt{tr}\,(\boldsymbol{d})}{\partial \boldsymbol{H}} = \frac{\partial \boldsymbol{d}}{\partial \boldsymbol{H}} : \boldsymbol{I} = \left(\boldsymbol{H}^{-2}\underline{\otimes}\boldsymbol{H}^{-1} + \boldsymbol{H}^{-1}\underline{\otimes}\boldsymbol{H}^{-2}\right) : \boldsymbol{I} = 2\boldsymbol{H}^{-3} \tag{Equ. C.30}$$

As $\boldsymbol{H}$ is a polynomial function of $\boldsymbol{d}$, the derivative given by Equ. C.29 can be computed by the use of a spectral decomposition of $\boldsymbol{d}$.

Appendix D
Deriving the Anisotropic Damage Variation for a Bone Remodeling Problem

This appendix relates the details of the equations needed to derive the damage variation for the remodeling problem introduced in section 5.2.3.
Using Equ. 5.35 defining the damage tensor and a normalization condition for the fabric tensor such that $\mathtt{tr}(\boldsymbol{T}) = 3$, one can write for the density:

$$\rho = \rho_0 \left(\frac{1 - d^H}{A} \right)^{1/\beta} \tag{Equ. D.1}$$

Therefore, the density evolution can be written (using Equ. C.30):

$$\dot{\rho} = -\frac{2\rho}{3\beta} \frac{1}{1 - d^H} \boldsymbol{H}^{-3} : \dot{\boldsymbol{H}} \tag{Equ. D.2}$$

Using an associated evolution law for the remodeling tensor (Equ. 5.76), we can write in formation conditions:

$$\dot{\rho} = -\frac{2\rho}{3\beta} \frac{1}{1 - d^H} \boldsymbol{H}^{-3} : \left(\mu^f \frac{\partial g^f}{\partial \boldsymbol{Y}} \right) \tag{Equ. D.3}$$

with (deriving Equ. 5.74 with respect to $\boldsymbol{Y}$)

$$\begin{aligned} \frac{\partial g^f}{\partial \boldsymbol{Y}} &= C\, 3^{1/4} \left(\frac{1}{4} (\boldsymbol{J} : \boldsymbol{J})^{-3/4} 2\boldsymbol{J} : \frac{\partial \boldsymbol{J}}{\partial \boldsymbol{Y}} \right) \\ &= \frac{3^{1/4}\, C}{2} (\boldsymbol{J} : \boldsymbol{J})^{-3/4} \mathbb{W} : \boldsymbol{J} \\ &= \alpha^f \mathbb{W} : \boldsymbol{J} \end{aligned} \tag{Equ. D.4}$$

Therefore, Equ. D.3 can be written:

$$\dot{\rho} = -\frac{2\rho}{3\beta} \frac{1}{1 - d^H} \mu^f \alpha^f \underbrace{\boldsymbol{H}^{-3} : (\mathbb{W} : \boldsymbol{J})}_{= \mathtt{tr}\left(\boldsymbol{H}^{-3}(\mathbb{W}:\boldsymbol{J})\right)} \tag{Equ. D.5}$$

which, together with Equ. 5.1 (to retrieve the density evolution of the Stanford model), gives:

$$\mu^f = -\frac{3}{2} \beta k S_v \dot{r} \underbrace{(1 - d^H)}_{= \frac{1}{3}\mathtt{tr}(\boldsymbol{H}^{-2})} \frac{1}{\alpha^f \mathtt{tr}\left(\boldsymbol{H}^{-3}(\mathbb{W} : \boldsymbol{J})\right)} \frac{\rho_0}{\rho} \tag{Equ. D.6}$$

and finally:

$$\dot{\boldsymbol{H}}^f = \mu^f \alpha^f \mathbb{W} : \boldsymbol{J} = -\frac{1}{2}\beta k S_v \dot{r} \frac{\mathtt{tr}\left(\boldsymbol{H}^{-2}\right)}{\mathtt{tr}\left(\boldsymbol{H}^{-3}(\mathbb{W} : \boldsymbol{J})\right)} \frac{\rho_0}{\rho} \mathbb{W} : \boldsymbol{J} \tag{Equ. D.7}$$

The same approach gives in resorption conditions:

$$\begin{aligned} \frac{\partial g^r}{\partial \boldsymbol{Y}} &= -3^{1/4}\left(\frac{1}{4}(\boldsymbol{J} : \boldsymbol{J})^{-3/4} 2\boldsymbol{J} : \frac{\partial \boldsymbol{J}}{\partial \boldsymbol{Y}}\right) \\ &= -\frac{3^{1/4}\, C}{2}(\boldsymbol{J} : \boldsymbol{J})^{-3/4} \mathbb{W} : \boldsymbol{J} \\ &= \alpha^r \mathbb{W} : \boldsymbol{J} \end{aligned} \tag{Equ. D.8}$$

and eventually:

$$\dot{\boldsymbol{H}}^r = \mu^r \alpha^r \mathbb{W} : \boldsymbol{J} = -\frac{1}{2}\beta k S_v \dot{r} \frac{\mathtt{tr}\left(\boldsymbol{H}^{-2}\right)}{\mathtt{tr}\left(\boldsymbol{H}^{-3}(\mathbb{W} : \boldsymbol{J})\right)} \frac{\rho_0}{\rho} \mathbb{W} : \boldsymbol{J} = \dot{\boldsymbol{H}}^f \tag{Equ. D.9}$$

Appendix E
Morphological Data of the Samples Used for the Validation Process

This appendix gives, for each sample tested for the validation in section 5.4, the morphological data exploited in this work (D.F. stands for Duocel Foam): `BV/TV`, `Tb.Th`, fabric tensor $\boldsymbol{T}$ eigenvalues, T_1 and T_2 (T_3 is computed so that $\mathrm{tr}(\boldsymbol{T}) = 3$) and eigenvectors, $\mathbf{T}_1$ and $\mathbf{T}_2$ ($\mathbf{T}_3$ is orthogonal to those two), `D.A.`, as well as an ellipsoid representation of the fabric tensor (Figs E.1 to E.17 - colormaps are proportional to the fabric values along the vertical axis).

TABLE E.1: *Morphological data of the tested samples*

Sample	BV/TV	Tb.Th	T_1	T_2	D.A.	$\mathbf{T}_1$	$\mathbf{T}_2$
	%	mm	-	-	-	-	-
D.F. high density - $D1$	11.865	0.352	1.022	1.005	1.051	(0.9,-0.0,1.5)	(-1.4,0.8,0.8)
D.F. high density - $D2$	13.463	0.376	1.023	1.006	1.053	(1.5,0.8,-0.5)	(0.5,-1.5,-0.8)
D.F. high density - $D3$	11.897	0.353	1.032	0.992	1.056	(0.1,-1.8,0.6)	(-1.3,-0.5,-1.1)
D.F. high density - $D4$	12.601	0.353	1.038	0.983	1.061	(1.4,-1.1,0.4)	(-1.0,-0.8,1.2)
D.F. high density - $D5$	14.175	0.366	1.044	0.985	1.074	(0.4,-1.4,-1.0)	(-1.3,0.3,-1.0)
D.F. middle density - $M1$	7.248	0.271	1.044	0.995	1.086	(0.4,-0.0,-2.5)	(-1.7,1.1,-0.3)
D.F. middle density - $M2$	6.533	0.248	1.047	0.983	1.079	(0.0,0.2,2.3)	(-1.7,-1.4,0.2)
D.F. middle density - $M3$	7.404	0.258	1.062	0.977	1.104	(-0.2,-0.1,2.3)	(-2.2,0.7,-0.1)
D.F. middle density - $M4$	7.935	0.259	1.040	0.998	1.081	(0.0,0.1,2.5)	(-1.1,2.1,-0.0)
D.F. middle density - $M5$	7.191	0.270	1.030	1.007	1.070	(0.0,0.0,-2.4)	(-1.8,-1.3,-0.0)
D.F. low density - $L1$	4.649	0.162	1.068	0.993	1.136	(0.1,0.1,2.0)	(0.0,1.9,-0.1)
D.F. low density - $L2$	4.762	0.173	1.084	1.008	1.193	(0.3,-0.1,2.1)	(-2.0,0.3,0.3)
D.F. low density - $L3$	4.167	0.161	1.047	1.009	1.109	(-0.5,0.1,2.0)	(-1.7,-0.8,-0.3)
D.F. low density - $L4$	4.153	0.169	1.063	0.992	1.125	(0.1,-0.0,1.9)	(-0.6,1.7,0.0)
D.F. low density - $L5$	4.423	0.170	1.061	0.993	1.121	(0.3,0.3,2.0)	(0.1,2.0,-0.3)
PLA	14.499	0.098	1.828	0.774	4.596	(1.0,-0.1,0.0)	(0.1,1.0,-0.0))
Deer antler	8.526	0.125	0.544	1.056	2.588	(0.1,0.9,0.0)	(1.0,-0.1,0.0)

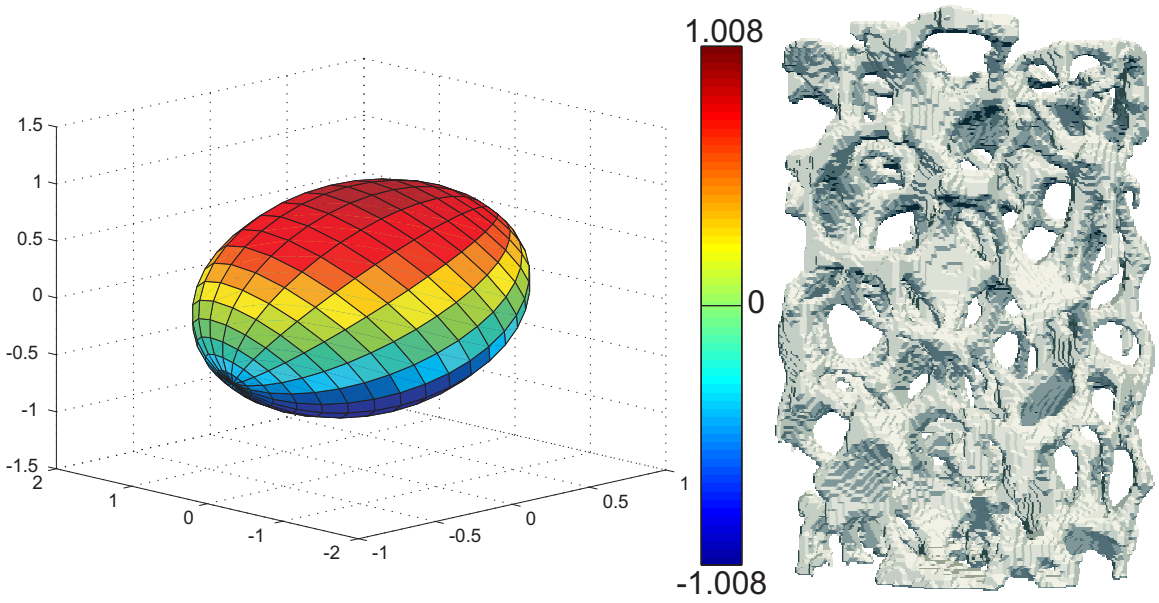

FIGURE E.1: *Duocel Foam high density - D1: fabric ellipsoid and 3D reconstruction from CT scan (both figures are depicted with the same orientation)*

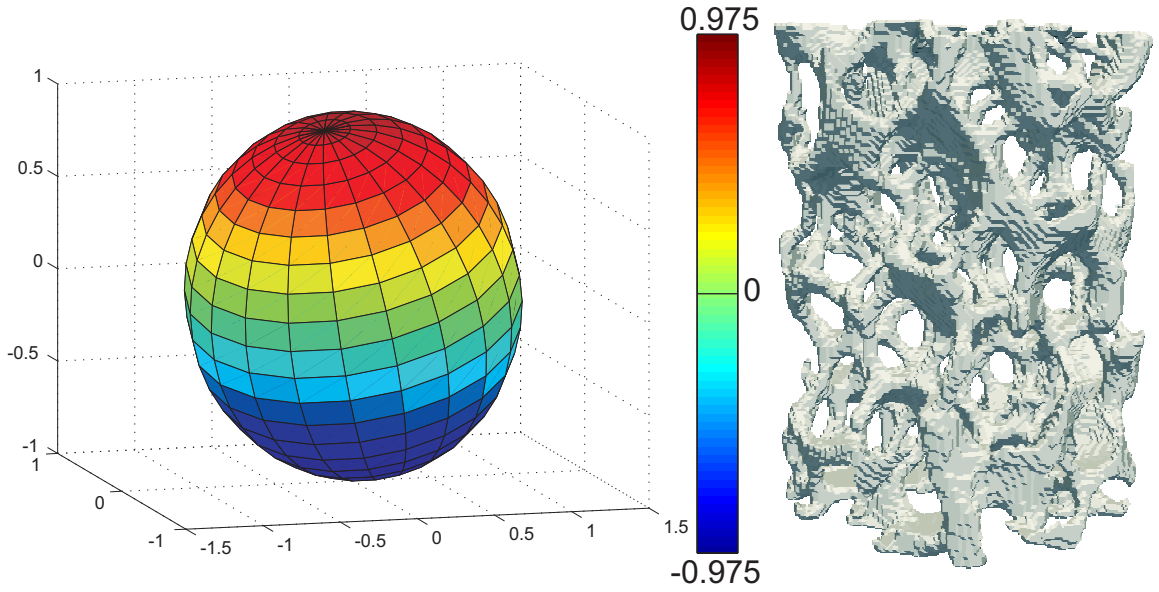

FIGURE E.2: *Duocel Foam high density - D2: fabric ellipsoid and 3D reconstruction from CT scan (both figures are depicted with the same orientation)*

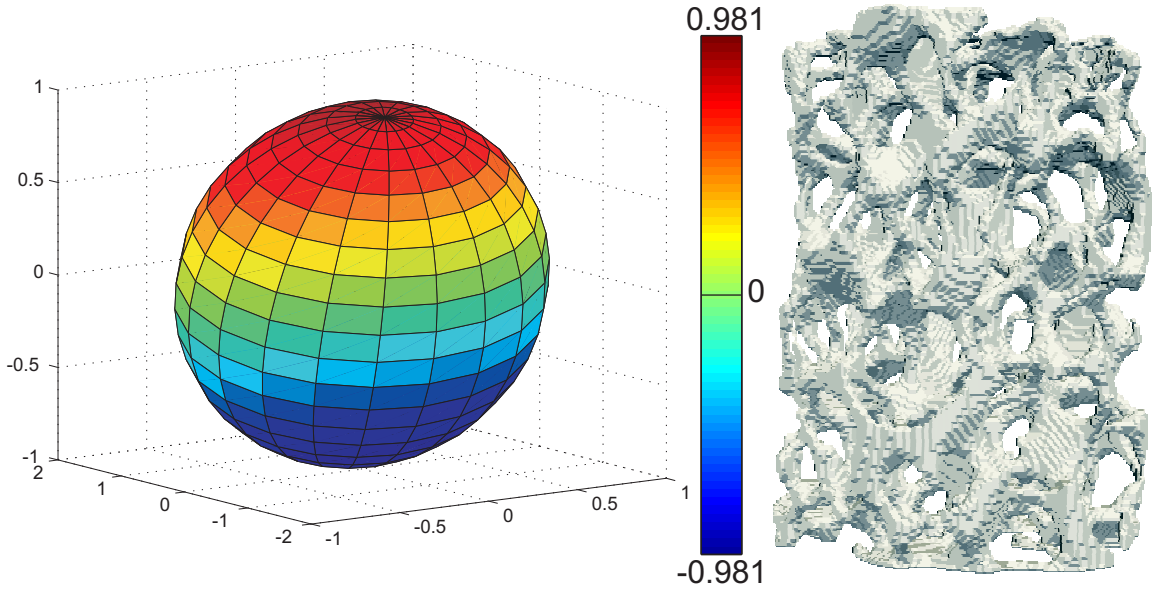

FIGURE E.3: *Duocel Foam high density - D3: fabric ellipsoid and 3D reconstruction from CT scan (both figures are depicted with the same orientation)*

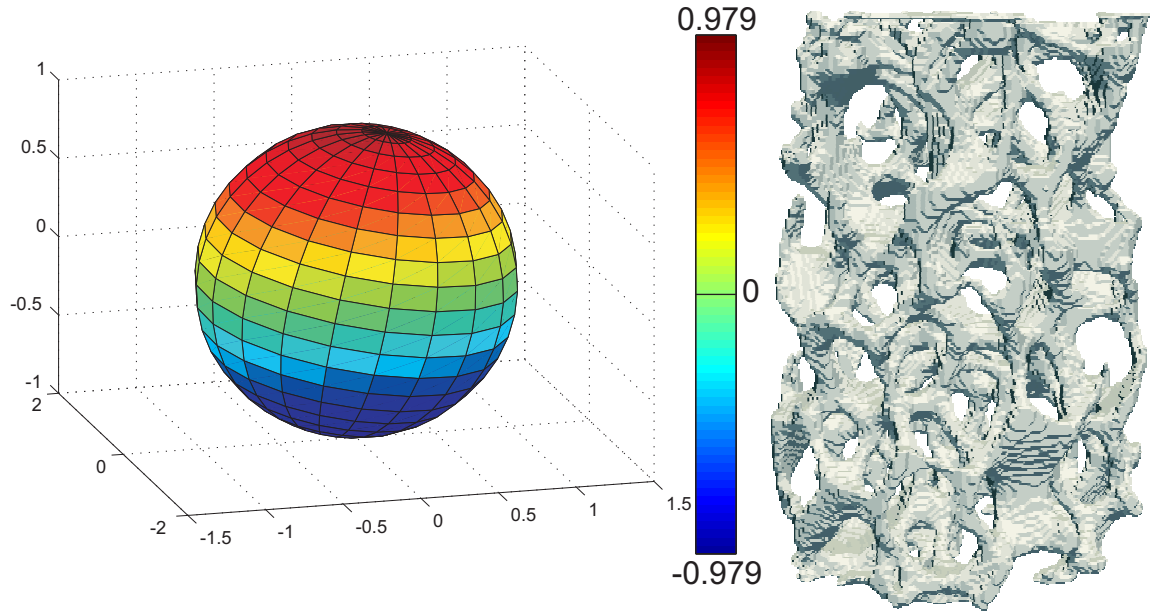

FIGURE E.4: *Duocel Foam high density - D4: fabric ellipsoid and 3D reconstruction from CT scan (both figures are depicted with the same orientation)*

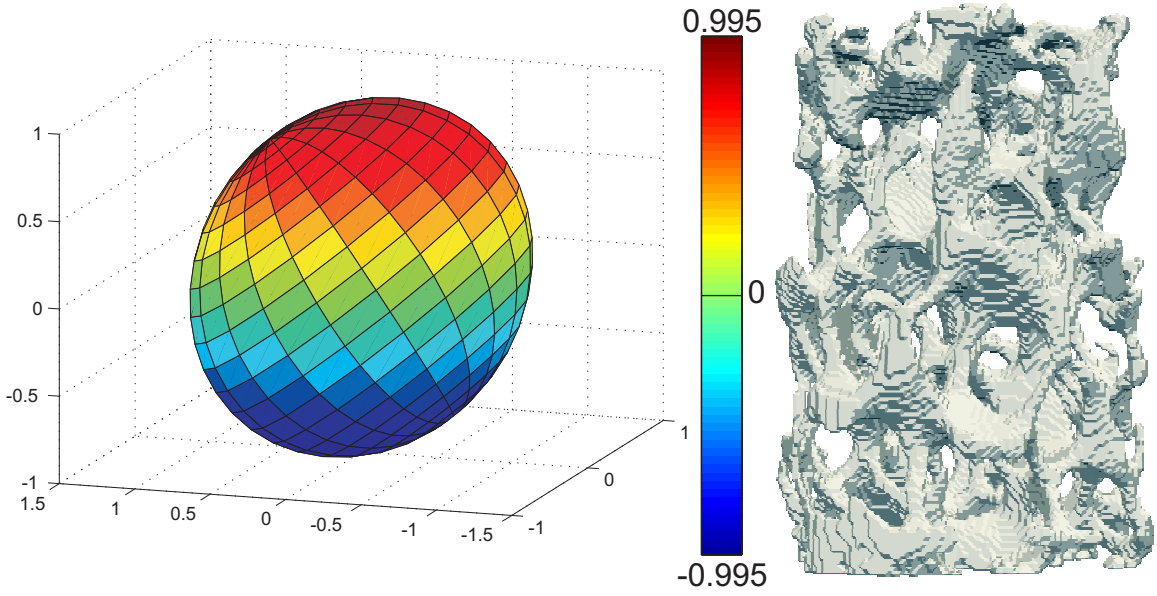

FIGURE E.5: *Duocel Foam high density - D5: fabric ellipsoid and 3D reconstruction from CT scan (both figures are depicted with the same orientation)*

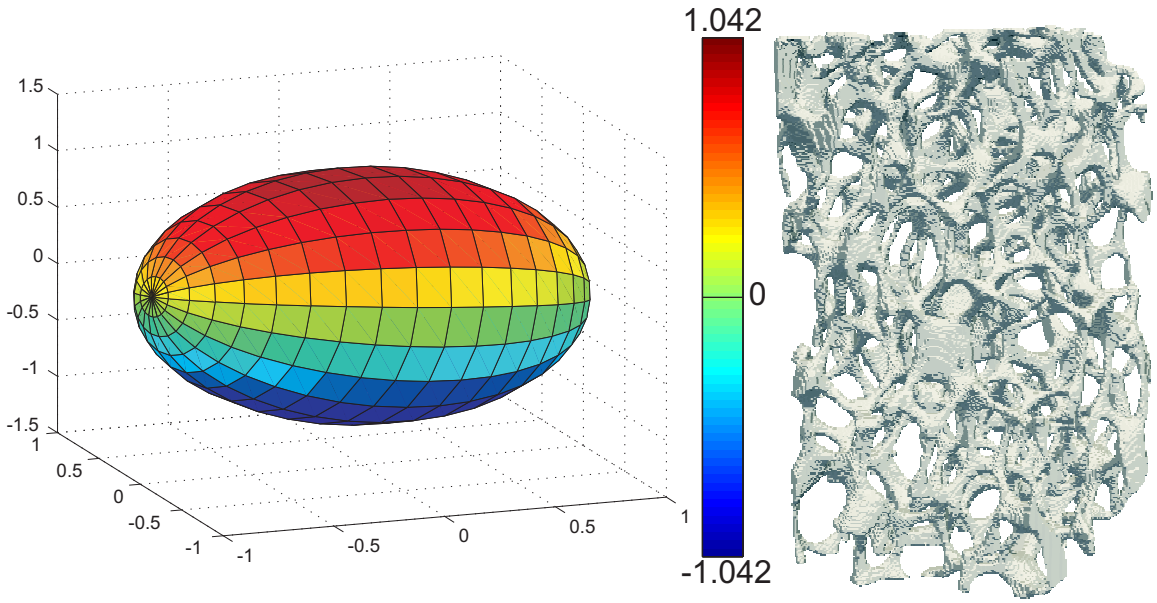

FIGURE E.6: *Duocel Foam middle density - M1: fabric ellipsoid and 3D reconstruction from CT scan (both figures are depicted with the same orientation)*

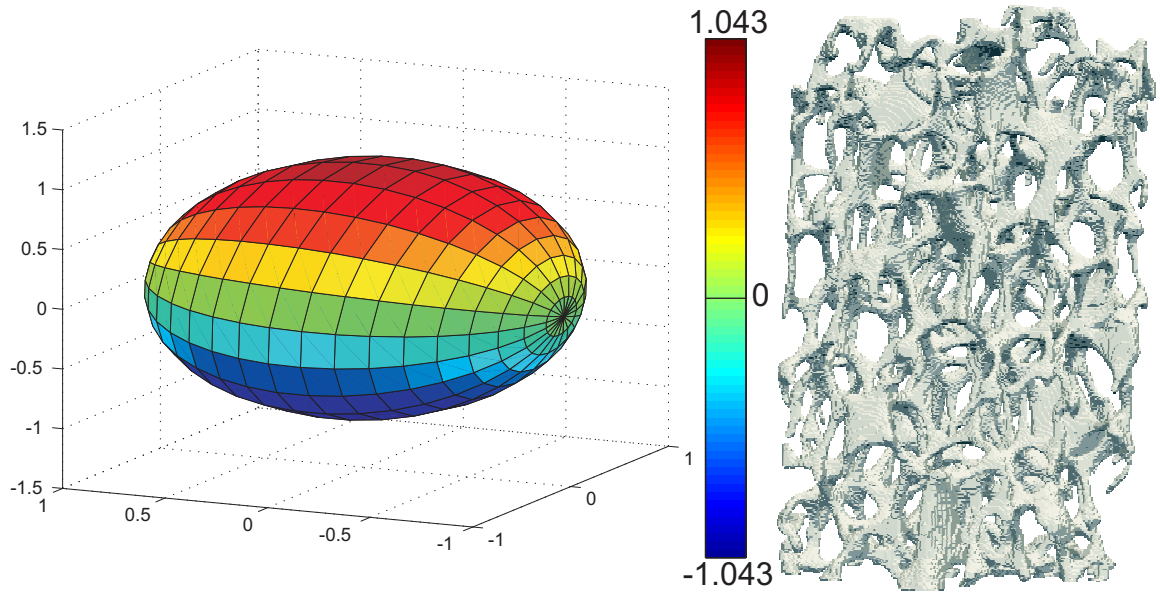

FIGURE E.7: *Duocel Foam middle density - M2: fabric ellipsoid and 3D reconstruction from CT scan (both figures are depicted with the same orientation)*

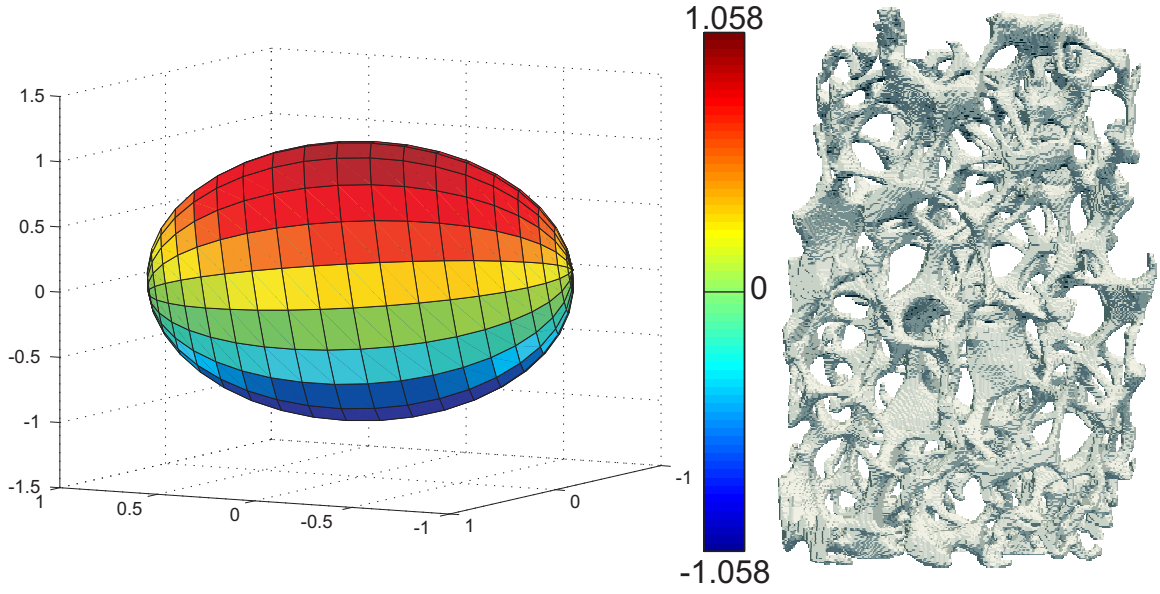

FIGURE E.8: *Duocel Foam middle density - M3: fabric ellipsoid and 3D reconstruction from CT scan (both figures are depicted with the same orientation)*

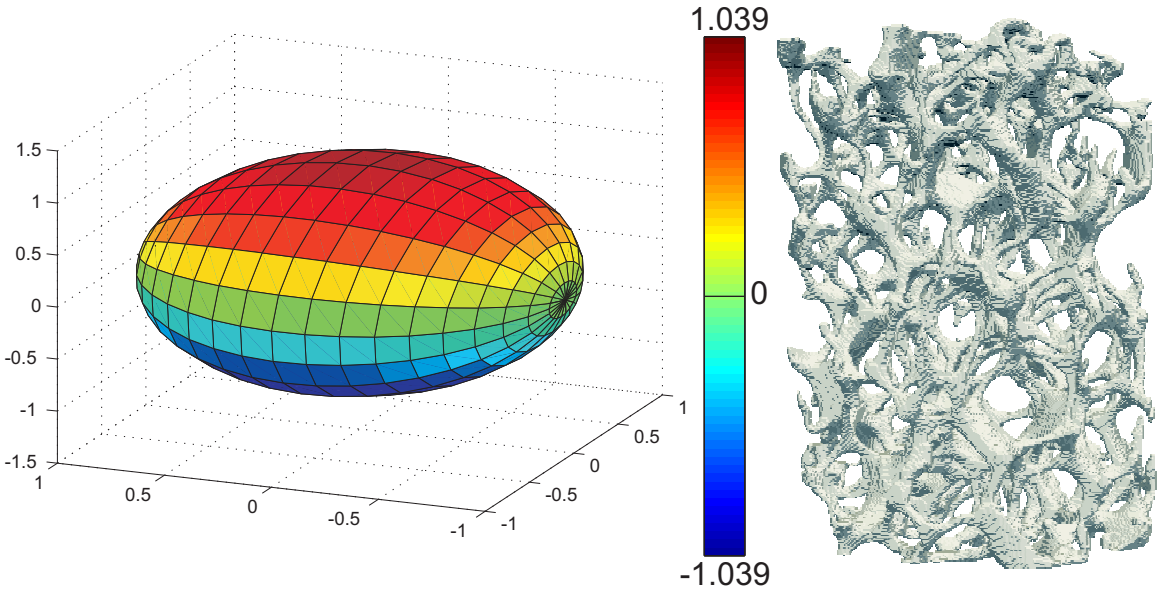

FIGURE E.9: *Duocel Foam middle density - M4: fabric ellipsoid and 3D reconstruction from CT scan (both figures are depicted with the same orientation)*

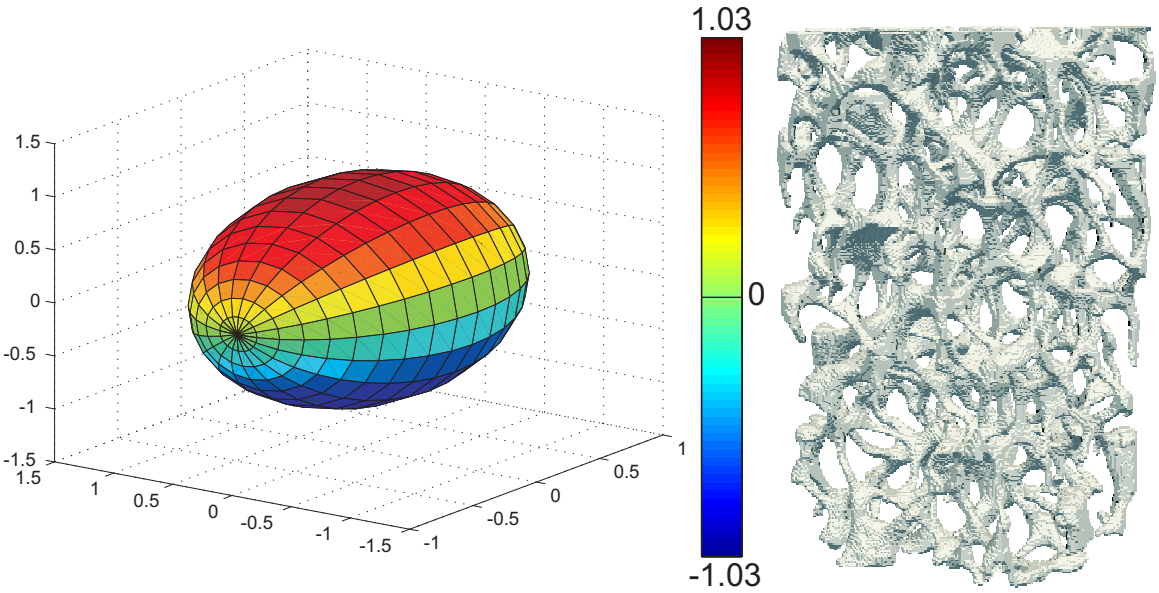

FIGURE E.10: *Duocel Foam middle density - M5: fabric ellipsoid and 3D reconstruction from CT scan (both figures are depicted with the same orientation)*

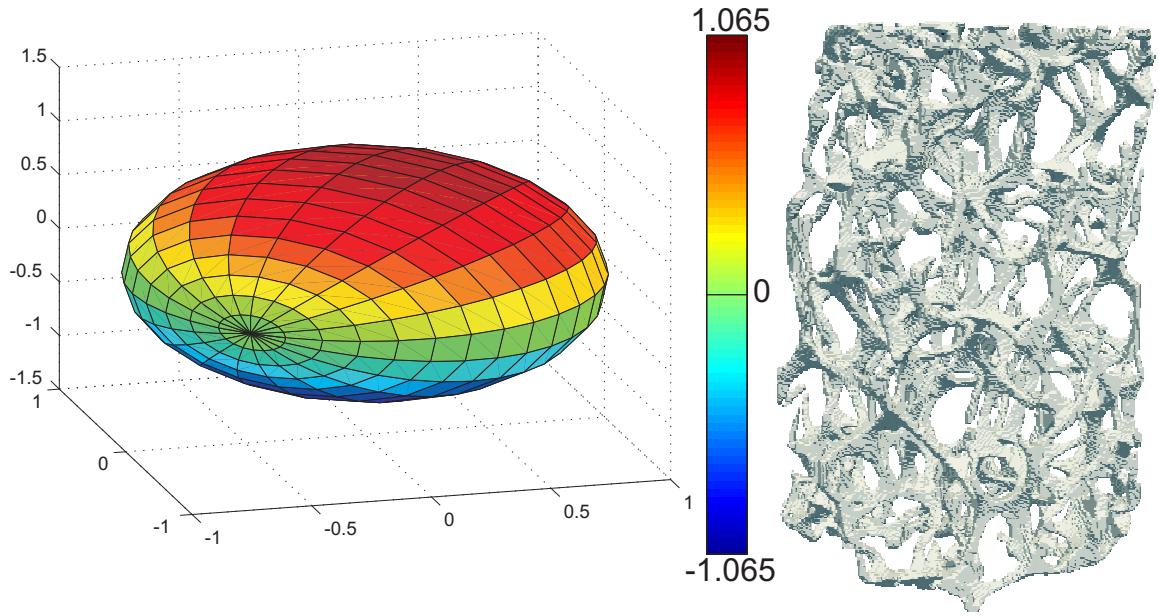

FIGURE E.11: *Duocel Foam low density - L1: fabric ellipsoid and 3D reconstruction from CT scan (both figures are depicted with the same orientation)*

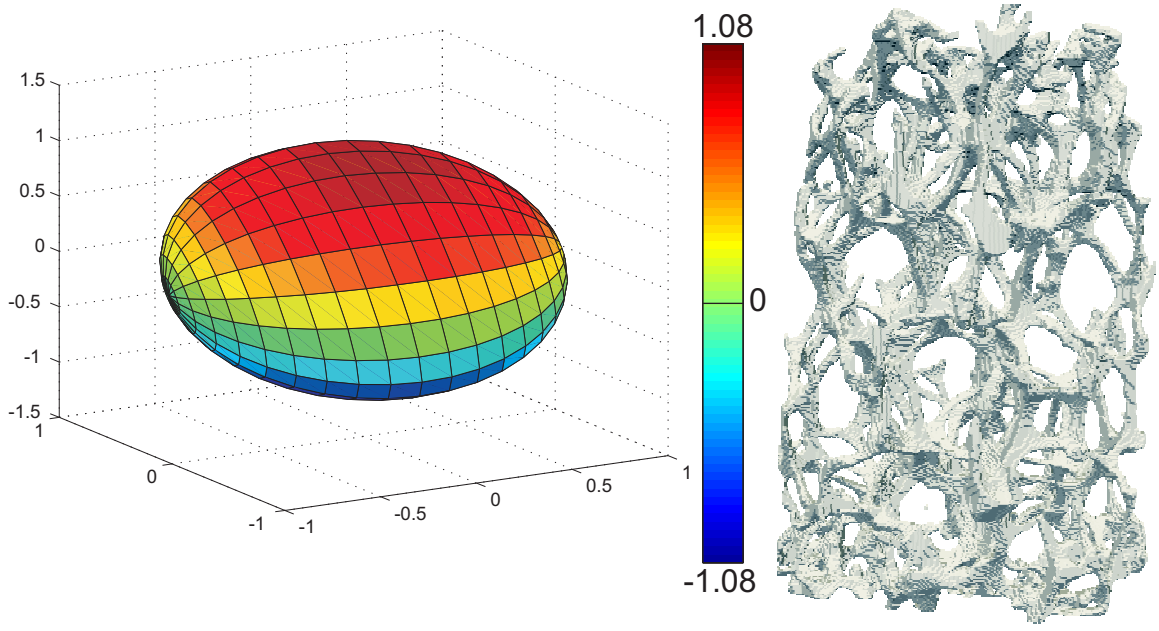

FIGURE E.12: *Duocel Foam low density - L2: fabric ellipsoid and 3D reconstruction from CT scan (both figures are depicted with the same orientation)*

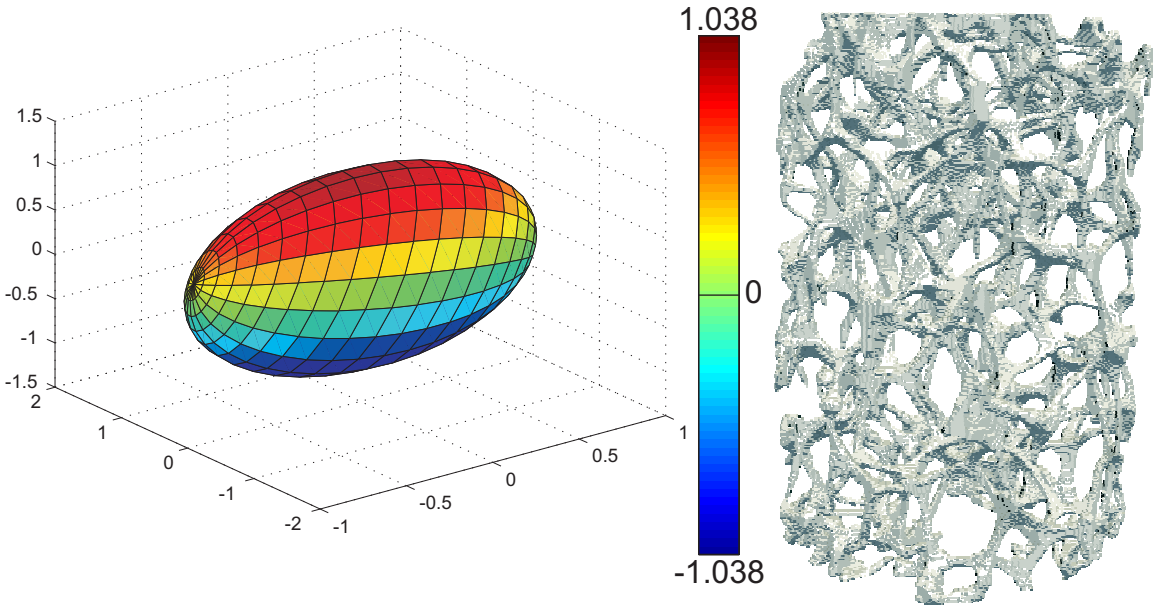

FIGURE E.13: *Duocel Foam low density - L3: fabric ellipsoid and 3D reconstruction from CT scan (both figures are depicted with the same orientation)*

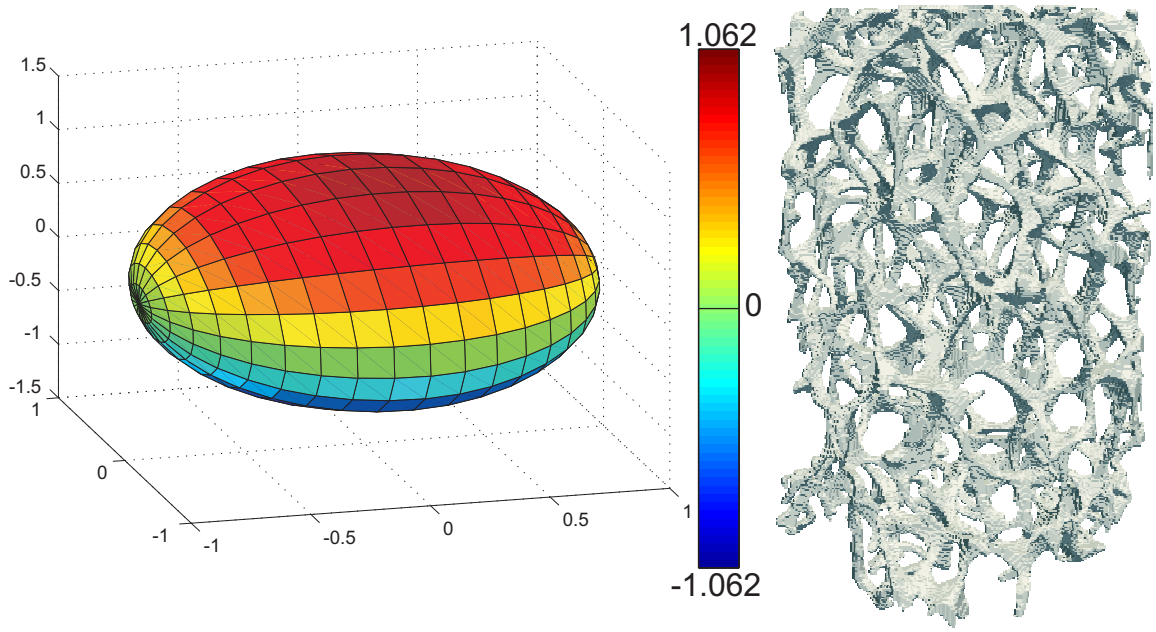

FIGURE E.14: *Duocel Foam low density - L4: fabric ellipsoid and 3D reconstruction from CT scan (both figures are depicted with the same orientation)*

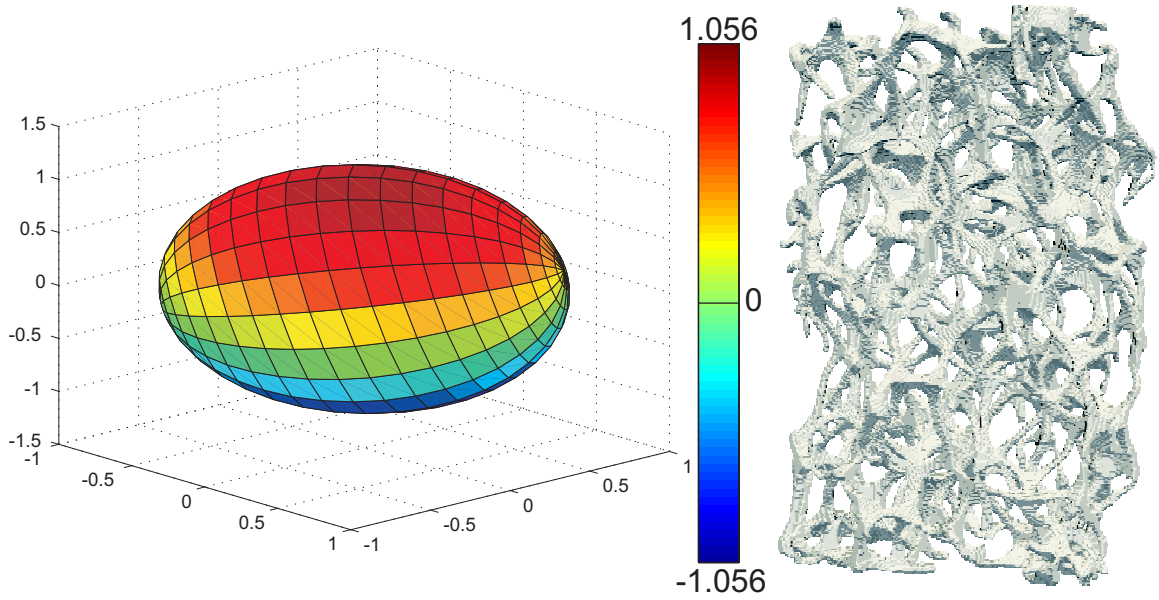

FIGURE E.15: *Duocel Foam low density - L5: fabric ellipsoid and 3D reconstruction from CT scan (both figures are depicted with the same orientation)*

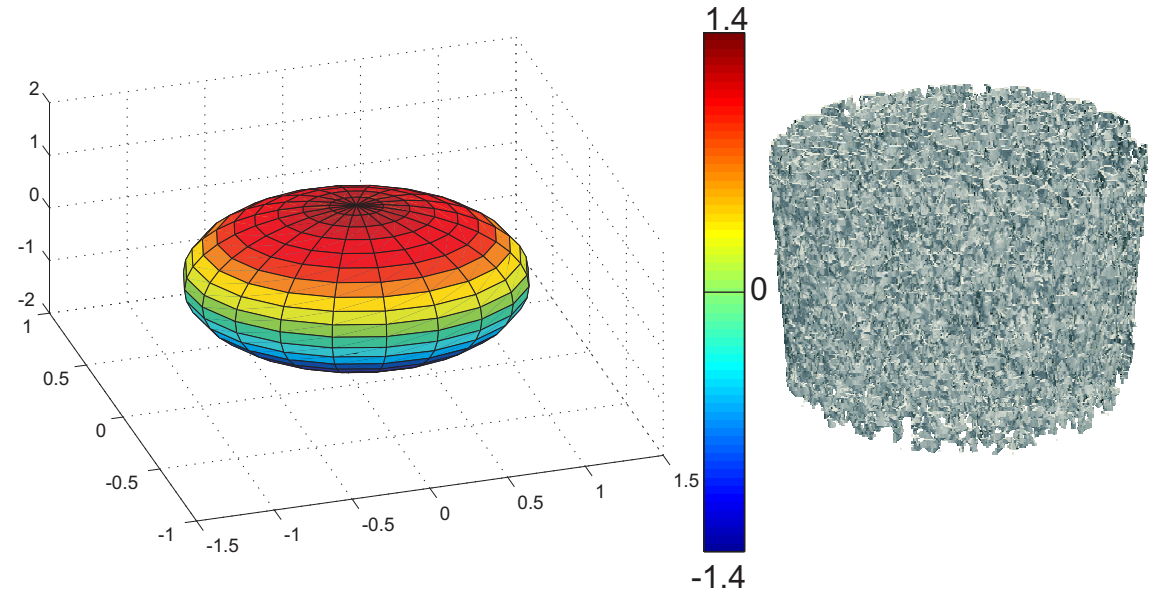

FIGURE E.16: *Deer antler: fabric ellipsoid and 3D reconstruction from CT scan (both figures are depicted with the same orientation)*

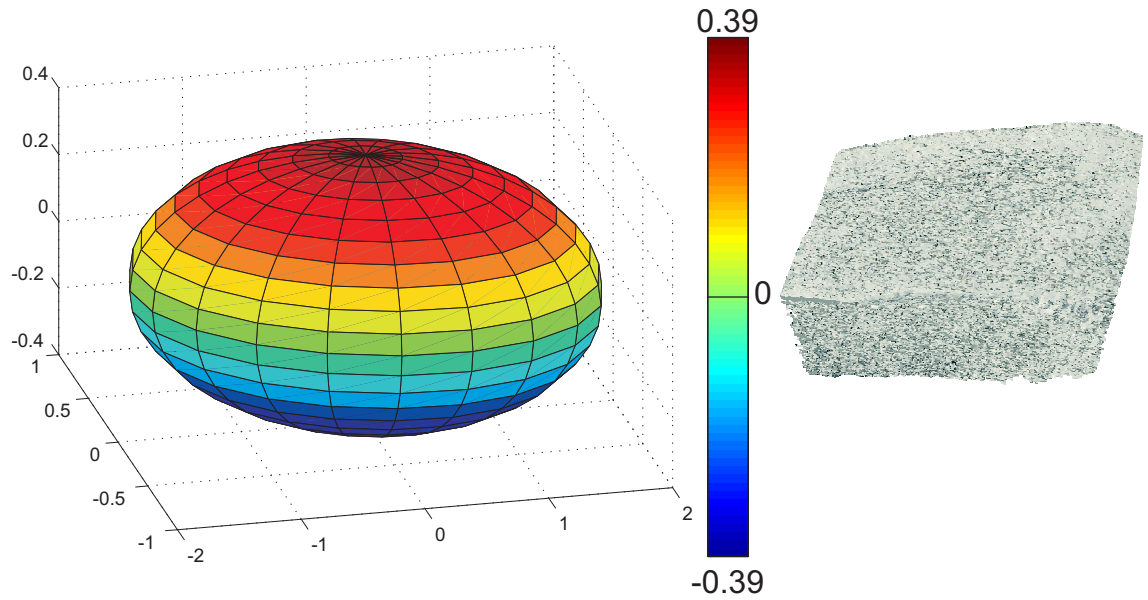

FIGURE E.17: *PLA: fabric ellipsoid and 3D reconstruction from CT scan (both figures are depicted with the same orientation)*

Appendix F
A Piecewise Linear Model for the Periodontal Ligament

This appendix details the results obtained for a piecewise linear model fitted on the experimental data presented in section 6.1.
As depicted on Figure F.1, we propose a model that lays between Cattaneo *et al.*'s model, softer on the whole strain range and Borák *et al.*, Qian *et al.*'s model, stiffer in traction (no data available in compression). The model values are given in Table F.1, it leads to a progressive stiffening in compression as well as in traction. However, to model the loosening of stiffness when fibers start to break, a low value is attributed for engineering strains beyond 0.63.

	Engineering Strain [-]	**Tangential Modulus** [MPa]
Compression	0.0	0.068 (i.e. Young's modulus)
	$0.0 \rightarrow -0.25$	linear variation up to 0.68
	$-0.25 \rightarrow -0.31$	linear variation up to 8.5
	$-0.31 \rightarrow -0.82$	constant value of 8.5
	< -0.82	13.5
Traction	0.0	0.068 (i.e. Young's modulus)
	$0.0 \rightarrow 0.14$	linear variation up to 1.35
	$0.14 \rightarrow 0.63$	constant value of 8.5
	> 0.63	0.01

TABLE F.1: *Values of the mechanical model for the periodontal ligament*

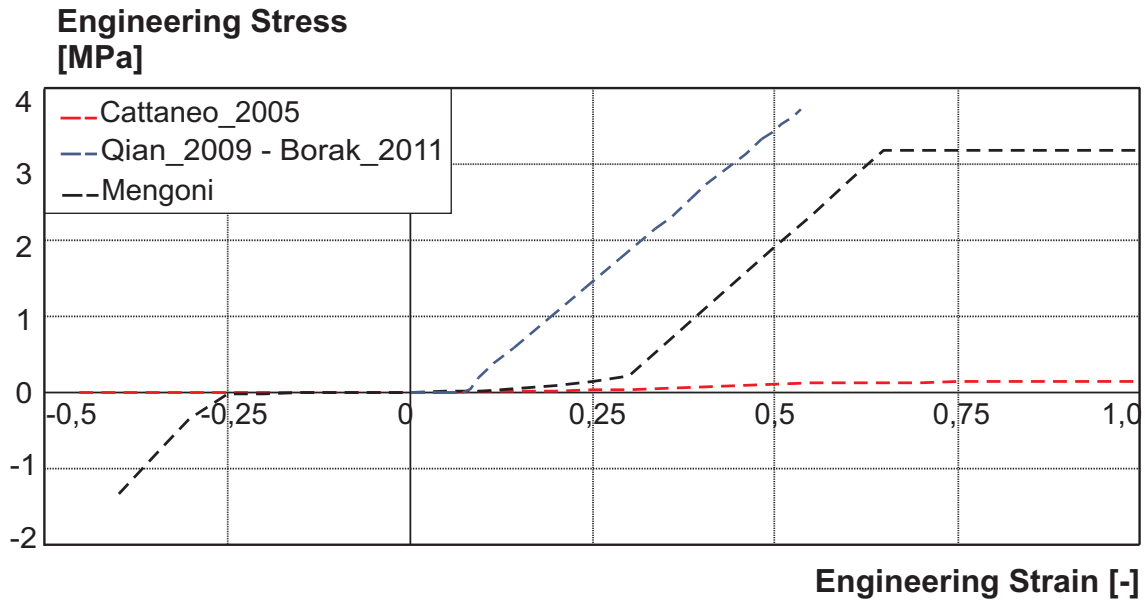

FIGURE F.1: *Periodontal Ligament - piecewise linear models [24, 34, 218]. In black dashed line, the model used in this work.*

Appendix G
A Brief Introduction to Contact Problems

This appendix gives a very brief introduction to the treatment of contact problems in the Finite Element Methods and is inspired from [29]. The interested reader should refer for instance to [277].
In contact problems, the principle of virtual works (see Equ. 3.13 in section 3.2) becomes, for $\mathbf{u}$ and $\delta\mathbf{u}$ the real and virtual displacement fields, and not accounting for inertia effects:

$$\delta W_{\text{int}}(\mathbf{u},\delta\mathbf{u}) = \delta W_{\text{ext}}(\mathbf{u},\delta\mathbf{u}) + \delta W_{\text{cont}}(\mathbf{u},\delta\mathbf{u})$$

The virtual work associated to contact forces can be written:

$$\delta W_{\text{cont}}(\mathbf{u},\delta\mathbf{u}) = \int_{\mathbb{S}_1(t)} \mathbf{t}^c.\delta\mathbf{u}\, d\mathbb{S}_1 + \int_{\mathbb{S}_2(t)} \mathbf{t}^c.\delta\mathbf{u}\, d\mathbb{S}_2$$

where $\mathbb{S}_1$ and $\mathbb{S}_2$ are the two surfaces of the two bodies potentially in contact (the contact boundaries) and $\mathbf{t}^c$ are the surface traction on the contact boundaries.
Using Newton's third law and splitting the virtual relative displacement field ($\delta\Delta\mathbf{u}$) into its normal and tangential components ($\delta\Delta\mathbf{u} = \delta g\mathbf{e}_n + \delta\xi^\alpha\mathbf{e}_{t_\alpha} \quad \alpha \in [1,2]$) this can be written:

$$\delta W_{\text{cont}}(\mathbf{u},\delta\mathbf{u}) = \int_{\mathbb{S}_1(t)} t_n^c\delta g + t_{t_\alpha}^c\delta\xi^\alpha\, d\mathbb{S}_1$$

for $\mathbf{t}^c = t_n^c\mathbf{e}_n + t_{t_\alpha}^c\mathbf{e}_{t_\alpha}$.
This weak form of the mechanical equilibrium is completed with the contact laws (Kuhn-Tucker's conditions), i.e. either unilateral contact conditions and Coulomb's friction law:

$$\text{unilateral contact: } g_n \geq 0, t_n^c \leq 0, g_n t_n^c = 0$$
$$\text{Coulomb's friction law: } ||\mathbf{t}_t^c|| - \mu t_n \leq 0, \zeta \geq 0, \zeta(||\mathbf{t}_t^c|| - \mu t_n) = 0$$

with g_n the normal gap, $\mathbf{t}_t^c = t_{t_\alpha}^c\mathbf{e}_{t_\alpha}$, ζ the rate of sliding, and μ Coulomb's friction coefficient. The rate of sliding is associated to the speed of sliding $\mathbf{v}_t$ with the following relationship:

$$\mathbf{v}_t - \zeta\frac{\mathbf{t}_t^c}{||\mathbf{t}_t^c||} = 0$$

Several numerical methods exist to solve the contact problem. We will here only present the global picture of the *Penalty Method* used in this work.

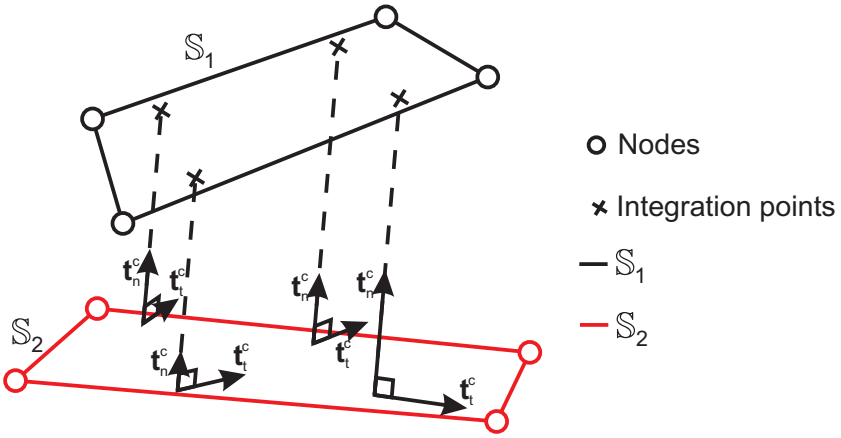

FIGURE G.1: *Orthogonal projection for the detection of contact between two surfaces (adapted from [29])*

The contact surface tractions are computed using to a node-to-segment algorithm. The equations of contact are solved for every integration point of each element on the contact surface $\mathbb{S}_1$ (called the slave surface). So, the contact surface tractions are known through their values at integration points. The link between one point of the slave surface and the master surface $\mathbb{S}_2$ is done by orthogonal projection on the closer element of the boundary $\mathbb{S}_2$ (see Fig. G.1). This projection is performed for each integration point of each element of the slave surface so that we can compute the virtual work of the contact forces for each element of this surface.

The penalty method (only the treatment of the normal surface traction is presented here after, the sticking tangential contact is treated in the same way, replacing the normal gap by the tangential displacement) ensures a continuous relation between the contact surface tractions and the displacements. The idea is to regularize the contact laws allowing penetration of the two bodies provided that the contact surface tractions are proportional to the normal gap (with a proportionality coefficient called the penalty, p_n):

$$t_n^c = p_n g_n$$

This method is a regularization method based on the penalty principle, it does not exactly fulfill the conditions of impenetrability and perfect sticking: the violation of these two conditions is therefore penalized through a penalty coefficient, p_n.

The penalty method needs some non zero penetration to generate a normal contact force (this penetration can be physically described in terms of an elastic deformation of the contact surface), as well as some tangential motion to generate the tangential forces, even if the contact is sticking (here again, this might correspond to some elastic shear deformation of the asperities produced by the tangential forces).

The idea to use a contact formulation to describe the PDL comes from this observation. Using a piecewise linear penalty coefficient can be physically related to a piecewise linear stiffness of the contact surface.

Bibliography

[1] **Abu, A. R., Rashid, K., and Voyiadjis, G. Z.** A finite strain plastic-damage model for high velocity impact using combined viscosity and gradient localization limiters: Part I-theoretical formulation. *International Journal of Damage Mechanics*, 15(4):293, 2006.

[2] **Adachi, T., Tsubota, K., Tomita, Y., and Hollister, S. J.** Trabecular surface remodeling simulation for cancellous bone using microstructural voxel finite element models. *Journal of Biomechanical Engineering*, 123(5):403–409, Oct 2001.

[3] **Adachi, T., Kameo, Y., and Hojo, M.** Trabecular bone remodelling simulation considering osteocytic response to fluid-induced shear stress. *Philosophical Transactions of the Royal Society A: Mathematical, Physical and Engineering Sciences*, 368(1920):2669, 2010.

[4] **Akhtar, R., Daymond, M. R., Almer, J. D., and Mummery, P. M.** Elastic strains in antler trabecular bone determined by synchrotron X-ray diffraction. *Acta Biomaterialia*, 4 (6):1677–1687, 2008.

[5] **Ammar, H. H., Ngan, P., Crout, R. J., Mucino, V. H., and Mukdadi, O. M.** Three-dimensional modeling and finite element analysis in treatment planning for orthodontic tooth movement. *American Journal of Orthodontics and Dentofacial Orthopedics*, 139(1):e59–e71, 2011.

[6] **Andrews, E., Sanders, W., and Gibson, L. J.** Compressive and tensile behaviour of aluminum foams. *Materials Science and Engineering A*, 270(2):113–124, 1999.

[7] **Arola, D. and Reprogel, R.** Effects of aging on the mechanical behavior of human dentin. *Biomaterials*, 26(18):4051–4061, June 2005.

[8] **Aversa, R., Apicella, D., Perillo, L., Sorrentino, R., Zarone, F., Ferrari, M., and Apicella, A.** Non-linear elastic three-dimensional finite element analysis on the effect of endocrown material rigidity on alveolar bone remodeling process. *Dental Materials*, 25(5):678–690, 2009.

[9] **Bagge, M.** A model of bone adaptation as an optimization process. *Journal of Biomechanics*, 33(11):1349–1357, Nov 2000.

[10] **Bailon-Plaza, A. and Van Der Meulen, M.** A mathematical framework to study the effects of growth factor influences on fracture healing. *Journal of Theoretical Biology*, 212(2):191–209, 2001.

[11] **Baïotto, S. and Zidi, M.** Un modèle viscoélastique de remodelage osseux : approche unidimensionnelle. *Comptes Rendus de Mécanique*, 332(8):pp. 633–638, 2004.

[12] **Bart-Smith, H., Bastawros, A. F., Mumm, D. R., Evans, A. G., Sypeck, D. J., and Wadley, H. N. G.** Compressive deformation and yielding mechanisms in cellular Al alloys determined using X-ray tomography and surface strain mapping. *Acta Materialia*, 46(10): 3583–3592, 1998.

[13] **Bayraktar, H. H. and Keaveny, T. M.** Mechanisms of uniformity of yield strains for trabecular bone. *Journal of Biomechanics*, 37(11):1671–1678, 2004.

[14] **Bayraktar, H. H., Morgan, E. F., Niebur, G. L., Morris, G. E., Wong, E. K., and Keaveny, T. M.** Comparison of the elastic and yield properties of human femoral trabecular and cortical bone tissue. *Journal of Biomechanics*, 37(1):27–35, 2004.

[15] **Beaupré, G. S. and Hayes, W. C.** Finite element analysis of a three-dimensional open-celled model for trabecular bone. *Journal of biomechanical engineering*, 107:249, 1985.

[16] **Beaupré, G. S., Orr, T. E., and Carter, D. R.** An approach for time-dependent bone modeling and remodeling-theoretical development. *Journal of Orthopedic Research*, 8 (5):651–661, 1990.

[17] **Beaupré, G. S., Orr, T. E., and Carter, D. R.** An approach for time-dependent bone modeling and remodeling-application: a preliminary remodeling simulation. *Journal of Orthopedic Research*, 8(5):662–670, 1990.

[18] **Belytschko, T., Liu, W., and Moran, B.** *Nonlinear finite elements for continua and structures*, volume 36. Wiley, 2000.

[19] **Besdo, S.** Determination of dynamically adapting anisotropic material properties of bone under cyclic loading. *Journal of Biomechanics*, 44(2):272–276, January 2011.

[20] **Bessho, M., Ohnishi, I., Matsumoto, T., Ohashi, S., Matsuyama, J., Tobita, K., Kaneko, M., and Nakamura, K.** Prediction of proximal femur strength using a CT-based nonlinear finite element method: Differences in predicted fracture load and site with changing load and boundary conditions. *Bone*, 45(2):226–231, 2009.

[21] **Boccaccio, A., Lamberti, L., Pappalettere, C., Carano, A., and Cozzani, M.** Mechanical behavior of an osteotomized mandible with distraction orthodontic devices. *Journal of Biomechanics*, available online decembre 2005:corrected proof, Nov 2005.

[22] **Boman, R.** *Développement d'un formalisme Arbitraire Lagrangien Eulérien tridimensionnel en dynamique implicite. Application aux opérations de mise à forme.* Phd thesis (in french), University of Liège (Belgium), School of Engineering, Aerospace and Mechanics Department, 2010.

[23] **Bonnet, A., Postaire, M., and Lipinski, P.** Biomechanical study of mandible bone supporting a four-implant retained bridge: Finite element analysis of the influence of bone anisotropy and foodstuff position. *Medical Engineering & Physics*, 31(7):806–815, 2009.

[24] **Borák, L., Florian, Z., Bartáková, S., Prachár, P., Murakami, N., Ona, M., Igarashi, Y., and Wakabayashi, N.** Bilinear elastic property of the periodontal ligament for simulation using a finite element mandible model. *Dental Materials Journal*, 30(4):448–454, 2011.

[25] **Boryor, A., Hohmann, A., Geiger, M., Wolfram, U., Sander, C., and Sander, F. G.** A downloadable meshed human canine tooth model with PDL and bone for finite element simulations. *Dental Materials*, 25(9):e57–e62, 2009.

[26] **Bourauel, C., Freudenreich, D., Vollmer, D., Kobe, D., Drescher, D., and Jäger, A.** Simulation of orthodontic tooth movements. A comparison of numerical models. *Journal of Orofacial Orthopedics*, 60(2):136–151, 1999.

[27] **Bourauel, C., Vollmer, D., and Jäger, A.** Application of bone remodeling theories in the simulation of orthodontic tooth movements. *Journal of Orofacial Orthopedics*, 61 (4):266–279, 2000.

[28] **Boutroy, S., van Rietbergen, B., Sornay-Rendu, E., Munoz, F., Bouxsein, M., and Delmas, P.** Finite element analysis based on in vivo HR-pQCT images of the distal radius is associated with wrist fracture in postmenopausal women. *Journal of Bone and Mineral Research*, 23(3):392–399, 2008.

[29] **Bussetta, P., Marceau, D., and Ponthot, J.-P.** The adapted augmented lagrangian method: a new method for the resolution of the mechanical frictional contact problem. *Computational Mechanics*, 49:259–275, 2012.

[30] **Carter, D. R.** Mechanical loading history and skeletal biology. *Journal of Biomechanics*, 20(11-12):1095–1109, 1987.

[31] **Carter, D. R. and Hayes, W. C.** Fatigue life of compact bone-I Effects of stress amplitude, temperature and density. *Journal of Biomechanics*, 9(1):27–30, 1976.

[32] **Carter, D. R., Hayes, W. C., and Schurman, D. J.** Fatigue life of compact bone-II. Effects of microstructure and density. *Journal of Biomechanics*, 9(4):211–214, IN1–IN3, 215–218, 1976.

[33] **Carter, D. R., Orr, T. E., and Fyhrie, D. P.** Relationships between loading history and femoral cancellous bone architecture. *Journal of Biomechanics*, 22(3):231–244, 1989.

[34] **Cattaneo, P. M., Dalstra, M., and Melsen, B.** The finite element method : a tool to study orthodontic tooth movement. *Journal of Dental Research*, 84(5):428–433, 2005.

[35] **Cattaneo, P. M., Dalstra, M., and Melsen, B.** Strains in periodontal ligament and alveolar bone associated with orthodontic tooth movement analyzed by finite element. *Orthodontics & Craniofacial Research*, 12(2):120–128, 2009.

[36] **Chan, E. and Darendeliler, M. A.** Physical properties of root cementum: Part 7. extent of root resorption under areas of compression and tension. *American Journal of Orthodontics and Dentofacial Orthopedics*, 129(4):504–510, April 2006.

[37] **Charlebois, M.** *Constitutive Law for Trabecular Bone in Large Strain Compression*. PhD thesis, Technische Universitat Wien, Institute of Lightweight Design and Structural Biomechanics, 2008.

[38] **Charlebois, M., Jirásek, M., and Zysset, P. K.** A nonlocal constitutive model for trabecular bone softening in compression. *Biomechanics and Modeling in Mechanobiology*, 9(5):597–611, 2010.

[39] **Charlier, R.** *Approche unifiée de quelques problèmes non linéaires de mécanique des milieux continus par la méthode des éléments finis (grandes déformations des métaux et des sols, contact unilatéral de solides, conduction thermique et écoulements en milieu poreux)*. PhD thesis, Université de Liège - Faculté de Sciences Appliquées, 1987.

[40] **Chen, G., Pettet, G., Pearcy, M., and McElwain, D.** Modelling external bone adaptation using evolutionary structural optimisation. *Biomechanics and Modeling in Mechanobiology*, 6(4):275–285, July 2007.

[41] **Chen, P.-Y., Stokes, A., and McKittrick, J.** Comparison of the structure and mechanical properties of bovine femur bone and antler of the North American elk (Cervus elaphus canadensis). *Acta Biomaterialia*, 5(2):693–706, 2009.

[42] **Christen, D., Webster, D., and Müller, R.** Multiscale modelling and nonlinear finite element analysis as clinical tools for the assessment of fracture risk. *Philosophical Transactions of the Royal Society A-Mathematical, Physical and Engineering Sciences*, 368(1920):2653–2668, 2010.

[43] **Cohen-Solal, M. and de Vernejoul, M. C.** Régulation du remodelage osseux. Bases physiologiques. *Archives de Pédiatrie*, 9(Supplement 2):pp. 92–94, 2002.

[44] **Committee, A. I. H.** *ASM Handbook: Properties and selection*, volume 2. ASM International, 1990.

[45] **Cowin, S. C.** The mechanical and stress adaptive properties of bone. *Annals of Biomedical Engineering*, 11(3-4):263–295, 1983.

[46] **Cowin, S. C.** *Bone mechanics handbook*. CRC press USA, 2001.

[47] **Cowin, S. C.** Tissue growth and remodeling. *Annual Reviews of Biomedical Engineering*, 6:77–107, 2004.

[48] **Cowin, S. C. and Doty, S.** *Tissue Mechanics*. Springer Verlag, 2007. Ch. 11 : Bone tissue.

[49] **Cowin, S. C. and Hegedus, D.** Bone remodeling I: theory of adaptive elasticity. *Journal of Elasticity*, 6(3):313–326, 1976.

[50] **Cowin, S. C. and Nachlinger, R.** Bone remodeling III: uniqueness and stability in adaptive elasticity theory. *Journal of Elasticity*, V8(3):285–295, July 1978.

[51] **Cowin, S. C.** Wolff's law of trabecular architecture at remodelling equilibrium. *Journal of Biomechanical Engineering*, 108(1):83–88, 1986.

[52] **Cowin, S. C., Hart, R. T., Balser, J. R., and Kohn, D. H.** Functional adaptation in long bones: establishing in vivo values for surface remodeling rate coefficients. *Journal of Biomechanics*, 18(9):665–684, 1985.

[53] **Crigel, M.-H., Balligand, M., and Heinen, E.** Les bois de cerf : revue de littérature scientifique. *Annales de Médecine Vétérinaire*, 145(1):25–38, 2001.

[54] **Cronau, M., Ihlow, D., Kubein-Meesenburg, D., Fanghänel, J., Dathe, H., and Nägerl, H.** Biomechanical features of the periodontium: an experimental pilot study in vivo. *American Journal of Orthodontics and Dentofacial Orthopedics*, 129(5):599.e13–599.e21, May 2006.

[55] **Currey, J.** Strain rate dependence of the mechanical properties of reindeer antler and the cumulative damage model of bone fracture. *Journal of Biomechanics*, 22(5):469–475, 1989.

[56] **de Bien, C.** Analyse de la relation entre les propriétés mécaniques et la microstructure de matériaux cellulaires : contribution au développement d'une méthodologie basée sur le suivi microtomographique de tests de compression. Master's thesis (in French), Université de Liège, Faculté des Sciences Appliquées, Département de Chimie Appliquée, 2010.

[57] **de Giorgi, M., Carofalo, A., Dattoma, V., Nobile, R., and Palano, F.** Aluminium foams structural modelling. *Computers & Structures*, 88(1-2):25–35, 2010.

[58] **del Pozo, R., Tanaka, E., Tanaka, M., Kato, M., Iwabe, T., Hirose, M., and Tanne, K.** Influence of friction at articular surfaces of the temporomandibular joint on stresses in the articular disk: a theoretical approach with the finite element method. *Angle Orthodontist*, 73(3):319–327, Jun 2003.

[59] **Desmorat, R. and Otin, S.** Cross-identification isotropic/anisotropic damage and application to anisothermal structural failure. *Engineering Fracture Mechanics*, 75(11): 3446–3463, 2008.

[60] **Dizier, A.** *Caractérisation des effets de température dans la zone endommagée autour de tunnels de stockage de déchets nucléaires dans des roches argileuses.* PhD thesis, Université de Liège - Faculté de Sciences Appliquées - ArgEnCo, 2011.

[61] **Doblaré, M. and García, J.-M.** Application of an anisotropic bone-remodelling model based on a damage-repair theory to the analysis of the proximal femur before and after total hip replacement. *Journal of Biomechanics*, 34:1157–1170, 2001.

[62] **Doblaré, M. and García, J.-M.** Anisotropic bone remodelling model based on a continuum damage-repair theory. *Journal of Biomechanics*, 35(1):1–17, 2002.

[63] **Donea, J., Huerta, A., Ponthot, J., and Rodriguez-Ferran, A.** Encyclopedia of computational mechanics, vol. 1: Fundamentals, chapter chapter 14: Arbitrary lagrangian-eulerian methods, 2004.

[64] **Dorow, C., Krstin, N., and Sander, F.-G.** Experiments to determine the material properties of the periodontal ligament. *Journal of Orofacial Orthopedics*, 63(2):94–104, Mar 2002.

[65] **Dorow, C., Krstin, N., and Sander, F.-G.** Determination of the mechanical properties of the periodontal ligament in a uniaxial tensional experiment. *Journal of Orofacial Orthopedics*, 64(2):100–107, Mar 2003.

[66] **d'Otreppe, V., Boman, R., and Ponthot, J.-P.** Generating smooth surface meshes from multi-region medical images. *International Journal for Numerical Methods in Biomedical Engineering*, in press, 2011.

[67] **Duncanson, M. G. and Korostoff, E.** Compressive viscoelastic properties of human dentin: I. stress-relaxation behavior. *Journal of Dental Research*, 54(6):1207–1212, 1975.

[68] **Fernandes, P., Rodrigues, H., and Jacobs, C.** A model of bone adaptation using a global optimisation criterion based on the trajectorial theory of Wolff. *Computer Methods in Biomechanics & Biomedical Engineering*, 2(2):125–138, 1999.

[69] **Fernandez, J., Garciá-Aznar, J., Martínez, R., and Viaño, J.** Numerical analysis of a strain-adaptive bone remodelling problem. *Computer Methods in Applied Mechanics and Engineering*, 199:1549–1557, 2010.

[70] **Field, C., Li, Q., Li, W., Thompson, M., and Swain, M.** Prediction of mandibular bone remodelling induced by fixed partial dentures. *Journal of Biomechanics*, 43(9):1771–1779, 2010.

[71] **Field, C., Ichim, I., Swain, M. V., Chan, E., Darendeliler, M. A., Li, W., and Li, Q.** Mechanical responses to orthodontic loading: A 3-dimensional finite element multi-tooth model. *American Journal of Orthodontics and Dentofacial Orthopedics*, 135(2): 174–181, 2009.

[72] **Folgado, J., Fernandes, P. R., Guedes, J. M., and Rodrigues, H. C.** Evaluation of osteoporotic bone quality by a computational model for bone remodeling. *Computers and Structures*, 82(17-19):1381–1388, July 2004.

[73] **Follet, H.** *Caractérisation Biomécanique et Modélisation 3D par Imagerie X et IRM haute résolution de l'os spongieux humain : Evaluation du risque fracturaire*. PhD thesis, Laboratoire de Mécanique des Solides, Institut National des Sciences Appliquées de Lyon (France), 2002.

[74] **Frost, H.** *Bone remodelling dynamics*. Henry Ford Hospital surgical monographs. Henry Ford Hospital surgical monographs, 1963.

[75] **Frost, H.** *The laws of bone structure*. Henry Ford Hospital surgical monographs, 1964.

[76] **Frost, H.** Bone "mass" and the "mechanostat": a proposal. *The anatomical record*, 219 (1):1–9, 1987.

[77] **Frost, H.** Skeletal structural adaptations to mechanical usage (SATMU): 1. Redefining Wolff's law: the bone modeling problem. *The Anatomical Record*, 226(4):403–413, 1990.

[78] **Frost, H.** Skeletal structural adaptations to mechanical usage (SATMU): 2. Redefining Wolff's law: the remodeling problem. *The Anatomical Record*, 226(4):414–422, 1990.

[79] **Fyhrie, D. and Carter, D.** A unifying principle relating stress to trabecular bone morphology. *Journal of Orthopaedic research*, 4(3):304–317, 1986.

[80] **Gal, J. A., Gallo, L. M., Palla, S., Murray, G., and Klineberg, I.** Analysis of human mandibular mechanics based on screw theory and in vivo data. *Journal of Biomechanics*, 37(9):1405–1412, Sep 2004.

[81] **Garcia, D., Zysset, P. K., Charlebois, M., and Curnier, A.** A three-dimensional elastic plastic damage constitutive law for bone tissue. *Biomechanics and Modeling in Mechanobiology*, 8(2):149–165, 2009.

[82] **García, J.-M., Martinez, M. A., and Doblaré, M.** An anisotropic internal-external bone adaptation model based on a combination of CAO and continuum damage mechanics technologies. *Computer Methods in Biomechanics & Biomedical Engineering*, 4:355 – 377, 2001.

[83] **García, J.-M., Doblaré, M., and Cegonino, J.** Bone remodelling simulation: a tool for implant design. *Computational Materials Science*, 25(1-2):100–114, September 2002.

[84] **García-Aznar, J., Rueberg, T., and Doblaré, M.** A bone remodelling model coupling microdamage growth and repair by 3D BMU-activity. *Biomechanics and Modeling in Mechanobiology*, 4(2):147–167, November 2005.

[85] **Geiger, M., Schneider, J., and Sander, F. G.** Finite element calculation of bone remodeling in orthodontics by using forces and moments. *Journal of Mechanics in Medicine & Biology*, 3(2):123, 2003.

[86] **Geng, J., Tan, K., and Liu, G.** Application of finite element analysis in implant dentistry: a review of the literature. *The Journal of Prosthetic Dentistry*, 85(6):585–598, 2001.

[87] **Geramy, A.** Initial stress produced in the periodontal membrane by orthodontic loads in the presence of varying loss of alveolar bone: a three-dimensional finite element analysis. *European Journal of Orthodontics*, 24(1):21–33, Feb 2002.

[88] **Geris, L., Gerisch, A., Vander Sloten, J., Weiner, R., and Van Oosterwyck, H.** Angiogenesis in bone fracture healing: A bioregulatory model. *Journal of Theoretical Biology*, 251(1):137–158, 2008.

[89] **Geris, L., Vander Sloten, J., and Van Oosterwyck, H.** Connecting biology and mechanics in fracture healing: an integrated mathematical modeling framework for the study of nonunions. *Biomechanics and Modeling in Mechanobiology*, 9(6):713–724, 2010.

[90] **Gibson, I. and Ashby, M.** *Cellular solids: structure and properties.* Cambridge University Press, Cambridge, 1999.

[91] **Gibson, L.** Biomechanics of cellular solids. *Journal of Biomechanics*, 38(3):377–399, 2005.

[92] **Gray, H.** *Anatomy of the Human Body.* Lea & Febiger, Philadelphia, 1918. available online at `www.bartleby.com/107/`.

[93] **Gröning, F., Fagan, M., and O'Higgins, P.** The effects of the periodontal ligament on mandibular stiffness: a study combining finite element analysis and geometric morphometrics. *Journal of Biomechanics*, 44(7):1304 – 1312, 2011.

[94] **Guo, X.-D. E., McMahon, T. A., Keaveny, T. M., Hayes, W. C., and Gibson, L. J.** Finite element modeling of damage accumulation in trabecular bone under cyclic loading. *Journal of Biomechanics*, 27(2):145–155, 1994.

[95] **Gupta, A., Bayraktar, H. H., Fox, J. C., Keaveny, T. M., and Papadopoulos, P.** Constitutive modeling and algorithmic implementation of a plasticity-like model for trabecular bone structures. *Computational Mechanics*, 40(1):61–72, 2007.

[96] **Gurson, A.** Continuum theory of ductile rupture by void nucleation and growth. I. yield criteria and flow rules for porous ductile media. *Transactions of the ASME. Series H, Journal of Engineering Materials and Technology*, 99(1):2–15, January 1977.

[97] **Harrigan, T. and Mann, R.** Characterization of microstructural anisotropy in orthotropic materials using a second rank tensor. *Journal of Materials Science*, 19(3): 761–767, 1984.

[98] **Harrison, N. M., McDonnell, P. F., O'Mahoney, D. C., Kennedy, O. D., O'Brien, F. J., and McHugh, P. E.** Heterogeneous linear elastic trabecular bone modelling using micro-CT attenuation data and experimentally measured heterogeneous tissue properties. *Journal of Biomechanics*, 41(11):2589–2596, 2008.

[99] **Hattori, Y., Satoh, C., Seki, S., Watanabe, Y., Ogino, Y., and Watanabe, M.** Occlusal and TMJ loads in subjects with experimentally shortened dental arches. *Journal of Dental Research*, 82(7):532–536, Jul 2003.

[100] **Hayashi, K., Uechi, J., Murata, M., and Mizoguchi, I.** Comparison of maxillary canine retraction with sliding mechanics and a retraction spring: a three-dimensional analysis based on a midpalatal orthodontic implant. *European Journal of Orthodontics*, 26 (6):585–589, 2004.

[101] **Hayashi, K., Hamaya, M., and Mizoguchi, I.** Simulation study for a finite helical axis analysis of tooth movement. *Angle Orthodontist*, 75(3):350–355, May 2005.

[102] **Hazelwood, S. J., Martin, R. B., Rashid, M. M., and Rodrigo, J. J.** A mechanistic model for internal bone remodeling exhibits different dynamic responses in disuse and overload. *Journal of Biomechanics*, 34(3):299–308, March 2001.

[103] **Hegedus, D. H. and Cowin, S. C.** Bone remodeling II: small strain adaptive elasticity. *Journal of Elasticity*, V6(4):337–352, October 1976.

[104] **Helgason, B., Perilli, E., Schileo, E., Taddei, F., Brynjólfsson, S., and Viceconti, M.** Mathematical relationships between bone density and mechanical properties: a literature review. *Clinical biomechanics*, 23(2):135–146, 2008.

[105] **Hernandez, C. J., Hazelwood, S. J., and Martin, R. B.** The relationship between basic multicellular unit activation and origination in cancellous bone. *Bone*, 25(5):585–587, Nov 1999.

[106] **Hildebrand, T. and Rüegsegger, P.** A new method for the model-independent assessment of thickness in three-dimensional images. *Journal of microscopy*, 185(1):67–75, 1997.

[107] **Hinterkausen, M., Bourauel, C., Siebers, G., Haase, A., Drescher, D., and Nellen, B.** In vitro analysis of the initial tooth mobility in a novel optomechanical set-up. *Medical Engineering & Physics*, 20(1):40–49, 1998.

[108] **Howard, P., Kucich, U., Taliwal, R., and Korostoff, J.** Mechanical forces alter extracellular matrix synthesis by human periodontal ligament fibroblasts. *Journal of periodontal research*, 33(8):500–508, 1998.

[109] **Huiskes, R.** Stress patterns, failure modes, and bone remodeling. In R. H. Fitzgerald, editor, "Non-cemented Total Hip Arthroplasty," pages 283–302. Raven Press, New York, 1988.

[110] **Huiskes, R., Weinans, H., Grootenboer, H., Dalstra, M., Fudala, B., and Slooff, T.** Adaptive bone-remodeling theory applied to prosthetic-design analysis. *Journal of Biomechanics*, 20(11-12):1135–1150, 1987.

[111] **Huiskes, R., Ruimerman, R., van Lenthe, G. H., and Janssen, J. D.** Effects of mechanical forces on maintenance and adaptation of form in trabecular bone. *Nature*, 405 (6787):704–706, Jun 2000.

[112] **Ichim, I., Kieser, J., and Swain, M.** Functional significance of strain distribution in the human mandible under masticatory load: Numerical predictions. *Archives of Oral Biology*, 52(5):465–473, 2007.

[113] **Ichim, I., Li, Q., Li, W., Swain, M., and Kieser, J.** Modelling of fracture behaviour in biomaterials. *Biomaterials*, 28(7):1317–1326, 2007.

[114] **Ichim, I., Li, Q., Loughran, J., Swain, M., and Kieser, J.** Restoration of non-carious cervical lesions:: Part i. modelling of restorative fracture. *dental materials*, 23(12):1553–1561, 2007.

[115] **Ihlow, D., Cronau, M., Kubein-Meesenburg, D., Heine, G., Dathe, H., Hansen, C., and Nägerl, H.** An experimental method for in vivo analysis of biomechanical asymmetries of the periodontium. *Journal of Orofacial Orthopedics*, 64(5):321–329, Sep 2003.

[116] **Iwasaki, L. R., Baird, B. W., McCall, W. D., Jr, and Nickel, J. C.** Muscle and temporomandibular joint forces associated with chincup loading predicted by numerical modeling. *American Journal of Orthodontics and Dentofacial Orthopedics*, 124(5):530–540, November 2003.

[117] **Jacobs, C. R.** *Numerical simulation of bone adaptation to mechanical loading*. PhD thesis, Department of Mechanical Engineering - Stanford University, 1994.

[118] **Jacobs, C. R.** The mechanobiology of cancellous bone structural adaptation. *Journal of Rehabilitation Research and Development*, 37(2):209–216, 2000.

[119] **Jacobs, C. R., Simo, J. C., Beaupre, G. S., and Carter, D. R.** Adaptive bone remodeling incorporating simultaneous density and anisotropy considerations. *Journal of Biomechanics*, 30(6):603–613, 1997.

[120] **Jantarat, J., Palamara, J. E. A., Lindner, C., and Messer, H. H.** Time-dependent properties of human root dentin. *Dental Materials*, 18(6):486–493, Sep 2002.

[121] **Jeon, P. D., Turley, P. K., and Ting, K.** Three-dimensional finite element analysis of stress in the periodontal ligament of the maxillary first molar with simulated bone loss. *American Journal of Orthodontics and Dentofacial Orthopedics*, 119(5):498–504, May 2001.

[122] **Jeunechamps, P. P.** *Simulation numérique, à l'aide d'algorithmes thermomécaniques implicites, de matériaux endommageables pouvant subir de grandes vitesses de déformation. Application aux structures aéronautiques soumises à impact.* PhD thesis (in French), University of Liège (Belgium), School of Engineering, Aerospace and Mechanics Department, 2008.

[123] **Jones, M. L., Hickman, J., Middleton, J., Knox, J., and Volp, C.** A validated finite element method study of orthodontic tooth movement in the human subject. *Journal of Orthodontics*, 28(1):29–38, Mar 2001.

[124] **Jonoobi, M., Harun, J., Mathew, A. P., and Oksman, K.** Mechanical properties of cellulose nanofiber (CNF) reinforced polylactic acid (PLA) prepared by twin screw extrusion. *Composites Science and Technology*, 70(12):1742–1747, 2010.

[125] **Kak, A. C. and Slaney, M.** *Principles of computerized tomographic imaging*. IEEE Press, Philadelphia, 1988. available online at `http://www.slaney.org/pct/`.

[126] **Kawarizadeh, A., Bourauel, C., and Jäger, A.** Experimental and numerical determination of initial tooth mobility and material properties of the periodontal ligament in rat molar specimens. *European Journal of Orthodontics*, 25(6):569–578, Dec 2003.

[127] **Kawarizadeh, A., Bourauel, C., Zhang, D., Götz, W., and Jäger, A.** Correlation of stress and strain profiles and the distribution of osteoclastic cells induced by orthodontic loading in rat. *European Journal of Oral Sciences*, 112(2):140–147, Apr 2004.

[128] **Keaveny, T. M., Morgan, E. F., Niebur, G. L., and Yeh, O. C.** Biomechanics of trabecular bone. *Annual Review of Biomedical Engineering*, 3(1):307–333, 2001.

[129] **Keyak, J. H.** Improved prediction of proximal femoral fracture load using nonlinear finite element models. *Medical Engineering & Physics*, 23(3):165–173, 2001.

[130] **Kojima, Y. and Fukui, H.** Numeric simulations of en-masse space closure with sliding mechanics. *American Journal of Orthodontics and Dentofacial Orthopedics*, 138(6): 702–e1, 2010.

[131] **Kojima, Y., Mizuno, T., and Fukui, H.** A numerical simulation of tooth movement produced by molar uprighting spring. *American Journal of Orthodontics and Dentofacial Orthopedics*, 132(5):630–638, 2007.

[132] **Kojima, Y. and Fukui, H.** A numerical simulation of tooth movement by wire bending. *American Journal of Orthodontics and Dentofacial Orthopedics*, 130(4):452–459, October 2006.

[133] **Kojima, Y. and Fukui, H.** Effects of transpalatal arch on molar movement produced by mesial force: A finite element simulation. *American Journal of Orthodontics and Dentofacial Orthopedics*, 134(3):335.e1–335.e7, 2008.

[134] **Komatsu, K., Sanctuary, C., Shibata, T., Shimada, A., and Botsis, J.** Stress-relaxation and microscopic dynamics of rabbit periodontal ligament. *Journal of Biomechanics*, 40(3):634–644, 2007.

[135] **Koolstra, J. and van Eijden, T.** The jaw open-close movements predicted by biomechanical modeling. *Journal of Biomechanics*, 30(9):pp. 943–950, 1997.

[136] **Koolstra, J. and van Eijden, T.** A method to predict muscle control in the kinematically and mechanically indeterminate human masticatory system. *Journal of Biomechanics*, 34:pp. 1179–1188, 2001.

[137] **Koolstra, J. and van Eijden, T.** Combined finite element and rigid body analysis of human jaw joint dynamics. *Journal of Biomechanics*, 38:2431–2439, 2005.

[138] **Kopperdahl, D. L. and Keaveny, T. M.** Yield strain behavior of trabecular bone. *Journal of Biomechanics*, 31(7):601–608, 1998.

[139] **Korioth, T. W. and Versluis, A.** Modeling the mechanical behavior of the jaws and their related structures by finite element (FE) analysis. *Critical Reviews in Oral Biology and Medicine*, 8(1):90–104, 1997.

[140] **Krauss, S., Fratzl, P., Seto, J., Currey, J. D., Estevez, J. A., Funari, S. S., and Gupta, H. S.** Inhomogeneous fibril stretching in antler starts after macroscopic yielding: indication for a nanoscale toughening mechanism. *Bone*, 44(6):1105–1110, 2009.

[141] **Krishnan, V. and Davidovitch, Z.** Cellular, molecular, and tissue-level reactions to orthodontic force. *American Journal of Orthodontics and Dentofacial Orthopedics*, 129 (4):469.e1–469.32, 2006.

[142] **Krishnan, V. and Davidovitch, Z.** On a path to unfolding the biological mechanisms of orthodontic tooth movement. *Journal of dental research*, 88(7):597–608, 2009.

[143] **Lambers, F., Schulte, F., Kuhn, G., Webster, D., and Müller, R.** Mouse tail vertebrae adapt to cyclic mechanical loading by increasing bone formation rate and decreasing bone resorption rate as shown by time-lapsed in vivo imaging of dynamic bone morphometry. *Bone*, 2011.

[144] **Lambrechts, P., Goovaerts, K., Bharadwaj, D., De Munck, J., Bergmans, L., Peumans, M., and Van Meerbeek, B.** Degradation of tooth structure and restorative materials: A review. *Wear*, 261(9):980–986, November 2006.

[145] **Lemaire, V., Tobin, F. L., Greller, L. D., Cho, C. R., and Suva, L. J.** Modeling the interactions between osteoblast and osteoclast activities in bone remodeling. *Journal of Theoretical Biology*, 229(3):293–309, August 2004.

[146] **Lemaitre, J. and Desmorat, R.** *Engineering Damage Mechanics: Ductile, Creep, Fatigue and Brittle Failures*. Springer, 2005.

[147] **Lemaitre, J., Desmorat, R., and Sauzay, M.** Anisotropic damage law of evolution. *European Journal of Mechanics - A/Solids*, 19(2):187–208, 2000.

[148] **Lennon, A. and Prendergast, P.** Modelling damage growth and failure in elastic materials with random defect distributions. In "Mathematical Proceedings of the Royal Irish Academy," volume 104, pages 155–171. The Royal Irish Academy, 2004.

[149] **Léonard, A., Guiot, L., Pirard, J. P., Crine, M., Balligand, M., and Blacher, S.** Non-destructive characterization of deer antlers by X-ray microtomography coupled with image analysis. *Journal of Microscopy*, 225(3):258–263, 2007.

[150] **Levenston, M. E. and Carter, D. R.** An energy dissipation-based model for damage stimulated bone adaptation. *Journal of Biomechanics*, 31(7):579–586, July 1998.

[151] **Li, H. and Zhou, Z. R.** Wear behaviour of human teeth in dry and artificial saliva conditions. *Wear*, 249(10-11):980–984, November 2001.

[152] **Li, J., Li, H., Shi, L., Fok, A. S., Ucer, C., Devlin, H., Horner, K., and Silikas, N.** A mathematical model for simulating the bone remodeling process under mechanical stimulus. *Dental Materials*, 23(9):1073–1078, September 2007.

[153] **Lin, D., Li, Q., Li, W., Duckmanton, N., and Swain, M.** Mandibular bone remodeling induced by dental implant. *Journal of Biomechanics*, 43(2):287–293, 2010.

[154] **Lindauer, S.** The basics of orthodontic mechanics. *Seminars in Orthodontics*, 7(1): 2–15, 2001.

[155] **Lindauer, S. and Britto, A.** Biological response to biomechanical signals: orthodontic mechanics to control tooth movement. *Seminars in Orthodontics*, 6(3):145–154, 2000.

[156] **Liu, X. S., Bevill, G., Keaveny, T. M., Sajda, P., and Guo, X. E.** Micromechanical analyses of vertebral trabecular bone based on individual trabeculae segmentation of plates and rods. *Journal of Biomechanics*, 42(3):249–256, 2009.

[157] **Mackerle, J.** Finite element modelling and simulations in dentistry: a bibliography 1990-2003. *Computer Methods in Biomechanics & Biomedical Engineering*, 7(5):277–303, Oct 2004.

[158] **Malek, S., Darendeliler, M. A., and Swain, M. V.** Physical properties of root cementum: Part i. a new method for 3-dimensional evaluation. *American Journal of Orthodontics and Dentofacial Orthopedics*, 120(2):198–208, August 2001.

[159] **Malek, S., Darendeliler, M. A., Rex, T., Kharbanda, O. P., Srivicharnkul, P., Swain, M. V., and Petocz, P., PhD**. Physical properties of root cementum: Part 2. effect of different storage methods. *American Journal of Orthodontics and Dentofacial Orthopedics*, 124(5):561–570, November 2003.

[160] **Maquet, V., Martin, D., Scholtes, F., Franzen, R., Schoenen, J., Moonen, G., and Jérôme, R.** Poly(D,L-lactide) foams modified by poly(ethylene oxide)-block-poly(D,L-lactide) copolymers and a-FGF : in vitro and in vivo evaluation for spinal cord regeneration. *Biomaterials*, 22(10):1137–1146, 2001.

[161] **Marangalou, J. H., Ghalichi, F., and Mirzakouchaki, B.** Numerical simulation of orthodontic bone remodeling. *Orthodontic Waves*, 68(2):64–71, 2009.

[162] **Martin, R. B.** Porosity and specific surface of bone. *Critical Reviews in Biomedical Engineering*, 10(3):179–222, 1984.

[163] **Martin, R. B.** Mathematical model for repair of fatigue damage and stress fracture in osteonal bone. *Journal of Orthopaedic Research*, 13-3:309–316, 1995.

[164] **Martin, R. B.** Is all cortical bone remodeling initiated by microdamage? *Bone*, 30(1): 8–13, Jan 2002.

[165] **Martin, R. B., Burr, D., and Sharkey, N.** *Skeletal Tissue Mechanics*. Springer, New York., 1998.

[166] **Masella, R. S. and Meister, M.** Current concepts in the biology of orthodontic tooth movement. *American Journal of Orthodontics and Dentofacial Orthopedics*, 129(4): 458–468, 2006.

[167] **Matsuura, M., Eckstein, F., Lochmueller, E.-M., and Zysset, P. K.** The role of fabric in the quasi-static compressive mechanical properties of human trabecular bone from various anatomical locations. *Biomechanics and Modeling in Mechanobiology*, 7(1): 27–42, FEB 2008.

[168] **McMinn, R., Hutchings, R., and Pegington, J.** *A colour atlas of human anatomy*. Wolfe Medical Publications, 1977.

[169] **McNamara, L. M. and Prendergast, P. J.** Bone remodelling algorithms incorporating both strain and microdamage stimuli. *Journal of Biomechanics*, article in press: available online 18–10–2006, Aug 2006.

[170] **Melchels, F. P., Bertoldi, K., Gabbrielli, R., Velders, A. H., Feijen, J., and Grijpma, D. W.** Mathematically defined tissue engineering scaffold architectures prepared by stereolithography. *Biomaterials*, 31(27):6909–6916, 2010.

[171] **Melsen, B.** Tissue reaction to orthodontic tooth movement-a new paradigm. *European Journal of Orthodontics*, 23(6):671–681, 2001.

[172] **Mengoni, M. and Ponthot, J.-P.** Isotropic continuum damage/repair model for alveolar bone remodeling. *Journal of Computational and Applied Mathematics*, 234(7): 2036–2045, 2010.

[173] **Mengoni, M., Voide, R., Toye, D., Léonard., A., van Lenthe, G. H., and Ponthot, J.-P.** A non-linear homogeneous model for bone-like materials under compressive load. In P. Nithiarasu, R. Löhner, R. van Loon, I. Sazonov, and X. Xie, editors, "Conference Proceedings-2nd International Conference on Computational & Mathematical Biomedical Engineering," pages 355–358, Swansea, UK., March 2011. Alexandria, VA, US: All American Printing inc. First Edition.

[174] **Mengoni, M., Voide, R., de Bien, C., Freichels, H., Jérôme, C., Léonard, A., Toye, D., van Lenthe, G. H., Müller, R., and Ponthot, J.-P.** A non-linear homogeneous model for bone-like materials under compressive load. *International Journal for Numerical Methods in Biomedical Engineering*, 28(2):334–348, 2012.

[175] **Menicucci, G., Mossolov, A., Mozzati, M., Lorenzetti, M., and Preti, G.** Tooth-implant connection: some biomechanical aspects based on finite element analyses. *Clinical Oral Implants Research*, 13(3):334–341, Jun 2002.

[176] **Menzel, A., Ekh, M., Steinmann, P., and Runesson, K.** Anisotropic damage coupled to plasticity: Modelling based on the effective configuration concept. *International Journal for Numerical Methods in Engineering*, 54:1409–1430, 2002.

[177] **Metafor**. *A finite strain finite element code*. LTAS-MN2L - University of Liège, `http://metafor.ltas.ulg.ac.be/`, 2011.

[178] **Meyer, B. N., Chen, J., and Katona, T. R.** Does the center of resistance depend on the direction of tooth movement? *American Journal of Orthodontics and Dentofacial Orthopedics*, 137(3):354–361, 2010.

[179] **Middleton, J., Jones, M. L., and Wilson, A. N.** Three-dimensional analysis of orthodontic tooth movement. *Journal of Biomechanical Engineering*, 12(4):319–327, Jul 1990.

[180] **Milan, J.-L., Planell, J. A., and Lacroix, D.** Computational modelling of the mechanical environment of osteogenesis within a polylactic acid-calcium phosphate glass scaffold. *Biomaterials*, 30(25):4219–4226, 2009.

[181] **Milne, T., Ichim, I., Patel, B., McNaughton, A., and Meikle, M.** Induction of osteopenia during experimental tooth movement in the rat: alveolar bone remodelling and the mechanostat theory. *The European Journal of Orthodontics*, 31(3):221–231, 2009.

[182] **Müller, R. and Rüegsegger, P.** Three-dimensional finite element modelling of non-invasively assessed trabecular bone structures. *Medical Engineering & Physics*, 17(2): 126–133, 1995.

[183] **Natali, A. N.**, editor. *Dental Biomechanics*. Taylor and Francis, 2003.

[184] **Natali, A. N., Pavan, P. G., Carniel, E. L., and Dorow, C.** A transversally isotropic elasto-damage constitutive model for the periodontal ligament. *Computer Methods in Biomechanics & Biomedical Engineering*, 6(5-6):pp. 329–336, 2003.

[185] **Natali, A. N., Carniel, E. L., Pavan, P. G., Bourauel, C., Ziegler, A., and Keilig, L.** Experimental-numerical analysis of minipig's multi-rooted teeth. *Journal of Biomechanics*, 40(8):1701–1708, 2007.

[186] **Natali, A. N., Pavan, P. G., and Scarpa, C.** Numerical analysis of tooth mobility: formulation of a non-linear constitutive law for the periodontal ligament. *Dental Materials*, 20(7):623–629, September 2004.

[187] **Nazarian, A. and Müller, R.** Time-lapsed microstructural imaging of bone failure behavior. *Journal of Biomechanics*, 37(1):55–65, 2004.

[188] **Negus, C. and Impelluso, T.** Continuum remodeling revisited. *Biomechanics and Modeling in Mechanobiology*, 6(4):211–226, 2007.

[189] **Nickel, J., Spilker, R., Iwasaki, L., Gonzalez, Y., McCall, W., Ohrbach, R., Beatty, M., and Marx, D.** Static and dynamic mechanics of the temporomandibular joint: plowing forces, joint load and tissue stress. *Orthodontics & craniofacial research*, 12(3):159–167, 2009.

[190] **Nickel, J. C., Yao, P., Spalding, P. M., and Iwasaki, L. R.** Validated numerical modeling of the effects of combined orthodontic and orthognathic surgical treatment on TMJ loads and muscle forces. *American Journal of Orthodontics and Dentofacial Orthopedics*, 121(1):73–83, 2002.

[191] **Nicosia, M.** A planar finite element model of bolus containment in the oral cavity. *Computers in Biology and Medicine*, 37(10):1472–1478, 2007.

[192] **Niebur, G. L., Yuen, J. C., Hsia, A. C., and Keaveny, T. M.** Convergence behavior of high-resolution finite element models of trabecular bone. *Journal of Biomechanical Engineering*, 121:629, 1999.

[193] **Niebur, G. L., Feldstein, M. J., Yuen, J. C., Chen, T. J., and Keaveny, T. M.** High-resolution finite element models with tissue strength asymmetry accurately predict failure of trabecular bone. *Journal of Biomechanics*, 33(12):1575–1583, 2000.

[194] **Oates, T. and Cochran, D.** Dental applications of bone biology. *Engineering of functional skeletal tissues*, pages 129–140, 2007.

[195] **Odgaard, A., Kabel, J., van Rietbergen, B., Dalstra, M., and Huiskes, R.** Fabric and elastic principal directions of cancellous bone are closely related. *Journal of Biomechanics*, 30(5):487–495, 1997.

[196] **Pahr, D. H. and Zysset, P. K.** A comparison of enhanced continuum FE with micro FE models of human vertebral bodies. *Journal of Biomechanics*, 42(4):455–462, 2009.

[197] **Panagiotopoulou, O., Kupczik, K., and Cobb, S.** The mechanical function of the periodontal ligament in the macaque mandible: a validation and sensitivity study using finite element analysis. *Journal of Anatomy*, 2010.

[198] **Parfitt, G.** Measurement of the physiological mobility of individual teeth in an axial direction. *Journal of Dental Research*, 39(3):608–615, 1960.

[199] **Pashley, D. H., Agee, K. A., Wataha, J. C., Rueggeberg, F., Ceballos, L., Itou, K., Yoshiyama, M., Carvalho, R. M., and Tay, F. R.** Viscoelastic properties of demineralized dentin matrix. *Dental Materials*, 19(8):700–706, December 2003.

[200] **Pattin, C. A., Caler, W. E., and Carter, D. R.** Cyclic mechanical property degradation during fatigue loading of cortical bone. *Journal of Biomechanics*, 29(1):69–79, January 1996.

[201] **Peck, C., Langenbach, G., and Hannam, A.** Dynamic simulation of muscle and articular properties during human jaw opening. *Archives of Oral Biology*, 45:pp. 963–982, 2000.

[202] **Pietrzak, G., Curnier, A., Botsis, J., Scherrer, S., Wiskott, A., and Belser, U.** A nonlinear elastic model of the periodontal ligament and its numerical calibration for the study of tooth mobility. *Computer Methods in Biomechanics & Biomedical Engineering*, 5(2):91–100, 2002.

[203] **Pilon, J., Kuijpers-Jagtman, A., and Maltha, J.** Magnitude of orthodontic forces and rate of bodily tooth movement. An experimental study. *American Journal of Orthodontics and Dentofacial Orthopedics*, 110(1):16–23, 1996.

[204] **Pini, M., Wiskott, H. W. A., Scherrer, S. S., Botsis, J., and Belser, U. C.** Mechanical characterization of bovine periodontal ligament. *Journal of Periodontal Research*, 37 (4):237–244, Aug 2002.

[205] **Pini, M., Zysset, P. K., Botsis, J., and Contro, R.** Tensile and compressive behaviour of the bovine periodontal ligament. *Journal of Biomechanics*, 37(1):111–119, Jan 2004.

[206] **Pistoia, W., van Rietbergen, B., Lochmüller, E. M., Lill, C. A., Eckstein, F., and Rüegsegger, P.** Estimation of distal radius failure load with micro-finite element analysis models based on three-dimensional peripheral quantitative computed tomography images. *Bone*, 30(6):842–848, 2002.

[207] **Poiate, I. A., Vasconcellos, A. B., Andueza, A., Pola, I. R., and Poiate, E. J.** Three dimensional finite element analyses of oral structures by computerized tomography. *Journal of Bioscience and Bioengineering*, 106(6):606–609, 2008.

[208] **Poiate, I. A., Vasconcellos, A. B., Santana, R., and Poiate, E. J.** Three-dimensional stress distribution in the human periodontal ligament in masticatory, parafunctional, and trauma loads: Finite element analysis. *Journal of Periodontology*, 80(11):1859–1867, 2009.

[209] **Ponthot, J.-P.** *Traitement unifié de la Mécanique des Milieux Continus solides en grandes transformations par la méthode des éléments finis*. PhD thesis (in French), University of Liège (Belgium), School of Engineering, LTAS/MC&T, 1995.

[210] **Ponthot, J.-P.** Unified stress update algorithms for the numerical simulation of large deformation elasto-plastic and elasto-viscoplastic processes. *International Journal of Plasticity*, 18(1):91–126, 2002.

[211] **Poppe, M., Bourauel, C., and Jäger, A.** Determination of the elasticity parameters of the human periodontal ligament and the location of the center of resistance of single-rooted teeth a study of autopsy specimens and their conversion into finite element models. *Journal of Orofacial Orthopedics*, 63(5):358–370, Sep 2002.

[212] **Pothuaud, L., van Rietbergen, B., Mosekilde, L., Beuf, O., Levitz, P., Benhamou, C. L., and Majumdar, S.** Combination of topological parameters and bone volume fraction better predicts the mechanical properties of trabecular bone. *Journal of Biomechanics*, 35(8):1091–1099, 2002.

[213] **Prendergast, P., Huiskes, R., and Søballe, K.** Biophysical stimuli on cells during tissue differentiation at implant interfaces. *Journal of Biomechanics*, 30(6):539–548, 1997.

[214] **Provatidis, C. G.** A comparative FEM-study of tooth mobility using isotropic and anisotropic models of the periodontal ligament. Finite Element Method. *Medical Engineering & Physics*, 22(5):359–370, 2000.

[215] **Provatidis, C. G.** Parametric finite element analysis and closed-form solutions in orthodontics. *Computer Methods in Biomechanics & Biomedical Engineering*, 5(2):101–112, Apr 2002.

[216] **Provatidis, C. G.** A bone-remodelling scheme based on principal strains applied to a tooth during translation. *Computer Methods in Biomechanics & Biomedical Engineering*, 6(5-6):347–352, 2003.

[217] **Qian, H., Chen, J., and Katona, T. R.** The influence of PDL principal fibers in a 3-dimensional analysis of orthodontic tooth movement. *American Journal of Orthodontics and Dentofacial Orthopedics*, 120(3):272–279, Sep 2001.

[218] **Qian, L., Todo, M., Morita, Y., Matsushita, Y., and Koyano, K.** Deformation analysis of the periodontium considering the viscoelasticity of the periodontal ligament. *Dental Materials*, 25(10):1285–1292, 2009.

[219] **Qian, Y., Fan, Y., Liu, Z., and Zhang, M.** Numerical simulation of tooth movement in a therapy period. *Clinical Biomechanics*, 23(Supplement 1):S48–S52, 2008. Research and Development on Biomechanics in China.

[220] **Rahmoun, J., Chaari, F., Markiewicz, E., and Drazetic, P.** Micromechanical modeling of the anisotropy of elastic biological composites. *Multiscale Modeling & Simulation*, 8:326, 2009.

[221] **Ramtani, S. and Zidi, M.** Damaged-bone remodeling theory : thermodynamical approach. *Mechanics Research Communications*, 26(6):pp. 701–708, 1999.

[222] **Ramtani, S. and Zidi, M.** A theoretical model of the effect of continuum damage on a bone adaptation model. *Journal of Biomechanics*, 34:pp. 471–479, 2001.

[223] **Redlich, M., Rahamim, E., Gaft, A., and Shoshan, S.** The response of supraalveolar gingival collagen to orthodontic rotation movement in dogs. *American Journal of Orthodontics and Dentofacial Orthopedics*, 110(3):247–255, September 1996.

[224] **Rees, J. S. and Jacobsen, P. H.** Elastic modulus of the periodontal ligament. *Biomaterials*, 18(14):995–999, Jul 1997.

[225] **Reimann, S., Keilig, L., Jäger, A., Brosh, T., Shpinko, Y., Vardimon, A., and Bourauel, C.** Numerical and clinical study of the biomechanical behaviour of teeth under orthodontic loading using a headgear appliance. *Medical engineering & physics*, 31(5): 539–546, 2009.

[226] **Rex, T., Kharbanda, O. P., Petocz, P., and Darendeliler, M. A.** Physical properties of root cementum: Part 6. A comparative quantitative analysis of the mineral composition of human premolar cementum after the application of orthodontic forces. *American Journal of Orthodontics and Dentofacial Orthopedics*, 129(3):358–367, March 2006.

[227] **Roberts, W. E.** Bone physiology of tooth movement, ankylosis, and osseointegration. *Seminars in Orthodontics*, 6(3):173–182, 2000.

[228] **Roberts, W. E., Huja, S., and Roberts, J. A.** Bone modeling: biomechanics, molecular mechanisms, and clinical perspectives. *Seminars in Orthodontics*, 10(2):123–161, 2004.

[229] **Ruimerman, R.** *Modeling and remodeling in bone tissue.* PhD thesis, Technische Universiteit Eindhoven, The Netherlands, 2005.

[230] **Ruse, N.** Propagation of erroneous data for the modulus of elasticity of periodontal ligament and gutta percha in FEM/FEA papers: a story of broken links. *Dental Materials*, 24(12):1717–1719, 2008.

[231] **Sajewicz, E.** On evaluation of wear resistance of tooth enamel and dental materials. *Wear*, 260(11-12):1256–1261, June 2006.

[232] **Sanctuary, C.** *Experimental investigation of the mechanical behaviour and structure of the bovine periodontal ligament.* PhD thesis (in French), Faculté Sciences et Techniques de l'Ingénieur-Ecole Polytechnique Fédérale de Lausanne (Switzerland), 2003.

[233] **Schneider, J., Geiger, M., and Sander, F.-G.** Numerical experiments on long-time orthodontic tooth movement. *American Journal of Orthodontics and Dentofacial Orthopedics*, 121(3):257–265, 2002.

[234] **Schulte, F., Lambers, F., Webster, D., Kuhn, G., and Müller, R.** In vivo validation of a computational bone adaptation model using open-loop control and time-lapsed micro-computed tomography. *Bone*, 2011.

[235] **Si, H.** *Tetgen, a quality tetrahedral mesh generator and three-dimensional Delaunay triangulator.* http://tetgen.berlios.de, 2006.

[236] **Simo., J. and Ju, J.** Strain- and stress-based continuum damage models. I formulation. *International Journal of Solids Structures*, 23:821–840, 1987.

[237] **Simoes, J., Vaz, M., Blatcher, S., and Taylor, M.** Influence of head constraint and muscle forces on the strain distribution within the intact femur. *Medical engineering & physics*, 22(7):453–459, 2000.

[238] **Skedros, J. G. and Baucom, S. L.** Mathematical analysis of trabecular 'trajectories' in apparent trajectorial structures: The unfortunate historical emphasis on the human proximal femur. *Journal of Theoretical Biology*, 244(1):15–45, 2007.

[239] **Slomka, N., Vardimon, A., Gefen, A., Pilo, R., Bourauel, C., and Brosh, T.** Time-related PDL: viscoelastic response during initial orthodontic tooth movement of a tooth with functioning interproximal contact-a mathematical model. *Journal of Biomechanics*, 41(9):1871–1877, 2008.

[240] **Smith, R. and Burstone, C.** Mechanics of tooth movement. *American Journal of Orthodontics and Dentofacial Orthopedics*, 85(4):pp. 294–307, 1984.

[241] **Soncini, M. and Pietrabissa, R.** Quantitative approach for the prediction of tooth movement during orthodontic treatment. *Computer Methods in Biomechanics & Biomedical Engineering*, 5(5):361–368, Oct 2002.

[242] **Song, G.-Q.** Three dimensional finite element stress analysis of post-core restored endodontically treated teeth. Master's thesis, Universtity of Manitoba (Canada), 2005.

[243] **Stauber, M. and Müller, R.** Volumetric spatial decomposition of trabecular bone into rods and plates-a new method for local bone morphometry. *Bone*, 38(4):475–484, 2006.

[244] **Stölken, J. and Kinney, J.** On the importance of geometric nonlinearity in finite-element simulations of trabecular bone failure. *Bone*, 33(4):494–504, 2003.

[245] **Tabor, Z.** On the equivalence of two methods of determining fabric tensor. *Medical Engineering & Physics*, 31(4):1313–1322, 2009.

[246] **Tanne, K., Matsubara, S., and Sakuda, M.** Stress distributions in the maxillary complex from orthopedic headgear forces. *Angle Orthodontist*, 63(2):111–118, 1993.

[247] **Tanne, K., Inoue, Y., and Sakuda, M.** Biomechanical behavior of the periodontium before and after orthodontic tooth movement. *Angle Orthodontist*, 65(2):pp. 123–128, 1995.

[248] **Tanne, K., Yoshida, S., Kawata, T., Sasaki, A., Knox, J., and Jones, M. L.** An evaluation of the biomechanical response of the tooth and periodontium to orthodontic forces in adolescent and adult subjects. *British Journal of Orthodontics*, 25(2):109–115, May 1998.

[249] **Taylor, D.** Fatigue damage in bone: links to adaptation. In P. Pedersen and M. Bendsøe, editors, "Solid Mechanics and Its Applications," volume 69 - IUTAM Symposium on Synthesis in Bio Solid Mechanics, pages 175–186. Kluwer academic publishers, 2002.

[250] **Toms, S. R. and Eberhardt, A. W.** A nonlinear finite element analysis of the periodontal ligament under orthodontic tooth loading. *American Journal of Orthodontics and Dentofacial Orthopedics*, 123(6):657–665, 2003.

[251] **Toms, S. R., Lemons, J. E., Bartolucci, A. A., and Eberhardt, A. W.** Nonlinear stress-strain behavior of periodontal ligament under orthodontic loading. *American Journal of Orthodontics and Dentofacial Orthopedics*, 122(2):174–179, August 2002.

[252] **Tsubota, K.-I., Suzuki, Y., Yamada, T., Hojo, M., Makinouchi, A., and Adachi, T.** Computer simulation of trabecular remodeling in human proximal femur using large-scale voxel FE models: Approach to understanding Wolff's law. *Journal of Biomechanics*, 42 (8):1088–1094, 2009.

[253] **Ulrich, D., van Rietbergen, B., Weinans, H., and Rüegsegger, P.** Finite element analysis of trabecular bone structure: a comparison of image-based meshing techniques. *Journal of Biomechanics*, 31(12):1187–1192, 1998.

[254] **vakhum**. *Virtual Animation of the Kinematics of the Human for Industrial, Educational and Research Purposes*. European Project (# IST-1999-10954), www.ulb.ac.be/project/vakhum/ , 2009.

[255] **van Driel, W. D., van Leeuwen, E. J., den Hoff, J. W. V., Maltha, J. C., and Kuijpers-Jagtman, A. M.** Time-dependent mechanical behaviour of the periodontal ligament. *Proceedings of the Institution of Mechanical Engineers - Part H - Journal of Engineering in Medicine*, 214(5):497–504, 2000.

[256] **van Leeuwen, E., Maltha, J., and Kuijpers-Jagtman, A.** Tooth movement with light continuous and discontinuous forces in beagle dogs. *Eur. J. Oral Sci.*, 107(6):468–74, 1999.

[257] **van Lenthe, G. H. and Huiskes, R.** Can the mechanical trabecular bone quality be estimated reliably from mean intercept length or other morphological parameters? In P. Pedersen and M. Bendsøe, editors, "Solid Mechanics and Its Applications," volume 69 - IUTAM Symposium on Synthesis in Bio Solid Mechanics, pages 349–360. Kluwer academic publishers, 2002.

[258] **van Lenthe, G. H., Stauber, M., and Müller, R.** Specimen-specific beam models for fast and accurate prediction of human trabecular bone mechanical properties. *Bone*, 39(6):1182–1189, 2006.

[259] **van Rietbergen, B. and Huiskes, R.** *Bone Mechanics Handbook (Ed. Cowin S.C.)*, chapter 15 - Elastic Constants of Cancellous Bone., pages 15.1–15.24. CRC press USA, 2001.

[260] **van Rietbergen, B., Weinans, H., Huiskes, R., and Odgaard, A.** A new method to determine trabecular bone elastic properties and loading using micromechanical finite-element models. *Journal of Biomechanics*, 28(1):69–81, 1995.

[261] **van Rietbergen, B., Weinans., H., Huiskes, R., and Polman, B.** Computational strategies for iterative solutions of large fem applications employing voxel data. *International journal for numerical methods in engineering*, 39(16):2743–2767, 1996.

[262] **van Schepdael, A.** *Biomechanical and mechanobiological modelling of orthodontic tooth movement*. Phd thesis, KU Leuven (Belgium), Faculty of Engineering, Department of Mechanical Engineering, 2011.

[263] **Vanderoost, J., Jaecques, S., Van der Perre, G., Boonen, S., D'hooge, J., Lauriks, W., and Lenthe, G. H.** Fast and accurate specimen-specific simulation of trabecular bone elastic modulus using novel beam-shell finite element models. *Journal of Biomechanics*, 2011.

[264] **Vanheudsen, A.** *Anatomie de l'appareil masticateur, cours de 2eme bachelier sciences dentaires*. University of Liège, 2008.

[265] **Varga, P. and Zysset, P. K.** Sampling sphere orientation distribution: An efficient method to quantify trabecular bone fabric on grayscale images. *Medical Image Analysis*, 13(3):530–541, 2009.

[266] **Verhulp, E., van Rietbergen, B., and Huiskes, R.** Load distribution in the healthy and osteoporotic human proximal femur during a fall to the side. *Bone*, 42(1):30–35, 2008.

[267] **Verhulp, E., van Rietbergen, B., Müller, R., and Huiskes, R.** Micro-finite element simulation of trabecular-bone post-yield behaviour–effects of material model, element size and type. *Computer Methods in Biomechanics and Biomedical Engineering*, 11(4): 389–395, 2008.

[268] **Verna, C., Dalstra, M., Lee, T. C., Cattaneo, P. M., and Melsen, B.** Microcracks in the alveolar bone following orthodontic tooth movement: a morphological and morphometric study. *European Journal of Orthodontics*, 26(5):459–467, 2004.

[269] **Vollmer, D., Bourauel, C., Maier, K., and Jäger, A.** Determination of the centre of resistance in an upper human canine and idealized tooth model. *European Journal of Orthodontics*, 21(6):633–648, Dec 1999.

[270] **Von Böhl, M., Maltha, J., and Von den Hoff, H.** Changes in the periodontal ligament after experimental tooth movement using high and low continuous forces in beagle dogs. *Angle Orthodontist*, 74(1):16–25, 2004.

[271] **Voyiadjis, G. Z. and Kattan, P. I.** *Advances in Damage Mechanics: metals and metal matrix composites with an introduction to fabric tensors.* Elsevier Science Ltd, second edition, 2006.

[272] **Wakabayashi, N., Ona, M., Suzuki, T., and Igarashi, Y.** Nonlinear finite element analyses: Advances and challenges in dental applications. *Journal of Dentistry*, 36(7):463–471, 2008.

[273] **Weinans, H., Huiskes, R., and Grootenboer, H.** The behavior of adaptive bone-remodeling simulation models. *Journal of Biomechanics*, 25(12):1425–1441, 1992.

[274] **Weinstein, A., Klawitter, J., and Cook, S.** Implant-bone interface characteristics of bioglass dental implants. *Journal of Biomedical Materials Research*, 14(1):23–29, 1980.

[275] **Williams, M. O. and Murphy, N. C.** Beyond the ligament: A whole-bone periodontal view of dentofacial orthopedics and falsification of universal alveolar immutability. *Seminars in Orthodontics*, 14(4):246–259, 2008. Emerging Concepts in Orthodontic Periodontal Interactions for the 21st Century.

[276] **Wise, G. E. and King, G. J.** Mechanisms of tooth eruption and orthodontic tooth movement. *Journal of Dental Research*, 87(5):414–434, MAY 2008.

[277] **Wriggers, P.** *Computational contact mechanics.* Springer, Berlin, 2006.

[278] **Wriggers, P.** *Nonlinear finite element methods.* Springer Verlag, 2008.

[279] **Wu, T., Liao, W., Dai, N., and Tang, C.** Design of a custom angled abutment for dental implants using computer-aided design and nonlinear finite element analysis. *Journal of Biomechanics*, 43(10):1941–1946, 2010.

[280] **Yoshida, N., Koga, Y., Peng, C.-L., Tanaka, E., and Kobayashi, K.** In vivo measurement of the elastic modulus of the human periodontal ligament. *Medical Engineering & Physics*, 23:pp. 567–572, 2001.

[281] **Yousefian, J., Firouzian, F., Shanfeld, J., Ngan, P., Lanese, R., and Davidovitch, Z.** A new experimental model for studying the response of periodontal ligament cells to hydrostatic pressure. *American Journal of Orthodontics and Dentofacial Orthopedics*, 108(4):402–409, October 1995.

[282] **Zhao, Z., Fan, Y., Bai, D., Wang, J., and Li, Y.** The adaptive response of periodontal ligament to orthodontic force loading-a combined biomechanical and biological study. *Clinical Biomechanics*, 23(Supplement 1):S59–S66, 2008. Research and Development on Biomechanics in China.

[283] **Zheng, J. and Zhou, Z.** Friction and wear behavior of human teeth under various wear conditions. *Tribology International*, 40(2):278–284, February 2007.

[284] **Zidi, M.** Contribution à la modélisation du remodelage de l'os trabéculaire. *Comptes Rendus de l'Académie des Sciences de Paris- Series IIb - Mechanics-Physics-Chemistry-Astronomy*, 326(2):pp. 121–128, 1998.

[285] **Ziegler, A., Keilig, L., Kawarizadeh, A., Jäger, A., and Bourauel, C.** Numerical simulation of the biomechanical behaviour of multi-rooted teeth. *European Journal of Orthodontics*, 27(4):333–339, Aug 2005.

[286] **Zysset, P. K. and Rincón, L.** *Mechanics of Biological Tissues*, chapter IV.10 - An alternative fabric-based yield and failure criterion for trabecular bone, pages 457–470. Springer, 2006.

[287] **Zysset, P. K.** A review of morphology-elasticity relationships in human trabecular bone: theories and experiments. *Journal of Biomechanics*, 36(10):1469–1485, 2003. Bone Cell and Tissue Mechanics.

[288] **Zysset, P. and Curnier, A.** An alternative model for anisotropic elasticity based on fabric tensors. *Mechanics of Materials*, 21(4):243–250, NOV 1995.